

Proceedings ICSBM 2019 Volume 2 - New cementitious binders

Citation for published version (APA):

Caprai, V., & Brouwers, J. (Eds.) (2019). *Proceedings ICSBM 2019 Volume 2 - New cementitious binders*. Technische Universiteit Eindhoven.

Document status and date:

Published: 01/11/2019

Document Version:

Publisher's PDF, also known as Version of Record (includes final page, issue and volume numbers)

Please check the document version of this publication:

- A submitted manuscript is the version of the article upon submission and before peer-review. There can be important differences between the submitted version and the official published version of record. People interested in the research are advised to contact the author for the final version of the publication, or visit the DOI to the publisher's website.
- The final author version and the galley proof are versions of the publication after peer review.
- The final published version features the final layout of the paper including the volume, issue and page numbers.

[Link to publication](#)

General rights

Copyright and moral rights for the publications made accessible in the public portal are retained by the authors and/or other copyright owners and it is a condition of accessing publications that users recognise and abide by the legal requirements associated with these rights.

- Users may download and print one copy of any publication from the public portal for the purpose of private study or research.
- You may not further distribute the material or use it for any profit-making activity or commercial gain
- You may freely distribute the URL identifying the publication in the public portal.

If the publication is distributed under the terms of Article 25fa of the Dutch Copyright Act, indicated by the "Taverne" license above, please follow below link for the End User Agreement:

www.tue.nl/taverne

Take down policy

If you believe that this document breaches copyright please contact us at:

openaccess@tue.nl

providing details and we will investigate your claim.



Organized by
Eindhoven University
of Technology

TU/e

In cooperation with
Wuhan University
of Technology

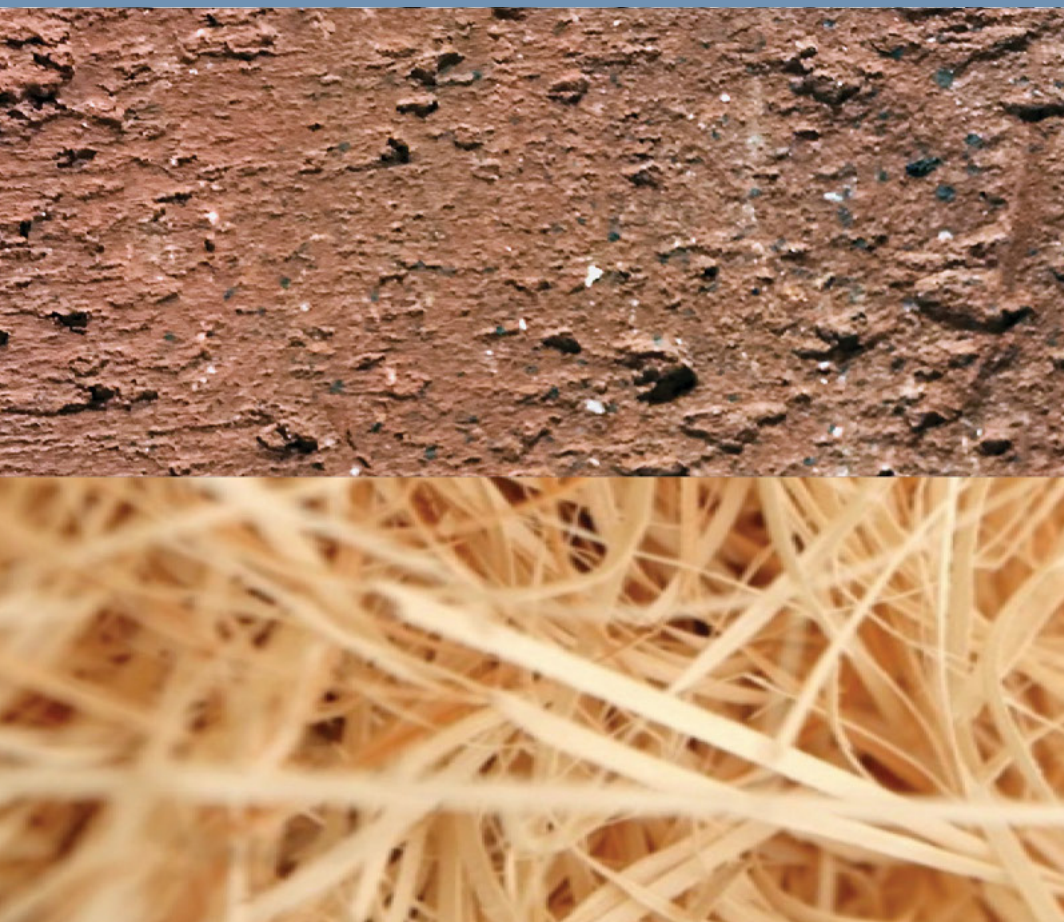


PROCEEDINGS ICSBM 2019

VOLUME 2 - New cementitious binders

2nd International Conference on Sustainable Building Materials

August 12-15, 2019 - Eindhoven, The Netherlands
Editors: V. Caprai and H.J.H. Brouwers



and supported by



ICSBM 2019, Conference proceedings

A catalogue record is available from the Eindhoven University of Technology Library

ISBN of the volumes set: 978-90-386-4898-9

ISBN of Volume 2: 978-90-386-4911-5

Sponsored by: CRH, Eltomation - Wood cement board plant, Tata Steel Europe (Gold sponsors), VDZ, PCA (Bronze Sponsors).

Front page image: V. Caprai

Editors: V. Caprai and H.J.H. Brouwers

Organizing committee:

Conference Chairman: Prof. H.J.H. (Jos) Brouwers, Eindhoven

Conference Co-Chairman: Prof. Wen Chen, Wuhan

Conference Secretary: Mrs V. (Veronica) Caprai and Dr. M.V.A. (Miruna) Florea, Eindhoven

Dr. Qiu Li, Wuhan

Dr. Bo Yuan, Wuhan

Dr. Q. Yu, Eindhoven

Dr. F. Gauvin, Eindhoven

Dr. K. Schollbach, Eindhoven

Mr. Y. Chen, Eindhoven

Mrs. L.T.J. Harmsen, Eindhoven

Mrs. N.L. Rombley, Eindhoven

Table of Contents

Performance of SCMs – Chemical and Physical Principles

H. Justnes 8

Specification of building materials for in service durability

C. Gehlen, C. Thiel..... 31

Design of reinforced concrete slabs with consideration of the construction joints

V. Kurochkina, I. Yakovleva, A. Deineko, A. Starostin 42

Eco-efficiency in cement use analysed by the concept of distance among particles in concrete phases

M. F. L. Menezes, R.G. Pileggi, M. Rebmann, C. Massucato..... 57

HYDCEM: A new cement hydration model

N. Holmes, D. Kelliher and M. Tyrer 66

Chloride Ingress and Degradation of Portland Cement Mortar Exposed to Seawater Attack Coupling with Drying-wetting Cycle

S. Cheng, Z. Shui, T. Sun, X. Gao..... 75

Locally available material (manufactured sands) impacts on properties for an Ultra-High Performance Concrete (UHPC)

R. Yang, R. Yu, Z. Shui, C. Guo, S. Wu, X. Gao 88

Application of Krstulovic-Dabic model on early hydration analysis of Portland cement under Mg²⁺ influence

X.S. Li, Z.H. Shui, X. Gao 101

Recent Sustainable Development of Ultra-High Performance Concrete (UHPC)

R. Yu, Z. Liu, X. Wang, Q. Song, Z. Shui, C. Hao 110

Influence of External Water Introducing by Coral Sand on Autogenous Shrinkage and Microstructure of Ultra-High Performance Concrete (UHPC)

K. Liu, Z. Shui, R. Yu, S. Yi 119

Neutron radiography to study water ingress via the interlayer of 3D printed cementitious materials

J. Van Der Putten, M. Azima, P. Van den Heede, T. Van Mullem, G. De Schutter and K. Van Tittelboom 130

Influence of heat treatment and mechanical activation on reactivity of natural pozzolan for geopolymer synthesis

R. Firdous, D. Stephan 138

Effect of calcium hydroxide on the hydration of sulphoaluminate cement with high concentration of borate solution	
Q. Li, H. Ma, X. Ling, B. Yuan, W. Chen.....	156
The effect of MgO on the structure and chemical composition of C-S-H gels	
Y. Tang, W. Chen.....	167
Impact of steel fibre content on the fibre network structure of ultra-high performance fibre reinforced concrete (UHPFRC)	
Q. Song, Z. Shui, R. Yu, S. Rao	176
Investigation of the zonation of thermally treated ultra high performance concrete	
M. Voigt, J. von Werder, B. Meng.....	185
Role of Mg²⁺ stabilized amorphous calcium carbonate on the early reaction of sodium carbonate activated slag	
B. Yuan, Q.L. Yu, W. Chen, H.J.H. Brouwers.....	194
Pozzolanic reactivity of size-classified siliceous fly ashes	
R. Snellings, H. Kamyab, S. Joseph, P. Nielsen, M. Loots, L. Van den Abeele	199
Evaluation of calcined dredged sediments as supplementary cementitious materials	
H. Kazemi-Kamyab, L. Van den Abeele, M. Henry, L. Haouche, R. Snellings	214
The Effects of Epoxy Resin as Partial Cement Replacement on the Mechanical Properties of Concrete	
G.A. Jokhio, Y. Gul, A. Abu-Tair, G. S. Wei.....	224
Polycarboxylate Superplasticizer Modified Fly Ash: Its Effects on Fluidity and Mechanical Properties of Cement Paste	
P. Liu, M. Qu, F. Wang, G. Hu, L. Yang, W. Zhang	232
Understanding Hydrogen Bonding in Calcium Silicate Hydrates	
B. Li ¹ , H.J.H. Brouwers, Q. Yu, W. Chen.....	233
Concrete with High-purity Volcanic Glass Powder Manufactured from Pyroclastic Deposit through Dry Gravity Classification and Pulverization	
T. Noguchi, A. Tomoyose, K. Sodeyama and K. Higashi	244
Manufacturing high-performance supplementary cementitious materials from pyroclastic deposit through dry gravity classification and pulverization	
A. Tomoyose, T. Noguchi, K. Sodeyama, K. Higashi.....	256
Early hydration of C₂S doped with combination of S and Li	
M. Boháč, T. Staněk, A. Rybová, A. Zezulová, F. Bellmann, H.-M. Ludwig.....	269
Safe Use of Sustainable Building Materials: A reappraisal of Adobe	
T. Li Piani, J. Weerheijm, L. Koene and L. J. Sluys	278

Microstructural changes in porosity due to carbonation of fly ash blended pastes assessed by dynamic vapour sorption	
Y. Villagrán-Zaccardi, N. Alderete, N. De Belie.....	297
Isothermal Calorimetric Study on Heat Evolution and of Apparent Activation Energy of Alkali-activated Slag/Fly ash Pastes	
S. Zhang, Y. Zuo, Z. Li, G. Ye	304
Uncovering strength developing regularities of ultra-high performance concrete cured under high temperature	
Z. Liu, Z. Shui, R. Yu, Q. Song.....	312
Depth of penetration for steel-tube-confined concrete targets penetrated by rigid sharp-nosed projectiles	
Q. Tan, D. Song, Z. Jiang.....	320
Ballistic performances of multi-layered Ultra-high Performance Fibre Reinforced Concrete	
Y.Y.Y. Cao, M. Sluijsmans, Q.L. Yu , H.J.H. Brouwers	337
Effect of MgO, nitrate intercalated LDH and Calcined-LDH on chloride resistance of alkali-activated fly ash /slag mortar	
T. Liu, Y. Chen, Q.L.Yu, H.J.H. Brouwers	344
Recent development on sustainable ultra-high performance concrete design with low cement consumption: a review	
P.P. Li, Q.L. Yu, H.J.H. Brouwers	353
Suitability of phenolphthalein indicator method for alkali activated concrete	
O.O. Ojedokun, P.S. Mangat	363
Activation of binary binder containing fly ash and cement with red mud as alkali source and application in controlled low strength materials	
B. Yuan, S. Yuan, C. Straub, W. Chen	373

Volume 2

New cementitious binders

Performance of SCMs

– Chemical and Physical Principles

H. Justnes

SINTEF Building and Infrastructure, Trondheim, Norway. E-mail: harald.justnes@sintef.no

Abstract

The influence of supplementary cementing materials (SCMs) on the hydration and durability of blended cement has been evaluated using chemical and physical principles. Similarities and differences between various SCMs have been considered grouping them into latent hydraulic or pozzolanic with sub-division into siliceous, aluminous, carbonaceous etc. Synergy between SCMs producing calcium aluminate hydrate and calcium carbonate maximize water binding leading to reduced porosity and increased strength by forming calcium monocarboaluminate hydrate. Any magnesium content in the carbonate leads to hydrotalcite formation in the presence of aluminates.

The interaction of SCMs with plasticizers and use of hydration accelerators are also treated.

The influence of SCMs on durability issues like chloride ingress, carbonation, alkali aggregate reactions, sulphate resistance and freeze-thaw resistance is discussed as well. Generally speaking SCMs improve the resistance of blended cements to most degradation mechanisms at equal w/c, except for carbonation resistance that can be improved by reducing w/c.

Keywords: Supplementary cementing material, hydration, durability, microstructure, porosity.

1. Introduction

1.1 Reason for extended use of SCMs

The cement industry world-wide is calculated to bring about 5-8% of the total global anthropogenic carbon dioxide (CO₂) emissions. The general estimate is about 1 tonne of CO₂ emission per tonne clinker produced, if fossil fuel is used and no measures are taken to reduce it. The 3rd rank after heating/cooling of buildings and transport is not because cement is such a bad material with respect to CO₂ emissions, but owing to the fact that it is so widely used to construct the infrastructure and buildings of modern society as we know it. Concrete is actually among the more environmentally friendly materials since it is composed in general of about 1 part cement, 0.5 parts water and 5-6 parts of sand and gravel (i.e. aggregate). The world's cement production was roughly 4 billion tonnes in 2013, meaning roughly 24 billion tonnes concrete or 1·10¹⁰ m³ concrete. This quantity can be translated into making a concrete cylinder of about ϕ 20 cm reaching the moon and back to earth every day or building a solid concrete block with 1 km² base reaching higher (10 000 m) than Mount Everest (8 848 m) in a year!

A lot is done by cement producers to reduce the global carbon footprint, in particular to replace coal with waste having a calorific value equivalent to (fossil) fuel and by making blended cement where parts of the clinker is replaced with supplementary cementing materials (SCMs). However, cement is a bulk product that should cover a wide range of applications and serve different customers, giving limitations on clinker

replacements.

Concrete, on the other hand, is the end product where the performance criteria are already specified and depending on application more can be done to increase its sustainability. As pointed out by Justnes [1] the shortest route to make cement and concrete more sustainable, is to replace clinker in cement or cement in concrete by supplementary cementing materials (SCMs). This paper discusses how SCMs affect cement and concrete principally in chemical and physical ways and what this means in terms of durability.

Classes of SCMs

One can divide SCMs into *latent hydraulic* and *pozzolanic*. Latent hydraulic SCMs are inorganic additives that only need an activator to react with water and form a cementitious binder. Examples are ground, granulated blast furnace slag (GGBS), synthetic calcium aluminate glasses and to some extent high calcium fly ash. Pozzolanic SCMs are mineral additives that form cementitious binders in reaction with calcium hydroxides. Pozzolanic SCMs can be sub-divided by their major oxides like silicas (e.g. silica fume, nano-silica, rice husk ash, hydrothermal silica and diatomaceous earth or kieselgur), aluminosilicates (e.g. siliceous fly ash, calcined clays like metakaolin, burnt shale and natural pozzolana of volcanic origin like trass, scoria etc) and alumina (e.g. nano-alumina). Lothenbach *et al* [2] have given an overview of the performance of the most common SCMs (i.e. silica fume, fly ash and GGBS) in blended cements, while Thomas [3] published a book on SCMs in concrete. Carbonates as SCM are in a class by itself since they need aluminate hydrates to react with and they were for a long time considered inert, or at best accelerating the cement setting acting as nucleation sites, since there were relatively little aluminate in cement clinker not tied up by sulphates to ettringite and thereby the carbonate reactivity was difficult to observe. However, the reactivity of calcium carbonate becomes first observable on a macro level in ternary systems with fly ash producing extra calcium aluminate hydrates in its pozzolanic reaction (De Weerd and Justnes [4]) and recently the strength increase of fly ash blended cement with dolomite versus limestone was found to be due to hydrotalcite formation also requiring aluminates (Zajac *et al* [5]).

1.1.1 Physical Principles

The physical principles include particle packing, pore refinement and connectivity of pores reducing the transport of aggressives into the concrete. The two latter points are actually indirectly chemical since they are a consequence of hydration and depend on how much liquid water is transferred into solid hydrates. The effect improves as a function of time.

1.1.2 Chemical Principles

The chemical principles involve the chemical nature of the hydration products and how they interact with aggressives forming new products.

2. Physical effects of SCMs

2.1 Initial particle packing

SCMs have often higher surface and consist of smaller particles than portland cement and also lower density. Hence, in the practical approach of just replacing cement with SCM by mass, there will be an increased volume of binder (cement + SCM + water) relative to the aggregate. The same goes for *adding* SCM to cement instead of *replacing* cement, which is common in many former studies, in particular for silica fume. In more scientific studies it is therefore recommended to use *volume replacement* of cement by SCM in order to sort out the physical and chemical effects of the SCM compared to cement.

If one considers a portland cement with average particle size $d_{50} \approx 20 \mu\text{m}$, it still has a particle size distribution

(psd) allowing smaller particles to pack in between the larger particles. For a particle with radius r to fit into a tetrahedral hole created by 4 spheres of $20\ \mu\text{m}$ diameter (radius $R = 10\ \mu\text{m}$); $r < (\sqrt{3}/2 - 1)R = 2.25\ \mu\text{m}$, and to fit in an octahedral hole of 6 spheres of diameter $20\ \mu\text{m}$; $r < (\sqrt{2}-1)R = 4.14\ \mu\text{m}$. An individual silica fume particle of $0.15\ \mu\text{m}$ can then even fit into a tetrahedral hole of cement particles as small as $1.33\ \mu\text{m}$ in diameter, while calcined clay particles with a typical diameter of $5\ \mu\text{m}$ only can pack in between coarser cement particles and compete with cement grains of similar size.

The simplest SCM example is silica fume (Justnes [6]) consisting of basically spherical individual particles with an average diameter of $0.15\ \mu\text{m}$, although usually occurring as aggregation of fused particles. As comparison, the irregular grains of a portland cement have typical average diameter of $15\text{-}20\ \mu\text{m}$. The chemical composition of silica fume (SF) is also rather simple as it usually contains more than 90% SiO_2 with a range of 85 to 99%. Because of its small particle size, SF will pack in the cavities formed by the irregular shaped cement grains until a certain dosage when the SF will disperse cement grains or its agglomerates in the fresh state. The result is a considerable void size refinement from the start.

Reduced permeability during setting, or shortly thereafter, is important for durability of concrete (for instance in marine environment) when made by slip forming or when demoulded early. Ingress of aggressive ions like water-borne chlorides can be very rapid during early exposure, in particular due to suction created by the under pressure in contraction pores formed as a consequence of hydration.

2.2 Increased volume of solids

Hydration reactions lead normally to an increased volume of solids as liquid water is transformed into hydrates. The strength increase after initial contact between the particles is mainly a consequence of reduced porosity, even though the mechanical properties of the formed compounds matters as well. One can use alite hydration as an example as illustrated in Eq. 1 where the increase in volume of solids during hydration is $(0.300+0.217)-0.317= 0.200\ \text{ml/g}\ \text{C}_3\text{S}$ corresponding to an increase of 63 vol%.

$2\ \text{C}_3\text{S}$	+	$6\ \text{H}$	=	$\text{C}_3\text{S}_2\text{H}_3$	+	$3\ \text{CH}$	(1)
$m=1.00\text{g}$		0.237		0.750		0.487	
$M=228.32\text{g/mol}$		18.02		342.46		74.09	
$n = 4.38\ \text{mmol}$		13.14		2.19		6.57	
$\rho = 3.15\ \text{g/ml}$		0.998		2.50		2.24	
$V=0.317\text{ml}$		0.237		0.300		0.217	

3. Chemical effects of SCMs

Scrivener *et al* [7] published a state of the art on methods to determine the degree of reaction of SCMs. The chemical effects of different SCMs are treated in the following:

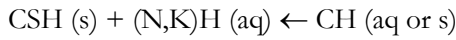
3.1 Silica

Using the cement chemist's notation the pozzolanic reaction of silica fume can be written:



A mixture of silica fume and pure lime needs weeks to harden properly. The acceleration of the pozzolanic reaction by alkalis creating high pH in the pore water was confirmed by Justnes [8] following the strength development for mortars with lime/silica fume cementitious materials. The presence of alkalis seems to

serve as a catalyst for a rapid pozzolanic reaction of silica fume (aq = aqueous, s = solid):



The nature of the CSH-gel from the pozzolanic reaction is different than the CSH gel formed by cement hydration. The two different gels coming from the cement hydration and the pozzolanic reaction, respectively, can be interwoven. The calcium silicate hydrate amorphous gel can exist in a wide range of compositions. The general difference between CSH from pozzolanic reaction and from cement hydration is that the former CSH has longer linear polysilicate anions and lower C/S-ratio than the latter (Justnes [9]).

In Fig. 1 (Justnes [10]) the relative compressive strength of mortar with lime/SF cementitious material (corresponding to C/S = 1.11, water-to-solid = 0.70 and alkalis of K/Na = 2 to pH = 13) is plotted versus curing time. In the same figure the degree of reaction of SF as measured by ²⁹Si MAS NMR versus curing time is plotted as well with a nearly identical trend indicating linearity between SF conversion and strength.

Justnes *et al* [11, 12] used ²⁹Si MAS NMR to study the influence of silica fume on the hydration rate of the silicate phases (sum of alite and belite) in ordinary and high strength cement, as well as the rate of silica fume reaction in such blends and the overall composition of the CSH gel under sealed conditions. Justnes *et al* [12] and Sellevold *et al* [13] showed that for low w/(c+s), the silica fume reacted faster than cement and left cement grains as micro-aggregate embedded in the CSH-gel. However, this is not necessarily negative for strength as cement grains are quite hard particles. Furthermore, some unreacted cement has potential in contributing to self-healing of microcracks during the service life of concrete.

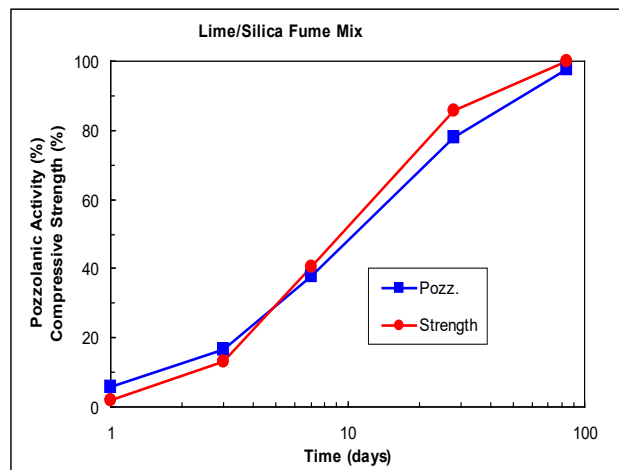


Figure 1: Comparison of compressive strength (100% = 63.9 MPa at 84 days) development of mortar with reactivity of silica fume in the cementitious material lime /SF with C/S = 1.11 and water-to-solid ratio 0.70 after Justnes [10].

3.2 Alumina and aluminosilicates

The chemical reaction of alumina, as in for instance nano-alumina (e.g. Barbhuiya *et al* [14]) or simply γ -Al₂O₃, is equally simple as for silica in reaction (2);



C₃AH₆ is the stable end-product in an isolated system of finely divided alumina and lime in spite of a number of metastable calcium aluminate hydrates (CAH₁₀, C₄AH₁₉, etc). As for silica in reaction (3), alkalis will also

here play a catalytic role with soluble aluminum hydroxide ions like $Al(OH)_4^-$ as the likely intermediate product. The difference is that the CAH products in general are crystalline rather than amorphous.

The pozzolanic reaction of the aluminosilicate (AS) glass phase in fly ash and the distorted aluminosilicate layers in calcined clays is complex but can be written in a non-balanced way;



A representative for calcium aluminate hydrate (CAH) will be C_3AH_6 and the mixed product CASH can be Strätlingite; C_2ASH_8 . In addition to that, it is typical that the CSH-gel will contain more aluminate than when it is formed by cement hydration only.

Ground blast-furnace slag (GGBS) contains sufficient calcium to react by itself when activated by alkalis. GGBS has a typical composition of 47% CaO+MgO, 35% SiO_2 and 12% Al_2O_3 . When activated with gypsum together with cement, the hydration products of slag are generally the same as for ordinary Portland cement (OPC); CSH-gel, Ettringite and monosulphate (Smocsyk [15] and Uchikawa [16]). The formation of Strätlingite (C_2ASH_8) is only to be expected if alkali hydroxide is added to the slag cement according to Richartz [17] or if the blast furnace slag is activated with alkali hydroxide (Regourd [18] and Forss [19]). Like fly ash, GGBS has a somewhat variable composition and it may not be entirely true that it does not consume calcium hydroxide during its reaction (Hinrichs and Odler [20]), which may depend on its content of CaO relative to SiO_2 and Al_2O_3 . The introduction of more calcium aluminate hydrate in the system by GGBS will destabilize ettringite (AFt) and form more calcium monosulphate hydrate (AFm), as for fly ash (Fig. 2).

3.3 Carbonates

Carbonates need CAH to react with. The combination of limestone together with an aluminate containing pozzolan (e.g. fly ash) makes calcium carbonate react more since it is too little CAH available from the clinker. This synergistic reaction lead to more bound water, reduced porosity and thereby higher strength has been documented by De Weerd and Justnes [4, 21] and De Weerd *et al* [22-26].

The synergetic effect between fly ash and limestone powder is attributed to the impact of $CaCO_3$ on the AFm phases which has been documented for pure OPC (Lothenbach *et al* [27]). AFm can in general be written $[Ca_2(Al,Fe)(OH)_6]X \cdot xH_2O$ where X denotes one formula unit of a singly charged anion or half a formula unit of a doubly charged anion (e.g. OH^- , SO_4^{2-} or CO_3^{2-} often referred to as OH-AFm, SO_4 -AFm and CO_3 -AFm. The impact of limestone powder is amplified as fly ash provides additional aluminates to the system by its pozzolanic reaction with calcium hydroxide from the cement hydration. The effect is demonstrated by Eqs. 6 and 7 showing the increased volume of the hydration phases in the reactions. The remains and original boundary of a partial reacted limestone grain in a cement-fly ash-limestone blend is shown in Fig. 2.

It is beneficial to blend calcium carbonate with something forming either more C_3AH_6 or sulphate-AFm that can react with calcium carbonate to bind more water and increase volume;



m = 1.00 g	3.78	0.90	5.68
M = 100.09 g/mol	378.29	18.02	568.50
n = 9.99 mmol	9.99	49.95	9.99
$\rho = 2.67$ g/ml	2.52	0.998	2.17

V = 0.375 ml 1.500 0.902 2.618

According to the reaction in Eq. 6, 100 g calcium carbonate (≈ 1 mol) would bind 90 g (≈ 5 mol) extra water. The total increase in volume of solids will then be $(2.618 - (0.375 + 1.500)) \cdot 100 \text{vol}\% / (0.375 + 1.500) = 39.6 \text{ vol}\%$. So with a lot of C_3AH_6 produced, this will matter. Alternatively, the reaction with sulphate AFm will be as follows;



m = 1.00 g	9.33	1.62	5.68	6.27
M = 100.09 g/mol	622.52	8.02	568.50	1255.11
n = 9.99 mmol	14.99	9.91	9.99	5.00
$\rho = 2.67 \text{ g/ml}$	2.015	0.998	2.17	1.778
V = 0.375 ml	4.630	1.623	2.618	3.526

According to the reaction in Eq. 7, 100 g calcium carbonate (≈ 1 mol) would bind 162 g (≈ 9 mol) extra water. The total increase in volume of solids will then be $((3.526 + 2.618) - (0.375 + 4.630)) \cdot 100 \text{vol}\% / (0.375 + 4.630) = 22.8 \text{ vol}\%$. This is just above half the volume increase compared to limestone reacting directly with C_3AH_6 in Eq. 6.

Small additions of limestone powder result in the formation of calcium hemicarboaluminate hydrate (“hemicarbonate”) instead of calcium monosulphoaluminate hydrate (“monosulphate”) and thereby stabilizing ettringite. Larger limestone additions lead to the formation of calcium monocarboaluminate hydrate (“monocarbonate”). Due to the difference in specific volume of these phases, and higher amount of hydrate water in ettringite or AFt (32 mole) vs. AFm (12 mole), an increase in the total volume of hydration phases can be observed. This will in turn lead to a reduction in porosity and consequently to an increase in strength. Segments of XRD profiles of paste showing how phases shift for different mixes of cement, cement with fly ash (FA), cement with limestone (L) and cement with limestone and fly ash (FA/L) are plotted in Fig. 2. The validity of the synergistic effect of limestone/fly ash for different clinker types and fly ash types was documented by De Weerd *et al* [28].

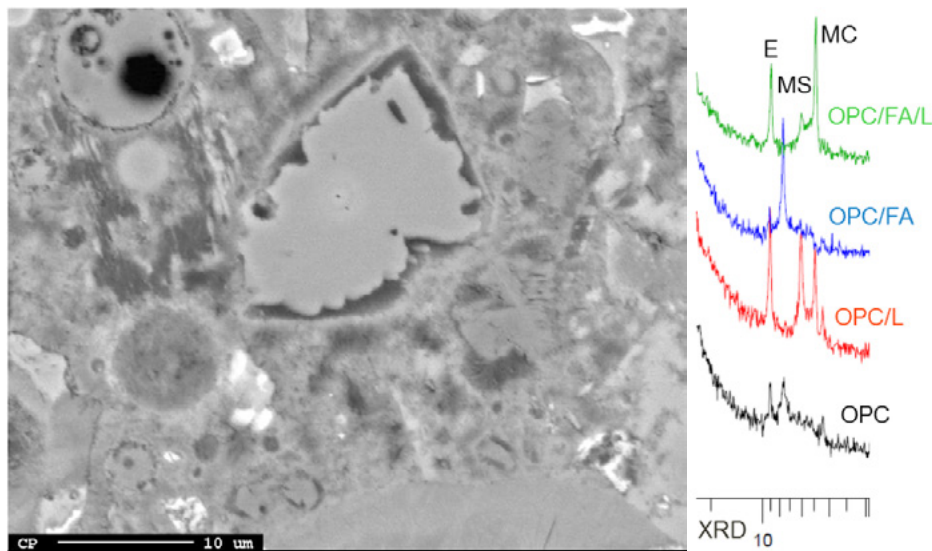


Figure 2: Left; BSE of paste consisting of cement/fly ash/limestone showing boundaries of a partly crystalline phase. Right; XRD profiles for OPC/FA/L, OPC/FA, OPC/L, and OPC.

reacted limestone in the centre and a circular fly ash particle in the upper left. Right; Segments of XRD profiles for OPC with combinations of fly ash (FA) and limestone (L). OPC alone gives a mixture of ettringite (E) and monosulphate (MS). OPC/L stabilises E and form hemihydrate and monocarbonate (MC). OPC/FA destabilises E and form MS. OPC/FA/L stabilises E and forms mainly MC.

It is of course not only fly ash that will form aluminates having a synergistic reaction with limestone, but also GGBS and calcined clay (Antoni *et al* [29]) or marl. Fig. 3 (photo to the left) shows a BSE image of a mortar where 35% of cement has been replaced with calcined marl, and the formation of CAH in the centre of the image. A wave length dispersive spectrum (WDS) revealed the composition 16.5 Ca, 8.3 Al and 0.4 Fe in atom% (mark of electron beam can be seen), giving Ca/Al = 2.0, so it is $C_4A\bar{C}H_{11}$. (Justnes and Østnor [30]). The segment of XRD to the right in Fig. 3 reveals the formation of $C_4A\bar{C}H_{11}$, calcium carboaluminate hydrate, in a mixture of calcined marl and calcium hydroxide (Justnes and Østnor [31]).

Neither is it necessary to use limestone, $CaCO_3$, as carbonate source, since dolomite, $CaMg(CO_3)_2$, will function as well and even lead to higher strength through formation of voluminous hydrotalcite; $Mg_6Al_2CO_3(OH)_{16} \cdot 4H_2O$, according to Zajac *et al* [5].

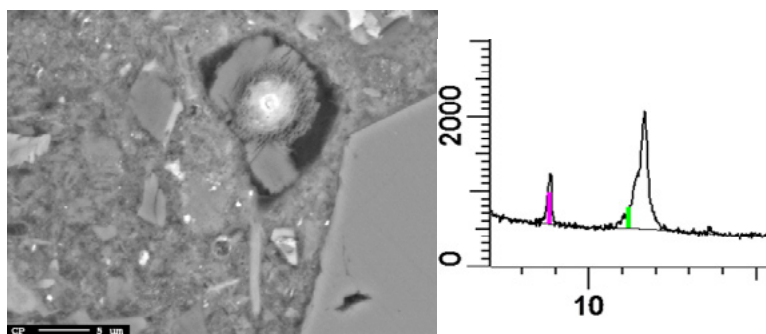


Figure 3: Left; BSE image of mortar where 35% cement is replaced with calcined marl and a CAH is formed in a void (Justnes and Østnor [30]). Right; XRD segment of a paste of calcined marl mixed with lime showing an illite peak (clay mineral) at $2\theta \approx 8.7^\circ$ and a peak from calcium monocarboaluminate hydrate at $2\theta \approx 11.7^\circ$ (Justnes and Østnor [31]).

4. Increasing reactivity of blended cements by accelerators

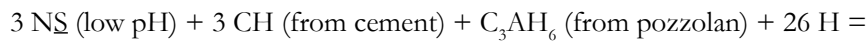
SCMs react in general slower than cement. Both GGBS and FA are activated by increased pH, but while GGBS is a latent hydraulic material, FA is a pozzolanic material consuming calcium hydroxide in producing hydraulic binder.

One advantage of using common potassium carbonate (K_2CO_3 or $K\bar{C}$ in short) or sodium carbonate (Na_2CO_3 or $N\bar{C}$ in short) as fly ash or slag activator, is that they are safe to handle and will form high pH *in situ* by reaction with calcium hydroxide from cement hydration;



and at the same time form calcium carbonate with high surface area that probably is faster reactive with calcium aluminate hydrates than limestone powder. Such *in situ* forming accelerators were utilized by Justnes [8] making lime-pozzolan mortars with high early strength. The disadvantage may be that alkali carbonates may retard the setting of cement and/or give somewhat lower long-term strength depending on total alkali content.

Sodium sulphate is also a good accelerator for aluminate containing pozzolana and slag involving in situ formation of NaOH (short hand notation NH) for further acceleration and formation of solid ettringite and/or monosulphate with increased water binding;



Shi and Day [32-25] studied the effect of Na_2SO_4 and CaCl_2 as chemical activators on the strength of lime-fly ash pastes. ASTM type C and F fly ashes were used in the 20% hydrated lime and 80% fly ash mixes (no cement) and the chemical activators were added in dosages up to 5% of the lime-fly ash mass. The pastes were prepared with a water/solid ratio of 0.35 for type F or 0.375 for type C fly ashes and cured moist at 50°C. Both Na_2SO_4 and CaCl_2 clearly increased the compressive strength of the mortars, but sodium sulphate was superior with respect to the 1 day strength. Unfortunately, are many chemical activation experiments performed at elevated temperatures being irrelevant for ready mix concrete, but still applicable for precast concreting.

Shi and Day [32] used X-ray diffraction (XRD) and scanning electron microscopy (SEM) to examine pastes with and without activators. The low lime fly ash (ASTM type F) without any activator had a CSH-like phase as principal hydration product, and the second major hydration product was found to be C_4AH_{13} . Minor products detected were ettringite (AFt) at early age and C_2ASH_8 at later age. The addition of sodium sulphate resulted in an increase of the AFt phase and a decrease in the C_4AH_{13} phase, which is in line with reaction 9. Calcium chloride activator led to formation of the solid solution $\text{C}_4\text{AH}_{13}\text{-C}_3\text{A-CaCl}_2\cdot 10\text{H}_2\text{O}$.

Qian *et al*[36] compared the effect of grinding for 30 minutes in a ball mill and chemical activation through the addition of 3-4% Na_2SO_4 . They found that chemical activation was more efficient than ordinary grinding. Chemical activation increased the 3 and 7 day-strength of cement replaced with 30% fly ash by 5-10 MPa.

Lee *et al* [37] studied the strength and microstructure of fly ash-cement systems containing the accelerators Na_2SO_4 , K_2SO_4 and triethanolamine. The accelerators increased the amount of ettringite at early ages. The authors concluded that accelerators were a viable solution to increase early compressive strength of concrete with high amounts of fly ash.

High dosages of alkaline salts as accelerators may give lower long-term strengths and may also be negative in terms of alkali-aggregate reactions (AAR). Another approach is to boost the cement reactivity rather than the SCM reactivity. Hoang [38] investigated accelerators for mortars where cement was replaced with 30% fly ash. He arrived at a ternary accelerator based on 0.2% sodium thiocyanate (NaSCN), 0.1% diethanolamine (DEA) and 0.05% glycerol and showed that a 0.35% dosage of this ternary accelerator gave same improved strength after 2 days at 5°C (41°F) as 4% sodium sulphate (Na_2SO_4) + 0.4% NaSCN (total 4.4%, more than 12x increased dosage), but the 28 days strength was higher for the low dosage of ternary accelerator. The ternary accelerator also fulfilled the requirements to a hardening accelerator according to EN 934-2 [39] at a 0.35% dosage with +60% 2 day strength at 5°C and +30% 1 day strength at 20°C relative to reference and was patented (Hoang *et al*[40]).

5. Rheology of blended cements

Cement blended with SCMs with substantially higher specific surface than cement, and in particular irregular particles shapes with voids, leads to inferior rheology compared to ordinary cement. Justnes and Ng [41] published a review on the influence of all components of a concrete matrix (i.e. cement type, SCMs and mineral fillers). Some information for the individual SCMs are repeated in the respective sub-sections.

4.1 Silica fume

Vikan and Justnes [42] made cement pastes with a constant total particle volume of 0.442 corresponding to w/c about 0.40 as basis, while the amount of silica fume (SF) was replacing cement in volume increments of 0.01 from 0.00 to 0.06. They concluded that the influence of SF replacement on the flow resistance (FR) depended on the plasticizer type: FR increased with increasing SF replacement when naphthalene sulphonated – formaldehyde condensate (NSF) was added as a plasticizer and decreased when polycarboxylic ether (PCE) was added. Increased FR and gel strength with SF replacement using SNF may be caused by early gel formation due to water binding by SF or the ionization of SF surface due to the high pH and possible bridging with polyvalent cations like calcium. Decreased FR with increasing SF replacement using PCE was explained by the dispersing power of PCE coupled with SF packing between cement grains displacing water or by a ball-bearing effect of silica spheres.

4.2 Fly ash

Ng and Justnes [43] studied cementitious paste where OPC were replaced by siliceous fly ash (FA) in increments of 20 to 60% by mass and with a constant water-to-powder ratio of 0.36. They investigated the effect of 5 plasticizers; lignosulfonate (LS), NSF and 3 PCEs. Some results are presented here, but Ng and Justnes [44] have presented detailed results for one PCE. The flow resistance (FR) decreased steadily with increasing replacement of OPC by FA as shown in Fig. 4 in spite of increased total volume of solids since the density of FA is lower than OPC. The decrease in FR is due to the spherical nature of FA and the low reactivity of the glass phase at this early stage. Furthermore, there is much lower interaction of the plasticizers with FA than with cement, so the effective plasticizer-to-cement ratio is increasing and thereby also the retardation of the cement as illustrated in Fig. 5 for NSF.

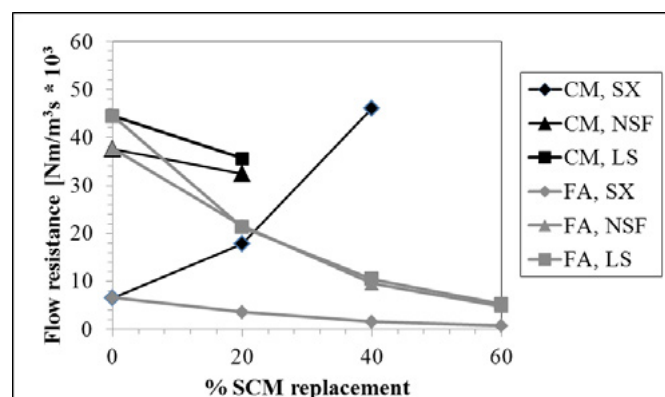


Figure 4: Flow resistance as a function of OPC replacement by SCM, fly ash (FA) or calcined marl (CM) with 0.2% dry plasticizer LS, NSF and a PCE named SX) of powder mass.

4.3 Blast furnace slag

Investigations on admixture interactions with cement blended with ground blast furnace slag are limited. Blast furnace slag consists of a glass phase with in the order of 40% CaO. The surface is believed to have calcium-sites capable of coordinating with plasticizers unlike the glassy phase of siliceous fly ash, but still to a smaller extent than for OPC.

Palacios *et al* [45] studied the effect of a number of plasticizers on the yield stress and plastic viscosity of alkali activated slag (AAS) and OPC pastes. They concluded that the adsorption of the plasticizers on AAS pastes was independent of the pH of the alkaline solutions used and lower than on OPC pastes. However, the effect of the admixtures on the rheological parameters depended directly on the type and dosage of plasticizer as well as of the binder used and, in the case of the AAS, on the pH of the alkaline activator solution. In 11.7-pH NaOH-AAS pastes the dosages of plasticizers required to attain similar reduction in

the yield stress were ten-fold lower than for Portland cement. For this pH the plasticizers showed a fluidizing effect considerably higher than in OPC pastes. In 13.6-pH NaOH-AAS pastes, the only plasticizer to affect the rheological parameters was NSF due to its higher chemical stability in such extremely alkaline media.

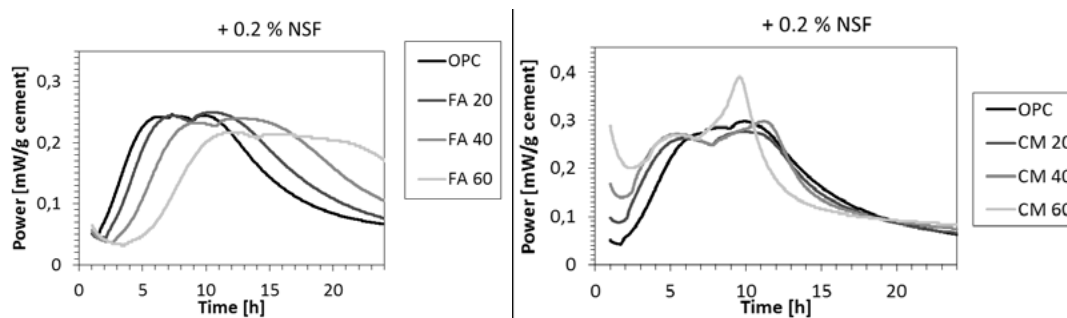


Figure 5: Heat of hydration (Power) evolution per cement mass for cementitious pastes with 0 (OPC), 20 (FA20), 40 (FA40) and 60% (FA60) replacement of OPC with FA to the left and with 0 (OPC), 20 (CM20), 40 (CM40) and 60% (CM60) replacement of OPC with CM to the right. All pastes are plasticized by 0.2% dry NSF of powder mass.

4.4 Calcined clay

Ng and Justnes [43] studied also cementitious paste where OPC were replaced by calcined marl (CM) in increments of 20 to 60% by mass and with a constant water-to-powder ratio of 0.36. They investigated the effect of the same 5 plasticizers; LS, NSF and 3 PCEs as for fly ash. The flow resistance (FR) plotted in Fig. 4 shows that it decreased slightly from 0 to 20% OPC replacement by CM and 0.2% addition of dry plasticizer for LS and NSF. Workable mixes were not attained for these plasticizers at a 0.2% dosage for higher CM replacements. For 0.2% PCE (SX) addition, FR increased with increasing OPC replacement by CM until 40%, while the 60% was not workable at this PCE dosage. Reasons for lower workability when OPC is replaced by CM are higher volume of solid due to lower density, higher water absorption by its porous nature and less reactive surface with less calcium sites than OPC. CM surface is assumed to be more reactive and have more Ca-sites than siliceous fly ash (FA) and adsorb more plasticizer. This is also reflected in the heat of hydration evolution curves when OPC is replaced with CM using NSF leading to acceleration rather than retardation for the FA replacement as seen in Fig. 5. This indicates that the effective plasticizer-to-cement ratio is less in the case of CM replacement than for FA replacement.

5. Influence of SCMs on durability of blended cements

5.1 General

There is a general dilemma in all accelerated durability testing: How can the exposure be sufficiently accelerated in order to give in a relative short time the same environmental load as a long-term natural exposure? This is usually sought achieved by increasing the exposure temperature (e.g. alkali aggregate reactions) or by increasing the concentration of the aggressive component (e.g. carbonation).

Increased temperature prior to exposure is also often used to achieve a more mature cementitious binder since SCMs often react much slower than the cement hydrate at ambient temperature and many of the degradation mechanisms happens slowly over years. However, it is important to not raise the temperature so high that changes occur in the binder that will not happen in practice. For instance it is well known, that the CSH gel becomes coarser and more porous already at 50°C (Kjellsen *et al* [46-48]) and fly ash/lime mixes might have a phase change when cured at 38°C relative to 20°C (De Weerd and Justnes [21]). Another example is paste where cement is partly replaced by calcined clay as SCM and cured at 38°C (Danner [49]) where dense areas of the hydrogarnet katoite formed and not seen at 20°C.

5.2 Chloride ingress

Chloride ingress is not detrimental to the binder itself but may induce corrosion of reinforcement steel in spite of high pH when exceeding a certain threshold value of chloride at the steel surface. The required total chloride content at the rebar to initiate corrosion is often taken as 0.1% Cl of concrete mass irrespectively of the binder type. Chloride binding is not taken into account even though it is the chlorides in the pore water next to the steel that are destabilizing the protective oxide layer created by the high pH. Many refer to a certain Cl⁻/OH⁻ ratio in order to initiate steel corrosion, but the values scatter. The following conclusions were made from a state-of-the-art report on critical chloride level (Angst and Vennesland [50]); “A lot of studies have been undertaken in the context of critical chloride content and the published results scatter in a wide range. The reported results span from 0.02 to 3.08% total chloride by weight of binder and thus over two orders of magnitude. Published Cl⁻/OH⁻ ratios even range from 0.03 to 45 and thus over three orders of magnitude.”

Even though pozzolanic SCMs consume calcium hydroxide (CH), the remaining CH will buffer pH to 12.5, albeit it may be reduced from pH 13.2 given by the alkali hydroxides as long as SCM prevails. Alumina containing SCMs may in addition form CAH that will lead to increased chemical binding of chlorides as Friedel’s salt; Ca₃Al₂O₆·CaCl₂·12H₂O, as well as increased adsorption on CSH-gel as more gel is formed on the expense of CH in the pozzolanic reaction. Thus, it is difficult to judge how SCMs will affect the Cl⁻/OH⁻ ratio. If properly dispersed, SCMs will in general also refine the porosity of the binder and reduce the diffusion rate of aggressives as chloride.

An example of chloride ingress profiles in mortars with increasingly volume replacement of cement by calcined marl is shown in Fig. 6 (Justnes and Østnor [30]) revealing that chloride ingress is substantially reduced up to a cement replacement of 50 vol%. Such profiles of *total* chloride content is often erroneously (Justnes and Geiker [51]) used to be fitted to solutions of Fick’s 2nd law of diffusion to yield a surface concentration of chlorides and an apparent diffusion coefficient that is further used in service life modelling of concrete structures, even though it is only the *free* chlorides that are moving. Another benefit of SCMs is increased electrical resistivity as exemplified in Fig. 7 for the same mortars as in Fig. 6. A high electrical resistivity brought about by a combination of porosity segmentation and reduced ion activity (i.e. hydroxyl ions are the most important charge carriers) in the pore fluid, may also reduce corrosion rate of steel once it is initiated.

Fidjestøl and Justnes [52] investigated the chloride profiles in a quay structure in Gothenburg harbor after 24 years of service. The water in the harbor is partly brackish with an average chloride concentration of 1.4% as opposed to 1.9% in Atlantic waters. The quay was cast with different segments of concrete with 5% silica fume and without, and if the chloride profiles are fitted to the solution of Fick’s 2nd law of diffusion it resulted in apparent diffusion coefficients of 0.32 and 0.90·10⁻¹²m²/s) for 5% and 0% silica fume, respectively.

Thomas and Bamforth [53] investigated the effect of cement replacement by 30% fly ash or 70% GGBS on chloride ingress in concrete blocks naturally exposed to seawater spray over a period of several years with the objective of finding the decay coefficient (m) of the apparent diffusion coefficient in Eq. 10;

$$D_t = D_{ref} \cdot (t_{ref}/t)^m \tag{10}$$

where

D_t = apparent diffusion coefficient at time t

D_{ref} = apparent diffusion coefficient at a given reference time, e.g. 28 days

m = decay coefficient

Thomas and Bamforth [53] found $D_{28\text{d}} = 8, 6$ and $25 \cdot 10^{-12} \text{m}^2/\text{s}$ for reference, 30 FA and 70% GGBS, respectively, with corresponding values $m = 0.1, 0.7$ and 1.2 . In spite of higher $D_{28\text{d}}$, the accumulated chloride ingress in concrete with 30% fly ash or 70% GGBS was about equal but much lower than reference after 2 years and onwards to 8 years. This illustrates the importance of mature samples with high dosages of SCMs prior to accelerated exposure.

Sometimes ternary mixes are beneficial, as shown by Thomas *et al* [54] where cement replaced by 25% FA and 8% SF resulted in lower chloride ingress than either component alone, probably by a combination of improved particle packing and increased reactivity.

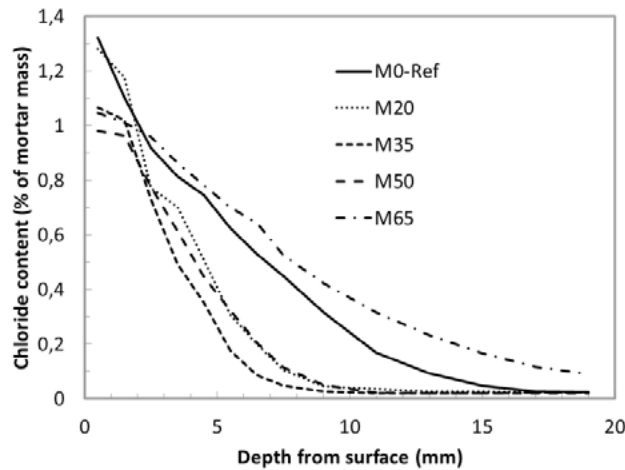


Figure 6: Chloride ingress in mortars where cement is replaced with 0 (M0), 20 (M20), 35 (M35), 50 (M50) and 65 (M65) vol% calcined marl after exposure for 35 days to 165 g NaCl/liter (Justnes and Østnor [30]).

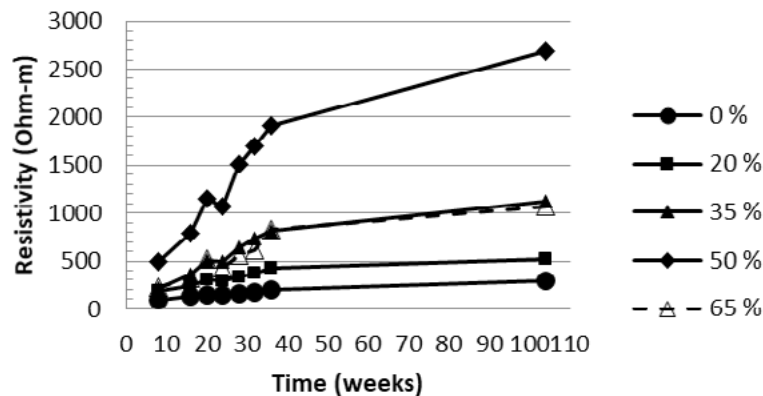
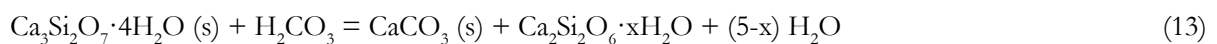


Figure 7: Resistivity of mortars where cement is replaced with calcined marl from 0-65 vol% as a function of time.

5.3 Carbonation

Carbonation is actually a neutralization reaction between carbonic acid, H_2CO_3 (i.e. CO_2 dissolved in water) and alkaline components in the blended cement;



According to Engelsen and Justnes [55], all hydrates formed by cement will carbonate, but CSH will probably only carbonate down to a Ca/Si of about 1. Based on stoichiometric considerations they calculated that about 72% of all CaO in an ordinary portland cement will carbonate. Visser [56] recently reviewed carbonation mechanisms and consequences of elevated CO₂ concentrations for accelerated testing. Carbonation reduces pH of the pore water from about 13 to around 9 and the carbonation front inwards is easily detected by spraying an indicator like phenolphthalein on a broken surface since it is colorless for pH <10 and pink above. The carbonation front is also believed to be relatively steep.

There are basically 2 reasons why cements blended with SCMs are more prone to carbonation than ordinary portland cements; 1) the physical thinning effect since there is less cement per volume unit to produce calcium hydroxide and 2) the chemical pozzolanic effect of some SCMs consuming calcium hydroxide. The question is whether or not their hydration products will carbonate as they tend to produce CSH of low C/S less prone to carbonation under natural conditions (≈0.04% CO₂) even though they might carbonate at ≥ 1% CO₂.

The water-to-cement ratio (w/c) together with the amount and volume of hydration products determines the connectivity of pores and also the carbonation depth as shown in Fig. 8 for mortar where OPC is replaced by FA and GGBS as function of w/c and compared to OPC. It can be seen that a mortar with 17% replacement of cement by FA carbonates only slightly faster than for cement replaced with 48% GGBS at the same w/c. Thus, it seems to be controlled by total CaO in the system which is about 52% for both.

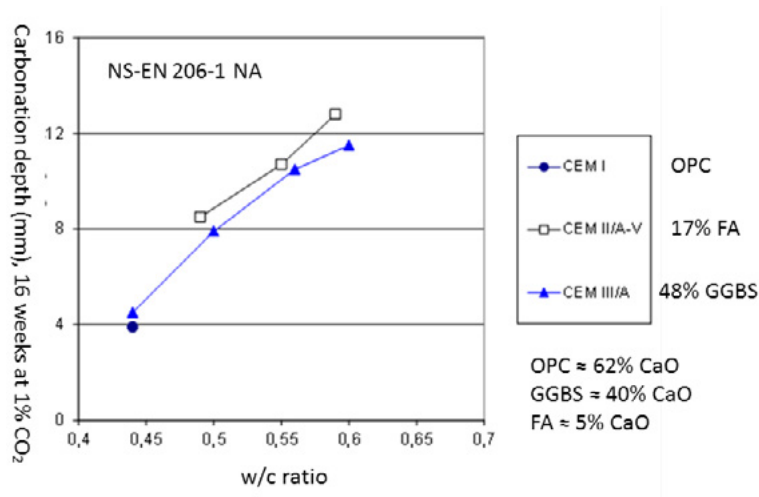


Figure 8: Carbonation depth (mm) of mortar where cement has been replaced with 17% fly ash containing ≈5% CaO or 48% GGBS containing ≈40% CaO as a function of w/c and compared to OPC (CEM I) containing ≈62% CaO after exposure for 16 weeks to 1% CO₂ at 60% RH and 20°C. Samples preconditioned 28 d in water and 14 d at 50% RH.

Justnes and Østnor [30] tested the carbonation rate of mortars with increasing volume replacement of cement by calcined marl and constant water-binder ratio for carbonation depth versus square root of time. Such a plot is expected to be linear if diffusion controlled, but in this case it is curved for replacement levels ≥ 35 vol%. This might be due to formation of increasing amount of AFt (stabilized by carbonate) and AFm rich in crystal water. When these phases carbonate, they form calcium carbonate and gibbsite while the crystal water goes back to liquid, which leads to increased porosity forming pathways for increased carbonation rate. Calcined clay/marl reacts much faster than for instance fly ash.

Generally speaking, the carbonation rate will increase with increasing SCM at constant w/c and curing time. However, when the concrete is proportioned to give same 28 days strength, the carbonation rate

seems to be similar irrespectively of SCM according to Thomas [3]. Studies that employ enriched CO₂ to accelerate carbonation tend to overestimate the carbonation rate in concrete with SCMs (Thomas *et al* [57]). Concluding from short-term tests (< 5 years) may overestimate the negative impact of fly ash on carbonation rates in concrete (Hobbs [58]).

5.4 Alkali aggregate reactions (AAR)

Alkali aggregate reactions (AAR) are most often caused by dissolution of reactive silica in the aggregate by alkali hydroxides in the pore solution, which turn into a viscous, swelling gel when it meets the paste binder and alkalis partly ion exchange with calcium.

Replacing cement with SCMs generally reduce expansion due to AAR (Thomas [59]). This has in general been thought to be caused by a reduction in pH (i.e. hydroxyl concentration) of pore water and a lower content of calcium hydroxide. In the author's opinion, the reduction in pH will be the case as long as the alkalis are busy in dissolving SCM in the catalytic way outlined in Eq. 3, but the implication is that this may cause only a delay of AAR until the SF has reacted totally. Bérubé and Duchesne [60] showed indeed that SF merely postpones expansion due to AAR. Nevertheless, SF as a preventative against AAR, together with other improvements in construction procedures, has found its application in Iceland where all cement has been interground with 7-8 % SF to combat the problem (Asgeirsson [61]). Fournier *et al* [62] also showed that >7% SF was able to control ASR.

According to Thomas [3] the level of cement replacement by SCM required to control AAR expansion increases as 1) SiO₂ content of SCM decreases, 2) CaO of SCM increases, 3) alkali content of SCM increases, 4) alkali availability in the concrete increases and 5) reactivity of the aggregate increases. Shehata and Thomas [63] showed that low calcium fly ashes (ASTM Class F) are much more effective in reducing AAR expansion (typical cement replacement level >20%) than high calcium fly ashes (ASTM class C). Shehata and Thomas [64] demonstrated that the required level of low calcium fly ash could be reduced to 10% when combined with 5% SF as a ternary blend. Thomas and Innis [65] found that North American GGBS at a cement replacement level of > 40% was able to control expansion caused by AAR. Bleszynski *et al* [66] showed that GGBS in combination with SF as a ternary blend including cement was better than GGBS replacement alone in reducing AAR expansion. Ramlochan *et al* [67] proved that highly reactive metakaolin at a cement replacement level > 10% was able to combat expansion due to AAR.

Some have suggested that the presence of alumina in SCMs contributes to prevent the release of alkali back to the pore solution by binding in the hydration products. However, Chappex and Scrivener [68] showed that this effect is extremely small, and instead it was found that alumina is an inhibitor of silica dissolution (Chappex and Scrivener [69, 70]) in their system with metakaoline as SCM. Favier *et al* [71] showed that AAR is prevented by calcined clay mixed with limestone as well.

5.5 Sulphate attack

There are 2 forms of sulphate attack; 1) external where sulphates from the surroundings are penetrating the hardened concrete forming expanding ettringite and 2) internal that can be caused by decomposition of ettringite during hot curing exceeding 70°C and later reformation and expansion after cooling (i.e. delayed ettringite formation shortened DEF). A special form of external sulphate attack can occur at low temperatures (<15°C) if the concrete contains limestone, namely the formation of thaumasite; Ca₃Si(OH)₆(CO₃)(SO₄)·2H₂O, that can take silicate from the CSH and turn it into a non-binding mush (Irassar [72]). A special form of internal sulphate attack is from aggregate containing iron sulfides that may oxidize to sulphates (Duchesne [73]).

The good performance of concrete with SCMs in a sulfate environment can be attributed to several

factors of which the most important are likely to be i) the refined pore structure and thus reduced mobility of harmful ions and ii) the lower calcium hydroxide content by thinning or pozzolanic reaction and iii) formation of more CAH that will at least delay formation of AFt since AFm must form first. The second factor leads to reduced formation of expansive gypsum (Eq. 14) and later ettringite from, for instance, calcium aluminate hydrates (Eq. 15) or monosulphate, AFm (Eq. 16), found in the hydrated concrete binder.



Based on molar volumes, it can be calculated that the reaction in Eq. 14 leads to 124% expansion of the solid (s). The reaction in Eq. 15 leads to 371% increase relative to the C_3AH_6 crystal (localized growth) or 89% relative to both C_3AH_6 and gypsum, while the reaction in Eq. 16 leads to 128 % expansion relative to the AFm phase only (localized growth) or 54 % expansion relative to both AFm and gypsum. These expansive reactions result in cracking and spalling if the stress exceeds the tensile strength of the binder. Scrivener [74] pointed out that ettringite needs to be supersaturated in order to create a pressure leading to expansion. Müllauer *et al* [75] studied sulfate attack mechanisms in detail.

When SF is used together with GGBS or FA as cement replacement (Carlsen and Vennesland [76] and Fidjestøl and Frearson [77]) these ternary mixtures have been found to be more resistant to sulfate attack than special sulfate resisting cements.

Kunther *et al* [78] showed an improvement of the sulphate resistance (50 g Na_2SO_4 /liter) for a cement with 70% GGBS relative to an OPC, and also that the expansion due to sulphate attack was substantially reduced when bicarbonate was present simultaneously (50 g Na_2SO_4 + 30 g NaHCO_3 /liter). They explained the latter effect by ettringite and gypsum becoming unstable in presence of bicarbonate and that the ettringite could not build up the crystallization pressure required to create expansion. An alternative explanation is that CO_3 -AFm is more stable than SO_4 -AFm and would prevent AFt formation.

Dehwah [79] exposed concrete specimen to 5% NaCl and sodium sulphate of concentrations 1, 2.5 and 4% solutions for up to 4 years. The concretes were based on two types of cement (ASTM C150 type I and V), as well as cement type I replaced by 10% silica fume, 20% fly ash or 70% GGBS. None of the concretes showed any deterioration after 4 years, indicating that Friedel's salt (Cl-AFm) may be more stable than monosulphate (SO_4 -AFm) at the experimental conditions.

Ghafoori *et al* [80] evaluated the sulfate resistance of concrete based on ASTM type V cement of different cement contents (and thereby w/c) when replaced with 0, 15, 20, 25 and 30% ASTM class F (siliceous) fly ash. They found that the improvement in sulfate resistance was only modest (15%) and that the required FA replacement increased with increasing cementitious content of the concrete.

Hossack and Thomas [81] studied the sulfate resistance at both 5 (41) and 23°C for mortars based on cements with limestone content varying from 4-22%. In their series cement was partly replaced with fly ash (ASTM types C and F), blast furnace slag, silica fume or metakaolin, as well as some ternary blends thereof. They found that SCMs greatly improved the sulfate resistance at 23°C, but higher SCM levels may be required when limestone is present. The greatest degree of resistance to sulphate attack was found with ternary mixes of silica fume with fly ash or blast furnace slag, as well as for high replacement levels of metakaolin. Ettringite, thaumasite and gypsum were found in all samples exposed to Na_2SO_4 at 5°C indicating a mixed form of sulfate attack. Abdalkader *et al* [82] investigated sulphate attack on mortars based on cement and cement blended with 10% limestone exposed for combined action of chloride (0,

0.5, 1 or 2% Cl and sulfate (0.6% SO₄²⁻) for 630 days at 5°C. All specimens suffered from the thaumasite form of sulfate attack, with the exception of the combination of sulfate with 2% Cl. The degradation was more severe for samples with limestone. The better performance in combination with the highest chloride concentration was explained by increased Friedel's salt formation, possibly preventing ettringite formation that many consider a prerequisite for the formation of the isostructural thaumasite. Even though chloride may prohibit thaumasite formation it was still found in concrete with limestone filler exposed to sea water (0.27% SO₄²⁻ and 1.9% Cl) for 10 years outside Trondheim, Norway (De Weerd *et al* [83]).

When it comes to the effect of SCMs on internal sulphate attack, Rønne *et al* [84] published the effect of SF on expansion due to delayed ettringite formation (DEF), and the measurements for 2 years are plotted in Fig. 9 for OPC with 0 and 8% SF and w/(c+SF) = 0.40. The concrete was resting for 6 hours before being heated to the set temperature of 20, 70 or 85 °C with a rate of 12°C/h in a water bath that thereafter cooled down slowly to the ambient temperature of 20°C to mimic the temperature evolution in a massive structure driven by heat of hydration. The rest of the curing time was at 20°C and the volume of the specimens was monitored by weighing in water and air according to the principle of Archimedes. SEM confirmed ettringite formation in aggregate interfaces and cracks for the expanding specimens.

Ramlochan *et al* [85, 86] initial cured mortar samples at 95°C followed by storage in limewater at 23°C up to 1500 days. They found that 25% replacement of cement by SCMs containing alumina; such as fly ash (both ASTM class C and F), blast furnace slag and metakaolin, was able to prevent DEF while 8% silica fume only had limited effect (expansion reached 1.0% compared to reference expanding 2.8%).

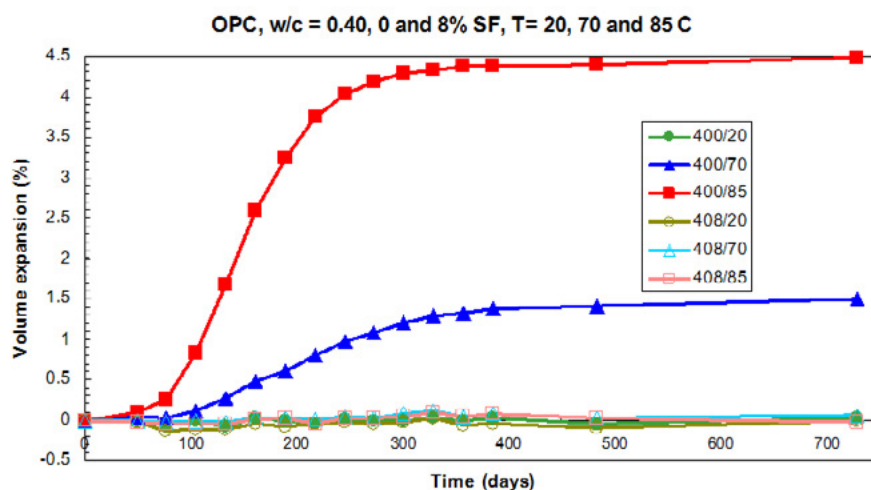


Figure 9: Volume changes of OPC concrete with w/cm = 0.40 with 0% (legend 400) and 8% (legend 408) SF initial cured at 20, 70 and 85°C followed by 20°C water curing > 2 years (Rønne *et al* [84]).

5.6 Freeze-thaw resistance

Concrete with a high degree of capillary saturation with water (>92%) can be damaged by repetitive freezing and thawing cycles (fatigue) since water expands 9% upon freezing and can create a hydraulic pressure forcing unfrozen water into smaller pores leading to cracking. This is usually mitigated by entraining small air bubbles with the help of appropriate admixtures. These well distributed air bubbles are empty and will function as pressure relief chambers upon freezing. Concrete with SCMs is believed to be equal resistant to freeze-thaw as concrete with ordinary portland cement providing that a good air void system is obtained by the aid of air entraining agents and that the concrete is well cured. SCMs react slower than OPC and concrete with SCM is thus more sensitive to improper workmanship.

There are indications that blended cement may be more sensitive to freeze-thaw under the influence of

thawing salts like sodium chloride (NaCl), and an interaction with aluminates forming Friedel's salt can not be ruled out. Residual carbon in fly ash is known to create a problem by adsorbing air entraining agents leading to the need of higher dosages to obtain a good air void system. This can also be omitted by adding sacrificial agents that will preferentially adsorb to the free carbon (Jolicoeur *et al* [87]). There have also been reports on concrete with high blast furnace slag content that become more prone to freeze-thaw damage under influence of thawing salts (Panesar and Chidiac [88], Giergiczny *et al* [89]), and in particular when carbonated (Utgenannt [90]). A possible remedy against the inferior freeze-thaw resistance of concrete with GGBS seems to be surface treatment with sodium monofluorophosphate (Sisomphon *et al* [91]).

7. Conclusions

Concrete based on cement blended with SCMs, or where ordinary cement is partly replaced with SCMs, is more durable in general than concrete based on ordinary portland cement at equal water-to-binder ratio, when well cured and when the SCM is properly dispersed. The main reasons are a denser microstructure either due to improved particle packing initially or more binder (CSH or CAH) formed on the expense of calcium hydroxide (CH) either due to displacement of cement or pozzolanic reaction.

The exception is carbonation resistance which is increasing with increasing cement replacement by SCMs at equal water-to-binder ratio due to less CH, even though most calcium containing components will carbonate in the end. However, the increased carbonation rate can be counteracted by reducing the water-to-binder ratio, but if this is achieved by increasing the binder content the positive effect of using SCMs for the sake of environment will be reduced.

Limestone can also be considered as a SCM, in particular in combination with other SCMs producing CAH that can be a reactant for a synergic reaction binding even more water that will help densifying the porosity of the binder.

The resistance to ingress of chemicals depends largely on the AFm phases in the binder and which one is the most stable. For instance, the binding of chlorides is improved by the presence of CAH forming Friedel's salt and ingress is delayed.

8. References

1. Justnes, H., "How to make concrete more sustainable", *1st International Conference on Concrete Sustainability*, May 27-29, 2013, Tokyo, Japan, Paper S1-1-2, 92-99 (ISBN 978-4-86384-041-6-C3050).
2. Lothenbach, B.; Scrivener, K. and Hooton, R.D., "Supplementary cementing materials". *Cement and Concrete Research*, V. 41, 2011, pp. 1244-1256.
3. Thomas, M., *Supplementary Cementing Materials in Concrete*. 1st Ed. CRC Press, Taylor & Francis Group, 2013, 190 pp. (ISBN 978-1-4665-7298-0).
4. De Weerd, K. and Justnes, H., "Synergic Reactions in Triple Blended Cements", *11th NCB International Seminar on Cement and Building Materials*, 17-20 November, 2009, New Delhi, India, pp. 257-261.
5. Zajac, M.; Bremseth, S.K.; Whitehead, M. and Ben Haha, M., "Effect of $\text{CaMg}(\text{CO}_3)_2$ on hydrate assemblages and mechanical properties of hydrated cement pastes at 40°C and 60°C", *Cement and Concrete Research*, V. 65, 2014, pp. 21 -29.
6. Justnes, H., "Silica Fume in High-Quality Concrete - A Review of Mechanism and Performance", *9th CANMET/ACI International Conference on Fly Ash, Silica Fume, Slag and Natural Pozzolans in Concrete*, ACI SP-242, Ed. Mohan Malhotra, Warszawa, Poland, 21-25th May, 2007, SP-242-6, 63-78.

7. Scrivener, K.L.; Lothenbach, B.; De Belie, N.; Gruyaert, E.; Skibsted, J.; Snellings, R. and Vollpracht, A., “RILEM TC 238-SCM: hydration and microstructure of concrete with SCMs”, *Materials and Structures*, 2015, DOI 10.1617/s11527-015-0527-4.
8. Justnes, H., “Accelerated Hardening of Mortars with Hydraulic Binders of Silica Fume/Lime”, *Nordic Concrete Research*, Publication No. 17, 2/1995, pp. 30-41.
9. Justnes, H., “Hydraulic binders based on condensed silica fume and slaked lime”, *9th International Congress on the Chemistry of Cement*, New Delhi, India, 23-28 November, 1992, V. III, pp. 284-290.
10. Justnes, H., “Kinetics of Reaction in Cementitious Pastes Containing Silica Fume as Studied by ²⁹Si MAS NMR”, in *Nuclear Magnetic Resonance Spectroscopy of Cement-based Materials* (Eds. P. Colombet, A.-R. Grimmer, H. Zanni and P. Sozzani), Springer Verlag, Berlin, 1998, pp. 245-268.
11. Justnes, H.; Meland, I.; Bjørgum, J.O. and Krane, J., «A ²⁹Si MAS NMR Study of the Pozzolanic Activity of Condensed Silica Fume and the Hydration of Di- and Tricalcium Silicate”, *Advances in Cement Research*, V. 3, 1990, pp. 111-116.
12. Justnes, H.; Sellevold, E.J. and Lundevall, G., “High Strength Concrete Binders. Part A: Reactivity and Composition of Cement Pastes with and without Condensed Silica Fume”, *4th ACI International Conference on Fly Ash, Silica Fume, Slag and Natural Pozzolana in Concrete*, Ed.: V.M. Malhotra, Istanbul, May 3-8, 1992, CANMET/ACI SP 132-47, V. 2, pp. 873-889.
13. Sellevold, E.J. and Justnes, H., “High-Strength Concrete Binders. Part B: Non-evaporable Water, Self-desiccation and Porosity of Cement Pastes with and without Condensed Silica Fume”, *4th CANMET/ACI International Conference on Fly Ash, Silica Fume, Slag and Natural Pozzolana in Concrete*, Ed.: V.M. Malhotra, Istanbul, May 3-8, 1992, CANMET/ACI SP 132-48, V. 2, pp. 891-902.
14. Barbhuiya, S.; Mukherjee, S. and Nikraz, H., “Effects of nano-Al₂O₃ on early-age microstructural properties of cement paste”, *Construction and Building Materials*, V. 52, 2014, pp. 189-193.
15. Smolczyk, H.-G., “The hydration products of cements with high contents of blast furnace slag”, *Zement-Kalk-Gips International*, V. 18, 1965, pp. 238-246.
16. Uchikawa, H., “Effect of blending components on hydration and structure formation”, *8th International Congress on the Chemistry of Cement*, Rio de Janeiro, V. 1, 1986, pp. 249-280.
17. Richartz, W., “On the formation of the aluminous hydrate phases during setting of cement”, *Tonind.-Ztg.*, V. 90, 1966, pp. 449-457.
18. Regourd, M., “Structure and behaviour of slag Portland cement hydrates”, *7th International Congress on the Chemistry of Cement*, Paris, 1980, Vol. I, pp. III-2/10-III-2/26.
19. Forss, B., “F-cement, a new low-porosity slag cement”, *Sil. Ind.* V. 48, 1983, pp. 79-82.
20. Hinrichs, W. and Odler, I., “Investigation of the hydration of Portland blast furnace slag cement: hydration kinetics”, *Advances in Cement Research*, V. 2, 1989, pp. 15-20.
21. De Weerd, K. and Justnes, H., “Microstructure of Binder from the Pozzolanic Reaction between Lime and Siliceous Fly Ash, and the Effect of Limestone Addition”, *1st International Conference on Microstructure Related Durability of Cementitious Composites*, 13-15 October, 2008, Nanjing, China, RILEM Proceeding PRO 61, pp. 107-116.
22. De Weerd, K.; Justnes, H.; Kjellsen, K.O. and Sellevold, E.J., «Fly Ash-Limestone Ternary Composite Cements: Synergy Effect at 28 days”, *Nordic Concrete Research*, Publication No. 42, 2/2010, pp. 51-70 (ISBN: 978-82-8208-023-1).

23. De Weerd, K.; Kjellsen, K.O.; Sellevold, E.J. and Justnes, H., "Synergy between Fly Ash and Limestone Powder in Ternary Cements", *Cement and Concrete Composites*, V. 33, 2011, pp. 30-38.
24. De Weerd, K.; Ben Ha-Ha, M.; Le Saout, G.; Kjellsen, K.O.; Justnes, H. and Lothenbach, B., "Hydration mechanism of ternary Portland cements containing limestone powder and fly ash", *Cement and Concrete Research*, V. 41, 2011, pp. 279-291.
25. De Weerd, K.; Sellevold, E.J.; Kjellsen, K.O. and Justnes, H., "Fly ash – Limestone Ternary Cements – Effect of Component Fineness", *Advances in Cement Research*, V. 23, 2011, pp. 203-214.
26. De Weerd, K.; Justnes, H. and Kjellsen, K.O., "Synergic Effect between Fly Ash and Limestone Powder in Portland Composite Cements", XXI Nordic Concrete Research Symposium, Hämeenlinna, Finland, May 2011, *Nordic Concrete Research Publication No. 43*, pp. 297-300.
27. Lothenbach, B.; Le Saout, G.; Gallucci, E. and Scrivener, K., "Influence of limestone on the hydration of Portland cements", *Cement and Concrete Research*, V. 38, 2008, pp. 848-860.
28. De Weerd, K.; Østnor, T.A.; Justnes, H.; Ben Haha, M. and Kjellsen, K.O., "Fly ash - limestone synergy in triple cement", *1st International Conference on Concrete Sustainability*, May 27-29, 2013, Tokyo, Japan, Paper S2-2-4, 510-515 (ISBN 978-4-86384-041-6-C3050).
29. Antoni, M.; Rossen, J.; Martirena, F and Scrivener, K., "Cement substitution by a combination of metakaolin and limestone", *Cement and Concrete Research*, V. 42, 2011, pp. 1579-1589.
30. Justnes, H. and Østnor, T.A., "Durability and microstructure of mortar with calcined marl as supplementary cementing material", *XIII conference on Durability of Building Materials and Components (DBMC)*, Sao Paulo, Brazil, September 3-5, 2014, pp. 771-780
31. Justnes, H. and Østnor, T.A., "Designing Alternative Binders Utilizing Synergic Reactions", *5th International Conference on Non-traditional Cement and Concrete (NTCC2014)*, Edited by V. Bilek and Z. Keršner, 16-19 June, 2014, Brno, Czech Republic, 101-104 (ISBN 978-80-214-4867-4).
32. Shi, C., and Day, L.R., "Acceleration of the reactivity of fly ash by chemical activation", *Cement and Concrete Research*, V. 25, 1995, pp. 15-21.
33. Shi, C. and Day, L.R., "Pozzolanic reaction in the presence of chemical activators, Part I. Reaction kinetics", *Cement and Concrete Research*, V. 30, 2000, pp. 51-58.
34. Shi, C. and Day, L.R., "Pozzolanic reaction in the presence of chemical activators, Part II. Reaction products and mechanisms", *Cement and Concrete Research*, V. 30, 2000, pp. 607-613.
35. Shi, C. and Day, L.R., "Comparison of different methods for enhancing reactivity of pozzolans", *Cement and Concrete Research*, V. 31, 2001, pp. 813-818.
36. Qian, J., Shi, C. and Wang, Z., "Activation of blended cements containing fly ash", *Cement and Concrete Research*, V. 31, 2001, pp. 1121-1127.
37. Lee, C.Y., Lee, H.K. and Lee, K.M., "Strength and microstructural characteristics of chemically activated fly ash-cement systems", *Cement and Concrete Research*, V. 33, 2003, pp. 425-431.
38. Hoang, K. D., "Hardening Accelerator for Fly Ash Blended Cement", Thesis (PhD) at NTNU (Norwegian University of Science and Technology) 2012:336, 195 pp.
39. EN 934-2:2009. "European Standard: Admixtures for Concrete, Mortar and Grout. Part 2: Concrete Admixtures – Definitions, Requirements, Conformity and Labelling", *CEN (European Committee for Standardization)*, 28 pp.

40. Hoang K.D.; Geiker, M.R.; Justnes, H.; Rudberg, E. and Myrdal, R., “Hardening-Accelerator and a Method for Accelerating the Hardening of Hydraulic Binders and Mixtures Thereof”, WO2013066192 (A1) — 2013-05-10.
41. Justnes, H. and Ng, S., “Concrete Admixtures – Interactions with Cement, Supplementary Cementing Materials and Fillers”, *3rd International Symposium on Design, Performance and Use of Self-Consolidating Concrete, SCC’2014-China*, June 5-8, 2014, Xiamen, China, RILEM Proceedings PRO 93, 2014, p. 138 (ISBN 978-2-35158-143-8, e-ISBN 978-2-35158-144-5).
42. Vikan, H. and Justnes, H., “Rheology of cementitious paste with silica fume and limestone”, *Cement and Concrete Research*, V. 37, 2007, pp. 1512-1517.
43. Ng, S. and Justnes, H., “A Comparison on the Roles of Plasticizers in the Rheology and Hydration of Blended Cements”, *6th International Conference of the Asian Concrete Federation (ACF)*, 21-24 September, 2014, Seoul, South Korea, pp. 614-618.
44. Ng, S. and Justnes, H., “Rheological Properties and Early Hydration of Blended Cement Pastes with PCE Plasticizers”, *3rd International Symposium on Design, Performance and Use of Self-Consolidating Concrete, SCC’2014-China*, June 5-8, 2014, Xiamen, China, RILEM Proceedings PRO 93, pp. 162-169 (ISBN 978-2-35158-143-8, e-ISBN 978-2-35158-144-5).
45. Palacios, M.; Houst, Y.F.; Bowen, P. and Puertas, F., “Adsorption of superplasticizer admixtures on alkali-activated slag pastes”, *Cement and Concrete Research*, V. 39, 2009, pp. 670–677.
46. Kjellsen, K.O.; Detwiler, R.J. and Gjørsv, O.D., ”Back scattered electron imaging of cement pastes hydrated at different temperatures”, *Cement and Concrete Research*, V. 20, 1990, pp. 308-311.
47. Kjellsen, K.O.; Detwiler, R.J. and Gjørsv, O.D., ”Pore structure of plain cement pastes hydrated at different temperatures”, *Cement and Concrete Research*, V. 20, 1990, pp. 927-933.
48. Kjellsen, K.O.; Detwiler, R.J. and Gjørsv, O.D., “Development of microstructure in plain cement pastes hydrated at different temperatures”, *Cement and Concrete Research*, V. 21, 1991, pp. 179-189.
49. Danner, T., “Reactivity of Calcined Clays”, Thesis (PhD) at NTNU (Norwegian University of Science and Technology), 2013:218, 229 pp.
50. Angst, U. and Vennesland, Ø., “COIN P4: Operational Service Life Design, SP 4.2: Critical chloride content. State-of-the-Art”, *SINTEF Report SBF BK A07037*, 2007-12-17, 54 pp. (downloadable from www.coinweb.no)
51. Justnes, H. and Geiker, M.R., “A Critical View on Service Life Predictions based on Chloride Induced Corrosion”, *2nd International Conference on “Microdurability” (Microstructure Related Durability of Cementitious Composites)*. Amsterdam, the Netherlands, 11-13 April, 2012, 13 pp.
52. Fidjestøl, P. and Justnes, H., “Long Term Experience with Microsilica Concrete in a Marine Environment”, *Nordic Concrete Research*, Publication No. 31, 1/2004, pp. 30-39.
53. Thomas, M.D.A. and Bamforth, P.B., “Modelling chloride diffusion in concrete - Effect of fly ash and slag”, *Cement and Concrete Research*, V. 29, 1999, pp. 487-495.
54. Thomas, M.D.A.; Shehata, M.H.; Shashiprakash, S.G.; Hopkins, D.S. and Cail, K., “Use of ternary cementitious systems containing silica fume and fly ash in concrete”, *Cement and Concrete Research*, 29, 1999, pp. 1207-1214.

55. Engelsens, C.J. and Justnes, H., “CO₂-Binding by Concrete Structures during Life Cycle”, 2nd *International Congress on Durability of Concrete (2nd ICDC)*, 4-6 December 2014, New Delhi, India, Paper 65, 10 pp.
56. Visser, J.H.M., “Influence of the carbon dioxide concentration on the resistance to carbonation of concrete”, *Construction and Building Materials*, V. 67, 2014, pp. 8-13.
57. Thomas, M.D.A.; Matthews, J.D. and Haynes, C.A., “Carbonation of fly ash concrete”, 4th *CANMET/ACI International Conference on Durability of Concrete*, 2000, ACI SP-192, V. 1, pp. 539-556.
58. Hobbs, D.W., “Carbonation of concrete containing pfa”, *Magazine of Concrete Research*, V. 40, 1986, p. 143.
59. Thomas, M.D.A., “The effect of supplementary cementing materials on alkali silica reaction: A review”, *Cement and Concrete Research*, V. 41, 2011, pp. 1224-1231.
60. Bérubé, M.-A. and Duchesne, J., “Does Silica Fume merely postpone Expansion due to Alkali-Aggregate Reactivity?”, 9th *International Conference on Alkali-Aggregate Reaction in Concrete*, 27-31 July, 1992, London, 71-80.
61. Asgeirsson, H., “Silica Fume in Cement and Silane for counteracting of Alkali-Silica Reactions in Iceland”, *Cement and Concrete Research*, V. 16, 1986, pp. 423-428.
62. Fournier, B.; Nkinamubanzi, P.C. and Chevrier, R., “Comparative field and laboratory investigations on the use of supplementary cementing materials to control alkali-silica reactions in concrete”, 12th *International Conference on Alkali-Aggregate Reaction in Concrete* (ed. T. Mingshu and D. Min), V. 1, 2004, pp. 528-537.
63. Shehata, M.H. and Thomas, M.D.A., “The effect of fly ash composition on the expansion of concrete due to alkali silica reaction”, *Cement and Concrete Research*, V. 30, 2000, pp. 1063-1072.
64. Shehata, M.H. and Thomas, M.D.A., “Use of ternary blends containing silica fume and fly ash to suppress expansion due to ASR in concrete”, *Cement and Concrete Research*, V. 32, 2002, pp. 341-349.
65. Thomas, M.D.A. and Innes, F.A., “Effect of slag on expansion due to alkali aggregate reaction in concrete”, *ACI Materials Journal*, V. 95 (6), 1998
66. Bleszynski, R.; Hooton, R.D.; Thomas, M.D.A. and Rogers, C.A., “Durability of ternary blend concrete with silica fume and blast-furnace slag: Laboratory and exposure site studies”, *ACI Materials Journal*, V. 99, 2002, pp. 499-508.
67. Ramlochan, T.; Thomas, M.D.A. and Gruber, K.A., “The effect of metakaolin on alkali-silica reaction in concrete”, *Cement and Concrete Research*, V. 30, 2000, pp. 339-344.
68. Chappex, T. and Scrivener, K.L., “Alkali fixation of C–S–H in blended cement pastes and its relation to alkali silica reaction”, *Cement and Concrete Research*, V. 42, 2012, pp. 1049–1054.
69. Chappex, T. and Scrivener, K.L., “The influence of aluminum on the dissolution of amorphous silica and its relation to alkali silica reaction”, *Cement and Concrete Research*, V. 42, 2012, pp. 1645–1649.
70. Chappex, T. and Scrivener, K.L., “The Effect of Aluminum in Solution on the Dissolution of Amorphous Silica and its Relation to Cementitious Systems”, *J. Am. Ceram. Soc.*, V. 96, 2013, pp. 592–597.
71. Favier, A.R.; Dunant, C.F. and Scrivener, K.L., “Alkali silica reaction mitigation properties of ternary

- blended cements with calcined clay and limestone”, 2nd *International Congress on Durability of Concrete (2nd ICDC)*, 4-6 December 2014, New Delhi, India, Paper 11, 7 pp.
72. Irassar, E.F., “Sulfate attack on cementitious materials containing limestone filler – A review”, *Cement and Concrete Research*, V. 39, 2009, pp. 241-254.
 73. Duchesne, J., “Deterioration of concrete by the oxidation of sulphide minerals in the aggregate”, 1st *International Congress on Durability of Concrete (1st ICDC)*, Trondheim, Norway, 18-21 June, 2012 (ISBN 978-82-8208-031-6).
 74. Scrivener, K.L., “Understanding and establishing sulfate resistance of cementitious materials”, 1st *International Congress on Durability of Concrete (1st ICDC)*, Trondheim, Norway, 18-21 June, 2012 (ISBN 978-82-8208-031-6). KN2, 8 pp.
 75. Müllauer, W.; Beddoe, R.E.; Hilbig, H. and Heinz, D., “Mechanisms of sulfate attack for plain and fly ash cements at different storage temperatures and sulfate concentrations”, 1st *International Congress on Durability of Concrete (1st ICDC)*, Trondheim, Norway, 18-21 June, PP3, 12 pp.
 76. Carlsen, R. and Vennesland, Ø., “Sulfate and sea water durability of concrete” (In Norwegian), *SINTEF Report STF65 F82010*, 1982.
 77. Fidjestøl, P. and Frearson, J., “High-performance concrete using blended and triple blended binders”, *ACI International Conference on High Performance Concrete*, Singapore, ACI SP-149, 1994.
 78. Kunther, W.; Lothenbach, B. and Scrivener, K.L., “Influence of bicarbonate ions on the deterioration of mortar bars in sulfate solutions”, *Cement and Concrete Research*, V. 44, 2013, pp. 77-86.
 79. Dehwah, H.A.F., “Effect of sulfate concentration and associated cation type on concrete deterioration and morphology changes in cement hydrates”, *Construction and Building Materials*, V. 21, 2007, pp. 29-39.
 80. Ghafoori, N.; Najimi, M.; Diawara, H. and Islam, M.S., “Effects of class F fly ash on sulphate resistance of Type V Portland cement concretes under continuous and interrupted sulfate exposures”, *Construction and Building Materials*, V. 78, 2015, pp. 85-91.
 81. Hossack, A.M. and Thomas, M.D.A., “Varying fly ash and slag contents in Portland limestone cement mortars exposed to external sulfates”, *Construction and Building Materials*, V. 78, 2015, pp. 333-341.
 82. Abdalkader, A.H.M.; Lynsdale, C.J. and Cripps, J.C., “The effect of chloride on cement mortar subjected to sulfate exposure at low temperature”, *Construction and Building Materials*, V. 78, 2015, pp. 102-111.
 83. De Weerd, K.; Justnes, H. and Geiker, M.R., “Changes in the phase assemblage of concrete exposed to sea water”, *Cement and Concrete Composites*, V. 47, 2014, pp. 53-63
 84. Rønne, M.; Hammer, T.A.; Justnes, H.; Meland, I.S. and Jensen, V., «Chemical Stability of LWAC Exposed to High Hydration Generated Temperatures”, *International Symposium on Structural Lightweight Aggregate Concrete*, Sandefjord, Norway, 20-24 June, 1995, pp. 505-516.
 85. Ramlochan, T.; Zacarias, P.; Thomas, M.D.A. and Hooton, R.D., “The effect of pozzolans and slag on expansion of mortars cured at elevated temperature. Part I. Expansive behavior”, *Cement and Concrete Research*, V. 33, 2003, pp. 807-814.
 86. Ramlochan, T.; Thomas, M.D.A. and Hooton, R.D., “The effect of pozzolans and slag on expansion of mortars cured at elevated temperature. Part II. Microstructural and microchemical investigations”, *Cement and Concrete Research*, V. 34, 2004, pp. 1341-1356.

-
87. Jolicoeur C.; To T.C.; Benoît, É.; Hill, R.; Zhang, Z. and Pagé, M., “Fly Ash Carbon Effects on Air-Entrainment: Fundamental Studies on their Origin and Chemical Mitigation”, *World of Coal Ash (WOCA)*, May 4-7, 2009, Lexington, KY, USA, 23 pp.
 88. Panesar, D.K. and Chidiac, S.E., “Multi-variable statistical analysis for scaling resistance of concrete containing GGBFS”, *Cement & Concrete Composites*, V. 29, 2007, pp. 39-48.
 89. Giergiczny, Z.; Glinicki, M.A.; Sokolowski, M. and Zielinski, M., “Air void system and frost-salt scaling of concrete containing slag-blended cement”, *Construction and Building Materials*, V. 23, 2009, pp. 2451-2456.
 90. Utgennant, P., “The influence of ageing on the salt-frost resistance of concrete”, Thesis (PhD) 2004, Report TVBM-1021, Division of Building Materials, Lund Institute of Technology, Lund University, Sweden, 346 pp (ISBN 91-628-6000-3).
 91. Sisomphon, K.; Copuroglu, O. and Fraaij, A.L.A., “Development of blast furnace slag mixtures against frost salt attack”, *Cement & Concrete Composites*, V. 32, 2010, pp. 630-638.

Specification of building materials for in service durability

C. Gehlen, C. Thiel

Department of Civil, Geo and Environmental Engineering, Technical University of Munich.

Abstract

To assess whether a structural element made of a given building material can withstand the expected mechanical load and environmental exposure in service, designers need information on the material resistances and loads as well as the local conditions. The durability of a building material in the structure can only be assessed if these factors are taken into account. Usually, the material resistances are obtained from laboratory tests. However, the performance of materials under standardized laboratory conditions differs from those occurring in the field. This paper considers this assessment problem and develops a solution strategy based on carbonation-induced corrosion as an example.

Keywords: durability design, concrete, reinforcement, material resistances, modeling.

1. Introduction

Infrastructure made of structural concrete is an essential part of our modern built environment. Supply of goods and services, individual and public transport, all services are very dependent on the technical reliability of concrete structures.

Not only is the preservation of the existing built infrastructure a tremendous task, but also the resource-saving construction of new, permanent infrastructure. The current high degree of worldwide construction activity is driven mainly by the population explosion and the dramatically increasing urbanization. More than 1.7 billion people in the world are under 20 years old, and in future most of them will move to the rapidly growing urban centres. There, all these people will require housing and infrastructure, offices and production facilities, food, consumables, water and energy supplies, as well as schools, universities and hospitals. In just a few years, a construction volume will be required which amounts to more than the total volume created over 150 years since 1800.

Sustainable construction and economical preservation of structures are required to ensure the availability of infrastructure at the high level needed. Premature failure or unexpectedly high maintenance costs can result in economic expenditure amounting to billions of Euros.

Structural elements are generally subjected to mechanical loads and the action of the service environment. Mechanical, thermal, chemical and hygric actions always occur together and affect the serviceability, structural capacity, deformation, and the building-physics of structural elements over time, Figure 1. Consequently, the design and dimensioning of each structural element must take the provision of adequate durability into account.

The underlying interactions between simultaneous chemical and physical processes in the micro-structure of mineral and metallic building materials are not fully understood. In view of the importance of this, there is an urgent need for research: how does the material behave regarding effects which limit durability. What

are the decisive factors affecting and limiting durability? How should the material be designed in future? How can the material be characterized by fair standard tests and qualified for particular applications? How can sufficient durability be proven? How can the durability of reinforced structures be assessed as a whole? How can existing structures be efficiently protected against damaging influences or repaired?

At present, the durability of the majority of civil engineering structures is ensured by approximate prescriptive rules based on experience in field practice. The disadvantage of this approach is that new materials cannot be taken into account, as well as the effect of changing exposure conditions or load during service cannot be estimated (e.g. conversion of buildings, increasing heavy goods traffic, climate change).



Figure 1: Mechanically loaded concrete column, affected by chloride in de-icing salts which has induced corrosion of rebar and freeze-thaw scaling, photo Gehlen

Moreover, studies have shown that classical durability design concepts, in which requirements on concrete composition and cover are based on decades of experience, lead, depending on the exposure class, to uneconomic solutions or solutions which are uncertain, [1]. This approach stifles innovation, [2], and is hard to verify in the field. It is almost impossible to estimate how deviations from the requirements affect the actual component behaviour.

On the contrary, performance-based durability design provides a justified calculation of the time-dependent behaviour of structural components taking statistical uncertainties into account, [3].

For these alternative, probabilistic-based approaches, a probability of occurrence of an unwanted structural condition (failure) p_f remains below a given target probability p_{target} within the prescribed service life (Eq. 1). The occurrence of an unwanted structural condition (failure) is defined when a limiting state is exceeded, i.e. the stress S exceeds the resistance R , Eq. 1.

$$p_f = p\{R - S < 0\} \leq p_{target} \tag{1}$$

The implementation and fulfilment of Eq. 1 is illustrated in Fig. 2.

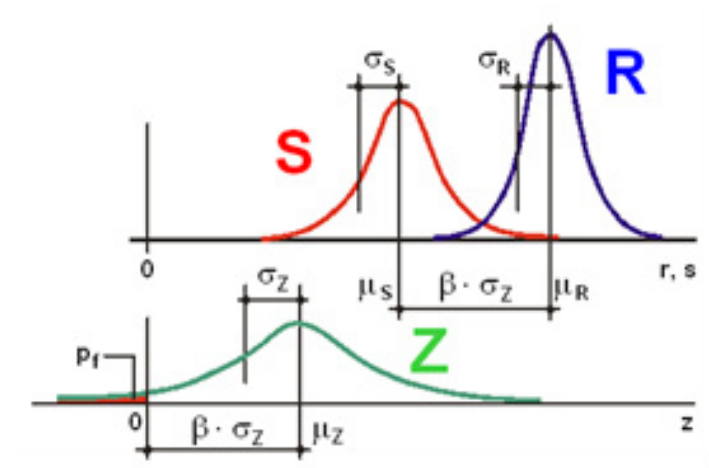


Figure 2: Definition of the probability of occurrence (failure) p_f (μ : mean; σ : standard deviation, β : reliability index) [4].

Since both, S and R , are distributed variables, the result Z is also a distributed variable. The probability of occurrence (failure) is defined by the region of Z for negative values. However, rather than the probability of failure, the reliability index β is commonly used. The reliability index is the factor by which the standard deviation of the variable Z is multiplied to yield the distance of the mean value from zero. The probability of failure p_f and the reliability index β may be calculated for normal distributions of R and S by using Eq. 2 and the mathematical definition of the standard normal distribution Φ .

$$p_f = \Phi\left(-\frac{\mu_Z}{\sigma_Z}\right) = \Phi(-\beta) \quad (2)$$

In the case of a full probabilistic calculation in accordance with Eqs 1 and 2, all the parameters in the stress and resistance models must be defined as statistical parameters each with mean value, standard deviation and distribution type (e.g. [4]).

In field practice, however, the probabilistic analysis is only required in special cases. Usually, the full probabilistic calculation is adapted thereby becoming semi-probabilistic. In this case, stress and resistance are introduced as characteristic variables and the scatter taken into account by partial safety factors, Eq. 3.

$$\frac{R_k}{\gamma_M} - S_k \cdot \gamma_E \geq 0 \quad (3)$$

Here R_k is the characteristic value for resistance, S_k the characteristic value for stress, γ_M is the partial safety factor for the material resistance and γ_E the partial safety factor for the environmental stress.

Often, complex models with different parameters are required. In case of carbonation or chloride-induced corrosion, transport models are generally used for the time until depassivation (initiation phase) and afterwards deterioration models for the propagation phase. Both these phases must be taken into account for the computation of the limiting load-bearing capacity. Eq. (4) can be used to prove that the chosen design provides the target service life, [4].

$$t_{SL} = t_{ini} + t_{prop} \geq t_{SL,target} \quad (4)$$

Here t_{SL} is the service life of structural member, $t_{SL,target}$ the target service life, t_{ini} the time to depassivation and t_{prop} the corrosion period to the ultimately acceptable service condition.

An important advantage of probabilistic durability design compared to prescriptive design is that the service life prediction can be significantly improved during the actual service of the structure, thus becoming more

accurate. The distribution of concrete cover and the penetration of depassivating substances in concrete (for example CO₂) can be determined by measurements on the structure during service. Thus as time passes, the prognosis of service life or the reliability index expected at the end of the target service life can be calculated with increasing accuracy. Moreover, a fundamental basis is available for expert decisions regarding economical concepts for tailored maintenance and repair throughout the target service life of the structure.

In the following, carbonation-induced corrosion is used to demonstrate the diffusion/chemical and electrochemical mechanisms (transport- and deterioration models) and the corresponding models for durability design.

2. Mechanisms

The evolution of the carbonation process is summarized schematically in Fig. 3.

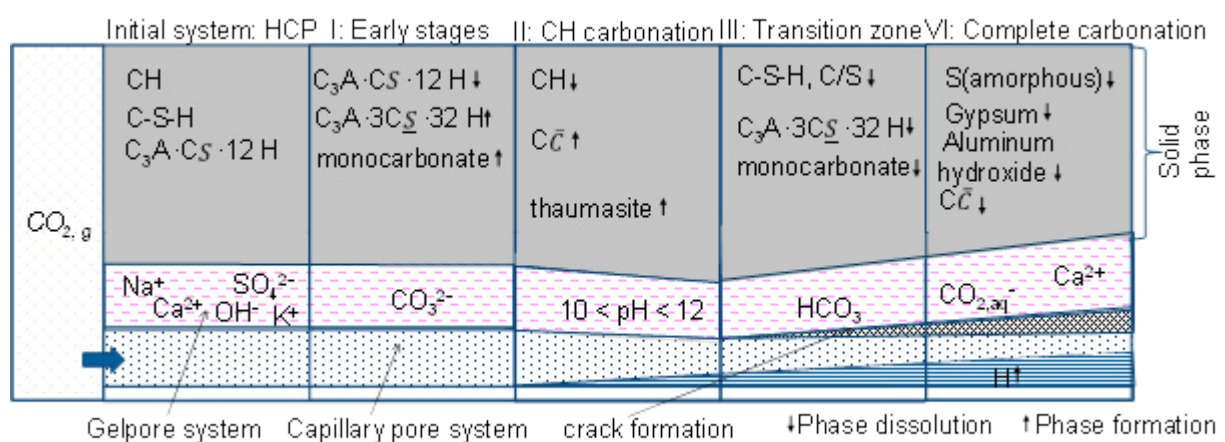


Figure 3: Phase transformations during carbonation according to [5]

Gaseous CO₂ diffuses through the pores in the hardened cement paste (HCP) matrix and dissolves in the pore solution forming carbonic acid. Consequently, dissolved calcium in the alkaline pore solution reacts to form calcium carbonate. The carbonation reactions continue as long as sufficient calcium is available in the pore solution. This is maintained by the dissolution of, in particular, portlandite and the C-S-H phases. Other phases in the hardened cement paste matrix also undergo carbonation. During carbonation the C/S ratio of the C-S-H phases progressively decreases owing to decalcification until ultimately complete degradation occurs. In addition, other phases in HCP carbonate as well. Phases such as monocarbonate, strätlingite and thaumasite can form as intermediate products which are finally followed by calcite, Al(OH)₃, gypsum and an amorphous SiO₂ gel.

The carbonation kinetics of hcp depends on concrete moisture content as well as the concentration and the pressure of CO₂. The material resistance itself mainly depends on the pore structure of the HCP matrix and the amount components that can carbonate [6]. Concrete with water-saturated pores carbonates very slowly because the pore water inhibits the penetration of CO₂ gas into the concrete [7]. Concrete carbonation at ambient relative humidities below about 30% is very slow because a water film is not available for the dissolution of CO₂. The most rapid carbonation of concrete occurs at a relative humidity near 50% [8].

After the carbonation front has reached the reinforcement corrosion can be initiated. The corrosion process takes place in two sub-processes: At the anode, iron ions pass into solution, separating from the electrons. They are converted into rust products in further reactions. At the cathode, electrons, water and oxygen are converted into hydroxyl ions. The cathodic process does not cause any deterioration of the steel.

These hydroxyl ions transport the negative charge in the electrolyte through the electrical field created between the anode and the cathode, towards the direction of the anode. Near the anode, they react with the iron ions in solution. Depending on moisture and aeration conditions, this intermediate product may continue to react, producing the final corrosion products. The individual processes are in fact much more complicated.

- In order for the corrosion process to take place, a number of preconditions for the anodic and cathodic process and for the electrolytic process must be satisfied simultaneously:
- There must be differences in potential between anodes and cathodes. The preconditions for sufficiently large differences in potential are, however, usually met.
- Anodic and cathodic surface zones of the steel must be connected electrically and electrolytically, i.e. a flow of electrons and ions between them must be possible. The metallic connection necessary for an electron flow from the anode to the cathode is provided by the reinforcement system in the reinforced concrete. The electrolytic connection is represented by the concrete. This must, however, be sufficiently moist, since otherwise there can be virtually no migration of ions. In dry interior situations, for example, the electrolytic conductivity of the concrete is too low to permit corrosion of the reinforcement, even if the carbonation front reaches the reinforcement, leading to loss of alkaline protection.
- Anodic dissolution of iron must be possible due to depassivation of the steel surface. The cathodic process can, however, take place even in zones with a passive steel surface.

Sufficient oxygen must be available at the cathode. There must be continuous diffusion of oxygen from the surface of the concrete to the steel surface acting as the cathode. There is therefore practically no risk of corrosion to reinforced concrete components which are permanently and completely immersed in (deep) water.

If all conditions for corrosion are fulfilled simultaneously, the reinforcement will corrode. If only one of the conditions can be eliminated, corrosion can be prevented or halted. Fundamental repair principles may be deduced from this knowledge.

If depassivation is caused by carbonation of the concrete generally uniform corrosion takes place. This leads to the formation of micro-corrosion-cells, consisting of pairs of immediately adjacent anodes and cathodes. These are microscopic in size, so that externally they appear to produce uniform removal of the steel.

3. Models

In [9] it was proposed to describe mathematically the evolution of carbonation depth $x_c(t)$ vs time t by utilizing a Fick's law diffusion model, Eq. 5,

$$x_c(t) = k_{NAC} \cdot \sqrt{k_e \cdot k_c \cdot k_a} \cdot \sqrt{t} \cdot W(t) \text{ with } k_a = \frac{c_a}{c_t} \quad (5)$$

where $x_c(t)$ [mm] is the carbonation depth at time t , k_{NAC} [$\sqrt{\text{mm}^2/\text{year}}$] the carbonation rate measured under standard laboratory test conditions on specimens exposed to a standard climate at atmospheric pressure, k_e [-] a function accounting for the environmental effect of relative humidity (RH_a) on carbonation, k_c [-] a function for the effect of curing/execution on the carbonation, k_a [-] a function describing the effect of CO_2 -concentration in the ambient air on carbonation, C_a [kg/m^3] the CO_2 concentration in the ambient air, C_t [kg/m^3] the CO_2 concentration during the concrete test, t [year] the exposure time, $W(t)$ [-] a function describing the effect of wetting events which partly block CO_2 transport. The last parameter becomes more relevant with increasing carbonation depth and therefore with increasing time. More details on the

functions can be found in [9].

If $x_c(t)$ equals the concrete cover, depassivation of rebar takes place and initiation period t_{ini} is over. Corrosion of reinforcement can then occur, i.e. propagation starts. If a certain degree of propagation is acceptable (for example until the concrete cover cracks), a propagation model is needed. An example of a simple one is given in Eq. (6).

$$x_{corr}(t_{prop}) = V_{corr} \cdot t_{prop} \quad (6)$$

Here $x_{corr}(t_{prop})$ [mm] is the uniform corrosion penetration depth, V_{corr} [$\mu\text{m}/\text{year}$] the corrosion rate and t_{prop} [year] the propagation period, i.e. the time period after depassivation during which the rebar can corrode.

Depending on the specifically chosen design criteria, i.e. depending on the structural condition, the designer wants to avoid unwanted structural conditions. Possible unwanted conditions are, for example: Rebars located in carbonated concrete (limit state: depassivation) or corrosion attack on rebars with depths larger than $x_{corr,max} = 100 \mu\text{m}$.

5. Material tests

Material testing plays a central role in the verification of the durability of building materials which means that material compliance tests must be performed. Compliance tests are used to determine reliably the performance of the material, e.g. strength, or carbonation resistance. A compliance test must fulfil the following requirements:

1. Accurate and precise; every measurement method produces errors which are, in general, systematic or random. Systematic errors can be minimized by appropriate calibration, choice of equipment and careful measurement. Unavoidable systematic errors due to variations in experimental conditions or inaccurate measuring equipment can be taken into account by suitable correction factors or equations [4]. In addition, the results of measurements scatter around a true value. Although such random errors cannot be avoided, their effect can be calculated. In this case, the precision of the test method is decisive. The real difference between two materials or a material from a specified limiting value can be determined, [10]. The decisive factor here is the precision of reproducibility as determined in round robin tests.
2. Reliable results consistent with observations in-field practice; a procedure is only suitable as a compliance test if its results agree with the corresponding observations in the field, i.e. the transferability of the results to field practice should not be worsened by acceleration factors which do not occur in service. A compromise must be found between testing on the safe side and the consideration of the real, highly scattered parameters.
3. Fast and easy to perform; a robust test procedure should be performed easily by appropriately trained laboratory staff. In addition, time is crucial in construction practice. To minimize disruption of the production process, the test should be as fast as possible and commercially available.
4. Cost-effective; in order to increase the acceptance of a compliance test, the cost should also be kept as low as possible.

Generally, direct or indirect test methods may be applied. Direct test methods reproduce the real, almost unmodified behaviour of the material in field practice for given boundary conditions (production, storage conditions, test procedure). Natural conditions are simulated over a long time period or accelerated in a compliance test by using extreme conditions (e.g. simulation of extreme freeze-thaw variations with high minimum temperature and constant moisture supply for the determination of freeze-thaw resistance).

In the case of indirect test methods, a property A of the material is measured which is then used to determine a different property B which is not (directly) measured. This is only possible if a mathematical relationship between the two quantities A and B is known. For example, the freeze-thaw resistance of hardened concrete can be determined from the amount of entrained air measured in the fresh concrete or the resistance of concrete to chloride diffusion determined from the measurement of the chloride migration coefficient. The DuraCrete project drew up the state-of-the-art of compliance testing in 1997 [11] and analysed suitable test methods with regard to duration, reproducibility, simplicity and commercial availability [12]. Standard committee CEN TC51(CEN TC 104)/WG12/TG5 created a series of technical specifications prEN 12390-XX in which generally accepted test procedures are described for the measurement of material resistances against various forms of environmental attack. The tests measure the relevant resistances directly or indirectly, and are performed either under natural or accelerated conditions.

DIN EN 12390-10 [13] can be applied for the direct determination of carbonation resistance under natural conditions. The results obtained from this laboratory test can be transferred into a carbonation rate k_{NAC} . In [14], the measurement and subsequent classification of concrete material according to test specification [13] is described in detail.

6. Transfer methods

For design purposes, the laboratory performance must be transferred to field performance. By utilizing models, outlined in Section 3 and described more in detail in [9], and introducing (partial) safety factors, Eq. (3), Greve-Dierfeld and Gehlen [15] developed and proposed a design chart. In this chart material laboratory performance is first transferred into the corresponding field performance and then related to the minimum concrete cover necessary to avoid unwanted structural conditions during a specified period of service. By using this chart, the depassivation of steel in structural members due to carbonation can be avoided for a targeted reliability level of $\beta = 1.5$, Fig. 4, which corresponds to a probability of occurrence of approximately 7%.

This semi-probabilistic based design starts with information on the mean material resistance (in this case mean carbonation rate) k_{NAC} measured in the laboratory. In addition, information is required on the mean specified curing time t_i [d], the expected mean relative humidity of ambient air RH_a [% RH] at the location of the structure, the expected mean amount of precipitation expressed by the weather function, i.e. the expected time of wetness ToW and probability of driving rain p_{dr} on location, and the targeted design service life which can range between 10 to 100 years. The chart yields the minimum concrete cover which is needed to achieve the targeted design service life with material and execution selected at a reliability level of $\beta = 1.5$. As an example, the following specific design situation is considered.

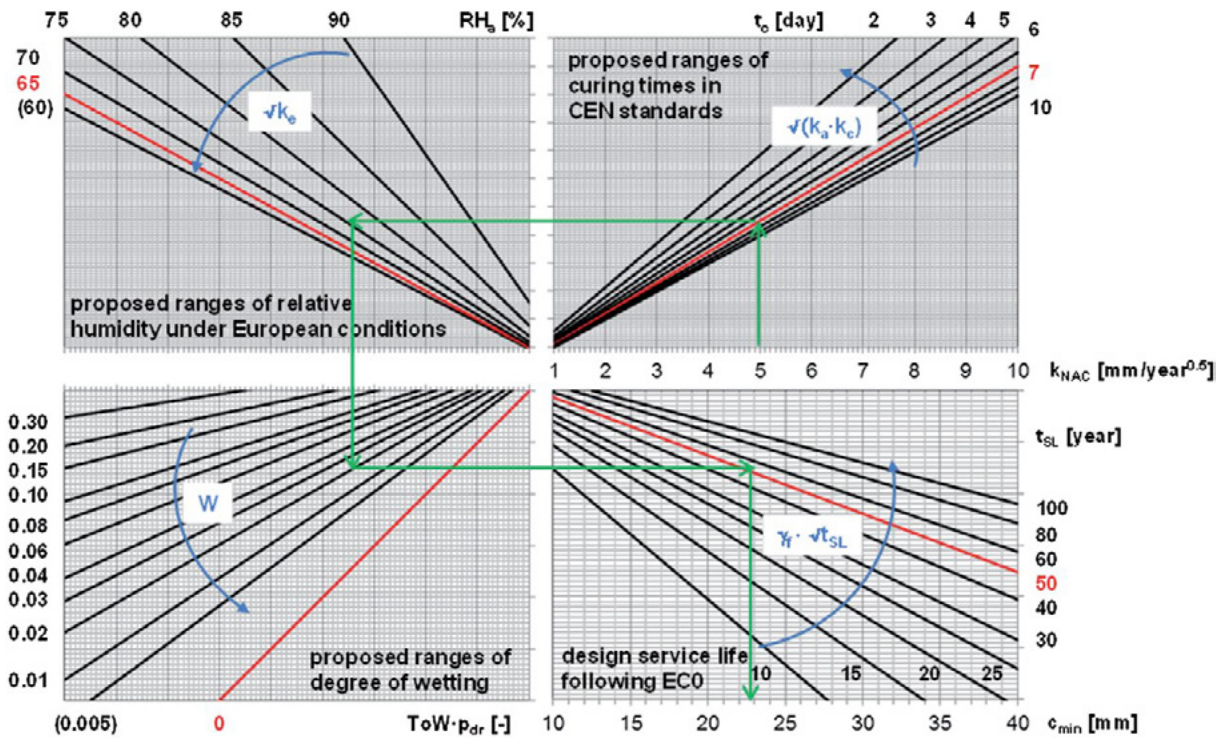


Figure 4: Design chart for carbonation of structural concrete members, target reliability level $\beta = 1.5$, according to [15]

7. Field study

The subject of this study is a reinforced concrete pillar which has already been damaged by carbonation-induced reinforcement corrosion, Fig. 5. Based on the apparent corrosion damage, the remaining service life (before repair) was rated as “expired”. The investor wanted an “extension of the remaining service life” by 50 years, i.e. the quality and thickness the concrete replacement was to be designed for a total of 50 years.

The repair material, whose composition was unknown (trade secret), was subjected to a standardized carbonation test according to DIN EN 12390-10 [13] which yielded a mean carbonation rate of $k_{NAC} = 5.0 \text{ mm}/\sqrt{a}$.

In this case, the curing time t_c was specified at 7 days by an expert planner. According to data provided by the weather service, the average ambient humidity RH_a expected at the location is 75% RH, the expected mean probability of driving rain (north exposure) p_{dr} is 12%, and the expected average rain frequency ToW (proportion of days in the year with precipitation $b_{rain} \geq 2.5 \text{ mm}$) is 17%. The required minimum layer thickness of the replacement concrete was then determined from this data using a design nomogram, Fig. 4. The input values for the nomogram must always be mean values. The safety (by means of partial safety factors) is included by changing the slope of the parameter curves, in order that the required minimum layer thickness of the replacement concrete is obtained.

In the present example, the required minimum layer thickness $d_{c,min}$ is 23 mm, see Figure 4. In order that the minimum layer thickness, like the minimum concrete cover, is defined as a quantile value (usually 95%) a tolerance must be allowed for; fulfilled by 95 % of all cases on the construction site. The tolerance for layer thickness depends on the substrate and the type of execution and is usually between 10 mm and 15 mm.

According to the expert planning described above, the executing company has to use a product of specifically tested performance ($k_{NAC} \leq 5.0 \text{ mm}/\sqrt{a}$). It should be noted that the requirements regarding curing time ($t_c \geq 7\text{d}$) and minimum layer thickness ($d_{c,min} = 23 \text{ mm}$) specified by the designer are to be met and an

adequately tolerance taken into account. In this specific case a nominal cover of 35 mm was appropriate.



Figure 5: Reinforced concrete pillar, photo Gehlen

8. References

- [1] Gehlen, C.; Schießl, P.; Schießl-Pecka, A. (2008): Hintergrundinformationen zum Positionspapier des DAfStb zur Umsetzung des Konzepts von leistungsbezogenen Entwurfsverfahren unter Berücksichtigung von DIN EN 206-1, Anhang J für dauerhaftigkeitsrelevante Problemstellungen. Beton- und Stahlbetonbau, 103, 12 (in German).
- [2] Bickley, J.A.; Hooton, D.; Hover, K.C. (2006): Performance specifications for durable concrete, Concrete International 28(9): 51-57
- [3] Bunte, D. (1994): Zum karbonatierungsbedingten Verlust der Dauerhaftigkeit von Außenbauteilen aus Stahlbeton, PhD-Thesis, Technische Universität Braunschweig (in German).
- [4] Gehlen, C. (2000): Probabilistische Lebensdauerbemessung von Stahlbetonbauwerken – Zuverlässigkeitsberechnungen zur wirksamen Vermeidung von Bewehrungskorrosion, Deutscher Ausschuss für Stahlbeton, Heft 510, Beuth-Verlag, Berlin (in German).
- [5] Glasser, F. P., Matschei, T. (2007): Interactions between Portland Cement and Carbon Dioxide. 12th Int. Cong. on the Chem. of Cem., Montreal, Canada, 8-13 July 2007.
- [6] Papadakis, V.G.; Vayenas, C. G.; Fardis, M. N. (1991): Fundamental modeling and experimental investigation of concrete carbonation, ACI Material Journal, 1, pp 363-373.
- [7] Verbeck, G. J. (1958): Carbonation of Hydrated Portland Cement. In: ASTM Special Technical Publication No. 205 pp. 17-36.
- [8] Papadakis, V.G.; Fardis, M. N., Vayenas, C. G. (1992): Effect of composition, environmental factors and

cement-lime mortar coating on concrete carbonation, *Materials and Structures*, 25, pp. 293-304

[9] Greve-Dierfeld v., S.; Gehlen, C. (2016): Performance based durability design, carbonation part 1 - Benchmarking of European present design rules. *Structural Concrete*, 17: 309-328. DOI: 10.1002/suco.201600066

[10] DIN ISO 5725-2 (2002): Accuracy of measurement methods and results - Part 2: Basic method for the determination of repeatability and reproducibility of a standard measurement method, Beuth Verlag, Berlin.

[11] DuraCrete (1997): Summary and Suitability of Existing Compliance Tests. Brussels: European Union – Brite EuRam, 1997. - Project BE95-1347, Document BE95-1347/R6, 1

[12] Gehlen, C.; Ludwig, H.M. (1999): Compliance Testing for Probabilistic Design Purposes. Brussels: European Union – Brite EuRam, 1999. - Project BE95-1347, Document BE95-1347/R8,

[13] DIN EN 12390-10 (2019): Determination of the carbonation resistance of concrete at atmospheric levels of carbon dioxide, Beuth Verlag, Berlin.

[14] Greve-Dierfeld v., S.; Gehlen, C. (2016), Performance-based durability design, carbonation part 2 – Classification of concrete. *Structural Concrete*, 17: 523–532. DOI: 10.1002/suco.201600067

[15] Greve-Dierfeld v., S.; Gehlen, C. (2016), Performance-based durability design, carbonation, part 3: PSF approach and a proposal for the revision of deemed-to-satisfy rules. *Structural Concrete*, 17: 718–728. DOI: 10.1002/suco.201600085

Parallel session contributions

Design of reinforced concrete slabs with consideration of the construction joints

V. Kurochkina¹, I. Yakovleva², A. Deineko³, A. Starostin⁴

¹Dr., Associate Professor, , Department of Engineering Survey and Geoecology, National Research Moscow State University of Civil Engineering, 26, Yaroslavskoe shosse, Moscow, 129337 Russia, kurochkina@mgsu.ru

²Ph.D. Student, Senior Lecturer, , Department of Engineering Survey and Geoecology, National Research Moscow State University of Civil Engineering, 26, Yaroslavskoe shosse, Moscow, 129337 Russia, YakovlevaIYU@mgsu.ru

³Deputy Director for Science and Technology, Spectrum Group of Companies, Building 15, Complex 29, Academica Tupoleva Embankment, Moscow, 105005, Russia, deineko@spgr.ru

⁴Head of Architectural and Civil Engineering Group, Spectrum Group of Companies, Building 76, Letter "A", 7th Line of Vasilievskiy Island, St. Petersburg, 199178, Russia, Starostin@spgr.ru.

Abstract When erecting monolithic reinforced concrete slabs, construction joints have to be installed. Construction joints are the area of weakness of the construction. The evidence from construction practice shows that the compliance with the correct technology of the installation of the construction joint according to the regulations is not a sufficient condition to ensure the strength balance of reinforced concrete slabs. The article considers approaches to calculations of monolithic reinforced concrete slabs taking into account construction joints. The relevance of the task is determined by the fact that the correct calculation of construction joints determines the conformity of design and actual characteristics of the in-situ reinforced concrete constructions as a whole. The problem of the monolithic slabs construction joints was considered in one of the residential buildings under construction. In course of construction, pre-construction land surveys were carried out in the areas of the construction joints installation. Calculations of reinforced concrete structures using finite element method were also performed. As a result of the study, the actual deflections of the floor slabs in the areas of the construction joints were measured, and calculations were made using the finite element method of the same floor slabs, both those erected only a short time ago and those erected in stages, considering the construction joints. The difference between the calculated and actual deflections is conditioned upon the inaccurate conformity of the design diagram (mathematical model) of the real reinforced concrete construction, and its erection and operation conditions. It should be noted that the deflection of horizontal reinforced concrete constructions is only one of the parameters of the stress-strain state, which is best measured. It is shown that if the deflection of a real reinforced concrete construction does not correspond to the estimates, the other parameters of the stress-strain state will also differ from the estimates. The field data shows that the vertical construction concrete joints in the slabs weaken their solidity. However, the installation of joints is necessary due to organization and techniques issues. What is more, their location can be predicted at the stage of development of the project documentation.

Keywords: construction concrete joints, reinforced concrete constructions, framed buildings, concrete slabs deflections, deformations, finite element method, solid compositional modelling of reinforced

concrete.

1. Introduction

Currently, monolithic buildings are very common. The use of in-situ reinforced concrete constructions allow to construct a building of almost any configuration and height (Fig. 1). The frame of the building is often made of in-situ reinforced concrete constructions, consisting, as a rule, of walls, columns and concrete floors.

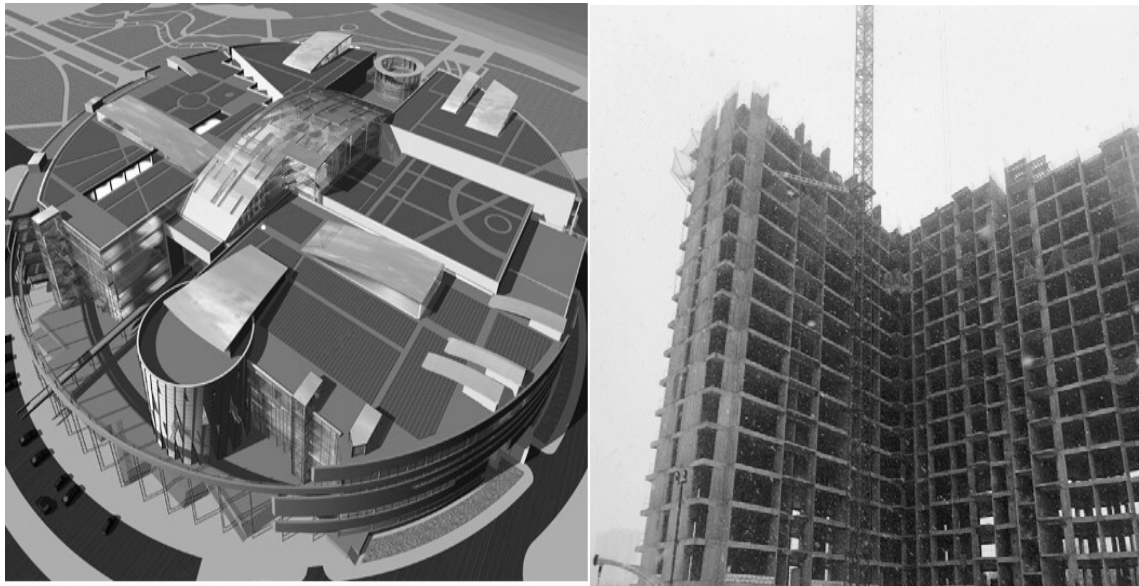


Figure 1: Monolithic frame buildings.

Wherein, it is impossible to install all monolithic constructions at the same time, therefore, construction is carried out in a specific sequence. As a rule, the foundation comes first, then vertical basement structures (walls, columns, piers), then the concrete floor of the basement, the walls of the next floor, and so on. As a result, it is necessary to install horizontal and vertical joints. At the same time, if the installation of horizontal construction joints [1] is often provided by the project, then vertical construction joints arise unplanned, directly during in-situ floor slabs concrete works.

According to common standard 70.13330.2012, installation of construction joints has requirements. The surface of construction joints, installed when pouring concrete intermittently, shall be perpendicular to the axis of the concreted columns and beams, the surface of the slabs and walls. It is allowed to keep pouring concrete when it reaches strength of at least 1.5 MPa. It is allowed to install construction joints in coordination with the design contractor when pouring concrete:

- in columns and piers – at the elevation of the top of the foundation, the bottom of the sills, beams and crane cantilevers, the top of the crane beams, the bottom of the column's beds;
- large beams, integrally connected to the floor slabs – 20–30 mm below the elevation of the lower surface of the slab, and if there are capitals in the slab – at the lower elevation of the capitals of the slab; - flat slabs – in any place parallel to the smaller side of the slab;
- ribbed coatings – in the direction parallel to the secondary girders;
- separate beams – within the middle third of the span of the beams, in the direction parallel to the main beams (girders) within two middle quarters of the span of the girders and slabs;

- bulk concrete, arches, vaults, tanks, bunkers, hydraulic structures, bridges and other complex engineering structures and constructions – in the places specified in the project.

In practice, the design contractors recommend installing construction joints in $1/3-1/4$ of the span, which does not contradict common standard 70.13330.2012. The design of the construction joint (Fig. 2) shall be given in the work production plan.

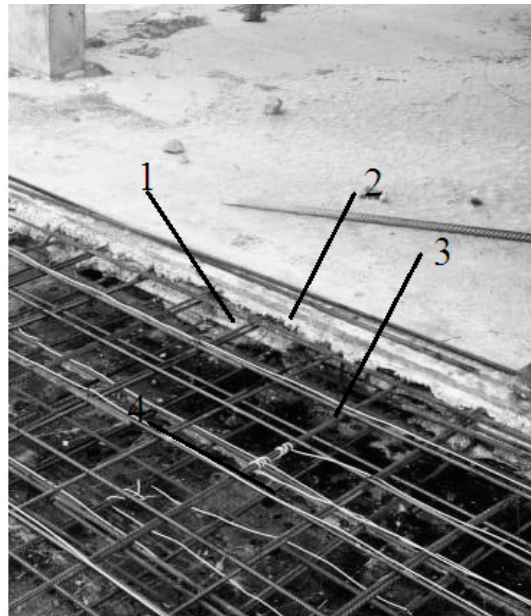


Figure 2: Construction joint structure: 1 - metal grid; 2 - protective concrete layer; 3 - top reinforcement; 4 - bottom reinforcement.

Many authors [2–11] consider the construction joint installation procedure. In their works, they emphasize that the joint shall be cleaned of dirt and garbage, rinsed with water and dried with a stream of air. Also, the authors cite laboratory studies of various constructions that confirm the reduction in strength and stiffness characteristics, as a result, deformations occur in places where the joints are made. The authors also note that when designing a monolithic building, it is calculated as a complete monolithic one.

Authors [8,9], describing the structure of construction joints in the base plates, come to the conclusion that “the ideal position of the concrete joint shall coincide with the position of the zero transverse force of the structure, i.e. the joint is installed in the place where the transverse force is minimal, and better where it is equal to zero. This is determined by the results of the calculation, namely, by the diagram of transverse forces”. The authors [2–12] concur that this issue is poorly studied and the regulatory framework does not give unambiguous answers on how to properly install construction joints. However, they note that construction joints are a weak point and can adversely affect the load bearing capacity of the structure as a whole.

The authors [2, 8, 9] consider one of the reasons for the negative impact of concrete joints to be that they cannot foresee at the design stage the actual places where concrete construction joints will be installed. At the same time, according to common standard 70.13330.2012, the in-situ structures shall provide the structural strength, taking into account the concrete construction joints. To minimize the effect of construction joints on the load bearing capacity of constructions, this paper considers the possibility of construction joints accounting at the design stage

2. Methodology

Consider the vertical concrete construction joints in in-situ reinforced concrete slabs on one of the residential buildings under construction with a height of up to 20 floors. The locations of the construction joints were selected on the basis of the planned average daily volume of concrete or from the shipping length of the reinforcement bars, equal to 11.70 m. During the construction process, preconstruction geodetic surveys were performed at the joint's installation sites. The survey was performed with the Sokkia CX 105 total station. Also, calculations of reinforced concrete structures by the finite element method (FEM) were carried out [13–15].

FEM is the most common method used in practice for numerical (mathematical, computer) simulation of building structures and is used in most specialized design programs. The principle of the method as applied to the calculations of in-situ reinforced concrete structures consists in the approximation of structures by laminar (shell) and beam (bar) bending finite elements (FE) with 6 nodal degrees of freedom (3 degrees of freedom in displacements, 3 degrees of freedom in turns). From the point of view of geometric simulation, planes and segments, that do not have their own volume, are constructed, and they are assigned the geometric characteristics of the section (cross-sectional area A , moment resistance W , moment of inertia I). This allows you to reproduce the stress-strain state (SSS) of an elastic isotropic body with a similar cross-section shape. Bending structure SSS is conveniently represented in the form of internal forces: bending moment M , axial force N , transverse force Q , and also torque, if necessary. To determine the required number of longitudinal reinforcement, internal forces are decomposed into a couple of forces using semi-empirical engineering formulas: the compressive force from the compressed zone of the concrete (as well as in the compressive reinforcement, if any) and the tensile force in the tensile reinforcement. Concrete tensile strength is assumed to be equal to zero. A similar approach is used to determine the required amount of transverse reinforcement and the crack opening width.

Note that the representation of SSS by internal forces involves the postulation of a linear diagram of the distribution of normal stresses σ over the thickness of the structure, while the extreme values of the stresses are determined by formula:

$$\sigma_{\min}^{\max} = \frac{N}{A} \pm \frac{M}{W} \quad (1)$$

The tangential stresses τ in this case are distributed along a parabolic diagram according to the D. I. Zhuravskii formula. For the particular case of a cross-section, the maximum tangential stresses on the neutral axis are:

$$\tau_{\max} = \frac{3}{2} \cdot \frac{Q}{A} \quad (2)$$

The use of internal forces in a solid isotropic bending body to represent the SSS in reinforced concrete structures is due to the need to ensure the compatibility of the results of numerical calculations with semi-empirical engineering techniques given in regulatory documents. The accuracy of this approach is limited by two main conditions:

- rather high (not specified in regulatory documents) ratio of the length of the structure to the characteristic dimension of the cross section, which allows considering the structure as a slab or beam, and not as a volumetric body of arbitrary configuration;
- the stress state is close to the limit state, since otherwise SSS decomposition on the forces in the concrete and reinforcement will not be accurate.

The above approach is called classical theory of reinforced concrete.

A promising alternative to it is the volumetric compositional simulation of reinforced concrete with the reproduction of concrete and reinforcement as independent materials, taking into account their real physical and mechanical properties and mutual spatial arrangement. The main advantage of this approach is its versatility, i.e. in the possibility of calculating reinforced concrete structures of arbitrary configuration with any reinforcement layout in terms of any SSS.

Engineering semi-empirical formulas of regulatory documents are not used in the framework of volumetric compositional simulation of reinforced concrete, since all SSS parameters (concrete stresses, reinforcement stresses, deflection, crack opening width) are clearly determined as a result of numerical simulation.

The SSS calculation in the FEM framework is based on the generalized Hooke's law, which makes the connection between normal σ and tangential τ stress, linear ϵ and shear γ relative deformations

$$\{\sigma\} = [D]\{\epsilon\} \quad (3)$$

$$\begin{Bmatrix} \sigma_x \\ \sigma_y \\ \sigma_z \\ \tau_{xy} \\ \tau_{yz} \\ \tau_{xz} \end{Bmatrix} = \frac{E}{(1+\nu)(1-2\nu)} \begin{bmatrix} \nu & 1-\nu & \nu & 0 & 0 & 0 \\ \nu & \nu & 1-\nu & 0 & 0 & 0 \\ 0 & 0 & 0 & \frac{1-2\nu}{2} & 0 & 0 \\ 0 & 0 & 0 & 0 & \frac{1-2\nu}{2} & 0 \\ 0 & 0 & 0 & 0 & 0 & \frac{1-2\nu}{2} \end{bmatrix} \begin{Bmatrix} \epsilon_x \\ \epsilon_y \\ \epsilon_z \\ \gamma_{xy} \\ \gamma_{yz} \\ \gamma_{xz} \end{Bmatrix} \quad (4)$$

where $[D]$ is a stiffness matrix; $\{\sigma\}$ is a stress vector; $\{\epsilon\}$ is a relative deformations vector.

Each element of the stiffness matrix D_{ij} characterizes the stress arising in the i -th direction from the deformation in the j -th direction, here i and j , respectively, are lines and columns indexes corresponding to the indexes of the $\{\sigma\}$ and $\{\epsilon\}$ column members.

In the framework of statical calculations, the resolving equation of the FEM is a static equilibrium equation:

$$\{F\} = [K]\{u\} \quad (5)$$

where $[K]$ is the global stiffness matrix; $\{F\}$ is a global load vector; $\{u\}$ is a global displacement vector.

The global stiffness matrix is obtained by combining local stiffness matrices of each FE. The total number of lines is equal to the number of nodal degrees of freedom of the finite element model. Due to the application of boundary conditions (loads and supporting fixtures), some members become known, which allows us to calculate unknown members by solving a system of linear algebraic equations.

In the general case, the FEM resolving equation becomes more complicated and is the equation of motion:

$$\{F\} = [M]\{\ddot{u}\} + [C]\{\dot{u}\} + [K]\{u\} \quad (6)$$

where $[M]$ is a mass matrix, $[C]$ is a damping matrix, $\{\dot{u}\}$ is a nodal speed vector; $\{u\}$ is a nodal displacement vector.

A key tool for improving the accuracy of calculations is taking into account nonlinearity (Fig. 3).

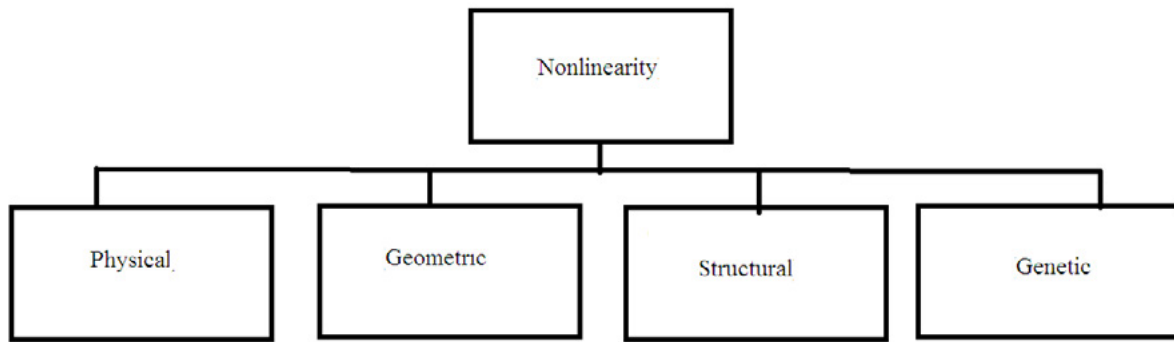


Figure 3. Nonlinear analysis.

Physical nonlinearity is dependence of the nature of the material deformation on the magnitude of stresses accounting, for example, the ability of reinforcement to plastic deformations, and concrete to cracking and creep.

Geometric nonlinearity is a consideration of the influence of the deformation of the model on the spatial distribution of forces, for example, on the eccentricity of the applied load or the span length. Design nonlinearity is taking into account changes in the design diagram depending on the loading conditions, for example, contact closing and opening. Genetic nonlinearity is a phased change in the design diagram accounting by activating and deactivating finite elements. From a computational viewpoint, nonlinearity accounting is a modification of the matrices $[K]$, $[C]$, $[M]$, which occurs automatically depending on the values $\{F\}$, $\{u\}$, $\{\dot{u}\}$, $\{\ddot{u}\}$. The above FEM principles are universal. However, the possibility of their implementation depends on the topology of the finite element model. The stress state represented by volumetric (SOLID) and bending plate (SHELL) FE is outlined in Fig. 4.

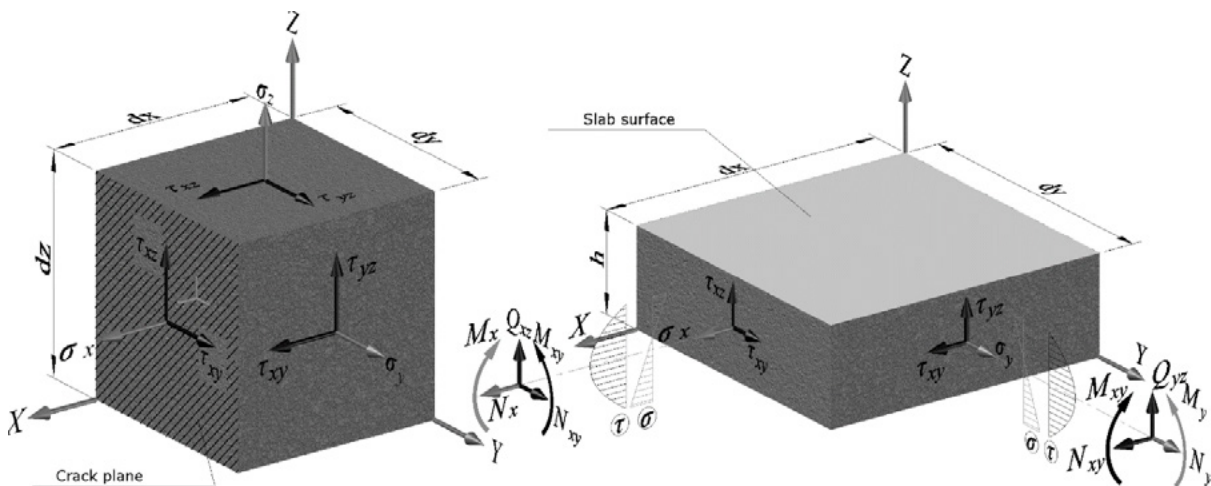


Figure 4. Stress state diagram for solid and thick shell finite elements.

In volumetric FE (SOLID), each integration point reproduces elementary volume with a full stress tensor. In FE (SHELL) plate, each integration point reproduces a volume with a certain size in the Z direction equal to the plate thickness. There are no normal and tangential stresses on the edges of the slab in the XOY plane. Stresses σ_x and σ_y are distributed over the thickness of the slab along a linear diagram and

reach extreme values on the edges of the slab. Stresses τ_{yz} and τ_{xz} are distributed over the thickness of the slab along a parabolic diagram and reach zero values on the edges of the slab. Thus, volumetric FE makes it possible to reproduce the stress state in detail (as compared with plate, as well as beam FE). Consequently, volumetric compositional simulation of reinforced concrete provides the greatest opportunities for accounting for all sorts of manifestations of nonlinearity. For example, consider crack formation in YOZ plane, perpendicular to X-axis, as shown in Fig. 4a. Crack formation can be interpreted as the cessation of the effect of stresses σ_y and σ_z on stress σ_x , with simultaneous σ_x stress relief and lowering τ_{xy} and τ_{xz} tangential stresses (depending on the crack roughness). Stiffness matrix takes shape:

$$[D]_{crack.YOZ} \sim \begin{bmatrix} \rightarrow 0 & 0 & 0 & 0 & 0 & 0 \\ 0 & \dots & \dots & 0 & 0 & 0 \\ 0 & \dots & \dots & 0 & 0 & 0 \\ 0 & 0 & 0 & \dots & 0 & 0 \\ 0 & 0 & 0 & 0 & x & 0 \\ 0 & 0 & 0 & 0 & 0 & \dots \end{bmatrix} \quad (7)$$

where “ $\rightarrow 0$ ” is a member of the matrix characterizing σ_x stress relief, “...” are nonzero members of the matrix, requiring transformations within the applicable nonlinear model of reinforced concrete [16]; “x” is a member of the matrix that does not require conversions.

In particular, such transformations of the stiffness matrix are implemented in FE like SOLID65 of the ANSYS software package. The specified FE is based on the Willam-Warnke [17] concrete strength criterion and allows taking into account up to three reinforcement directions. The reinforcement is an evenly distributed throughout the volume of the FE. Therefore, to simulate the main longitudinal working reinforcement of slabs, the surface layer of the final elements shall be located along the axis of the reinforcement bars and have a size equal to twice the protective layer of concrete (counting from the centre of gravity of the reinforcement bar). SOLID65, apparently, is the most well-known and widely used tool for volumetric composite simulation of reinforced concrete for solving a wide range of practical problems [18–22].

Currently, the use of universal FE reinforcement is being expanded, which allows flexible positioning of reinforcement inside volumetric FE of concrete. This increases opportunities for the development of effective mesh approximations of reinforced concrete structures.

The topology of the finite element model is chosen in accordance with the objectives of the calculation and the adopted design diagram. Consider the main approaches in the framework of the volumetric compositional simulation of reinforced concrete.

1. The reinforcement and concrete are reproduced together (by one FE, or by several geometrically coinciding FE, when one FE reproduces concrete, and the rest are reinforcement in it, possibly made of different materials and with different spatial orientation).

1a. Reinforcement is evenly distributed over the FE volume. The reinforcement diagram is reproduced by combining volumetric FE with different reinforcement percentage, provided that FE dimensions are accurately determined. Changing the reinforcement diagram requires FE mesh redesign.

1b. Reinforcement is arbitrarily positioned in volumetric FE. Changing the reinforcement diagram does not require FE mesh redesign.

2. Reinforcement and concrete are reproduced separately by non-intersecting volumetric FE, i.e. inside the volume of concrete there are cavities that are filled with reinforcement. Changing the reinforcement

diagram requires FE mesh redesign.

2a. Reinforcement is modelled in a simplified way, down to a rectangular cross-sectional shape reproducible by a single volumetric FE.

2b. Reinforcement is modelled in detail, up to periodic profile of the reinforcement and the reproduction of the “concrete-steel” contact with the possibility of slipping reinforcement accounting.

3. Reinforcement and concrete are reproduced separately by intersecting FE, and the concrete is reproduced by volumetric finite elements, and the reinforcement is reproduced by bar torque-free (LINK), bending beam (BEAM), shell torque free or bending plate FE (SHELL). The change in reinforcement does not require FE mesh complete redesign, since mesh approximations of reinforcement and concrete are independent of each other. Connection of reinforcement with concrete is carried out by assigning links of degrees of freedom by displacements of the FE nodes of concrete and FE of reinforcement.

From the point of view of practical engineering calculations, options 1b and 3 are most preferable, which allow changing the reinforcement diagram without redesigning the FE mesh, which makes it possible to perform optimization calculations with sufficient efficiency. In general, composite simulation of reinforced concrete is advisable to apply for design substantiation of structures that, for one reason or another, fall outside the limits of applicability of semi-empirical engineering techniques:

- check calculations of the actual work of the structure for all types of beyond design SSS;
- strengthening calculations, including overlaid reinforcement;
- calculations of structures with internal cavities, for example, from embedded ductwork in flat slabs;
- calculations of structures with non-metallic reinforcement with nonstandard physical and mechanical characteristics;
- calculations of any nonstandard configuration designs.

Concrete construction joint is a structural imperfection in the form of a layer of concrete decompaction, in which the strength and deformation characteristics are lowered. This layer in the compressed zone of concrete at the initial stage of the construction of the structure causes additional deformations similar to the joint closure, which lead to an increase in the deflection of the structure. Within the framework of composite concrete simulation, the concrete construction joint can be considered as a preliminary open joint, the closure of which under load introduces additional deformation into the compressed zone of concrete with a corresponding additional deflection of the structure. The specified imperfection in the finite element model can be reproduced by the introduction of a contact FE with preliminary disclosure, where the width of the disclosure is a parameter of the FE and can be selected from the field data without FE mesh redesign.

The longitudinal reinforcement crosses concrete construction joint without weakening, which can be reproduced by simulation of the reinforcement with torque-less bar FE (LINK) passing through volumetric FE and contact FE. The transition of the reinforcement through the joint is optimally performed with one FE, in which the ends are located on both sides of the joint. This simulation technique corresponds to the above option 3. It is advisable to reproduce transverse reinforcement, if available, together with concrete reinforcing FE. Depending on the uniform distribution of transverse reinforcement according to the reinforcement diagram, transverse reinforcement can be considered evenly distributed over the slab area, or positioned precisely. This simulation technique corresponds to the above 1b option. The basic diagram of the corresponding finite element approximation of the floor plate is shown in Fig. 5.

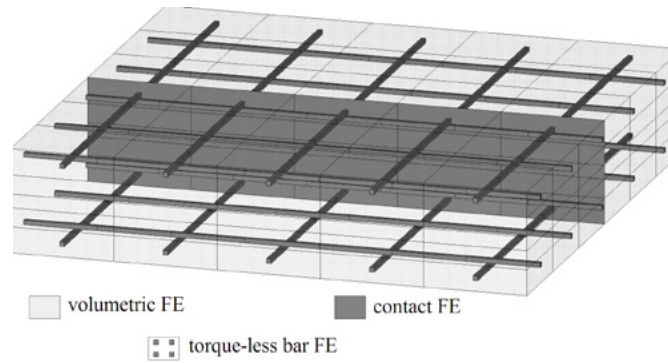


Figure. 5. Schematic finite element mesh of a monolithic reinforced concrete slab with a construction joint.

A practical difficulty in the implementation of volumetric compositional simulation of reinforced concrete is the limited initial data on the physical and mechanical characteristics of concrete for nonlinear simulation, which are specified in the regulatory documents. The available data in common standards 70.13330.2012 and 52-103-2007 are focused on the application of the classical theory of reinforced concrete according to the calculation of slabs and beams in combination with engineering approaches to taking into account nonlinearity, which consists in lowering the effective modulus of deformation of reinforced concrete in accordance with the concrete state diagrams and in accordance with a creep coefficient of concrete. When using modern computational programs, this allows in finite element models of plate and beam FEs to adjust the stiffness individually in each FE with the construction of the corresponding isofields or stiffness diagrams [23, 24]. At the same time, from the point of view of the FEM, the final design diagram continues to remain linear with the effective moduli of deformation of reinforced concrete specified for each FE.

Volumetric compositional simulation of reinforced concrete is based on the use of a universal nonlinear material model, which involves building a yield surface (in the general case, also a loading surface taking into account the material strengthening) in the main stress space, representing the state of the material for any combination of stress and strain tensor components. For this, additional data are needed, which are not included in regulatory documents, for example, concrete strength under a flat (biaxial) stressed state, as well as the dilatancy of concrete under compression and tension.

Practical implementations of concrete models in universal software and computing suites of numerical simulation, as a rule, provide for the possibility of accounting the minimum amount of input data, assuming the rest of the data automatically as default. For example, in the above-mentioned type SOLID65, the concrete adopted for biaxial compression is adopted by default 20% higher than the uniaxial compression strength. Due to the fact that, as a rule, volumetric compositional simulation of reinforced concrete is applied to nonstandard working conditions of structures, the initial data taken automatically require compliance monitoring with the actually considered SSS. Also, when using foreign programs and methods, differences in the designation of the standard strength of concrete in different countries, interconnected with the standardized method of testing samples of different shapes and sizes, shall be taken into account.

3. Results and discussion

As a result of executive geodetic surveys of 6 floors, floor slabs deflections were obtained at the construction joints locations. Magnitudes and location of the deflections are similar on all floors. Therefore, the 10th floor was adopted for a more detailed analysis. As built drawing of which is given in Fig. 6.

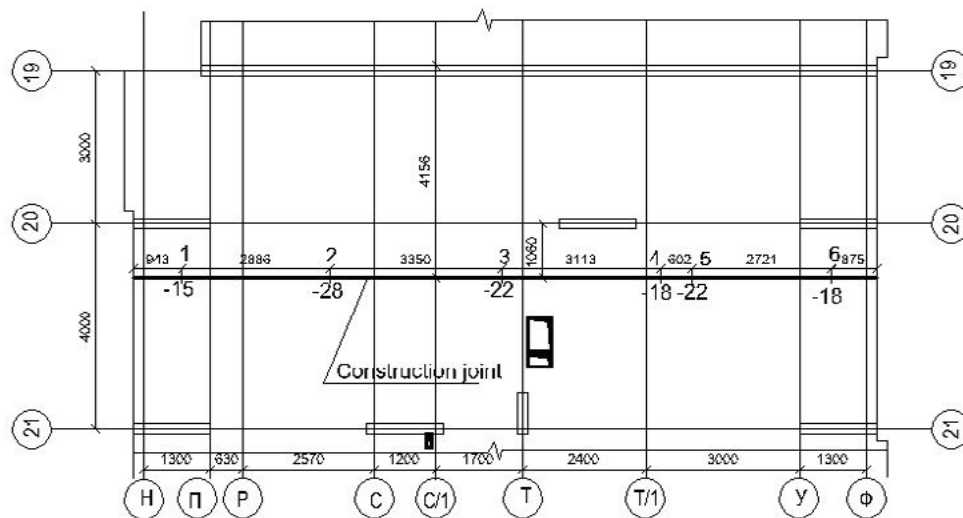


Figure 6. Scheme for the definition of deflections of concrete in the places of the construction joint (10 floor).

Factual measured data of deformations in the construction joint are presented in Table 1.

Table 1: Factual data of deformations in the construction joint.

Stage	Description	Vertical displacement at the check point, mm					
		1	2	3	4	5	6
	Actual deformation measurements	15	28	22	18	22	18

During the calculation using the finite element method, a section of the 10th floor slab was modelled at three stages of construction in accordance with present day practice of performing mass calculations using engineering nonlinearity accounting methods.

1. The initial stage of the slab installation on one pour, while the pattern of the static slab structural behaviour is based on three sides.
2. Topping up the slab to the design dimensions, while the pattern of the static work of the slab is a four-side support.
3. Slab loading with a useful standard load after the strength gain.

For the first and second stage, reduced values of concrete strength and deformation modulus were taken, thus the guidance of common standard 70.13330.2012 on the minimum strength of concrete when stripping unloaded slabs was considered. At each stage of the calculation, a reduction factor was determined for the concrete deformation modulus, taking into account the properties of concrete under load, as well as the presence of cracks in the finished structure and the actual reinforcement. During the calculations, the deformations were analyzed at the check points of the construction joint zone. The calculation results are given in Table 2.

Table 2: The results of the calculation of deformations in the construction joint.

Stage	Description	The strength of concrete is relative to the design strength	The value of the reduction factor to the concrete deformation modulus	Vertical displacement at the check point, mm					
				1	2	3	4	5	6
1	Initial stage	70%	0.118	0.59	19.76	4.89	0.74	1.32	0.30
2	Topping up the slab to the design dimensions	70%	0.354	0.37	1.42	0.65	1.15	1.27	0.39
3	Loading the slab with a useful design load.	100%	0.203	0.21	1.75	0.59	0.63	0.77	0.18
Total deformations taking into account the formation of a construction joint				1.17	22.93	6.13	2.52	3.36	0.87
	Calculation without taking into account the phased construction	100%	0.203	0.86	7.02	1.95	2.97	3.09	0.74

After analyzing the factual measured data in table 1 and the results of the calculation in table 2, we can note the following:

1. Actual deflections exceed the calculated deflections obtained without taking into account the phasing of the construction. At the same time, at the point of maximum deflection, the actual deflections are 4 times higher than the calculated deflections.
2. Actual deflections exceed the calculated deflections obtained taking into account the phasing of the construction. At the same time, at the point of maximum deflection, the actual deformations are 1.3 times higher than the calculated deflections.
3. Calculated deflections, obtained with consideration of the stage of installation, are much closer to the actual deflections.

Based on the above stated, it should be assumed that, in practice, the difference between the calculated deflection of a reinforced concrete structure and the actual one is due to inaccurate correspondence of the design diagram (mathematical model) to a real reinforced concrete structure, the conditions of its installation and operation. It is important to stress that the deflection of horizontal reinforced concrete structures is only one of the parameters of the SSS, which is best measured. Deflection, i.e. the difference in vertical displacements of the structure in the span and on the supports is interconnected with other SSS parameters, such as stresses in concrete and reinforcement, relative deformations of concrete and reinforcement, crack opening width. Thus, if the actual deflection of the reinforced concrete structure does not correspond to the design estimate, then other SSS parameters will also differ from the design estimate, although this is usually not fixed during construction, since full scale measurements of the relevant SSS parameters are not made.

Any calculation operates with a mathematical model that is an idealized reflection of a real building structure. In practice, mathematical models with a limited account of nonlinearity, or fully linear mathematical models, are often used. The linear model uses the principle of superposition (independence of action of forces), which is an extremely important practical advantage of linear models. This allows you to combine the results of the statical calculations for different loads, generating results for combinations of these loads without solving the FEM equation (3) for each new combination.

In the linear model, the deformations are directly proportional to the loads; the strength of the material is infinite; displacements, deformations and stresses are not limited. Linear models do not reproduce the limits of the construction work, i.e. allow you to get in the SSS calculation, which cannot be in reality (assessment of the performance of the structure is carried out analytically according to engineering criteria,

such as the calculated strength of materials, permissible structural deflections, adequacy of the required reinforcement).

The above facts convincingly demonstrate that the most significant differences between the estimated and actual SSS are accumulated at the stage of formwork removal before the construction is put into operation. Thus, the conditions of construction with the introduction of imperfections in the form of concrete construction joints, as well as the conditions of loading the structure up to the set of design strength with its own weight and temporary loads of technological nature in the partial removal of formwork with the redistribution of the load on the posts of crossover, and then with the complete removal of formwork have a significant impact on the subsequent SSS in the operation of the structure.

In terms of design, these processes are a phased construction and structural loading, coordinated with the concrete strength. This characterizes the genetic nonlinearity of the floor slab.

The concrete construction joint is a structural imperfection, which can be represented as the ability of compressive zone of the concrete to a limited increment of deformations at the initial loading stage, which can be interpreted as a certain crack closing before concrete begins to perceive compression. Thus, as the load increases, the workflow changes, which is characterized by the structural nonlinearity of the floor slab operation.

Deformation of the structure leads to a change in the distances between the application of loads parts and supporting fixtures, to a change in the characteristic spans, lengths and eccentricities. This characterizes the geometric nonlinearity. With regard to slabs of civic buildings, the influence of geometric nonlinearity should be expected from the influence of other structures in the calculation of the supporting system of the building as a whole.

The nonlinear relationship between stresses and deformations is a physical nonlinearity. The nature of the physically nonlinear work of the materials, from which reinforced concrete (concrete steel reinforcement, non-metallic reinforcement) is made, differs, which requires the use of various mathematical models of materials that can be taken into account in the framework of volumetric composite modelling of reinforced concrete. The engineering approach is to account for the reduced effective modulus of elasticity of reinforced concrete, which is used in the framework of the classical modelling of reinforced concrete with plate and beam FE (finite elements).

Engineering approaches to the accounting of nonlinearity make it possible to consider various types of nonlinearity together. For example, structural nonlinearity can be taken into account by lowering the effective modulus of deformation of reinforced concrete, i.e. methods of accounting for physical nonlinearity. In this case, it is assumed that the distribution of internal forces in the elements of the bearing system of a building depends mainly not on the value but on the ratio of the stiffness of these elements. Accordingly, the accuracy of the calculation depends on the representativeness of the adopted stiffness ratios within the framework of the calculation of the carrier system of the building as a whole.

4. Conclusions

1. The installation of vertical concrete construction joints in floor slabs that were not originally provided by the project documentation is necessary due to a number of organizational and technical reasons related to the limitations of the possibility of continuous concrete supply and the duration of work shifts.
2. The location of vertical concrete construction joints is predictable based on the basic organizational and technical indicators of construction (number of work shifts, number and performance of cranes and concrete pumps). Therefore, concrete construction joints can reasonably be assigned in the development

of project documentation and taken into account when carrying out calculations of reinforced concrete structures.

3. The field studies data show that the concrete construction joints in the floor slabs, installed in accordance with common standard 70.13330.2012, weaken the solidity of the structure. The results of calculations carried out without taking into account the concrete construction joints do not accurately predict the actual SSS of the structure.

4. The effect of concrete construction joints can be taken into account when using common calculation programs that implement FEM, while explicitly taking into account the phasing of the construction of the structure by pours, using engineering approaches to taking into account nonlinearity based on the introduction of reduction factors to the effective modulus of elasticity of reinforced concrete, calculated taking into account the degree of strength and characteristic intermediate operation schemes of construction work during the construction period. Geometrical nonlinearity shall be taken into account, especially when calculating the spatial formulation of the full model of the building's carrier system.

5. The greatest accounting opportunities for all possible manifestations of nonlinearity are provided by volumetric compositional simulation of reinforced concrete, which is advisable to use for calculations of structures that for one reason or another go beyond the limits of the applicability of semiempirical engineering techniques, in particular, for check calculations and calculations of the reinforcement of structures that have switched to no design SSS as a result of beyond-design opening of concrete construction joints.

6. It is advisable to supplement the regulatory and technical documentation with basic data for the bulk composite modelling of reinforced concrete, in particular, with data on the strength of concrete for biaxial compression and dilatancy under compression and tension.

5. References

- [1] Biswajit Roy, Aminul Islam Laskar 2018 Cyclic Performance of Beam-Column Subassemblies with Construction Joint in Column Retrofitted with GFRP // Structures. Vol. 14. Pp. 290-300. <https://doi.org/10.1016/j.istruc.2018.04.002>
- [2] Koyankin A.A., Beletskaya V.I., Guzhevskaya A.I. 2014 The influence of concrete joints on the structural behavior // Vestnik MGSU [Proceedings of Moscow State University of Civil Engineering]. №. 3, pp. 76—81.
- [3] Nagib N. Gerges, Camille A. Issa, Samer Fawaz 2016 The effect of construction joints on the flexural bending capacity of singly reinforced beams // Case Studies in Construction Materials Vol. 5 Pp. 112-123. <http://dx.doi.org/10.1016/j.cscm.2016.09.004>
- [4] Nagib N. Gergesa, Camille A. Issab, Samer Fawaza 2015 Effect of construction joints on the splitting tensile strength of concrete// Case Studies in Construction Materials Vol. 3. Pp. 83-91 <http://dx.doi.org/10.1016/j.cscm.2015.07.001>
- [5] Camille A. Issaa, Nagib N.Gergesb, SamerFawaz 2014 The effect of concrete vertical construction joints on the modulus of rupture // Case Studies in Construction Materials. Vol. 1 Pp. 25-32. <https://doi.org/10.1016/j.cscm.2013.12.001>
- [6] Hyun-O Jang, Han-Seung Lee, Keunhee Cho, Jinkyu Kim 2017 Experimental study on shear performance of plain construction joints integrated with ultra-high performance concrete (UHPC) Construction and Building Materials. Vol. 152 pp.16-23. <http://dx.doi.org/10.1016/j.conbuildmat.2017.06.156>

- [7] Smoljago G.A., Krjuchkov A.A., Dronova A.V., Drokin C.V. 2011 Results of the experimental studies of bearing capacity, crack resistance and deformability of the precast-monolithic and monolithic overlaps // Proceedings of the south-west state university № 5-2 (38) Pp. 105-109.
- [8] Shpilevskaya N, Shvedov A. 2018 Peculiarities of normative support for designing organization and production of works by working sewing device concreting // Electronic collection of articles of the international scientific conference dedicated to the 50th anniversary of Polotsk State University Novopolotsk, 5-6 april 2018 (electronic materials) ed. A. A. Bakatovich, L.M. Parfenova. Pp. 311-315.
- [9] Shvedov A., Shpilevskaya N. 2018 Development of organizational-technological documentation on concreting of massive fundamental slabs // VESTNIK OF PSU №8. Pp. 49-55. (In Russian)
- [10] Wujun Zhou, Pangil Choi, Sureel Saraf, Sung Woo Ryu, Moon C. Won 2014 Premature distresses at transverse construction joints (TCJs) in continuously reinforced concrete pavements // Construction and Building Materials Vol. 55. Pp. 212-219. <https://doi.org/10.1016/j.conbuildmat.2014.01.042>
- [11] Keun-Hyeok Yang, Ju-Hyun Mun, Yong-Ha Hwang, Jin-Kyu Song 2017 Cyclic tests on slip resistance of squat heavyweight concrete shear walls with construction joints // Engineering Structures Vol. 141 Pp. 596-606. <https://doi.org/10.1016/j.engstruct.2017.03.0354>
- [12] Pikin D. Y., Kondrashkova V. A. 2016 The study of various approaches to the determination of the relative deformations of reinforced concrete structures // Youth and XXI century. Materials of the VI International Youth Scientific Conference (Kursk, 25-26 February 2016 r): in 4 volumes. Ed. Gorokhov A.A. Vol. 3 Pp.289-293
- [13] Manakhov P.V., Fedoseev O.B. 2008 On an alternative method of calculating the accumulated plastic strain in plastic problems using the finite element method // Bulletin of the Samara University. Natural Science Series №3(62). pp. 262-271
- [14] Karan Kumar Pradhan 2019 Chapter Four - Finite Element Method // Computational Structural Mechanics Static and Dynamic Behaviors Pp. 25-28. <https://doi.org/10.1016/B978-0-12-815492-2.00010-1>
- [15] Antipov I.V., Balagurov A.V. 2016 Analytical solution of the problem for generation of element stiffness matrix in FE-analysis // Proceedings of Republican Academic Research and Design Institute of Mining Geology, Geomechanics, Geophysics and Surveying №: 1 (16). Pp. 146-156
- [16] R. Raveendra Babua, Gurmail S. Benipala, Arbind K. Singh 2005 Constitutive Modelling of Concrete: an Overview // Asian Journal of Civil Engineering (Building and Housing) Vol. 6, No. 4. Pp. 211–246.
- [17] K.J. Willam, E.D. Warnke 1975 Constitutive Model for the Triaxial Behavior of Concrete // Proceedings, International Association for Bridge and Structural Engineering Vol. 19. ISMES. Bergamo, Italy. Pp. 1-30.
- [18] A.S. Zalesov, A.A. Pashchanin 2011 Strength calculation for ferroconcrete beams using volume finite elements within a framework of development of ferroconcrete beams design standards// Structural Mechanics and Analysis of Constructions №4. Pp. 66–71. (In Russian)
- [19] Piskunov A.A., Zinnurov T.A., Berezhnoi D.V., Umarov B.Sh., Volter A.R. 2018 Experimental and numerical studies of stress-strain state of concrete structures reinforced with polymer-composite reinforcement // Russian journal of transport engineering №2 (5). Pp. 1-18.
- [20] Shirko A.V., Kamlyuk A.N., Polevoda I.I., Zainudinova N.V. 2014 Strength calculation of reinforced concrete slabs in case of fire using ANSYS software environment // Bulletin of the Command Engineering

Institute of the Republic of Belarus № 1 (19). Pp. 45–58.

[21] Radaikin O.V., Sharafutdinov L.A. 2017 By evaluating the strength, hardness and fracture toughness of bent reinforced-concrete elements, strengthened concrete of steel fiber «jacket» on the basis of computer modeling in PC «ANSYS» // News KSUAE № 1 (39). Pp. 111–120.

[22] Mihub A., Polish P.P., Mailyan D.R., Blyagoz A.M. 2012 Comparison of experimental and theoretical strength of reinforced concrete beams strengthened with composite materials using different calculation methods. *New technologies* №4. C. 101–110.

[23] Gorodetsky A.S., Barabash M.S. 2016 Nonlinear behavior of reinforced concrete in Lira-SAPR software. *Nonlinear engineering method* // *International Journal for Computational Civil and Structural Engineering* № 2. Pp. 92–98

[24] Ivanova E.I., Kotov A.A. 2019 The stiffness of reinforced concrete beams in finite element analysis models of prefabricated buildings. // *Modern Construction and Architecture* № 1 (13). Pp 19–25. DOI: <https://doi.org/10.18454/mca.2019.13.4>

Eco-efficiency in cement use analysed by the concept of distance among particles in concrete phases

M. F. L. Menezes^{1,2}, R.G. Pileggi¹, M. Rebmann¹, C. Massucato²

¹Universidade de São Paulo, São Paulo, Brazil.

²InterCement, São Paulo, Brazil.

Abstract

Concrete greenhouse gas emissions are mostly from cement. A relevant strategy for the concrete greenhouse gas emissions abatement is the increase of the efficiency in binder usage. For this, it is important to understand the packing and the distance of concrete particles and their effects on its rheological behaviour in the fresh state and its mechanical properties in the hardened state. Currently, mix design methods are empirical, as opposed to this experimental optimization, computational optimization emerges, based on predictive models. Thus, the objective of this study is to use a model based on particle distance in phases to predict the rheological behaviour of concrete. The method consisted in the following steps: characterization of raw materials; eco-efficiency analysis of 120 formulations of a concrete plant with two different material sets using the binder intensity concept; and a parameter estimation for a descriptive model of the slump in function of particle distance variables. These concrete binder intensities were between 7.5 and 10.5 kg/m³/MPa, in which the rise of specified f_{ck} and maximum aggregate size have a positive impact on this index, while the specified slump growth has a negative effect. For these concretes, the distance variable MPT (Maximum Paste Thickness) for f_{ck} showed good correlations with the specified slump (R^2 0.97 and 0.98), as well as the model presented a good adjustment to the data (R^2 0.91). These results allow an improvement in the mix design methodology – using computational optimization –, which can lead to an increase in concrete eco-efficiency.

Keywords: Particle packing, interparticle separation distance, slump, rheological behaviour.

1. Introduction

Greenhouse gas emissions from concrete are mostly from cement, with the cement industry accounting for approximately 7% of global CO₂ emissions [1]. The levers for reducing these emissions are increasing energy efficiency, using alternative fuels, increasing clinker replacement and using innovative technologies such as carbon capture and storage [1]. In the concrete field, a relevant strategy is to increase the efficiency in binder use, that is, to achieve better properties with lower binder consumption [2]. Besides, because the binder represents the most significant fraction of the concrete cost, increasing efficiency is also a cost-saving solution.

To increase the efficiency of concrete binders, it is necessary to understand the structure of this material and its consequences on the concrete properties, both in the fresh and hardened state. For this, it is important to understand packing and distance among particles of concrete particles and their effects on the material rheological behaviour in the fresh state and on the mechanical properties in the hardened state, a theme that has already been widely discussed by several concrete researchers [3-17].

The concrete can be divided into two phases: the paste and the aggregates. The paste consists of the fine particles and the fluid that moves them away: the water. In this context, the predominant forces are the surface forces. In aggregates, the fluid that moves them away is the paste, and the most relevant forces in this context are the mass forces. Thus, the diameter of 100 μm is defined as the border between the fine and coarse particle – and the phases - since this diameter is in the region of transition between the predominance of each type of force [4], [12].

Seeking a better concrete eco-efficiency, using different materials, the concrete mix design was evaluated from the perspective of packing and particle distance concepts. Currently, mix design methods are empirical, that is, based on experience from concrete operations over years and experiments results [18]. In contrast to experimental optimization, computational optimization emerges, in which an optimization problem is used based on a model to point out the best solution, which is verified experimentally. In the literature, several types of models are available for predicting concrete properties, including linear, statistical, automatic and physical combinations [19].

The present work was developed using materials and formulations of a concrete plant in São Paulo, Brazil, with the objective of using a model based on particle distance in the phases to predict the rheological behaviour of concrete to improve the current mix design methodology.

2. Methodology

2.1 Materials

Two material sets were collected at a concrete plant in São Paulo, Brazil, to be used in this study. The aggregates of the Material Set 1 were granitic and the ones of the Material Set 2 were calcitic. Particle size distribution was determined by laser granulometry, using Helos equipment from Sympatec, and dynamic image analysis, using Camsizer equipment from Retsch and Qicpic made by Sympatec, density by helium pycnometry, using a Multipycnometer of Quantachrome, and specific area by BET method, using a Belsorp produced by Bel Japan. The Material Set 1 characterization is presented in Table 1 and Figure 1, and the Material Set 2 characterization is presented in Table 2 and Figure 2. Cement and Natural Sand are the same for both Material Sets.

Table 1: Material Set 1 Characteristics

Characteristic	19mm Gravel	9.5mm Gravel	Artificial Sand	Natural Sand	Cement
Density (kg/m ³)	2.71	2.70	2.70	2.65	3.06
Granulometric					
Volumetric Area (m ² /	7.8 x 10 ⁻³	4.0 x 10 ⁻³	8.2 x 10 ⁻²	4.2 x 10 ⁻²	1.17
BET Specific Area (m ² /g)	0.01	0.01	0.26	0.30	1.48
Median Aspect Ratio	0.65	0.63	0.62	0.74	0.75

(1) Granulometric volumetric area was calculated from particle size distribution assuming spherical particles

Comparing the two Material Set, it can be noticed that Artificial Sand from Material Set 1 shows a lower amount of fines (below 100 μm) than the one from Material 2. Material Set 1 presents a finer 19mm Gravel than Material Set 2, though the other materials are coarser, this impacts on packing porosity and, also, on volumetric granulometric area, that is higher for Material Set 1 19mm Gravel and lower for Material Set 1 9.5mm Gravel and Artificial Sand. Besides, the granulometric curves from Material Set 2 are broader than the Material Set 1's.

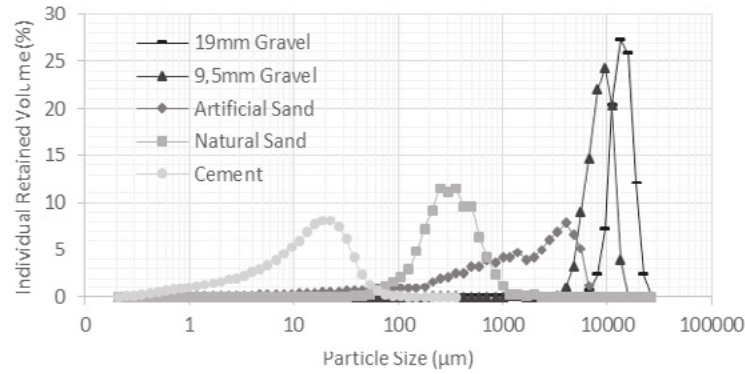


Figure 1: Material Set 1 Particle Size Distribution

Table 2: Material Set 2 Characteristics

Characteristic	19mm Gravel	9.5mm Gravel	Artificial Sand	Natural Sand	Cement
Density (kg/m ³)	2.66	2.65	2.86	2.65	3.06
Granulometric					
Volumetric Area (m ² /cm ³)	6.9x10 ⁻³	4.6x10 ⁻³	0.12	4.2 x 10 ⁻²	1.17
BET Specific Area (m ² /g)	0.02	0.02	0.23	0.30	1.48
Median Aspect Ratio	0.70	0.67	0.68	0.74	0.75

(1) Granulometric volumetric area was calculated from particle size distribution assuming spherical particles

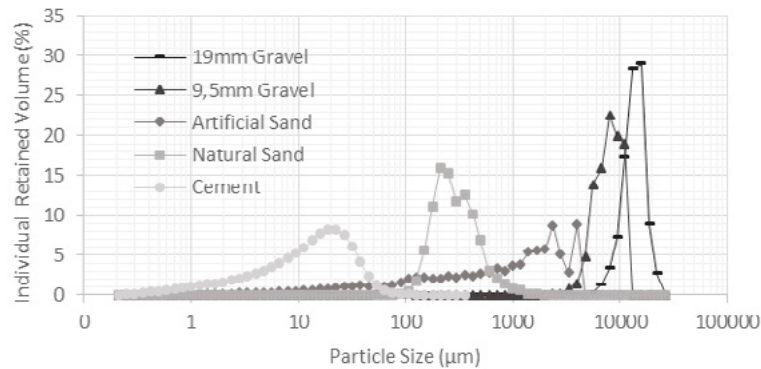


Figure 2: Material Set 2 Particle Size Distribution

In order to understand the current logic of mixture design, data were obtained from conventional concrete formulations of a concrete operation in São Paulo/Brazil. This concrete plant has 60 base formulations for each Material Set (Formulation Set). These concretes have specified compressive strength (f_{ck}) ranging from 20 to 40MPa, slump between 90 and 200mm and maximum aggregate size 19mm or 9.5mm. In concrete operation, the way to adjust the specified slump after all the materials are mixed is adding more water.

2.2 Methods

With this data, the concrete binder intensities (Equation 1) were evaluated to understand their eco-efficiency. In order to elucidate the observed trends, the models of packing and distance between particles were used to evaluate the formulations. In this study, the packing porosity was calculated by the Compressive Packing

Model [8] and mean distances between particles (Equation 2) were calculated: IPS (Interparticle Separation Distance, for the particles finer than 100 μm) and MPPT (Maximum Paste Thickness, for the particles greater than 100 μm) [20]. These two variables were correlated with the fresh concrete property, slump, and a model was adjusted.

$$BI = b/pr \tag{1}$$

BI is Binder Intensity (kg/m³/MPa)

b is binder content (kg/m³)

pr is performance requirement, adopted as cylindrical compressive strength at 28 days (MPa)

$$D = \frac{2}{V_{SA}} \left[\frac{1}{V_{sol}} - \left(\frac{1}{1-\epsilon} \right) \right] \tag{2}$$

D is Distance between particles - IPS for fine or MPPT for coarse (μm)

VSA is volumetric surface area (m²/cm³)

V_{sol} is solids volumetric fraction

ε is packing porosity

For the IPS, the VSA used was the one obtained by BET method. For MPPT, the VSA was evaluated based on the granulometric volumetric area, using its sphericity and aspect ratio.

3. Results and discussion

3.1 Binder intensity evaluation

Concrete eco-efficiency can be first analysed by binder intensity since clinker is the most intense source of CO₂ emissions in concrete. So, for concrete using the same binder and produced at the same place, the lower is its binder intensity, the higher is its eco-efficiency.

Looking at the change of binder intensity in function of f_{ck} for the Formulation Set 1, as shown in Figure 3, it is possible to notice that there is a decrease of this index between 20 and 30MPa, but, from 30 to 35MPa the intensity stagnates and grows slightly when reaching 40MPa. Comparing the results with Daminelli [21], the intensities of the evaluated concretes are in the same experimental region of concretes mapped by him, however with binder intensities well above the best-found intensities, which are below 5kg/m³/MPa. The name of each series was given using the following pattern: it starts with “form1” for the Formulation Set 1 or “form2” for the Formulation Set 2, followed by the maximum aggregate size (“b1” for 19mm and “b0” for 9.5mm), and then the slump (ex. 140).

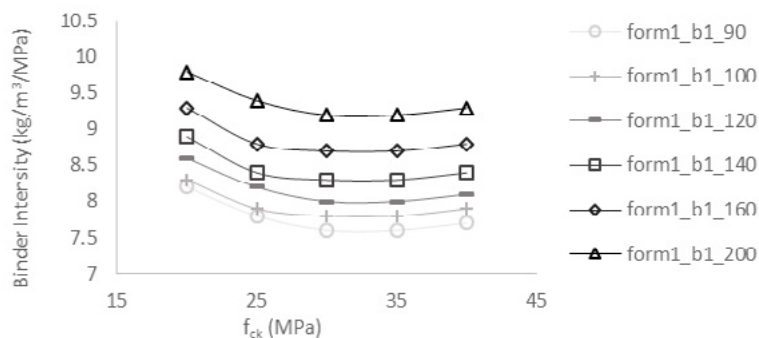


Figure 3: Binder intensity per f_{ck} for different slumps

For a given strength, concretes with the lowest binder intensity are those with maximum aggregate size 19mm and lower slump: about 7.5 to 8 kg/m³/MPa. The concretes with the lowest eco-efficiency are those with a maximum aggregate size 9.5mm and higher slump, reaching values between 9 and 10kg/m³/MPa.

Analysing the mix design strategy, Figure 3 shows the negative effect on binder intensity by the specified slump raise, while a broader particle size distribution, allowed by increasing maximum aggregate size, has a positive impact (Figure 4a). Figure 4b shows that concretes from Formulation Set 2 have a slightly lower binder intensity than those from Formulation Set 1.

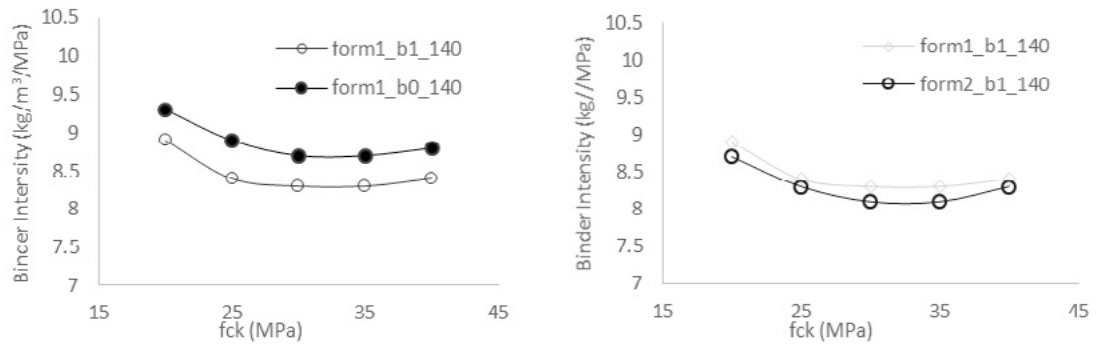


Figure 4: Binder intensity per f_{ck} (a) for different maximum aggregate sizes and (b) for different Formulation Sets

3.2 Distance among particles

In order to understand concrete flowability, coarse packing porosity, MPT and IPS, as defined by Equation 2, were calculated. First, concretes for different f_{ck} – consequently different paste compositions - were analysed plotting the slump as a function of the coarse packing porosity (Figure 5). With these results, it is not possible to find a correlation between the slump and coarse packing porosity. Different concretes with the same slump present different porosities. It can be noticed that for each specified compressive strength that is two groups of data, one with coarse porosity between 16,8% and 17,5% and another one starting from 18,0%. These two groups are the ones with maximum aggregate size 19mm and 9,5mm. The group with 19mm maximum size achieves a lower coarse packing porosity because it has a broader particle size distribution than the 9,5mm.

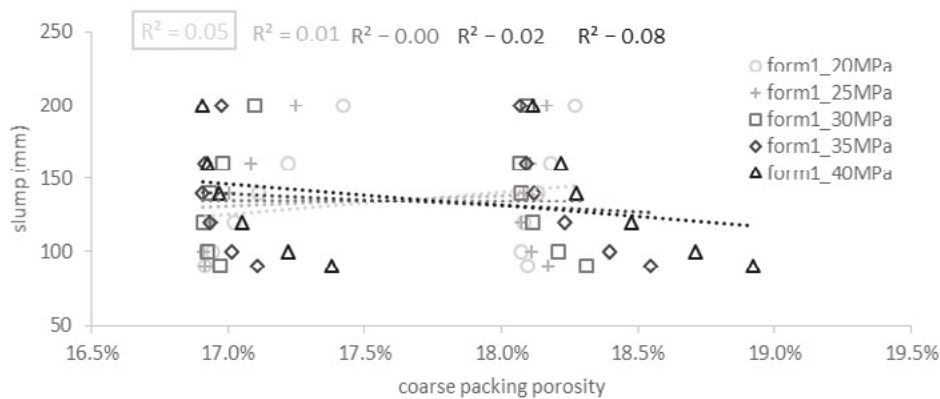


Figure 5: Slump in function of coarse packing porosity per f_{ck}

Porosity is a property of the granular size distribution and does not comprehend the pasta volume either the superficial area, so, in different concretes with the same slump, different material proportions are used,

but also a different paste content, which is not addressed by the porosity.

MPT considers the paste volume and the area as well. Thus, the slump was plotted as a function of MPT (Figure 6) for both Formulation Sets. A high correlation between MPT and slump was observed, with the coefficient of correlation of the adjusted linear regression (R^2) between 0.97 and 0.98, given a paste composition. That is, formulations that use different types of paste (in the graph represented by f_{ck}) do not present the same MPT for a slump, because of the different rheological behaviour of these pastes. But if this variable (paste) is fixed, slump varies linearly with MPT.

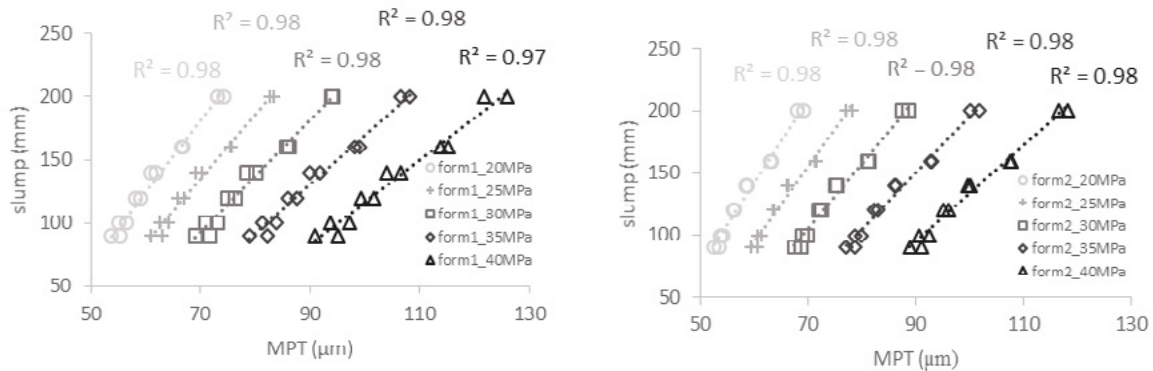


Figure 6: Slump in function of MPT per f_{ck} for (a) Formulation Set 1 (a)Formulation Set 2

The second distance parameter refers to the distance between fine particles (IPS). A high correlation (R^2 0,98), with f_{ck} for both Formulation Sets, were observed (Figure 7). The cause for this negative correlation is that the strategy to increase f_{ck} is to reduce the water/cement ratio, which leads to less fluid to separate the particles, diminishing the IPS. For concretes without other fine particles rather than cement and aggregates fines, this trend is likely to be repeated.

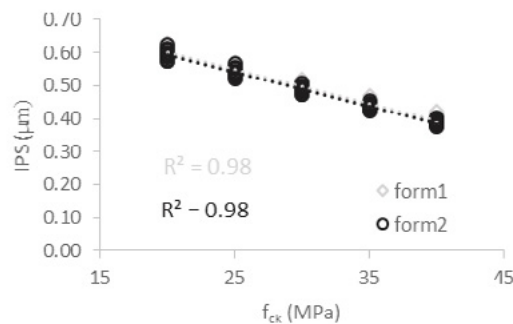


Figure 7: Correlation between IPS and f_{ck}

3.3 Descriptive model

The previous section showed the impact of two distance variables (IPS and MPT) on concrete flowability. Based on the hypothesis that these two variables could describe slump, a linear model was adjusted (Equation 3) to predict slump.

The estimated parameters are shown in Table 3. Figure 8 shows how well expected slump fits to model slump. For an individual Formulation Set, R^2 are between 0.97 and 0.98. When both Formulation Sets are considered together a lower value, but still good, correlation (R^2 0.91) was achieved.

$$s = a + b \times IPS + c \times MPT + d \times IPS * MPT \tag{3}$$

Table 3: Estimated parameters

Parameter	Formulation Set 1	Formulation Set 2	Formulation Set 1 and 2
a	-210.4	-229.5	-197.26
b	124.7	111.8	115.05
c	-0.189	-0.260	-0.175
d	7.58	8.89	7.56

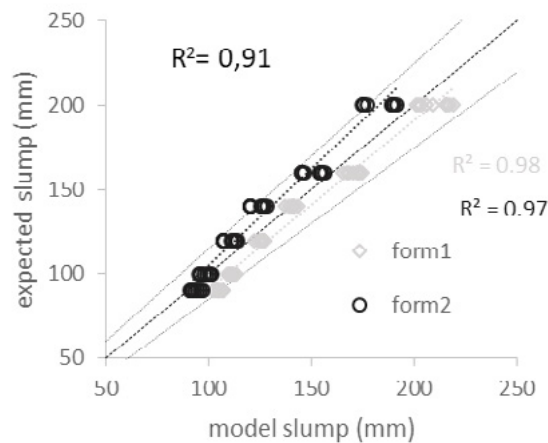


Figure 8: Correlation between the expected slump and model slump

This model is able to describe the slump for two different material sets and 120 concretes. This high correlation can be explained because the distance between particles in phases governs the concrete rheological behaviour, the correlation shows that its three variables present relevance on the physical phenomenon and its equation can quantitatively describe the slump.

This realization allows the creation of a concrete design strategy. The water/cement ratio governs the IPS and, consequently, the viscosity of the paste in this experimental region. As the water/cement ratio is determined by the specified compressive strength, the gain in binder efficiency should be obtained by reducing paste consumption, that is, increasing the coarse solid fraction in the formulation. Thus, for a specified concrete (f_{ck} , slump and maximum aggregate size), it is desired to increase the coarse solid fraction keeping a fixed MPT by reducing the coarse packing porosity. Computational optimization can minimize the coarse packing porosity keeping the specified slump, strategy that will reduce the concrete paste and binder intensity, increasing eco-efficiency.

4. Conclusions

This study analysed eco-efficiency of concrete produced by a concrete plant in São Paulo/Brazil, through binder intensity. For a given strength, concretes with the lowest binder intensity are those with maximum aggregate size 19mm and lower slump, reaching 7.5 to 8 kg/m³/MPa. The lowest eco-efficiency was obtained by those with a maximum aggregate size of 9.5mm and higher slump, reaching values between 9 and 10kg/m³/MPa. The Material Set 2 led to a slightly lower binder intensity than the Material Set 1.

For the concrete rheological behaviour, there is a high correlation between the MPT and the slump, with the correlation coefficient of the adjusted linear curve (R^2) between 0.97 and 0.98, for both Formulation

Set, given a paste composition and a f_{ck} . Based on that, a descriptive model of the slump in function of MPT and IPS was adjusted getting R^2 0.91 between the expected slump and the model slump when both Formulation Set are considered together. This high correlation shows that these three variables used to evaluate particle distance present relevance on the physical phenomenon and its equation can quantitatively describe the slump.

This model can be used by computational optimization of mixture design, in order to reduce the paste volume and increase concrete eco-efficiency.

5. Acknowledgment

This research was partially supported by InterCement. We thank InterCement technical team who provided materials, data, insight and expertise that greatly assisted the research.

6. Reference

- [1] IEA and WBCSD, 2018, Technology Roadmap: Low-Carbon Transition in the Cement Industry.
- [2] R. J. Flatt, N. Roussel, and C. R. Cheeseman, 2012, Concrete: An eco material that needs to be improved, *J. Eur. Ceram. Soc.*, vol. 32, no. 11, pp. 2787–2798.
- [3] T. C. Powers, 1968, *The properties of fresh concrete*, 1st ed. Michigan.
- [4] R. G. Pileggi, 2001, *Ferramentas para o estudo e desenvolvimento de concretos refratários*, São Carlos, UFSCar.
- [5] B. L. Damineli, V. M. John, B. Lagerblad, and R. G. Pileggi, 2016, Viscosity prediction of cement-filler suspensions using interference model: A route for binder efficiency enhancement, *Cem. Concr. Res.*, vol. 84, pp. 8–19.
- [6] N. Roussel, A. Lemâitre, R. J. Flatt, and P. Coussot, 2010, Steady state flow of cement suspensions: A micromechanical state of the art, *Cem. Concr. Res.*, vol. 40, no. 1, pp. 77–84.
- [7] H. Hafid, G. Ovarlez, F. Toussaint, P. H. Jezequel, and N. Roussel, 2016, Effect of particle morphological parameters on sand grains packing properties and rheology of model mortars, *Cem. Concr. Res.*, vol. 80, pp. 44–51.
- [8] F. de Larrard, *Concrete mixture proportioning a scientific approach*, 1999, 1st ed. London: E & FN Spon.
- [9] F. Larrard and T. Sedran, 1994, Optimization of ultra-high-performance concrete by the use of a packing model, *Cem. Concr. Res.*, vol. 24, no. 6, pp. 997–1009.
- [10] O. H. Wallevik and J. E. Wallevik, 2011, Rheology as a tool in concrete science: The use of rheographs and workability boxes, *Cem. Concr. Res.*, vol. 41, no. 12, pp. 1279–1288.
- [11] R. J. Flatt and P. Bowen, 2006, Yodel: A Yield Stress Model for Suspensions, *J. Am. Ceram. Soc.*, vol. 89, no. 4, pp. 1244–1256.
- [12] R. J. Flatt, 2004, Towards a prediction of superplasticized concrete rheology, *Mater. Struct.*, vol. 37, no. 5, pp. 289–300.
- [13] A. Arora et al., 2018, Microstructural packing- and rheology-based binder selection and characterization for Ultra-high Performance Concrete (UHPC), *Cem. Concr. Res.*, vol. 103, pp. 179–190.

- [14] S. T. Erdoğan, A. M. Forster, P. E. Stutzman, and E. J. Garboczi, 2017, Particle-based characterization of Ottawa sand: Shape, size, mineralogy, and elastic moduli, *Cem. Concr. Compos.*, vol. 83, pp. 36–44.
- [15] K. Sobolev and A. Amirjanov, 2010, Application of genetic algorithm for modeling of dense packing of concrete aggregates, *Constr. Build. Mater.*, vol. 24, no. 8, pp. 1449–1455.
- [16] A. Dörr, A. Sadiki, and A. Mehdizadeh, 2013, A discrete model for the apparent viscosity of polydisperse suspensions including maximum packing fraction, *J. Rheol. (N. Y. N. Y.)*, vol. 57, no. 3, pp. 743–765.
- [17] I. Mehdipour and K. H. Khayat, 2017, Effect of particle-size distribution and specific surface area of different binder systems on packing density and flow characteristics of cement paste, *Cem. Concr. Compos.*, vol. 78, pp. 120–131.
- [18] B. F. Tutikian and P. Helene, 2011, Dosagem dos Concretos de Cimento Portland, in *Concreto: Ciência e Tecnologia*, 1st ed., no. 1927, G. C. ISAIA, Ed. São Paulo, IBRACON, pp. 439–471.
- [19] M. A. DeRousseau, J. R. Kasprzyk, and W. V. Srubar, 2018, Computational design optimization of concrete mixtures: A review, *Cem. Concr. Res.*, vol. 109, pp. 42–53.
- [20] F. Larrard and T. Sedran, 2002, Mixture-proportioning of high-performance concrete, *Cem. Concr. Res.*, vol. 32, no. 11, pp. 1699–1704.
- [21] B. L. Daminieli, 2013, *Conceitos para formulação de concretos com baixo consumo de ligantes: controle reológico, empacotamento e dispersão de partículas*. São Paulo, Universidade de São Paulo.

HYDCEM: A new cement hydration model

N. Holmes¹, D. Kelliher² and M. Tyrer³

¹School of Civil & Structural Engineering, Technological University Dublin, Ireland

²School of Civil, Structural & Environmental Engineering, University College Cork, Ireland;

³Centre for research in the built and natural environment, Coventry University, UK

Abstract

Hydration models are useful to predict, understand and describe the behaviour of different cementitious-based systems. They are indispensable for undertaking long-term performance and service life predictions for existing and new products for generating quantitative data in the move towards more sustainable cements while optimising natural resources. One such application is the development of cement-based thermoelectric applications.

HYDCEM is a new model to predict the phase assemblage, degree of hydration, heat release and changes in pore solution chemistry over time for cements undergoing hydration for any w/c ratio and curing temperatures up to 45°C. HYDCEM, written in MATLAB, is aimed at complementing more sophisticated thermodynamic models to predict these properties over time using user-customisable inputs. A number of functions based on up to date cement hydration behaviour from the literature are hard-wired into the code along with user-changeable inputs such as the cement chemical (oxide) composition, cement phase densities, element molar mass, phase and product densities and heat of hydration enthalpies. HYDCEM uses this input to predict the cement phase and gypsum proportions, volume stoichiometries and dissolution and growth of hydration products from the silicates, aluminates and ferrites, including C-S-H, calcium hydroxide, hydrogarnet (if applicable) ettringite and monosulphate. A number of comparisons are made with published experimental and thermodynamic model results and HYDCEM predictions to assess its accuracy and usefulness.

The results show that HYDCEM can reasonably accurately predict phase assemblages in terms of volume change and behaviour for a range of cements and curing temperatures. It is proposed that HYCEM can complement more sophisticated thermodynamic models to give users a reasonable prediction of cement behaviour over time.

Keywords: Cement; Hydration; microstructure; model; MATLAB

1. Introduction

Cement hydration and microstructure development is a complex process. However, the advances in computing power and range of programmable software in recent years has made the modelling of cement hydration achievable. A comprehensive review of other cement hydration and microstructure models over the past 45 years including single particle models, mathematical nucleation and growth models and vector and lattice-based approaches to simulating microstructure development can be found at [1]. While computer modelling should never completely replace experimental analysis, it does provide valuable insights into the process particularly with the increased use of supplementary cementitious and other sustainable materials [2]. Model outputs here are based on the cements chemical (oxide) composition and element molar masses

to calculate phase proportions (based on modified Bogue equations [3]) and volume stoichiometries to improve the accuracy of the predictions. Previous work to compare simulation and measured properties have been presented [3-6] but, in order to accelerate the acceptance of prediction models, direct comparisons are best [8].

Cement particles at the micro-scale are made up of four main phases, namely tri-calcium silicate (C_3S)¹, di-calcium silicate (C_2S), tri-calcium aluminate (C_3A) and tetra-calcium aluminate ferrite (C_4AF) with particle size distributions ranging from 60-100 μ m to less than 1 μ m. Of the four phases above, C_3S is by far the most influential in terms of chemical reactivity and contribution to long term strength gain making up approximately 65-70% of overall cement content. It is no surprise therefore that the hydration of C_3S alone has been the focus of several numerical models [1,9] due to its influence and relative straightforward reaction and product development. Upon reaction with water, C_3S produces calcium silicate hydrate (written as C-S-H) and calcium hydroxide (CH)². However, in order for a full prediction of the hydration of a cement, it is important that all cement phases are included in any analysis.

One way of predicting the performance of a hydrating cement is by thermodynamic modelling which provides, amongst others, phase assemblage and pore concentration predictions. Such hydration predictions allow cement scientists assess the performance, troubleshoot short and long-term problems and even help design new cement-based materials. Despite significant effort and progress, the ability to perform such a complete simulation has not been developed, mainly because cement hydration is one of the more complex phenomena in engineering science.

This paper presents a new model, HYDCEM, written in MATLAB to undertake cement hydration analysis to predict phase assemblage, degree of hydration, heat release and pore solution chemistry over time for any w/c ratio and curing temperatures up to 45°C. HYDCEM is aimed to complement the more sophisticated thermodynamic models giving users an accurate prediction of how their Portland cement will perform by demonstrating cement phase and gypsum dissolution and the development of hydration products over time.

All input parameters required by the model are fully defined by the user including the cement chemical (oxide) composition, element molar mass, cement phase densities, phase and product densities and heat of hydration enthalpies. It uses this information to calculate the unhydrated cement proportions, gypsum content and magnesium and volume stoichiometries, which in turn determines the volumes of silicates, aluminates and ferrites hydration products namely, C-S-H, calcium hydroxide, hydrogarnet, ettringite, monosulphate and hydrotalcite. The model employs the empirical-based Parrot and Killoh [10] approach for the degree of hydration for the cement phases with an input file read in that includes the Blaine surface area of the cement, temperature, phases activation energies and the constants developed by Lothenbach [11,12] for the three reaction regimes, namely nucleation and growth, shell formation and diffusion.

The initial design of the model is presented along with worked examples to compare HYDCEM phase assemblage predictions with results from the literature. Phase assemblage predictions provide a much better insight how the microstructure is developing. MATLAB is particularly well suited to this type of analysis due to its 'engineering-like' architecture both in terms of coding language and background calculations. Also, the significant amount of help available for MATLAB programmers online make writing and understanding the code very straightforward.

1 Conventional cement chemistry notation: C=CaO, S=SiO₂, A=Al₂O₃, F=Fe₂O₃, and H=H₂O.

2 H = water; CH = Calcium Hydroxide; CAH = Hydrogarnet; GYP = Gypsum; ETTR = Ettringite; MONO = Monosulphate; FH = Iron Oxide

2. Model Design

2.1 Input files

HYDCEM was developed with the user in mind by providing clearly laid out and easy to change flat text input files. The analysis/calculation flow for HYDCEM is shown in Figure 1. As may be seen, when the input data files are read into the model, the analysis follows a well-structured methodology by using multiple functions within the main HYDCEM script along with pre-allocation of single precision outputs for quicker analysis. The data is stored within predefined single column vectors with the number of rows equal to the number of hourly time steps. There is an expected increase in analysis time with the duration of hydration (Figure 2) with 10,000 hourly time steps analysed in less than 1/2 second.

2.2 Chemical Properties

Using four customisable input files (oxide_proportions.txt, densities.txt, molar_mass.txt & molar_mass_reaction.txt) as shown in Figure 1, the four cement phase and gypsum proportions are determined using the Bogue equations [3] shown in Equations 1-5 below. The volume stoichiometries are calculated based on the molar mass reaction of the cement phase, the molar mass of the phase (C3S, etc.)

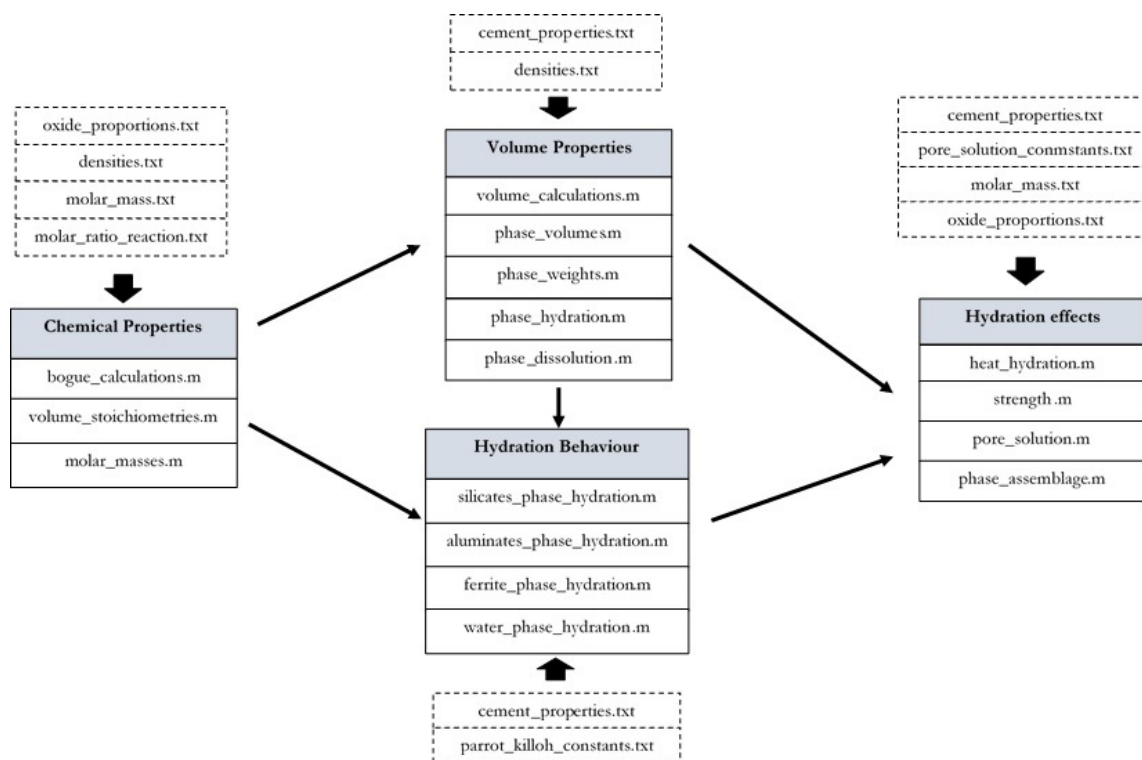


Figure 1: Diagram of HYDCEM's Matlab functions (*.m) and customisable input text files (*.txt)

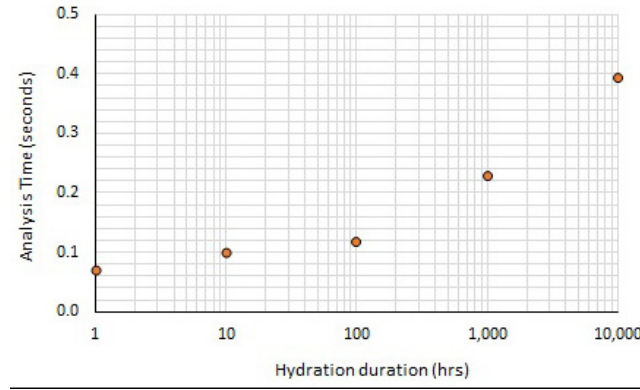
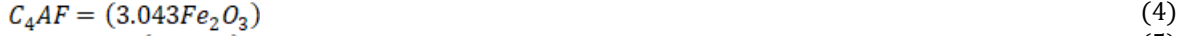
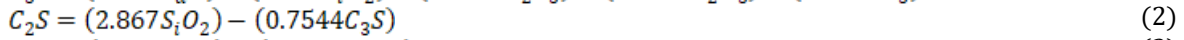
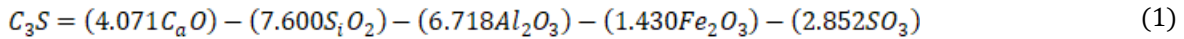


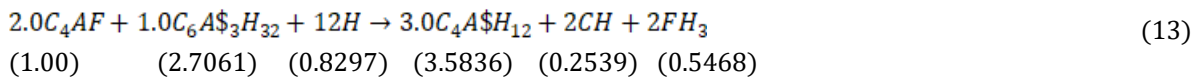
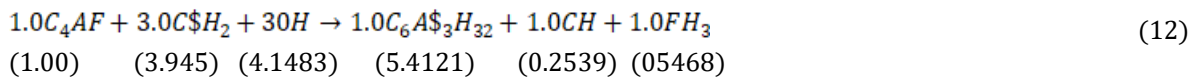
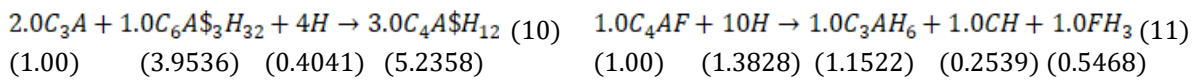
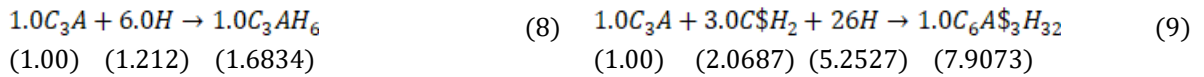
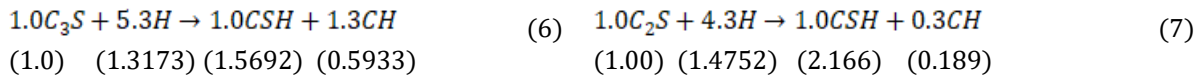
Figure 2: Analysis time for increasing hydration durations



or hydration product (C-S-H, etc.) and the density, all of which are customisable by the user. The molar mass reaction for the four cement phases and magnesium (Mg) are shown in Equations 6-14 with their calculated volume stoichiometries shown in brackets below.

2.3 Dissolution of cement phases

The dissolution of the four cement phases are calculated in HYDCEM using the approach presented by Parrot and Killoh [10] that uses a set of empirical expressions to estimate the degree of hydration of each phase as a function of time. The dissolution of each phase is determined using Equations 15 to 17 where the lowest hydration rate R_t is taken as the rate-controlling value.



The degree of hydration (α) is expressed as $\alpha_t = \alpha_t - 1 + \Delta_t \cdot R_{t-1}$. The K, N and H values used for the three phases are those proposed by Lothenbach *et al* [11,12]. The influence of the surface area on the initial hydration are included as well as the influence of w/c ($= (1 + 3.333 (H * w/c - \alpha_t))^4$; for $\alpha_t > H * w/c$).

$$R_t = \frac{K}{N} (1 - \alpha_t) (-\ln(1 - \alpha_t))^{(1-N)} \quad (15)$$

$$R_t = \frac{K(1 - \alpha_t)^{\frac{2}{3}}}{1 - (1 - \alpha_t)^{\frac{1}{3}}} \tag{16}$$

$$R_t = K(1 - \alpha_t)^N \tag{17}$$

2.4 Hydration Behaviour

The change in volume of cement phases, gypsum, hydration products and water are calculated using the volume stoichiometries calculated from the molar ratios in reactions (Equations 6-14) within using a series of programming operations. HYDCEM has implemented well accepted cement hydration behaviour found in the literature as shown Figure 3, for example where the growth in monosulfate (for limestone free cements) begins after gypsum has been depleted [12,13] with increased ettringite volume until all gypsum is depleted [11,13]. The following section presents a worked example to show HYDCEM predictions of hydration behaviour over time.

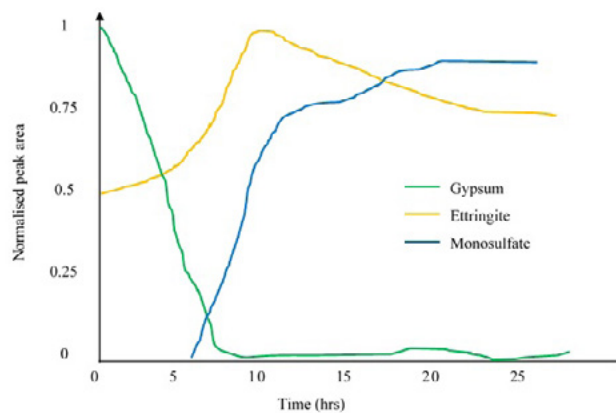


Figure 3: Kinetics of aluminate hydration for limestone-free cements (after Scrivener, 1984 [13])

3. Worked Example

The worked example is based on work by Lothenbach *et al* [11] with the cement properties shown in Table 1. The published phase assemblages or thermodynamic modelling shown here to compare the HYDCEM output with were carried out using the Gibbs free energy minimization program GEMS [14,15]. GEMS is a broad-purpose geochemical modelling code which computes equilibrium phase assemblage and speciation in a complex chemical system from its total bulk elemental composition. A detailed description of GEMS can be found elsewhere in the literature [14-17].

Table 1: Sample of input for worked example

Cement composition [11]		Enthalpy (J/g) [2]		Parameters for degree of hydration analysis [11]				
CaO	63.9	C3S	517	Parameter	C3S	C2S	C3A	C4AF
SiO ₂	20.2	C2S	262	K1	1.5	0.5	1.0	0.37
Al ₂ O ₃	4.9	C3A	1144	N1	0.7	1.0	0.85	0.7
Fe ₂ O ₃	3.2	C4AF	725	K2	0.05	0.02	0.04	0.015
CaO(free)	0.93			K3	1.1	0.7	1.0	0.4
MgO	1.8			N3	3.3	5.0	3.2	3.7
K ₂ O	0.78			H	1.8	1.35	1.6	1.45
Na ₂ O	0.42							
CO ₂	0.26			Blaine surface area (m ² /kg)		413		
SO ₂	2.29			w/c ratio		0.4		
K ₂ O (soluble)	0.72			Temperature (°C)		20		
Na ₂ O (soluble)	0.09							

The (a) HYDCEM predicted and (b) published cement dissolution of the four phases are shown in Figure 4. As may be seen, there is close agreement between the measured and predicted phase dissolution values.

Figure 5 shows (a) the HYDCEM and (b) published phase assemblage diagrams [11] for the cement described in Table 1. Figure 5(b) shows small quantities of monocarbonate, brucite and hemicarbonate that are not included in the HYDCEM model. Despite this, the HYDCEM predictions are very close to the measured phase assemblage with the products of hydration forming at a similar rate over time. Also, the dissolution of gypsum is very similar with both predictions showing it completely depleted within 10 hours. As expected, both show similar reductions in the volume of ettringite with increasing monosulfate volume over time. Figure 6 shows the modelled aluminates products of hydration over time. Again, there is a reasonably close agreement between both.

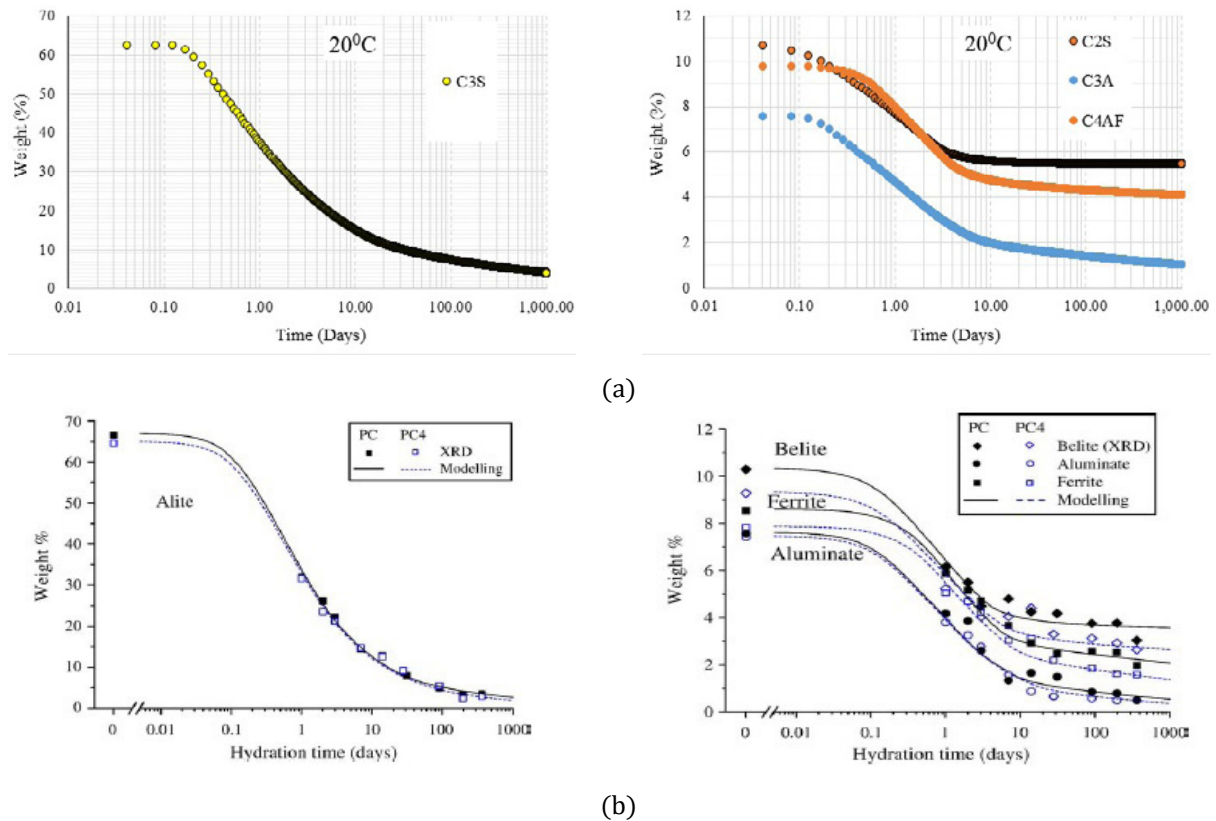


Figure 4: (a) Predicted (HYDCEM) and (b) published [11] cement phase dissolution at 20°C.

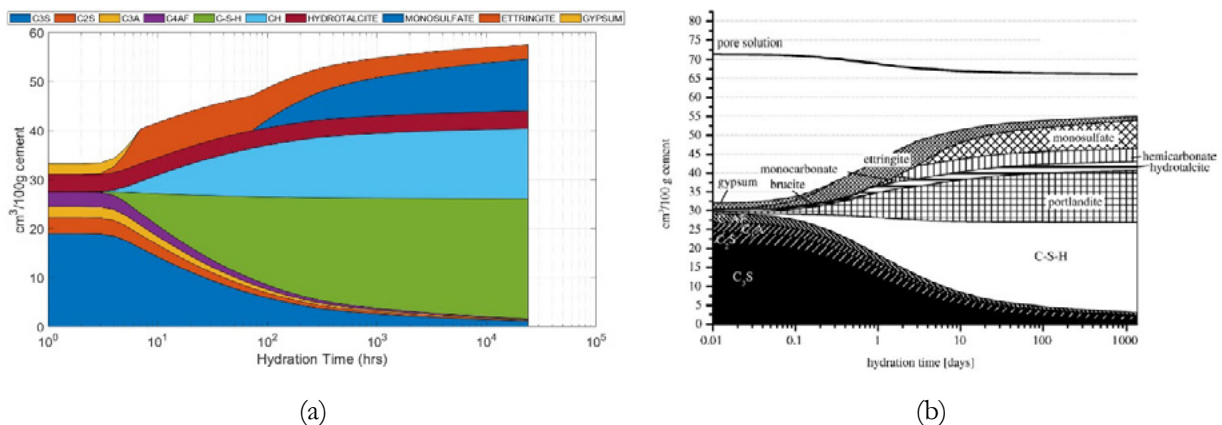


Figure 5: (a) Predicted (HYDCEM) and (b) GEMS modelled phase assemblages [11] at 20°C.

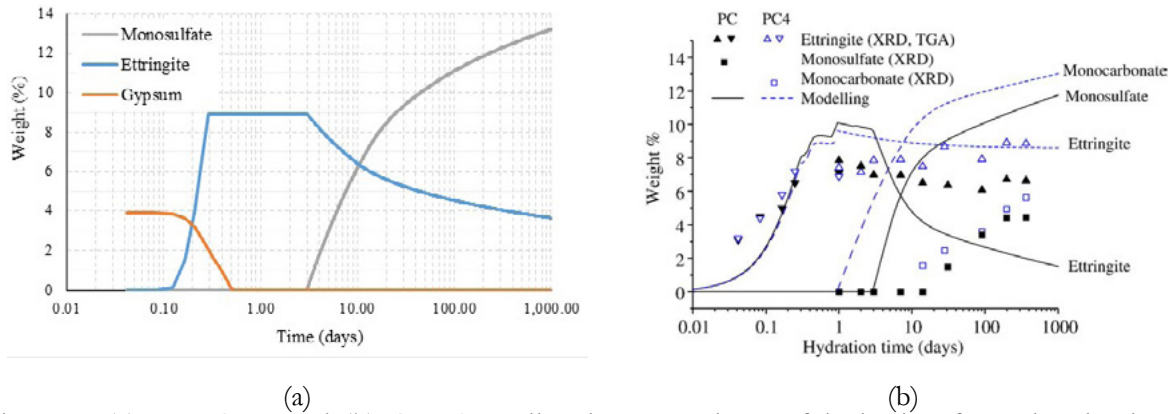


Figure 6: (a) HYDCEM and (b) GEMS predicted [11] products of hydration from the aluminate phase.

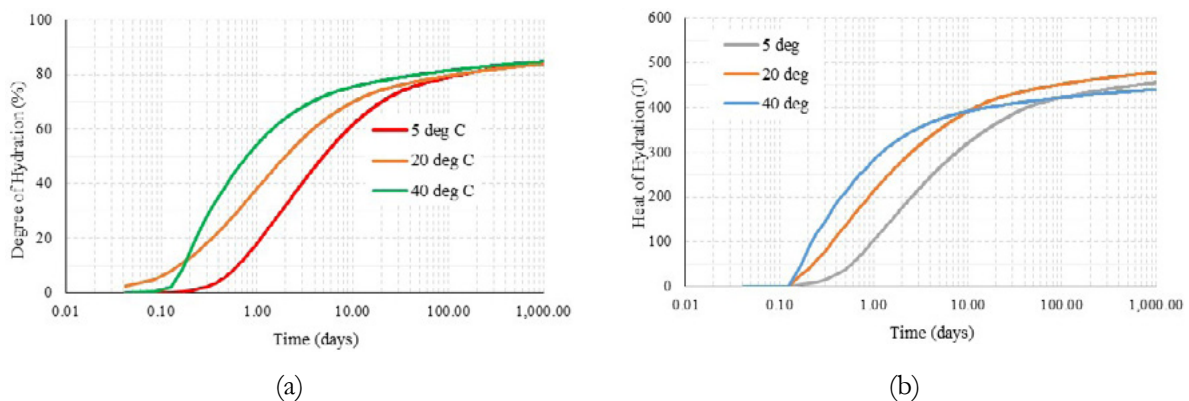


Figure 7: HYDCEM predicted (a) degree of hydration and (b) heat of hydration at (a) 5^oC, 20^oC and 40^oC over time.

Figure 7 shows a suite of HYDCEM predictions of the (a) degrees of hydration and (b) heat release over time for curing temperatures of 5, 20 and 40^oC. Lower curing temperatures cause hydration to start very slowly allowing the dissolved ions more time to diffuse prior to precipitation of hydrates along with the slower dissolution of gypsum [18]. This leads to a less dense C-S-H, a more even distribution of hydration products and a less coarse porosity [18-22]. The effect of the higher temperature can be observed with an initially fast dissolution of the four cement phases and a more rapid precipitation of hydration products early on. This is responsible for the early strength development observed at higher temperatures along with a more heterogeneous distribution of hydration products in and around the clinker particles [20]. The effect of the higher temperature demonstrates a much more rapid rate of hydration, as discussed above. The predicted degree of hydration (Figure 7(a)) at the three temperatures are as expected. At 5^oC, the degree of hydration is slower whereas at 40^oC, it is more rapid early on quickly slowing down over time. For instance, after 10 hours of hydration, the overall degree of hydration at 5^oC, 20^oC and 40^oC is 7, 18 and 36% respectively. However, after 100 hours of hydration, the overall degree of hydration at the three temperatures is 47, 61 and 71% respectively, which clearly shows the effect of curing temperature as discussed above.

4. Conclusions

The HYDCEM model has been found to simulate the hydration and microstructure development of Portland cements. Using cement composition and reaction relationships, the cement phase and products of hydration are determined in volumetric terms over time for any w/c ratio and curing temperatures up to 45^oC. Results presented here have shown good agreement with published hydration behaviour. HYDCEM can therefore become a useful tool for the initial prediction of cement hydration and microstructure

behaviour before the use of more sophisticated thermodynamic models. Development of the model is ongoing with additional features being added to include limestone and predictions of the pore solution chemistry by coupling with the PHREEQC geochemical model [23]. Future developments also include predictions of electrical and thermal conductivities to better understand the potential of cement based thermoelectric materials.

5. Acknowledgement

The authors would like to thank the financial assistance provided by Science Foundation Ireland as part of the ThermoConc research project.

6. References

- [1] Thomas, J.J., Biernacki, J.J., Bullard, J.W., Bishnoi, S., Dolado, J.S., Scherer, G.W. and Luttge, A. (2011) Modeling and simulation of cement hydration kinetics and microstructure development, *Cement and Concrete Research* 41, pp. 1257–1278.
- [2] Garbozi, E.J., Bentz, D.P. and Frohnsdorff, G.J (2000) The Past, Present, and Future of Computational Materials Science of Concrete, *Materials Science of Concrete Workshop*, Centre for Advanced-Cement-Based Materials, April 27-29, Lake Shelbyville, IL, 10 pages.
- [3] ASTM C150-09, standard specification for portland cement. *Annual Book of ASTM Standards*, ASTM International, West Conshocken, PA, 4.
- [4] D.P. Bentz, Three-dimensional computer simulation of Portland cement hydration and microstructure development, *J. Am. Ceram. Soc.* 80 (1) (1997) 3– 21.
- [5] D.P. Bentz, E.J. Garbozi, C.J. Haecker, O.M. Jensen, Effects of cement particle size distribution on performance properties of cement-based materials, *Cem. Concr. Res.* 29 (1999) 1663–1671.
- [6] C.J. Haecker, D.P. Bentz, X.P. Feng, P.E. Stutzman, Prediction of cement physical properties by virtual testing, *Cem. Int.* 1 (3) (2003) 86– 92.
- [7] A. Princigallo, P. Lura, K. van Breugel, G. Levita, Early development of properties in a cement paste: a numerical and experimental study, *Cem. Concr. Res.* 33 (2003) 1013– 1020.
- [8] Bentz, D.P (2006) Quantitative comparison of real and CEMHYD3D model microstructures using correlation functions, *Cement and Concrete Research* 36, pp. 259 – 263.
- [9] Holmes, N., Griffin, A., Enright, B. and Kelliher, D (2018) Introducing a new cement hydration and microstructure model, *Civil Engineering Research in Ireland (CERI) conference*, UCD Ireland, Editors Vikram Pakrashi and Jennifer Keenahan, pp. 202-207.
- [10] L.J. Parrot, D.C. Killoh, Prediction of cement hydration, *Br. Ceram. Proc.* 35 (1984) 41–53.
- [11] Lothenbach, B., Le Saout, G., Gallucci, E. and Scrivener, K. (2008) Influence of limestone on the hydration of Portland cements, *Cement and Concrete Research* 38 pp. 848–860.
- [12] Lothenbach, B., Winnefeld, F., Alder, C., Wieland, E., and Lunk, P. (2007) Effect of temperature on the pore solution, microstructure and hydration products of Portland cement pastes, *Cement and Concrete Research* 37 (4) pp. 483–491.
- [13] Scrivener, K.L and Pratt, P.L (1984) Microstructural studies of the hydration of C3A and C4AF independently and in cement paste, *The Chemistry and Chemically related properties of cement*, Edited

by F.P. Glaser, Proceedings of the British Ceramic Society, Vol. 35, pp. 207-20.

- [14] D. Kulik, GEMS-PSI 2.1, 2007, available at <http://gems.web.psi.ch/>, PSI-Villigen, Switzerland.
- [15] T. Thoenen, D. Kulik, Nagra/PSI chemical thermodynamic database 01/01 for the GEM-Selektor (V.2-PSI) geochemical modeling code, PSI, Villigen, 2003, available at <http://gems.web.psi.ch/doc/pdf/TM-44-03-04-web.pdf>.
- [16] W. Hummel, U. Berner, E. Curti, F.J. Pearson, T. Thoenen, Nagra/PSI chemical thermodynamic data base 01/01, Universal Publishers/uPUBLISH.com, USA, also published as Nagra Technical Report NTB02-16, Wettingen, Switzerland, 2002.
- [17] B. Lothenbach, T. Matschei, G. Möschner, F.P. Glasser, Thermodynamic modelling of the effect of temperature on the hydration and porosity of Portland cement Cement and Concrete Research 38 (1) (2008) 1–18.
- [18] Lothenbach, B. Thermodynamic modelling of the effect of temperature on the hydration of Portland cement, International RILEM Symposium on Concrete Modelling – CONMOD 2008, 26-28 May, Delft, The Netherlands.
- [19] Kjellsen, K.O., Detwiler, R.J., (1992) Reaction-kinetics of Portland-cement mortars hydrated at different temperatures, Cement & Concrete Research 22 (1), pp. 112-120.
- [20] Escalante-Garcia, J.I., Sharp, J.H. (1998) Effect of temperature on the hydration of the main clinker phases in Portland cements: Part I, neat cements, Cement & Concrete Research 28 (9), pp. 1245-1257.
- [21] Komonen, J., Penttala, V. (2003) Effects of high temperatures on the pore structure and strength of plain and polypropylene fiber reinforced cement pastes, Fire Technol 39 (1), pp. 23-34.
- [22] Thomas, J.J., Rothstein, D., Jennings, H.M., Christensen, B.J. (2003), Effect of hydration temperatures on the solubility behaviour of Ca-, S-, Al- and Al- and Si- bearing solid phases in Portland cement pastes, Cement & Concrete Research 33 (12), pp. 2037-2047.
- [23] David L. Parkhurst and C.A.J. Appelo (2013) Description of input and examples for PHREEQC version 3: a computer program for speciation, batch-reaction, one-dimensional transport, and inverse geochemical calculations, Techniques and Methods 6-A43, Chapter 43, Section A.

Chloride Ingress and Degradation of Portland Cement Mortar Exposed to Seawater Attack Coupling with Drying-wetting Cycle

S. Cheng¹, Z. Shui¹, T. Sun^{1,2}, X. Gao^{1,2}

¹State Key Laboratory of Silicate Materials for Architectures, Wuhan University of Technology, Wuhan 430070, China.

²School of Civil Engineering and Architecture, Wuhan University of Technology, Wuhan 430070, China.

Abstract

The chloride, sulphate and magnesium ion attack usually occur together in marine environment. The corrosion of concrete in seawater is mainly caused by the chloride induced reinforcement corrosion, the exfoliation of magnesium salt and the volume expansion due to sulphate attack. In addition to ions attack, the drying-wetting cycles always cause a severe deterioration of concrete structures. This study aims to identify the chloride ingress and mechanisms of degradation in Portland cement mortar exposed to simulated seawater attack under drying-wetting cycle conditions. Mortar mixtures are prepared and exposed to NaCl, NaCl+MgCl₂, NaCl+Na₂SO₄ and NaCl+Na₂SO₄+MgCl₂ solutions with a fixed chloride concentration. Chloride transportation and binding capacity of Portland cement based mortars are investigated by titration. In order to identify phase assemblages and microstructural evolutions under exposure, samples are examined by applying XRD, TGA, SEM-EDS and MIP. The analysis of the physical aspect reveal that after 90 days of drying-wetting, the outmost layer (0-5mm) is enriched in sulphate and magnesium ion, and present the highest chloride ion content when exposed to NaCl+MgCl₂ solutions. Moreover, the presence of Mg²⁺ and Mg²⁺+SO₄²⁻ in chloride solution accelerates the chloride ingress, increases the apparent chloride diffusion coefficient and reduces the chloride binding capacity. However, the presence of SO₄²⁻ in NaCl solution retards the chloride ingress and enhances the chloride binding capacity. On the other hand, the chemical composition analysis highlights the conspicuous consumption of portlandite in the outmost layer, the decalcification of C-S-H, and the ettringite (AFt) formation from AFm and aluminium phases. The microstructure analysis shows a refined pore size and significant micro-cracking formation in the sulphate and chloride conditions due to formation of AFt. These phase changes are generally agreed with the predictions of a thermodynamic model.

Keywords: Chloride ingress; Sulfate; Magnesium; Drying-wetting cycle; Thermodynamic model.

1. Introduction

Reinforced concrete is an important construction material for marine exposed structures due to its ability to withstand the harsh marine environment. However, the service life of reinforced concrete structures can be limited by several deterioration mechanisms. Concerning the chemical attacks, the chloride induced reinforcement corrosion is one of the main degradations of concrete, and the simultaneous presence

of corrosive ions such as chloride, sulfate and magnesium in seawater even shows a combined effect on chemical corrosion [1-4]. On the other hand, the physical degradation of concrete under marine environment is non-ignorable factor that can accelerate the chemical attacks. Typical physical degradations such as leaching, wave erosion, repeated dry and wet usually leads to the dissolution of hydrated products and increases the porosity [5-7], and then the concrete matrix is more vulnerable to ingress of aggressive ions and results in surface crack.

The tidal zone is the most serious damage area of concrete structures in marine environment, where usually presents the most complicated degradations including both physical and chemical attacks. However, the degradation mechanisms of cementitious materials under multiple ions attack and drying-wetting cycles have not been studied in detail. This work highlights the degradation mechanisms of Portland cement mortar by multiple corrosive ions under the drying-wetting zone. First of all, the degradation behaviors including mass changes and relative dynamic modulus of elasticity of samples exposed to simulated seawater and the impacts of sulfate and magnesium ions on the chloride ion ingress are investigated. Then, the multiple corrosive ion induced phase changes under drying-wetting cycles are presented. Furthermore, the phase changes are compared with the predictions of a thermodynamic model. Lastly, the microstructure characteristics of mortar samples under different corrosive environments are identified by scanning electron microscopy-energy dispersive spectrometer (SEM-EDS) and mercury intrusion porosimetry (MIP).

2. Methodology

2.1 Materials

The Portland cement type CEM I (strength class 42.5) was used to produce the mortar specimens according to European standard EN 197-1, the chemical composition of cement was determined by X-ray fluorescence (XRF) and shown in Table 1. The analytical reagents sodium chloride, hexahydrate magnesium chloride and anhydrous sodium sulfate were utilized to simulate the major elements in seawater.

Table 1: Chemical composition of ordinary Portland cement by X-ray fluorescence.

Constituents	SiO ₂	Al ₂ O ₃	CaO	MgO	Fe ₂ O ₃	K ₂ O	Na ₂ O	SO ₃	LOI
wt.%	21.76	5.83	62.69	1.72	3.41	1.22	0.07	1.09	1.11

2.2 Sample preparation and exposed to corrosive solution

According to Chinese standard GB/T 29756-2013, mortar mixtures with water to cement ratio of 0.5 and sand to binder ratio of 3 were prepared. Samples were cast in steel molds of 40×40×160 mm³, and then demould after 1 day and cured under the condition of 20±2°C and 98±2% relative humidity for 7 days. Mortar samples were also prepared and filled into 50 mL centrifuge tube, then stored in standard curing chamber. The cement pastes with the same w/c ratio were produced for microstructure analysis.

Table 2: Detailed composition of the exposure solutions.

Conc. (M)	NaCl	MgCl ₂	Na ₂ SO ₄	Cl conc. (M)
NaCl	0.56	-	-	0.56
NaCl+MgCl₂	0.46	0.05	-	0.56
NaCl+Na₂SO₄	0.56	-	0.028	0.56
NaCl+MgCl₂+Na₂SO₄	0.56	0.05	0.028	0.56

The physical and chemical degradation of samples in the ocean tidal zone was simulated by using a self-made drying-wetting cycle test chamber. The corrosion solutions were used: NaCl solution (N), NaCl+MgCl₂ solution (N+M), NaCl+Na₂SO₄ solution (N+S) and NaCl+MgCl₂+Na₂SO₄ solution

(N+M+S). Compared with the seawater, the detailed composite of each corrosive solution were presented in Table 2. All solutions were having a fixed chloride concentration of 0.56 mol/L, and then they were stored in four self-regulating polymethyl methacrylate boxes.

The drying-wetting cycle was set as follows: Firstly, samples were immersed in corrosive solution for 18 h, and then dried for 0.5 h in the air. Afterwards, the samples were dried for 5 h at a temperature of 60°C and followed by cooling down at the room temperature for 0.5 h. Thus, the 24 h represent one drying-wetting cycle. The schematic of drying-wetting cycle box is shown in the Fig. 1. In order to maintain concentration stability of all ions, the exposed solutions were replaced every two weeks.

2.3 Methods

2.3.1 Chloride diffusion

The specimens in the centrifuge tubes were analyzed after 30, 60, 90 and 120 days of exposure. The exposed surfaces were used for profile grinding according to the following intervals: 0-5, 5-10, 10-15 and 15-20 mm. Then, the ground samples were stored in plastic sample sack and placed in a desiccator until analysis. According to the technical specification for chloride ion content test in concrete (JGJ/T 322-2013), the specimen was grinding and passed through a 0.15mm square hole. Then, the collected powder was dried at 105 °C for 2 h, followed by taking about 5 g and mixing the powder with about 50 mL (V₃) diluted nitric acid (water: nitric acid=15:85), and then shocked for 1~2 minutes and stored for 24 h. Afterwards, 10 mL of the supernatant was taken by pipette and placed in a conical flask, and added with 10 mL silver nitrate solution. Finally, the mixtures were titrated with potassium thiocyanate. The total chloride content of specimen can be calculated by Eq. (1).

$$P = \frac{0.3545(C \times V - C' \times V_1)}{G \times \frac{V_2}{V_3}} \times 100\% \quad (1)$$

where P denotes the total chloride content (%); C is the concentration of silver nitrate solution (mol/L); C' is the potassium thiocyanate solution (mol/L); V and V₁ respectively denotes the volume of the added silver nitrate solution and the consumed volume of potassium thiocyanate solution at each test (mL); G is the sample mass of exposed mortar (g); V₂ and V₃ are the selected amount for titration and the amount of dilute nitric acid for dissolved sample (mL).

The apparent chloride ion diffusion coefficient (D_a) is an important index which can be used to characterize the speed of chloride ingress. The apparent chloride diffusion coefficient and the concentration at the surface of sample are determined by fitting experimental data using the solution of Fick's second law fitting Eq. (2).

$$C_{x,t} = C_s [1 - \text{erf} \left(\frac{x}{2\sqrt{D_a t}} \right)] \quad (2)$$

where C_{x,t} is the free chloride content at depth x (m) and exposure time t (s), C_s is the chloride content at the surface and D_a is the apparent diffusion coefficient. The chloride content at the surface (C_s) and apparent diffusion coefficient (D_a) were obtained from the best fit by least squares.

2.3.2 Degradation performance

The mass change measurements after different exposure times can be used to characterize the surface changes of specimen, which can be regarded as an indicator of physical degradation. The mass change of specimen at different exposure time can be calculated by Eq. (3), according to the China standard GB/T50082-2009.

$$\Delta W = \frac{G_t - G_0}{G_0} \times 100\% \quad (3)$$

where ΔW is mass change rate of specimens after corrosion (%); G_0 is the mass of specimen after erosion (g); G_t is the mass of specimen before erosion (g).

A nonmetal ultrasonic analyzer was used to determine the modulus of elasticity of mortar samples at different erosion cycles. The measurement length in this study is 160 mm. The acoustic time value is converted into the relative dynamic modulus of elasticity by Eq. (4).

$$E_{rd} = \frac{E_{dn}}{E_{do}} = \frac{V_n^2}{V_o^2} = \frac{t_o^2}{t_n^2} \quad (4)$$

where E_d and E_{rd} are the dynamic modulus of elasticity (GPa) and the relative dynamic modulus of elasticity, respectively; V represents the ultrasonic velocity of specimen (m/s); ρ denotes the density of specimen (kg/m^3); ν is the Poisson's ratio; V_o is initial ultrasonic velocity of specimen before erosion (m/s); V_n is the ultrasonic velocity of specimen after erosion (m/s); t_o denotes the initial ultrasonic time of specimen before erosion (μs); t_n represents the ultrasonic time of specimen after erosion (μs).

2.3.3 Microstructure characterization

Cement paste from the exposure surface (0-5mm) was characterized by X-Ray diffraction (XRD). The Empyrean X-ray diffractometer produced by PANalytical B.V. (Netherlands) was performed for the test experiment using $\text{Cu K}\alpha = 1.5406 \text{ \AA}$, step size of 0.019° , measuring time 141.804 s/step , start position 5° and end position 70° . The thermogravimetric analysis (TG) was applied by using a Netzsch STA449F3. The samples were heated from $30 \text{ }^\circ\text{C}$ to $1000 \text{ }^\circ\text{C}$ at a rate of $10 \text{ }^\circ\text{C/min}$ while the oven was purged under an inert atmosphere with N_2 flow of 30 mL/min . The exposed surface of mortar sample was further characterized by QUANTA FEG 450 field emission environment scanning electron microscopy (SEM) with energy dispersive spectrometer (EDS). The specimens were coated by epoxy resin and further polished with diamond polishing machine. The point analysis was used to identify the composites of matrix. The effective capillary pore volume and pore size distribution of mortar samples were measured by mercury intrusion porosimetry (MIP), which were conducted on the polished mortars with an age of 90 days exposure. MIP analysis was carried out by using a micromeritics mercury porosimeter (Auto Pore IV-9500, pore size $6 \text{ nm-360 } \mu\text{m}$). About $1\sim 2$ grams specimen were prepared and soaked in acetone, and then they were dried in a vacuum atmosphere at $60 \pm 2 \text{ }^\circ\text{C}$ for 8 h.

2.3.2 Thermodynamic modelling

Gibbs free energy minimisation program (GEMS 3.3) was utilized to simulate the changes in phase assemblage of binder. The default databases were obtained from the CEMDATA14 database, which contains solubility products of solids relevant for cementitious systems. The data-set includes thermodynamic data for common cement minerals such as ettringite (AFt) and alumina-ferric monophases (AFm), hydroalcite, hydrogarnet and C-S-H phases. The following simplifications of equilibrium system were conducted: (i) assumed that 10% cement was not reacted; (ii) there were not containing Fe-AFm and Fe-AFt phases in equilibrium system.

3. Results and discussion

3.1 Chloride diffusion behaviour

3.1.1 Chloride content

Fig. 1 shows the total chloride profiles of mortar specimens exposed to different solutions under drying-wetting cycles. With the increase of mortar depths, the total chloride content decreases, and the total chloride content exhibits a distinctive increase with the increase of exposure time. In contrast to the N solution, samples exposed to the N+M and N+M+S solution show higher total chloride content. However, the total chloride content for samples exposed to the N+S solutions is lower than the N solution with

increasing exposure time. It can be revealed that the presence of sulfate ion in chloride solution obstructs the chloride ingress into mortar. This phenomenon can be attributed to two aspects: 1) According to the charges-equilibrium and mass-equilibrium principle, the diffusion rate of sulfate and chloride ion for mortar exposed to the combined solution is less than their single diffusion. 2) The formation of ettringite refines the pore structure and leads to a densification of the matrix, which block the channels of chloride ion penetration [8]. It is clear that the simultaneous presences of sulfate and magnesium ion in NaCl solution exhibit higher chloride ingress. This is because the magnesium ion can react with hydroxyl ions and result in a reduction pH in the pore solution, promoting the chloride ingress based on the charges-equilibrium [9].

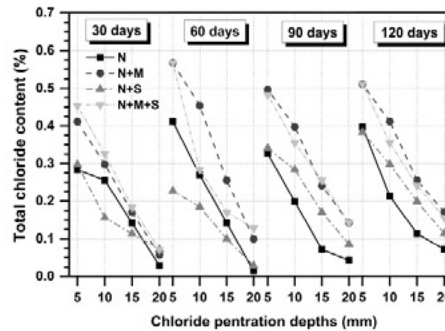


Figure 1: Chloride content of mortar specimens after different exposure time under corrosive solution and drying-wetting cycles.

3.1.2 Apparent chloride diffusion coefficient

The apparent chloride diffusion coefficient (D_{app}) of mortar samples exposed different solutions under drying-wetting cycles are presented in Fig. 2. With increasing of exposure time, the D_{app} exhibits a distinct reduction correspondingly. It is clear that the samples exposed to the N+M solution shows the highest D_{app} regardless of exposure time. The D_{app} of samples in the N+M+S solution is higher than the N solution. It is also found that the N+S solution seems decrease the D_{app} at 60 and 90 days exposure, while it increase the D_{app} after 120 days exposure. Overall, the D_{app} of samples follows $N+M > N+M+S > N+S > N$. It indicates the SO_4^{2-} and Mg^{2+} has different impacts on the D_{app} . Namely, the presence of SO_4^{2-} firstly reduces but later increases the D_{app} of mortar in chloride solution, whereas the $SO_4^{2-} + Mg^{2+}$ in NaCl solution lead to an increase in the D_{app} . The results are in accordance with previous studies, which reveal that the SO_4^{2-} can refine the pore structure of matrix and reduce the D_{app} of mortar when exposed to the combined NaCl and Na_2SO_4 solution at the short exposure time [10]. However, the formation of expansion corrosive product will generate crack occurrence and thereby promote the chloride diffusion. The presence of $SO_4^{2-} + Mg^{2+}$ increases the D_{app} significantly. This may be attributed to the fact that the degradation caused by $SO_4^{2-} + Mg^{2+}$, which aggravates the chloride ingress.

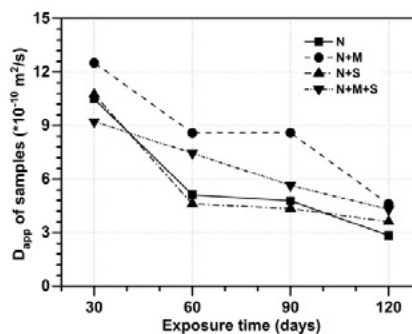


Figure 2: D_{app} of samples after different exposure time under corrosive solution and drying-wetting cycles.

3.2 Magnesium and sulfur profiles

Fig. 3 shows the elemental concentration of magnesium (Mg) and sulfur (S) determined by ICP-OES for the exposed mortar samples at different exposure time. Since the NaCl solution does not contains sulfur and magnesium, samples exposed to solutions of N+M, N+S and N+M+S are selected for analysis. It can be observed that the magnesium content in the outermost layer for mortar exposed to the N+M+S solution is increased with increasing exposure time. The outermost layers (0-5 mm) of the mortar specimens exposed to the N+M+S solution are enriched in magnesium. As for the sulfate ion, although the sulfur content shows a variation between 30 and 120 days of exposure, there is no increase in sulfur content at the outmost layer for the samples exposed to the N+M+S solution. The magnesium profiles in the mortar samples exposed to the N+M reveal that there is no clear increase in the magnesium content at the outermost layer except for 120 days of exposure. For samples exposed to the N+S, the sulfur content also does not further increase at the outmost layer. Compared with the chloride ingress (Fig. 1), it is clear evident that the penetration depths of magnesium ion and sulfate ion are much smaller. The precipitation of brucite occurs at higher pH values ($pH > 10$) and reduces the magnesium concentrations, resulting in limited mobility of magnesium in cementitious systems [11]. Indeed, the formation of brucite is observed on the surface of mortar but its content in the mortar does not increase with the increasing of exposure time. Similar as the results presented in, the magnesium and sulfur were enriched in the outmost section (0-1 mm) [12].

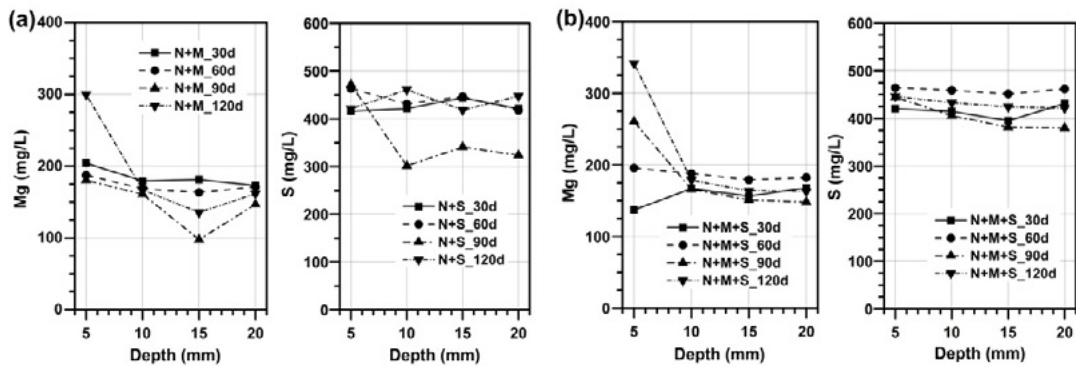


Figure 3: Total magnesium (Mg) and sulfur (S) content determined by ICP-MS for profile ground mortar samples.

3.3 Degradation progress

3.3.1 Mass change

Fig. 4 shows the mass change of mortar specimens exposed to different corrosive solutions under drying-wetting cycle. It is clear that the mass changes of samples exposed to the N solution are increased with the increasing of exposure age. However, for the samples exposed to the N+M solutions, the mass changes show an increase and reach the maximum until the exposure age of 90 days. Afterwards, it shows a decrease after 120 days of exposure. It is also obvious that the mass changes curves of samples exposed to the N+S and N+S+M solution are similar to the group of N+M. The specimens exposed to the N solution show the maximum mass gain of 1.10%, while the mass gains of samples exposed to the combined solution N+M, N+S, and N+M+S reach the maximum of 2.74, 2.34% and 2.51%, respectively. The combined solutions exhibit greater mass changes than those exposed to the N solution under drying-wetting cycles. Initially, the mass of specimens in the N+M solution under drying-wetting cycles increases to 2.74% until 90 days and follows by a slight decrease down to 2.68%. The mass changes of samples exposed to the N+S and N+S+M solutions show a similar tendency. When exposed to corrosive solutions, the presence

of sulfate and magnesium ion in the chloride environment leads to a higher mass gain than the sodium chloride solution. This may be caused by the precipitation of brucite and AFt, which could adhere on the surface of pore walls and inside the pore space in cement matrix. Moreover, it is clear that the solution with sulfate, magnesium and chloride ions results in larger mass change than that with sulfate and chloride. The results in accordance with a previous finding, which revealed that the ordinary Portland concrete immersed in the magnesium sulfate plus sodium chloride solution showed a larger mass decrease than the magnesium sulfate solution [13]. The magnesium ion does not cause obvious mass loss in the chloride solution, this can be attributed to magnesium ion attack, which only reacts with hydroxyl ions at the outmost surface and limit internal erosion, resulting in indistinctive degradation of mortar.

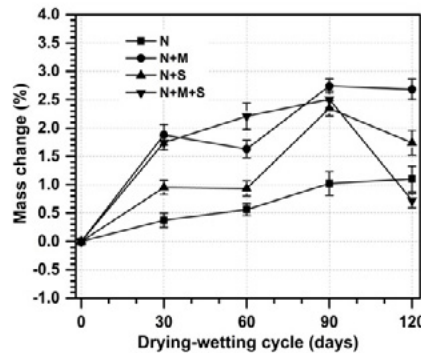


Figure 4: Mass change vs. time for mortar specimens exposed to different solution under drying-wetting cycles.

3.3.2 Dynamic of modulus of elasticity

The dynamic modulus of elasticity for mortar exposed to different exposure solutions under drying-wetting cycles are presented in Fig. 5. It can be noticed that the curves of relative dynamic modulus of elasticity (E_{rd}) is increased with the increasing of exposure age when exposed to the N, N+M and N+S solution, respectively. .

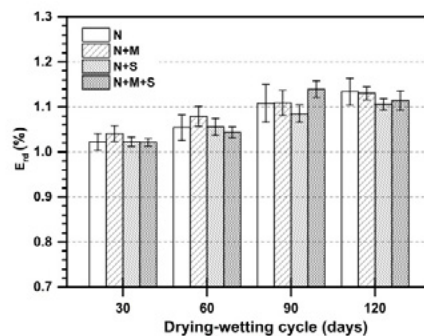


Figure 5: Variation of dynamic modulus of elasticity vs. time for mortar specimens exposed to different solution under drying-wetting cycles

While the E_{rd} of mortars in the N+M+S solution firstly increases until 90 days of exposure and then slightly decreases after 120 days. After 90 days of exposure, the E_{rd} for the mortar exposed to the N+M+S solution reaches the maximum. It can be seen that the presence of sulfate and magnesium in chloride environment has impacts on the variation of E_{rd} , which also proves that the presence of sulfate ion in chloride solution reduces the damage of mortar under drying-wetting cycles. However, the coexistence of sulfate, magnesium and chloride ion intensifies the degradation of mortar. This may indicates that when exposed to sulfate and chloride attack, the generated corrosion products such as ettringite and Friedel’s salt (Fig. 6) fill the pore walls and densify the cement matrix. At the early stage of seawater attack, the corrosion

products also refines the pore structure, however, the attacks of multiple corrosive ions lead to corrosion intensification at later stages of exposure

3.4 Phase assemblage

3.4.1 Phase composition

The hydration products and corrosion products of cement paste in different solution after 120 days of exposure are analyzed by XRD and the results are illustrated in Fig. 6. The patterns show that the hydrated products contain hemicarbonate (Hc) and monocarbonate (Mc) before exposure and Friedel's salt (Fs) is observed in all samples after exposed to corrosive solutions. Actually, both Hc and Mc could directly convert to Fs with high chloride concentrations. The TGA analysis of exposed hydrated cement for 120 days of exposure (0-5 mm) shows that the phase assemblages contain C-S-H, ettringite (AFt), portlandite (CH) as well as calcium carbonate (Cc), as shown in Fig. 7. It is suggested that the peak ranges from 230~410°C is referred to the decomposition of Fs and the interval of 410-500°C is mainly ascribed to the dehydration of portlandite.

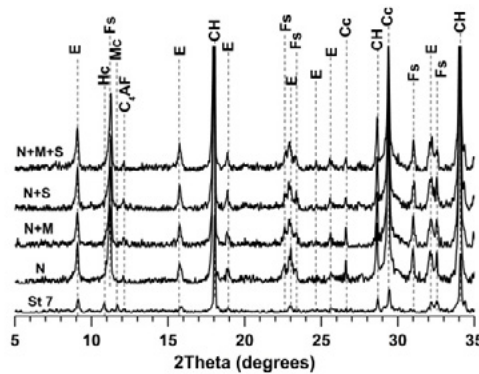


Figure 6: XRD patterns for cement paste samples exposed to different solutions after 120 days drying-wetting cycles

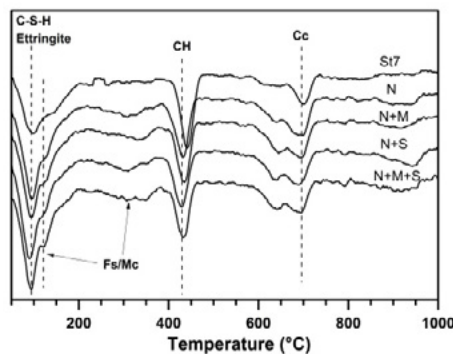


Figure 7: DTG curves of cement paste samples exposed to different solutions after 120 days drying-wetting cycles.

The amount of CH and Fs are determined by DTG and the results are presented in Fig. 8. In contrast to sample exposed to N solution, the amount of Fs decreases in the one exposed to N+S solution, indicating that the formation of Fs is limited by sulfate ions. This is attributed to the fact that C-S-H gels can absorb more sulfates instead of chlorides when exposed to the sulfate + chloride solution. The sulfate presented in combined solution (N+S) reduces the chloride binding and part of Fs converted to Ettringite as a result. Similarly, the presence of $SO_4^{2-}+Mg^{2+}$ in chloride solution declines the content of Fs, which suggests that the combined $SO_4^{2-}+Mg^{2+}$ decreased the chloride uptake in the C-S-H and induce increased formation of corrosion products [14]. Moreover, it is obvious that the CH content in the N+M+S solution is lower than that exposed to the N solution. The precipitation of brucite reduced the content of CH. Previous study

also indicated that the $\text{SO}_4^{2-} + \text{Mg}^{2+}$ in chloride solution reduce the formation of Fs at the outmost layer.

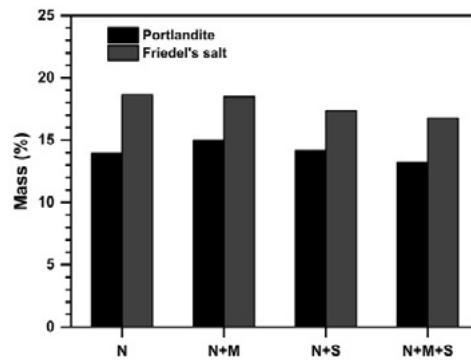


Figure 8: Portlandite and Friedel's salt determined by DTG in the cement paste samples exposed to different solution after 120 days drying-wetting cycles

3.4.2 Modelling of phase change

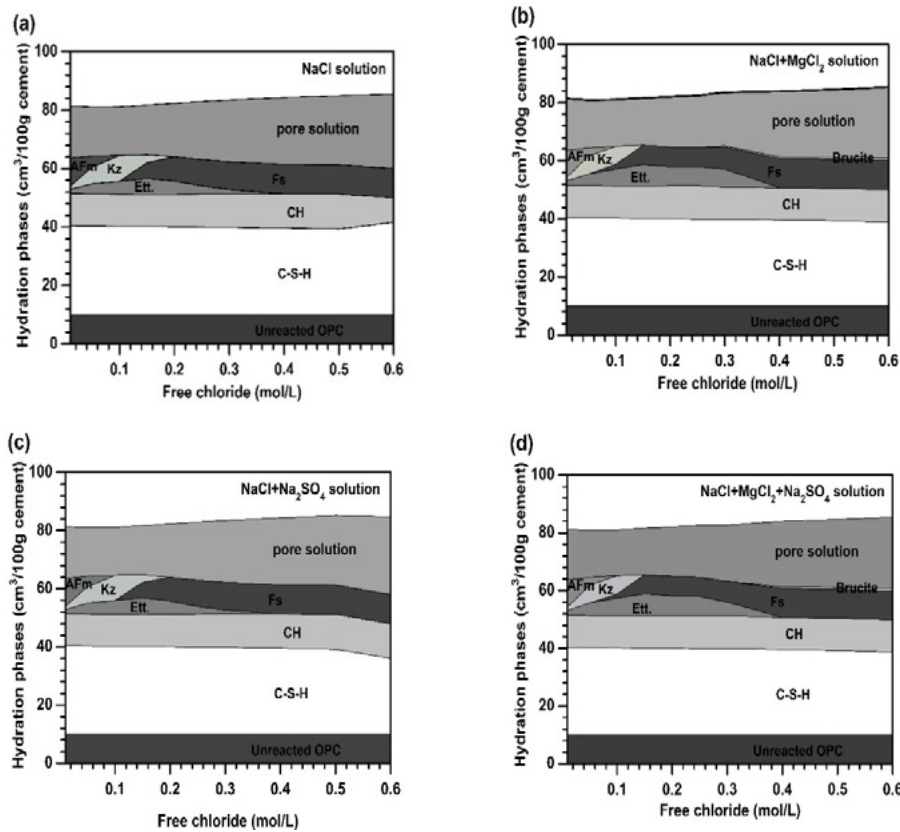


Figure 9: Hydration phases vs. the free chloride concentration for different exposure solutions by GEMS modelling.

Fig. 9 illustrates changes of predicted hydration phases vs. the free chloride present exposed to different solution by GEMS modelling. It is clear that the free chloride concentrations have significant impacts on the phase assemblage of cement. The phase assemblages include C-S-H gel, portlandite, ettringite, monosulphate (AFm) and Kuzel's salt (Ks) in the exposure solutions at low chloride concentrations[15]. However, at high chloride concentration levels, The Fs is the only AFm phase. The results indicate that, with the increasing chloride concentration, the presence of magnesium ion in chloride solution forms to brucite and hence cause a decrease in calcium hydroxide, which is also confirmed by TGA analysis.

Similarly, the changes in hydration phases exposed to N+M+S solutions appear to formation of brucite at high chloride concentration (Fig. 9d). Additionally, it is clear that the content of ettringite is increased when sulfate ion presence in chloride solutions. Thus, GEMS model can predict the hydration phases formed in equilibrium system.

3.5 Microstructure

3.5.1 SEM-EDS

To determine the influence of exposed solutions on the microstructure, mortar matrixes are characterized at 120 days using a Scanning Electron Microscope (SEM) so as to observe their morphology. Fig. 10 shows that the region of SEM observation in mortar matrix generates micro cracking and pores. There are more micro cracking and pores in mortar exposed to the chloride and sulfate solutions (Fig. 10c). However, Mg^{2+} and $SO_4^{2-}+Mg^{2+}$ ion in chloride solution show not significant micro cracking in SEM observation (Fig. 10b and Fig. 10d). This may be attributed to ettringite crystals and resulted in micro cracking occurrence. Fig. 11 shows the SEM-EDS plots for the selected specimens immersed in simulated solutions. The SEM-EDS measurements indicate that, compared with the NaCl solution, the Si/Ca ratios the sample exposed to N+M solutions are decreased. The cloud of points which represent C-S-H gel shifts to left as shown in Fig. 11. This might lead to an increase in the absorption of hydroxyl ions and results in lower pH values. Additionally, the cloud of points of specimens exposed to NaCl+Na₂SO₄ solutions shows higher Si/Ca ratios than the NaCl solution. The change of AFm phases in the composition of the C-S-H can also be observed in the SEM-EDS plots, which are confirmed from XRD spectra and TG curves.

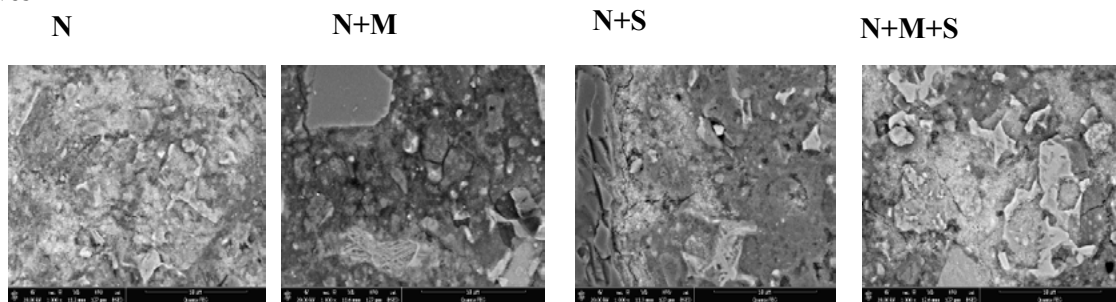


Figure 10: SEM observations of mortar matrices exposed to different solutions after 120 days exposure.

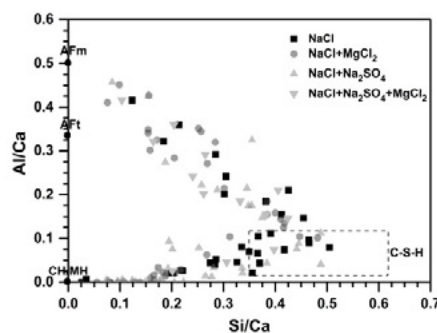


Figure 11: SEM-EDS plots for the mortar specimens exposed to different simulated solutions after 120 days exposure

3.5.2 Pore structure

The MIP analysis is conducted to clearly clarify the pore characteristics. The detailed pore parameters and pore size distribution for samples exposed to different solutions are illustrated Fig. 10. It can be observed that the incremental intrusion follows a similar pattern and there are two main incremental intrusion

distribution peaks in the exposed mortar samples. One peak is ranged from 10 to 50 nm, which is usually considered as less harmful pore (20-50 nm). For the samples in N+S solutions, the pore volume (<20 nm) is higher than that exposed to the N solution, while the volume of pore size between 100 and 200 nm are lower. The pore size volume (<20 nm) of samples exposed to the N+M+S solutions is less than the N solution, whereas the pore size volume (>200 nm) are higher. The results demonstrate that the presence of sulfate ion in chloride solution decrease less harmful pore size, while the presences of sulfate and magnesium ion in NaCl solution increase the harmful pore size. The formation of AFt by sulfate ion precipitates inside the pores and refines the pores size, which declines the chloride penetration channels and retards the chloride ingress. However, the degradations caused by magnesium and sulfate result in increase of porosity and harmful pore size and thus promote the chloride ingress.

Table 3: Detailed composition of the exposure solutions.

Exposure solution	Pore structure information				Porosity (%)
	<20 nm volume (%)	20-100 nm volume (%)	100-200 nm volume (%)	>200 nm volume (%)	
N	55.606	22.564	6.519	15.310	12.977
N+M	57.308	25.267	6.368	11.057	9.006
N+S	58.391	22.819	5.965	12.825	13.681
N+M+S	51.797	21.212	5.987	21.004	13.031

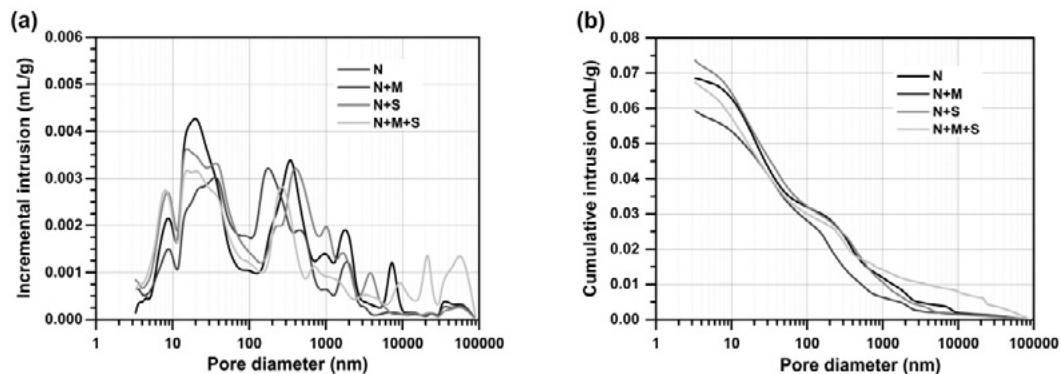


Figure 12: Pore size distribution for mortar samples exposed to different solutions after 120 days drying-wetting cycles.

4. Conclusions

- (1) The presence of sulfate ion in the chloride solution inhibits the chloride ingress, while the $SO_4^{2-}+Mg^{2+}$ in chloride ion environment increase the chloride ingress of mortar. In addition, the ingress of magnesium and sulfate ion is limited to the outmost (0-5mm) at the surface.
- (2) The combined corrosive ions have significant effects on the mass loss and relative dynamic modulus of elasticity of Portland cement mortar. The presence of SO_4^{2-} in the chloride solution decreases the mass loss and the dynamic modulus of elasticity change of mortar. However, the simultaneous presences of $SO_4^{2-}+Mg^{2+}$ in NaCl solution aggravate the damages of mortar. The SO_4^{2-} in chloride environment reduced the content of Friedel's salt and CH. The presence of sulfate and magnesium ion in chloride solution can further declines the content of Fs and CH and causes decalcification of C-S-H.
- (3) The synergy effects of SO_4^{2-} in chloride environment refine the pore structure and decrease the total

porosity. The coexisting of $\text{SO}_4^{2-} + \text{Mg}^{2+}$ in chloride solution increases the porosity and harmful pore volume, and thus aggravates the ingress of corrosive ions into the matrix.

5. Acknowledgements

This study was financially supported by the National Natural Science Foundation Project of China (No. 51679179) and National Key Research and Development Program of China (No. 2017YFB0310905).

6. References

- [1] M. Maaga, S. Helland, J.E. Cafilsen, Exposure to marine environment of chloride penetration of high performance concrete, Science Press, Beijing, 1998.
- [2] M. Santhanam, M. Otieno, 5 - Deterioration of concrete in the marine environment, in: M.G. Alexander (Ed.) Marine Concrete Structures, Woodhead Publishing 2016, pp. 137-149.
- [3] S.-J. Kwon, H.-S. Lee, S. Karthick, V. Saraswathy, H.-M. Yang, Long-term corrosion performance of blended cement concrete in the marine environment – A real-time study, Contribution and Building Materials, 154 (2017) 349-360.
- [4] F.P. Glasser, J. Marchand, E. Samson, Durability of concrete - Degradation phenomena involving detrimental chemical reactions, Cement and Concrete Research, 38 (2008) 226-246.
- [5] T. Simčič, S. Pejovnik, G. De Schutter, V.B. Bosiljkov, Chloride ion penetration into fly ash modified concrete during wetting–drying cycles, Contribution and Building Materials, 93 (2015) 1216-1223.
- [6] Y. Chen, J. Gao, L. Tang, X. Li, Resistance of concrete against combined attack of chloride and sulfate under drying–wetting cycles, Contribution and Building Materials, 106 (2016) 650-658.
- [7] J. Yuan, Y. Liu, Z. Tan, B. Zhang, Investigating the failure process of concrete under the coupled actions between sulfate attack and drying–wetting cycles by using X-ray CT, Contribution and Building Materials, 108 (2016) 129-138.
- [8] M. Zhang, J. Chen, Y. Lv, D. Wang, J. Ye, Study on the expansion of concrete under attack of sulfate and sulfate–chloride ions, Contribution and Building Materials, 39 (2013) 26-32.
- [9] S. Cheng, Z. Shui, T. Sun, X. Gao, C. Guo, Effects of sulfate and magnesium ion on the chloride transportation behavior and binding capacity of Portland cement mortar, Contribution and Building Materials, 204 (2019) 265-275.
- [10] J. Zuquan, S. Wei, Z. Yunsheng, J. Jinyang, L. Jianzhong, Interaction between sulfate and chloride solution attack of concretes with and without fly ash, Cement and Concrete Research, 37 (2007) 1223-1232.
- [11] N.R. Buenfeld, J.B. Newman, The development and stability of surface layers on concrete exposed to sea-water, Cement and Concrete Research, 16 (1986) 721-732.
- [12] K. De Weerd, B. Lothenbach, M.R. Geiker, Comparing chloride ingress from seawater and NaCl solution in Portland cement mortar, Cement and Concrete Research, 115 (2019) 80-89.
- [13] M. Maes, N. De Belie, Influence of chlorides on magnesium sulphate attack for mortars with Portland cement and slag based binders, Contribution and Building Materials, 155 (2017) 630-642.
- [14] K. De Weerd, D. Orsáková, M.R. Geiker, The impact of sulphate and magnesium on chloride binding in Portland cement paste, Cement and Concrete Research, 65 (2014) 30-40.

[15] Z. Shi, M.R. Geiker, B. Lothenbach, K. De Weerd, S.F. Garzón, K. Enemark-Rasmussen, J. Skibsted, Friedel's salt profiles from thermogravimetric analysis and thermodynamic modelling of Portland cement-based mortars exposed to sodium chloride solution, *Cement Concrete Composites*, 78 (2017) 73-83.

Locally available material (manufactured sands) impacts on properties for an Ultra-High Performance Concrete (UHPC)

R. Yang^{1,2}, R. Yu^{1,4*}, Z. Shui^{1,4}, C. Guo^{1,2}, S. Wu¹, X. Gao³

¹State Key Laboratory of Silicate Materials for Architectures, Wuhan University of Technology, Wuhan 430070, China

²School of Materials Science and Engineering, Wuhan University of Technology, Wuhan 430070, China

³School of Civil Engineering and Architecture, Wuhan University of Technology, Wuhan, 430070, China

⁴Wuhan University of Technology Advanced Engineering Technology Research Institute of Zhongshan City, Zhongshan, 528400, China.

Abstract

In this paper, the physical and chemical characteristics of local material (manufactured sands) impacts on properties for Ultra-High Performance Concrete (UHPC) are studied. Based on the modified Andersen & Andresen (MAA) model, the natural river sand (RS) is partially replaced by manufactured sand (MS) to design UHPC. Then, the properties of the developed UHPC are evaluated. The obtained results show that the particle packing model of UHPC can be disturbed by the addition of MS. Moreover, the flowability and volume stability of the developed UHPC can also be negatively affected by the inclusion of MS. Additionally, based on the chemical reaction and microstructure development points of view, the addition of MS has limited influence on the hydration process and pore size distribution of UHPC, the SEM measurements show that the connection of cementitious matrix with MS is more compact than that with RS, which should be attributed to the typical surface characteristics of the utilized MS particles.

Keywords: Ultra-High Performance Concrete (UHPC), Physical and chemical characteristics, Manufactured sands, Microstructures, Local material.

1. Introduction

Ultra High Performance Concrete (UHPC) is one of the most advanced cement-based construction material. It has outstanding mechanical and durability properties, such as compressive strength [1,2], malleability [3,4], impact resistance [5], chloride penetration resistance and freezing-thawing resistance[6-8]. Compared with other building material (e.g, high performance concrete (HPC)), UHPC can extend service cycle and requires less maintenance costs during their service time, which is fit for structures in harsh working environment, where the durability performance is a primary demand [9]. A representative UHPC mixture proportion consist of binders (cement, fly ash , and silica fume), aggregate (fine sand, quartz or glass power), chemical admixtures, steel fiber, and a small amount of water[10-15]. For UHPC, the aggregate plays an important role in UHPC that occupies about 50% be weight [16-19], which directly influences the cost and mechanical properties of UHPC. Natural river sand has been widely used for producing concrete [20-23]. However, one alarming fact, which should never be ignored, is that the natural river sand (RS) is non-renewable resource. In some regions, RS has already been exceedingly exploited,

which has threatened the safety of bridges and the stability of river banks, and creating environmental problems [24-26]. In addition, the natural river sand is also a typical local material, for instance, there is no RS in Guizhou, China. It must be transported by car from a distance of 1000 kilometers, if this place prepare UHPC use RS which will be generated transportation cost. However, there are a lot of mechanical sand which employed to concrete [27-29]. Therefore, the development of UHPC employing mechanical sand can create additional opportunities for the UHPC applications. The use of mechanical sand not only decreases the cost of UHPC but also eliminates the time in Guizhou. Thus, there is a need to development using mechanical sand which help engineers to use UHPC when necessary without enhances in cost.

Manufactured sand (MS) is a kind of artificial fine aggregates from natural stone based on a series of breaking and grinding techniques. Due to the difference among mother rock composition during crushing, and the reduction ratio, the produced MS grains normally show distinctive particle shapes compared to natural river sand [30-32]. The crushing process tends to produce sharp edged, and angular particles. Compared with more rounded natural sands, the rough-angular particles yield a granular critical state friction angle [33-36]. To clearly understand the influence of MS on the properties of concrete, many investigations have been executed and shown in available literature [37-42]. For instance, Shen et al [43] studied the characterization of MS, for example, surface properties, particle shape, and behavior in concrete. Prakash et al [44] studied the mechanical properties of MS concrete and RS concrete. The experimental results show that the mechanical properties of MS concrete are better than RS concrete. Donza et al [45] investigated the effect of MS on the mechanical properties of concrete. The results show that the shape and physical properties of MS could increase the interlocking between paste and aggregate, thus improving the compressive strength of the concrete. Sahu.Sunil Kumar et al [46] studied the properties of the concrete with RS and MS simultaneously. The results show that the concrete working performance could be reduced by the addition of MS. Li et al [47] studied the influence of MS characteristics on the abrasion resistance and mechanical properties of pavement concrete, and the effect of limestone filler content in MS on durability of different class of concrete. The obtained results indicate that the MS is comparable with RS, and a certain stone powder content in MS can contribute to the strength development, abrasion resistance and durability of the concrete. In general, it can be noticed that, in most cases, the MS is applied in the production of normal or normal strength concrete. With an increase of the requirements on concrete properties from construction industry, it is needed to clarify whether the MS is also suitable to be utilized in producing advanced concrete (e.g. UHPC).

Based on the premises mentioned above, the object of this study is to clarify the physical and chemical characteristics of manufactured sands induced impacts on properties for UHPC. The MS is utilized to partial replace RS by 10-50% in producing UHPC. Then, the macro and micro properties of the developed UHPC are evaluated, such as flowability, mechanical properties, micro-hardness, pore structure and microstructure development.

2. Methodology

2.1 Materials

CEM II, fly ash, and silica fume are used as binding materials in this study. Their chemical constitution is displayed in Table 1. Two types of natural aggregates (0–0.6 mm and 0.6-1.25 mm natural river sand) and two manufactured fine sand (0–0.6 mm and 0.6-1.25 mm manufactured sand). A Polycarboxylic ether based superplasticizer is used to adjust the workability of UHPC.

Table 1: Chemical composition of the used powders in this study (wt. %)

Compositions	Na ₂ O	MgO	Al ₂ O ₃	SiO ₂	P ₂ O ₅	SO ₃	K ₂ O	CaO	Fe ₂ O ₃	LOI
C	0.09	1.61	4.18	19.2	0.09	3.35	0.78	64.93	3.32	2.49
SF	0.13	0.47	0.25	94.65	0.17	0.69	0.84	0.36	0.15	2.29
FA	0.33	0.23	38.01	46.44	0.06	0.69	0.88	7.5	3.12	2.79

(C: Cement, SF: Silica Fume, FA: Fly Ash,)

X-ray diffraction (XRD) patterns of fine aggregates are showed in Fig. 1. As can be seen in figure, their composition is different from each other. The main ingredients of RS are SiO₂, however, the main components of MS are CaCO₃. Fig. 2 shows Scanning Electron Microscopic (SEM) images of particles of RS and MS. The RS grain has round appearance, whose surface is smooth, and the particle has good regularity. Compared with RS, the MS grain has surface asperities, sharp edges and corners.

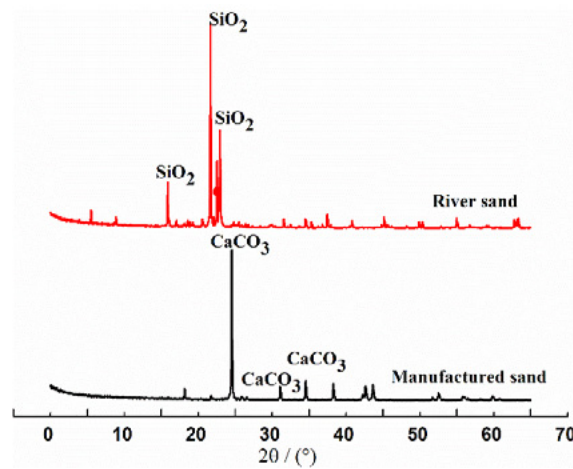


Fig.1 X-Ray diffraction (XRD) patterns of RS and MS

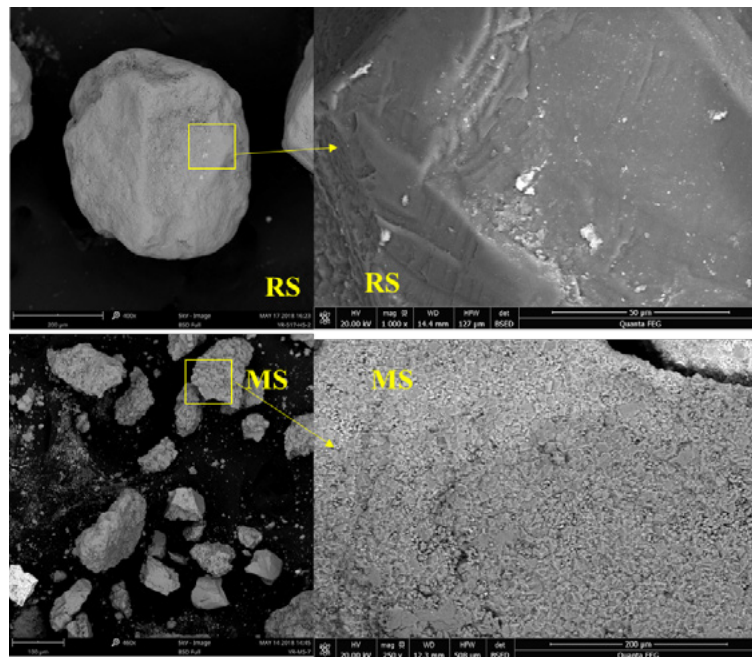


Fig.2 SEM images of NS and MS

2.2 Methods

2.2.1 Mix design

Particle packing theory is used for design the UHPC mixtures in this study. Modified Andreasen &Andersen model was used which is shown in Eq. (1).

$$P(D) = \frac{D^q - D_{min}^q}{D_{max}^q - D_{min}^q} \tag{1}$$

Where P(D) is represented the cumulative percent finer than size D by volume, D is the particle size, Dmin represent to the minimum particle size, Dmax is the maximum particle size, and q is coefficient , in this paper, the value of q is set 0.23. The target function play an important role in the optimization of the composition of mixture modified Andreasen&Andersen model. By adjusting the proportion of various materials, an optimum solution is closest to the target curve based on the Least Squares Method (LSM), the result in Eq.(2)

$$RSS = \sum_{i=1}^n (P_{mix}(D_i^{i+1}) - P_{tar}(D_i^{i+1}))^2 \tag{2}$$

Where RSS is the sum of the squares of the residuals (RSS), Pmix represents the composed mix and the Ptar represents the target grading calculated form Eq.(1). When the deviation between the target curve and the calculated curve is minimized, the concrete design is considered to be the best one. In this paper, UHPC which replace RS according to MS is list in table.2. Compared with the reference samples, 10%, 20%,30%, 40% and 50% of RS (by mass) are replaced by MS in the mixture, four examples of integral gradation curves are given in the figure.3 (due to the fact that the PSD of all the used substitutive are similar). The smaller the integral gradation curve deviates from the target curve, the closer the real accumulation of particles is to the ideal accumulation; the greater the deviation from the target curve, the greater the deviation from the ideal accumulation, and the greater the porosity in the UHPC system. The mixture of RS50-2 is closer to the target curve than the reference RS100, the mixture of RS50-1, RS50-3 deviates from the target curve. This indicates that the particle accumulation of the mixture of RS50-2 is better than that as the reference sample of the mixture of RS100, the MS (0.6-1.25) replaced RS with the same particle size can make the compactness of solid particles pile up maximum. When the MS (0-0.6mm) substitutive to the RS of the same size, the piling between particles becomes worse. The MS (0-1.25mm) replaces the worst stacking between RS particles of the same size

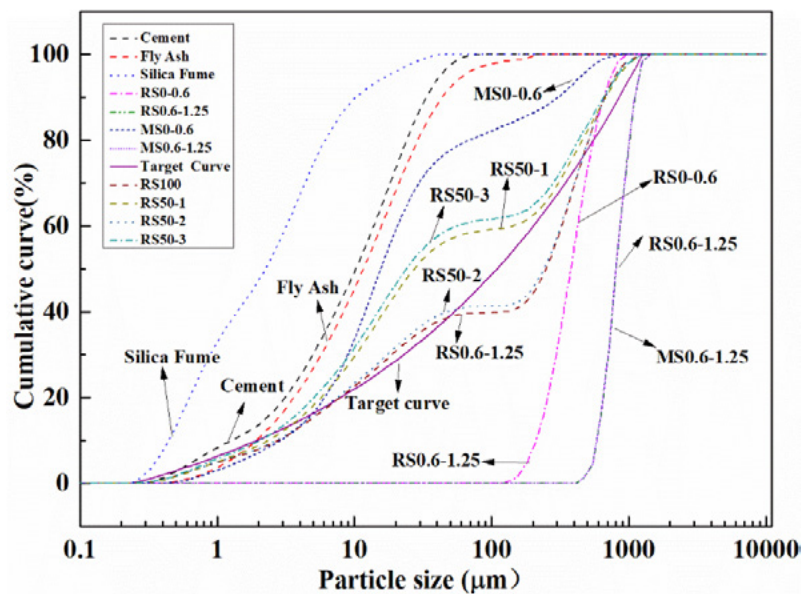


Fig .3 Particle size distribution of the solid constituents and optimized grading curves of different

mixtures.

Table.2 Mix proportion of UHPC

Mixture	C	SF	F	RS _{0-0.6}	RS _{0.6-1.25}	MS _{0-0.6}	MS _{0.6-1.25}	W	SP
RS100	1	0.192	0.267	1.027	0.293	0	0	0.28	0.41
RS10-1	1	0.192	0.267	0.924	0.293	0.103	0	0.28	0.41
RS10-2	1	0.192	0.267	1.027	0.264	0	0.029	0.28	0.41
RS10-3	1	0.192	0.267	0.924	0.264	0.1037	0.029	0.28	0.41
RS20-1	1	0.192	0.267	0.821	0.293	0.235	0	0.28	0.41
RS20-2	1	0.192	0.267	1.027	0.234	0	0.059	0.28	0.41
RS20-3	1	0.192	0.267	0.827	0.235	0.235	0.059	0.28	0.41
RS30-1	1	0.192	0.267	0.719	0.293	0.308	0	0.28	0.41
RS30-2	1	0.192	0.267	1.027	0.205	0	0.088	0.28	0.41
RS30-3	1	0.192	0.267	0.719	0.205	0.308	0.088	0.28	0.41
RS40-1	1	0.192	0.267	0.616	0.293	0.411	0	0.28	0.41
RS40-2	1	0.192	0.267	1.027	0.176	0	0.117	0.28	0.41
RS40-3	1	0.192	0.267	0.616	0.176	0.411	0.117	0.28	0.41
RS50-1	1	0.192	0.267	0.513	0.293	0.513	0	0.28	0.41
RS50-2	1	0.192	0.267	1.027	0.147	0	0.147	0.28	0.41
RS50-3	1	0.192	0.267	0.513	0.147	0.513	0.147	0.28	0.41

(C: cement, F: fly ash, SF: silica fume, RS_{0-0.6} and RS_{0.6-1.25}: natural river sand 0-0.6 mm and 0.6-1.25mm, MS_{0-0.6} and MS_{0.6-1.25}: manufactured sand 0-0.6 mm and 0.6-1.25mm, W: water, SP: superplasticizer)

2.2.2 Flowability test

To evaluate the fresh behavior of the developed UHPC, EN1015-3 is applied in this research. Two diameters perpendicular to each other are measured. Their mean value is used as the slump flow of the designed UHPC.

2.2.3 Mechanical properties test

All the fresh concrete is cast in moulds with the sizes of 40 × 40 × 160 mm, the block are demold about 24h, after place and cured in standard maintenance room, after curing 3,7,28 days, the flexural and compressive strength are tested according to the standard- EN196-1.

2.2.4 Hydration kinetics test

To understand the influence of fine particles (≤ 0.125 mm) of MS on the hydration process of cement, a heat flow calorimetry test is employed. The isothermal heat of each sample was measured by ATM AIR isothermal calorimeter at 25 °C. When the mortar is made, put 24.75g into the volumetric flask, mechanically seal, the container was placed into the calorimeter. The heat evolution and total heat released of the sample was continuously monitored for the first 7 days of hydration.

2.2.5 Microstructure analysis

To clearly understand the effect of the MS on the microstructure development of the design UHPC, three test methods are applied. The pore (pore size distribution and total porosity) of the UHPC measured

by a Micromeritics mercury Porosimeter (namely AutoPore IV-9500, pore size range: 6 nm-360µm). The pore structure was test on 7 days and 28 days respectively. The Scanning Electron microscopy (SEM) is characterized the microstructure of UHPC in Backscattered electron mode.

3. Results and discussion

3.1 Fresh behavior of the developed UHPC with manufactured sand

The flowability of UHPC in this research is shown in Fig.4. It is clear that the fluidity is continuously reduced with the increase of the substitution rate of the MS. Compared with reference sample, the fluidity decreased 35mm when the replacement(0-1.25mm) rate is 50% and the fluidity only decreased 15mm when the substitute ratios(0.6-1.25mm) is 50%. This indicated the MS impact on flowability, and then the MS (0-1.25mm) has greater effect than MS (0.6-1.25mm). The main reason is caused by the surface properties of the MS and the particle size distribution. Firstly, the surface of MS is rough, multi-ridges. The increase of internal friction between the paste and the MS in UHPC, result in the slurry flow needs to be overcome greater resistance. Secondly, the accumulation of MS is worse than that of RS, led to the free water reduction of UHPC.

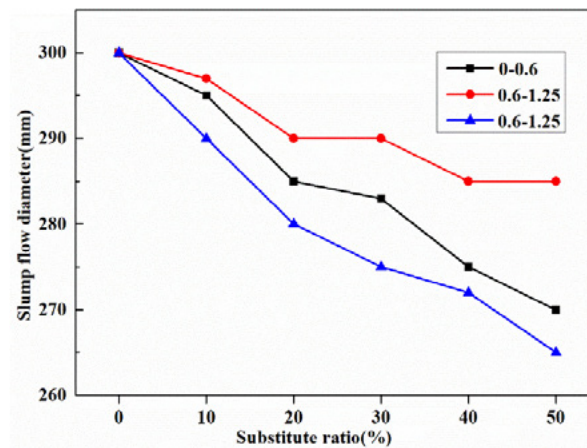


Fig .4 Results of slump flow test

3.2 Mechanical properties of the developed UHPC with manufactured sand

Fig. 5 shows the compressive strength when the different particle size of RS are replaced by MS in designed UHPC matrix at 3, 7, and 28 days, respectively. It can be noticed that the compressive strength increased, when the RS is replaced by the MS (0-0.6 mm and 0-1.25 mm, respectively). The increased value of compressive strength is 0.2-16.8 MPa. When the substitution rate is less than 30%, the compressive strength is not noticeably. When the substitution rate is more than 40%, the value of compressive strength increase more than 10 MPa. The maximum compressive strength increasement is 16.8MPa when the RS substitution ratio is 40% and the 0-1.25 mm. The compressive strength does not increase significantly when the RS is replaced by the MS (0.6-1.25 mm).

Based on appropriate application of modified Andreasen & Andersen particle packing model. Firstly, good stacking generate better mechanical properties in UHPC. Although the strength should be the highest because the MS (0.6-1.25 mm) are the best substitute for stacking. However, the experimental showed opposite result. When MS (0-0.6 mm and 0~ 1.25 mm) are replaced by the same particle size RS, the strength of RS is improved, especially when the substituted rate is considerable, the strength increase is more obvious. Secondly, when the RS is replaced by the MS, there are interlockings between slurry and aggregate in MS UHPC, which would increase the coupling force between slurry and aggregate because

of the edge-angle of the MS particle. Compared with RS, the surface of MS is rough, and the effect of UHPC matrix and aggregate is enhanced by rough surface. In addition, the rough surface makes the C-S-H gel grow nondirective, thus increasing the ratio of crystal to gel. In summary, the compressive strength is determined by the particle accumulation and the surface properties of aggregate in UHPC system.

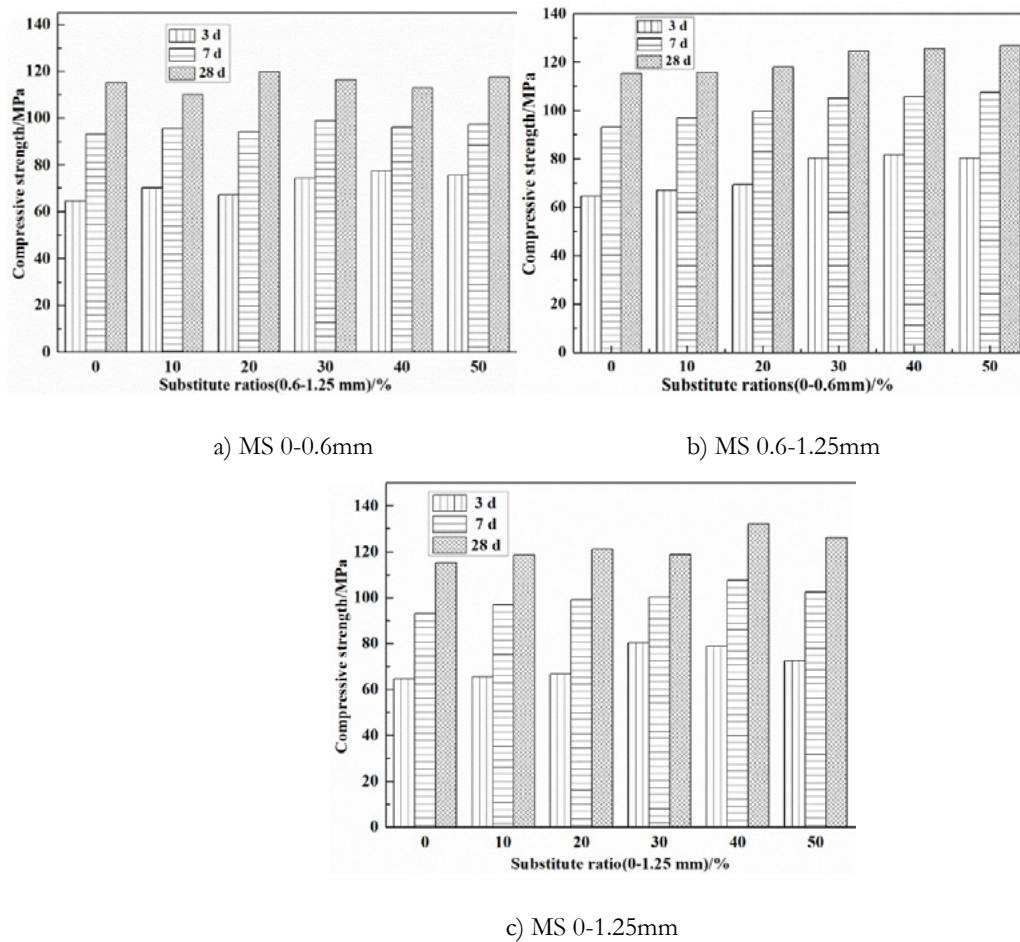


Fig. 5: Results of compressive strength

3.3 Pores structure of the developed UHPC with manufactured sand

To clearly understand the influence of MS on the microstructure development of UHPC, the MIP is used to evaluate the development of UHPC pore structures. The results are shown Fig.6. It can be seen from the figure that the pore size of UHPC is mainly between 5-20 nm at 7days, with the increase of age, the cement continues to hydrate and fill the void between particles. At 28days of age, the pore size of UHPC is mainly are in 3-11nm. The critical pore size is decreasing, the density of concrete increasing. The reason for this phenomenon is that there are more MS particles which less than 125 μ m, and the grain surface is rough, which can be better combined with cement paste. The ITZ can be improved and the density of the ITZ can be increased, the porosity of ITZ is reduced. In addition, the composition of MS is CaCO₃, it can be react with cement hydration product and improve the connection between MS and slurry, therefore the ITZ becoming denser.

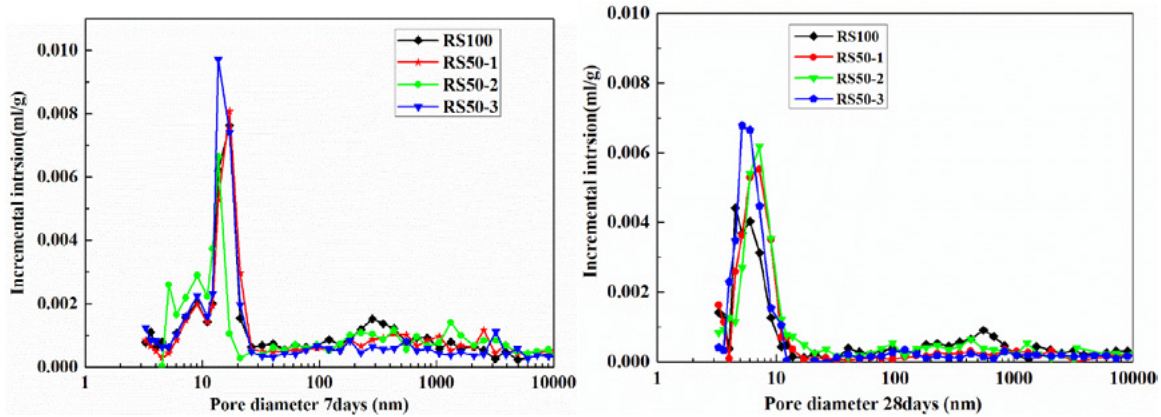


Fig .6 Pore structure analysis results of the UHPC

3.4 Isothermal calorimetry

To clearly understand the impact of these sand particles on cement hydration in UHPC. The hydration heat test was carried out in cement hydration process in UHPC, the results are shown in Fig. 7 (hydration heat release rate curve). The as seen in figure, this results in a slightly different looking the RS100 than the RS50-3 in hydration heat release curve and cumulative heat release curve, this is consistent with previous reseach. This indicates those grain do not affect the hydration process in cement, or has weakness nucleation effect. Therefore, they have very limited influence on cement hydration and most likely act as filler in the developed UHPC.

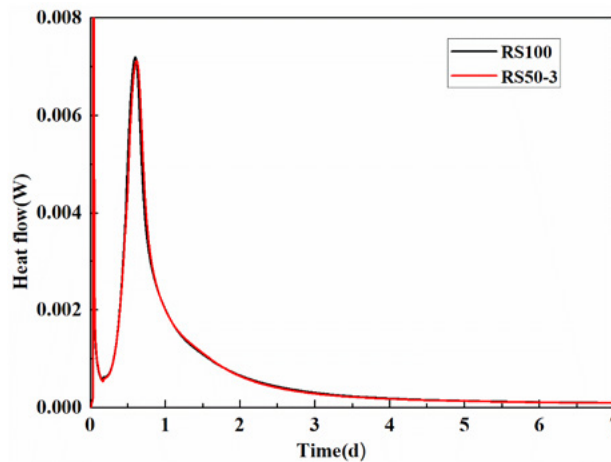


Fig.7 Effect of different sand on the hydration kinetics of the UHPC cementitious system

3.5 Microstructure development and ITZ analysis

To observe the ITZ between aggregate and cement paste, the backsacatter scanning electron was used to study the ITZ. The results are shown in Fig. 8. As can be seen from the figure, there are obvious cracks in the ITZ between RS and paste, but the cracks were not found in ITZ of MS. The reason is mainly due to the nature of the surface properties and particles shape of aggregate. Fig. 2 shows that the surface of RS is smooth, the particles are regular, but the grain of MS is multi-angled and the surface is rough. When the cement is hydrated, the contact area between the rough surface and cement paste increases, which can be better combined with the paste. In addition, the MS particles have edge-angles, there are interlocks between MS and the cement paste. In the complex process of cement hydration, it is difficult to slip the cement paste and the MS. Therefore, compared with the RS, the MS can be better combined with the cement paste and restrain the slippage of the slurry on the surface of the aggregate during the cement hydration process,

forming a denser ITZ.

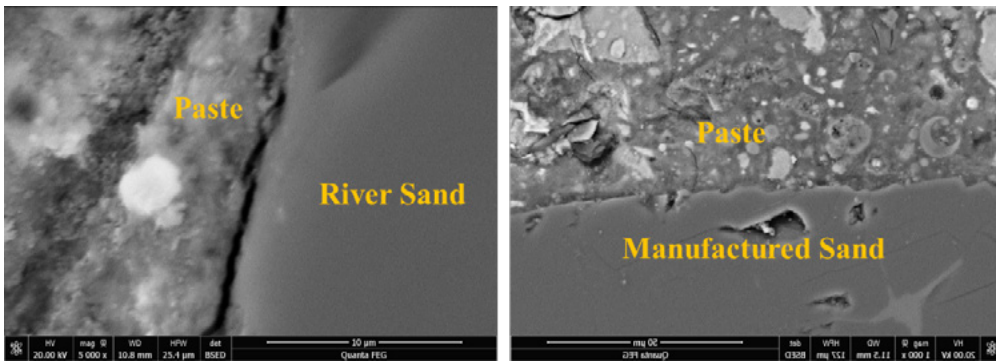


Fig .8 BSE/SEM images for the mixture at 28 days

Fig. 9 shows the relationship between the porosity and strength of UHPC at 28days. In generally, the strength of concrete decrease with the increase of porosity, the strength concrete increase with the decrease porosity. It can be seen from the Fig. 9, the mixture of RS100 has the highest porosity, and the lowest corresponding strength, the macro-porosity of the mixture of RS50-1 and RS50-3 is equivalent and the strength is also equivalent. The reason is mainly caused by the surface characteristics and composition of the MS. The main component of MS is CaCO₃, it could have a weak chemical reaction with the cement paste, the interface between aggregate and paste is closely connected, in addition, the surface of the MS is rough, compared with the volume of the MS and RS, its specific surface area is large, and it can be better combined with the slurry. The MS particles have multiple edges and corners, thus the interlockings exist between the cement pastes. The results are in good agreement with the results of BES. There is no obvious crack between the MS and the slurry, but it can be found between the RS and the slurry.

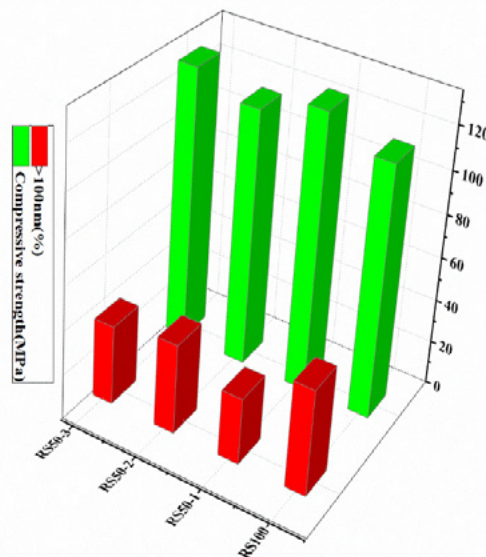


Fig.9 Compressive strength and Macro-porous percentage

4. Conclusions

Based on closest packing theory, a study on the replacement of RS by limestone MS is carried out. The properties of MS UHPC are analyzed in terms of fluidity, mechanical properties, and 2.2.5

Microstructure analysis. The key survey and findings of this research can be summarized as follows:

1. The MS has great influence on fluidity, the UHPC which is made up of MS has worse fluidity;
2. Under certain conditions, particle accumulation determining the mechanical properties of UHPC. The surface properties of aggregate also affect the mechanical properties of UHPC. Namely, the mechanical properties of UHPC are determined by particle packing, aggregate morphology and surface properties;
3. Based on the chemical reaction point of view, the included fine particles from MS have limited effect on the cement hydration kinetics of UHPC. However, the typical physical characteristics of MS (rough surface, multi-edges, and interlocks) are the key factor to obtain UHPC with advanced mechanical properties and optimized microstructure (e.g. ITZ of UHPC)

5. Acknowledgment

The authors acknowledge the financial supports of National Nature Science Foundation Project of China (51608409), Major science and technology project in Zhongshan city, Guangdong province (2017A1021), Yang Fan plan of Guangdong Province (201312C12), Science and Technology Program of Guangdong Province in 2016 (2016A090924002), Science and Technology Program of Guangdong Province in 2017 (2017B090907009), Late-model Research Institute Development Program of Zhongshan in 2016: Subsidy for Major Research Platform Construction (2016F2FC0008), and open research project of Advanced Engineering Technology Research Institute of Wuhan University of technology in Zhongshan city (WUT201802).

6. References

- [1] K. Wille, A.E. Naaman, G.J. Parra-Montesinos, Ultra-high performance concrete with compressive strength exceeding 150 MPa (22 ksi): a simpler way, *ACI Mater. J.*108 (1) (2011) 46–54.
- [2] De Larrard F, Sedran T. Optimization of ultra-high-performance concrete by the use of a packing model. *Cem. Concr. Res.* 24(6) (1994) 997-1009.
- [3] Pyo S, Wille K, El-Tawil S, Naaman AE. Strain rate dependent properties of ultra high performance fiber reinforced concrete (UHP-FRC) under tension. *Cem. Concr. Compos.* 56 (2015) 15–24.
- [4] Yoo D-Y, Bantia N. Mechanical properties of ultra-high-performance fiber-reinforced concrete: A review. *Cem. Concr. Compos.*73 (2016) 267-80.
- [5] Tran NT, Tran TK, Jeon JK, Park JK, Kim DJ. Fracture energy of ultra-high-performance fiber-reinforced concrete at high strain rates. *Cem. Concr. Res.* 79 (2016) 169–184.
- [6] Shi C, Wu Z, Xiao J, Wang D, Huang Z, Fang Z. A review on ultra high performance concrete: Part I. Raw materials and mixture design. *Constr. Build. Mater.* 101 (2015) 741-51.
- [7] Hooton R, Titherington M. Chloride resistance of high-performance concretes subjected to accelerated curing. *Cem. Concr. Res.*34 (2004)1561–1567.
- [8] Abbas S, Soliman AM, Nehdi ML. Exploring mechanical and durability properties of ultra-high performance concrete incorporating various steel fiber lengths and dosages. *Constr. Build. Mater.* 75 (2015) 429-41.
- [9] Kono K, Musha H, Kawaguchi T, Eriguchi A, Tanaka S, Kobayashi T, et al. Durability study of the first PC bridge constructed with ultra high strength fiber reinforced concrete in Japan. *Proceedings of the RILEM-fib-AFGC International Symposium on Ultra-High Performance Fibre-Reinforced Concrete*2013,

239-48.

[10] Kim H, Koh T, Pyo S. Enhancing flowability and sustainability of ultra high performance concrete incorporating high replacement levels of industrial slags. *Constr. Build. Mater.* 123 (2016) 153-160.

[11] Wu Z, Khayat KH, Shi C. Effect of nano-SiO₂ particles and curing time on development of fiber-matrix bond properties and microstructure of ultra-high strength concrete. *Cem. Concr. Res.* 95 (2017) 247-56.

[12] Ngo TT, Park JK, Pyo S, Kim DJ. Shear resistance of ultra-high-performance fiber-reinforced concrete. *Constr. Build. Mater.* 151 (2017) 246-257.

[13] Meng W, Khayat KH. Improving flexural performance of ultra-high-performance concrete by rheology control of suspending mortar. *Composites Part B*, 117 (2017) 26-34.

[14] Richard P, Cheyrezy M. Composition of reactive powder concretes. *Cem. Concr. Res.* 25(7) (1995) 1501-1511.

[15] Yu R, Spiesz P, Brouwers H. Mix design and properties assessment of ultra-high performance fibre reinforced concrete (UHPFRC). *Cem. Concr. Res.* 56 (2014) 29-39.

[16] Lee Y, Kang S-T, Kim J-K. Pullout behavior of inclined steel fiber in an ultra-high strength cementitious matrix. *Constr. Build. Mater.* 24(10) (2010) 2030-2041.

[17] Ghafari E, Ghahari SA, Costa H, Júlio E, Portugal A, Durães L. Effect of supplementary cementitious materials on autogenous shrinkage of ultra-high performance concrete. *Constr. Build. Mater.* 127 (2016) 43-48.

[18] Yu R, Spiesz P, Brouwers H. Development of an eco-friendly Ultra-High Performance Concrete (UHPC) with efficient cement and mineral admixtures uses *Cem. Concr. Compos.* 55 (2015) 383-394.

[19] Alsalman A, Dang CN, Hale WM. Development of ultra-high performance concrete with locally available materials. *Constr. Build. Mater.* 133 (2017) 135-145.

[20] Wang X, Yu R, Shui Z, Song Q, Zhang Z. Mix design and characteristics evaluation of an eco-friendly Ultra-High Performance Concrete incorporating recycled coral based materials. *J Clean Prod*, 165 (2017) 70-80.

[21] Chen Y, Yu R, Wang X, Chen J, Shui Z. Evaluation and optimization of Ultra-High Performance Concrete (UHPC) subjected to harsh ocean environment: Towards an application of Layered Double Hydroxides (LDHs). *Constr. Build. Mater.* 177 (2018) 51-62.

[22] Song Q, Yu R, Shui Z, Wang X, Rao S, Lin Z. Optimization of fibre orientation and distribution for a sustainable Ultra-High Performance Fibre Reinforced Concrete (UHPFRC): Experiments and mechanism analysis. *Constr. Build. Mater.* 169 (2018) 8-19.

[23] Su Y, Wu C, Li J, Li Z-X, Li W. Development of novel ultra-high performance concrete: From material to structure. *Constr. Build. Mater.* 135 (2017) 517-528.

[24] Raman SN, Ngo T, Mendis P, Mahmud H. High-strength rice husk ash concrete incorporating quarry dust as a partial substitute for sand. *Constr. Build. Mater.* 25 (2011) 3123–3130.

[25] Manning D, Vetterlein J. Exploitation and Use of Quarry Fines; Report No: 087. MIST2/DACM/01; Mineral Solutions Limited: Manchester, UK; March; 2004; pp. 1–60. Available online: <http://www>.

sustainableaggregates.com/library/docs/mist/10066_ma_2_4_003.pdf (accessed on 5 August 2015).

- [26] Thomas T, Dumitru I, van Koeverden M, West G, Basford G, Lucas G, et al. Manufactured Sand. National Test Methods and Specification Values Available online: http://www.ccaa.com.au/imis_prod/documents/Library%20Documents/CCAA%20Reports/ManSand.pdf (accessed on 7 April 2016).
- [27] Singh S, Nagar R, Agrawal V. A review on Properties of Sustainable Concrete using granite dust as replacement for river sand. *J CLEAN PROD*, 126 (2016) 74-87.
- [28] Joudi-Bahri I, Lecomte A, Ouezdou MB, Achour T. Use of limestone sands and fillers in concrete without superplasticizer. *Cem. Concr. Compos.* 34(6) (2012) 771-780.
- [29] Shen W, Li X, Gan G, et al. Experimental investigation on shrinkage and water desorption of the paste in high performance concrete[J]. *Constr. Build. Mater.* 114(2016): 618-624.
- [30] Chi C, Wu Y, Riefler C. The use of crushed dust production of self-consolidating concrete (SCC), Recycling Concrete and other materials for sustainable development, Editors Tony C. Liu Christian Meyer. ACI International SP-219. 2004.
- [31] Kenai S, Benna Y, Menadi B. The effect of fines in crushed calcareous sand on properties of mortar and concrete. *Infrastructure regeneration and rehabilitation improving the quality of life through better construction International conference1999*: 253-261.
- [32] F.L. Li, C.J. Liu, L.Y. Pan, C.Y. Li, *Machine-Made Sand Concrete*, China Water Power Press, Beijing, China, 2013 (in Chinese with English content).
- [33] Ji T, Chen C-Y, Zhuang Y-Z, Chen J-F. A mix proportion design method of manufactured sand concrete based on minimum paste theory. *Constr. Build. Mater.* 44 (2013) 422-426.
- [34] Zhao S, Ding X, Zhao M, Li C, Pei S. Experimental study on tensile strength development of concrete with manufactured sand. *Constr. Build. Mater.* 138 (2017) 247-253.
- [35] Cepuritis R, Wigum B, Garboczi E, Mørtzell E, Jacobsen S. Filler from crushed aggregate for concrete: Pore structure, specific surface, particle shape and size distribution. *Cem. Concr. Compos.* 54 (2014) 2-16.
- [36] Cepuritis R, Jacobsen S, Smeplass S, Mørtzell E, Wigum BJ, Ng S. Influence of crushed aggregate fines with micro-proportioned particle size distributions on rheology of cement paste. *Cem. Concr. Compos.* 80 (2017) 64-79.
- [37] Donza H, Cabrera O, Irassar E. High-strength concrete with different fine aggregate. *Cem. Concr. Res.* 32(11) (2002) 1755-1761.
- [38] Cortes D, Kim H-K, Palomino A, Santamarina J. Rheological and mechanical properties of mortars prepared with natural and manufactured sands. *Cem. Concr. Res.* 38(10) (2008) 1142-1147.
- [39] Shen W, Liu Y, Cao L, Huo X, Yang Z, Zhou C, et al. Mixing design and microstructure of ultra high strength concrete with manufactured sand. *Constr. Build. Mater.* 143 (2017) 312-321.
- [40] Nanthagopalan P, Santhanam M. Fresh and hardened properties of self-compacting concrete produced with manufactured sand. *Cem. Concr. Compos.* 33(3) (2011) 353-358.
- [41] Li H, Huang F, Cheng G, Xie Y, Tan Y, Li L, et al. Effect of granite dust on mechanical and some durability properties of manufactured sand concrete. *Constr. Build. Mater.* 109 (2016) 41-46.

- [42] Cepuritis R, Jacobsen S, Pedersen B, Mørtzell E. Crushed sand in concrete—effect of particle shape in different fractions and filler properties on rheology. *Cem. Concr. Compos.* 71 (2016) 26-41.
- [43] Shen W, Yang Z, Cao L, Cao L, Liu Y, Yang H, et al. Characterization of manufactured sand: Particle shape, surface texture and behavior in concrete. *Constr. Build. Mater.* 114 (2016) 595-601.
- [44] Prakash Rao D, Giridhar Kumar V. Investigations on concrete with stone crusher dust as fine aggregate. *The Indian Concrete Journal*, July, 2004.45-50.
- [45] Bonavetti V, Donza H, Rahhal V, Irassar E. High-strength concrete with limestone filler cements. *Special Publication.* 186 (1999) 567-80.
- [46] Sahu A, Kumar S, Sachan A. Crushed stone waste as fine aggregate for concrete.. *The Indian Concrete Journal*, January, 2003.845-848.
- [47] Li B, Ke G, Zhou M. Influence of manufactured sand characteristics on strength and abrasion resistance of pavement cement concrete. *Constr. Build. Mater.* 25(10) (2011) 3849-3853.

Application of Krstulovic-Dabic model on early hydration analysis of Portland cement under Mg^{2+} influence

X.S. Li ^{1,2}, Z.H. Shui ¹, X. Gao ³

¹ State Key Laboratory of Silicate Materials for Architectures, Wuhan University of Technology, Wuhan 430070, China

² School of Materials Science and Engineering, Wuhan University of Technology, Wuhan 430070, China

³ School of Civil Engineering and Architecture, Wuhan University of Technology, Wuhan 430070, China

Abstract - Fresh water is the natural resource for human survival, and it is widely used in human life and production. Due to the increasing scarcity of freshwater resources, more and more freshwater applications need to find alternatives to other substances. Concrete production needs a large amount of fresh water. Processes including mixing and maintenance all require massive fresh water. In coastal areas far from the interior, sea water is used to produce concrete. However, there are still many problems to be verified during seawater mixing, one of which is Mg^{2+} interaction with matrix. In this study, the effect of Mg^{2+} on early hydration of Portland cement is discussed. Heat flow calorimetry is employed to characterize influence of Mg^{2+} on early hydration of cement. The obtained results reveal that hydration during induction and acceleration periods is significantly influenced after incorporation of Mg^{2+} . Mg^{2+} induces hydration inhibition during deceleration and stabilization period. The results from this study can provide more supporting materials for verification on seawater mixing.

Keywords: Mg^{2+} ; calorimetry; Krstulovic-Dabic model; C_3S dissolution

1. Introduction

With the growing shortage of drinking water and constantly increasing on global population, insufficient supply of freshwater has become a severe problem in the front of human races [1]. It is predicted that half of global population will be lack of freshwater at the end of 2025 [2]. Development of concrete industry requests huge consumption of freshwater. In the year of 2016, the whole production amount of cement worldwide was 4.2 billion tons [3]. It is estimated that over 3.0 tons of freshwater has consumed in concrete mixing and curing in one year. In coastal areas far from continent, seawater is considered to be an alternative of freshwater and it is concluded that seawater can be employed in concrete structures without reinforced rebars [4-6]. However, there are still many problems to be solved concerning about safe utilization of seawater mixing, one of which is concerns about interactions of Mg^{2+} from seawater with cement-based materials.

Mixing with Mg^{2+} solutions could induce significant hydration delay in cement system. Reddy et al incorporate $MgCl_2$ with different concentrations into ordinary Portland cement system and find that both initial and final setting time are prolonged. More importantly, the elongation degree increases with increase on $MgCl_2$ concentrations [7]. Thomas et al apply seawater in the peninsular area of Sierra Leone as mixing water in ordinary Portland cement system and conclude that seawater in Goderich, Sussex, Bawbaw and No. 2 River significantly delay setting time of cement [8].

In previous study, research about internal corrosion of Mg^{2+} mainly analysis with calorimetry analysis [9-12]. However, effect of Mg^{2+} on cement hydration should be further carried out. Discussion on this part requires more comprehensive understanding on hydration process.

In this study, research is concentrated on Mg^{2+} induced influences on early age cement hydration. Heat flow calorimetry is employed to characterize influence of Mg^{2+} on early hydration of cement. Hydration kinetics analysis is carried out with Krstulovic-Dabic model. The results from this study can provide more supporting materials for verification on seawater mixing.

2. Methodology

2.1 Materials

P I 52.5 Portland cement is used in this study. Chemically pure magnesium nitrate is applied to provide magnesium into hydration system. The chemical composition of P I 52.5 Portland cement is presented in Table 1.

Table 1: Chemical composition of main materials (wt. %).

Material	SiO ₂	Al ₂ O ₃	CaO	Fe ₂ O ₃	SO ₃	MgO	Na ₂ O	K ₂ O	P ₂ O ₅	LOI
PC	20.04	5.27	63.19	3.24	2.59	1.59	0.17	0.83	0.06	2.06

2.2 Methods

The w/c ratio of cement paste is fixed at 0.3. 0.055 mol/L (M1 group), 0.110 mol/L (M2 group) and 0.22 mol/L (M3 group) magnesium nitrate solution are prepared to introduce different concentration of magnesium during mixing. The group (R group) without magnesium added is employed as reference.

Hydration heat test is carried out with TAM AIR microcalorimeter from TA instruments, USA. Based on consistence on specific heat with reference, 15 g paste is prepared and examined. The heating rate is fixed from 0.1 - 2.0 °C/min.

3. Results and discussion

3.1 Hydration heat release

The heat flow of Portland cement with different Mg^{2+} concentration is presented in Figure 1. It can be seen the heat release during induction period is promoted after Mg^{2+} incorporation. The improvement degree is proportional to the concentration of Mg^{2+} , especially when concentration of Mg^{2+} reaches 0.22 mol/L. In terms of acceleration period, it can be seen from Figure 1 that heat release presented limited difference when Mg^{2+} concentration is below 0.11 mol/L. While significant promotion on heat evolution is observed when concentration of Mg^{2+} reaches 0.22 mol/L. The lowest heat flow during induction period is 0.75 mW/g, 0.85 mW/g, 0.92 mW/g and 1.14 mW/g for R, M1, M2 and M3, respectively. The enhancement on heat release is inherited from induction period to acceleration period. As the heat release between 1 and 12 h of Portland cement is mainly brought by reaction of C_3S and to C-S-H and $Ca(OH)_2$ as presented by Jansen et al, it can be seen that incorporation of Mg^{2+} could somehow influence C_3S reaction, especially under high concentrations [13]. More importantly, it can be seen that Mg^{2+} also induces regular decline on maximum heat flow and advance on time of maximum heat flow. This will be further discussed in the following part. The maximum heat flow is also considered to be controlled by C_3S hydration [13-14].

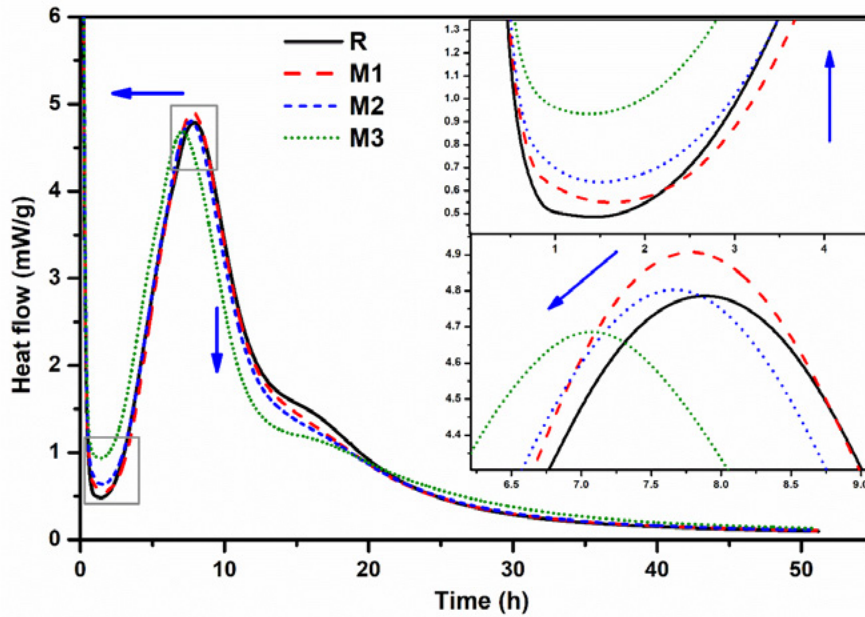


Figure 1: Heat flow of Portland cement with different Mg^{2+} concentration.

Figure 2 presents heat of Portland cement with different Mg^{2+} concentration. As all groups possess the same mix proportion, the heat released is in consistent with hydration degree. It can be seen when Mg^{2+} concentration is below 0.11 mol/L, influence from Mg^{2+} is not obvious in first 12 hs. However, when Mg^{2+} concentration is reaches 0.22 mol/L, significant hydration promotion is exhibited in first 12 hs. The reaction from C_3S to C-S-H and $Ca(OH)_2$ during acceleration period is more significant in M3 group and that in reference group. The promotion on heat evolution should be attributed to changes on pore solution environment [15-17].

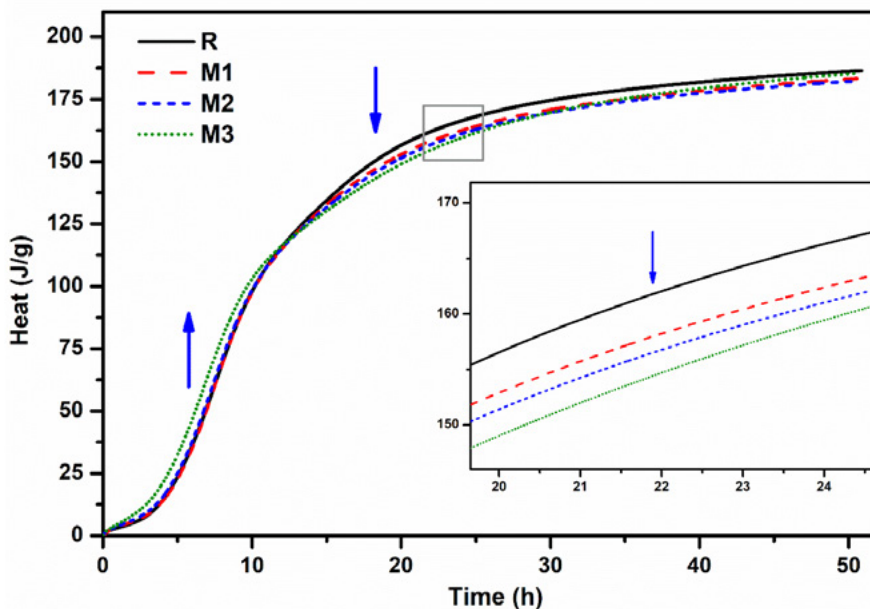


Figure 2: Heat of Portland cement with different Mg^{2+} concentration.

However, after hydrated for 12 hs, the decrease on heat release is presented in groups with Mg^{2+} incorporated. This is consistent with research from Agatzini et al [18-20]. The M3 group also exhibits some specific characteristics. Except for acceleration during acceleration period and inhibition during deacceleration period, decreased difference between R and M3 groups during stabilization period is observed.

Furthermore, the main information of heat release characteristics of Portland cement with different Mg^{2+} concentration is presented in Table 2. Mg^{2+} increases maximum heat flow when Mg^{2+} concentration is 0.055 mol/L and 0.110 mol/L but decreases maximum heat flow when Mg^{2+} concentration is 0.220 mol/L. Meanwhile, Mg^{2+} decreases time of maximum heat flow. The time of maximum heat flow of R, M1, M2 and M3 is 7.88 h, 7.78 h, 7.66 h and 7.07 h, respectively. The onset of acceleration period of R, M1, M2 and M3 are 2.28 h, 2.92 h, 2.87 h and 2.54 h, respectively. More importantly, the delay degree decreases with increase on Mg^{2+} added. Simultaneously, Mg^{2+} decreases hydration heat after hydrated for 24 h. As presented in Table 2, the heat release at 24 h of R, M1, M2 and M3 is 166.3 J/g, 162.4 J/g, 161.0 J/g and 159.5 J/g, respectively. The inhibition effect is proportional to Mg^{2+} addition. However, after hydrated for 48 h, the heat release of R, M1, M2 and M3 is 185.5 J/g, 182.2 J/g, 181.3 J/g and 184.1 J/g, respectively. The M3 group does not exhibit the most significant inhibition.

Table 2: Heat release characteristics of Portland cement with different Mg^{2+} concentration.

	R	M1	M2	M3
maximum heat flow [mW/g]	4.76	4.91	4.80	4.69
time of maximum heat flow [h]	7.88	7.78	7.66	7.07
Onset of acceleration period [h]	2.28	2.92	2.87	2.54
24 h heat release [J/g]	166.3	162.4	161.0	159.5
48 h heat release [J/g]	185.5	182.2	181.3	184.1

3.2 Hydration kinetics analysis

Krstulovic-Dabic model is employed to analyze the hydration kinetics analysis of Portland cement [21]. Based on Krstulovic-Dabic model, hydration of cement should be divided into three stages, including nucleation and growth process (NG), phase boundary process (I), diffusion process (D) [22-23]. Determination of kinetic factors from linear regression and fitting curves of hydration rate are presented in Figure 3, Figure 4, Figure 5 and Figure 6. It can be seen R^2 during linear fitting are all above 0.9950, indicating the fitting is credible.

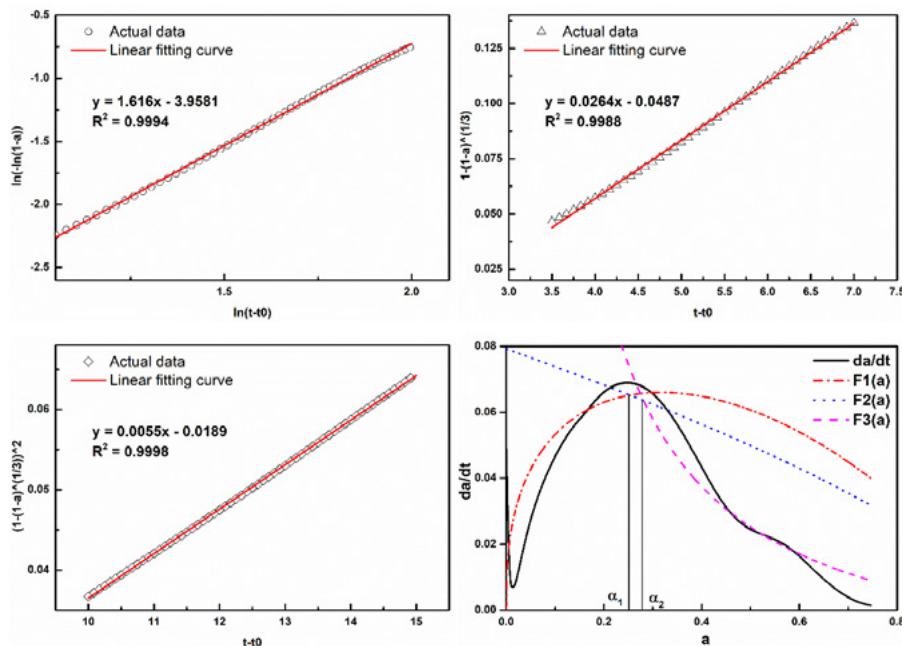


Figure 3: Determination of kinetic factors from linear regression for R group.

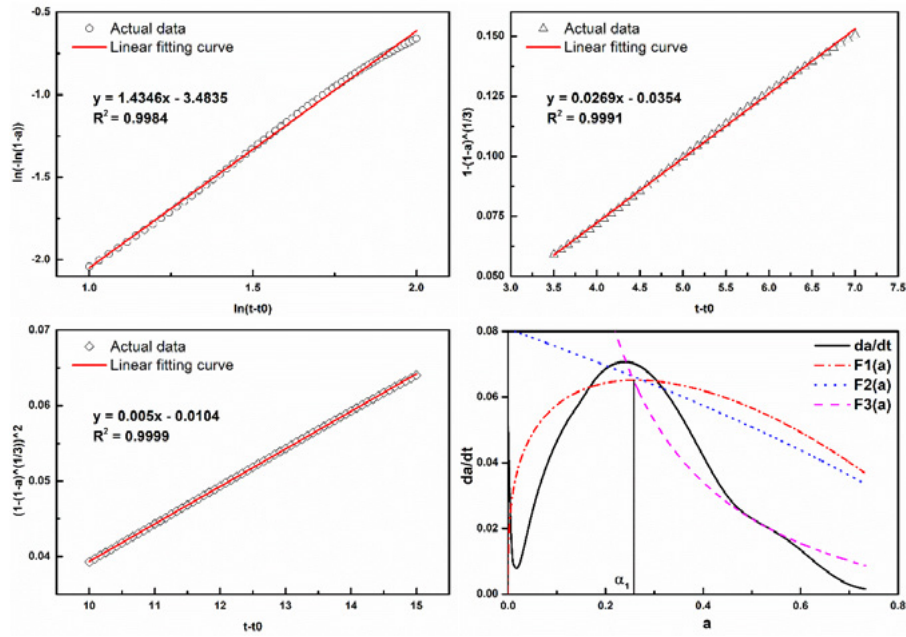


Figure 4: Determination of kinetic factors from linear regression for M1 group.

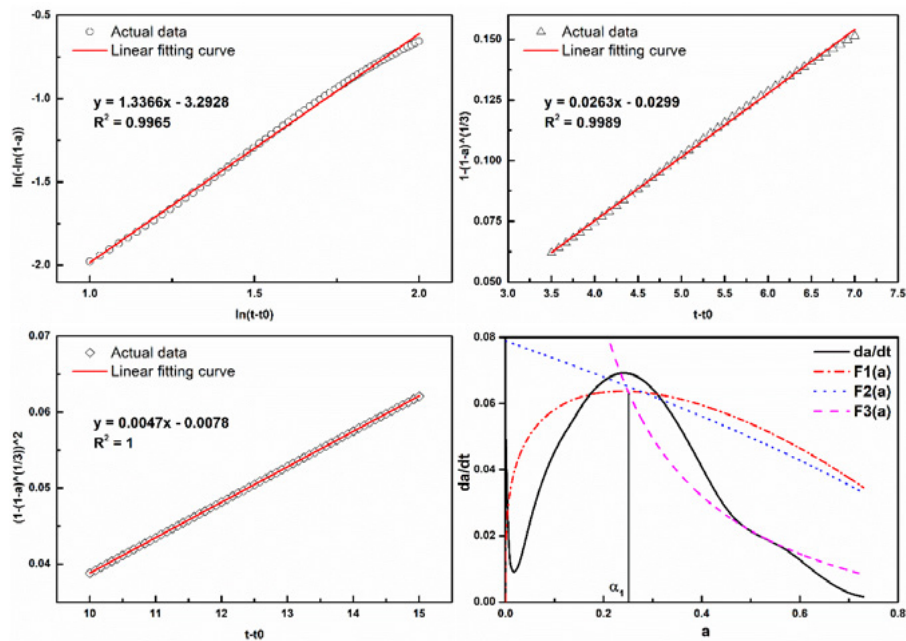


Figure 5: Determination of kinetic factors from linear regression for M2 group.

Furthermore, the kinetic parameters determined by Krstulovic-Dabic model are presented in Table 3. The n value of R, M1, M2 and M3 is 1.6160, 1.4346, 13724 and 1.2666, respectively.

The hydration rate during D process of R, M1, M2 and M3 is 0.005, 0.0050, 0.0047 and 0.0041, respectively. It is proposed by Zheng et al that brucite precipitates on cement particles in micro-crystalline size and form a “protective layer”, which hinders the further cement hydration [19]. Moreover, it can be seen hydration mechanism in group without Mg²⁺ is NG-I-D. Addition of Mg²⁺ limits development of I process and makes hydration mechanism become NG-D.

The hydration degree during NG process of R, M1, M2 and M3 is 0.2463, 0.2533, 0.2466 and 0.2267,

respectively. Decreased hydration degree is observed when Mg²⁺ concentration increases from 0.055 mol/L to 0.220 mol/L.

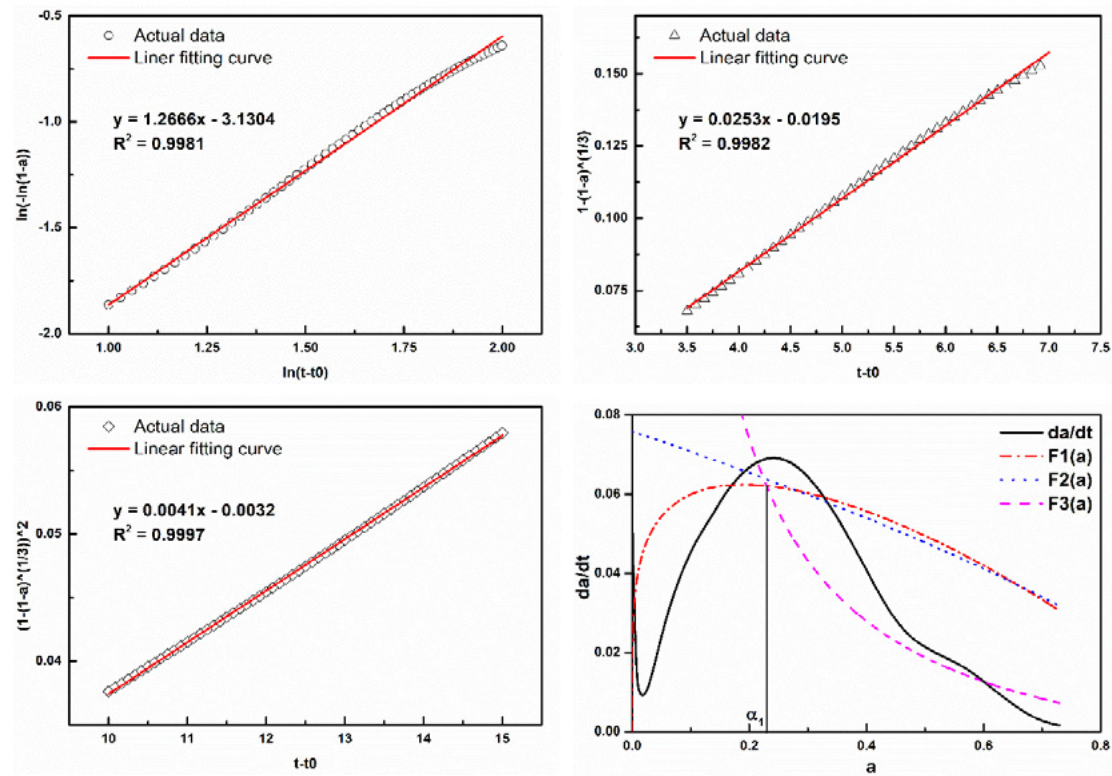


Figure 6: Determination of kinetic factors from linear regression for M3 group.

Table 3: Kinetic parameters determined by Krstulovic-Dabic model.

	n	K _{NG} [h ⁻¹]	K _I [μm·h ⁻¹]	K _D [μm ² ·h ⁻¹]	hydration mechanism	α ₁	α ₂	α ₁ -α ₂
R	1.6160	0.0864	0.0264	0.0055	NG-I-D	0.2463	0.2470	0.0007
M1	1.4346	0.0882	0.0269	0.0050	NG-D	0.2533	0.2533	0
M2	1.3724	0.0893	0.0263	0.0047	NG-D	0.2466	0.2466	0
M3	1.2666	0.0907	0.0253	0.0041	NG-D	0.2267	0.2267	0

Table 4: Share of individual processes up to 48 h of hydration /h.

Sample	Induction period	NG	I	D
R	2.28	5.28	0.01	40.43
M1	2.92	4.76	0	40.32
M2	2.87	4.57	0	40.56
M3	2.54	4.05	0	41.41

Share of individual processes up to 48 h of hydration is presented in Table 4. It can be seen the duration of induction period R, M1, M2 and M3 is 2.28 h, 2.92 h, 2.87 h and 2.54 h, respectively. The most significant extension is presented when Mg²⁺ concentration is 0.055 mol/L. The duration of NG process decreases regularly as increase on Mg²⁺ added from 0 mol/L to 0.22 mol/L. The duration of R, M1, M2 and M3 is 5.28 h, 4.76 h, 4.57 h and 4.05 h, respectively. Within 48 hs hydration, the share of D process of R, M1, M2 and M3 is 40.43 h, 40.32 h, 40.56 h and 41.41 h, respectively.

4. Conclusions

In this study, effect of Mg^{2+} on early hydration of Portland cement is discussed. Based on calorimetry test and hydration kinetic analysis, the following conclusions can be drawn:

1. Mg^{2+} increases heat release during induction and acceleration period, especially under high Mg^{2+} concentrations.
2. Mg^{2+} induces hydration inhibition during deacceleration and stabilization period.

5. Acknowledgment

This research has been financially supported by the National Natural Science Foundation of China (No. 51679179), National Nature Science Foundation Project of China (No. 51608409), Major science and technology project in Zhongshan city, Guangdong province (2017A1021), Yang Fan plan of Guangdong Province (201312C12), Open research project of Advanced Engineering Technology Research Institute of Wuhan University of technology in Zhongshan city (WUT201802).

1 References

1. T. Nishida, N. Otsuki, H. Ohara, Z.M. Garba-Say, T. Nagata, Some Considerations for Applicability of Seawater as Mixing Water in Concrete, *J. Mater. Civ. Eng.* 27 (2015) B4014004.
2. Nobuaki, Otsuki, Tsuyoshi, Saito, Yutaka, Tadokoro, Possibility of Sea Water as Mixing Water in Concrete, *J. Civ. Eng. Arch.* 6 (2012) 1273-1279.
3. <https://www.statista.com/statistics/219343/cement-production-worldwide/>
4. S.K. Kaushik, S. Islam, Suitability of sea water for mixing structural concrete exposed to a marine environment, *Cem. Concr. Comp.* 17 (1995) 177-185.
5. O.O. Akinkurolere, C. Jiang, O.M. Shobola, The Influence of Salt Water on the Compressive Strength of Concrete, *J Eng Appl Sci*, 2 (2012) 412-415.
6. W.J. McCoy, Water for mixing and curing concrete. In *Significance of Test and Properties of Concrete and Concrete Aggregates*, ASTM STP. 169 (1956) 352-357.
7. V.V. Reddy, N.V. Ramana, K. Gnaneswar, C. Sashidhar, Effect of magnesium chloride ($MgCl_2$) on ordinary Portland cement concrete, *Indian J. Sci. Technol.* 4 (2011) 643-645.
8. K. Thomas, W.E.A. Lisk, Effect of sea water from tropical areas on setting times of cements, *Mater. Struct.* 3 (1970) 101-105.
9. P.K. Mehta, J.M. Monteiro, *Concrete Microstructure Properties and Materials*, McGraw-Hill Professional, 2006 (Third Edition).
10. A. Tangen, W. Lund, J. Frederiksen, J. Determination of Na^+ , K^+ , Mg^{2+} , and Ca^{2+} in mixtures of seawater and formation water by capillary electrophoresis, *J. Chromatogr. A.* 767 (1997) 311-317.
11. L. Shan, Y. Wang, J. Li, H. Li, X. Wu, J. Chen, Tribological behaviours of PVD TiN and TiCN coatings in artificial seawater, *Surf. Coat. Technol.* 226 (2013) 40-50.
12. J. Olek, M. Cohen, M. Santhanam, Differentiating seawater and groundwater sulfate attack in Portland cement mortars, *Cem. Concr. Res.* 36 (2006) 2132-2137.
13. D. Jansen, F. Götz-Neunhoeffler, B. Lothenbach, J. Neubauer, The early hydration of Ordinary Portland Cement (OPC): an approach comparing measured heat flow with calculated heat flow from QXRD, *Cem. Concr. Res.* 42 (2012) 134-138.
14. C. Hesse, F. Götz-Neunhoeffler, J. Neubauer, A new approach in quantitative in-situ XRD of cement pastes: correlation of heat flow curves with early hadration reactions, *Cem. Concr. Res.* 41 (2011) 123-128.
15. J.W. Bullard, G.W. Scherer, J.J. Thomas, Time dependent driving forces and the kinetics of tricalcium silicate hydration, *Cem. Concr. Res.* 74 (2015) 26-34.
16. G. Sandrine, B. Tanja, N. André, Formation of the C-S-H Layer during early hydration of tricalcium silicate grains with different sizes, *J. Phys. Chem. B* 110(1) (2006) 270.
17. P. Juilland, E. Gallucci, R. Flatt, K. Scrivener, Dissolution theory applied to the induction period in alite hydration, *Cem. Concr. Res.* 40(6) (2010) 831-844.
18. G.C. Edwards, R.L. Angstadt, The effect of some soluble inorganic admixtures on the early hydration

- of Portland cement, *J. Appl. Chem.* 16 (1966) 166-168.
19. L. Zheng, X. Cui, M. Tang, Hydration and setting time of MgO-type expansive cement, *Cem. Concr. Res.* 22(1) (1992) 1-5.
 20. S Agatzini-Leonardou, Karidakis T, Tsakiridis P E. Use of gypsum/brucite mixed precipitate instead of gypsum in Portland cement[J]. *J. Chem. Technol. Biotechnol.* 2005, 80(3):5.
 21. KRSTULOVIC, DABIC, A conceptual model of the cement hydration process, *Cem. Concr. Res.* 30(5) (2000) 693-698.
 22. W. Teng, Y. Xue, Z. Min, L. Yi, Y. Chen, S. Wu, H. Hou, Hydration kinetics, freeze-thaw resistance, leaching behavior of blended cement containing co-combustion ash of sewage sludge and rice husk, *Constr. Build. Mater.* 131(Complete) (2017) 361-370.
 23. X. Chang, X. Yang, W. Zhou, G. Xie, S. Liu, Influence of glass powder on hydration kinetics of composite cementitious materials, *Adv. Mater. Sci. Eng.* 2015 (2015).

Recent Sustainable Development of Ultra-High Performance Concrete (UHPC)

R. Yu^{1*}, Z. Liu^{1,2}, X. Wang^{1,2}, Q. Song^{1,2}, Z. Shui¹, C. Hao³

¹State Key Laboratory of Silicate Materials for Architectures, Wuhan University of Technology, Wuhan 430070, China;

²School of Materials Science and Engineering, Wuhan University of Technology, Wuhan 430070, China

³Zhonganruibao Construction Group CO., LTD, East Huizhan road 1, 528400, Zhongshan, Guangdong, China

Abstract

Ultra-high performance concrete (UHPC) is a relatively new building materials, which has superior durability, ductility and strengths in comparison with Normal Strength Concrete (NSC) and Fiber Reinforced Concrete (FRC) due to its extremely low porosity, dense matrix, high homogeneous system and the inclusion of various fibres. However, in recent years, due to the fact that more and more attentions have been paid on sustainable development and cleaner products, the high materials cost and high environmental impact of UHRC seem to be the main disadvantages that restrict its further development and application. Hence, to solve the problem mentioned above, a series of approaches have been proposed. In this study, based on the investigation by the authors, several key methods for developing eco-friendly UHPC are presented: 1) optimized design of UHPC particle packing skeleton; 2) appropriate application of cementitious materials; 3) appropriate application of aggregates; 4) effective increase of steel fibre efficiency. Moreover, some detailed mechanism for the properties and microstructure development in the developed sustainable UHPC are also discussed. At last, based on a large amount of experimental results and analysis, the development trend for sustainable UHPC in near future is suggested.

Keywords: Ultra-High Performance Concrete (UHPC), Sustainable development, optimized design, efficient application, mechanism analysis

1. Introduction

Nowadays, the sector of building materials (mainly cement based materials, as concrete) is the third largest CO₂ emitting industrial sector world-wide [1]. Therefore, to achieve a sustainable development of concrete industry, one of the promising approaches is to design and produce a type of concrete with less clinker [2-4], inducing lower CO₂ emissions than traditional ones [5], while providing the same or better reliability and durability [6].

Ultra-High Performance Fibre Reinforced Concrete (UHPFRC) is a relatively new construction material [7]. Considering the successful application of UHPFRC in practice (e.g. Mediterranean Culture Museum in Marseille of France, Gärtnerplatz bridge build in Kassel of Germany), UHPFRC seems to be one of the most suitable candidates to reduce the global warming impact of construction materials [8]. Due to the advanced mechanical properties and durability, the structure made of UHPFRC can be much more slender compared to normal concrete structure. However, the disadvantage of UHPFRC in reducing its environmental impacts can also be noticed. This can mainly attributed into following three aspects: 1) the

cement/binder amount in the production of UHPFRC is relatively high, and the cement/binder efficiency is relatively low; 2) the application of recycled materials or industry by products needs theoretical support; 3) the utilization of steel fibres can be treated as a black box, and the fibre efficiency is relatively low. Although, in available literature, many researchers have contributed a lot of experimental and theoretical results in developing sustainable UHPFRC, this field still needs further investigation and effort.

In general, based on these premises mentioned above, to promote the sustainable development of UHPFRC, its matrix and used fibres efficiencies should be optimized. Therefore, in this study, three strategies are mainly employed: 1) optimized design of the UHPFRC matrix based on modified Andreasen & Andersen particle packing model and appropriate application of substitutive materials; 2) appropriate utilization of recycled materials based on close packing theory; 3) efficient improve the fibre efficiency based on an optimized casting method.

2. Methodology

2.1 Materials

The cement used in this study is Ordinary Portland Cement (52.5). A polycarboxylic ether based superplasticizer is used to adjust the workability of concrete. Several supplementary cementing materials (SCM), such as fly ash (FA), ground granulated blastfurnace slag (GGBS) and silica particles (S-P) in slurry, are used as pozzolanic materials to replace cement. Limestone powder (LP) is treated as filler in this study. Four types of sand are used: micro-sand, sand (0-0.6), sand (0.6-1.25) and sand (0-2). The addition of construction and demolition wastes is used to reduce energy consumption. The particle size distribution, shape and texture of river sand and construction and demolition wastes have been compared and the detailed information is presented in Figures 1. The water absorption of construction and demolition wastes and river sand has also been measured (19.60% for construction and demolition wastes and 2.9% for river sand). Additionally, one type of steel fibres is utilized: length = 13 mm, diameter = 0.2 mm.

Based on the modified Andreasen & Andersen particle packing model, the optimized UHPFRC matrix is firstly designed (as shown in Table 1). Compared to the reference sample, about 30% of Portland cement (by mass) is replaced by FA, GGBS or LP in the mixtures. One of the resulting integral grading curves are shown in Figure 2.

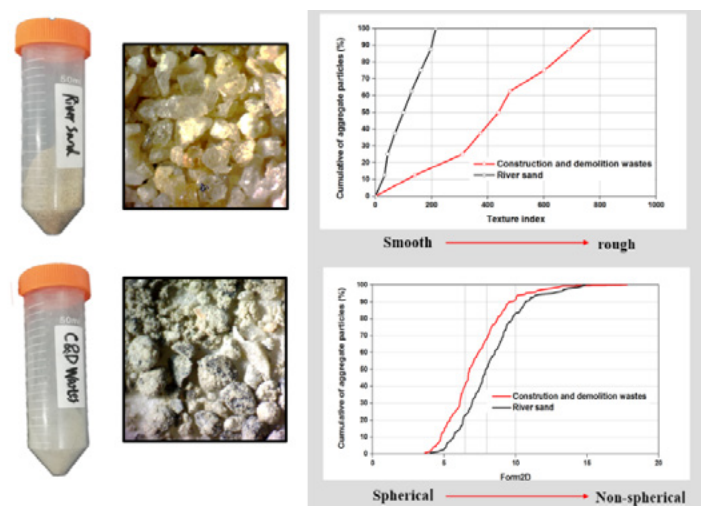


Figure 1: Properties of C&D (construction and demolition wastes) and river sand

Table 1: Mix recipes of the designed UHPFRC matrix (kg/m³ concrete)

NO.	C (kg/m ³)	FA (kg/m ³)	GGBS (kg/m ³)	LP (kg/m ³)	S (kg/m ³)	MS (kg/m ³)	S-P (kg/m ³)	W (kg/m ³)	SP (kg/m ³)
1	591.9	264.3	0	0	1057.0	220.2	24.7	159.3	44.0
2	606.4	0	270.7	0	1082.9	225.6	25.3	163.2	45.1
3	602.8	0	0	269.1	1076.5	224.3	25.1	162.2	44.9
Ref.	883.9	0	0	0	1091.2	227.3	25.5	164.4	45.5

(C: Cement, FA: Fly ash, GGBS: Ground granulated blast-furnace slag, LP: Limestone powder, S: sand, MS: Microsand, S-P: Silica particle, W: Water, SP: Superplasticizer, W/B: water to binder ratio, Ref.: reference samples without industry by-products, #: LP is considered as a binder in the calculation)

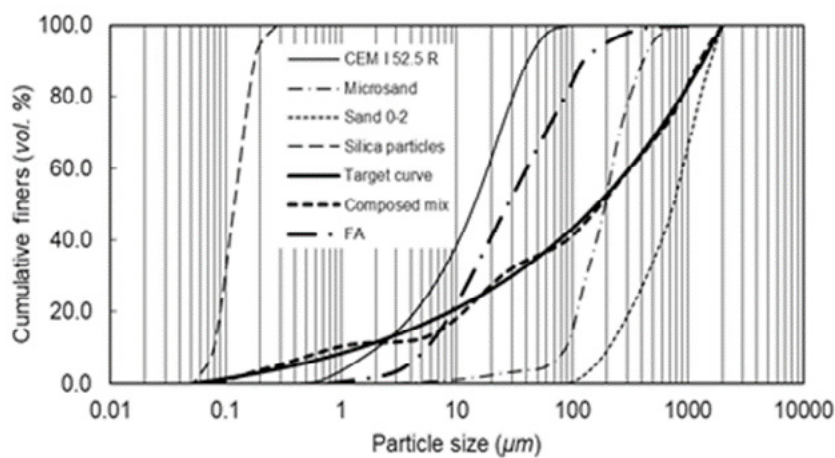


Figure 2: PSDs of the involved ingredients, the target and optimized grading curves of the developed UHPFRC matrix

After that, construction and demolition wastes with maximum size of 0.6mm are utilized to replace cement and natural river sand. The influence of the replacement by construction and demolition wastes on the solid particle system is illustrated in Figure 3 and results further confirm the feasibility. The mixing design and binder composition of UHPC mixtures including construction and demolition wastes are shown in table 2.

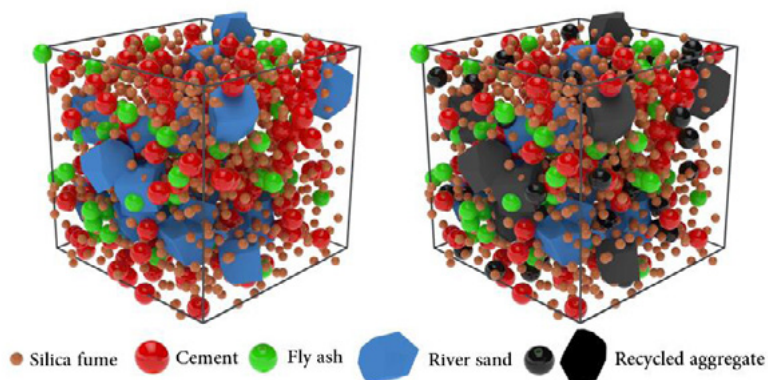


Figure 3: the replacement of cement and river sand by construction and demolition wastes on the packing system of UHPC

Table 2: Recipe of UHPFRC with different compounded high-active powders (kg/m³)

	C&D	C	SF	FA	S	Water	Sp	R ₁	R ₂
REF.	0	670	188	200	990	210	30	0	0
C&D 215	215	536	188	200	904	210	30	25	8.7
C&D 430	430	402	188	200	818	210	30	50	17.4

(C: Cement, FA: Fly Ash, SF: Silica Fume, C&D: construction and demolition wastes; R₁: Volume replacement ratio of cement by construction and demolition wastes; R₂: Volume replacement ratio of river sand by construction and demolition wastes; S: river sand with particle size of 0-0.6 mm; Sp: superplasticizer.)

Thirdly, to efficiently improve the fibre orientation and fibre efficiency, two cast methods (as shown in Figure 4) are used in this study: 1) A: cast at one side of the mould with flowing process (optimized casting); 2) B: cast randomly without flowing process (non-optimized casting).

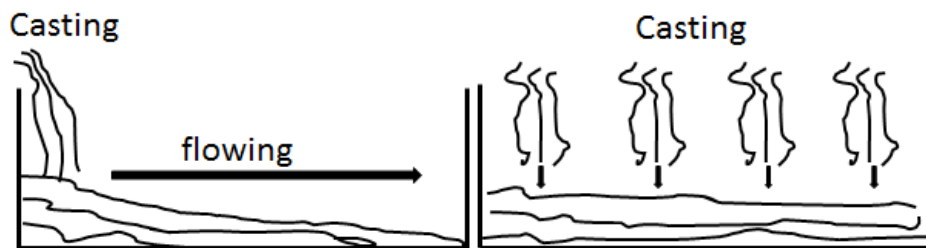


Figure 4: Employed casting methods: (a) cast at one side of the mould with flowing process (optimized casting); (b) cast randomly without flowing process (non-optimized casting)

3. Results and discussion

3.1 Properties evaluation of UHPFRC skeleton with low cement/binder amount

Figure 5 presents the compressive strength of the designed UHPFRC matrix (without fibres) at 28 and 91 days. It can be noticed that the reference sample always has the highest compressive strengths at both 28 and 91 days, which can be attributed to its high cement content. When the cement is partly replaced by industry by-products, it can be found here the mixture with GGBS has superior mechanical properties at both 28 and 91 day, while that the strengths of the mixtures with FA or LP are similar to each other. According to the compressive strength results obtained in this study, it can be summarized that based on appropriate application of modified Andreasen and Andersen particle packing model, a dense packed UHPFRC matrix skeleton can be obtained. When the unhydrated cement particles in this dense packed skeleton are replaced by industry by-products, the utilized cement amount can be reduced by about 30%, and the concrete mechanical properties are still acceptable.

To evaluate the eco properties of the designed UHPFRC matrix, the concept of embedded CO₂ emission is employed in this study, which focus on the amount of materials required for 1 m³ of compacted concrete. Based on the embodied CO₂ values for each components of concrete [9], the embedded CO₂ emissions of the designed UHPFRC matrix in this study are calculated and shown in Figure 6. It is obvious that the reference sample has the highest embedded CO₂ emission, while that value for the mixture with industry by-products are much lower (about 30% less) and similar to each other. This can be attributed to the large cement amount in reference sample and the relatively high environmental impact of cement material. Therefore, appropriately replace the cement by industry by-products is a promising method to promote the sustainable development of UHPFRC.

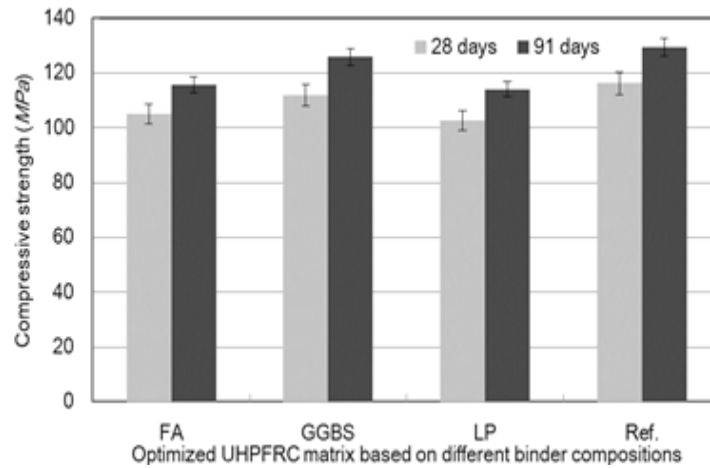


Figure 5: Compressive strengths of the designed UHPFRC matrix with different mineral admixtures

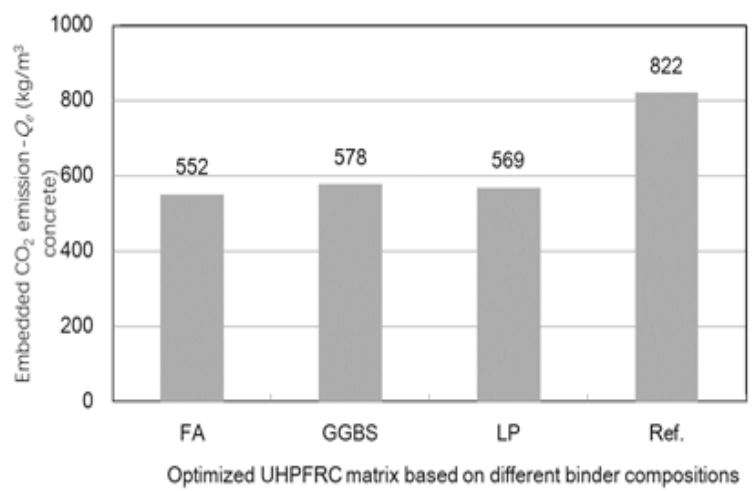


Figure 6: Comparison of embedded CO₂ emission (Q_e) for the optimized UHPFRC matrix based on different binder compositions

3.2 Appropriate application of recycled materials in UHPFRC

The compressive strength for the UHPC mixtures are presented in Figure 7. It can be noticed that with increase amount of C&D wastes, the 1d compressive strength of UHPC including construction and demolition wastes obvious decrease. However, it is important to notice that the addition of C&D wastes have limited effect on the compressive strength development of UHPC at 7 and 28 days. For instance, the maximum compressive strength for the UHPC produced is about 127 MPa (at 28 days), while the value for UHPC including 448kg/m³ C&D is around 116 MPa (at 28 days). Compared with other eco-efficient UHPC, it can be concluded that the compressive strength per cement is higher. This also highlights the advantage of substitution strategy based on maintaining the close packing system of UHPC. To evaluate the environmental contribution of UHPC mixtures including C&D wastes, the ecological indexes are calculated based on 1m³ designed materials. As shown in Figure 8, it is clear that the ecological overload can be significantly reduced with the addition of C&D wastes. For instance, C&D 448 (mixtures replacing 40% cement and 18.2% river sand) shows a significant reduction in environmental categories: about 39%, 20%, 33%, 11% and 16% reduction in renewable energy input, non-renewable energy input, global warming potential, nitrification potential and acidification potential, respectively, compared to that of reference specimens (REF). Hence, based on the obtained experimental results, it can be summarized that the outcome of this research can not only benefit for solving the landfill problem caused by C&D waste, but also provide UHPC with low environmental burden [10].

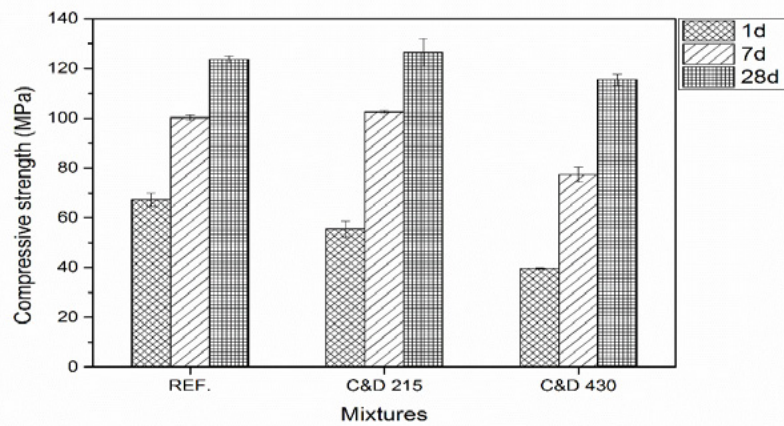


Figure 7: Compressive strengths for the UHPC with and without C&D wastes

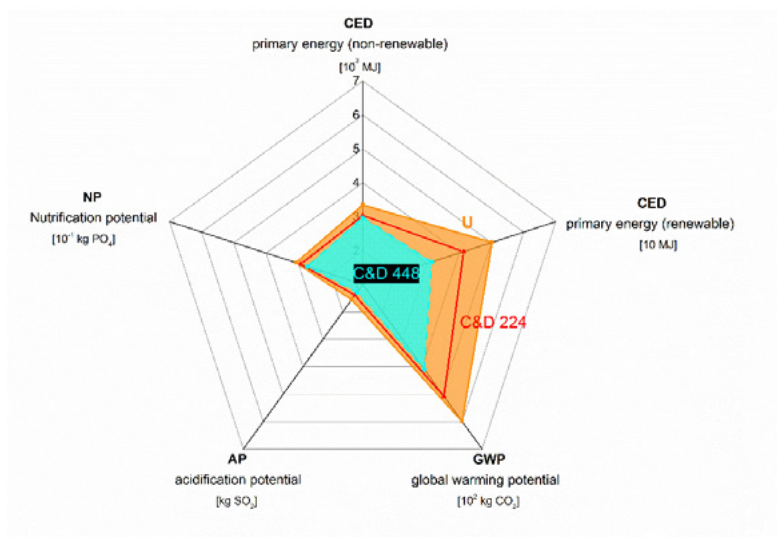


Figure 8: Comparison of the ecological characteristics of UHPC with different C&D wastes dosages

3.3 Improvement of fibre efficiency of UHPFRC based on optimized casting method

Figure 9 illustrates the flexural strength variation of the UHPFRC with different steel fibre content. The two curves represent the 28d flexural strength of UHPFRC based on optimized casting method (with flowing process) and non-optimized casting method (without flowing process). It is found that with an increase of the steel fibre content, the flexural strengths simultaneously increase. Moreover, it is important to notice that the UHPFRC produced based on optimized casting method always has higher flexural strength than that of the one produced based on non-optimized casting method, which proves that the UHPFRC cast at one side of the mould has higher flexural strength than randomly casting samples.

These difference flexural strength results obtained from two casting methods can be attributed to the influence of fibre orientation in UHPFRC. As commonly known, the fibre orientation has close relationship with the flexural strength of concrete. When a large amount of steel fibres are perpendicular to the flexural force direction, the steel fibres can significantly resist the cracks generation and growth, which is helpful for improving the concrete flexural strength. Hence, in this study, it can be predicted that in the UHPFRC produced based on the optimized casting method has more fibres perpendicular to the flexural force direction [11-12].

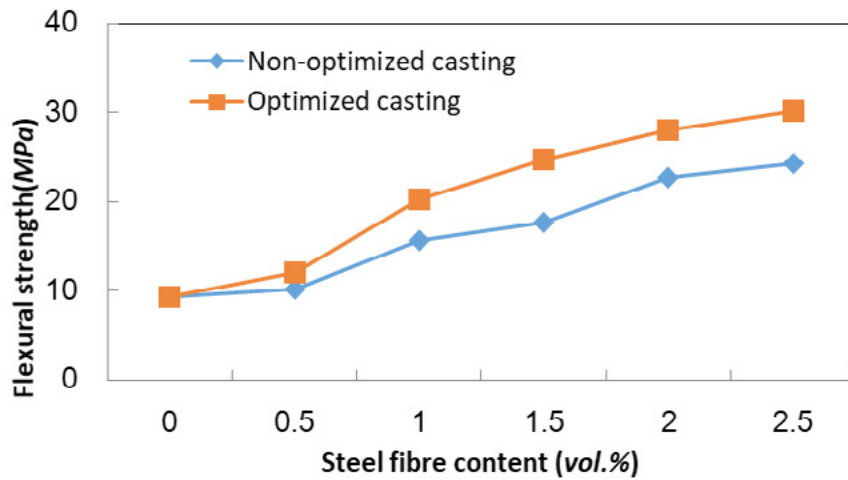


Figure 9: Flexural strength variation of the UHPFRC produced based on different casting methods

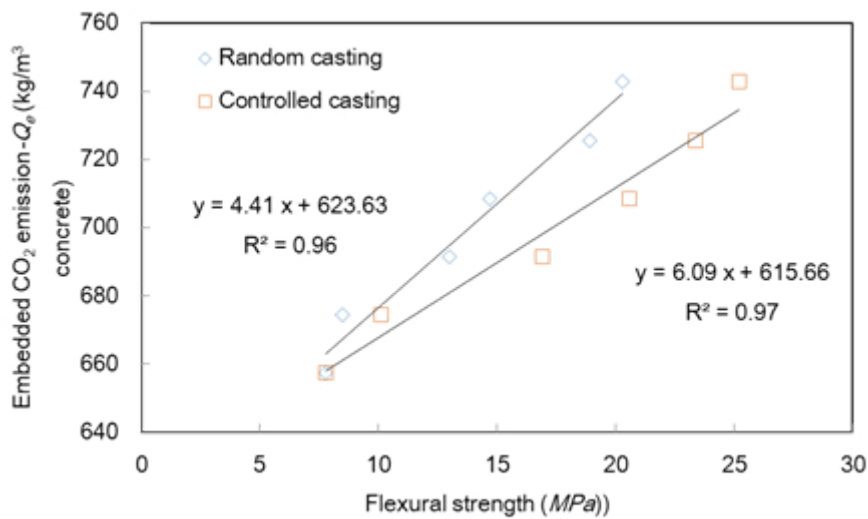


Figure 10: Comparison of embedded CO₂ emission (Q_e) for the designed UHPFRC based on different casting methods

As shown in previous sections, the concept of embedded CO₂ emission (EN ISO 14040 and 14044) is also employed to evaluate the eco properties of the optimized UHPFRC based on different casting methods (as presented in Figure 10). It is obvious that with almost the same flexural strength, the designed UHPFRC based on controlled casting method presents low environmental impact. For instance, when the flexural strength is about 20 MPa, the embedded CO₂ emissions are about 700 and 750 kg/m³ for the UHPFRC based on controlled casting and random casting. This further demonstrates the controlled casting method can effectively promote the sustainable development of UHPFRC for a cleaner production [13].

4. Conclusions

Based on the experimental investigations shown in this study, the following conclusions can be drawn:

- 1) Based on appropriate application of modified Andreasen and Andersen (A&A) particle packing model, a dense packed UHPFRC matrix skeleton can be obtained, which has relatively higher binder efficiency.
- 2) C&D wastes with maximum size of 0.6mm can be treated as mixture blending of cement and natural sand and the reasonable substitution of cement and sand has no negative effect on the deviation between mixtures and target curve calculated by modified A&A model.

3) When the developed UHPFRC cast at one side of the mould (optimized casting method), the fibres orientation can be well optimized, which is beneficial for improving the fibre efficiency and producing sustainable UHPFRC.

5. Acknowledgment

The authors acknowledge the financial supports of National Nature Science Foundation Project of China (No. 51608409), National Nature Science Foundation Project of China (51679179), Major science and technology project in Zhongshan city, Guangdong province (2017A1021), Yang Fan plan of Guangdong Province (201312C12), Open research project of Advanced Engineering Technology Research Institute of Wuhan University of technology in Zhongshan city (WUT201802).

6. References

- [1] UNSTATS, 2010. Greenhouse gas emissions by sector (absolute values).United Nation Statistical Division: Springer.
- [2] Yu, R., Spiesz, P., Brouwers, H.J.H., 2015. Development of an eco-friendly Ultra-High Performance Concrete (UHPC) with efficient cement and mineral admixtures uses. *Cem. Concr. Comp.*, 55, 383-394.
- [3] Yu R., Spiesz P., Brouwers H.J.H., Mix design and properties assessment of Ultra- High Performance Fibre Reinforced Concrete (UHPFRC), *Cement and Concrete Research*, 2014, 56: 29-39.
- [4] Yu R., Spiesz P., Brouwers H.J.H., Effect of nanosilica on the hydration and microstructure development of Ultra-High Performance Concrete (UHPC) with a low binder amount. *Construction and Building Materials*, 2014; 65: 140-150.
- [5] Igliński, B., Buczkowski, R., 2017. Development of cement industry in Poland – History, current state, ecological aspects. A review. *J. Clean. Prod.*, 141, 702-720.
- [6] Mohammadhosseini, H., Yatim, J.M., Sam, A.R.M., Abdul Awal, A.S.M., 2017. Durability performance of green concrete composites containing waste carpet fibers and palm oil fuel ash. *J. Clean. Prod.*, 144, 448-458.
- [7] Richard P., Cheyrezy M., Composition of reactive powder concretes, *Cement and Concrete Research*, 1995; 25 (7): 1501-1511.
- [8] Habert, G., Arribe, D., Dehove, T., Espinasse, L., Le Roy, R., 2012. Reducing environmental impact by increasing the strength of concrete: quantification of the improvement to concrete bridges. *J. Clean. Prod.*, 35, 250-262.
- [9] Randl N., Steiner T., Ofner S., Baumgartner E., Mészöly T., Development of UHPC mixtures from an ecological point of view. *Construction and Building Materials*, 2014; 67: 373-378.
- [10] Wang X.P., Yu R., Shui Z.H., Song Q.L., Liu Z., Bao M., Liu Z.J., Wu S., Optimized treatment of recycled construction and demolition waste in developing sustainable ultra-high performance concrete. *Journal of Cleaner Production*, 2019, 221: 805-816.
- [11] Song Q.L., Yu R., Shui Z.H., Wang X.P., Rao S.D., Lin Z.W., Optimization of fibre orientation and distribution for a sustainable Ultra-High Performance Fibre Reinforced Concrete (UHPFRC): Experiments and mechanism analysis. *Construction and Building Materials*, 2018, 169: 8-19.
- [12] Song Q.L., Yu R.*, Shui Z.H., Wang X.P., Rao S.D., Lin Z.W., Wang Z., Key parameters in optimizing fibres orientation and distribution for Ultra-High Performance Fibre Reinforced Concrete (UHPFRC). *Construction and Building Materials*, 2018, 188: 17-27.

[13] Yu R., Song Q.L., Wang X.P., Zhang Z.H., Shui Z.H., Brouwers H.J.H., Sustainable development of Ultra-High Performance Fibre Reinforced Concrete (UHPFRC): Towards to an optimized concrete matrix and efficient fibre application. *Journal of Cleaner Production*, 2017, 162: 220-233.

Influence of External Water Introducing by Coral Sand on Autogenous Shrinkage and Microstructure of Ultra-High Performance Concrete (UHPC)

K. Liu^{1,2}, Z. Shui¹, R. Yu¹, S. Yi²

1 State Key Laboratory of Silicate Materials for Architectures, Wuhan University of Technology, Wuhan 430070, China;

2 School of Materials Science and Engineering, Wuhan University of Technology, Wuhan 430070, China

Abstract

Ultra-High Performance Concrete (UHPC) is a new cement-based material with high strength, toughness and durability, which has broad application prospects in marine engineering. The biggest disadvantage of UHPC is large early autogenous shrinkage and cracking risk. Coral sand as an internal curing agent employed in UHPC can effectively inhibit the self-desiccation inside the concrete and reduce its autogenous shrinkage. In this paper, 0-0.6 mm river sand was replaced by the same size of pre-wetting coral sand (water absorption rate of 19.0%, 24.7% and 31.2%, respectively) by a certain volume fraction (10%, 20% and 30%, respectively), and the early autogenous shrinkage and development of microstructure of UHPC were evaluated. The experimental results show that the introduction of wet coral sand improves the fluidity of UHPC fresh slurry and prolong the setting time. Meanwhile, the development of mechanical properties and early autogenous shrinkage of UHPC hardened paste are inhibited as a whole. The optimum mixture design is that 20% (vol. %) of river sand is replaced by coral sand with 19.0% (wt. %) water absorption rate, and UHPC fluidity increases by 43.2%, 28 d compressive strength increases by 1.3%, 28 d flexural strength decreases by 4.8%, 7 d autogenous shrinkage decreases by 42.2%. Image analysis of pore structure presents that the porosity of micron-scale coarse pores in UHPC increase, and that porosity of millimeter-scale stomata decreases. Environmental Scanning Electron Microscope and Electron Backscattered Diffraction photomicrographs show that Interfacial Transition Zone (ITZ) of damp coral sand and matrix becomes homogenized and densified, and micro-cracks are more difficult to initiate and propagate.

Keywords: ultra-high performance concrete (UHPC), coral sand, water absorption, autogenous shrinkage, microstructure

1. Introduction

Ultra-high Performance Concrete (UHPC), as a new type of cement-based material, is designed based on the tightest accumulation of component particles at low water/binder ratio ($w/b < 0.2$) [1-3]. Compared with ordinary concrete, UHPC has excellent performance such as ultra-high strength, toughness and durability, leading to wide application prospect and development potential in construction and restoration engineering fields [4,5]. However, due to the low water/binder ratio of UHPC, the early autogenous shrinkage caused by the self-desiccation phenomenon is extremely large, which makes the concrete have poor volume stability and cracking risk. Therefore, how to effectively reduce the early contraction of UHPC is particularly important.

The commonly method for controlling of the early autogenous shrinkage of concrete is adding expansion agent, shrinkage reducing agent and introduce internal curing agent. However, the action time of expansive agents and the scale of expansion are quite difficult to control [6-8]. Shrinkage reducing agent can inhibit the early strength development of concrete, and it is easy to interact with admixtures, resulting in further degradation of performance [8-10]. Internal curing can radically solve the problem of self-shrinkage by compensating the internal humidity of concrete through the water slow-release effect of the medium and delay the self-desiccation. Recent research on super absorbent polymer (SAP) and porous mineral materials are the main internal curing media studied. SAP has a good internal curing effect, which can completely eliminate self-shrinkage and even cause the matrix to slightly expand [11-14]. However, the holes caused by SAP after water release will reduce the density of concrete matrix, resulting in a decrease in the mechanical properties and durability. Therefore, the use of porous mineral materials as internal curing agent is an effective way to reduce the early autogenous shrinkage of UHPC.

Nowadays, the research on using porous mineral materials as internal curing agent in UHPC is still at initial stage. Meng et al. [15,16] designed UHPC by replacing river sand with saturated expansion shale and light sand respectively. The results showed that the compressive strength of UHPC introducing saturated expansion shale (25%, vol. %) increased from 130 MPa to 158 MPa after 28 days, and the corresponding self-shrinking deformation decreased from 489 $\mu\text{m}/\text{m}$ to 365 $\mu\text{m}/\text{m}$. When saturated light sand replaced river sand, UHPC 28 d compressive strength increased from 145 MPa to 160 MPa, 28 d self-shrinking deformation decreased from 406 $\mu\text{m}/\text{m}$ to 72 $\mu\text{m}/\text{m}$. Liu et al. [17] used saturated coral sand as internal curing agent in UHPC, and revealed that the early self-shrinking deformation of UHPC decreased with the increase of coral sand. When the content of saturated coral sand exceeded 35% (vol. %), the micro-expansion began to appear. Meanwhile, the strength of UHPC decreased, as well as the degree of reduction was positively correlated with the content of that saturated coral sand. When the dosage reached 35% (vol. %), the compressive strength decreased by 19.6% on the 28th day. Wang et al. [18] not only prepared the ecological UHPC by using saturated micro-coral powder and coral sand to replace cement and river sand respectively, but also evaluated its early self-shrinking development. The results indicated that saturated coral sand had significant internal curing effect, and the content of 30% (vol. %) saturated coral sand reduced the 7 d self-shrinkage of UHPC from 1175 $\mu\text{m}/\text{m}$ to 617 $\mu\text{m}/\text{m}$. At the same time, under the condition that saturated coral sand replaced river sand at a lower level, mechanical properties of UHPC would not be significantly degraded, or even improved to a certain extent (< 20%, vol. %). However, it has not systematically studied about the water absorption rate of porous mineral materials curing agent and the total amount of water introduced on the internal curing effect in UHPC.

In this paper, UHPC was prepared using water-absorbing coral sand with different water absorption rates to replace river sand with a certain volume fraction, and its influence on the performance of UHPC was studied. The macroscopic properties of UHPC such as working performance, mechanical properties and early autogenous shrinking were characterized according to relevant standards. Besides, the pore structure and microstructure development of UHPC were evaluated.

2. Methodology

2.1 Materials

Cementitious materials used in the experiment include OPC 52.5 cement, fly ash (FA), silica fume (SF). Fine aggregates include two particle sizes of natural river sand (0-0.6 mm and 0.6-1.25 mm) and coral sand (0-0.6 mm) from south China sea. The XRF analysis results of cementitious materials and coral sand (CS) are shown in Table 1. Admixture is a polycarboxylic ether based superplasticizer (SP) with a solid content of 20% and water reduction rate of 40%.

Table 1 Chemical compositions of cementitious materials and coral sand (wt. %)

Compositions	Na ₂ O	MgO	Al ₂ O ₃	SiO ₂	P ₂ O ₅	SO ₃	K ₂ O	CaO	Fe ₂ O ₃	LOI
Cement	0.09	1.61	4.18	19.20	0.09	3.35	0.78	64.93	3.32	2.49
SF	0.13	0.47	0.25	94.65	0.17	0.69	0.84	0.36	0.15	2.29
FA	0.33	0.23	38.01	46.44	0.06	0.69	0.88	7.50	3.12	2.79
CS	0.38	2.00	0.25	0.98	0.07	0.74	0.03	50.42	0.09	44.32

The apparent densities of 0-0.6 mm natural river sand and crushed coral sand are 2.66 kg/m³ and 2.57 kg/m³ respectively, and their particle morphology is shown in Figure 1. As a naturally formed porous mineral material, the SEM photomicrograph of coral sand is shown in Figure 2. The saturated water absorption rate of 0-0.6 mm coral sand is 31.2% (wt. %) [19].

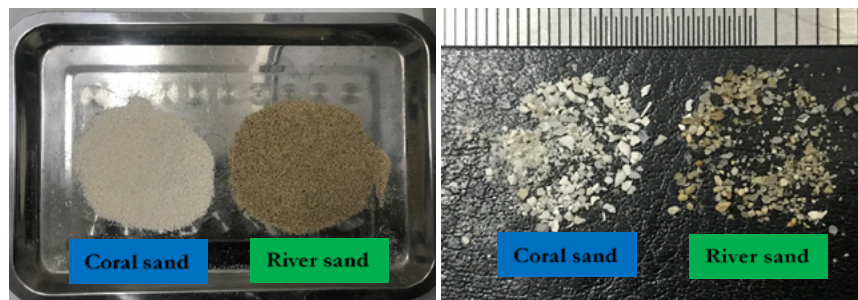


Figure 1 Images of 0-0.6 mm nature river sand and broken coral sand particles

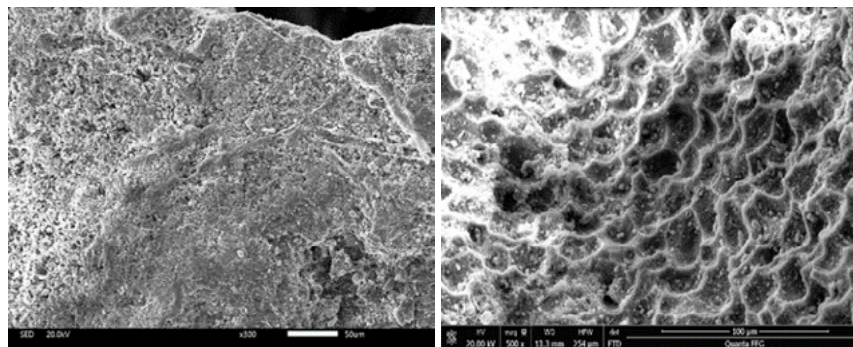


Figure 2 SEM photomicrographs of coral sand

2.2 Methods

2.2.1 UHPC mix design method

The modified Andreasen-Andersen (A&A) model is the most widely used mix design method for UHPC, as shown in equation (1). Where, P(D) represents the total amount of particles under sieve (%), D is the current particle size (μm), D_{min} and D_{max} represent the minimum and maximum particle size (μm), q is the distribution modulus. In this paper, the q value is 0.23 [18,20,21].

$$P(D) = \frac{D^q - D_{min}^q}{D_{max}^q - D_{min}^q} \tag{1}$$

According to the particle size distribution of cement, fly ash, silica fume, river sand and coral sand, the least square method is used to evaluate the packing state between particles of each component, as shown

in equation (2). Among them, the D_i^{i+1} represents particles of a certain level of distribution scope, n represents the number of particles selected, P_{mix} and P_{tar} represent the actual accumulation curve and target curve between particles respectively. RSS represents the sum of squares of residuals. The smaller the value of RSS is, the smaller the error between the actual accumulation curve and the target curve will be.

$$RSS = \frac{\sum_{i=1}^n (P_{mix}(D_i^{i+1}) - P_{tar}(D_i^{i+1}))^2}{n} \tag{2}$$

According to the cementitious materials (cement, fly ash and silica fume) and the fine aggregates (river sand and coral sand) particle size distributions to adjust their volume fractions, the mix proportion of UHPC system was designed. The closer the actual accumulation curve and the target curve was, UHPC components between particles reached the more compact packing. The mix design of UHPC was prepared with 0-0.6 mm coral sand particles with different water absorption rates (19.0%, 24.7% and 31.2%, wt. %) instead of a certain amount (10%, 20% and 30%, vol. %) of same size river sand. The mix design is shown in Table 2 and the accumulation curve is shown in Figure 3. The results showed that although the gradation of coral sand particles in the same size range was not completely the same as that of river sand, the actual accumulation curve of each substitution ratio was in good agreement with the target curve. It meant that the particles accumulation form of UHPC components mixed with coral sand was not obviously destroyed, and the matrix was still in a compact packing state.

Table 2 Mix design of UHPC combined with pre-wetting coral sand (kg/m³)

Group	Cement	FA	SF	River sand		Pre-wetting coral sand		Water	SP
				0-0.6 mm	0.6-1.25 mm	Drying coral sand	Extra water		
RE	750	200	144	770	220	0	0	175	31
C1	750	200	144	693	220	74.33	14.12	175	31
C2	750	200	144	616	220	148.66	28.25	175	31
C3	750	200	144	539	220	222.99	42.37	175	31
C4	750	200	144	693	220	74.33	18.36	175	31
C5	750	200	144	616	220	148.66	36.72	175	31
C6	750	200	144	539	220	222.99	55.08	175	31
C7	750	200	144	693	220	74.33	23.19	175	31
C8	750	200	144	616	220	148.66	46.38	175	31
C9	750	200	144	539	220	222.99	69.57	175	31

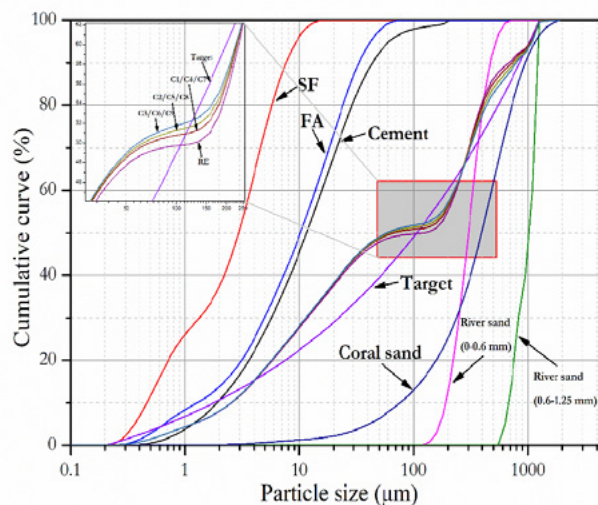


Figure 3 Particle accumulation curve of UHPC raw materials

2.2.2 *Fluidity*

The fluidity of UHPC slurry was tested according to the related Chinese standard GB/T 2419-2005.

2.2.3 *Setting time*

The setting time of UHPC slurry was tested according to the related Chinese standard JGJ/T 70-2009.

2.2.4 *Mechanical properties*

The compressive and flexural strength of UHPC samples were tested according to the related Chinese standard GB/T 17671-1999. The sample size was 40 mm×40 mm×160 mm and cured in water (20±2℃).

2.2.5 *Autogenous shrinkage*

The Autogenous shrinkage of UHPC was tested according to the related Chinese standard GB/T 50082-2009, and the device was shown in Figure 4. The temperature and humidity of deposited surrounding were 20±2℃ and 60±5%, respectively, and setting time was the beginning of the test.



Figure 4 UHPC autogenous shrinkage testing device

2.2.6 *Pore structure*

The pore structure of UHPC was evaluated by Image J software with image analysis on cross-sectional morphology of matrix.

2.2.7 *Microstructure*

The development of microstructure of UHPC was evaluated by image analysis of SEM and EBSD (Electron BackScattered Diffraction). SEM and EBSD were used to observe the structure of ITZ and the development of microcrack in matrix, respectively.

3. Results and discussion

3.1 Fresh behavior

Figure 5 shows the fluidity and setting time of fresh UHPC slurry with different mixing ratios. The fluidity of C1~C9 was 115.3%, 143.2%, 148.6%, 147.0%, 170.0%, 174.3%, 105.5%, 157.4% and 168.9% of the reference group, respectively. The results show that the fluidity of UHPC fresh slurry can be improved by adding wet coral sand, and the growth is positively correlated with the total amount of introducing water as a whole. This is because during mixing process of UHPC, the water introduced by water-absorbing coral sand breaks away under the action of rotor centrifugal force and enters into the slurry, which increases the free water in the system. As more free water can participate in the lubrication between particles, the fluidity of the paste increases. The fluidity of C7 group was not significantly improved compared with the reference group, because the content of water-absorbing coral sand was relatively high, which increased

the contact opportunities with the cementitious material, so that part of free water released by wet coral sand was adsorbed on the surface of cementitious material particles. The amount of water introduced into effective lubrication was limited, and the fluidity of slurry was not significantly increased.

The setting time of C1~C9 was 75.0%, 150.0%, 168.8%, 156.3%, 164.6%, 187.5%, 158.3%, 187.5% and 187.5% of the reference group. The results show that the addition of water-absorbing coral sand will lead to prolonged setting time of UHPC slurry. The setting time of UHPC mortar is directly proportional to the total amount of introduced water. This is because the moisture released by the wet coral sand promotes the hydration of cement and generates more hydration products, which thickens the film layer of hydration products covering cement particles, and delays the formation of the gel network and prolongs the setting time. However, the shortened setting time of group C1 is due to the fact that the coral sand with low water absorption rate and content will continuously absorb free water out from the system, so as to thin the film of hydration product encapsulating cement particles, accelerating the continuous hydration of cement particles and the formation of cementitious structure network.

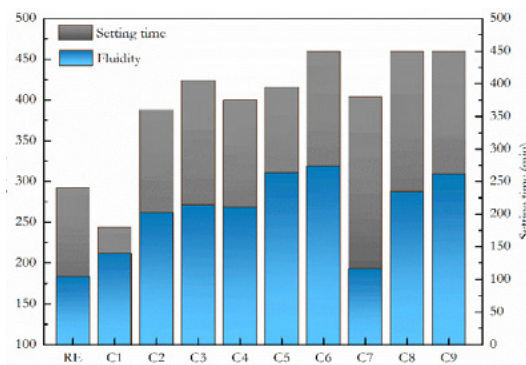


Figure 5 Fluidity and setting time of UHPC fresh slurry with different mixture ratios

3.2 Mechanical properties

The development of compressive and flexural strength of UHPC with different mixing ratios is shown in Figure 6 and 7 respectively. The compressive strength of C1~C9 on the 28th day was 105.6%, 101.3%, 96.1%, 93.9%, 90.1%, 87.8%, 91.0%, 77.3% and 68.5% of the reference group respectively. The results showed that the introduction of water-absorbing coral sand could inhibit the development of early compressive strength of UHPC. As the total amount of introduced water was low, UHPC had a significant strength compensation development after 7 days, and the compressive strength of 28 days would exceed that of the reference group (C1 and C2). This is because the introduction of water-absorbing coral sand has positive and negative effects on the development of mechanical properties of UHPC. The negative effect is mainly due to the fact that the water introduced by the wet coral sand increases the actual water-binder ratio of the UHPC system, increasing the porosity of the hardened paste and decreasing the mechanical properties. The positive effect is that the water released from the water-absorbing coral sand can continuously promote the hydration of cement and the secondary hydration of active mineral admixtures (SF and FA), and improve the hydration rate of the cementitious system and promote the development of UHPC strength, especially in the later stage. The development of compressive strength of UHPC is the result of these two effects.

The 28 d flexural strength of C1~C9 was 112.5%, 95.2%, 85.6%, 87.5%, 82.7%, 73.1%, 83.7%, 71.2% and 68.3% of the reference group. The results show that, except for group C1, the addition of water-absorbing coral sand not only leads to the reduction of the flexural strength of UHPC, but also the flexural strength will retract obviously with the extension of age. This is because the coral sand is more porous than river sand, which easily leads to stress concentration and micro cracks [22]. With the extension of age,

the continuous expansion of micro-cracks causes more defects and the bending strength of UHPC matrix decreases.

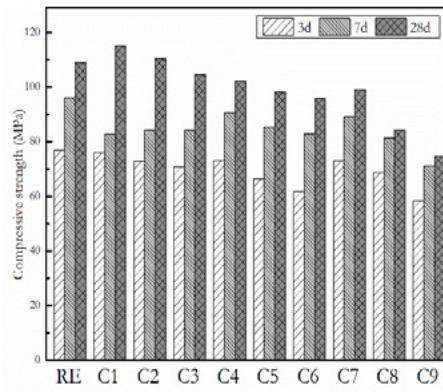


Figure 6 Development of compressive strength of UHPC with different mixture ratios

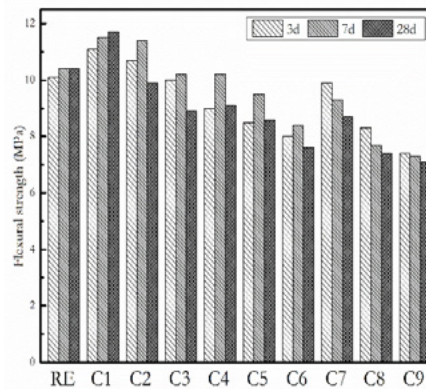


Figure 7 Development of flexural strength of UHPC with different mixture ratios

3.3 Autogenous shrinkage

The development of early autogenous shrinking of UHPC with different mix ratios is shown in Figure 8. The self-shrinking evolution of UHPC could be divided into three stages: rapid growth, callback and stable growth. The contraction of UHPC increased rapidly within 12 h after hardening, and the shrinkage accounts for more than 40% of the total shrinkage deformation at 7 d, which is the most important stage determining the volume stability of UHPC matrix [23].

Compared with the reference group, the total amount of 7 d autogenous shrinking deformation of C1~C9 decreased by -16.1%, 42.2%, 59.1%, 20.3%, 30.2%, 35.5%, 24.4%, 47.2% and 47.9%. The results show that the water-absorbing coral sand has good internal curing effect, and the shrinkage reducing efficiency is proportional to the amount of water introduced. This is because the slow-release effect of moisture from wet coral sand can compensate for the decline of relative humidity in UHPC, delaying the self-desiccation and inhibiting the early self-shrinking development of UHPC matrix.

Compared with the reference group, the autogenous shrinkage of group C1 increased by 16.1%. The water-absorbing coral sand did not reach the state of saturation, and the total amount of introduced water was too low. Hence, the coral sand would continue to absorb water from the system, which aggravated the decrease of relative humidity inside the matrix and caused the contraction to increase. Consequently, the water absorption rate of wet coral sand and the total amount of water introduced have a great influence on its internal curing effect. Too little water will lead to the increase of UHPC autogenous shrinkage. If

excessive water is introduced, the mechanical properties of UHPC will decrease significantly. The optimal mix ratio given in this experiment was C2, the fluidity of UHPC increased by 43.2%, the 28 d compressive strength increased by 1.3%, the 28 d flexural strength decreased by 4.8%, and the total autogenous shrinkage deformation within 7 d decreased by 42.2%.

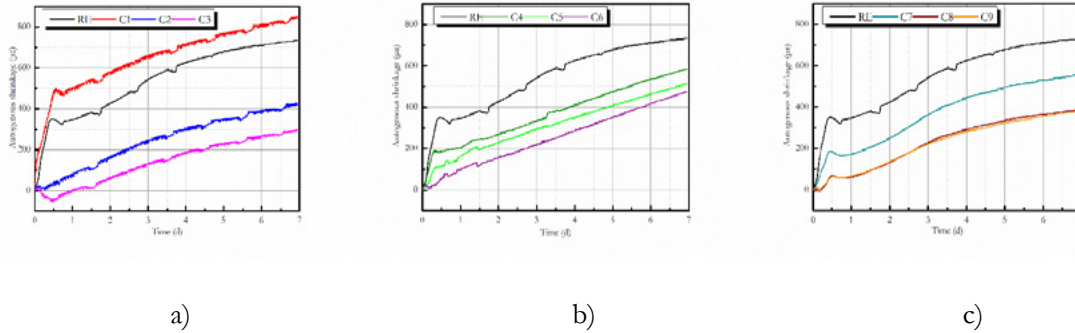


Figure 8 Early autogenous shrinkage development of UHPC with different mixture ratios: a) C1~C3; b) C4~C6; c) C7~C9;

3.4 Pore structure

Due to the porous structure of coral sand particles, it is not accurate to characterize pore structure of UHPC hardened paste mixed with coral sand by means of mercury intrusion porosimetry, which is difficult to eliminate the disturbance of pores of coral sand. Therefore, this paper intends to evaluate the pore structure of UHPC matrix by image analysis on cross-sectional morphology.

Figure 9 shows the image analysis on cross-sectional morphology of representative UHPC specimens after 28 d curing, such as RE, C2, C5 and C8 groups. The pore of micron size is coarse pore, the hole of millimeter size is stomata. The results of pore structure analysis are shown in Table 3. The results show that the porosity of UHPC matrix mixed with water-absorbing coral sand is proportional to the total amount of water introduced. The higher the porosity of coarse pore, the lower the compressive strength of UHPC hardened paste. The higher the porosity of stomata, the lower the fluidity of UHPC fresh slurry. The results of pore structure analysis are completely consistent with the preceding performance of UHPC.

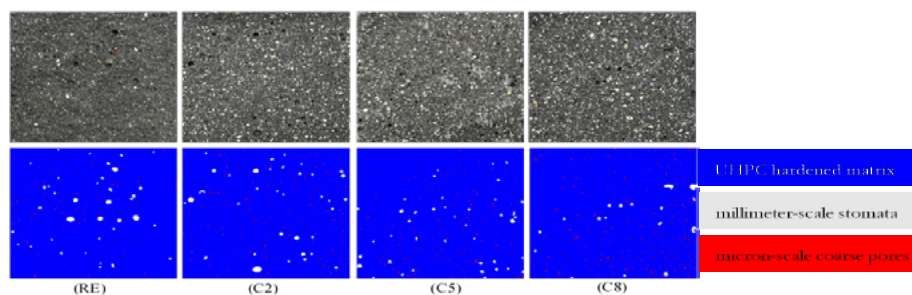


Figure 9 Cross-sectional image analysis of UHPC specimens

Table 3 Cross-sectional pore structure of UHPC specimens (area. %)

Code	RE	C2	C5	C8
Coarse pore	2.178	2.421	2.948	3.751
Stomata	1.247	1.224	1.042	0.732
Total porosity	3.425	3.645	3.990	4.483

3.5 Microstructure

The morphological characteristics of ITZ structure between river sand/coral sand and paste in hardened UHPC after 28 d curing are shown in Figure 10 and Figure 11. Figure 10 photomicrographs display that compared with the ITZ between river sand and paste, the ITZ boundary between coral sand and that paste is not obvious, and the structure is more uniform and dense. Figure 11 images exhibit that micro-cracks around the ITZ region between coral sand and paste are more difficult to initiate and expand under stress conditions compared with that ITZ structure between river sand and paste. It can be summarized that the ITZ structure between fine aggregate and paste is significantly improved and optimized in UHPC mixed with wet coral sand. Main reasons can be concluded as follow: (1) The slow release of water from the wet coral sand can promote the hydration of ITZ reaction layer. (2) The shape of coral sand is irregular (the river sand is spherical), increasing the contact area with paste, and the mechanical meshing force between fine aggregate and paste is strengthened. (3) The moisture released from wet tank promotes secondary hydration of FA and SF, consuming flaky $\text{Ca}(\text{OH})_2$ crystal and inhibiting its directional distribution near ITZ. The optimization of ITZ between fine aggregate and paste also contributes positively to mechanical properties of UHPC.

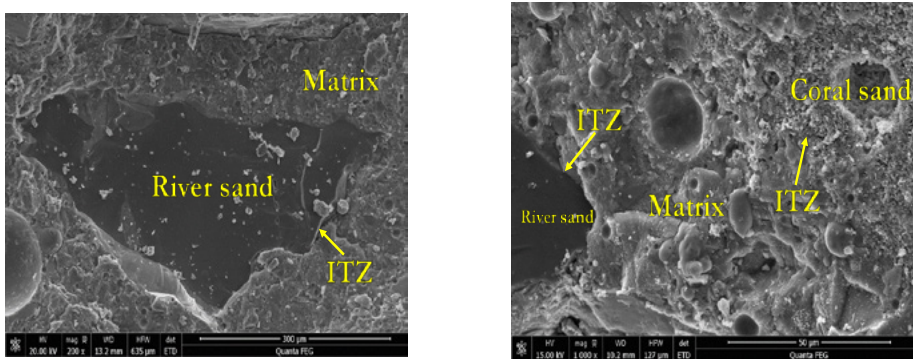


Figure 10 SEM photomicrographs of river sand/coral sand and paste ITZ structure

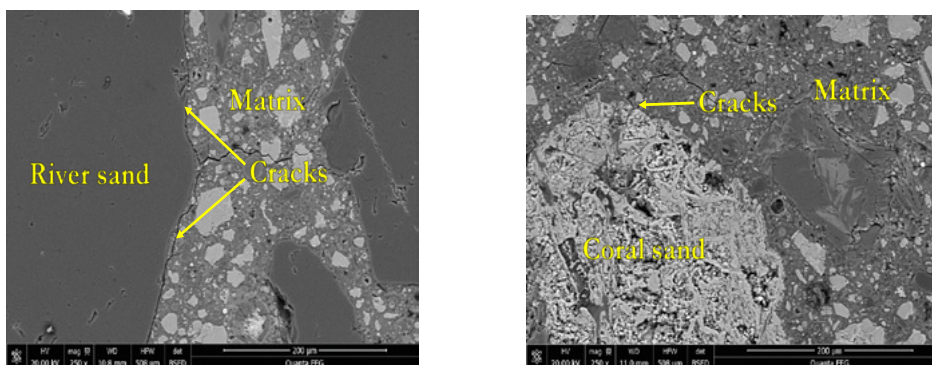


Figure 11 EBSD photomicrographs of river sand/coral sand and paste ITZ structure

4. Conclusions

- (1) UHPC is prepared by mixing with water-absorbing coral sand, the fluidity of fresh slurry is increased and the setting time is prolonged. The fluidity and setting time of UHPC fresh slurry are positively correlated with the total amount of water introduced by wet coral sand as a whole.
- (2) The addition of damp coral sand inhibits the development of mechanical properties of UHPC, especially during the early strength. Coral sand with a low water absorption rate (19.0%, wt. %) replaces river sand at a low level (< 20%, vol. %), there is a significant strength compensation development of

UHPC after 7 days, and the compressive strength at 28 days will exceed that of the reference group. At the same time, the introduction of water-absorbing coral sand will lead to a retraction of the flexural strength of UHPC.

3. (3) Water-absorbing coral sand has significant internal curing effect, and the shrinkage reducing efficiency is proportional to the amount of water introduced in the mass. Under substitution system of unsaturated coral sand with low content (< 10%, vol. %), the early autogenous shrinkage of UHPC will be increased.
4. (4) The optimal conditions for water-absorbing coral sand to be used as internal curing agent for UHPC are: replacing 20% (vol. %) river sand with 19.0% (wt. %) water absorption rate coral sand, the fluidity of UHPC increases by 43.2%, the 28 d compressive strength increases by 1.3%, the 28 d flexural strength decreases by 4.8%, and the autogenous shrinking deformation decreases by 42.2% within 7 d.
5. (5) The introduction of wet coral sand will lead to an increase in the porosity of micron-scale coarse pores in UHPC matrix, and that porosity of millimeter-scale stomata will decrease.
6. (6) The ITZ structure of damp coral sand and matrix is more uniform and dense, and micro-cracks are more difficult to initiate and expand.

5. Acknowledgment

The authors acknowledge the financial supports of National Nature Science Foundation Project of China (51608409), Major science and technology project in Zhongshan city, Guangdong province (2017A1021), Yang Fan plan of Guangdong Province (201312C12), Science and Technology Program of Guangdong Province in 2016 (2016A090924002), Science and Technology Program of Guangdong Province in 2017 (2017B090907009), Late-model Research Institute Development Program of Zhongshan in 2016: Subsidy for Major Research Platform Construction (2016F2FC0008), and open research project of Advanced Engineering Technology Research Institute of Wuhan University of technology in Zhongshan city (WUT201802).

6. References

- [1] Richard P, Cheyrezy M., Composition of reactive powder concretes, *Cem Concr Res*, 1995, 25(7): 1501-1511.
- [2] Shi C, Wu Z, Xiao J, et al., A review on ultra high performance concrete: Part I. Raw materials and mixture design, *Constr Build Mater*, 2015, 101: 741-751.
- [3] Wang D, Shi C, Wu Z, et al., A review on ultra high performance concrete: Part II. Hydration, microstructure and properties, *Constr Build Mater*, 2015, 96: 368-377.
- [4] Yoo D Y.; Yoon Y S., A Review on Structural Behavior, Design, and Application of Ultra-High-Performance Fiber-Reinforced Concrete, *Int J Concr Struct Mater*, 2016, 10(2): 125-142.
- [5] Zhou M.; Lu W.; Song J W. et al., Application of Ultra-High Performance Concrete in bridge engineering, *Constr Build Mater*, 2018, 186: 1256-1267.
- [6] Sun W, Chen H, Luo X, et al., The effect of hybrid fibers and expansive agent on the shrinkage and permeability of high-performance concrete, *Cem Concr Res*, 2001, 31(4): 595-601.
- [7] Corinaldesi V, Nardinocchi A, Donnini J., The influence of expansive agent on the performance of fibre

reinforced cement-based composites, *Constr Build Mater*, 2015, 91: 171-179.

[8] Yoo D Y, Kim S W, Yoon Y S, et al., Benefits of using expansive and shrinkage-reducing agents in UHPC for volume stability, *Mag Concr Res*, 2014, 66(14): 745-750.

[9] Yoo D Y, Banthia N, Yoon Y S., Effectiveness of shrinkage-reducing admixture in reducing autogenous shrinkage stress of ultra-high-performance fiber-reinforced concrete, *Cem Concr Comp*, 2015, 64: 27-36.

[10] Rajabipour F; Sant G.; Weiss J., Interactions between shrinkage reducing admixtures (SRA) and cement paste's pore solution, *Cem Concr Res*, 2008, 38(5): 606-615.

[11] Craeye B, Geirnaert M, Schutter G., Super absorbing polymers as an internal curing agent for mitigation of early-age cracking of high-performance concrete bridge decks, *Constr Build Mater*, 2011, 25(1):1-13.

[12] Soliman A M, Nehdi M L., Effect of partially hydrated cementitious materials and superabsorbent polymer on early-age shrinkage of UHPC, *Constr Build Mater*, 2013, 41(41): 270-275.

[13] Justs J, Wyrzykowski M, Bajare D, et al., Internal curing by superabsorbent polymers in ultra-high performance concrete, *Cem Concr Res*, 2015, 76: 82-90.

[14] Kang S H.; Hong S G.; Moon J., Shrinkage characteristics of heat-treated ultra-high performance concrete and its mitigation using superabsorbent polymer based internal curing method, *Cem Concr Comp*, 2018, 89: 130-138.

[15] Meng W, Khayat K., Effects of saturated lightweight sand content on key characteristics of ultra-high-performance concrete, *Cem Concr Res*, 2017, 101: 46-54.

[16] Meng W, Samaranyake V, Khayat K., Factorial Design and Optimization of Ultra-High-Performance Concrete with Lightweight Sand, *ACI Mater J*, 2018, 115(1):129-138.

[17] Liu J, Ou Z, Mo J, et al., Effectiveness of Saturated Coral Aggregate and Shrinkage Reducing Admixture on the Autogenous Shrinkage of Ultrahigh Performance Concrete, *Adv Mater Sci Eng*, 2017, 2017(4): 1-11.

[18] Wang X, Yu R, Shui Z, et al., Mix design and characteristics evaluation of an eco-friendly Ultra-High Performance Concrete incorporating recycled coral based materials, *J Cleaner Prod*, 2017, 165: 70-80.

[19] ASTM Committee C09, C1761: Standard Specification for Lightweight Aggregate for Internal Curing of Concrete, ASTM, 2013.

[20] Yu R, Spiesz P, Brouwers H J H., Mix design and properties assessment of Ultra- High Performance Fibre Reinforced Concrete (UHPRFC), *Cem Concr Res*, 2014, 56: 29-39.

[21] Liu K, Yu R, Shui Z, et al., Effects of Pumice-Based Porous Material on Hydration Characteristics and Persistent Shrinkage of Ultra-High Performance Concrete (UHPC), *Materials*, 2019;12(1):11.

[22] Cheng S, Shui Z, Yu R, et al., Multiple influences of internal curing and supplementary cementitious materials on the shrinkage and microstructure development of reefs aggregate concrete, *Constr Build Mater*, 2017, 155(30): 522-530.

[23] Liu K, Yu R, Shui Z, et al., Optimization of autogenous shrinkage and microstructure for Ultra-High Performance Concrete (UHPC) based on appropriate application of porous pumice, *Constr Build Mater*, doi: [10.1016/j.conbuildmat.2019.04.089](https://doi.org/10.1016/j.conbuildmat.2019.04.089).

Neutron radiography to study water ingress via the interlayer of 3D printed cementitious materials

J. Van Der Putten ¹, M. Azima ¹, P. Van den Heede ¹, T. Van Mullem ¹, G. De Schutter¹ and K. Van Tittelboom ^{1*}

¹Magnel Laboratory for Concrete Research, Department of Structural Engineering, Faculty of Engineering and Architecture, Ghent University, Tech Lane Ghent Science Park/Campus A, Technologiepark-Zwijnaarde 60, 9052 Ghent, Belgium

*Corresponding author: Kim.VanTittelboom@UGent.be

Abstract

3D printing of cementitious materials is a newly developing technology in which structural elements are built via a layer-by-layer process. Among the many advantages of this technique, it is also expected to lead to more sustainable structures due to a reduced waste generation and more efficient structural design, placing materials only where needed. However, the result of this technique is a layered and anisotropic specimen, creating weak interlayers which will not only endanger the structural behaviour, but also affect the durability as they form a preferential path for the ingress of aggressive substances. For that reason, this research study focuses on the transport of water through printed elements, fabricated with different print velocities (i.e. 1.7 cm/s and 3.0 cm/s) and with special attention for the interlayer interface. Water transport was visualised by means of neutron radiography, performed at the Paul Sherrer institute in Villigen. The effect of an increased print velocity is investigated through qualitative and quantitative analyses of the obtained radiographs. First qualitative results showed that for samples printed with a lower printing speed, the water uptake occurs in a more uniform way compared to specimens printed with a higher velocity. In case of a higher printing speed, the water ingress starts more at the sides and this effect becomes more and more pronounced due to the non-uniform distribution of sand particles through the sample. These results are confirmed by representing the water profile at the interface in a quantitative way. Calculation of the amount of water in a specified zone at the interface shows that, independently from the water distribution, the water uptake after 60 minutes of exposure is higher in case of a low printing speed.

Keywords: 3D printing, cementitious materials, interlayer, water ingress, neutron radiography

1. Introduction

3D printing of cementitious materials enlarges the possibilities in construction, especially in terms of geometrical freedom and flexibility. This newly developing technique not only reduces construction time, it also leads to more sustainable structures due to a reduced waste generation and more efficient structural design. Notwithstanding the many advantages, this technique includes a layer-by-layer deposition of the material, introducing an additional amount of voids. These voids will create a weak interface between two super positioned layers and deteriorate the mechanical performance of the printed element. Due to the absence of moulding, also drying shrinkage will become more pronounced when comparing 3D printing with traditional casting, creating cracks all over the printed specimens. The combination of an increased

amount of voids and cracks will endanger the durability as both result in capillary suction of aggressive liquids from the concrete surface to the interior.

Visual impressions of several existing 3D-printed elements have already disclosed that there is a preferential water uptake via the interlayer [1]. However, further research on the transport properties on the meso- and microscale has not been performed yet and a lot of parameters in this research field are still unknown. Therefore, the current study aims at further developing the correlation between the print process parameters and the transport properties of a printed element. In particular, the effect of an increased printing speed has been investigated and neutron radiography was used to visualise and quantify the capillary sorption behaviour of 3D printed cementitious materials along the interface at different times after water exposure. Prior to neutron radiography testing, basic capillary sorption tests were performed in order to select the maximal exposure time.

2. Methodology

2.1 Materials and mix compositions

Ordinary Portland Cement (CEM I 52.5 N) was combined with standardized sand ($D_{max} = 2 \text{ mm}$) and a water to cement ratio equal to 0.35 was applied. To increase the flowability of the mix composition, a polycarboxylic ether (PCE) with a molecular weight of approximately 4000 g/mol and 35% solids was used as superplasticizer. The exact mix composition can be found in Table 1.

Table 1: Mix composition

Mix component [-]	Amount [kg/m ³]
CEM I 52.5 N	620.5
Sand 0/2	1241.0
Water	226.5
PCE	0.15% [WOC]

The printability of the cementitious material was evaluated based on three different parameters: extrudability, buildability and workability. To classify the mixture as extrudable, it was mandatory that one layer with a total length of 300 mm could be expelled without blocking or segregation and that the deformation after extrusion was limited to 10%. Buildability was obtained when at least 5 layers could be printed on top of each other and a general conclusion about the workability was made by performing VICAT tests in an automated way.

2.2 Sample preparation

An in house developed apparatus was used to simulate the 3D printing process. The extrusion-based system is capable of printing up to 300 mm long specimens at different speeds and different interlayer time intervals between the depositions of two layers. For the purpose of this research, two different printing speeds were applied (1.7 cm/s and 3.0 cm/s, respectively). The height of each layer is manually adjustable and to ensure the same print quality in both cases, layer heights of respectively 15 mm and 20 mm were selected for both printing speeds. The nozzle of the print equipment was elliptical shaped (28 mm x 18 mm), creating layers with an average width of 30 mm. Consequently, a different printing speed and layer height introduce a different flow rate. In case of a low printing speed, the flow rate is equal to 0.028 m³/h, a higher printing speed induces a flow rate of 0.065 m³/h.

Sample preparation consists of filling the equipment and extruding the material through the nozzle with a constant speed. A base layer ($l = 300 \text{ mm}$) was extruded for each specimen and the second layer was

immediately deposited on top of the previous one. Due to the zero minute time gap, both layers were printed from the same batch of material in order to induce layers with the same rheological behaviour. After changing the height of the nozzle, the second layer was printed at the same position to create a similar time gap at every position. After printing, the specimens were stored during 28 days in a standardized environment ($20 \pm 3^\circ\text{C}$, 60% RH) and saw-cut to a thickness of maximum 20 mm (Figure 1). Afterwards, the specimens were placed in an oven. Based on previous research [2], a temperature of 35°C was selected in order to minimize microstructural damage. After two days, the specimens were removed from the oven and sample dimensions were determined. Due to the very irregular shape of the specimens (Figure 1 and Figure 2) and in order to create unidirectional water uptake, lateral surfaces were not sealed by self-adhesive aluminium tape in order to simulate real life printing conditions as much as possible.

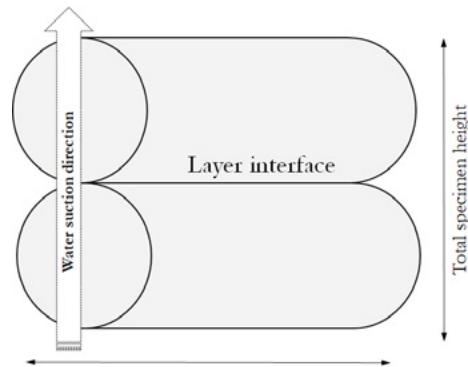


Figure 1: Schematic representation of a printed specimen, saw-cut from an original printed element, used for visualizing the capillary water uptake based on neutron radiography

2.3 Capillary water sorption

Capillary water sorption tests were performed on three cylindrical specimens with a diameter equal to 14 mm. These specimens were drilled out of an original printed specimen, stored in standardized conditions ($20 \pm 3^\circ\text{C}$, 60% RH) until the age of 28 days and dried in a ventilated oven at $35 \pm 5^\circ\text{C}$ for 7 days. A capillary sorption test was performed by placing the cylinders on circular rods in a small water bath, locating the water level at 2 ± 1 mm above the bottom side of the specimens. After wiping them with a towel, capillary sorption was measured by weighing the specimens with a Kern Electronic balance (accuracy 0.01 g) at different times (1, 3, 4, 24 and 72 hours).

2.4 Neutron radiography

Visualisation of the moisture distribution and quantification of the water content was done by using neutron radiography. The measuring principle consists of recording the radiation passing through an object by a position sensitive detector. The beam used for performing these measurements was the neutron beam line at the measuring station NEUTRA. This beam line is situated at the thermal neutron radiographic institute at the Swiss spallation source SINQ of the Paul Scherrer Institute (PSI). Measurements resulted in a radiograph consisting out of an array of grey level intensity values.

Before starting the test, specimens were weighted with a Sartorius BP 3100 S balance (accuracy 0.01 g) and afterwards placed on line supports into a water basin mounted on a support frame (Figure 2). Before the water basins were filled with water, reference images of the samples were taken in dry state. Subsequently, water was added manually 3 min before the actual start of neutron radiography measurements. The samples were approximately 4 mm immersed in the liquid. Subsequent radiographs were made every 20 seconds for a total measurement time of 6 hours. In this way, the water penetration through capillary suction could be followed as a function of time. After the 6 hours test, the wet mass was determined using the same

mass scale and the total amount of absorbed moisture was quantified and compared to the values obtained by post-processing the neutron radiographs. After 24 hours of water suction, the mass of the specimen was measured again and a last neutron radiograph was made to correlate with the other specimens in a qualitative way.

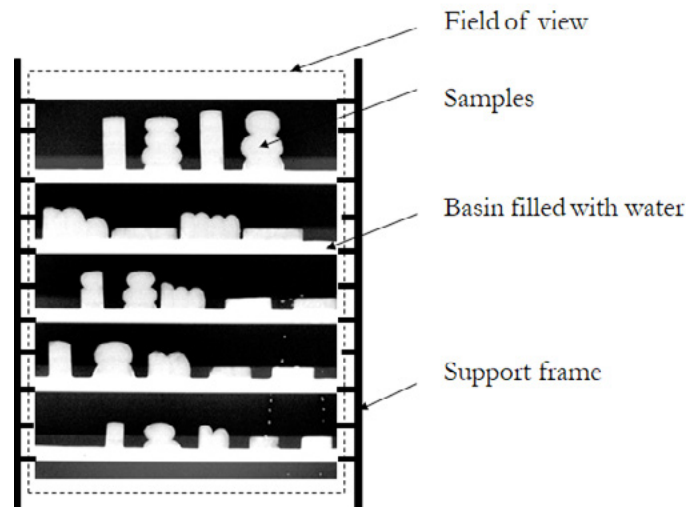


Figure 2: Test setup for neutron radiography testing

Based on previous research [1, 3, 4], a comparison was made by calculating the water content W [kg/m³] at different time steps by comparing the wet and dry radiographs (Eq. [1]).

$$W = -\frac{\rho_w}{\sum_w \cdot d} \cdot \ln\left(\frac{I_w}{I_{dry}}\right) \quad [1]$$

Where ρ_w [kg.m⁻³] is the density of water, \sum_w [m⁻¹] the attenuation coefficient of water (3.64 cm⁻¹), d [m] the thickness of the specimen, I_w [cm⁻².s⁻¹.μA⁻¹] the flux through wet material and I_{dry} [cm⁻².s⁻¹.μA⁻¹] the flux through dry material. More in depth information about the before mentioned parameters can be found in [3, 4].

For qualitative information, each image obtained with neutron radiography needed to be filtered with the image correction tool “Quantitative Neutron Imaging (QNI)”, provided and developed at the PSI institute. The reason for this processing is that the exponential law of attenuation is influenced by several deviations. The images were corrected using the dark current, the open beam (flat field) and the black body radiographs with and without samples. These separate radiographs were made before every new test series. All corrections were based on an average of five radiographs per correction factor, to further optimize the obtained results. After post-processing of these radiographs, all further image operations were performed using ImageJ. Within this software, a distinct water content profile along a rectangular zone (Figure 3) at the interlayer of the printed specimen was calculated using a grey-level profile plot. In case of a low printing speed, the rectangular zone had a width of 12 mm and a height equal to 0.1 mm. In case of a higher printing speed, the width and height of this zone of interest were respectively 15 mm and 0.1 mm. In this way, the water uptake over time could be studied and visualized in detail. The profiles were made and a precise calculation of the water amount in this interlayer zone was done after 5 min, 60 min and 360 min of water exposure.

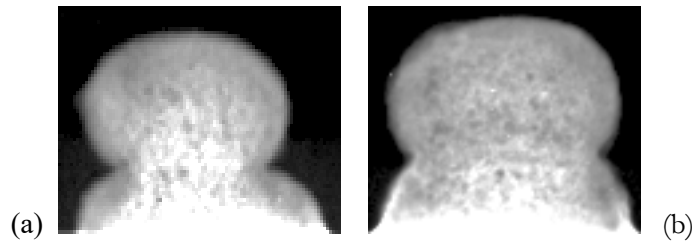


Figure 3: Representation of the rectangular zone used for calculation of the capillary water uptake in case of specimens printed on (a) low speed and (b) high speed.

3. Results and discussion

3.1 Capillary water sorption

Figure 4(a) shows the capillary water sorption capacity of a specimen, fabricated with a low printing speed. Based on this, one can conclude that the highest water uptake occurs within the first 4 hours. For that reason, a water exposure time equal to 6 hours is selected for neutron radiography and the relevance of the selected exposure time is confirmed by measurements with neutron radiography (Figure 4(b)).

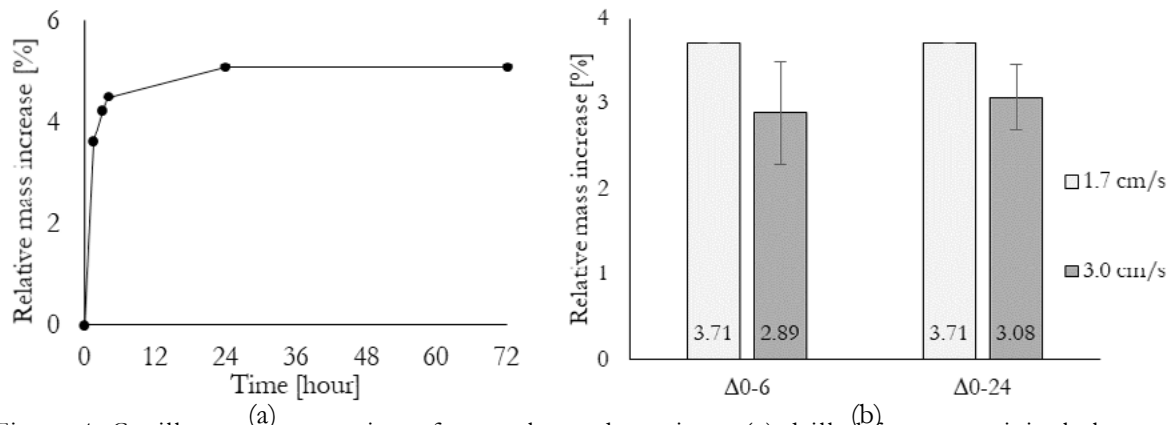


Figure 4: Capillary water sorption of a two layered specimen (a) drilled from an original element and measured in standardized conditions, (b) saw-cut from an original printed element and measured by using neutron radiography (error bars represent standard deviation)

3.2 Neutron radiography

3.2.1 Qualitative analysis

Figure 5 visualizes the capillary water uptake of specimens, fabricated with different print velocities, after different water exposure times. In case of elements fabricated with a low printing speed, the water front (white region) rises in a very consistent way through the material. Immediately after being placed in contact with water (0 minutes), one can see that the water uptake is most pronounced in the central part of the specimen. With an increased exposure time, the water front rises gradually and reaches the interface between the two super positioned layers around 60 minutes. After crossing this weak zone, the water front rises in the same way. After 24 hours, the specimen is almost completely saturated.

Increasing the printing speed of the element introduced a change in water front behaviour. Within the first minutes after exposure, the water amount is higher at the sides compared to the bulk material. This effect becomes more pronounced with an increased exposure time (Figure 5). After 30 minutes, the water front at the sides reaches, but even after 360 minutes the water front in the bulk material did not yet completely cross the interface. After 24 hours, the water front looks similar as the one of the sample printed at low printing speed.

This different water front behaviour can be explained based on previous research [5]. Within this research,

it was observed that a higher printing speed introduces a lower surface roughness. This lower roughness could be explained by a higher kinetic energy working on the sand particles, forcing them deeper into the layer. Consequently, the bulk material of layers printed with a higher velocity will contain a higher sand fraction and be more compacted compared with the interface, limiting the water ingress and creating a non-uniform water front. In case of a low printing speed, the composition of the bulk material and the interface are more or less comparable, resulting in an uniform water ingress over the whole specimen.

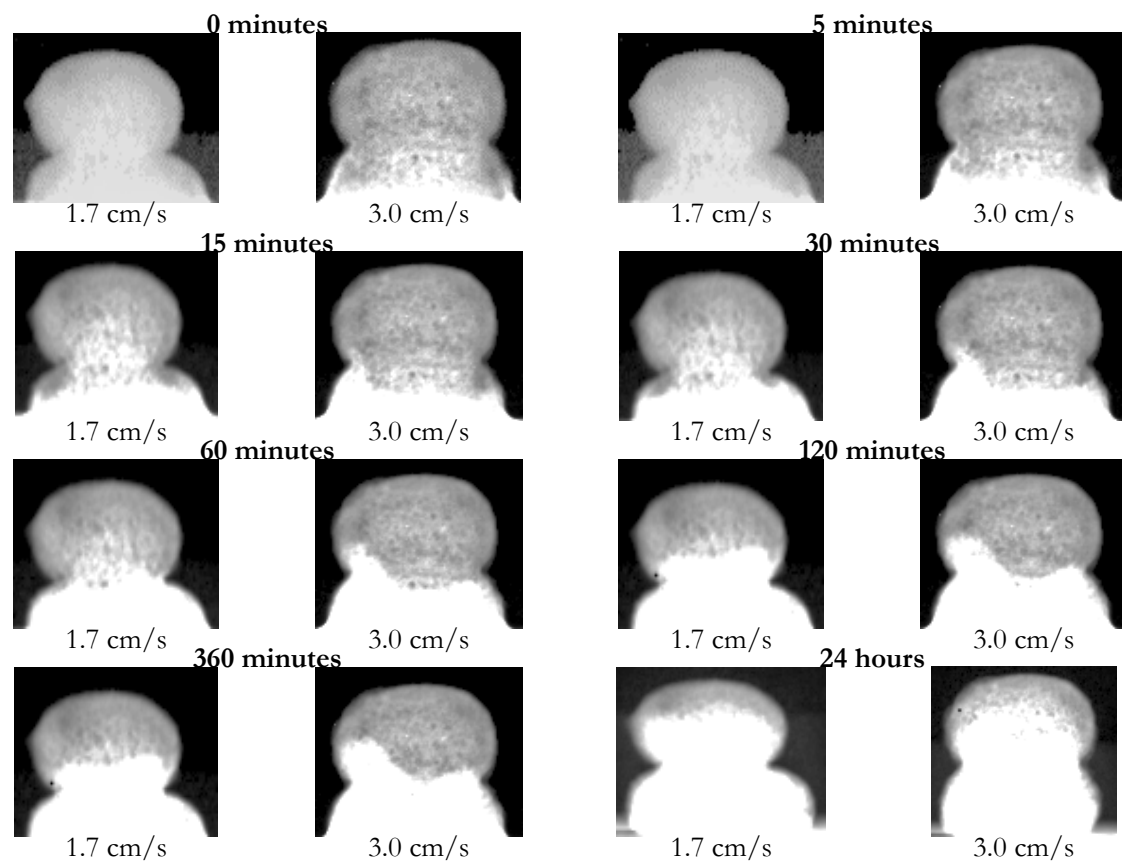


Figure 5: Qualitative comparison of the capillary water uptake capacity at different water exposure times of specimens fabricated with different printing speeds. For each test series, a representative sample is pictured.

3.2.2 Quantitative analysis

Based on Eq. [1], the exact amount of water in a specified region (Figure 3) can be calculated and these results are represented in Table 2. One can conclude that after 5 minutes of water exposure, the amount of water calculated based on the obtained grey levels in ImageJ is almost zero in case of specimens printed with a low velocity.

Comparing the samples after an exposure time of 60 minutes, one can see that the water amount is higher in case of a low printing speed, indicating that a higher amount of water was able to reach the interlayer zone. This phenomenon can be explained by the microstructural change induced by a higher print velocity. As mentioned before, the sand fraction in the bulk material is higher, creating a denser structure in the bulk of the printed specimen, limiting the water uptake capacity, introducing a lower amount of water at the interface. After 360 minutes (6 hours), the water amount in the interface region is higher in case of a higher printing speed.

Figure 6 shows the water amount at the interlayer on different positions in the horizontal direction. These results confirm in a qualitative way the results showed in Figure 5. After 5 minutes of water exposure, the

amount of water in the interface is zero in case of a low printing speed. In case of an increased printing speed, some of the water already reached the interface at the left side of the specimen. With an increased exposure time, one can see that the water amount is more equally distributed in case of a lower printing speed. After 60 minutes, the water amount through the interface region is comparable, while in case of a higher printing speed, the water uptake at the sides of the element is more pronounced. One can also see that in both cases, after 60 minutes of water exposure, the water has not completely reached the interlayer.

Table 2: Calculated amount of water at the interface region after different exposure times

Exposure time [minutes]	Water amount [g/cm ³]	
	1.7 cm/s	3.0 cm/s
5 minutes	0.00001	0.00011
60 minutes	0.00073	0.00041
360 minutes	0.00101	0.00121

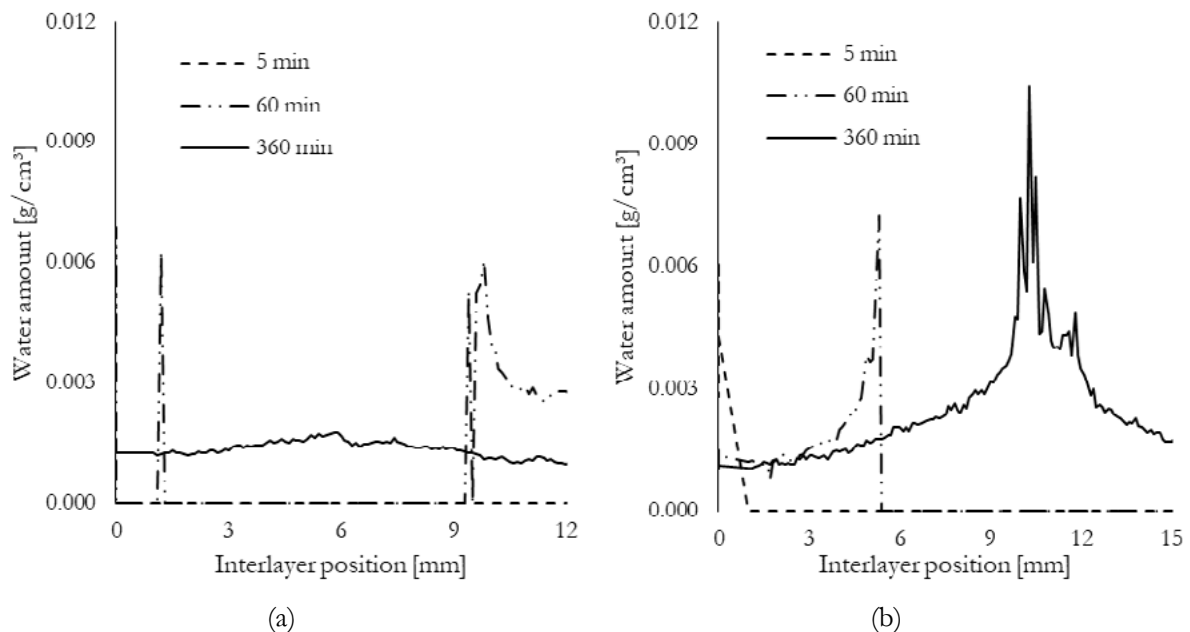


Figure 6: Water absorption at the interlayer at different exposure times for samples printed on (a) 1.7 cm/s and (b) 3.0 cm/s

4. Conclusions

The effect of an increased print velocity on the water uptake of printed specimens was investigated in this research. Visualisation of the moisture distribution and quantification of the water content was done by using neutron radiography and image analysis. From this study, the following conclusions can be drawn:

- Capillary water absorption measurements, performed under standardized circumstances, showed that the highest amount of water is absorbed during the first 4 – 6 hours of exposure. These results were confirmed by measurements performed by neutron radiography and therefore, a total exposure time of 6 hours was selected;
- In case of a low printing speed (1.7 cm/s), the water ingress occurs in a more uniform way compared to specimens fabricated with a higher velocity;

- Increasing the printing speed to 3.0 cm/s will induce a higher amount of water at the sides due to the non-uniform distribution of sand particles through the sample;
- After a water exposure time of 60 minutes, the water front did not reach the predefined interlayer zone completely. This phenomenon could be observed in case of both a low and high printing speed;
- After a water exposure time of 360 minutes, the samples were not completely saturated;
- The water amount at the interlayer is higher in case of an increased printing speed.

5. Acknowledgements

The authors would like to thank the Neutron Image and Activation Group of Paul-Scherrer-Institute (PSI Switzerland), and especially Mr. J. Hovind, for experimental support and useful discussions during operation of neutron radiography. J. Van Der Putten would like to acknowledge the support by EFRO for the C3PO-project (B/15100/01). T. Van Mullem also acknowledges the support of the grant (19SCIP-B103706-05) from the Construction Technology Research Program funded by the Ministry of Land, Infrastructure and Transport of the Korean government and P. Van den Heede is a postdoctoral fellow of Research Foundation-Flanders (FWO) (project No. 3E013917) and acknowledges its supports.

6. References

1. Schröfl, C., V.N. Nerella, and V. Mechtcherine. *Capillary Water Intake by 3D-Printed Concrete Visualised and Quantified by Neutron Radiography*. 2019. Cham: Springer International Publishing.
2. Brew, D.R.M., et al., *Water transport through cement-based barriers—A preliminary study using neutron radiography and tomography*. Nuclear Instruments and Methods in Physics Research Section A: Accelerators, Spectrometers, Detectors and Associated Equipment, 2009. **605**(1): p. 163-166.
3. Van Tittelboom, K., et al., *Use of neutron radiography and tomography to visualize the autonomous crack sealing efficiency in cementitious materials*. Materials and Structures, 2013. **46**(1): p. 105-121.
4. Snoeck, D., et al., *Visualization of water penetration in cementitious materials with superabsorbent polymers by means of neutron radiography*. Cement and Concrete Research, 2012. **42**(8): p. 1113-1121.
5. Van Der Putten, J., et al., *Microstructural characterization of 3D printed cementitious materials*. In preparation, 2019

Influence of heat treatment and mechanical activation on reactivity of natural pozzolan for geopolymer synthesis

R. Firdous¹, D. Stephan^{1*}

¹Technische Universität Berlin, Department of Civil Engineering, Building Materials and Construction Chemistry, Gustav-Meyer-Allee 25, 13355 Berlin, Germany

*Corresponding author E-mail: stephan@tu-berlin.de

Abstract

Natural pozzolans are suitable raw material for geopolymer synthesis as they are a tremendous source of silica and alumina with ease of mining and transportation accompanying lesser cost and lower environmental footprint than for artificial precursors. In this research study, a natural pozzolan formed as a result of meteorite impact has been used for the production of geopolymers. A comparative study has been made between heat treatment and mechanical activation as reactivity alteration methods. The geopolymer samples have been synthesised using raw and altered pozzolans. Several silica moduli of the alkaline solution and curing at ambient conditions were used. Results show that the heat treatment is more suitable as a reactivity alteration method compared to the mechanical activation as indicated by higher compressive strength and accelerated geopolymer reaction. Based on these results, microstructural characteristics have been studied for the geopolymer samples made with raw natural pozzolan and heat-treated pozzolan. Findings indicate that the heat-treated pozzolan has higher reactivity because of partial conversion of calcite to lime. A shift of optimum silica modulus to higher value in order to achieve maximum compressive strength has also been observed. Results of ATR-FTIR show the shift of various bands with the time due to uptake of Al into the structure. On the one hand, broadening of the band corresponding to Al/Si-O-Si indicates disorder introduced by initial geopolymerization. On the other hand, sharpening of this band denotes an increase in order with the age of geopolymer. TGA gives insight about the changes occurred during geopolymerization and shows the formation of C-S-H gel in geopolymer of heat-treated natural pozzolan. Results of XRD and SEM reveal that geopolymer gel is nevertheless mainly a mixture of N-A-S-H and (C)-N-A-S-H phase with the incorporation of Mg, Fe and K as charge-balancing cations.

Keywords: Geopolymer, natural pozzolan, compressive strength, alkaline solution, heat treatment.

1. Introduction

Global warming is the increase in the average atmospheric temperature over long-time, and it is one of the major issues which the world is facing currently. Scientists around the globe are thriving to find ways to reduce the green-house gas emissions. Building industry is one of the major contributors to global warming because of high production and consumption of cement [1]. Hence, there is a need to develop building materials with comparatively low CO₂ emissions for specific applications in order to cut short the use of cement. In this context, geopolymers have gained a lot of interest in recent decades. Comparatively low green-house gas emission, good mechanical and durability properties make them a foreseeable material for specific applications [1–3]. Geopolymers are a class of inorganic binders which possess a polymeric

Si-O-Al framework structure and can be synthesised by reaction of aluminosilicate source material with a concentrated alkaline solution [2, 4, 5]. Several aluminosilicate sources including natural and artificial pozzolans can be used as geopolymer precursor. Studies conducted till to date show that the natural pozzolans of volcanic origin can be used for geopolymer synthesis [6–13]. However, there is limited published data on the usability of other natural pozzolans for geopolymer synthesis which include diatomaceous earths, opaline cherts, shales, pumicites and materials formed by meteorite impact. This research study focusses on the use of natural pozzolan formed as a result of meteorite impact for geopolymer synthesis. The material named as breccia Suevite or Bavarian trass was formed approx. 14.5 million years ago when a meteorite hit the earth in a region later called the Nördlinger Ries, Germany [14].

Studies show that natural pozzolans have lower reactivity in alkaline medium in comparison to artificial pozzolans such as fly ash and metakaolin [8, 15]. Several methods have been applied to improve their reactivity including mechanical activation, heat treatment, partial replacement by secondary cementitious materials and alkali fusion [8, 16–19]. Bondar et al. applied heat treatment by calcinating four different natural pozzolans at different temperatures. Results showed that the calcination can have positive and negative effects on the reactivity of natural pozzolan depending on the mineralogy of the raw sample [18]. Djobo et al. investigated the effect of mechanical activation on Cameroonian volcanic ash and found that mechanical activation helps in improving the reactivity, however, excess milling beyond a certain limit can have adverse effect on the reactivity of volcanic ash [16]. Alkali fusion includes calcination in the presence of alkali hydroxides. Tchakoute et al. applied the alkali fusion technique on Cameroonian volcanic ash using NaOH pellets and burning at 550 °C for 1 h. Geopolymer samples synthesised using this fused volcanic ash and metakaolin showed good mechanical properties, short setting time and low shrinkage [19]. Several materials such as kaolinite, metakaolin, bauxite, calcined oyster shell and slag have been used as partial replacement of natural pozzolan for geopolymer synthesis [17, 20–22]. Results pointed out that the addition of kaolinite give similar compressive strength has no appreciable effect on the improvement of compressive strength [17]. Whereas, replacement by slag and metakaolin improves the properties of resultant geopolymer [21, 22]. The inclusion of bauxite has been found a promising way to reduce efflorescence while the addition of calcined oyster shell helps in reduction of setting time [20].

However, there are limited published studies available on the comparison of different reactivity enhancement methods and their effect on the properties of the geopolymer product. This research study aims to compare two reactivity alteration methods, i.e. heat treatment and mechanical activation and to study their effect on final geopolymer product. Geopolymer samples have been obtained by mixing raw natural pozzolan, heat-treated or mechanical activated natural pozzolan with an alkaline solution. For the purpose, three different silica moduli of alkaline solution have been used. Based on the results of compressive strength and reaction kinetics, one reactivity enhancement method has been chosen to study its effect on the microstructural properties of final geopolymer made with several silica moduli at various ages. TGA, XRD, ATR-FTIR and SEM have been used to study the microstructural characteristics.

2. Materials and methods

2.1 Materials and characterization

2.1.1 Pozzolans

Natural pozzolan from Germany named as Bavarian trass (BT) has been used in this study. Bavarian trass was supplied by Märker Zement GmbH, Germany. Chemical composition was determined by XRF analysis using PW 2400, PHILIPS and is given in Table 1. Bavarian trass (BT) was subjected to heat treatment and mechanical activation. Heat treatment was conducted by calcining the sample at 700 °C for 3 h, followed by cooling to room temperature in a desiccator with silica gel. While, the mechanical activation was performed

by milling in a planetary ball mill (PULVERISETTE 5 classic line, Fritsch GmbH, Germany) at a speed of 200 rpm for 5 min or 10 min with media to material ratio of 1:0.16.

Table 1: Chemical composition of all natural pozzolans.

Sample / wt.%	Total	LOI	SiO ₂	Al ₂ O ₃	Fe ₂ O ₃	MnO	MgO	CaO	Na ₂ O	K ₂ O	TiO ₂	P ₂ O ₅	SO ₃
BT	100.25	11.24	52.35	12.25	4.15	0.09	0.91	13.85	1.67	2.44	0.61	0.22	0.47

The grinding bowl made of hardened steel consisting of 125 ml capacity was filled with 80 g of pozzolan sample. 15 grinding balls made of hardened steel of 20 mm diameter were used for milling. The calcined Bavarian trass has been named as BTC and milled Bavarian trass for 5 and 10 min has been named as BT5 and BT10, respectively. It should be noted here that applying reactivity alteration methods add additional cost to the production of the building material. Therefore, from economical and industrial perspective more practical methodology was adopted. Specific surface area as measured by Blaine fineness according to EN 196-6 [23] was recorded as 6746 cm²/g for BT sample. For BTC as a result of heat treatment specific surface area increased to 7141 cm²/g. While for BT5 and BT10 the specific surface area was recorded as 7018 cm²/g and 11721 cm²/g. Figure 1a presents the particle size distributions of BT, BTC, BT5 and BT10 samples measured using Mastersizer 2000 of Malvern Instruments and Figure 1b shows the d₅₀ particle size for BT, BT5 and BT10 samples. With the applied mechanical activation method, a reduction of 23% and 43% in d₅₀ has occurred for BT5 and BT10, respectively. X-ray diffraction analysis was performed on BT, BTC, BT5 and BT10 using the method as described in section 2.2. Figure 2 presents the X-ray diffractograms of all pozzolans with the mineralogical phases. The mineralogical phases were determined in accordance with the literature [24–29]. In addition to mentioned crystalline phases, BT sample also contain a glass phase. Due to heat treatment, some amount of calcite has been found to decompose (calcite peaks reduced in height) and formation of lime has been observed in XRD in BTC sample (as shown in Figure 2). Partially crystalline phases present in BT which may correspond to the presence of clay and zeolite minerals also decomposed as a result of heat treatment. XRD detects entirely no differences between BT, BT5 and BT10.

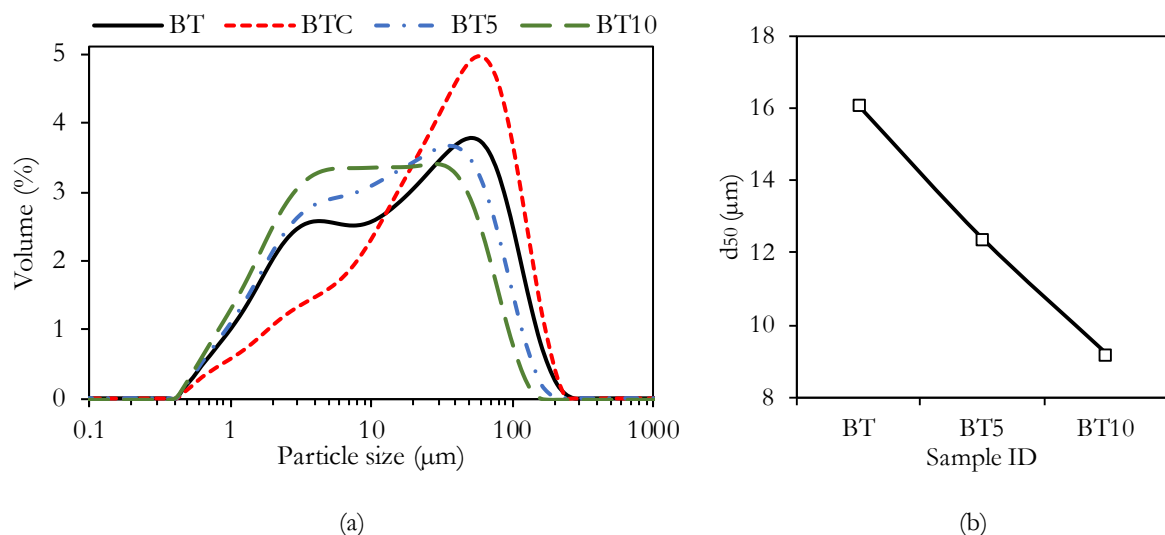


Figure 1: (a) Particle size distribution for BT, BTC, BT5 and BT10 samples, (b) d₅₀ for BT, BT5 and BT10 samples.

2.1.2 Alkaline activator

Alkaline activator consisting of combinations of sodium hydroxide (NaOH) and sodium silicate solutions (Na₂SiO₃) were used. NaOH of 99 wt.% purity was obtained from VWR International GmbH in pellets.

NaOH solutions were prepared by dissolving NaOH pellets in deionized water at least 24 h before use. Sodium silicate solution (Betol 52T) was obtained from Woellner GmbH with silica modulus of 2.12. The NaOH solution and Na₂SiO₃ solution were mixed in different fractions to obtain the alkaline solutions of desired silica modulus. Three silica moduli of alkaline solution of 0.707 (H₂O/Na₂O molar ratio = 9.7), 0.797 (H₂O/Na₂O molar ratio = 11.4) and 1.061 (H₂O/Na₂O molar ratio = 10.5) were used for BT and BTC geopolymers, while silica modulus of 0.707 was used for BT5 and BT10 geopolymer samples.

2.2 Experimental methodology

The geopolymer paste samples were prepared using a laboratory hand mixer with a mixing time of 3 min. In-between break of 30 s was taken after mixing the sample for 90 s to collect all the sample in the centre of the bowl for homogeneous mixing. After complete mixing, the paste was poured in 20 mm cubic molds and was compacted using vibration table for 2 min. Samples were sealed using plastic foil from all sides and were cured at 21 ± 1 °C and 100% relative humidity till test age. Alkaline solution to solid ratio was kept equal to 0.75 for all geopolymer samples to achieve good workability.

The compressive strength of cubic samples was determined at 7, 28, 90 and 180 d age. Pieces of broken samples were collected at 7, 28 and 90 d age and geopolymer reaction was stopped for examination by TGA, XRD, ATR-FTIR and SEM-EDX. The reaction was stopped by solvent exchange using isopropanol. Samples were submerged in isopropanol for 24 h followed freeze-drying for 7 d. Afterwards, samples were ground by hand in mortar and pestle to a size <125 µm. In the case of storing, the samples were stored in a desiccator with sodium hydroxide (on support) obtained from Merck, KGaA, Germany to avoid environmental carbonation.

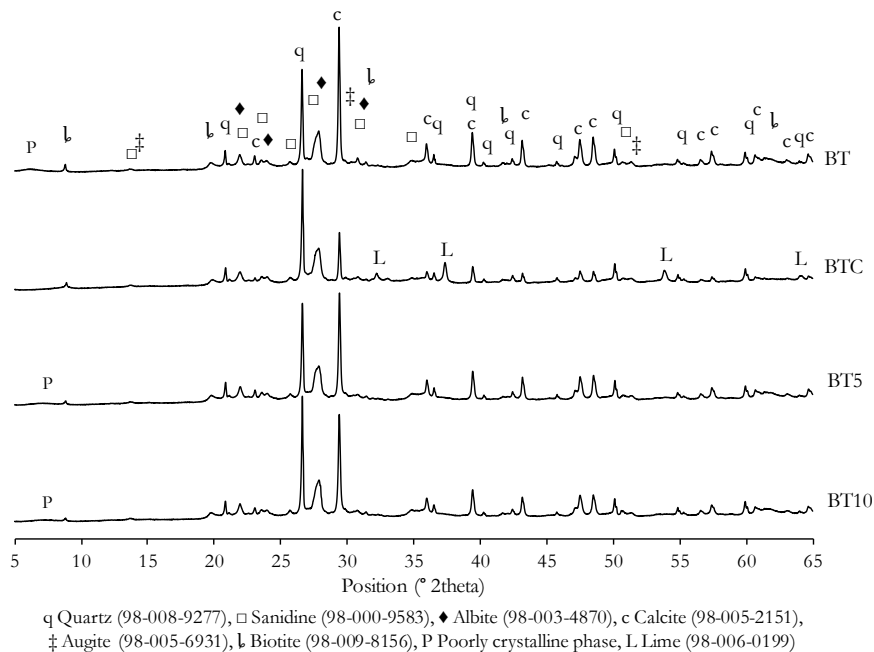


Figure 2: X-ray diffractograms of BT, BTC, BT5 and BT10 samples.

Isothermal conduction calorimetry was performed to understand the reaction kinetics and to study the effect of heat treatment and grinding on the reactivity of natural pozzolan. For the calorimetric study, device MC-CAL 100P, C3 Prozess- und Analysetechnik GmbH, Germany was used. Samples were mixed outside the device for 45 s each with vortexer. Therefore, zero in the calorimetric curves is the point when samples were placed inside the device.

Thermogravimetric analysis (TGA) was performed using TG 209, Tarsus F3, Netzsch Instruments under a nitrogen atmosphere at a flow rate of 250 mL/min. For each test, 10 ± 1 mg of sample was used. The sample was first held at 25 °C for 20 min, and then heated from 25 °C to 850 °C at a heating rate of 10 °C/min.

Fourier transform infrared spectroscopy (FTIR) was performed on raw natural pozzolan and respective geopolymer samples using Spectrum Two of PerkinElmer fitted with diamond crystal via the attenuated total reflection (ATR) method. IR spectra were obtained between 4000 to 400 cm^{-1} with a resolution of 1 cm^{-1} .

X-ray diffraction analysis (XRD) was performed using an Empyrean PANalytical diffractometer with Ni filter and $\text{CuK}\alpha$ radiation ($k = 1.540598 \text{ \AA}$), operating at 40 kV and 40 mA in continuous mode with a resolution of 0.0131° and speed of $0.0176^\circ/\text{s}$ for a range of 5° to 65° for 1 h. The phase evaluation was performed using HighScore Plus software with ICDD and ICSD.

Polished freeze-dried samples were impregnated in epoxy resin to study the microstructure and elemental distribution. For the purpose, scanning electron microscopy fitted with energy-dispersive X-ray spectrometer (SEM-EDX) was performed using device GeminiSEM500, ZEISS operated at 15 kV.

Throughout the manuscript, the geopolymer samples made with BT, BTC, BT5 and BT10 are labelled with the respective raw sample, silica modulus used to prepare each geopolymer and the age of the sample.

3. Results and discussion

3.1 Effect of heat treatment on compressive strength

Figure 3 presents the compressive strength development of BT and BTC geopolymer samples. Results indicate that heat treatment of BT improved the reactivity as found by an increase of compressive strength in BTC geopolymer samples. An increase of 32% and 45% in compressive strength has been observed at 90 d age for samples BTC-0.797 and BTC-1.061, in comparison to corresponding BT samples. While for sample BTC-0.707, 7- and 28-d compressive strength was improved and thereafter, no significant improvement in compressive strength has been observed. Considering the BT geopolymer, the optimum silica modulus to achieve highest compressive strength was recorded as 0.707, while for BTC geopolymers it is found as 0.797. Thus, the optimum silica modulus shifted to higher silica modulus for BTC geopolymers in comparison to BT geopolymers. This confirms the improvement in reactivity of this natural pozzolan and a reduction in the alkali concentration of the solution used, which is beneficial from both economic and environmental perspective.

Table 2 presents the visual observation of BT and BTC samples prepared with various silica moduli at 90 d. The pictures presented in Table 2 show that for sample BTC-0.707, efflorescence formation increased in comparison to sample BT-0.707. While for sample BTC-0.797 and BTC-1.061, the formation of efflorescence decreased in comparison to samples BT-0.797 and BT-1.061. The formation of efflorescence is because of an excess of free alkalis in geopolymer matrix which react with carbon dioxide from the environment and produce sodium carbonate which precipitates at the surface or in pores of geopolymer matrix.

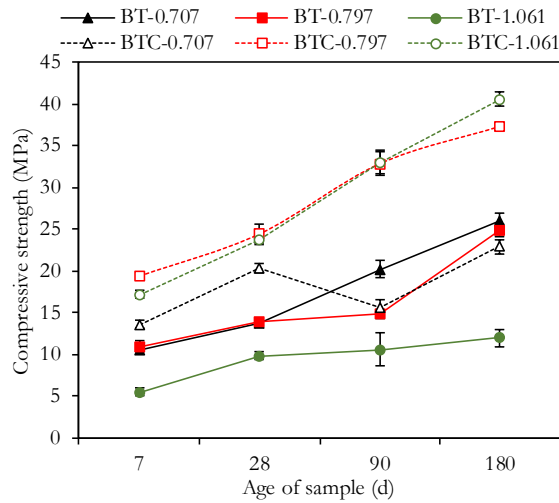








Figure 3: Compressive strength of BT and BTC geopolymers at different ages.

Table 2: Visual observation of BT and BTC sample at 90 d age.

Silica modulus	0.707	0.797	1.061
BT			
BTC			

3.2 Effect of mechanical activation on compressive strength

The effect of mechanical activation as the reactivity alteration process has also been studied by compressive strength and the results are presented in Figure 4.

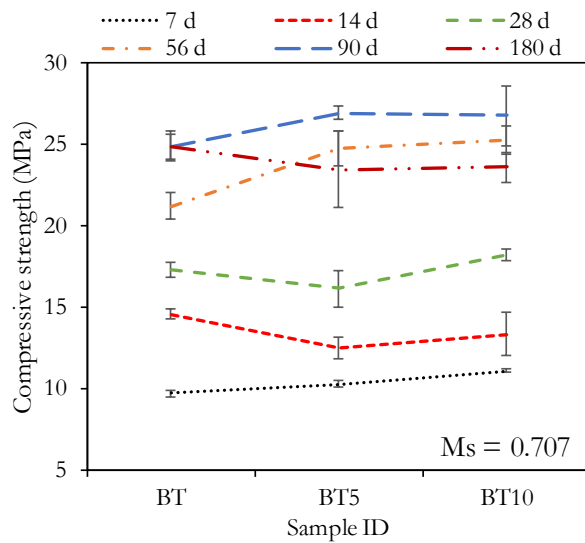


Figure 4: Effect of mechanical activation on the compressive strength of BT sample.

A slight improvement in strength with grinding has been found. However, no significant improvement in strength has been observed at all ages of the sample, and the values are mostly within the range of standard deviation.

3.3 Effect of heat treatment on reaction kinetics

Figure 5 presents the calorimetric curves for BTC compared to BT samples. Results show that geopolymer reaction for BT geopolymer samples is characterised by two exothermic peaks. The initial peak occurs when natural pozzolan and alkaline solution come in contact and is therefore attributed to wetting and dissolution of reactive phases. This peak is followed by deceleration which is associated with polycondensation thus the amount of heat released decreases. Thereafter, a second exothermic peak has been observed which is assigned to a delayed dissolution of some phases. Delayed dissolution of calcium-rich phases leading to a second exothermic peak was observed by Gebregziabihier et al. [30]. The formation of early product in alkali-activated system depletes the alkalis and the relative silica concentration increases, which in turn retards the dissolution of calcium phases [30]. For samples BT-0.707, BT-0.797 and BT-1.061, second exothermic peak was observed at 11 h, 12.6 h and 28.3 h with a maximum at approx. 12.5 h, 14.5 h and 34.7 h, respectively.

Comparing BT and BTC geopolymer samples, the rate of reaction increased for all calcinated samples in comparison to BT samples indicated by higher heat evolved over 168 h, higher heat flow in first hours and shift of second exothermic peak to an earlier time or complete disappearance. For sample BTC-0.797 and BTC-1.061 this peak was not observed at all. For BTC-0.707 sample, this peak moved to approx. 8 h and appears only as a slight hump (Figure 5). These findings are in accordance with the results of compressive strength, as for sample BTC-0.707 compressive strength is also lower than for sample BTC-0.797 and BTC-1.061 which can be described by the delayed dissolution and therefore, lack in a gain of compressive strength. Comparing BTC-0.707, BTC-0.797 and BTC-1.061 to each other, the rate of dissolution increases with the decrease of silica modulus.

The improvement of pozzolanic reactivity as a result of calcination for this natural pozzolan has also been reported by [25], however the authors found that a possible reason of such improvement was presence of smectite minerals. In the current research, this mineral group has not been identified. Therefore, the reason for such improvement in reactivity as a result of the heat treatment is most likely the conversion of calcite to lime which imparts higher reactivity [31]. This is because the reaction of lime with water leads to a rise in the pH of the system which enhances the dissolution of aluminosilicate species [32]. Thus, the rate of reaction increases and 2nd exothermic peak shifts to earlier times. Henceforth, the increase in dissolution rate results in a higher amount of precipitated geopolymer gel associated with an increase of compressive strength in most cases (Figure 3) and heat evolved over 168 h (Figure 5) of calcinated samples in comparison to BT samples. This finding also enables to explain the alteration of efflorescence development depicted in Table 2. The samples with silica moduli 0.797 and 1.061 precipitate enough geopolymer gel to incorporate most of the alkalis of activator solution. Therefore, lower efflorescence product is formed. On the other hand, the alkaline concentration in sample BTC-0.707 is too high and most of it has not been incorporated in geopolymer gel and thus it leads to formation of higher amount of efflorescence (as seen in Table 2).

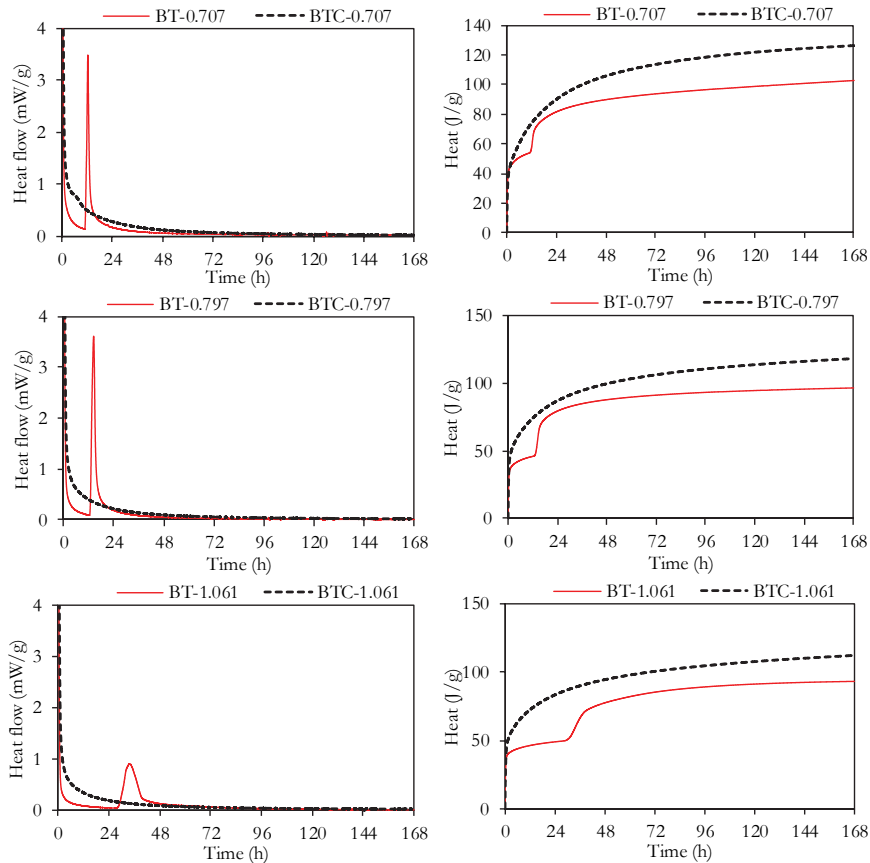


Figure 5: Heat evolution curves for BT and BTC geopolymers.

3.4 Effect of mechanical activation on reaction kinetics

To study the influence of mechanical activation on reaction kinetics, isothermal conduction calorimetry was conducted. Firstly, BT, BT5 and BT10 raw samples were separated in two fractions by a 40 μm sieve, afterwards, calorimetry was conducted on these separated fractions. The fractions of material were separated to understand the effectiveness of mechanical activation on the fine and coarse fractions of the sample, such that the first hump of bimodal particle size distribution was separated (Figure 1). Geopolymer samples were prepared with silica modulus of 0.707 for each fineness and are labelled as BT-0.707, BT5-0.707 and BT10-0.707. The results of the calorimetric study are presented in Figure 6 for both fractions of samples.

Results indicate that the fraction $<40 \mu\text{m}$ exhibits higher reactivity than fraction $>40 \mu\text{m}$. Mechanical activation in the ball mill is more effective in reducing the size of larger particles. The calorimetry curves of BT samples show that the part of sample $<40 \mu\text{m}$ develops approx. twice as much hydration heat after 168 h as that $>40 \mu\text{m}$. Total heat slightly increases with increasing fineness of sample (from BT over BT5 to BT10) for fraction $<40 \mu\text{m}$. While for the fraction $>40 \mu\text{m}$, total heat released stays nearly unchanged from BT to BT5 but increases significantly for BT10-0.707.

It is important to note here that the second exothermic peak occurs only for fraction $<40 \mu\text{m}$ for sample BT-0.707 and BT5-0.707. While for sample BT10-0.707, it occurs for both fractions. By increasing the overall fineness of sample (from BT over BT5 to BT10), this reaction triggers to earlier time and heat flow value decreases but time span over which reaction occurs is increased. These observations indicate that with the increase in fineness the reaction degree is increasing at a lower rate; therefore, only a slight improvement in compressive strength has been observed. However, to see a significant impact of mechanical activation,

sample may be milled for a longer time, but care must be taken while choosing a reactivity alteration method and its economic advantages.

XRD analysis was performed on the separated fractions of BT, BT5 and BT10 as shown in Figure 7 to understand calorimetric analysis. The results show that the fractions <40 μm have excess amount of calcite while the fractions >40 μm are enriched in minerals such as quartz, sanidine and albite which have higher Mohs scale hardness. Further the fraction BT <40 μm has highest amount of calcite while as a result of milling the calcite content is slightly decreasing in BT5 <40 μm and BT10 <40 μm. Therefore, as a result in calorimetric analysis the height of 2nd exothermic peak is decreasing with increasing milling time.

With increasing milling time, the calcite content in fraction >40 μm is consequently increasing. This is because of possible agglomeration of soft and small calcite particles during milling. In BT10 geopolymers samples both fractions exhibit the 2nd exothermic peak. This can be because of sufficiently high content of calcite in both fractions. The agglomeration leads also in coarse fraction to a sufficient amount of calcite content to develop the 2nd peak. While the hard minerals are not much effected by grinding and therefore, doesn't exhibit any appreciable differences in their reactivity.

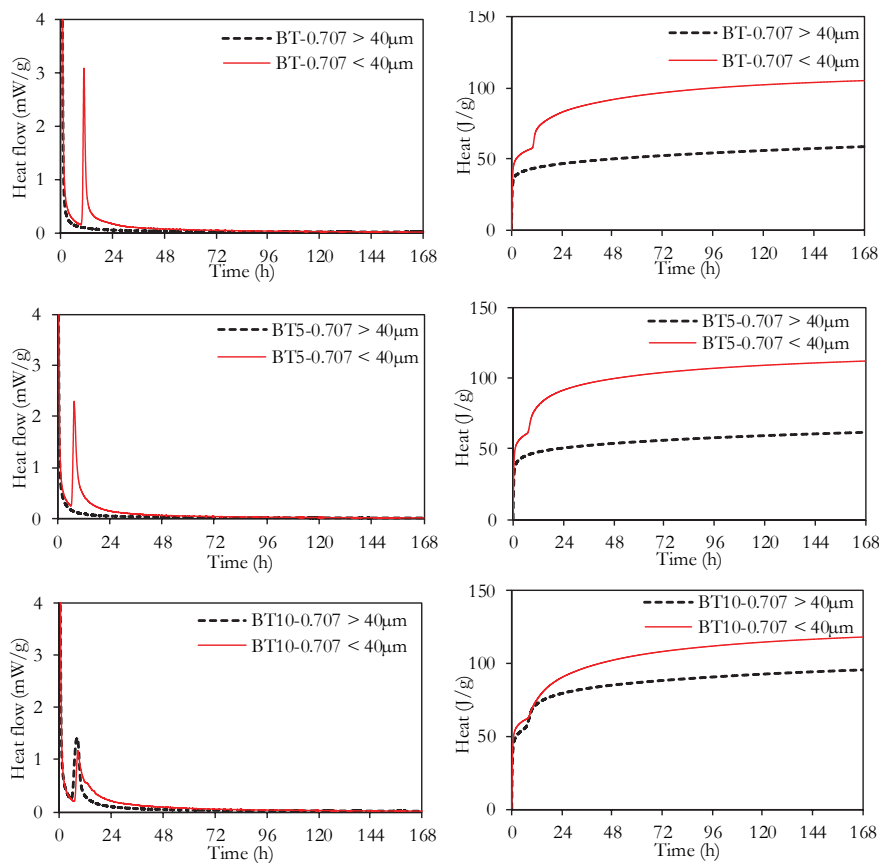


Figure 6: Heat evolution curves for BT, BT5 and BT10 geopolymers.

Comparing both reactivity alteration methods, the effect of heat treatment is more prominent than reduced particle size. Looking at Figure 1, BTC sample has a higher fraction of coarser particles in comparison to BT5 and BT10 samples. But the inclusion of more reactive phases such as lime imparts higher reactivity than reduced size of particles. Based on these results, heat treatment has a higher influence on the reactivity of BT. Therefore, further detailed microstructural analysis has been made only on BT- and BTC-based geopolymers in following sections.

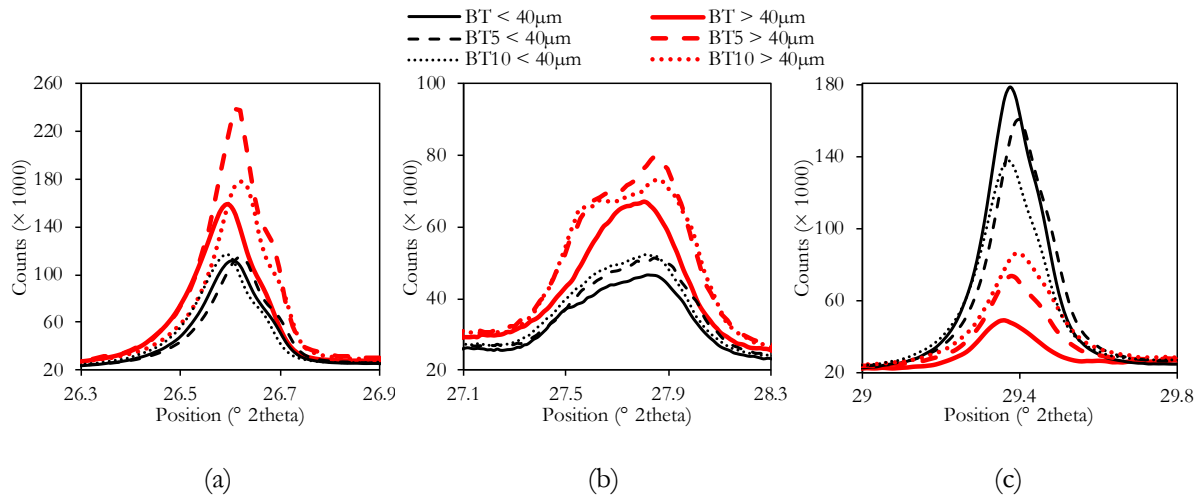


Figure 7: Diffractograms of BT, BT5 and BT10 fractions below and above 40 µm showing reflexes for (a) quartz (b) sanidine and albite (c) calcite.

4. Microstructural characteristics

4.1 Thermogravimetric analysis (TGA)

Thermogravimetric analysis was performed on BT and BTC geopolymers samples at the age of 7, 28 and 90 d. Results for the sample prepared with silica modulus of 0.797 for both pozzolans are presented in

Figure 8.

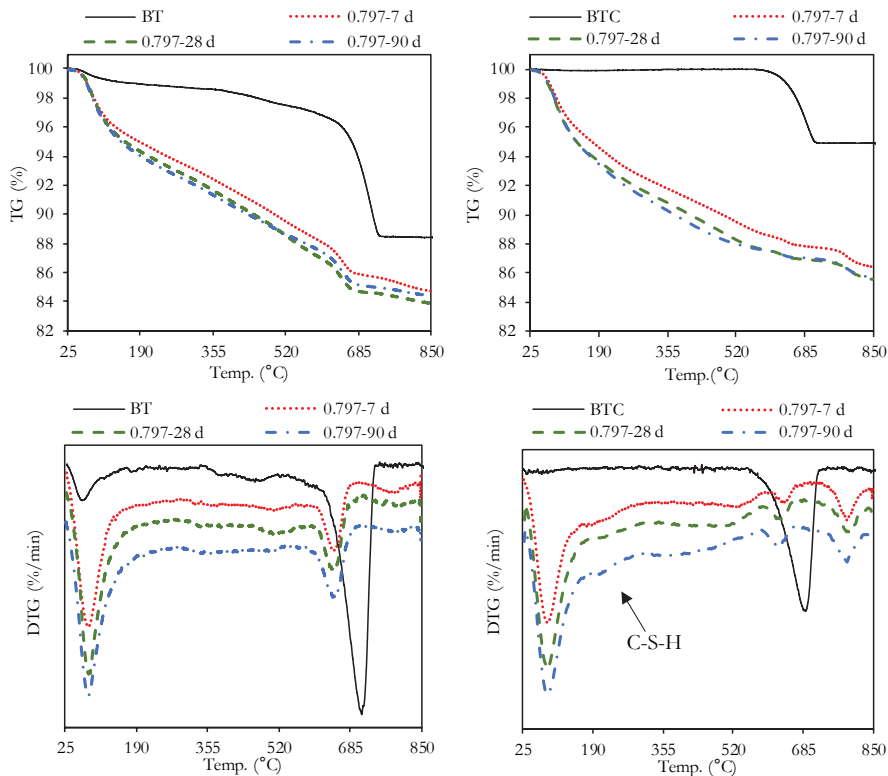


Figure 8: TG and DTG curves of BT and BTC samples at 7, 28 and 90 d age.

The overall mass loss for BT and BTC geopolymers prepared with silica modulus of 0.797 is higher at all ages than in raw pozzolans. Similar behaviour has been also observed for BT and BTC geopolymer samples prepared with silica modulus of 0.707 and 1.061 which are not shown here. The overall mass loss seems to increase with the age of sample slightly. This increase in the mass loss is attributed to geopolymerization

reaction. Mass loss till approx. 150 °C is considered as the liberation of loosely bound water. Mass loss from 150 – 600 °C is attributed to liberation of stronger chemically bound water. As a result of geopolymerization, bound water is introduced in the system as a part of geopolymer gel which is formed due to dissolution and subsequent precipitation of aluminate and silicate species. This mass loss in the range of 30 – 600 °C can be correlated to the amount of reaction product formed [33]. Results presented in Table 3 show that dehydration in the temperature range of 30 – 600 °C is affected by the change of silica modulus of alkaline solution used and the age of the sample. For samples BTC-0.797 and BTC-1.061, the mass loss in mentioned temperature range increases with age while for all others it initially increases from 7 to 28 d and then decreases till 90 d. Such a reduction in water content with the age can be caused by efflorescence formation in these samples with age [34]. The last stage in TG refers to decarbonization (600 – 850 °C) and shows that the carbonate content of samples is reduced as a result of geopolymerization [35, 36].

Table 3: Mass losses in the temperature range of 30 – 600 °C for BT and BTC geopolymer samples at various ages.

Age of sample	Mass loss (wt.%)					
	BT-0.707	BT-0.797	BT-1.061	BTC-0.707	BTC-0.797	BTC-1.061
7 d	11.87	11.88	10.76	11.44	11.40	10.38
28 d	13.25	12.98	12.38	11.74	12.40	10.98
90 d	13.00	12.48	12.17	11.43	12.77	11.40

The effects mentioned above are observed in both BT and BTC geopolymers. Additionally, for BTC geopolymers, two other peaks in DTG have also been found, i.e. a diffuse peak in the temperature range of 160 – 300 °C with its centre at approx. 200 °C and a sharp peak above 790 °C with a maximum at approx. 795 °C. The first peak is attributed to dehydration of C-S-H gel which has been observed to form in case of availability of reactive calcium [35, 36]. This peak has been observed in all BTC geopolymer samples but in none of the BT geopolymer samples. This shows that as a result of calcination, calcite converts to lime which imparts more reactive calcium. After that, the second peak observed only in BTC geopolymer samples is attributed to the decomposition of C-S-H to wollastonite; such decomposition has been also observed in the literature and was also confirmed here by conducting XRD on the decomposed residue [36, 37].

4.2 X-ray diffraction analysis (XRD)

Figures 9 and 10 show the XRD diffractograms of BT and BTC geopolymers at the age of 7, 28 and 90 d prepared with silica modulus of 0.797, respectively. XRD analysis was made on all samples, but for easy understanding selected samples have been shown here.

In raw BT and BT geopolymer samples, two amorphous humps were recorded ranging approx. 5° – 8° and 24° – 34°. While in raw BTC and BTC geopolymer samples only the second hump mentioned above has been recorded. The first hump in raw BT and BT-based geopolymers was not identifiable, but it may correspond to the presence of clay or zeolite minerals. As a result of geopolymerization the shape of this amorphous hump changed indicated by the shift of the centre of the hump. This may be due to the formation of aluminosilicate gel phase.

In both raw pozzolans, the centre of the second amorphous hump was recorded at 27°. While in both pozzolan-based geopolymer samples the centre of the second amorphous hump shifted to higher 2 theta values i.e. 31°. Such a shift has been described to occur due to the formation of geopolymeric gel [38–40]. Further, in BT geopolymer sample made with silica modulus of 0.707 at 7 d and in BTC geopolymer samples made with silica modulus of 1.061 at 28 d a new reflex has been observed to form at approx. 27°. This reflex has not been observed in all other samples. It is attributed to the formation of aragonite (98-028-0991) which is a polymorph of calcium carbonate and may form under high alkaline conditions [41, 42]. However, the lower stability of this phase is the reason that it has been not observed in other samples.

As seen earlier, efflorescence formation was observed for BT and BTC geopolymer samples. XRD results reveal that efflorescence is caused by precipitation of natrite ($\gamma\text{-Na}_2\text{CO}_3$, 98-009-5549). This is formed because of the reaction of excess free alkalis in the geopolymer system with environmental carbon dioxide. Looking at Figures 9 and 10, the participation of calcite and lime in geopolymer reaction can be clearly observed as indicated by the reduction of reflex height of calcite while reflexes of lime are completely absent in geopolymer samples.

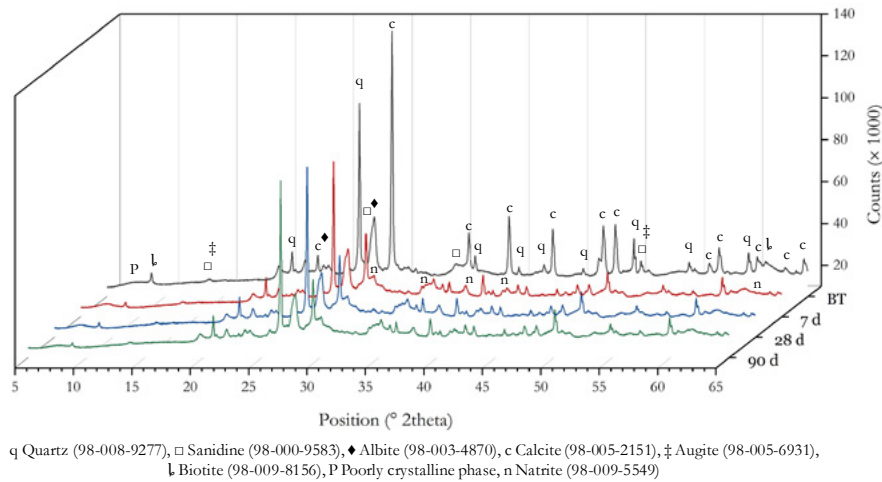


Figure 9: Comparison of raw BT and BT geopolymer sample at the age of 7, 28 and 90 d for geopolymer sample prepared with silica modulus of 0.797.

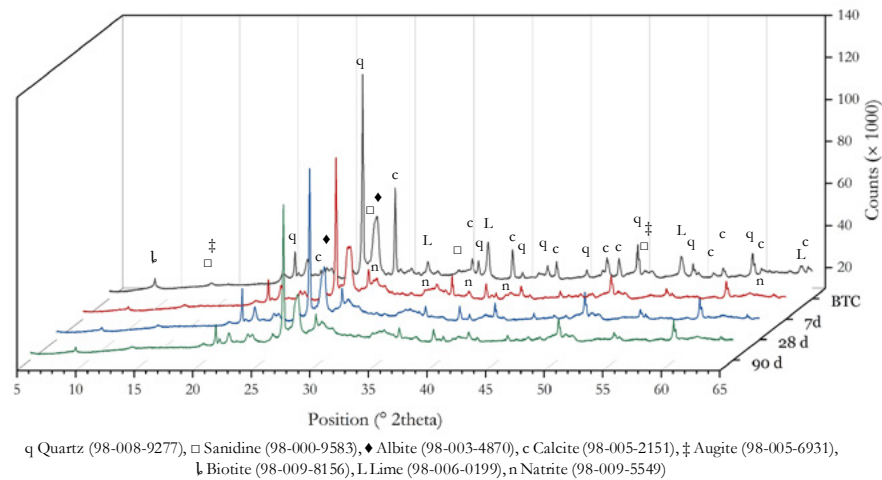


Figure 10: Comparison of raw BTC and BTC geopolymer sample at the age of 7, 28 and 90 d for geopolymer sample prepared with silica modulus of 0.797.

This confirms the previous finding that lime imparts higher reactivity than calcite as indicated by its complete participation in geopolymer reaction. Other crystalline phases may be participating in geopolymer reaction include biotite and sanidine, as indicated by slight changes in the reflexes for these minerals.

4.3 Fourier transform infrared spectroscopy (FTIR)

ATR-FTIR spectra were collected for the BT and BTC raw samples and their respective geopolymer samples at 7, 28 and 90 d ages. Results have been presented in Figure 11. FTIR analysis was made on all geopolymer samples and they showed comparable characteristics; therefore, for the easy understanding sample prepared with silica modulus of 0.707 has been shown here. The major characteristic peaks have been observed in region 1600 to 400 cm^{-1} . In region 4000 to 1600 cm^{-1} only one broad hump around 3100

cm⁻¹ has been observed which indicates the OH stretching vibration.

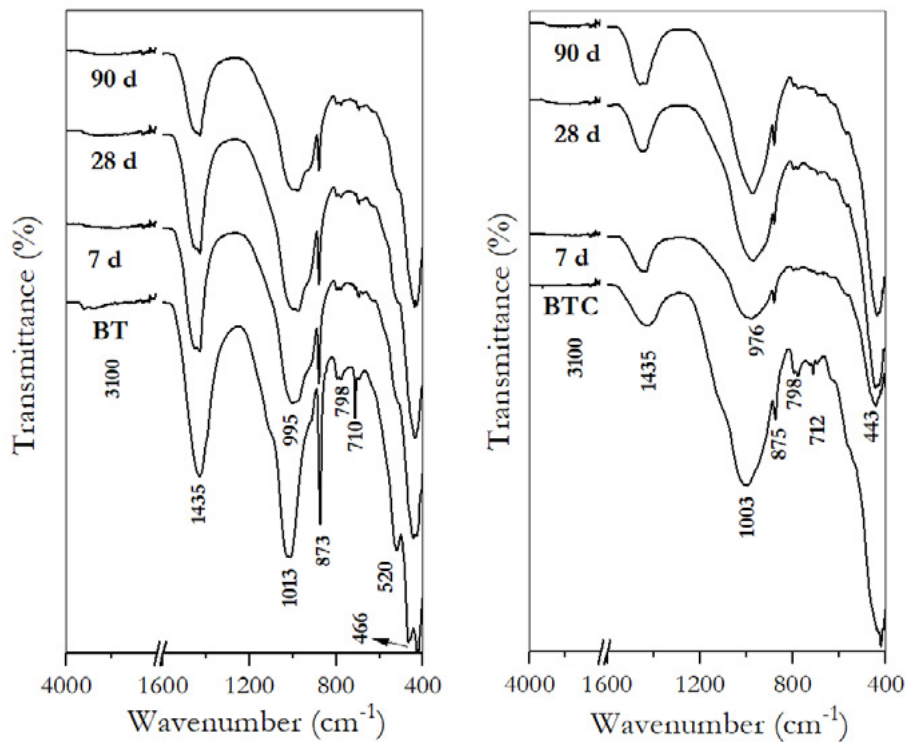


Figure 11: ATR-FTIR spectra of raw BT and BTC samples and BT and BTC geopolymer samples prepared with silica modulus of 0.707 at 7, 28 and 90 d age.

An intense band in raw BT and raw BTC samples at 1013 and 1003 cm⁻¹, respectively, attributed to asymmetric stretching of Al/Si-O-Si has been found to move to lower wavenumber i.e. 995 and 976 cm⁻¹ in respective geopolymer samples. This is significant of changes that occurred as a result of the dissolution of the raw sample to form Al-rich geopolymer gel. As the SiO₄ tetrahedra of silica-rich network of the raw sample are broken and precipitates take AlO₄ tetrahedra up [9, 43]. Further, broadening of bands observed at 995 and 976 cm⁻¹ in comparison to respective raw sample has been observed. This broadening is significant of structural disorder with the addition of water in structure [44]. Moreover, in BTC geopolymers the band present at 976 cm⁻¹ is sharpening with age, which indicates the increasing order in the phase [43].

Another significant change observed between raw BT and BTC samples is the reduction of the carbonate group as a result of heat treatment. As the stretching bands of O-C-O observed at 1435, 873 and 710 cm⁻¹ in raw BT sample and at 1435, 875 and 712 cm⁻¹ in raw BTC sample reduced in intensity while comparing BT and BTC samples to each other. Moreover, comparing the BT and BTC geopolymer samples, a clear reduction in this band has been observed as a result of geopolymerization. This indicates the participation of carbonates in geopolymer reaction. Further, a characteristic band corresponding to symmetrical stretching of Si-O-Si has been observed in both geopolymer samples at 798 and 520 cm⁻¹. Bending vibration band of Si-O-Si has been observed at 466 cm⁻¹ in BT geopolymers and at 420 cm⁻¹ in BTC geopolymers. This shift from higher to lower wavenumber is significant of incorporation of Al in gel structure [43].

4.4 Scanning electron microscopic (SEM) analysis coupled with energy dispersive X-ray spectroscopy (EDX)

Figures 12 and 13 show the scanning electron microscope micrographs and elemental maps of same region of the selected samples obtained for BT and BTC geopolymers, respectively. The microstructure illustrates a heterogeneous morphology, while elemental maps show a nonhomogeneous distribution of

several elements. Looking at the micrographs of BT geopolymers, three different zones in microstructure labelled as 1, 2 and 3 and microcracks are visible (Figure 12). The microcracks may appear as a result of the sample preparation method. Zone 1 in the micrograph shows a sponge-like structure which corresponds to Na-rich aluminosilicate geopolymer gel as indicated by the presence of Na, Al, Si and O in this zone from elemental maps. In addition to Na, the presence of Mg and Fe has also been recorded in this zone. While the elemental maps of K and Ca show that there is a small amount of K present while no Ca has been observed. Comparison of Si and Al elemental maps in this zone shows that the reaction product is richer in Al. Thus, it signifies that zone 1 potentially consists of N-A-S-H geopolymer gel incorporating Mg and Fe cations.

Zone 2 shows a natural pozzolan particle under alkali attack and dissolution of the particle. The particle has broken to small fragments under alkaline solution attack. Meanwhile, the reaction product is precipitated in cavities as indicated by the elemental map. Further, the elemental maps show that K and Ca are non-uniformly distributed in gel structure in contrast to zone 1. Zone 3 shows an unreacted particle of natural pozzolan which is rich in Si and O, and can be a quartz particle.

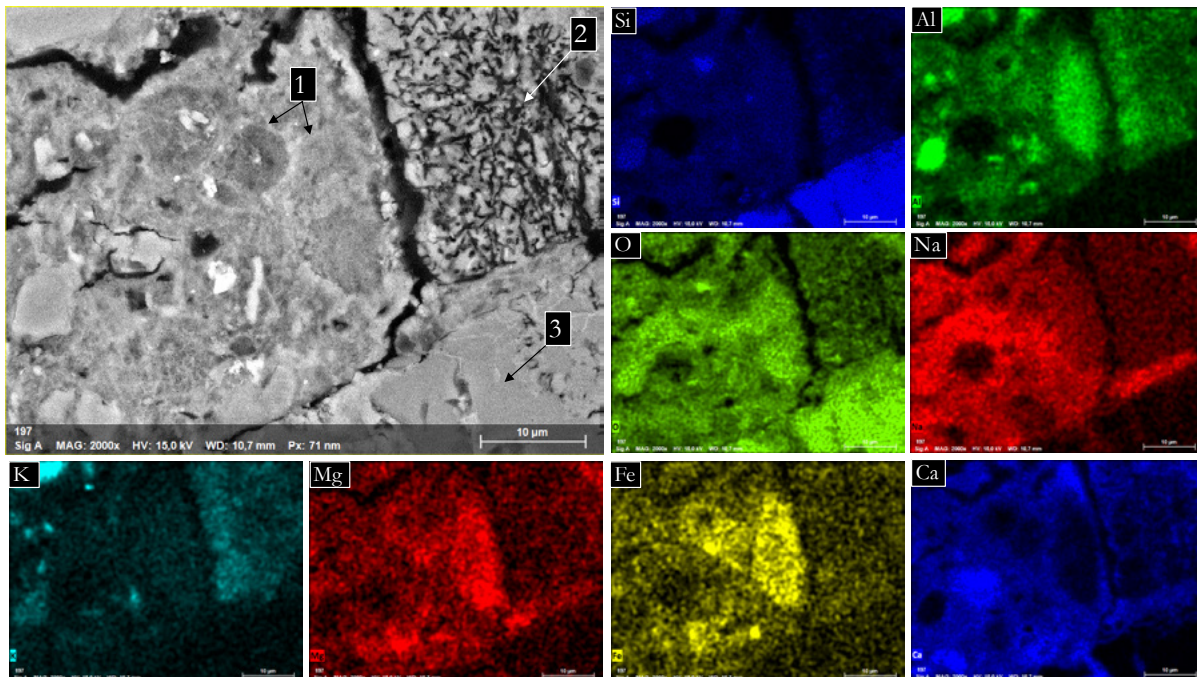


Figure 12: SEM image and elemental maps of BT geopolymer made with silica modulus of 0.707 at 7 d age.

Figure 13 presents a micrograph and elemental maps for BTC geopolymer sample. At least two types of gel phases can be seen marked as 1 and 2. The micrograph of the BTC geopolymer sample depicts a more homogeneous and compact microstructure with a more uniform distribution of several elements than the BT geopolymer. Like BT geopolymers, zone 1 shows Na-rich aluminosilicate gel, with an absence of Ca and the presence of Mg and Fe cations. As seen in BT geopolymers, this gel also has sponge-like structure. Zone 2 is characterized by a heterogeneous morphology with a compact gel structure where Na- and Ca-rich regions are overlapping each other. Further, in BTC micrograph a clear reduction in the size of unreacted particles of natural pozzolan can be seen in comparison to BT geopolymer sample. The geopolymer binder strongly binds the unreacted particles present. Comparing the elemental maps of Si and Al, the geopolymer gel in BTC geopolymers is rich in Si. This justifies the higher reactivity of BTC and higher compressive strength as Si-O bonds are stronger than corresponding Al-O bonds [2]. Combining the results of BT and BTC geopolymers, it is obvious that the geopolymer binder is heterogeneous in nature and consists majorly

of N-A-S-H, within cooperation of Mg, K, Fe and Ca.

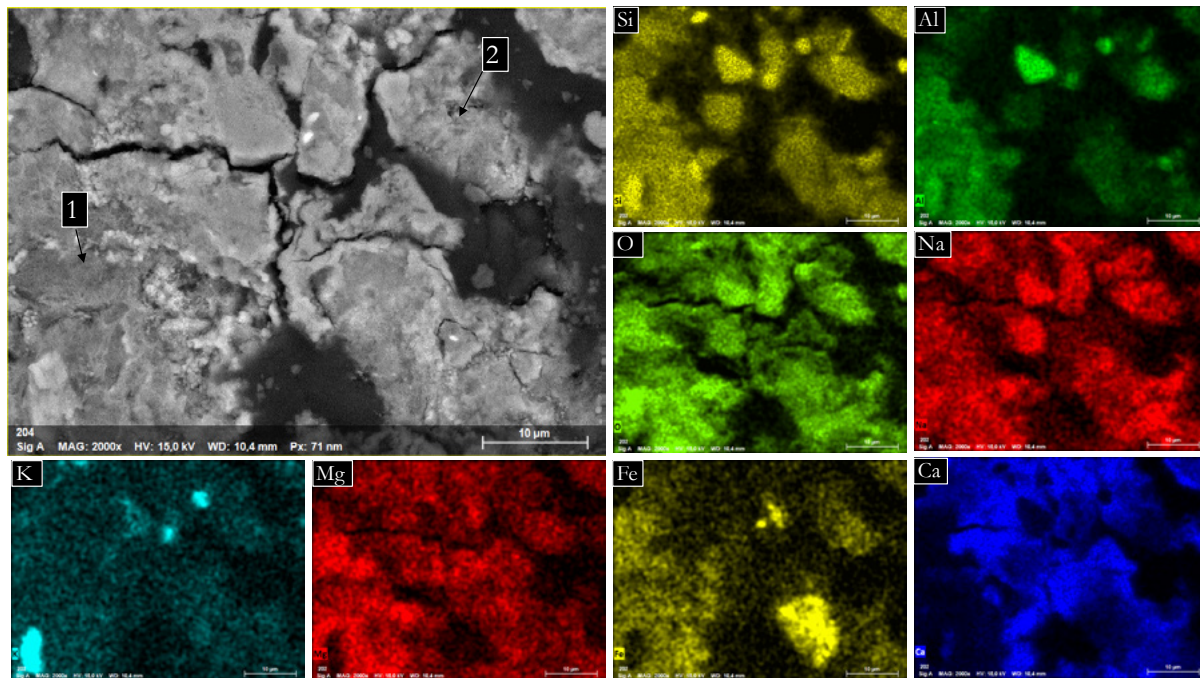


Figure 13: SEM image and elemental maps of BTC geopolymers made with silica modulus of 0.707 at 7 d age.

5. Conclusions

In this work, the natural pozzolan Bavarian trass obtained from Germany has been subjected to heat treatment and mechanical activation as reactivity enhancement methods. Results show that pozzolans in their natural state and after implementation of reactivity enhancement methods can be used as a precursor for geopolymer synthesis. The chemical composition, particle size and mineralogical phase composition of natural pozzolan affects the properties of resultant geopolymer product. The calcite-rich natural pozzolans can be used as geopolymer precursor by heat treatment, as the conversion of calcite to lime imparts higher reactivity and thus, an increase in compressive strength. An economical mechanical activation method was applied as reactivity enhancement method. However, no significant improvement in compressive strength has been observed as a result of mechanical activation. The calorimetric study showed that the fine fraction of natural pozzolan largely contributes to the reactivity. While mechanical activation helps majorly in reducing the size of coarser fraction thus only a slight improvement in reactivity has been observed. Comparing both reactivity enhancements methods, it is seen that the effect of calcination is more prominent than the reduced particle size.

For geopolymer samples prepared with calcined Bavarian trass (BTC), less amount of efflorescence was observed in comparison to BT samples for high silica modulus samples. As a result of heat treatment, an increase in the optimum silica modulus required to achieve higher compressive strength has also been observed. Therefore, the choice of reactivity enhancement method should be made depending on the properties, economic and environmental advantages. The second exothermic peak observed in the calorimetric study of BT geopolymers is assigned to the delayed dissolution of some phase(s) likely calcium rich phases. This delayed dissolution shifted to an earlier time for BTC geopolymers because of higher reactivity of BTC. The chemically bound water in the geopolymer structure gives insight about the dependence of the rate of reaction on silica modulus and age of the sample. Crystalline mineral phases such as calcite, lime, biotite and sanidine participate in geopolymer reaction by either complete or partial

dissolution in alkaline medium. Phase composition of geopolymer gel shows that it consists of N-A-S-H and (C)-N-A-S-H with the incorporation of Mg, Fe and K in the structure for both BT and BTC geopolymers.

6. Acknowledgements

The support of German Academic Exchange Service (DAAD) and Higher Education Commission of Pakistan (HEC) under funding programme “Faculty Development for PhD Candidates (Balochistan), 2016 (Programme ID: 57245990)” is acknowledged. The authors are thankful to Dr. Christian Lehmann for performing SEM-EDX experiment.

7. References

1. Robayo-Salazar R, Mejía-Arcila J, Mejía de Gutiérrez R et al. (2018) Life cycle assessment (LCA) of an alkali-activated binary concrete based on natural volcanic pozzolan: A comparative analysis to OPC concrete. *Constr. Build. Mater.* 176: 103–111. doi: 10.1016/j.conbuildmat.2018.05.017
2. Pacheco-Torgal F, Labrincha JA, Leonelli C et al. (eds) (2012) *Handbook of Alkali-activated Cements, Mortars and Concretes*. Woodhead Publishing in materials. Woodhead Publishing, Cambridge, Philadelphia, PA
3. Duxson P, Fernández-Jiménez A, Provis JL et al. (2007) Geopolymer technology: The current state of the art. *J. Mater. Sci.* 42(9): 2917–2933. doi: 10.1007/s10853-006-0637-z
4. Provis JL, van Deventer JSJ (eds) (2009) *Geopolymers - Structure, processing, properties and industrial applications*. Woodhead Publishing Limited
5. Provis JL, van Deventer JSJ (2014) *Alkali Activated Materials, State-of-the-Art Report*, RILEM TC 224-AAM. Springer, Dordrecht, Heidelberg, New York, London
6. Firdous R, Stephan D, Jin Y (2018) Investigation of Rhenish and Bavarian Trass as Geopolymer Precursor. 20th International Conference of Building Materials - Ibausil 2018, 12 – 14 September 2018, Weimar, Germany (Book 2): 617–624.
7. Firdous R, Stephan D (2019) Effect of silica modulus on the geopolymerization activity of natural pozzolans. *Constr. Build. Mater.* 219: 31–43. doi: 10.1016/j.conbuildmat.2019.05.161
8. Firdous R, Stephan D, Djobo JNY (2018) Natural pozzolan based geopolymers: A review on mechanical, microstructural and durability characteristics. *Constr. Build. Mater.* 190: 1251–1263. doi: 10.1016/j.conbuildmat.2018.09.191
9. Djobo JNY, Elimbi A, Tchakouté HK et al. (2016) Reactivity of volcanic ash in alkaline medium, microstructural and strength characteristics of resulting geopolymers under different synthesis conditions. *J. Mater. Sci.* 51(22): 10301–10317. doi: 10.1007/s10853-016-0257-1
10. Allahverdi A, Mehrpour K, Kani EN (2008) Investigating the possibility of utilizing pumice-type natural pozzolan in production of geopolymer cement. *Ceram. – Silik.* 52(1): 16–23
11. Bondar D, Lynsdale CJ, Milestone NB et al. (2011) Effect of type, form, and dosage of activators on strength of alkali-activated natural pozzolans. *Cem. Concr. Compos.* 33(2): 251–260. doi: 10.1016/j.cemconcomp.2010.10.021
12. Ghafoori N, Najimi M, Radke B (2016) Natural pozzolan-based geopolymers for sustainable construction. *Environ. Earth Sci.* 75:1110(14): 1–16. doi: 10.1007/s12665-016-5898-5
13. Haddad RH, Alshbuol O (2016) Production of geopolymer concrete using natural pozzolan: A

parametric study. *Constr. Build. Mater.* 114: 699–707. doi: 10.1016/j.conbuildmat.2016.04.011

14. Hewlett PC (ed) (1988) *Lea's Chemistry of Cement and Concrete*, 4th edn. Elsevier Ltd.
15. Djobo JNY, Elimbi A, Tchakouté HK et al. (2017) Volcanic ash-based geopolymer cements/concretes: The current state of the art and perspectives. *Environ. Sci. Pollut. Res.* 24(5): 4433–4446. doi: 10.1007/s11356-016-8230-8
16. Djobo JNY, Elimbi A, Tchakouté HK et al. (2016) Mechanical activation of volcanic ash for geopolymer synthesis: Effect on reaction kinetics, gel characteristics, physical and mechanical properties. *R. Soc. Chem. (RSC Adv.)* 6(45): 39106–39117. doi: 10.1039/C6RA03667H
17. Bondar D, Lynsdale CJ, Milestone NB et al. (2011) Effect of adding mineral additives to alkali-activated natural pozzolan paste. *Constr. Build. Mater.* 25(6): 2906–2910. doi: 10.1016/j.conbuildmat.2010.12.031
18. Bondar D, Lynsdale CJ, Milestone NB et al. (2011) Effect of heat treatment on reactivity-strength of alkali-activated natural pozzolans. *Constr. Build. Mater.* 25(10): 4065–4071. doi: 10.1016/j.conbuildmat.2011.04.044
19. Tchakoute HK, Mbey JA, Elimbi A et al. (2013) Synthesis of volcanic ash-based geopolymer mortars by fusion method: Effects of adding metakaolin to fused volcanic ash. *Ceram. Int.* 39(2): 1613–1621. doi: 10.1016/j.ceramint.2012.08.003
20. Djobo YJN, Elimbi A, Dika Manga J et al. (2016) Partial replacement of volcanic ash by bauxite and calcined oyster shell in the synthesis of volcanic ash-based geopolymers. *Constr. Build. Mater.* 113: 673–681. doi: 10.1016/j.conbuildmat.2016.03.104
21. Robayo RA, Mejía de Gutiérrez R, Gordillo M (2016) Natural pozzolan and granulated blast furnace slag-based binary geopolymers. *Mater. Constr.* 66(321): e077. doi: 10.3989/mc.2016.03615
22. Djobo JNY, Tchadjíé LN, Tchakoute HK et al. (2014) Synthesis of geopolymer composites from a mixture of volcanic scoria and metakaolin. *J. Asian Ceram. Soc.* 2(4): 387–398. doi: 10.1016/j.jascer.2014.08.003
23. EN 196-6 (2010) *Methods of testing cement – Part 6: Determination of fineness*
24. Schwiete H-E, Ludwig U, Wigger K-H (1961) *Die Konstitution einiger rheinischer und bayrischer Trasse*. Westdeutscher Verlag, Köln Opladen
25. Liebig E, Althaus E (1998) Pozzolanic activity of volcanic tuff and suevite: effects of calcination. *Cem. Concr. Res.* 28 (4): 567–575
26. Chukanov NV, Chervonnyi AD (2016) *Infrared spectroscopy of minerals and related compounds*. Springer Berlin Heidelberg
27. Ludwig U, Schwiete HE (1963) *Untersuchungen an Deutschen Trassen*. *Silicates Ind.*: 439–447
28. Fleischer M (1965) New mineral names. *Am. Miner.* 50: 2096–2111
29. Stark J, Wicht B (2000) *Zement und Kalk: Der Baustoff als Werkstoff*. Springer Berlin Heidelberg
30. Gebregziabihier BS, Thomas RJ, Peethamparan S (2016) Temperature and activator effect on early-age reaction kinetics of alkali-activated slag binders. *Constr. Build. Mater.* 113: 783–793. doi: 10.1016/j.conbuildmat.2016.03.098
31. Triantafyllou G, Christidis G, Markopoulos T (2003) Influence of porosity and grain size of carbonate rocks in the reactivity of lime. *Mineral Exploration and Sustainable Development*, Eliopoulos et al., eds. Millpress, Rotterdam: 931–934

32. Černý R, Rovnaníková P (2002) *Transport processes in concrete*. Spon Press, Taylor & Francis Group, London
33. Ben Haha M, Le Saout G, Winnefeld F et al. (2011) Influence of activator type on hydration kinetics, hydrate assemblage and microstructural development of alkali activated blast-furnace slags. *Cem. Concr. Res.* 41(3): 301–310. doi: 10.1016/j.cemconres.2010.11.016
34. Zhang Z, Provis JL, Reid A et al. (2014) Fly ash-based geopolymers: The relationship between composition, pore structure and efflorescence. *Cem. Concr. Res.* 64: 30–41. doi: 10.1016/j.cemconres.2014.06.004
35. Djobo JNY, Tchakouté HK, Ranjbar N et al. (2016) Gel Composition and Strength Properties of Alkali-Activated Oyster Shell-Volcanic Ash: Effect of Synthesis Conditions. *J. Am. Ceram. Soc.* 99(9): 3159–3166. doi: 10.1111/jace.14332
36. Scrivener K, Snellings R, Lothenbach B (eds) (2016) *A Practical Guide to Microstructural Analysis of Cementitious Materials*. Taylor & Francis Group
37. Tajuelo Rodriguez E, Garbev K, Merz D et al. (2017) Thermal stability of C-S-H phases and applicability of Richardson and Groves' and Richardson C-(A)-S-H(I) models to synthetic C-S-H. *Cem. Concr. Res.* 93: 45–56. doi: 10.1016/j.cemconres.2016.12.005
38. Zhang Z, Provis JL, Wang H et al. (2013) Quantitative kinetic and structural analysis of geopolymers. Part 2. Thermodynamics of sodium silicate activation of metakaolin. *Thermochim. Acta* 565: 163–171. doi: 10.1016/j.tca.2013.01.040
39. Sun Z, Vollpracht A (2018) Isothermal calorimetry and in-situ XRD study of the NaOH activated fly ash, metakaolin and slag. *Cem. Concr. Res.* 103: 110–122. doi: 10.1016/j.cemconres.2017.10.004
40. Lecomte I, Henrist C, Liégeois M et al. (2006) (Micro)-structural comparison between geopolymers, alkali-activated slag cement and Portland cement. *J. Eur. Ceram. Soc.* 26(16): 3789–3797. doi: 10.1016/j.jeurceramsoc.2005.12.021
41. van Deventer JSJ, San Nicolas R, Ismail I et al. (2015) Microstructure and durability of alkali-activated materials as key parameters for standardization. *J. Sustain. Cem. Mater.* 4(2): 116–128. doi: 10.1080/21650373.2014.979265
42. Komnitsas K, Zaharaki D, Perdikatsis V (2007) Geopolymerisation of low calcium ferronickel slags. *J. Mater. Sci.* 42(9): 3073–3082. doi: 10.1007/s10853-006-0529-2
43. Walkley B, San Nicolas R, Sani M-A et al. (2016) Phase evolution of C-(N)-A-S-H/N-A-S-H gel blends investigated via alkali-activation of synthetic calcium aluminosilicate precursors. *Cem. Concr. Res.* 89: 120–135. doi: 10.1016/j.cemconres.2016.08.010
44. Baykara H, Cornejo MH, Murillo R et al. (2017) Preparation, characterization and reaction kinetics of green cement: Ecuadorian natural mordenite-based geopolymers. *Mater. Struct.* 50: 188. doi: 10.1617/s11527-017-1057-z

Effect of calcium hydroxide on the hydration of sulphoaluminate cement with high concentration of borate solution

Q. Li¹, H. Ma², X. Ling², B. Yuan², W. Chen^{1*}

¹ State Key Laboratory of Silicate Materials for Architectures, Wuhan University of Technology, 430070 Wuhan, P.R. China

² School of Material Science and Engineering, Wuhan University of Technology, 430070 Wuhan, P.R. China

Abstract

The effect of calcium hydroxide on the hydration of CSA cement with high concentration of borate solution were investigated by a range of analytical techniques, aiming to accelerate the hydration of CSA cement and prevent the retardation by borate solution. The results indicate that the hydration of CSA cement was severely retarded by borate solution through formation of dense layer of amorphous ulexite on the surface of cement particles, preventing further dissolution of anhydrous cement particles. No hydration product was identified by up to 28 days. The amorphous ulexite transformed into crystalline ulexite by 56 days of hydration in borate solution. By addition of sodium hydroxide, the hydration of CSA cement in borate solution accelerated through formation of foil-like hexahydroborite and borate-incorporating ettringite, resulting in the prevention of formation of ulexite. The main hydration products for CSA cement in borate solution with sodium hydroxide addition were ettringite, AFm and hexahydroborite.

Keywords: Ulexite, Hexahydroborite, Borate solution, Sulphoaluminate cement, Borate-incorporating ettringite.

1. Introduction

Radioactive waste is produced from nuclear power plant, scientific research and medicine industry[1], which is classified into four levels according to radioactivity, namely high-level waste (HLW), intermediate-level waste (ILW), low-level waste (LLW) and very low-level waste (VLLW)[2]. The latter three types of radioactive waste take up approximately 99% in volume globally, but with lower radioactive content[3]. With long decays period of radionuclides in the radioactive waste, ionized radiation severely harms humans and the environment[4].

The radioactive waste liquid is mainly produced from cooling system of nuclear power plants, and usually contains high concentration of boron [5]. Borate compound or boric acid is used to control the rate of nuclear reaction in a pressurized water reactor (PWR)[6]. Borate compound is well known as set retarder during the hydration of cement [7-10], which will affect the effectively consolidation of radioactive waste liquid during the successful disposal of ILW and LLW. Several types of calcium borate ($2\text{CaO}\cdot 3\text{B}_2\text{O}_3\cdot 8\text{H}_2\text{O}$, $\text{CaO}\cdot \text{B}_2\text{O}_3\cdot 6\text{H}_2\text{O}$ [11, 12]) were identified during the hydration of cement in borate solution under various pH values, resulting in the retardation of hydration. Using alkaline additive to react with borate acid was suggested to solve the retardation of hydration[13]. Retardation phases still formed after addition of alkaline additives. More effective method could be to decompose unstable calcium hexahydroborite[14].

Calcium sulphoaluminate (CSA) cement is manufactured by calcining gypsum, bauxite and limestone at 1300°C, with less energy consumption and less carbon footprint[15-17]. CSA cement is widely used in applications such as fast construction, fast repair[18] and permeability resistance project[19, 20] due to its high early-age strength and short setting time. CSA cement is a potential candidate to consolidate the radioactive waste with high concentration of borate because borate ions demonstrated less effect on the hydration of CSA cement than Portland cement[21-23]. The hydration of CSA cement has been intensively studied by many researchers. Ettringite and monosulphate are identified as main hydration products (Eq. 1 and 2)[24]. High-density and low-porosity microstructure are obtained during the early age hydration due to the formation of ettringite, monosulphate and alumina hydrate, resulting in the high early strength and short setting time[19].



Previous study on the hydration of CSA cement in 1M borate solution under pH of 11 indicates that the hydration is retarded by 15 hours, comparing to that in deionized water, due to the formation of poorly-crystallized borate compound (ulexite, $NaCaB_5O_6(OH)_6 \cdot 5H_2O$)[25], although no direct observation of the compound. Ulexite, a crystalline borate mineral containing three borate tetrahedra and two borate triangular groups, is fibrous. There is little literature reporting the formation of poorly crystalline ulexite. Potential methods to prevent the retardation during the hydration of CSA cement with high concentration boron solution are to avoid the ulexite formation or accelerate the phase transformation of ulexite to other minerals.

In this study, the effects of calcium hydroxide on the hydration of CSA cement with high concentration of borate solution were investigated by a range of analytical techniques, aiming to accelerate the hydration of CSA cement and prevent the retardation by borate solution, and to provide feasible solution to improve the hydration and properties of CSA cement on radioactive waste liquid solidification in the future.

2. Methodology

2.1 Materials

Sulphoaluminate cement and sulphoaluminate cement clinker from Anda Special Cement Ltd. (Yicheng, Hubei, China) were used. Chemical composition of CSA clinker and CSA cement are shown in Table 1, which were quantitatively analysed by X-ray fluorescence spectroscopy (XRF, PANalytical Axios advanced, Netherlands). Solid sodium hydroxide (NaOH, Sinopharm, AR grade, CAS code:1310-73-2), boric acid (H_3BO_3 , Sinopharm, AR grade, CAS code:10043-35-3), calcium hydroxide ($Ca(OH)_2$, Sinopharm, AR grade, CAS code:1305-62-0) and deionized water were used for simulated highly-concentrated borate liquid waste and paste specimens. Zeolite with specific surface area of 740 m²/g was used during the paste specimen preparation.

Table 1 Chemical composition of CSA clinker and CSA cement determined by XRF (wt%)

Oxides	SiO ₂	Al ₂ O ₃	Fe ₂ O ₃	CaO	SO ₃	TiO ₂	MgO	Na ₂ O	K ₂ O	SrO	LOI*
C S A clinker	12.92	25.99	8.38	39.83	7.82	1.93	1.26	0.30	0.20	0.12	1.25
C S A cement	10.67	13.99	5.60	36.98	20.92	1.12	1.76	0.24	0.40	0.23	8.09

*Loss on ignition at 1000 °C.

2.2 Specimen preparation

Simulated liquid waste with high concentration of borate was prepared as follows. Boric acid solution of 0.5M was used as the boron solution. After dissolution of boric acid in deionized water, sodium hydroxide was added in the solution to modify the pH value to 7, which is the pH value specified by LLW and ILW effluent produced from PWR nuclear plants in China.

To investigate the effect of calcium hydroxide on the properties of CSA cement with high concentration borate solution, the water/cement (w/c) ratio was set at 0.6, which could prevent the potential early age bleeding and the stop of hydration resulted from the lack of water[25]. Calcium hydroxide was added as the mole ratio of borate, namely 0, 0.22, 0.44, 0.66, 0.88, 1.10, 1.32, 1.44 and 1.56. Paste specimens were cast in cylinder moulds of 50 mm in diameter and 50 mm in height. After demoulded at 1 day, the cylinder specimens were cured at temperature of 20 °C and relative humidity of 98%.

To characterize the effects of borate on the hydration of main mineral phases of CSA cement, the powder of CSA clinker was mixed with 0.5 M borate solution at a w/c ratio of 25, where 500 g of borate solution of 0.5 M were mixed with 20 g powder of CSA clinker in a sealed container stirring by a magnetic stirrer. The hydration of CSA clinker powder was stopped at 0, 1, 3, 6, 10, 18, 24 hours, and 3, 7 and 28 days, respectively, by immersing the clinker powder in ethanol and drying at room temperature (20±2 °C). Similarly, the effects of calcium hydroxide on the hydration of CSA cement in the borate solution were characterized. CSA cement was mixed with calcium hydroxide under the ratio of 1:1 and hydrated in 0.5 M borate solution at w/c of 25. The hydration was stopped at 5, 15, 30 and 45 min, and 1, 2, 18, 24 and 72 hours by immersing the paste in ethanol and drying at room temperature.

2.3 Analytical techniques

2.3.1 Calorimetry

The heat evolved during the hydration of CSA cement in borate solution with and without calcium hydroxide was measured by Thermometric TAM Air under isothermal conditions at 20 °C. 10 g of CSA cement and 6 g of 0.5 M borate solution with or without calcium hydroxide were mixed in a flask. After stirring for 1 min, the paste was sealed with cap in the container and transferred into the calorimeter for 72 hours. The heat evolved from specimens during the first hour was excluded due to the external mixing. The total evolved heat during hydration was calculated by integration of heat flow rate excluding those from the first hour.

2.3.2 X-ray powder diffraction (XRD)

XRD was performed to characterize the phase assemblage in the specimens with w/c of 25 by a Bruker D8 Advance diffractometer with Cu K α radiation (1.5406Å), under conditions of step size of 0.02° 2 θ /step, measuring time of 0.24 s/step, start position 5° (2 θ) and end position 60° (2 θ). After stopping hydration at various ages, approximately 1 g of paste was finely ground until passing 0.063 mm sieve. The fine powder was backfilled in the sample holder before being transferred for characterization. The XRD patterns obtained were analysed and the mineral phases were identified by PANalytical Highscore Plus with PDF 2004 database.

2.3.3 Thermal analysis

Thermal analysis was conducted on the specimens by a Netzsch STA 499 simultaneous thermal analyser under N₂ atmosphere with flow rate of 50 ml/min on approximately 15 mg of fresh finely-ground specimen at a heating rate of 10 K/min up to 1000 °C. Differential thermogravity (DTG) results were calculated from thermogravity (TG).

2.3.4 Fourier-transform infrared spectroscopy

Fourier-transform infrared (FTIR) spectroscopy was performed to identify the bonding in the mineral phases in the specimens with w/c of 25. Thermo Nicolet Nexus FTIR spectroscopy was employed under attenuated total reflectance (ATR) mode in the wavenumber range of 4000–400 cm⁻¹ under 4 cm⁻¹ resolution. Specimens were freshly finely ground to powder before transferred for analysis.

2.3.5 Scanning electron microscopy (SEM)

The development of microstructure of specimens was characterized by FEI Quanta 450FEG Environmental SEM under the conditions of spot size 5, accelerating voltage 20 kV. The specimens were coated with Pt before transferred to the vacuum chamber of SEM. Images were taken under secondary electron mode.

2.3.6 Electron probe micro-analysis (EPMA)

The morphology and elements distribution on the surface of specimens were characterized by JEOL JXA-8230 electron probe microanalyser equipped with Oxford Instruments INCA X-Act energy dispersive spectrometer (EDS). The specimens were coated with carbon before transferred for analysis.

3. Results and discussion

3.1 Hydration kinetics

The mineral phases of CSA clinker and CSA cement used in this study were identified by XRD and shown in Figure 1. The main mineral phases in the clinker were ye'elimite and belite, with minor minerals, namely perovskite and calcite. Anhydrite was identified in the CSA cement together with those minerals identified in the CSA clinker.

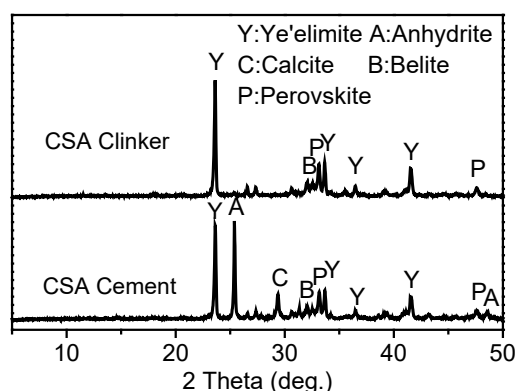


Figure 1 XRD patterns of CSA clinker and CSA cement.

The heat evolution rate and cumulative heat in the first 72 hours of hydration of CSA cement in deionized water and borate solution were characterized (Figure 2(a)). For CSA cement hydrating with deionized water, a dormant period of approximately 1.2 h was noted before the initial peak, which indicated the reaction of $C_4A_3\bar{S}$ with $C\bar{S}$. The second main hydration peak was at 3.2 h, due to the rapid dissolution of $C_4A_3\bar{S}$ after sulphates in solution were depleted. The total heat in the first 72 hours was approximately 149 J/g.

No peak was observed by up to 72 hours of hydration for CSA cement hydrated with 0.5 M borate solution, indicating that the hydration of CSA cement is greatly retarded. Borate solution retarded the hydration of both ordinary Portland cement and CSA cement. Borate anions reacted with calcium component in CSA cement by formation of various borate compounds. The retardation mechanism and chemical composition of borate compound will be discussed in the following sections.

Addition of calcium hydroxide accelerated the hydration of CSA cement with borate solution (Figure 2(b))

and (c)). The time of maximum heat evolution rate decreased with the increase of content of calcium hydroxide, indicating that the hydration of CSA cement was effectively accelerated by calcium hydroxide, possibly by formation of different borate mineral comparing to that in CSA cement with borate solution.

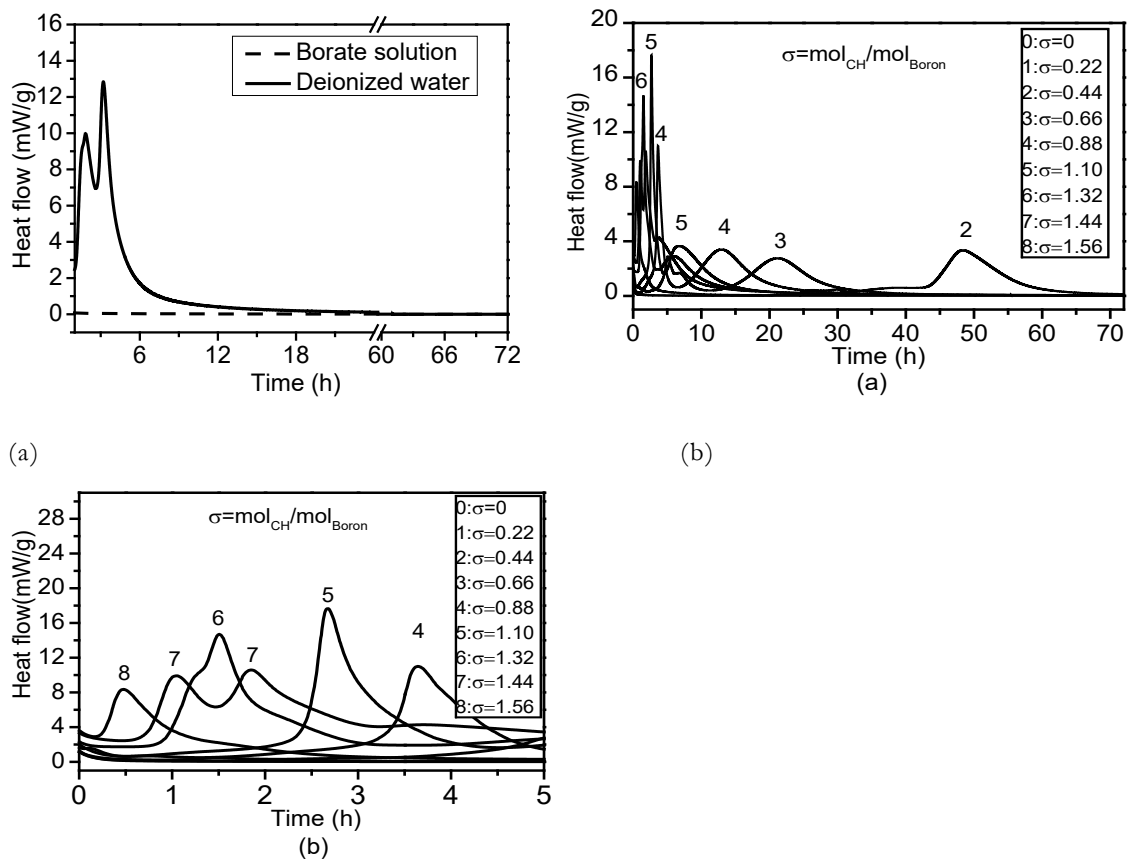


Figure 2 Heat evolution rate of (a) CSA cement hydrated with deionized water and borate solution (break from 24 h to 60 h) and (b) CSA cement hydrated in borate solution with various content of $\text{Ca}(\text{OH})_2$ in 72 h, and (c) first 5 h in (b).

3.2 Phase assemblage

The phase assemblage of CSA cement hydrated in borate solution for 28 d, together with anhydrous CSA cement is shown in Figure 3(a). According to these results, there was hardly any hydration products formed after 28 day of hydration in borate solution, indicating strong retardation of CSA cement hydration by borate. After 56 days of hydration in borate solution (Figure 3(b)), crystalline ulexite ($\text{NaCaB}_5\text{O}_8(\text{OH})_6 \cdot 5\text{H}_2\text{O}$) was identified as the main hydration products. By addition of the same amount of calcium hydroxide as CSA cement, the hydration of CSA cement in borate solution was accelerated and the hydration products were formed, namely hexahydroborite ($\text{Ca}[\text{B}(\text{OH})_4]_2 \cdot 2\text{H}_2\text{O}$) and ettringite as seen in Figure 3(c). By hydration of 5 min, most of CSA cement hydrated due to the high amount of calcium hydroxide addition. The main peak of ettringite shifted to the left (Figure 3(d)), indicating the increase of space of (001) plane due to the incorporation of boron in the ettringite crystal structure in the form of $\text{B}(\text{OH})_4^-$ [9, 25]. These results agree well with those from calorimetry.

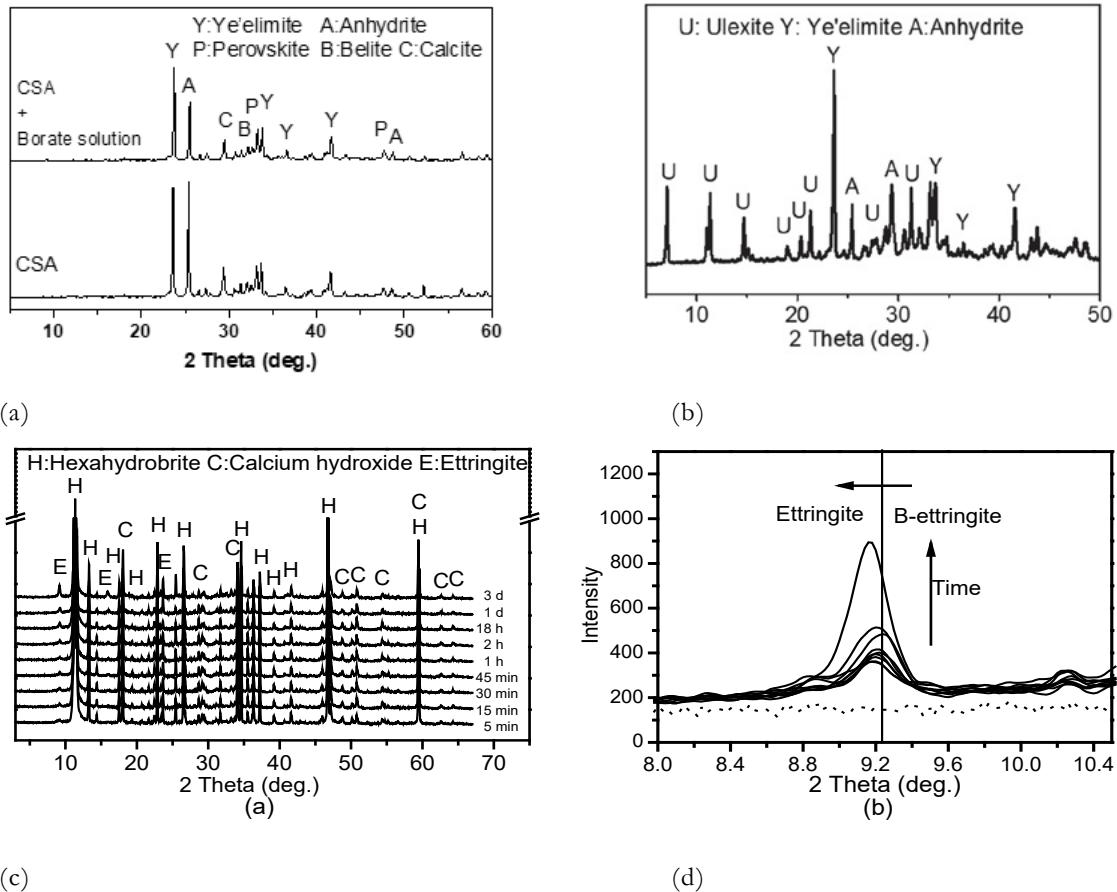
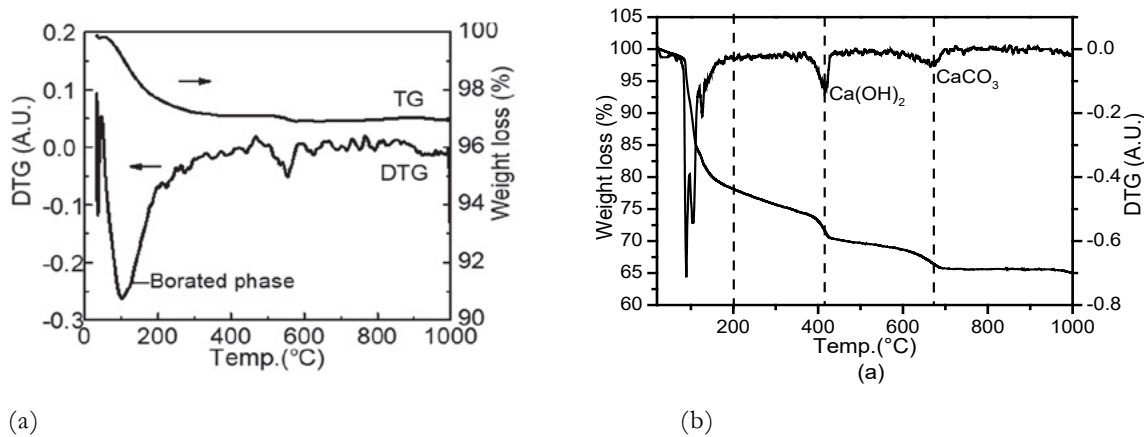
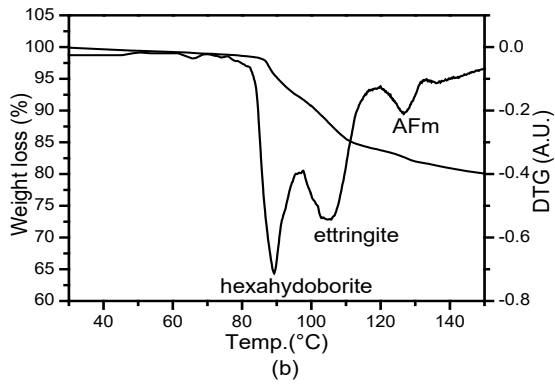


Figure 3 XRD results of CSA cement hydrated with borate solution at (a) 28 d and anhydrous CSA cement, (b) at 56 d, (c) CSA cement hydrated in borate solution with the same amount of $\text{Ca}(\text{OH})_2$ at various ages, and (d) first 5 h in (c).

Although there was no crystalline phase identified in CSA cement hydrated in borate solution for 28 days according to XRD results, amorphous borate phase was identified from TG/DTG results as weight loss at 100 °C [25](Figure 4(a)), due to the dehydration of borate related phases. After addition of the same amount of calcium hydroxide, the formation of hexahydroborite, ettringite, AFm and calcite were confirmed from TG/DTG results after 3 days of hydration, together with residue calcium hydroxide (Figure 4(b) and (c)). These results well agree with those from XRD, confirming the accelerated hydration of CSA cement in borate solution after calcium hydroxide addition by formation of hexahydroborite, ettringite and AFm phases.



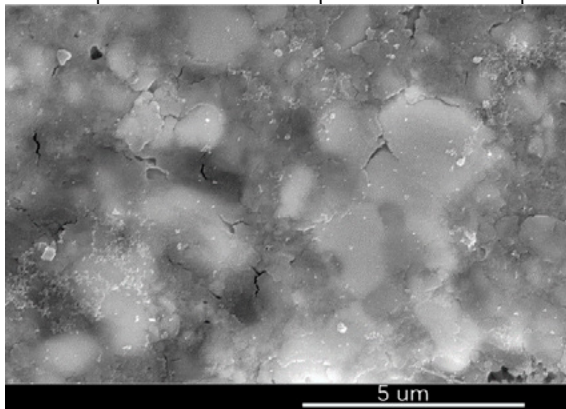


(c)

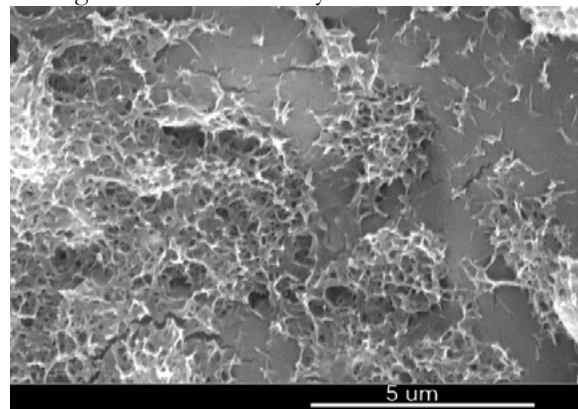
Figure 4 TG/DTG results of (a) CSA cement hydrated with borate solution at 28 d, (b) CSA cement hydrated in borate solution with the same amount of $\text{Ca}(\text{OH})_2$ at 3 d, and (c) 30-150 °C in (b).

3.3 Microstructure

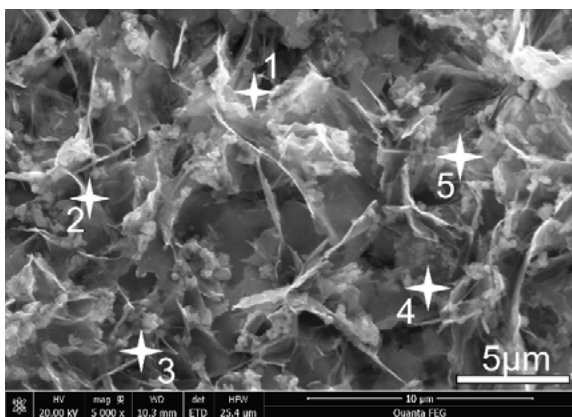
After hydrated in borate solution for 3 days, a dense layer of hydration products fully covered the surface of CSA cement particles (Figure 5(a)), preventing further dissolution of anhydrous phases and resulting in strong retardation of CSA cement hydration. While for CSA cement hydrated in the deionized water for 3 days (Figure 5(b)), foil-like hydration products formed on the surface of CSA cement particles with most part of surface exposed, resulting in the continuous hydration of CSA cement.



(a)



(b)



(c)

Figure 5 Microstructure of (a) CSA cement hydrated with borate solution at 3 days, (b) CSA cement hydrated in deionized water at 3 days, and (c) CSA cement hydrated in borate solution with the same amount of $\text{Ca}(\text{OH})_2$ at 1 day.

After addition of calcium hydroxide in the CSA cement with borate solution (Figure 5(c)), foil-like hydration products were observed after 1 day of hydration. Chemical composition of hydration products of CSA cement with addition of calcium hydroxide in borate solution was characterized by energy-dispersive X-ray spectroscopy (EDX). The average Ca/Al ratio in five positions was 4.38 (Table 2), indicating the hydration products were hexahydroborate and ettringite, which intermixed with residue calcium hydroxide.

Table 2 Chemical composition of points in Figure 5(c). (atom%)

	1	2	3	4	5	Ca/Al
Ca	24.6	27.1	26.9	24.5	28.6	
O	69.6	64.7	64	64.3	66.2	4.38
Al	5.7	8.2	9.1	4.2	5.2	

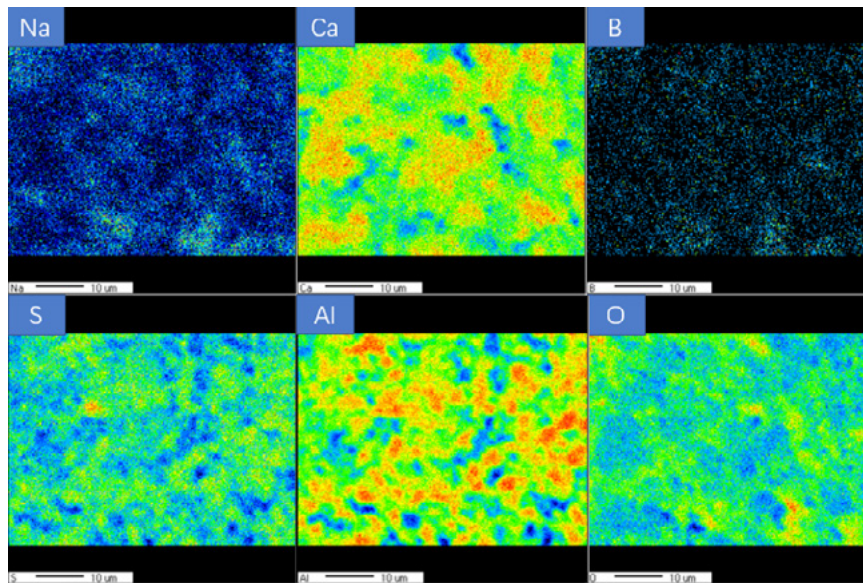


Figure 6 Element mapping of CSA cement hydrated with borate solution for 3 days

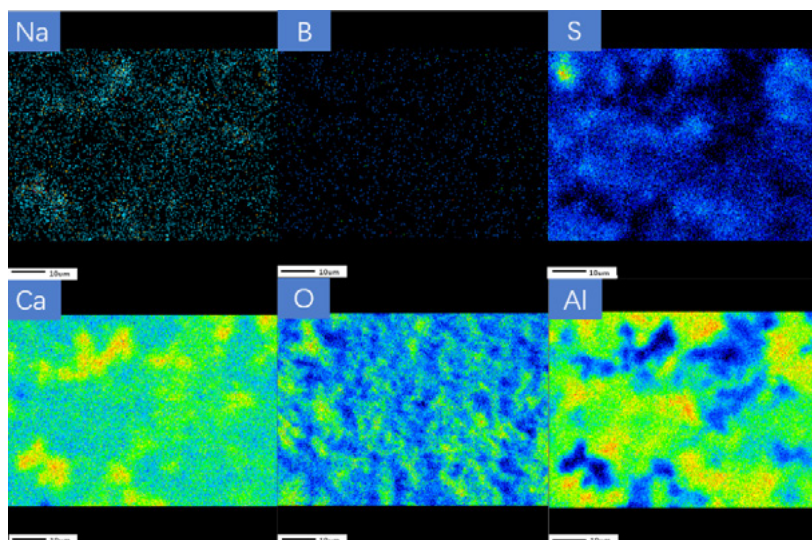


Figure 7 Element mapping of CSA cement hydrated in borate solution with addition of the same amount of Ca(OH)_2 at 1 day.

EPMA was performed on the CSA cement hydrated with borate solution for 3 days and CSA cement hydrated in borate solution with calcium hydroxide addition for 1 day, to characterize the chemical composition of hydration products. For CSA cement hydrated in borate solution for 3 days (Figure 6), the distributions of boron and sodium were similar, indicating the formation of borate mineral, which was ulexite according to XRD results. For CSA cement hydrated in borate solution with sodium hydroxide addition (Figure 7), there was hardly any boron on the surface of cement particles. The distribution of sulphur and aluminium were similar, indicating the formation of ettringite.

4. Conclusions

The effects of calcium hydroxide on the hydration of CSA cement with high concentration of borate solution were investigated by a range of analytical techniques. The hydration kinetics, phase assemblage and microstructure of CSA cement hydrated in borate solution with or without sodium hydroxide addition were characterized. According to the results obtained, the following conclusions can be drawn.

High concentration of borate severely retarded the hydration of CSA cement by formation of a dense layer of amorphous ulexite on the surface of cement particles, preventing further dissolution of anhydrous cement particles. The amorphous ulexite transformed into crystalline ulexite by 56 days of hydration.

Addition of sodium hydroxide accelerated the hydration of CSA cement in borate solution by formation of hexahydroborite and incorporation of borate in ettringite to prevent the formation of ulexite layer on the surface of cement particles. The main hydration products for CSA cement in borate solution with sodium hydroxide addition were ettringite, AFm and hexahydroborite.

5. Acknowledgment

This research was financially supported by the National Natural Science Foundation of China (grant numbers 51672199, 51611530545); the Fundamental Research Funds for the Central Universities (grant number WUT: 2017-YB-008) and the National Key Research and Development Program of China (grant number 2016YFB0303501, BY115J004).

6. Reference

- [1] W.E. Lee, M.I. Ojovan, *Fundamentals of Radioactive Waste (RAW): Science, Sources, Classification and Management Strategies*, Radioactive Waste Management and Contaminated Site Clean-Up, Woodhead Publishing 2013, pp. 3-50.
- [2] R. Burcl, *Radioactive Waste (RAW) Categories, Characterization and Processing Route Selection*, Radioactive Waste Management and Contaminated Site Clean-Up, Woodhead Publishing 2013, pp. 50-72.
- [3] IAEA, *Status and Trends in Spent Fuel and Radioactive Waste Management*, IAEA Nuclear Energy Series, International Atomic Energy Agency (IAEA), 2018, pp. 1-57.
- [4] IAEA, *Strategy and Methodology for Radioactive Waste Characterization*, 2007.
- [5] R. Ishihara, K. Fujiwara, T. Harayama, Removal of Cesium Using Cobalt-Ferrocyanide-Impregnated Polymer-Chain-Grafted Fibers, *Journal of Nuclear Science and Technology*, 48 (2011) 1281–1284.
- [6] P. Demirçivi, G. Nasün-saygılı, Removal of Boron from Waste Waters by Ion-Exchange in a Batch System, *World Academy of Science, Engineering and Technology*, 2 (2008) 95-98.
- [7] I.S. Bell, P.V. Coveney, Molecular Modelling of the Mechanism of Action of Borate Retarders on Hydrating Cements at High Temperature, *Molecular Simulation*, 20 (1998) 331-356.

- [8] L.J. Cseteyi, F.P. Glasser, Borate Retardation of Cement Set and Phase Relations in the System Na₂O—CaO—B₂O₃—H₂O, *Advances in Cement Research*, 7 (1995) 13-19.
- [9] J. Bensted, I.C. Callaghan, A. Lepre, Comparative Study of the Efficiency of Various Borate Compounds as Set-Retarders of Class G Oilwell Cement, *Cement and Concrete Research*, 125 (1991) 2384–2395.
- [10] Y. Hu, W. Li, S. Ma, X. Shen, Influence of borax and citric acid on the hydration of calcium sulfoaluminate cement, *Chemical Papers*, 71 (2017) 1909-1919.
- [11] S. Hernandez, A. Guerrero, S. Goni, Leaching of borate waste cement matrices: pore solution and solid phase characterization, *Advances in Cement Research*, 12 (2000) 1-8.
- [12] A. Guerrero, S. Goni, Efficiency of a blast furnace slag cement for immobilizing simulated borate radioactive liquid waste, *Waste Management*, 22 (2002) 831-836.
- [13] O. Gorbunova, Cementation of liquid radioactive waste with high content of borate salts, *J Radioanal Nucl Ch*, 304 (2015) 361-370.
- [14] B. Florence, F. Fabien, L. Sylvie, C.-d.-C. Céline, *Cement-Based Materials for Nuclear Waste Storage*, 2013.
- [15] E. Gartner, Industrially interesting approaches to “low-CO₂” cements, *Cement and Concrete Research*, 34 (2004) 1489-1498.
- [16] M.C.G. Juenger, F. Winnefeld, J.L. Provis, J.H. Ideker, *Advances in alternative cementitious binders*, *Cement and Concrete Research*, 41 (2011) 1232-1243.
- [17] D. Gastaldi, G. Paul, L. Marchese, S. Irico, E. Boccaleri, S. Mutke, L. Buzzi, F. Canonico, Hydration products in sulfoaluminate cements: Evaluation of amorphous phases by XRD/solid-state NMR, *Cement and Concrete Research*, 90 (2016) 162-173.
- [18] J. Qian, C. You, Q. Wang, H. Wang, X. Jia, A method for assessing bond performance of cement-based repair materials, *Construction and Building Materials*, 68 (2014) 307-313.
- [19] T. Kuryatnyk, M. Chabannet, J. Ambroise, J. Pera, Leaching behaviour of mixtures containing plaster of Paris and calcium sulphoaluminate clinker, *Cement and Concrete Research*, 40 (2010) 1149-1156.
- [20] K. Quillin, Performance of belite-sulfoaluminate cements, *Cement and Concrete Research*, 31 (2001) 1341-1349.
- [21] C.C.D. Coumes, S. Courtois, S. Peysson, J. Ambroise, J. Pera, Calcium sulfoaluminate cement blended with OPC: A potential binder to encapsulate low-level radioactive slurries of complex chemistry, *Cement and Concrete Research*, 39 (2009) 740-747.
- [22] J. Pera, J. Ambroise, New applications of calcium sulfoaluminate cement, *Cement and Concrete Research*, 34 (2004) 671-676.
- [23] Q. Sun, J. Li, J. Wang, Effect of borate concentration on solidification of radioactive wastes by different cements, *Nuclear Engineering and Design*, 241 (2011) 4341-4345.
- [24] F. Winnefeld, B. Lothenbach, Hydration of calcium sulfoaluminate cements - Experimental findings and thermodynamic modelling, *Cement and Concrete Research*, 40 (2010) 1239-1247.
- [25] J.-B. Champenois, M. Dhoury, C.C.D. Coumes, C. Mercier, B. Revel, P. Le Bescop, D. Damidot,

Influence of sodium borate on the early age hydration of calcium sulfoaluminate cement, Cement and Concrete Research, 70 (2015) 83-93.

The effect of MgO on the structure and chemical composition of C-S-H gels

Y. Tang^{1,2}, W. Chen¹

¹ School of Material Science and Engineering, Wuhan University of Technology, Wuhan 430070, China.

² State Key Laboratory of Silicate Materials for Architectures, Wuhan University of Technology, Wuhan 430070, China.

Abstract

As the amount of high-grade limestone decreases rapidly, limestone containing high amount of MgO could be applied as the supplement in the production of Portland cement clinker. This paper aims to study the effect of MgO on the structure and chemical composition of calcium silicate hydrates (C-S-H) gels during early stage hydration, which is the main product of Portland cement hydration. Magnesium oxide (MgO), silica fume (SiO₂) and calcium oxide (CaO) were used in the preparation of MgO modified C-S-H with (Ca + Mg)/Si ratio=0.8. A high water to solid ratio (around 10) and elevated temperature (60 C) were applied in order to ensure the sufficient water for reaction, promoting the ions diffusion and accelerating the reaction. The obtained solids were characterized by SEM, TEM-EDS, XRD, FT-IR and TG-DSC. The results show that the pure magnesium silicate hydrates (M-S-H) gels exhibit significantly different structure and chemical composition from C-S-H. The addition of MgO could retard the reaction of the entire MgO-CaO-SiO₂ system. The prepared MgO modified C-S-H gels have a poorly crystalline structure, which are similar to the synthesized pure C-S-H gels. The increasing initial amount of MgO lead to the formation of M-S-H gels and the possible formation of a new phase magnesium calcium silicate hydrates (M-C-S-H), showing the homogenous distribution of Mg, Si and Ca elements which was observed by TEM-EDS. The structure and chemical composition of reaction products is highly depending on the input molar ratio of Mg to Ca. However, the detailed reaction process still requires further investigations.

Keywords: magnesium silicate hydrates, calcium silicate hydrates, hydration, modification

1. Introduction

Cement remains the most used building materials and it will continue for a quite long time[1]. As the annual cement production is continuously increasing and high-grade limestone is not sufficiently available around the world, more low-grade limestone containing high magnesium content would be applied into the cement industry[2]. Some researchers have shown great interests in the effect of magnesium on calcium silicate hydrates[3–7]. Calcium silicate hydrate(C-S-H) gels are the primary hydration product and binding phase of Portland cement paste. It has a poor crystalline structure and variable composition controlled by initial Ca : Si ratio and the calcium ions content [8–10]. By mixing appropriate quantities of magnesium oxide, calcium oxide and silica fume, two sperate phases C-S-H and M-S-H (magnesium silicate hydrates) were observed by Bernard[4]. The structure of C-S-H which is based on single silica chains is clearly different from the sheet like structure of M-S-H. Although both phases are poorly crystalline, have loosely bound water and a variable chemical composition, M-S-H has higher silica polymerization degree than C-S-H[10–14]. In M-S-H, Q³ silicate tetrahedrons are present as the main silica network while C-S-H has mainly Q¹, Q²

silicate tetrahedrons corresponding to the single chain-like structure. As Chiang[15] reported before, the primary units of C-S-H gels are polydisperse multilayer disks while the M-S-H globules can be modelled as polydisperse spheres at nanoscale. As a result, the interaction between C-S-H and M-S-H is negligible.

With magnesium addition into CaO-SiO₂-H₂O system, the decomposition of C-S-H is possibly happened and the calcium concentration in the solution is increased. Magnesium facilitates the formation of brucite or reacts with dissolved silicon ions and leads to the formation of M-S-H[16]. The formation of M-S-H is a slow process at ambient temperature (20~25°C), which could continuous for a quite long time to consume the unreacted silica. At early age, only a small amount of M-S-H would be formed. Magnesium and silica exist as brucite and amorphous silica respectively. Therefore, in the mixed MgO-CaO-SiO₂-H₂O system, the formation of C-S-H and brucite is faster than that of M-S-H at room temperature[4,16]. The limited concentration of magnesium in the solution makes it difficult to be incorporated into the structure of C-S-H or form a single phase magnesium calcium silicate hydrates (M-C-S-H)[3,7]. However, under hydrothermal conditions, G. Qian[6] has confirmed the incorporation of magnesium into tobermorite and xonotlite. Brucite disappears with the increasing time and temperature. The possible presence of magnesium into C-S-H structure was also identified by L. Fernandez[17,18]. The magnesium might be incorporated into the octahedral sites in the interlayer space of dreierketten or the gap of Q^{3p} silicon tetrahedron as tetrahedral magnesium, which depends largely on Ca/Si ratio. The addition of magnesium can also increase crystallinity of C-S-H and the polymerization of silicate chains[19]. Elevating the reaction temperature in MgO-SiO₂-H₂O system has been claimed to have great influence of temperature on hydration behavior[20]. The samples with the same initial Mg/Si cured at different temperature shows quite different results. More brucite was observed in the XRD pattern from the sample cured at ambient temperature than these samples cured at elevated temperature, which shows more formation of M-S-H. The effect of magnesium on the chemical composition and structure of C-S-H is still unclear, which depends on the reaction temperature, the magnesium source and water/solid ratio etc. At present research, the MgO-CaO-SiO₂-H₂O system was investigated via mixing calcium oxide, silica fume and magnesium oxide at 60°C for 72h to obtain the products. The obtained solids were characterized by TEM/EDS, SEM, XRD, FT-IR and TG-DSC. The morphology, chemical composition and structure characteristics of the synthesized phase M-C-S-H would be discussed and compared to that of C-S-H and M-S-H gel.

2. Methodology

2.1 Materials

Pure C-S-H, M-S-H and MgO modified C-S-H gels were synthesized by mixing magnesium oxide (MgO), calcium hydroxide (CaO) and silica fume (SiO₂) at 60 °C. Different Ca/Si molar ratios (0, 0.2, 0.4, 0.5, 0.6 and 0.8) were used in the preparation of M-C-S-H with a total (Mg+Ca)/Si = 0.8. The samples are labelled according to the prepared Mg/Si atomic ratio, i.e. 0.8M, 0.6M, 0.4M, 0.3M, 0.2M and 0M, respectively, as shown in Table 1.

Table 1: Mix proportions.

Sample	CaO	SiO ₂	MgO	Water
	g	g	g	g
0.8M	0.00	10.00	5.33	153.33
0.6M	1.87	10.00	4.00	158.67
0.4M	3.73	10.00	2.67	164.00
0.3M	4.67	10.00	2.00	166.67
0.2M	5.60	10.00	1.33	169.33
0M	7.47	10.00	0.00	174.67

2.2 Methods

All samples were prepared in conical flasks sealed with plastic foils with a water/solid ratio of 10 in order to minimize CO₂ contamination. A high water/solid ratio of 10 was used to ensure sufficient water for dissolution and reaction. The samples were matured in a water bath at 60°C for 3d and then filtered with 0.45 μm Nylon filter. The residues were rinsed first with 50 mL of 1:1 water–ethanol solution and then flashed with 50 mL 94% ethanol solution. The obtained solids were freeze dried for 2d, and ground in an agate mortar before stored in desiccators using sodium hydroxide pellets as CO₂ trap until analysis[4].

XRD measurement was carried out on a D8 Advance X-ray diffractometer using CuKα radiation. The samples were scanned between 5° and 60° 2θ with the scanning speed of 5°/min. TG-DSC experiment was performed with sample mass of 30 to 40mg using a STA449F3 TG-DSC with a heating rate of 20°C/min from 50 to 980 °C. FT-IR spectra were recorded on a Nicolet 6700 FT-IR spectrometer using the attenuated total reflection (ATR) method. The investigated frequency range was from 400 to 4000 cm⁻¹ with a resolution of 1 cm⁻¹. SEM investigations were carried out with a JSM-IT300 SEM and TEM investigations were done with a JEM-2100F microscope.

3. Results and discussion

3.1 XRD

Figure 1 shows the XRD patterns of samples M-S-H, C-S-H and MgO modified C-S-H samples, respectively. As can be seen, the pure M-S-H (Mg/Si =0.8) has a semi-crystalline structure indicated by the broad Bragg reflections at 20.1, 35.1 and 59.9° (2θ). The result is in good agreement with previous finding about the crystalline structure of M-S-H[21–23]. Besides, the existence of silica fume is clearly shown by the broad peak of about 20° 2θ[12]. The reflection peaks of pure C-S-H (Ca/Si = 0.8) at 16.3, 29.3, 32.0, 43.0, 49.7 and 55.1 °2θ is attributed to a poorly-ordered 14Å tobermorite (5CaO·6SiO₂·9H₂O, PDF 00-029-0331). The XRD patterns of samples containing Mg and Ca show the Bragg reflections both shown in M-S-H and C-S-H, and the changes on Mg/Ca ratio makes no big difference. Besides, for the samples with higher initial Ca/Si ratio, the formation of brucite is also found. Furthermore, it can be seen that the intensity of M-S-H gel, magnesium hydroxide and unreacted silica fume gradually decreases with the decrease of Mg/Si ratio. For instance, the reflections of sample 0.4M at 20.1, 35.1 and 59.9° 2θ almost disappear. However, the intensity of C-S-H gel is gradually increased with the decrease of Mg/Si ratio, especially for the reflection located at 29.3 °2θ.

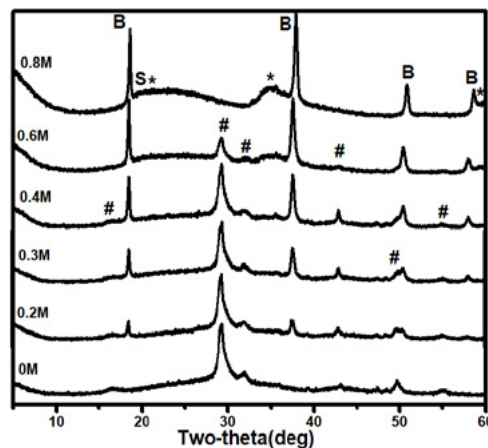


Figure 1: XRD patterns of the synthesized samples (S=silica fume, B=brucite, *=M-S-H, #=C-S-H).

3.2 FTIR

Figure 2 shows FT-IR spectra of six samples. The pure C-S-H ($\text{Ca/Si} = 0.8$) shows a OH stretching vibrations at 3442 cm^{-1} and H-OH bending vibrations of molecular water at 1639 cm^{-1} . Furthermore, the spectrum contains an Si-O-Si bending band at 662 cm^{-1} and Si-O stretching vibration bands at 971 cm^{-1} (Q^2 tetrahedra) and 876 cm^{-1} (Q^1 tetrahedra)[24]. The pure M-S-H ($\text{Mg/Si} = 0.8$) shows Mg-OH stretching vibrations at 3692 cm^{-1} and other OH vibrations at 3439 cm^{-1} together with H-OH bending vibrations of non-structural water at 1637 cm^{-1} . Besides, the sample also shows a Si-O-Si bending band at 899 cm^{-1} and Si-O stretching vibration bands at 798 cm^{-1} (unreacted silica fume), 1017 cm^{-1} (Q^3) [21]. The bands in the range of $1400\text{--}1500 \text{ cm}^{-1}$ correspond to the asymmetric stretching of CO_3^{2-} . It is difficult to prevent carbonation when the sample is exposed to air. 0.6M sample shows the similar spectra to that of 0.8M sample. It shows a Si-O-Si bending band at 899 cm^{-1} and Si-O stretching vibration bands at 798 cm^{-1} (unreacted silica fume), 1017 cm^{-1} (Q^3), indicating that M-S-H gel remains the major reaction product at higher Mg-Si ratios and the amount of unreacted silica fume decreases. The presence of magnesium (0.4M, 0.3M, 0.2M) does not further influence the position of the C-S-H band, but decreases its relative intensity. The disappearance of the Si-O stretching vibration bands at 798 cm^{-1} is in consistence with the XRD results that silica fume is completely consumed. It can be concluded that the formation of C-S-H is faster than that of M-S-H, which is in line with previous findings that the formation of M-S-H is extremely slow that equilibrium has not yet been reached even after 1 year[4]. The constant position of the bands in the presence of varying fractions of C-S-H and M-S-H is in consistence with the presence of two different phases.

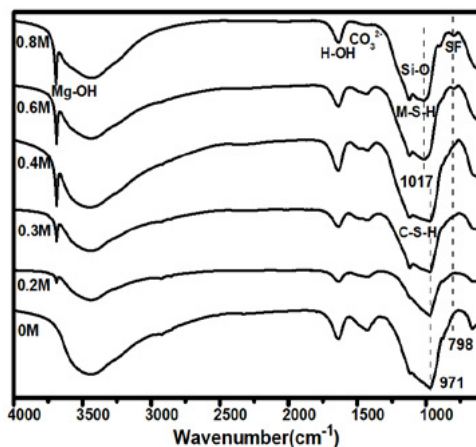


Figure 2: FT-IR spectra of the synthetic M-C-S-H samples

3.3 TG-DSC

Figure 3 shows the TG/DTG data of M-C-S-H sample. In general, the results can be classified into two stages [12]: the loss of loosely bound interlayer water between 50 and $250 \text{ }^\circ\text{C}$; weight loss between $250 \text{ }^\circ\text{C}$ and $800 \text{ }^\circ\text{C}$ associated with the dehydroxylation of magnesium hydroxide and silanol groups. The pure C-S-H ($\text{Ca/Si} = 0.8$) gel shows a main water loss between 50 and $250 \text{ }^\circ\text{C}$, which can be attributed to the dehydration of interlayer water. No weight loss is observed at $400 \text{ }^\circ\text{C}$ in the pure C-S-H gel, indicating that calcium hydroxide is absent and all calcium is incorporated in C-S-H. The TG-DTG data is in line with the differential scanning calorimeter (DSC) results (shown in Figure 4), and the peaks at $850 \text{ }^\circ\text{C}$ indicates a distinct exothermic transition, which can be attributed to the decomposition of wollastonite or enstatite [4,25]. The existence of brucite in

the sample containing magnesium indicates that C-S-H is more stable than M-S-H or alternatively that the formation of M-S-H is much slower than that of C-S-H, which is in line with the FT-IR data. The weight loss of interlayer water in samples containing magnesium shows no difference, while that of C-S-H is significantly larger. It indicates that more water molecules are incorporated into the structure of C-S-H and the transformation from SiO₂ to C-S-H is easier at high pH, consuming more water molecules to enhance the reaction.

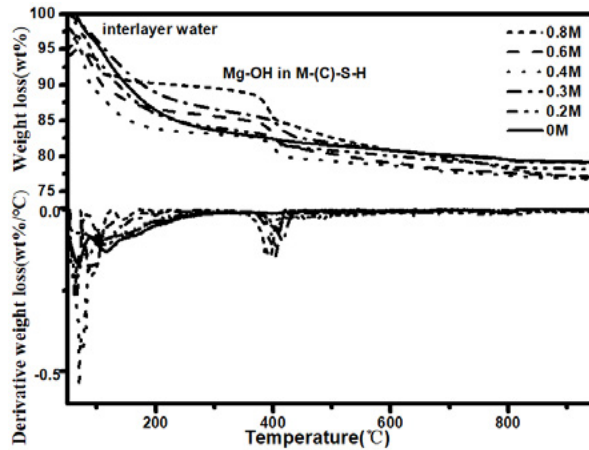


Figure 3: Weight loss determined by thermogravimetric analysis and 1st derivative of M-C-S-H samples

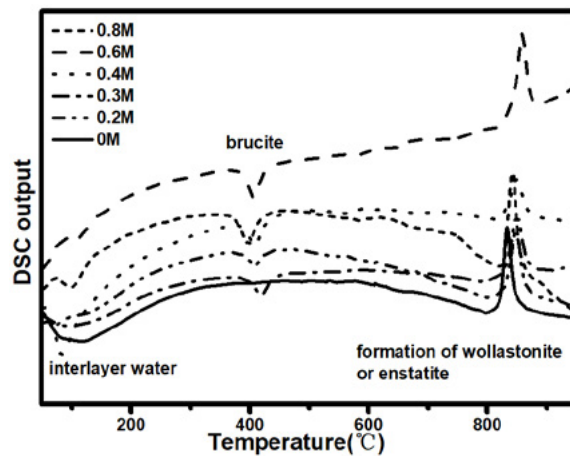


Figure 4: DSC curves of M-C-S-H samples

3.4 Microscopic analysis (SEM/TEM)

Fig. 5 shows the morphology of the pure C-S-H, M-S-H and MgO modified C-S-H gel obtained by SEM. Figure 5a) evidences an irregular porosity between interconnected and densely packed spherical particles at the micron level in M-S-H[26]. However, the morphology of pure C-S-H shows great difference from M-S-H. Figure 5c) exhibits foil-like objects arranging in a dense, laminar pattern. 0.4M Sample (shown in Figure 5b)) is similar in morphology to pure C-S-H. However, the foils are more distinct in a less extended network structure. The addition of MgO changes the microstructure of C-S-H and M-S-H more or less. Obviously, the formation of C-S-H play a dominant role in MgO-CaO-SiO₂ system.

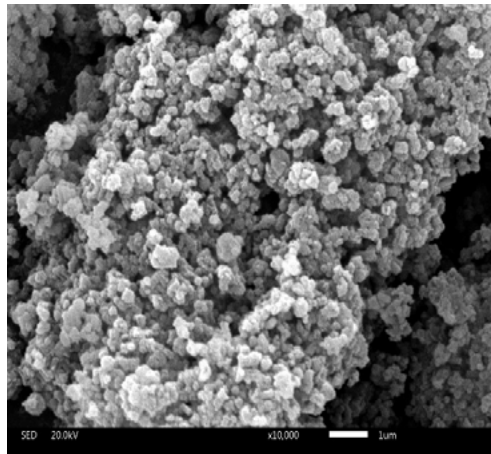


Figure 5a): SEM image of 0.8M sample

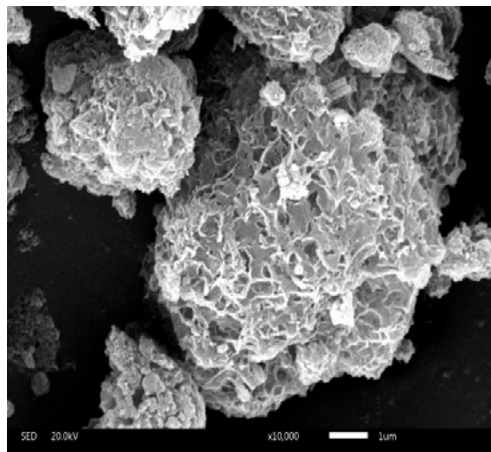


Figure 5b): SEM image of 0.4M sample

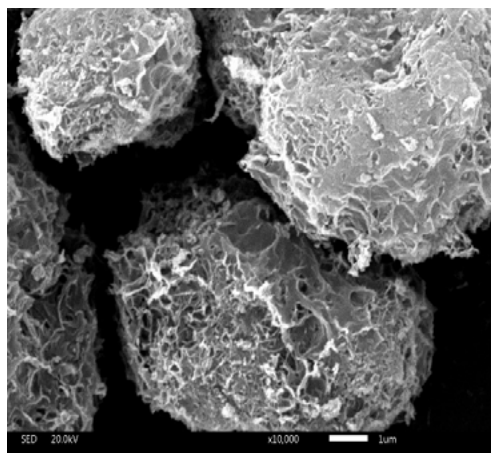


Figure 5c): SEM image of 0M sample

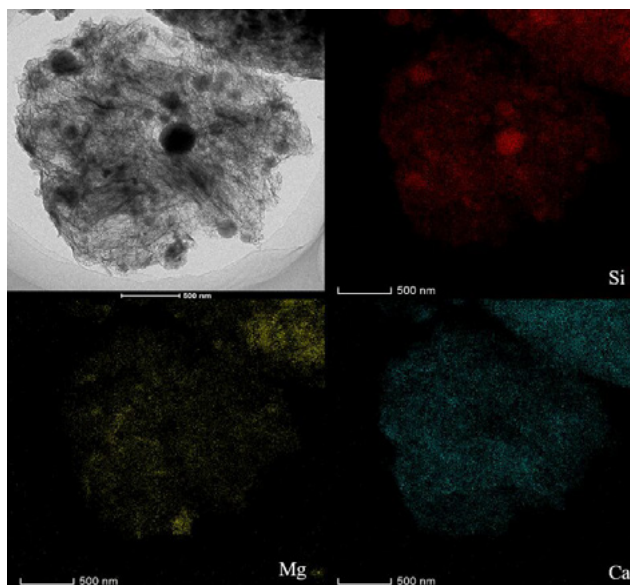


Figure 6: TEM characterizations of the 0.4M–0.4-C-S-H sample and EDS mappings of magnesium, calcium and silicon

The TEM picture of 0.4M sample in Figure 6 illustrates that MgO modified C-S-H gel exhibits a layered texture characteristic. This area is homogeneous and the SiO₂ grain is also shown, revealing that the formation of M-C-S-H gel is a process of dissolution, diffusion and precipitation, and the reaction starts on the surface of SiO₂ particles. The EDS data confirms the existence of an evenly distributed phase where the calcium and magnesium elements are distributed homogeneously, indicating the presence of large amounts of calcium in M-S-H or magnesium in C-S-H phase and the possible formation of the new phase M-C-S-H.

4. Conclusions

By mixing MgO, CaO with silica fume and water at 60°C for 3d, pure C-S-H, M-S-H and MgO modified C-S-H gels were successfully prepared. The structure and properties were confirmed by FT-IR, XRD, TG-DSC, SEM and TEM-EDS. Based on the results discussed above, the following conclusions can be drawn:

1. The hydration products in MgO-CaO-SiO₂ system are mainly brucite, M-S-H gel and C-S-H gel. The formation of C-S-H is faster than that of M-S-H under the same conditions, probably due to the higher dissolution of portlandite than brucite, strongly limiting the concentration of magnesium in the solution.
2. Increasing Ca/Si ratio in MgO-CaO-SiO₂ system benefits the reaction among silica fume, magnesium oxide and calcium oxide, which contributes to a more extended network structure.
3. The microstructure of M-S-H is different from that of C-S-H. In MgO-CaO-SiO₂ system, the hydration products show more similarities to C-S-H.
4. The possible formation of a new phase M-C-S-H where magnesium, calcium and silicon elements distribute homogeneously in a nanoscale was observed by TEM-EDS. However, the formation process of the new phases remains unclear, which requires further investigation.

5. Acknowledgment

This research has been financially supported by the National Natural Science Foundation of China (grant

numbers 51672199); the Fundamental Research Funds for the Central Universities (grant number WUT: 2017-YB-008□ 2019III018GX); and the 111 Project (No. B18038)

6. References

- [1] M. Schneider, M. Romer, M. Tschudin, H. Bolio, Sustainable cement production-present and future, *Cem. Concr. Res.* 41 (2011) 642–650. doi:10.1016/j.cemconres.2011.03.019.
- [2] A. Machner, M. Zajac, M. Ben Haha, K.O. Kjellsen, M.R. Geiker, K. De Weerd, Limitations of the hydrotalcite formation in Portland composite cement pastes containing dolomite and metakaolin, *Cem. Concr. Res.* 89 (2018) 89–106. doi:10.1016/j.cemconcomp.2018.02.013.
- [3] E. Bernard, B. Lothenbach, C. Cau-Dit-Coumes, C. Chlique, A. Dauzères, I. Pochard, Magnesium and calcium silicate hydrates, Part I: Investigation of the possible magnesium incorporation in calcium silicate hydrate (C-S-H) and of the calcium in magnesium silicate hydrate (M-S-H), *Appl. Geochemistry.* 89 (2018) 229–242. doi:10.1016/j.apgeochem.2017.12.005.
- [4] B. Lothenbach, D. Nied, E. L'Hôpital, G. Achiedo, A. Dauzères, Magnesium and calcium silicate hydrates, *Cem. Concr. Res.* 77 (2015) 60–68. doi:10.1016/j.cemconres.2015.06.007.
- [5] O.P. Shrivastava, S. Komarneni, E. Breval, Mg²⁺ uptake by synthetic tobermorite and xonotlite, *Cem. Concr. Res.* 21 (1991) 83–90. doi:10.1016/0008-8846(91)90034-F.
- [6] G. Qian, G. Xu, H. Li, A. Li, Mg-Xonotlite and its coexisting phases, *Cem. Concr. Res.* 27 (1997) 315–320. doi:10.1016/S0008-8846(97)00018-5.
- [7] E. Bernard, A. Dauzères, B. Lothenbach, Magnesium and calcium silicate hydrates, Part II: Mg-exchange at the interface “low-pH” cement and magnesium environment studied in a C-S-H and M-S-H model system, *Appl. Geochemistry.* 89 (2018) 210–218. doi:10.1016/j.apgeochem.2017.12.006.
- [8] H.F.W. Taylor, *Cement chemistry*. 2nd ed., Acad. Press. (1997). doi:10.1016/S0958-9465(98)00023-7.
- [9] A.J. Allen, J.J. Thomas, H.M. Jennings, Composition and density of nanoscale calcium-silicate-hydrate in cement, *Nat. Mater.* 6 (2007) 311–316. doi:10.1038/nmat1871.
- [10] I.G. Richardson, The calcium silicate hydrates, *Cem. Concr. Res.* 38 (2008) 137–158. doi:10.1016/j.cemconres.2007.11.005.
- [11] A. Hartmann, D. Schulenberg, J.-C. Buhl, Synthesis and Structural Characterization of CSH-Phases in the Range of C/S = 0.41 - 1.66 at Temperatures of the Tobermorite Xonotlite Crossover, *J. Mater. Sci. Chem. Eng.* 3 (2015) 39–55. doi:10.4236/msce.2015.311006.
- [12] E. Bernard, B. Lothenbach, D. Rentsch, I. Pochard, A. Dauzères, Formation of magnesium silicate hydrates (M-S-H), *Phys. Chem. Earth.* 99 (2017) 142–157. doi:10.1016/j.pce.2017.02.005.
- [13] D.A. Kulik, Improving the structural consistency of C-S-H solid solution thermodynamic models, *Cem. Concr. Res.* 41 (2011) 477–495. doi:10.1016/j.cemconres.2011.01.012.
- [14] D. Nied, K. Enemark-Rasmussen, E. L'Hôpital, J. Skibsted, B. Lothenbach, Properties of magnesium silicate hydrates (M-S-H), *Cem. Concr. Res.* 79 (2016) 323–332. doi:10.1016/j.cemconres.2015.10.003.
- [15] W. Chiang, G. Ferraro, E. Fratini, F. Ridi, Y. Yeh, U. Jeng, S. Chen, P. Baglioni, Multiscale structure of calcium- and magnesium-silicate-hydrate gels, *J. Mater. Chem. A Mater. Energy Sustain.* 2 (2014) 12991–

12998. doi:10.1039/C4TA02479F.

[16] E. Bernard, B. Lothenbach, F. Le Goff, I. Pochard, A. Dauzères, Effect of magnesium on calcium silicate hydrate (C-S-H), *Cem. Concr. Res.* 97 (2017) 61–72. doi:10.1016/j.cemconres.2017.03.012.

[17] L. Fernandez, C. Alonso, A. Hidalgo, C. Andrade, The role of magnesium during the hydration of C3S and C-S-H formation. Scanning electron microscopy and mid-infrared studies, *Adv. Cem. Res.* 17 (2005) 9–21. doi:10.1680/adcr.2005.17.1.9.

[18] L. Fernandez, C. Alonso, C. Andrade, A. Hidalgo, The interaction of magnesium in hydration of C3S and CSH formation using ²⁹Si MAS-NMR, *J. Mater. Sci.* 43 (2008) 5772–5783. doi:10.1007/s10853-008-2889-2.

[19] N.Y. Mostafa, E.A. Kishar, S.A. Abo-El-Enein, FTIR study and cation exchange capacity of Fe³⁺- and Mg²⁺-substituted calcium silicate hydrates, *J. Alloys Compd.* 473 (2009) 538–542. doi:10.1016/j.jallcom.2008.06.029.

[20] J. Szczerba, R. Prorok, E. Snie, D. Madej, K. Ma, Influence of time and temperature on ageing and phases synthesis in the MgO–SiO₂–H₂O system, *Thermochim. Acta.* 567 (2013) 57–64. doi:10.1016/j.tca.2013.01.018.

[21] D.R.M. Brew, F.P. Glasser, Synthesis and characterisation of magnesium silicate hydrate gels, *Cem. Concr. Res.* 35 (2005) 85–98. doi:10.1016/j.cemconres.2004.06.022.

[22] A.A.-T. Fei Jin, Strength and hydration products of reactive MgO–silica pastes, *Cem. Concr. Compos.* 37 (2008) 1285–1288. doi:10.1016/j.cemconcomp.2014.04.003.

[23] T. Zhang, C.R. Cheeseman, L.J. Vandeperre, Development of low pH cement systems forming magnesium silicate hydrate (M-S-H), *Cem. Concr. Res.* 41 (2011) 439–442. doi:10.1016/j.cemconres.2011.01.016.

[24] P. Yu, R.J. Kirkpatrick, B. Poe, P.F. McMillan, X. Cong, Structure of Calcium Silicate Hydrate (C-S-H): Near-, Mid-, and Far-Infrared Spectroscopy, *J. Am. Ceram. Soc.* 82 (1999) 742–748. doi:10.1111/j.1151-2916.1999.tb01826.x.

[25] Y. Wei, W. Yao, X. Xing, M. Wu, Quantitative evaluation of hydrated cement modified by silica fume using QXRD, ²⁷Al MAS NMR, TG-DSC and selective dissolution techniques, *Constr. Build. Mater.* 36 (2012) 925–932. doi:10.1016/j.conbuildmat.2012.06.075.

[26] W.S. Chiang, G. Ferraro, E. Fratini, F. Ridi, Y.Q. Yeh, U.S. Jeng, S.H. Chen, P. Baglioni, Multiscale structure of calcium- and magnesium-silicate-hydrate gels, *J. Mater. Chem. A.* 2 (2014) 12991–12998. doi:10.1039/c4ta02479f.

[27] H.M. Jennings, J.J. Thomas, J.J. Chen, D. Rothstein, Cement Paste as a Porous Material, *Handb. Porous Solids.* (2002) 2971–3028. doi:10.1002/9783527618286.

Impact of steel fibre content on the fibre network structure of ultra-high performance fibre reinforced concrete (UHPFRC)

Q. Song^{1,2}, Z. Shui¹, R. Yu^{1*}, S. Rao^{1,2}

¹State Key Laboratory of Silicate Materials for Architectures, Wuhan University of Technology, Wuhan 430070, China;

²School of Materials Science and Engineering, Wuhan University of Technology, Wuhan 430070, China

Abstract

This paper address the impact of steel fibre content on the fibre network structure of ultra-high performance fibre reinforced concrete (UHPFRC). Firstly, the design of the concrete mixtures is based on the aim to achieve a densely compacted cementitious matrix, employing the modified Andreasen & Andersen particle packing model. And, six fibre content, including 0, 0.5, 1, 1.5, 2, 2.5 and 3 vol.% are used in this study. Then, the effect of fibre content on the properties of UHPFRC is analysed, including the fresh properties and mechanics properties. Moreover, the X-ray CT is employed to evaluate the fibres distribution and directions in hardened UHPFRC. The obtained results show that with an increase of steel fibre content, the fresh properties of the UHPFRC and the fibre efficiency of mechanics properties improvement decrease. The X-ray CT results imply that with an increase of fibre content, the fibre connected probability will be increased and the 2 vol. % is a break point.

Keywords: Ultra-high performance fibre reinforced concrete (UHPFRC), fibre content, hybrid fibre, fibre network structure

1. Introduction

Ultra-High Performance Fibre Reinforced Concrete (UHPFRC) is a new kind of cement based composite material, which exhibits advanced mechanical properties, excellent durability, and high toughness. The main differences between UHPFRC and normal concrete (NC) or high-performance concrete (HPC) are high content of cementitious materials, low water to binder ratio (W/B), and high content of superplasticizer [1-11]. Moreover, to improve its ductility, toughness, flexural and shear strengths, steel fibres are normally used in the production of UHPFRC, since the utilized fibres can bridge cracks and prevent the cracks extended in the concrete [12-16]. Many studies have reported the positive influence of steel fibre on the UHPFRC, including the fibre content, fibre shape and fibre physical parameters (length, diameter etc.) [17-24]. However, in most cases, the fibres are added into the concrete directly and randomly, and the fibre network structure in the concrete are not clear, which is equal to a black box treatment. Based on available literatures [25-27], it can be concluded that the statement of fibre are important factors for improving concrete properties and fibre efficiency in fibre reinforced concrete. For example, the anisotropic properties of fibre reinforced concrete are caused by the orientation distribution of fibres [25, 26] and Bensaid et al. investigated the flexural behavior of steel fibre-reinforced concrete, it fund that the flexural behavior are significantly improved by the fibre orientation [27]. Hence, to effectively improve the fibre efficiency in

UHPFRC, the fibre network structure should be optimized.

In fact, the statement of fibres have been studied in normal concrete system and some achievements have already been obtained [28-35]. For instance, the distribution and orientation of steel fibres in the concrete can be adjusted by magnetic field, since the steel fibres are ferromagnetic. For instance, Torrents et al. [28] and Al-Mattarneh [29] investigated the effect of magnetic field on steel fibres distribution and orientation. It was found that the used magnetic field is beneficial for optimizing the fibre orientation. Nevertheless, due to the fact that the used steel fibres in concrete can also be magnetized and attracted to each other in the magnetic field, the homogeneity of the fibre distribution may be significantly disturbed, which cause that the mechanical properties of the fibre reinforced concrete are also decreased. Hence, it is logical to find other methods to control the fibre orientations and distributions.

As commonly known, the added steel fibres content in UHPFRC are much higher (2-6% by volume) than the normally steel reinforced concrete, which means there is a high chance for the fibres to connect/tough each other. When the amount of interconnected fibre is relatively large, a potential steel fibres network structure can be generated. Therefore, if one point of this potential steel fibres network structure is attacked by the harmful irons (e.g. Cl-) in the marine environment, the whole UHPFRC structure can be seriously corroded and damaged. In this case, the steel fibres network structure can be treated as a steel re-bar or other metal conductors that buried in the concrete materials without safe protection layer. Generally, the fibre interconnection induce corrosion problem in common concrete has not attracted enough attentions, since the added steel fibre amount is relatively low (about 0.5% vol.) in normal steel fibre reinforced concrete (SFRC), and very limited data can be found in available literature. Therefore, it is necessary and important to study the impact of fibre content on the fibre network of the UHPFRC.

Based on the entire premise listed above, the impact of steel fibres content on the fibre network of UHPFRC is investigated in this study. First of all, to obtain a densely packed concrete skeleton, the modified Andersen & Andreasen model is employed. Then, the properties of the UHPFRC with different fibre amount are evaluated, including flowability, mechanical. Lastly, X-ray computed tomography (X-ray CT) is utilized to detailed clarify the fibres network structure in hardened UHPFRC.

2. Methodology

2.1 Materials

PC 52.5 cement, fly ash, silica fume, metakaolin are treated as cementitious materials in this study, and their chemical compositions are shown in Table 1. Two types of fine aggregates (0–0.6mm and 0.6-1.25 mm natural river sand) are utilized. A polycarboxylic ether based superplasticizer is employed to meet the flowability requirements for the designed UHPFRC. Additionally steel fibre (13 mm length and 0.2 mm diameter) is also included in the UHPFRC production

Table 1: Chemical composition of the used powders in this study (wt. %)

Compositions	Na ₂ O	MgO	Al ₂ O ₃	SiO ₂	P ₂ O ₅	SO ₃	K ₂ O	CaO	Fe ₂ O ₃	LOI
Cement	0.09	1.61	4.18	19.2	0.09	3.35	0.78	64.93	3.32	2.49
Silica fume	0.13	0.47	0.25	94.65	0.17	0.69	0.84	0.36	0.15	2.29
Fly ash	0.33	0.23	38.01	46.44	0.06	0.69	0.88	7.5	3.12	2.79

In this research, the mixtures of the UHPFRC are presented in Table 2. It can be found that the fibres amount added in the UHPFRC are 0.5%, 1.0%, 1.5%, 2.0%, 2.5% and 3.0%(vol.), respectively. In addition, the particle size of materials and the derived comparison between the optimized and target grading curves of the UHPFRC matrix are presented in Figure 1.

Table 2: Recipe of the designed UHPFRC with different steel fibres dosage

	C (kg/m ³)	FA (kg/m ³)	SF (kg/m ³)	Sand-1 (kg/m ³)	Sand-2 (kg/m ³)	Water (kg/m ³)	Sp (kg/m ³)	SSF (vol.%)
1	750	200	144	770	220	190	30	0.0
2	750	200	144	770	220	190	30	0.5
3	750	200	144	770	220	190	30	1.0
4	750	200	144	770	220	190	30	1.5
5	750	200	144	770	220	190	30	2.0
6	750	200	144	770	220	190	30	2.5
7	750	200	144	770	220	190	30	3.0

(C: Cement, FA: Fly Ash, SF: Silica Fume, Sand-1: sand 0-0.6 mm, Sand-2: sand 0.6-1.25 mm, Sp: superplasticizer, SSF: straight steel fibres)

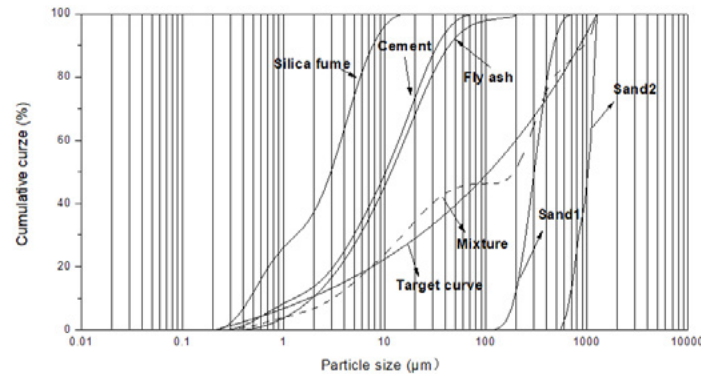


Figure 1: Particle size distributions (PSDs) of the involved ingredients, the target and optimized grading curves of the UHPFRC mixtures

2.2 Methods

After mixing, the flowability of the designed fresh UHPFRC is measured in accordance with the GB/T 2419-2005. Firstly, the mixtures are filled in a conical cone with the form of a frustum, respectively. Secondly, the molds are lifted vertically so as to allow a free flow for the paste without any jolting. Eventually, two diameters perpendicular to each other are measured, and their mean value is treated as the slump flow of the developed UHPFRC. The mechanical properties of concrete are tested according to EN 196-1(2005). Flexural strength tests are carried out at 28 days.

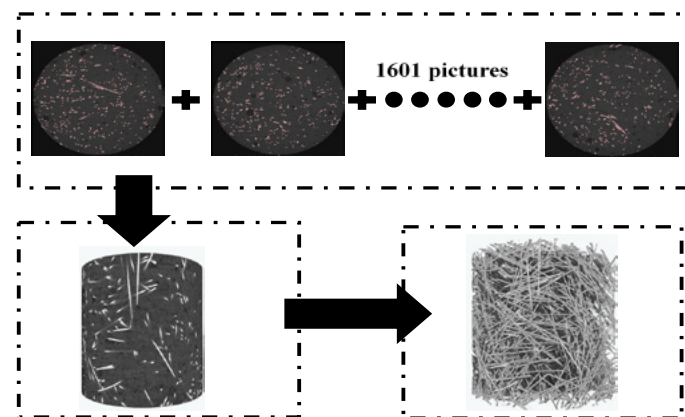


Figure 2: The rebuilt process of the designed UHPFRC 3D structure

The distribution of steel fibres is analyzed by the system of Zeiss Xradia 510 versa X-ray CT in this experiment. The general principle of this test can be summarized as follows: 1) The density of the fiber and the UHPFRC matrix is different; 2) Therefore, when the X ray passes through the specimen, different grayscales could be observed; 3) The utilized steel fibres have the largest density in the designed UHPFRC, so its gray value expressed should be also the largest, which cause that the steel fibres displayed in the

CT images are relatively white [30]. The X-ray CT system is composed by the X-ray source, detector and sample table. The three-dimensional structure information inside the sample can be obtained by rotating the sample in the range of 360 degrees. In order to clearly understand the network structure of steel fibres in UHPFRC, the sample size is 40mm×40mm×100mm and a total of 1601 sequential scan 2D-images are captured, which is 2048×2048 pixel². Then, the 3D structure of designed UHPFRC can be rebuilt with the soft of object research system (ORS) visual SI (as shown in Figure 2).

3. Results and discussion

3.1 Fresh properties of the designed UHPFRC

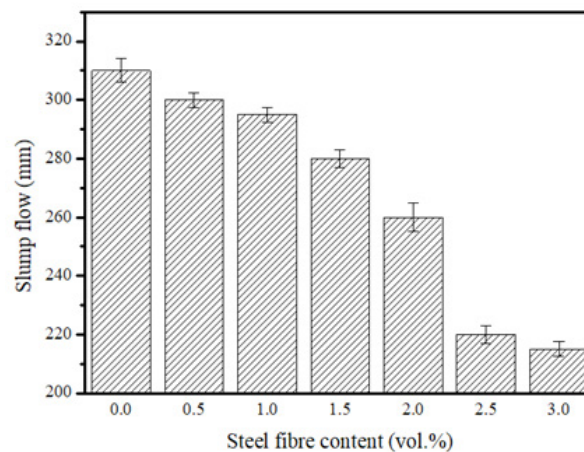


Figure 3: Flowability of the designed UHPFRC with different steel fibre amount

Figure 3 shows the flowability of the UHPFRC with different fibre amounts (0%~3%). It can be found that the flowability of the UHPFRC decreases with an increase of fibres amount. In general, the variation of the tested UHPFRC with different fibres content can be divided into three periods: Firstly, the decline of UHPFRC flowability is relatively slow (from 315mm to 260mm) with the increase of fibres amount increases from 0.5% to 2.0%; Then, the decline of UHPFRC flowability becomes quick (from 260mm to 220mm) when the added fibre is enhanced from 2.0% to 2.5%. Lastly, if the added steel fibre amount is further increased from 2.5% to 3.0%, the flowability of designed UHPFRC almost keeps stable (about 220mm).

These phenomena mentioned above may be caused by the formation of fibres network structure in UHPFRC, which could significantly enhance the flowing resistance for the tested fresh UHPFRC. Similar as the results presented in [31], the negative influence of fibres “skeleton” on the flowability of UHPFRC has already been investigated. Additionally, the three periods for the UHPFRC flowing process with different content of steel fibres can be explained by the relationship between the steel fibre numbers and the sample volume. For example, when the steel fibres content is relatively low (less than 2%), due to the activity space for steel fibres inside the UHPFRC is enough, very limited amount of fibres join the network formation, which simultaneously causes that the decreasing rate of the UHPFRC flowability is relatively small. However, when the added steel fibres content increases from 2.0% to 2.5%, the free activity space for the steel fibres is decreasing, and more fibres could connect to each other, which could significantly resistant the fibres movement and UHPFRC flowing. When the steel fibres content is further enhanced to about 3%, the fibres network structure could be further strengthened and improved, and the activity space for fibres is still very limited. Hence, the UHPFRC flowability still keeps at a relatively low level. In general, based on the fresh behavior of the designed UHPFRC, it can be summarized that the 2% (vol.) is a critical fibres amount to design UHPFRC with great flowability, with which the interconnection between fibres may be effectively limited.

3.2 Mechanical properties of the designed UHPFRC

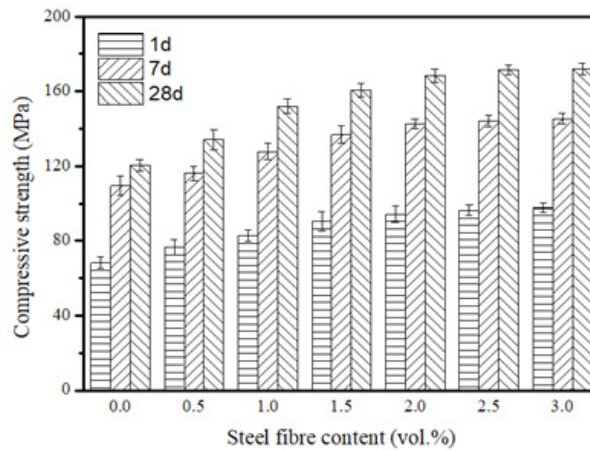


Figure 4: Compressive strength of the designed UHPFRC with different steel fibre amount at 1d, 7d, 28d

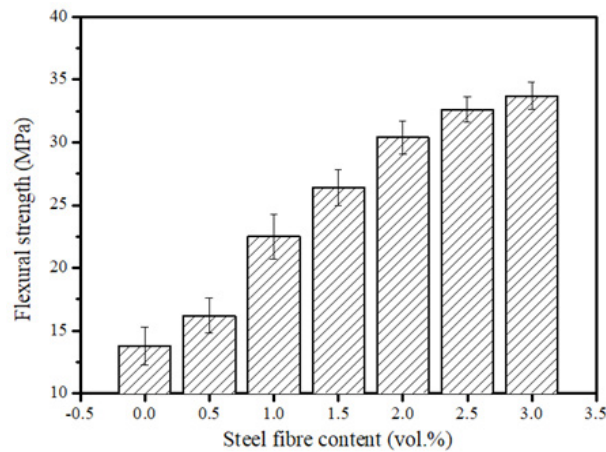


Figure 5: Flexural strengths of the designed UHPFRC with different steel fibre amount at 28d

The compressive strength of the developed UHPFRC are presented in Figure 4. It can be noticed that the compressive strength of the UHPFRC can be gradually enhanced with an increase of the fibres amount, which is similar as that presented in available literature [32]. Here, the compressive strength of the designed UHPFRC with 2% steel fibres can reach to about 168MPa at 28d, which can be explained by the role of high active powders and optimized particle packing model (as shown in [33]). However, when the fibres amount increased from 2.0% to 3.0%, the compressive strength improvement for the designed UHPFRC is limited. Furthermore, the flexural strength of the UHPFRC is presented in Figure 5. As it shown, the flexural strength of the UHPFRC significantly increases with the fibres amount increased. But, when the fibres amount increases from 2.0% to 2.5% or 2.5% to 3.0%, the flexural strength increasing rate is reduced, which implies that more steel fibres are connected to each other and the fibres efficiency is decreasing. Hence, it can be predicted that 2.0% (vol.) is an appropriate steel fibres content in UHPFRC produced.

Generally, based on the mechanical properties of the designed UHPFRC, it can be summarized that the 2% (vol.) is a critical steel fibres amount to effectively improve the fibres efficiency in UHPFRC, since the interconnection between fibres may be effectively limited in this case.

3.3 The 3D structure of the designed UHPFRC

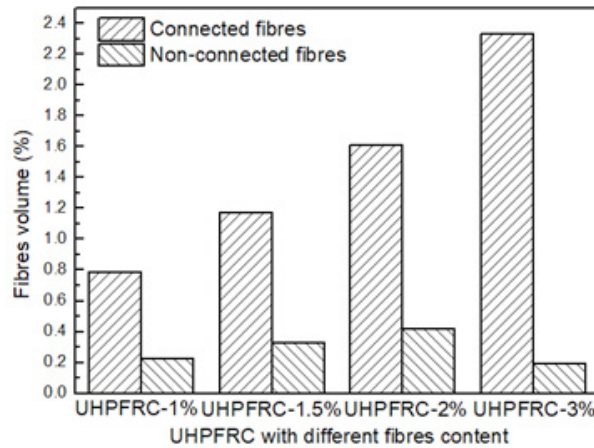


Figure 6: Results of the connected and non-connected steel fibres in the developed UHPFRC

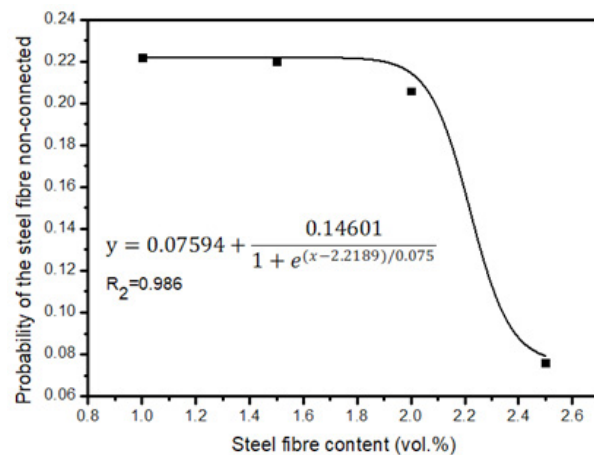


Figure 7: The probability for the steel fibres connecting to each other in the designed UHPFRC with different fibre amount

All the above shown experimental results imply the generation of steel fibres network structure in the developed UHPFRC. To more directly clarify the existence of the steel fibres network structure, the X-ray CT method is employed in this research. Figure 6 present the connected and non-connected steel fibres in the designed UHPFRC with 1.0%, 1.5%, 2.0% and 2.5% (vol.) steel fibres, respectively. Here, based on the obtained X-ray CT results, the total steel fibres amount can be measured by the software of object research system (ORS) visual SI, which is quite similar as the experimental addition. This also proves that the obtained X-ray CT results and relative software are reliable. Moreover, it is important to notice that the connected steel fibres volume increases (from about 0.79% to 2.33%) with an enhancement of the added steel fibres amount (from 1.0% to 2.5%, vol.). Nevertheless, different from the connected fibres amount variation trend, the non-connected steel fibres content is increased at first and then gradually decline. For example, when the added steel fibres content increases from 1.0% to 2.0% (vol.), the non-connected steel fibres volume also increases from about 0.23% to 0.42%. Meanwhile, when the added steel fibres content increases from 2.0% to 2.5% (vol.), the non-connected steel fibres volume decreases to only about 0.19%.

In general, these phenomena mentioned above could be attributed to the relationship between the steel fibres number and the UHPFRC internal space. To be specific, when the steel fibres content is relatively low (less than 2.0% vol.), there is enough space for the fibres movement inside the UHPFRC sample. Therefore, the originally added steel fibres can be easily divided into two parts: connected steel fibres and non-connected steel fibres. When the added steel fibres amount is increased from 1.0% to 2.0% (vol.), the connected steel fibres volume and non-connected steel fibres volume could be simultaneously enhanced.

However, when the steel fibres content is relatively high (more than 2.5% vol.), the remaining space for fibres movement inside the UHPFRC specimen is quite limited, which could cause a corresponding decline of the non-connected steel fibres volume. Similar as shown in Figure 7, the probability for the steel fibres connecting to each other will generally increase with an enhancement of the added total steel fibres amount. During this process, a great improvement of the probability can be observed when the steel fibres content is increased from 2.0% to 2.5% (vol.).

Based on the X-ray CT results, the interconnection of the steel fibres in UHPFRC is carefully clarified. It is important to notice that 2% (vol.) steel fibres can be treated as a critical value in restricting the fibres interconnection, which could also be used to explain the phenomena observed in Sections 3.1-3.2 (fresh behaviour and mechanical properties of the developed UHPFRC).

4. Conclusions

This research addresses the impact of steel fibre content on the fibre network structure of ultra-high performance fibre reinforced concrete (UHPFRC). Based on the experiment results, the following conclusions can be obtained:

1) As the fibres content increased, the flowability of the fresh UHPFRC gradually decreases. This UHPFRC flowability decline can be explained by the steel fibres interconnection in the UHPFRC. Additionally, the 2% (vol.) is a critical steel fibres amount to produce UHPFRC with great flowability, with which the interconnection between fibres may be effectively limited.

2) The compressive and flexural strengths could be improved by an increasing of added steel fibres content. Similar as the flowability test results, the 2% (vol.) is a critical steel fibres amount to effectively improve the fibres efficiency in UHPFRC, since the interconnection between fibres may be effectively limited in this case.

3) The X-ray CT method could be suitably used in investigating the fibres distribution in the hardened UHPFRC. It is important to found that, with an increase of the total added fibres amount, the non-connected steel fibres content is increased at first and then gradually decline. The 2% (vol.) steel fibres can be treated as a critical value in restricting the fibres interconnection.

5. Acknowledgment

The authors acknowledge the financial supports of National Nature Science Foundation Project of China (No. 51608409), National Nature Science Foundation Project of China (51679179), Major science and technology project in Zhongshan city, Guangdong province (2017A1021), Yang Fan plan of Guangdong Province (201312C12), Open research project of Advanced Engineering Technology Research Institute of Wuhan University of technology in Zhongshan city (WUT201802).

6. References

- [1] Richard P., Cheyrezy M., Composition of reactive powder concretes, *Cement and Concrete Research*, 1995; 25 (7): 1501-1511.
- [2] Habel K., Viviani M., Denarié E., et al. Development of the mechanical properties of an Ultra-High Performance Fibre Reinforced Concrete (UHPFRC). *Cement and Concrete Research*, 2006; 36:1362–1370.
- [3] Yu R., Spiesz P., Brouwers H.J.H., Mix design and properties assessment of Ultra- High Performance Fibre Reinforced Concrete (UHPFRC), *Cement and Concrete Research*, 2014; 56: 29-39.

-
- [4] N.V. Tuan, G. Ye, K.V. Breugel, et al. Hydration and microstructure of ultra-high performance concrete incorporating rice husk ash. *Cement and Concrete Research*, 2011; 41: 1104–1111.
- [5] Máca P., Sovják R., Konvalinka P., Mix design of UHPFRC and its response to projectile impact. *International Journal of Impact Engineering*, 2014; 63: 158-163.
- [6] Yu R., Spiesz P., Brouwers H.J.H., Effect of nanosilica on the hydration and microstructure development of Ultra-High Performance Concrete (UHPC) with a low binder amount. *Construction and Building Materials*, 2014; 65: 140-150.
- [7] Wu Z., Khayat K. H., Shi C., Effect of nano-SiO₂ particles and curing time on development of fiber-matrix bond properties and microstructure of ultra-high strength concrete. *Cement and Concrete Research*, 2017; 95: 247–256.
- [8] Yu R., Spiesz P., Brouwers H.J.H., Development of an eco-friendly Ultra-High Performance Concrete (UHPC) with efficient cement and mineral admixtures uses. *Cement and Concrete Composites*, 2015, 55: 383-394.
- [9] Yang S.L., Millard S.G., Soutsos M.N., Barnett S.J., Le T.T., Influence of aggregate and curing regime on the mechanical properties of ultra-high performance fibre reinforced concrete (UHPFRC). *Construction and Building Materials*, 2009; 23: 2291-2298.
- [10] Fehling E., Bunje K., Schmidt M., Schreiber W. (2008) The “Gärtnerplatzbrücke”: Design of First Hybrid UHPC-Steel Bridge across the River Fulda in Kassel, Germany. 2nd International Symposium on Ultra High Performance Concrete, March 05-07, Kassel, Germany, 581-588.
- [11] Wang X.P., Yu R.*, Shui Z.H., Song Q.L., Zhang Z.H., Mix design and characteristics evaluation of an eco-friendly Ultra-High Performance Concrete incorporating recycled coral based materials. *Journal of Cleaner Production*, 2017, 165: 70-80.
- [12] Randl N., Steiner T., Ofner S., Baumgartner E., Mészöly T., Development of UHPC mixtures from an ecological point of view. *Construction and Building Materials*, 2014; 67: 373-378.
- [13] Habel K., Gauvreau P., Response of ultra-high performance fibre reinforced concrete (UHPFRC) to impact and static loading. *Cement and Concrete Composites*, 2008; 30(10): 938-946.
- [14] Hassan A.M.T., Jones S.W., Mahmud G.H., Experimental test methods to determine the uniaxial tensile and compressive behaviour of ultra-high performance fibre reinforced concrete (UHPFRC). *Construction and Building Materials*, 2012; 37: 874-882.
- [15] Yoo D.Y., Banthia N., Kang S.T., et al. Size effect in ultra-high-performance concrete beams, *Engineering Fracture Mechanics*, 2016; 157:86–106.
- [16] Yu R., Spiesz P., Brouwers H.J.H., Development of Ultra-High Performance Fibre Reinforced Concrete (UHPFRC): towards an efficient application of binders and fibres. *Construction and Building Materials*, 2015, 79: 273-282.
- [17] Yoo D.Y., Yoon Y.S., Banthia N., Flexural response of steel-fibre-reinforced concrete beams: effects of strength, fibre content, and strain-rate. *Cement and Concrete Composites*, 2015; 64:84–92.
- [18] Wu Z., Shi C., He W., et al. Effects of steel fibre content and shape on mechanical properties of ultra-high performance concrete. *Construction and Building Materials*, 2016; 103: 8-14.
- [19] Yoo D.Y., Kang S.T., Yoon Y.S., Effect of fiber length and placement method on flexural behaviour,

tension-softening curve, and fiber distribution characteristics of UHPFRC. *Construction and Building Materials*, 2014; 64: 67-81.

[20] Kang S.T., Lee Y., Park Y.D., et al. Tensile fracture properties of an ultra-high performance fibre reinforced concrete (UHPFRC) with steel fibre, *Composite Structures*, 2010; 92 (1): 61–71.

[21] Park S.H., Kim D.J., Ryu G.S., et al. Tensile behavior of ultra-high performance hybrid fibre reinforced concrete, *Cement and Concrete Composites*, 2012; 34 (2):172–184.

[22] Yu R., Spiesz P., Brouwers H.J.H., Static and impact resistance of a green Ultra-High Performance Hybrid Fibre Reinforced Concrete (UHPHFRC): experiments and modeling. *Construction and Building Materials*, 2014, 68: 158-171.

[23] Wang W., Liu J., Agostini F., Davy C.A., Skoczylas F., Corvez D., Durability of an Ultra High Performance Fibre Reinforced Concrete (UHPFRC) under progressive aging. *Cement and Concrete Research*, 2014; 55: 1-13.

[24] Song Q.L., Yu R., Wang X.P., Rao S.D., Shui Z.H., A novel Self-Compacting Ultra-High Performance Fibre Reinforced Concrete (SCUHPFRC) derived from compounded high-active powders. *Construction and Building Materials*, 2018, 158: 883-893.

[25] Boulekbache B., Hamrat M., Chemrouk M., et al. Flexural behavior of steel fibre-reinforced concrete under cyclic loading. *Construction and Building Materials*, 2016; 126: 253-262.

[26] Martine L., Roussel N., Simple tools for fibre orientation prediction in industrial practice. *Cement and Concrete Research*, 2011; 41: 993-1000.

[27] Eik M., Puttonen J., Herrmann H., An orthotropic material model for steel fibre reinforced concrete based on the orientation distribution of fibres. *Composite Structures*, 2015; 121: 324-336.

[28] Torrents J.M., Blanco A., Pujadas P., et al. Inductive method for assessing the amount and orientation of steel fibres in concrete. *Materials and Structures*, 2012; 45:1577-1592.

[29] Al-Mattarneh H., Electromagnetic quality control of steel fibre concrete. *Construction and Building Materials*, 2014; 73:350-356.

[30] Z. Wu, C.J. Shi, W. He, et al. Effects of steel fibre content and shape on mechanical properties of ultra-high performance concrete. *Construction and Building Materials*, 2016; 103:8-14.

[31] R. Wang, X.J. Gao, J.Y. Zhang, et al. Spatial distribution of steel fibers and air bubbles in UHPC cylinder determined by X-ray CT method. *Construction and Building Materials*, 2018; 160:39-47.

[32] B. Boulekbache, M. Hamrat, M. Chemrouk, et al. Flowability of fibre reinforced concrete and its effect on the mechanical properties of the material. *Construction and Building Materials*, 2010; 24 (9): 1664–1671.

[33] D.X. Xuan, Z.H. Shui, S.P. Wu. Influence of silica fume on the interfacial bond between aggregate and matrix in near-surface layer of concrete. *Construction and Building Materials*, 2009; 23(7): 2631-2635.

Investigation of the zonation of thermally treated ultra high performance concrete

M. Voigt¹, J. von Werder¹, B. Meng¹

¹Bundesanstalt für Materialforschung und -prüfung, Unter den Eichen 87, 12205 Berlin, Germany

Abstract

Ultra high performance concrete (UHPC) is characterised by its high compressive strength of more than 150 MPa and its high durability. Due to thermal treatment at 90°C a strength comparable to the 28-days-strength can be achieved immediately after the treatment and in some cases can be even further increased up to 30 %. The explanations for the increase in strength are the accelerated hydration of the clinker minerals and the intensified pozzolanic reaction contributing to a denser microstructure and hence, a high performance in compressive strength.

Former research shows that thermal treatment can lead to inhomogeneities in form of a visible zonation within the cross-section. The width of the margin increases with shorter pre-storage time before the thermal treatment and with omitting protective measures against desiccation during the treatment. Specimens exhibiting a zonation typically show a lower compressive strength compared to the undisturbed reference whereas changes in chemistry, mineral content and microstructure were not reported in detail.

In this study the zonation of thermally treated UHPC is investigated with respect to its chemistry, mineral composition and microstructure to allow predictions on durability and strength development. Measurements show a change in pore sizes, minerals phase composition and element distribution leading to the visible zonation and weaker bending tensile strength compared to the reference.

Keywords: UHPC, thermal treatment, zonation, desiccation, microstructure, durability

1. Introduction

In 1994 the term ultra high performance concrete (UHPC) was introduced by [1]. It characterizes concrete with an exceptional compressive strength which was accomplished by optimizing the packing density and viscosity using a low water/binder ratio and moderate thermal treatment. In the last decades the term UHPC is used for concrete with a characteristic compressive strength over 150 MPa and high durability. These characteristics derive from the low water/binder ratio of < 0.3 and the high viscosity of the fresh concrete and thus a self-compacting behaviour facilitated by a superplasticizer. By its well-tuned mixture based on assorted additives UHPC obtains its typical high packing density, low porosity and homogeneous microstructure.

In the production of precast UHPC elements thermal treatment became a common practice to shorten fabrication times, as the 28-days-strength of UHPC specimens is achieved after 24h of thermal treatment up to 90 °C [2, 3]. The thermal treatment accelerates and intensifies the hydration process and the pozzolanic reaction so that shrinkage [4] is largely completed after the treatment. For the early and rapid precipitation of hydration products during exposure to higher temperatures [5] the presence of water is crucial. Thus, some guidelines like the German regulation [6] propose a protection from desiccation but do not clearly specify to which degree. To evaluate the impact of the lacking definition three different measures against

desiccation of UHPC during thermal treatment were investigated by [7]. In the study of [7] a zonation was observed in foil covered and unprotected UHPC samples after 90 °C thermal treatment (as in Figure 1). After optical assessment of the dimension of the zonation from high resolution scans of cross sections of standard prisms (4x4x16 cm³) it could be detected that the dimension of the zonation varied with the time span between demoulding and thermal treatment (pre-treatment time), the duration of the thermal treatment time (thermal-treatment time) and the level of protection against desiccation. Compressive strength is one of the key parameters defining concrete. Thermal treatment of UHPC in general was found not to be detrimental for the further strength development but on the contrary the compressive strength of later age was even increased [8, 9]. Specimens, however, which were treated at 90 °C in the oven without any protection performed inferior to the water cured reference samples at all times [7, 10].

This study focuses on the analysis of the microstructure of the zonation and aims to provide an insight into the processes leading to the diminished strength performance.

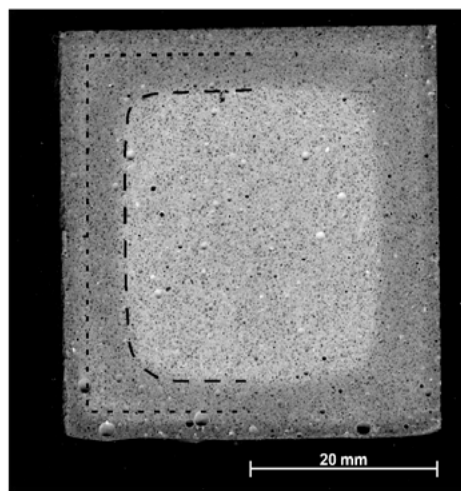


Figure 1: High resolution scan of a UHPC standard prism treated 6 days at 90 °C under dry conditions comparable to [7]. The zonation shows an inner lighter part and an outer darker part. At the rim there is a slim darker zone visible. The image was modified for better visibility of the zonation.

2. Methodology

2.1 Materials

To investigate the formation of the zonation during thermal treatment a well-established (M2Q) UHPC mixture design after [7, 11] was selected. The mixture is based on mainly SiO₂ containing components and CEM I 52,5 R as shown in table 1. The addition of fibres was omitted as the focus of the study lies on microstructure and mineral phase analysis.

The mixing was conducted in an Eirich intensive mixer with a volume of 10 l within 11 minutes. The homogenisation and mixing of the dry components were followed by the addition of water and the first half of the PCE superplasticizer. The remaining superplasticizer was added 5 minutes after the water admixture resulting in a flow spread of 30 cm.

Standard prisms of 4 x 4 x 16 cm³ were cast, prestored under water for one day at 23 °C, thermally treated in an oven with full circulation at 90 °C for six days (no protection from desiccation) and afterwards kept under water at 23 °C till strength testing after 28 days. These conditions for the thermal treatment were chosen after [7] to establish a “worst-case scenario” and ensure a strongly developed zonation of the cross section. The reference samples were immersed in water at 23 °C until testing after 28 days.

Table 1: Components of the UHPC mixture.

Components	Mass
	kg/m ³
CEM I 52,5 R	832
Microsilica	135
Quartz Powder	207
Quartz Sand	975
Superplasticizer(PCE)	25
Water	209

2.2 Methods

2.2.1 Strength testing

The prisms were tested after 28 days according to DIN EN 196-1 with a three-point bending-test set up in a universal testing machine. The bending test was followed by a compressive strength test according to DIN EN 196-1 with an area of 40 x 40 mm² using the two split halves of the prisms.

2.2.2 Pore Size Distribution

For the mercury intrusion porosity testing (MIP) the outer zone of the samples was cut off and parts of the rim and the inner zone were broken into 2-5 mm cubes so that the inner and outer parts of the samples could be measured individually. Before measuring the samples were dried at 40 °C under vacuum to avoid further hydration. The pressure applied was 410 MPa and a contact angle of 140 ° reaching a resolution of 3.6 nm as the finest pore diameter.

2.2.3 X-Ray diffraction (XRD)

The samples for the XRD measurements were prepared in the same way as for MIP so that the outer zonation and the inner part of the prisms could be analysed separately. After drying the samples were ground in an agate mortar and scanned in the 2theta range 5-65 ° with a step size of 0.02 ° and a speed of 0.5 °/min with a conventional XRD (CuK α radiation, 40 mA, 40 kV).

2.2.4 Micro X-Ray Fluorescence (μ XRF)

For μ XRF measurements cross sections of the prisms were polished with water and dried at 40 °C under vacuum to stop hydration. The measurements were conducted with 40 kV, 300 μ A and a spot size of 150 μ m.

2.2.5 Scanning Electron Microscope (SEM)

For the SEM analysis smaller cross sections of 20 x 20 mm² were embedded in epoxy resin and polished to perform qualitative and semi quantitative analysis on back scattered electron images and energy dispersive X-ray analysis (EDX). The samples for the SEM analysis represent a quarter of the overall cross section of the prisms and were selected corresponding to the outer and inner part of the sample. To recognize changes in microstructure punctual EDX mappings and backscattered electron (BSE) images were taken along a 10 mm linear line from the surface towards the core of the sample.

3. Results and discussion

3.1 Strength testing

The compressive strength of the prisms is shown in figure 2a and does not indicate a dependency on the thermal treatment after 28 days. As noted in [7] the compressive strength loss in standard prisms which are thermally treated without protection compared to thermally treated prisms immersed in water is marginal

compared to smaller sample sizes due to the basically intact core. Hence, the prisms tested after 28 days for compressive strength exhibit similar strength independent of the unprotected treatment. The bending strength however displays unambiguous lower strength values in thermally treated samples compared to the reference (Figure 2b). The reduction in bending tensile strength and compressive strength of samples cured at room temperature exposed to air compared to samples cured in water is a well-known phenomenon and due to the shrinkage stress during dry curing [12]. The resulting crack formation is likely to be increased by thermal stress arising from a temperature gradient during thermal treatment [13]. As the zonation is dependent on the degree of protection against desiccation during thermal treatment the loss in strength seems to be the logical consequence of an excessive drying process.

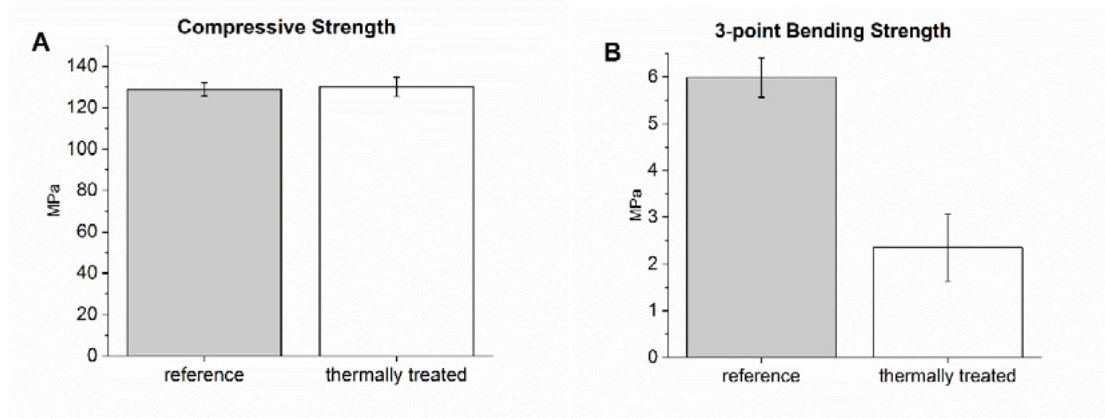


Figure 2: Test results of the compressive strength (a) and bending tensile strength (b).

3.2 Pore Size Distribution

In figure 3 the porosities of the inner and outer part of the thermally treated samples are shown in comparison to the reference sample cured in the water bath. As shown in figure 3a the outer part has a median pore size diameter of 12,5 nm, the inner part of 29 nm while the median pore size diameter of the reference lies in the middle and measures 24 nm. Figure 3b shows the cumulative intrusion and thus represents the total porosity which is comparable for the reference sample and the inner part with an average value of 10.2 Vol.-%. For the outer part, however, a noticeably smaller porosity of 8.9 Vol.-% was measured.

It is known [5] that cement matrix, exposed to elevated temperatures early during the hardening process, develops a more heterogeneous microstructure as the hydration products precipitate rapidly in a dense structure around the clinker minerals and lead to a coarser porosity. The coarser median pore diameter of the inner part of the thermally treated sample compared to the reference can therefore be explained with the thermal treatment. The fact that the outer part is mainly not characterized by a coarser but on the contrary by a finer porous structure is possibly due to the water storage after thermal treatment. In the water bath additional water is provided so that the remaining clinker phases can hydrate and thus reduce the pore size towards the surface. The weak bending tensile strength could be explained by possible microcracks occurring in the large pore size region due to the thermal stresses during thermal treatment. The lack of evidence for an accumulation of microcracks by the measurements is probably concealed by the self-healing taking place during the subsequent water storage to the thermal treatment and is matter of further research.

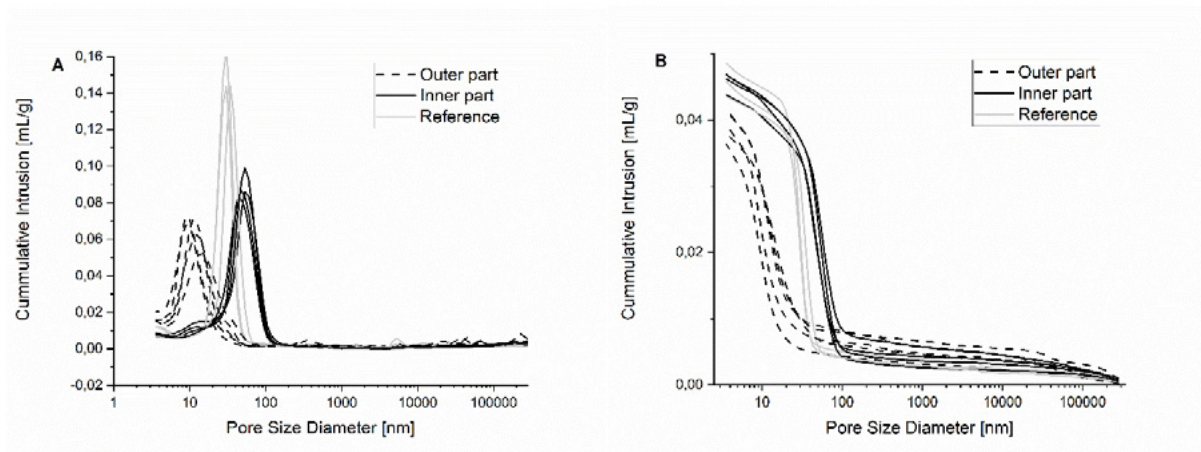


Figure 3: Pore size distribution of thermally treated and water cured (reference) UHPC at 28 days: (a) Log differential intrusions and (b) cumulative pore volume.

3.3 X-Ray diffraction

The diffraction patterns pictured in figure 4 show in general the same peak positions for the reference as well as the inner and the outer part of then thermally treated sample and therefore a similar composition of the crystalline phases. As it is typical for UHPC with a low w/c ratio alite peaks are observed as well as aluminate peaks as the remaining clinker phases besides the sharp quartz peaks from the aggregates. Focusing on the clinker mineral peaks of alite at 32.2 and 32.6 $^{\circ}2\theta$ it seems that in the outer part of the zonation peak intensities decrease compared to the reference and the inner part. In the detailed frame of figure 4 the AFm phase peak at 10.9 $^{\circ}2\theta$ is displayed to emphasize the decrease in the outer part of the zonation whereas the reference and the inner part show a distinct peak of lower intensity at this position. The peak position matches data from [14] and seems to represent a partly carbonated AFm phase like Hemicarboaluminate.

Even though the changes seem marginal it indicates that the clinker consumption at the rim of the thermally treated sample is slightly higher and hence, points to a continued hydration after thermal treatment via the renewed water influx during water storage. The change of the crystallinity of the AFm phase towards the rim is evidence for ongoing carbonatization even though it is not comprehensible from the calcite peak at 29.5 $^{\circ}2\theta$ as it is superimposed by alite and belite peaks.

3.4 Micro X-Ray Fluorescence

The mapping of the μ XRF in figure 5a shows an enriched potassium concentration in the outer zone and a depletion in the core. The sulphur content distribution is exactly diametrical to the potassium enrichment (Figure 5b). Thus, it is decreasing from the rim towards the outer zone followed by a sharp increase towards the core where it slightly declines in the thermally treated sample. The reference sample shows no distinct zonation in the potassium (Figure 5e) or sulphur distribution (Figure 5f) even though the distribution seems not entirely homogeneous. Especially in the case of the potassium a depletion in the concentration around the air pores is visible.

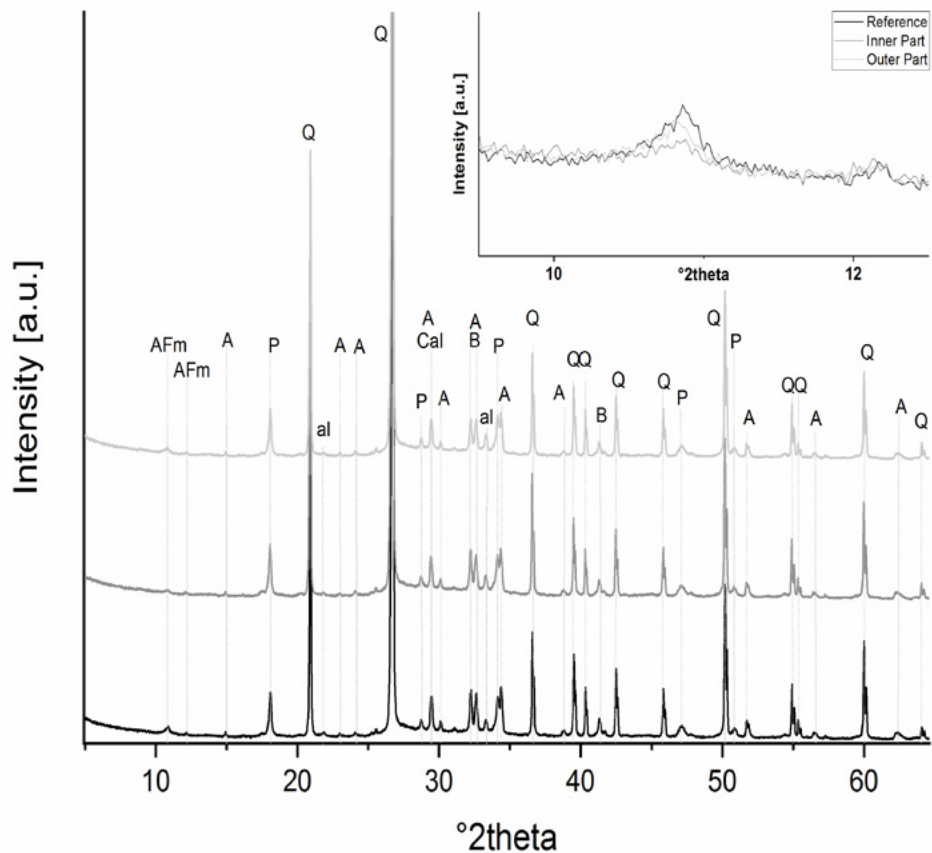


Figure 4: XRD patterns of UHPC at 28 days: q-quartz, a-alite, b-belite, p- portlandite, al-aluminates AFm-AFm phases, cal-calcite

Other elemental mappings e.g. Ca or Si in figure 5 c and d, do not exhibit any measurable shifts in element concentration across the cross-section due to the high intensities of either the chosen SiO₂-rich aggregates or the typical mineral phases expected in a Portland cement.

The low potassium content at the rim of the outer zone is probably caused by leaching during water storage subsequent to the thermal treatment. The depletion in the core, however could be assigned to the capillary transport of the K-rich pore solution from the inner core driven by the gradient in capillary pressure during thermal treatment.

The varying potassium and sulphur contents can be related to plural transport mechanisms through the capillary pores and diffusion during thermal treatment and subsequent storage in water. For more detailed insights of the element distribution the effects of the thermal treatment should be investigated separately without water storage.

3.5 Scanning Electron Microscope

The punctual EDX mappings of the cement matrix confirm the trends seen in the μXRF analysis. Qualitative it can be recognized that less clinker phases are found in the inner part of the thermal treated sample (Figure 6a) compared to the rim (Figure 6b) and the reference. For the thermally treated as well as the water cured sample clinker phases seem both diminished at the rim of the cross section and suggest an

external water influx and subsequent further hydration during water storage.

Portlandite crystals (Figure 7) appearing as stacks and agglomerates of crystals are found in all parts of the thermally treated sample and the reference sample. The composition is validated via EDX measurements where the Wt.% of Ca is noticeable increased whereas the C value is smaller compared to the mappings of the cement matrix.

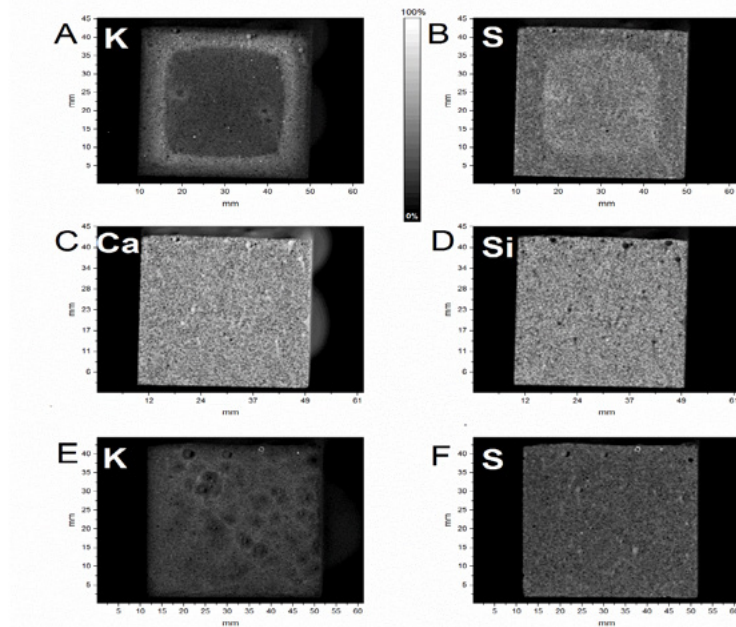


Figure 5: The μ XRF mappings of the potassium (a), the sulphur (b), the calcium (c) and the silicon (d) distribution of the thermally treated sample in comparison to the potassium (e) and sulphur (f) concentrations of the water immersed reference sample.

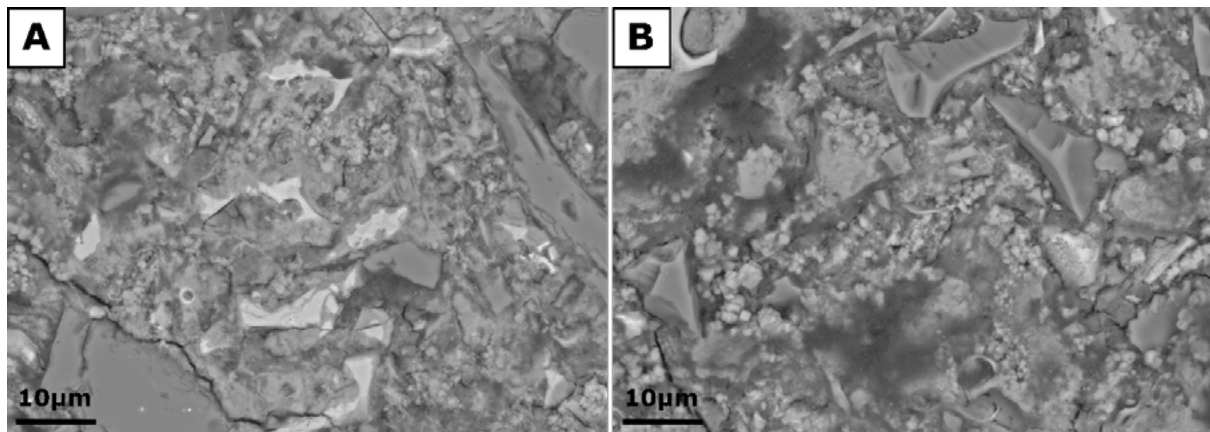


Figure 6: BSE images (4000x magnification) of the thermally treated sample of the core (a) and the outer zone (b).

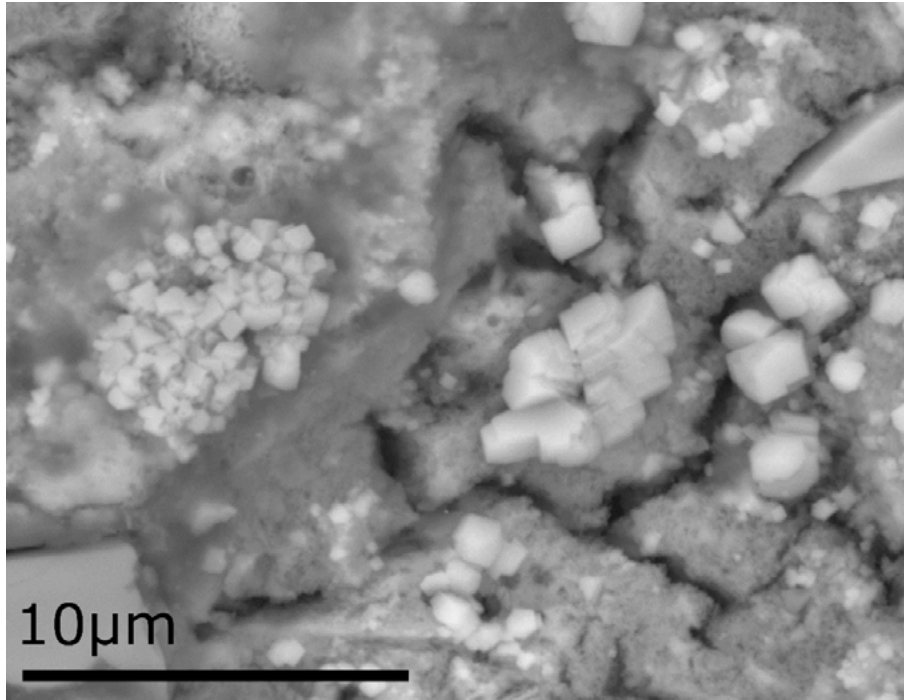


Figure 7: BSE image (8000x magnification) of the portlandite stacks and agglomerates of different crystal sizes in a water immersed reference sample.

4. Conclusions

The microstructure of the depth dependent zonation of unprotected, thermally treated UHPC was investigated. The results exhibited a different microstructure in the core of the thermally treated UHPC sample compared to the outer zone.

The dehydration effects near the surface during the thermal treatment appears to be responsible for the measured weaker bending tensile strength in that zone. For the outer zone, additionally the appearance of partly carbonated AFm points to ingress and reaction of CO₂ during the unprotected exposition.

The microstructure of the outer zone displayed consistently that the water storage following the treatment resulted in ongoing hydration effects, densifying the structure and consuming clinker minerals. Accordingly, the core of the thermal treated sample showed a larger median pore diameter and more remaining clinker minerals compared to the water immersed reference sample.

Additionally, the drying and wetting processes in the outer zone seem to provoke migration effects of ions mobilised with the pore solution. Such effects, which could not be explained in detail so far, were indicated by μ XRF mappings, indicating a depletion of potassium in the core and an enrichment towards the rim and an opposing sulphur distribution. Further research is needed to explain the interrelationships between element distributions and the transport mechanisms.

Also, the other zonation effects mentioned above desire a deepening investigation of dehydration and rehydration processes caused by treatment and storage parameters, because this knowledge is essential for durability performance of thermally treated UHPC.

5. Acknowledgment

The authors would like to thank P. Drabetzki, A. Gardei and S. Simon from BAM for assistance with XRD, XRF, MIP measurements, strength testing and stimulating discussions.

6. References

1. 1. De Larrad, F. and T. Sedran, *Optimization of ultra-high-performance concrete by the use of a packing model*. Cement and Concrete Research, 1994. **24**(6): p. 997-1009.
2. 2. NPCA, *Ultra High Performance Concrete (UHPC): Guide to Manufacturing Architectural Precast UHPC Elements*. 2013: Carmel, IN, USA.
3. 3. Kang, S., et al., *Microstructural Investigation of Heat-treated Ultra-High performance Concrete for Optimum Production*. Materials, 2017. **10**(1106): p. 1-13.
4. 4. Heinz, D. and H.-M. Ludwig, *Heat Treatment and the Risk of DEF Delayed Ettringite Formation in UHPC*, in *Proceedings of the International Symposium on Ultra High Performance Concrete*, M. Schmidt, E. Fehling, and C. Geisenhanslüke, Editors. 2004, Kassel University Press: Kassel. p. 717-730.
5. 5. Lothenbach, B., et al., *Effect of temperature on the pore solution, microstructure and hydration products of Portland cement pastes*. Cement & Concrete Research, 2007. **37**: p. 483-491.
6. 6. DAfStb, *Sachstandsbericht Ultrahochfester Beton*. DAfStb-Heft, ed. Deutscher Ausschuss für Stahlbeton. Vol. 561. 2008, Berlin: Beuth Verlag GmbH. 126.
7. 7. Selleng, C., et al., *Influencing factors for the effectivity of heat treatment of ultra-high performance concrete (UHPC)*. Beton- und Stahlbetonbau, 2017. **112**(1): p. 12-21.
8. 8. Schmidt, M., et al., *The German Guideline for ultra-high performance concrete*, in *AFGC-ACI-fib-RILEM Int. Symposium on Ultra-High Performance Fibre-Reinforced Concrete, Volume II*. 2017: Montpellier, Franca. p. 545-555.
9. 9. Schachinger, A.I., H. Hilbig, and T. Stengel, *Effect of Curing Temperature at an Early Age on the Long-Term Strength Development of UHPC*, in *2nd International Symposium on Ultra High Performance Concrete*, E. Fehling, M. Schmidt, and S. Stürwald, Editors. 2008, Kassel University Press: Kassel, Germany. p. 205-212.
10. 10. Gröger, K., et al., *Effect of 90 °C Thermal Treatment on Ultra High Performance Concrete*, in *GeoBerlin 2015 - Dynamic Earth from Alfred Wegener to today and beyond*, J. Wagner and K. Elger, Editors. 2015, GFZ German Research Centre for Geosciences: Berlin. p. 162.
11. 11. Bornemann, R., et al., *Ultra High Performance Concrete UHPC - Composition, Properties and Applications*. Beton- und Stahlbetonbau, 2001. **96**(7): p. 458-467.
12. 12. Graf, O. and K. Walz, *Vergleichende Prüfungen von Straßenbauementen in der Versuchsanstalt und in der Straße* Zement, 1939. **28**: p. 445-505.
13. 13. Ma, Q., et al., *Mechanical properties of concrete at high temperature—A review*. Construction and Building Materials, 2015. **93**: p. 371-383.
14. 14. Baquerizo, L., T. Matschei, and K.L. Scrivener, *Impact of water activity on the stability of systems containing ettringite*, in *19. ibausil*. 2015, F. A. Finger-Institut für Baustoffkunde: Weimar, Germany. p. 556-560.

Role of Mg^{2+} stabilized amorphous calcium carbonate on the early reaction of sodium carbonate activated slag

B. Yuan^{1,2}, Q.L. Yu³, W. Chen¹, H.J.H. Brouwers^{1,3}

¹State Key Lab of Silicate Materials for Architectures, Wuhan University of Technology, Wuhan 430070, PR China;

²School of Material Science and Engineering, Wuhan University of Technology, Wuhan 430070, PR China

³Department of the Built Environment, Eindhoven University of Technology, P.O. Box 513, 5600 MB Eindhoven, The Netherlands

Abstract

Amorphous calcium carbonate (ACC) is the least stable phase of calcium carbonate, and will quickly transfer to more stable phases, e.g. aragonite, vaterite and calcite, the phases of which are widely reported in sodium carbonate activated slag (SCAS). However, the existence of ACC was not reported in SCAS yet, probably because of its extreme instability at ambient condition. Mg^{2+} ion is known as an effective inorganic ion that increases the stability of ACC. In order to study the effect of ACC on the early age reaction of SCAS, Mg^{2+} ion is added to the SCAS system to increase the stability of ACC in order to evaluate the effect of ACC on the early age reaction. The results show that the reaction rate, reaction intensity and reaction products depend on the dosage of Mg^{2+} , providing that Mg^{2+} -stabilized ACC plays an important role on the early age reaction of SCAS. Due to the presence of Mg^{2+} , the precipitation of reaction product is clearly identified at different reaction stages as classified by the reaction kinetic results. The precipitation of calcium carbonate starts when the solids mix with the sodium carbonate solution, and the first reaction peak in the heat release curve assigns to the precipitation of gaylussite. The existence of ACC is observed by SEM. Furthermore, the role of ACC or Mg^{2+} -stabilized ACC on the early age reaction of sodium carbonate activated slag is discussed and a model is proposed.

Keywords: Sodium carbonate activated slag, amorphous calcium carbonate, Magnesium stabilization, early age reaction.

1. Introduction

Applying near neutral salts, e.g. sodium carbonate, as activator for alkali activated materials has received increased attention because of its good properties, low price and environmental benefits [1–4]. However, slow reaction of sodium carbonate activated slag (SCAS) are often reported, while current understandings about the long dormant period are still limited to the effect of CO_3^{2-} anion in controlling the Ca^{2+} ion at the early age reaction [5,6]. There 3 out of 4 polymorphous of calcium carbonate are widely reported as the secondary products of SCAS at the early stages, i.e. aragonite, vaterite and calcite. While the least stable phase of calcium carbonate, ACC, is not reported yet. It is known that high pH value and Mg^{2+} ion can

stabilize ACC [7,8], which indicates that the other three phases of CaCO₃ are originally converted from ACC. Considering the pore solution environment, ACC can potentially plays an important role on the early age reaction of SCAS.

This study aims to investigate the effect of Mg²⁺ ion on the early age reaction of SCAS. MgCl₂ is used as the Mg²⁺ ion source. The reaction kinetics and reaction products of the samples containing different amounts of Mg²⁺ ion are characterized with isothermal calorimeter, X-ray diffraction (XRD) and scanning electron microscope (SEM). Based on the results, the role of Mg²⁺-stabilized ACC on the early age reaction of SCAS is discussed.

2. Materials and experiments

2.1 Materials

Ground granulated blast furnace slag (GGBS) was used in this study (supplied by ENCI B.V, the Netherlands). The elemental composition and particle size distribution of the slag were determined by X-ray fluorescence (XRF) using a PANalytical Epsilon3 analyzer and the results are shown in Table 1, respectively. Sodium carbonate (powder, analytical grade) was applied as the activator in this study with different concentrations. The designed Na₂CO₃ concentrations (Table 2) were firstly mixed/dissolved in water followed by cooling down to room temperature (20 ± 1 °C) prior to further actions. MgCl₂ (powder, analytical grade) was used as the source of Mg²⁺ ion and mixed with the prepared Na₂CO₃ solutions about ≈20 s using a vibrator (ensuring the completed reaction of Mg²⁺ and CO₃²⁻) before mixing with the slag powders.

Table 1 Chemical composition of GGBS.

Oxidations (%)	SiO ₂	CaO	Al ₂ O ₃	MgO	Fe ₂ O ₃	SO ₃	K ₂ O	Cl	L.O.I
Slag	30.24	40.68	12.67	9.05	0.64	3.53	0.38	0.05	-0.36

Table 2 Mix proportions of specimens.

Items	Na ₂ CO ₃ dosage	MgCl ₂ dosage	W/S
Unit	[Na ₂ O wt.%]	[Na ₂ O wt.%]*	
Reference	4.00		0.4
Mg/Ca 1/9	4.44	0.44	
Mg/Ca 2/8	5.00	1.00	
Mg/Ca 3/7	5.71	1.71	

*means that the MgCl₂ dosage is calculated by the same mole of Na₂CO₃ and shown as the dosage of equivalent Na₂O wt.% by mass of slag. Due to the reaction of MgCl₂ + Na₂CO₃ = MgCO₃ + 2NaCl, the Na₂CO₃ dosage keeps the same to be 4.00 Na₂O wt.% for all the mixtures.

2.2 Experiments

The reaction kinetic of the samples with different amount of Mg²⁺ ion content is investigated using an isothermal calorimeter, set at 20 °C (TAM AIR Calorimeter). The microscopic analysis is performed using a JSM-IT100 InTouchScope™ Scanning Electron Microscope (SEM).

3. Results and discussion

3.1 Reaction kinetics

Fig. 1 shows the heat release of sodium carbonate activated slag with different dosage of Mg²⁺ ion. It is clear that the reaction process can generally be classified into five stages, and the duration of each stage is highly depending on the dosage of the Mg²⁺ ion. The reference sample shows a similar reaction pattern to previous studies [5,9], but with a shortened dormant period. This is explained by the fineness of the applied slag [10]. It is reported that the CO₃²⁻ anions concentration in the pore solution controls the reaction of

sodium carbonate activated slag [5]. In this case, more Ca²⁺ ions are dissolved from finer slag particles and precipitated with CO₃²⁻ anions, which consequently lead to a faster reaction.

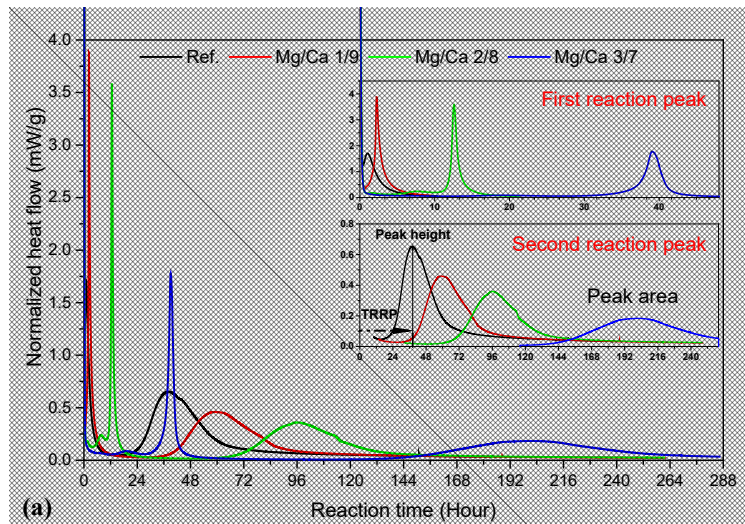


Fig. 1 Heat evolutions of sodium carbonate activated slag with different Mg²⁺ ion dosages. (TTRP is time to reach the reaction peak).

Table 3 Summarized results of TTRP (time to reach reaction peak), peak height (intensities), and peak area (identified in Fig. 1)

Items	Peak height	TTRP	Peak area
Reference	0.65	36.81	78.30
Mg/Ca 1/9	0.46	58.96	70.03
Mg/Ca 2/8	0.36	95.93	61.33
Mg/Ca 3/7	0.18	201.49	53.78*

*the value is relatively low because the main reaction (second reaction peak) is not finished yet.

After dosing a small amount of Mg²⁺ ion, the first peak on the heat release curve is slightly delayed by about 1 h (from 1 h to ≈ 2 h), as shown in Fig. 2. However, further increasing the Mg²⁺ ion dosage leads to a significant delay up to 12 h (mixture Mg/Ca 2/8) and 39 h (mixture Mg/Ca 3/7), respectively. The time to reach the second peak (i.e. the main reaction peak) is also significantly extended. Besides, the peak height of the samples decreases with the increase of Mg²⁺ ion content. The total heat release during the main reaction is estimated, as shown in Table 3. It is seen that the intensity of the second reaction peak decreases with the increasing content of Mg²⁺ ion, the total heat release of the mixtures is slightly reduced. It is obvious that the incorporated Mg²⁺ ion dominates the reaction kinetics of SCAS.

3.2 Role of Mg²⁺ stabilized ACC

Fig. 2 presents the SEM picture of the reference sample after 6 h of reaction. As can be seen, two distinguishable products are clearly identified, i.e. calcite with hexagonal crystalline structure and many clusters of irregular micro-particles. The sample is washed with distilled water and left dried on a silica plate. Considering the chemical reaction involved in the early reaction of SCAS, the micro-particles can be assigned to ACC, which is known as the least stable polymorphous structure of calcium carbonate. In most cases, ACC will quickly convert to more stable products, e.g. aragonite, vaterite and/or calcite. However, methods such as increasing the pH [11] or dosing stabilization agent [12] delay the process and improve the stability of ACC.

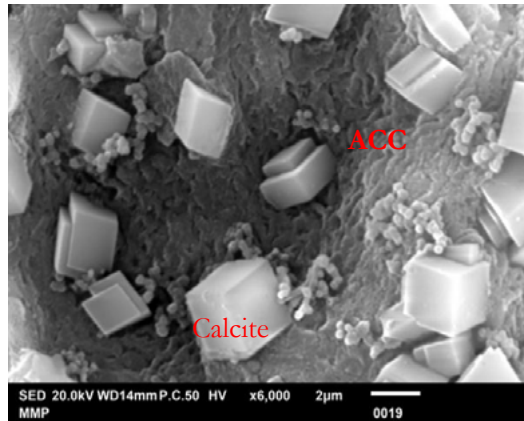


Fig. 2 SEM picture of the mixture Mg/Ca 2/8 after 7 h of curing (washed with water and then left dry).

It is clear that the incorporation of Mg^{2+} ion stabilizes ACC, which is responsible for the delayed initial precipitation peak of gaylussite. Why the main reaction peak, i.e. precipitation of C-(A)-S-H gel is significantly prolonged, however, is not clear understood yet. In theory, when the pH of the pore solution rises over 10.52, $MgCO_3$ will turn to a less soluble product $Mg(OH)_2$, and its ability in stabilizing ACC will not be prominent. In which case, the stabilization effect could be the synergetic effect of Mg, pH and SiO_3^{2-} that requires further study.

Fig. 4 presents the carbonate consumption routine of the samples after incorporating Mg^{2+} ion as an stabilization agent. If the initial precipitated ACC is not stabilized, it will quickly react with Na_2CO_3 forming gaylussite, or convert to other more thermodynamic stable polymorphous of $CaCO_3$, e.g. aragonite, vaterite and/or calcite. In which case, the reaction in stage 1 and stage 3 happens simultaneously. However, when the initially precipitated ACC is stabilized by Mg^{2+} ion (stage 2), the formation of gaylussite is delayed, as shown in Fig. 3. The duration of this stage is highly depending on the dosage of Mg^{2+} , which can vary from a few hours to days. The mechanism behind this phenomenon still requires further investigations.

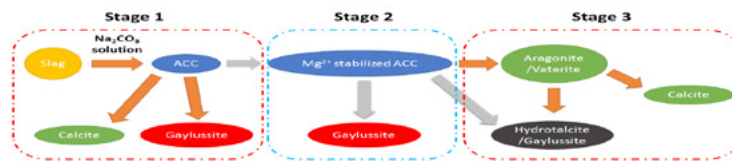


Fig. 3 Scheme of role of Mg^{2+} ion stabilized ACC on sodium carbonate activated slag.

4. Conclusions

The effect of Mg^{2+} -stabilized ACC on the reaction of sodium carbonate activated slag (SCAS). The results demonstrate that Mg^{2+} -stabilized ACC plays a significant role on the early age reaction of SCAS. The first reaction peak of SCAS is assigned to the precipitation of gaylussite, while the second reaction peak is attributed to the precipitation of C-A-S-H gel together with the generation of hydrotalcite-like structures.

5. Acknowledgment

Acknowledgments of people, grants, funds, etc. should be placed in a separate section before the reference list. The names of funding organizations should be written in full.

6. References

- [1] S.A. Bernal, Advances in near-neutral salts activation of blast furnace slags, RILEM Tech. Lett. (2016) 39–44.
- [2] A.F. Abdalqader, F. Jin, A. Al-Tabbaa, Development of greener alkali-activated cement: utilisation of sodium carbonate for activating slag and fly ash mixtures, J. Clean. Prod. 113 (2015) 66–75. doi:10.1016/j.jclepro.2015.12.010.
- [3] B. Yuan, C. Straub, S. Segers, Q.L.L. Yu, H.J. J.H. Brouwers, Sodium carbonate activated slag as cement replacement in autoclaved aerated concrete, Ceram. Int. 43 (2017) 6039–6047. doi:10.1016/j.ceramint.2017.01.144.
- [4] A.J. Moseson, D.E. Moseson, M.W. Barsoum, High volume limestone alkali-activated cement developed by design of experiment, Cem. Concr. Compos. 34 (2012) 328–336. doi:10.1016/j.cemconcomp.2011.11.004.
- [5] S.A. Bernal, J.L. Provis, R.J. Myers, R. San Nicolas, J.S.J. van Deventer, Role of carbonates in the chemical evolution of sodium carbonate-activated slag binders, Mater. Struct. 48 (2014) 517–529. doi:10.1617/s11527-014-0412-6.
- [6] M. Kovtun, E.P. Kearsley, J. Shekhovtsova, Chemical acceleration of a neutral granulated blast-furnace slag activated by sodium carbonate, Cem. Concr. Res. 72 (2015) 1–9. doi:10.1016/j.cemconres.2015.02.014.
- [7] J.D. Rodriguez-Blanco, S. Shaw, P. Bots, T. Roncal-Herrero, L.G. Benning, The role of pH and Mg on the stability and crystallization of amorphous calcium carbonate, J. Alloys Compd. 536 (2012) S477–S479. doi:10.1016/j.jallcom.2011.11.057.
- [8] J.D. Rodriguez-Blanco, S. Shaw, P. Bots, T. Roncal-Herrero, L.G. Benning, The role of Mg in the crystallization of monohydrocalcite, Geochim. Cosmochim. Acta. 127 (2014) 204–220. doi:10.1016/j.gca.2013.11.034.
- [9] B. Yuan, Q.L.L. Yu, H.J.H.J.H. Brouwers, Time-dependent characterization of Na₂CO₃ activated slag, Cem. Concr. Compos. 84 (2017) 188–197. doi:10.1016/j.cemconcomp.2017.09.005.
- [10] B. Yuan, Q.L. Yu, H.J.H. Brouwers, Evaluation of slag characteristics on the reaction kinetics and mechanical properties of Na₂CO₃ activated slag, Constr. Build. Mater. 131 (2017) 334–346. doi:10.1016/j.conbuildmat.2016.11.074.
- [11] N. Koga, Y. Nakagoe, H. Tanaka, Crystallization of amorphous calcium carbonate, Thermochem. Acta. 318 (1998) 239–244. doi:10.1016/S0040-6031(98)00348-7.
- [12] J. Ihli, W.C. Wong, E.H. Noel, Y.-Y. Kim, A.N. Kulak, H.K. Christenson, M.J. Duer, F.C. Meldrum, Dehydration and crystallization of amorphous calcium carbonate in solution and in air, Nat. Commun. 5 (2014) 3169. doi:10.1038/ncomms4169.

Pozzolanic reactivity of size-classified siliceous fly ashes

R. Snellings¹, H. Kamyab¹, S. Joseph², P. Nielsen¹, M. Loots³, L. Van den Abeele¹

¹Sustainable Materials, Flemish Institute of Technological Research (VITO), Boeretang 200, B-2400 Mol, Belgium

²Department of Civil Engineering, KU Leuven, Kasteelpark Arenberg 40/2448, B-3001 Heverlee, Belgium

³Value Ash Technologies NV, Centrum-Zuid 1111, B-3530 Houthalen-Helchteren, Belgium

Email of the corresponding author: ruben.snellings@vito.be

Abstract

High grade mineral powders are essential as high-quality supplementary cementitious materials and fillers for low carbon, high performance cement and concrete. In the FLAME project a new technology for size classification of mineral powders is upscaled from lab to pilot prototype. The new size classification technique operates on dry powders in a closed circuit. The pilot prototype was tested on a number of mineral powders, amongst which coal combustion ashes, and generated ultrafine (d_{50} of 2-3 μm), very fine (d_{50} of 4-5 μm), medium (d_{50} of 15-20 μm), and coarse (d_{50} >20 μm) size fractions.

This contribution reports on the physico-chemical properties and the pozzolanic reactivity of the size-separated siliceous coal combustion ashes. The particle size distribution, specific surface area, density and chemical, mineralogical composition were measured for all size fractions. Quartz, iron oxide and unburnt carbon were found to be concentrated in the coarser fractions, amorphous phases and trace elements were more abundant in the finer fractions.

The R3 heat release test for measuring chemical reactivity as supplementary cementitious material showed a strong dependence of reactivity on particle size. The finest fractions were found to be twice as reactive as the initial fly ash, the coarse fraction only half. The reactivity-particle size relationship was further investigated using a microstructure based kinetic model to calculate the intrinsic volumetric reaction rate of the fly ash. The model simulations confirm the first order impact of particle size on reactivity, however they indicate that also secondary effects such as density variations should be included to fully explain the reactivity measurements.

The impact of the very fine and medium fly ash size fractions on cement hydration was investigated on cement blends using isothermal calorimetry and X-ray diffraction. The effect on compressive strength development was measured on mortar bars with 30% replacement of Portland cement (CEM I 42.5 R) by fly ash. The results confirm the higher reactivity of the very fine fly ash by showing higher heat release, more portlandite consumption and more rapid and greater strength development.

Keywords: Coal combustion fly ash, Pozzolan, Reactivity, Hydration, Blended cement

1. Introduction

To keep the global temperature rise well below 2°C above pre-industrial levels, global anthropogenic greenhouse gas emissions will need to be drastically reduced on the short term [1, 2]. Already by 2030, the EU commits to a reduction of at least 40% of the 1990 emissions to avoid the far-reaching impacts of climate change [3]. To accomplish such drastic cuts at the short term, all greenhouse gas emitting human activities will need to be concerned and undergo intensive changes. Energy-efficiency measures need to find widespread adoption in appliances, buildings and industrial processes, while shifts towards low-carbon technologies in energy generation and transport gain impetus. Simultaneously also the global warming impact of the composing materials will need to be tackled by a transition to a more circular economy that makes more efficient use of materials that require carbon or energy intensive production processes [4].

In response to rising global demands for housing and transport infrastructure, the production of building materials such as concrete has increased strongly over the last decades, predominantly in rapidly developing countries such as China and India, reaching a global estimate of 30-40 Gt/y of produced concrete in 2017 [5]. In conventional concrete products the Portland cement binder is responsible for about 75-80% of the embodied CO₂ [6]. Pure Portland cement consists of 95% clinker and minor additives, mostly calcium sulphates. The production of Portland clinker from (impure) limestone and corrective raw meal additions emits about 0.9 tonne of CO₂ per tonne of clinker [7]. Since modern clinker production processes are nearing the thermodynamic energy efficiency limit, the most appropriate approach to reducing the global warming impact of concrete is by making efficient use of Portland clinker [8]. This approach can be adopted by various actors along the value chain. Cement producers blend in supplementary cementitious materials (SCMs) to partially substitute clinker in composite cements. Also concrete producers add in SCMs at the concrete mixing stage to replace clinker. Concrete producers can minimise clinker levels in their concrete design, e.g. by optimising the concrete particle size grading or by using microfillers. Finally designers and end-users may opt for low-impact high-performance products containing high-grade microfillers or SCMs and as such reduce material volumes as well as clinker volumes [9].

As such, high grade mineral powders suitable for use in concrete are essential in achieving substantial CO₂ emission savings in the clinker efficiency approach. In terms of fine mineral additions for concrete a distinction is made between inert and reactive materials. Largely inert materials comprise quartz dust or finely ground limestone and contribute to the properties mainly through physical interactions, such as improving particle packing. Reactive powders contribute to the concrete properties by undergoing a chemical reaction with the hydrating Portland cement. A distinction among reactive materials is generally made between (latent) hydraulic and pozzolanic materials. Latent hydraulic materials do not require a source of soluble Ca but will spontaneously hydrate when contacted with water and, if need be, small amounts of (alkali) activator to initiate the hydration. Pozzolanic materials, on the other hand, require a soluble source of Ca to form typical cement hydrates and trigger a continuous hydration reaction [10]. Blast furnace slag generated in the smelting of iron ore to pig iron behaves typically as a latent hydraulic material, fly ash generated during combustion of hard coal for electricity production typically behaves as a pozzolanic material. Given the scale of production of Portland clinker (3.2 Gt/y) it is obvious that large volumes of SCMs and fillers need to be available for substitution [5, 11]. In this respect, blast furnace slag supplies are practically exhausted by their use in cement in concrete and other materials are needed. Considerable research efforts are therefore directed towards extending supplies of SCMs. Different approaches are followed. Next to exploring the behaviour of materials for which little experience exists in terms of use as SCM, ternary blends of common SCMs, including limestone, and clinker have been thoroughly investigated to establish viable combinations and formulation boundaries [12-14]. This paper treats new SCMs that were obtained by post-processing of candidate SCMs, in this case coal combustion fly ashes. Post-processing is

generally applied to improve material quality, i.e. it can transform off-spec materials into candidate SCMs that comply to standard specifications, or it can generate SCMs that have superior properties to regular products. In view of enhancing clinker efficiency, processing of mineral powders can enable more dense particle packing and can increase SCM reactivity to obtain a denser and more durable microstructure of low-clinker cements.

Coal combustion fly ashes are globally one of the most used SCMs. Based on global coal consumption for electricity generation about 1 Gt/y of fly ashes are generated, of which an estimated third is used in cement and concrete applications [5, 11]. The rate of use is highly variable by region, depending partly on logistics and local incentives to accommodate reuse, but is also determined to a large extent by the actual material properties and associated quality as SCM. Coal quality, precombustion treatment, combustion conditions and fly ash collection technology all impact ash properties [15, 16]. Most common ash deficiencies are the content of unburnt carbon, excessive sulphate contents, free lime in calcareous fly ashes, and low reactivity for siliceous fly ashes. Low reactivity is generally related to large fractions of inert materials such as quartz, mullite or coarse particles [17]. To recover usable materials from low reactivity fly ashes or to tailor fly ash fineness, screening, classification and/or comminution treatments can be applied. Earlier work has shown clear positive effects of finer fly ash on reactivity with cement, and concrete properties such as strength development, pore structure and durability [18-20]. This paper describes how fly ash quality varies for a range of classified size fractions obtained from a dry powder classification device under development. Material properties of the classified fractions are characterised, including pozzolanic reactivity measured by the R3 calorimetry test, and the impact of the fly ash on the hydration kinetics and hydrate assemblage of composite cements are reported. Finally microstructure-based kinetic modelling is applied to quantitatively assign the impact of particle size on reactivity.

2. Methodology

2.1 Materials

The starting materials in this study were a siliceous fly ash and a pure Portland cement of type CEM I 42.5 R. The siliceous fly ash was classified by a proprietary prototype device into 4 fractions of different particle size distribution, henceforth they will be designated as ultrafine, very fine, medium, and coarse fraction. The prototype was developed and tested in the FLAME project, in the device fly ashes are separated based on size in a dry, closed system. For the pozzolanic reactivity test material replicates resulting from different classification runs on the same starting material were included.

The impact of fly ash fineness and processing on cement hydration was assessed for two different fractions, i.e. the very fine fraction and the medium fraction obtained through classification. A Portland cement replacement level of 30 wt.% was used. Thus, including the reference Portland cement, the hydration of a total of 3 cements was studied.

2.2 Methods

The bulk chemistry, mineralogy and physical properties of the starting materials as well as the classified fly ashes were measured. The chemical composition was measured by X-ray Fluorescence (XRF) spectroscopy on beads. Loss on Ignition (LOI) and Total Organic Carbon (TOC) were determined according to EN 196-2 and EN 15936. To investigate the distribution of trace elements acid digestates of the different size fractions were analysed by Inductively Coupled Plasma – Optical Emission Spectrometry (ICP-OES). The mineralogical composition was determined using Rietveld analysis of X-ray powder diffraction (XRD) scans. The amorphous phase was quantified using the external standard method applied to the Rietveld fitting results. Rietveld analysis was based on the procedure and starting crystal structures given by [21].

The particle size distribution of the materials was measured by a Microtrac s3500 laser diffractometer on samples dispersed in isopropanol suspensions using ultrasonication. The specific surface area was measured using BET analysis of N₂ sorption data of samples off-gassed at 40 °C overnight. The specific gravity of the samples was measured by He pycnometry. Scanning electron microscopy (FEI FEG NanoSEM) was applied on Pd-coated powder stubs for imaging of the size, shape and surface texture of the different size fractions.

The pozzolanic reactivity of the fly ashes was evaluated using the R3 calorimetry test [22]. This test measures the heat release of a model mixture of the SCM, Ca(OH)₂, H₂O and small additions of reagent grade CaCO₃, K₂SO₄ and KOH. The model system simulates the reaction environment of the SCM in a hydrating Portland cement, by eliminating the Portland cement component itself the reaction of the SCM can be measured directly. The test protocol is described in more detail in [23]. The isothermal calorimetry measurements were made using a TAM Air calorimeter calibrated at 40°C, heat flow data were recorded until 7 days after mixing.

The reaction kinetics for the different particle fractions of fly ash from the R3 test is modelled using CemRS assuming particles to be spherical [24]. The model uses the uniform reactive thickness concept [25] which assumes that the depth of dissolution is constant irrespective of the size of the particle. While most models use a time dependent variation in the reactive thickness [26, 27], the CemRS model uses a constant reactive thickness. Such a model assumes that the reaction is controlled by isotropic dissolution of the fly ash particles.

The impact of the classified fly ashes on the hydration and performance of blended cements was carried on the paste and mortar level. The cement replacement level by fly ash was 30 wt.% on a solids base. For the pastes a water to binder of 0.4 was used for all mixes. The solids were premixed by hand, and all materials were equilibrated at room temperature before mixing. About 120 g of cement paste was mixed at 1600 rpm during 2 min using an overhead mixer. 15 g of paste was immediately transferred to calorimeter flasks, closed, and introduced into the measurement channel for recording of the heat flow. Isothermal calorimetry measurements were made at 20°C for 28 days. The remainder of the paste was cast into HDPE containers, sealed air-tight using wax paper, and left to cure at 20 °C until the sampling time. After 1, 2, 7, 14, 28 and 90 days disks of the hardened paste were cut. The slices were slightly polished on sandpaper, flushed with water to remove polishing residue and superficially dried and subsequently measured by XRD as a “fresh” disk to study the hydration product assemblage.

Mortar bars of the reference and composite cements were prepared according to EN 196-1, the strength development was measured accordingly at 2, 7 and 28 days.

3. Results and discussion

3.1 Characterisation of the starting materials

The chemical and mineralogical composition of the fly ash and cement starting materials are reported in Table 1. The fly ash has a chemical composition typical for a siliceous fly ash, the amorphous content is relatively high, which could be indicative for above average reactivity. The Portland cement composition is normal for a good quality CEM I, the alite (C₃S M3) content is relatively high, C₃A and C₄AF are balanced. Limestone was to be added as minor constituent, but is below the 5% limit for CEM I. The physical properties of each are summarized in Table 2. The initial fly ash has a relatively broad particle size distribution, with a significant fraction under 3 µm. This makes the fly ash an interesting candidate material for further classification treatment. The Portland cement had a d₅₀ of 14 µm, this slightly coarse PSD is in line with the declared cement strength class of 42.5 R.

3.2 Characterisation of size-classified fly ashes

The classification device generated 4 different fractions of fly ash. The particle size distribution curves of these fractions and the initial fly ash are given in Figure 1. The classification mass balance, i.e. the mass fraction of each classified fly ash, and the particle size grading and physical properties of the fly ash fractions are summarized in Table 3. The ultrafine and very fine fractions are close in terms of physical properties; also the medium and coarse fractions are similar.

The ultrafine and very fine fractions represent the bulk of the fraction smaller than 10 µm in the initial fly ash, the recovery yield being 76 % based on the initial fly ash particle size distribution. It should be noted that a compilation of the different fly ash fractions results in a reconstituted particle size distribution which is considerably finer than the initial fly ash. This indicates that the classification treatment leads to particle refinement, either through particle deagglomeration or milling of fly ash particles.

Table 1. Chemical and mineralogical composition of the starting materials – siliceous fly ash and Portland cement

	Raw fly ash	Portland cement		Raw fly ash	Portland cement
	Wt.%	Wt.%		Wt.%	Wt.%
Al ₂ O ₃	22.7	5.2	Quartz	8.1	0.9
SiO ₂	54.4	20.8	Mullite	6.7	-
CaO	3.0	62.1	Magnetite	2.3	-
MgO	1.6	2.0	Hematite	1.4	-
K ₂ O	2.7	1.2	Calcite	0.7	4.8
Na ₂ O	1.1	0.2	Anhydrite	0.6	0.4
Fe ₂ O ₃	8.7	1.9	C ₂ S M3	-	65.7
Mn ₂ O ₃	0.1	-	β C ₂ S	-	13.1
TiO ₂	0.9	0.2	C ₃ A cubic	-	4.2
P ₂ O ₅	0.2	0.3	C ₄ AF	-	6.7
SO ₃	0.3	2.7	Periclase	-	0.9
LOI	4.2	2.4	Gypsum	-	1.8
TOC	3.9	-	Bassanite	-	0.7
			Aphthalite	-	1.0
			Amorphous	80.1	-

Table 2. Physical properties of the starting materials of this study – siliceous fly ash and Portland cement

Sample	Specific surface area	Specific gravity	Particle size distribution		
			d ₁₀ (µm)	d ₅₀ (µm)	d ₉₀ (µm)
Raw fly ash	4.6	2.40	3.0	21	88
Portland cement	1.2	3.13	2.4	14	42

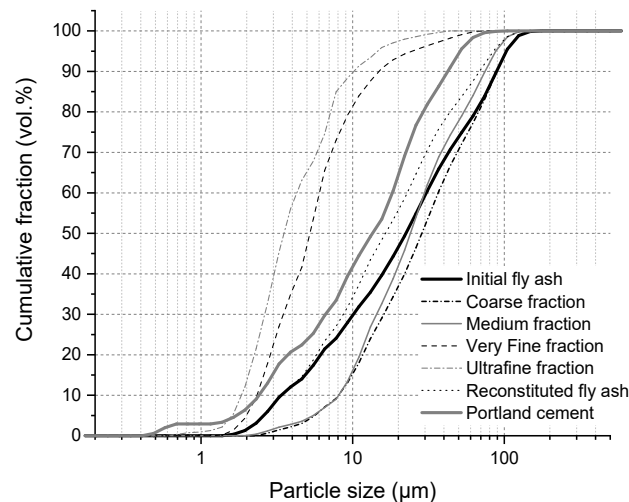


Figure 1. Particle size distribution of the initial and classified fly ashes measured by laser diffractometry.

The main oxide chemical composition of the classified fly ash fractions is given in Table 4. The trace element composition of the respective fractions is reported in Table 5. A distinction between the ultrafine and very fine fractions on the one hand, and the medium and coarse fraction is apparent. The fine fractions are enriched in Al_2O_3 , and to a lesser extent in alkalis and sulphate than the initial fly ash. In exchange the coarser fractions show higher SiO_2 , CaO and Fe_2O_3 than the feed material. A more pronounced repartitioning is noted for the trace element composition. The finer fractions show strong enrichment in As, Cd, Cr, Cu, Hg, Mo, Ni, Pb, V and Zn. Previous studies reported that these hazardous volatile elements (HVEs) metals are captured as condensates sorbed on or encapsulated in nanoparticles such as nano-sulphates, iron nano-hydroxides and residual carbonaceous materials [28].

Table 3. Physical properties of the classified fly ash fractions

Property	Ultrafine fraction	Very fine fraction	Medium fraction	Coarse fraction
Classification mass balance (wt.%)	2.6	25	61.2	11.2
d_{10} (μm)	1.6	2.2	6.8	6.9
d_{50} (μm)	3.0	5.0	22	27
d_{90} (μm)	9.3	12.5	73	90
Specific surface area (m^2/g)	7.1	6.9	4.4	3.6
Specific gravity (g/cm^3)	2.55	2.50	2.32	2.28

Table 4. Major element composition, expressed as oxides, of the classified fly ash fractions

Oxide	Ultrafine fraction	Very fine fraction	Medium fraction	Coarse fraction
	Wt.%	Wt.%	Wt.%	Wt.%
Al_2O_3	26.0	25.5	21.6	21.9
SiO_2	51.9	52.3	55.2	55.5
CaO	2.2	2.3	3.3	3.2
MgO	1.8	1.7	1.6	1.6
K_2O	3.4	3.3	2.5	2.6
Na_2O	1.4	1.4	1.0	1.0
Fe_2O_3	7.7	7.6	9.1	9.1
Mn_2O_3	0.09	0.08	0.11	0.10
TiO_2	1.0	1.0	0.9	0.9
P_2O_5	0.3	0.3	0.2	0.2
SO_3	0.5	0.5	0.2	0.2
LOI	4.3	4.5	4.1	4.7
TOC	3.2	3.7	3.9	4.7

The phase composition measured by XRD-Rietveld analysis of the classified fly ashes is shown in Table 6. The repartitioning of phases over the different fractions is in line with the observed contrasts in chemical composition and earlier characterisation studies on classified fly ash [29]. The enrichment of SiO_2 in the coarser fractions is largely explained by higher quartz and mullite levels. Also the concentration of Fe_2O_3 in the coarser fractions is clarified by an enrichment in crystalline iron oxides such as magnetite and hematite. In the finer fractions, anhydrite is slightly enriched in line with the higher SO_3 levels. Most important in terms of reactivity, however, is the significantly higher amorphous content of the finer fractions. A visual impression of particle size and shape was obtained through SEM imaging. Representative SEM pictures of the ultrafine and the medium size fractions are given in Figure 2. The ultrafine and very fine fractions consist predominantly of spherical particles, with a large fraction of spheres below $5 \mu m$. The medium fly ash fraction is generally more coarse and contains more irregularly shaped particles, such as flaky or angular particles. Still, spherical particles smaller than $5 \mu m$ are clearly present in the medium fraction. Part of these particles occur in agglomerates or are partially welded onto the surface of large particles.

Table 5. Trace element composition of the classified fly ash fractions

Element	Ultrafine fraction mg/kg	Very fine fraction mg/kg	Medium fraction mg/kg	Coarse fraction mg/kg
<i>As</i>	133	107	35.2	32.9
<i>Ba</i>	1670	1570	1350	1350
<i>Be</i>	10.2	9.8	6.7	6.5
<i>Cd</i>	4.88	3.97	1.46	1.36
<i>Co</i>	45.7	42.7	33.2	32.6
<i>Cr</i>	234	188	112	115
<i>Cu</i>	137	123	72	72
<i>Hg</i>	0.93	0.91	0.25	0.3
<i>Mo</i>	47.1	41.4	18.8	18.4
<i>Ni</i>	173	146	93.8	92.1
<i>Pb</i>	151	135	53	50
<i>Sr</i>	495	501	484	477
<i>V</i>	342	309	216	220
<i>Zn</i>	527	434	153	152
<i>Zr</i>	118	121	126	126

Table 6. Phase composition of the classified fly ash fractions

Phase	Ultrafine fraction Wt. %	Very fine fraction Wt. %	Medium fraction Wt. %	Coarse fraction Wt. %
<i>Quartz</i>	3.1	3.6	9.8	9.7
<i>Mullite</i>	5.4	5.7	7	7.5
<i>Hematite</i>	0.6	0.8	1.7	1.6
<i>Magnetite</i>	0.6	0.8	2.8	2.8
<i>Anhydrite</i>	0.8	0.8	0.5	0.7
<i>Calcite</i>	0.8	0.7	0.7	0.9
<i>Amorphous</i>	88.7	87.5	77.5	76.8

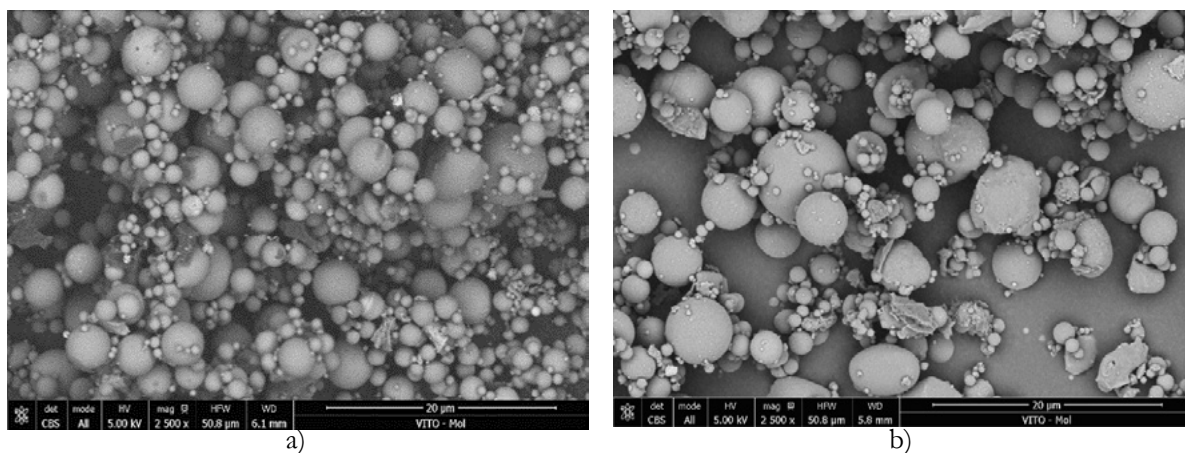


Figure 2. SEM pictures of a) ultrafine fly ash and b) medium size fly ash obtained through classification.

3.3 Reactivity of size-classified fly ashes

The R3 SCM reactivity test is used to measure the chemical (pozzolanic and hydraulic) reactivity of the fly ash fractions obtained by classification. For the ultrafine and very fine fractions, samples from different classification runs performed under different operating conditions were included to increase the number of different results. The particle size distribution of the tested materials is shown in Figure 3. The heat release by the hydration reaction of the fly ash fraction in combination with water, calcium hydroxide, calcium carbonate and small amounts of KOH and K₂SO₄ was measured by isothermal calorimetry at 40 °C. The cumulated heat results until 7 days of reaction are given in Figure 4.

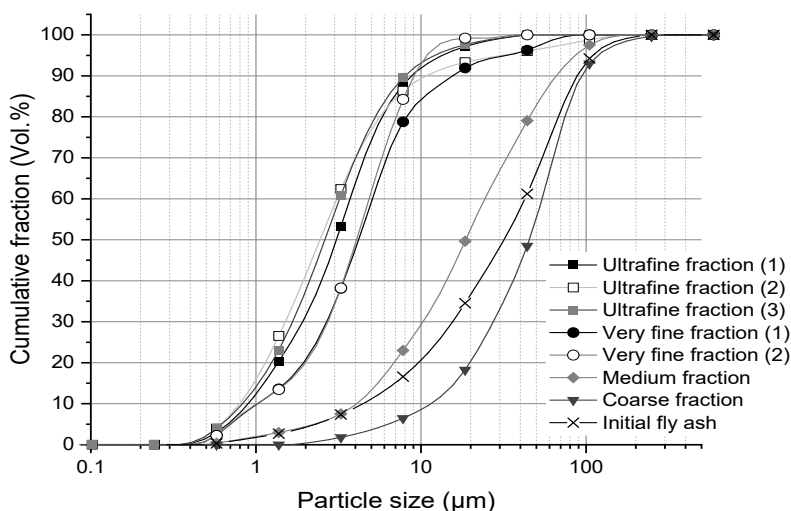


Figure 3. Particle size distribution of all fly ash fractions tested by the R3 reactivity test. The number in brackets indicates that the material was obtained by replicate classification runs.

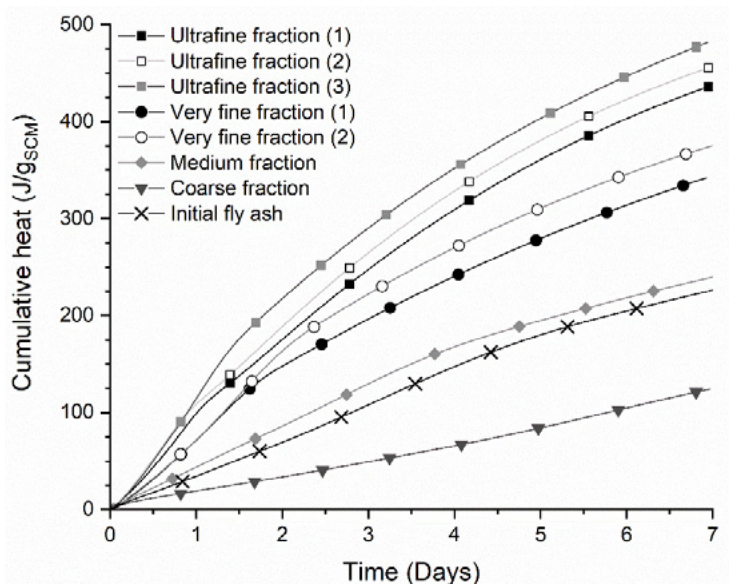


Figure 4. Fly ash reactivity as measured by the R3 calorimetry test. The cumulative heat released by the reaction of the fly ashes over time is a proxy for reactivity. The number in brackets indicates that the material was obtained by a replicate classification run.

The heat release at isothermal conditions can be related directly to the enthalpy difference between products and starting materials. Previous research has shown that the heat release is directly related to the water

bound [23], which is supported by the enthalpy calculations for common cement hydration reactions [30]. More than assessing pozzolanic reactivity, the test results relate to hydration reactivity of the SCM directly and thus avoid issues in determining portlandite consumption rates.

In case of the classified fly ashes, the test results clearly show that the reactivity increases with decreasing particle size. The initial fly ash and the medium fraction show similar heat release and are moderately reactive. The coarser fraction clearly shows reduced reactivity. The very fine and ultrafine fractions clearly show enhanced reactivity in order of decreasing particle size distribution.

To verify whether differences in particle size of the different fraction can explain the noted differences in reactivity microstructure based kinetic modelling was carried out using the particle size distributions from Figure 3. Figure 5 compares the cumulative heat release measured from the isothermal calorimeter and numerical simulations. Based on thermodynamic calculations the simulations assumed the enthalpy of reaction to be 600 J/g. The rate of dissolution was fitted to the experimental data. For both the ultrafine and very fine fractions good fits were obtained using 0.003 $\mu\text{m}/\text{h}$. For the medium and coarse fraction 0.006 $\mu\text{m}/\text{h}$ was obtained. For the initial fly ash 0.008 $\mu\text{m}/\text{h}$ was used. There can be different ways to explain the higher dissolution rates for the coarser fractions. On the one hand, a larger fraction of hollow particles in the coarser fractions (which were found to have significantly lower specific gravity) could positively affect the reaction rate by exposing additional reactive surface once the outer shell is partially consumed. On the other hand experimental effects such as agglomeration of fly ash particles could reduce the reaction rates for the finer fractions. It should also be noted that the simplified approach for modelling presumed isotropic dissolution which was constant over time which may conflict with experimental evidence. The reasons for the discrepancy in dissolution rates will be further investigated in the future.

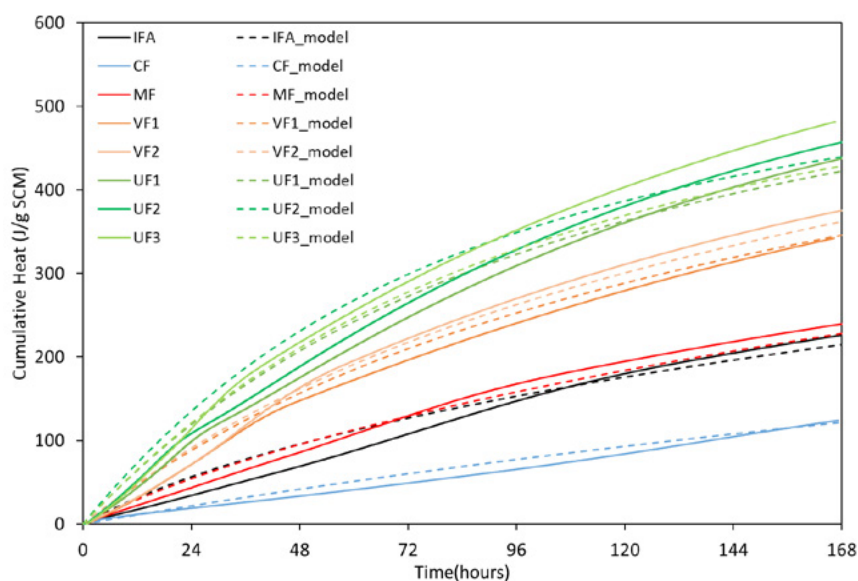


Figure 5 Comparison of experimental heat release from the R3 test (solid line) and simulations (dashed line).

3.4 Impact of fly ash fineness on cement hydration

The replacement of Portland cement by SCMs affects the hydration kinetics and hydration product assemblage. In return, also the strength of the cement changes. In this study the impact of fly ash fineness on cement hydration kinetics was evaluated through measurement of the hydration heat flow by isothermal calorimetry. During hydration the cements were kept at 20°C inside the calorimeter. The heat flow over the first seven days of hydration is shown in Figure 5. A comparison is made between the pure Portland

cement, and the composite cements in which 30 wt.% of the Portland cement is substituted by siliceous fly ash of different fineness, i.e. the very fine and the medium fractions obtained through classification. The calorimetry measurements did not show noticeable changes in the acceleration period of the main hydration peak. The duration of the main hydration peak is lengthened in the composite cements, in particular in case of Portland cement replacement by very fine fly ash. Even more clear is the delay and extension of the heat release peak (shoulder) in the deceleration period, usually explained as an increase in hydration of calcium aluminates upon depletion of solid sulphates. Possibly the presence of some anhydrite in the fly ashes may lead to the delay and extension of the peak.

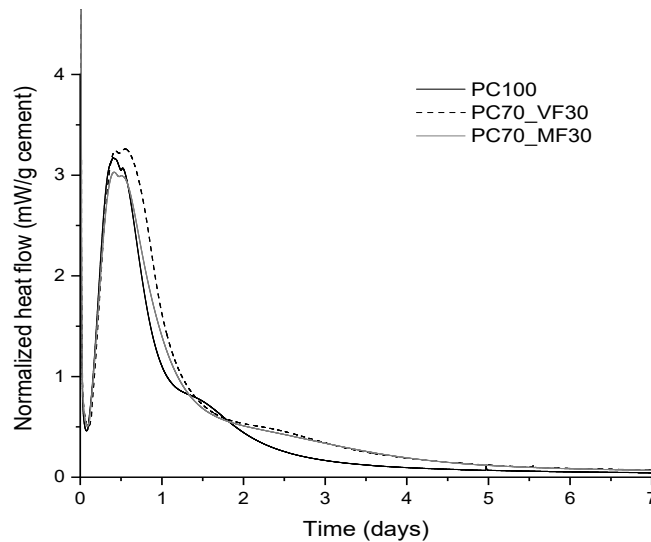


Figure 6. Heat flow measured by isothermal (20°C) calorimetry for the reference Portland cement paste (PC100), and composite cements in which 30% of Portland cement is replaced by the very fine (PC70_VF30) and the medium (PC70_MF30) particle size fractions of the classified fly ash. The heat flow data are normalised per gram of Portland cement.

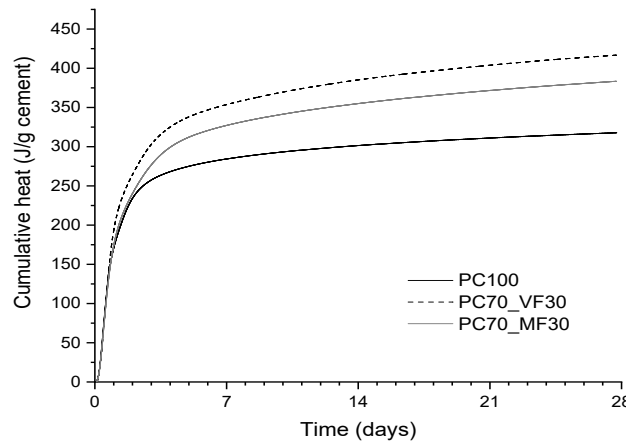


Figure 7. Cumulative heat measured by isothermal calorimetry for the reference Portland cement paste (PC100), and composite cements in which 30% of Portland cement is replaced by the very fine (PC70_VF30) and the medium (PC70_MF30) particle size fractions of the classified fly ash. The data are normalised per gram of Portland cement.

The shoulder peak in the composite cements between 2 to 5 days of hydration leads to a strong increase in cumulative heat signals of the composite cements compared to the reference cement in Figure 6. This overall increase in cumulative heat (normalised to Portland cement content) in composite cements is related to on the one hand additional reaction of the Portland cement also referred to as the filler effect, and on the other hand the reaction of the fly ash. The composite cement with the very fine fly ash shows, at the same

30 wt.% level, higher heat than the medium sized fly ash cement.

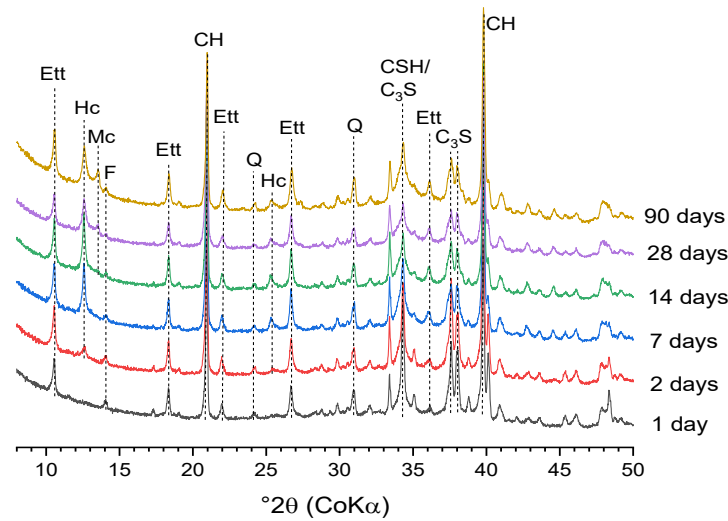


Figure 8. XRD scans of the hydrated composite cement with very fine fly ash (PC70_VF30). The development of the cement hydrate assemblage is shown for selected hydration ages. The main XRD peaks are labelled; Ett stands for ettringite, Hc for hemicarboaluminate, Mc for Monocarboaluminate; F for ferrite, CH for portlandite, Q for quartz, C₃S for alite and CSH for C-S-H.

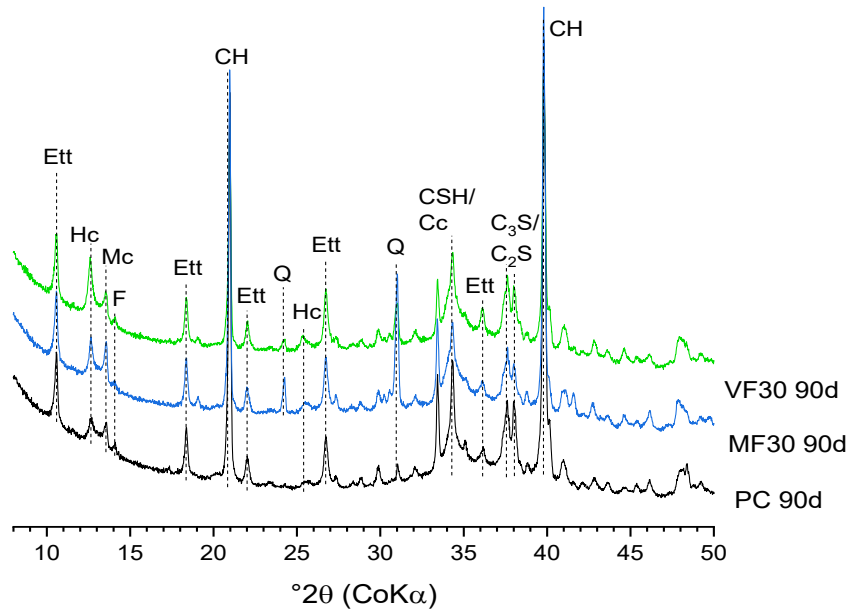


Figure 9. XRD scans of the studied cements at 90 days of hydration. The main XRD peaks are labelled; Ett stands for ettringite, Hc for hemicarboaluminate, Mc for Monocarboaluminate; F for ferrite, CH for portlandite, Q for quartz, C₃S for alite, C₂S for belite, Cc for calcite and CSH for C-S-H.

This implies that part of the additional heat is generated by the reaction of the fly ash, even at early ages of 1 to 2 days of hydration. Thus, it is apparent that the 2-5 days heat flow signal is not only related to renewed hydration of aluminate (C₃A), but also to the reaction of fly ash. In an extended study the reaction degree of the clinker phases and the fly ash will be quantified by Rietveld-PONKCS analysis of XRD data.

The formation of the cement hydration product assemblage was studied by qualitative XRD. XRD measurements on freshly cut disks were made up to 90 days of hydration. A representative time series is shown in Figure 7 for the composite cement containing very fine fly ash. At 1 day of hydration, ettringite is the main calcium aluminate hydrate product. C-S-H is present as well, but difficult to observe as broad

peak overlapping with the alite peaks. During further hydration the typical AFm phases appear. From 2 days onwards hemicarboaluminate can be discerned. Around 14 days, and more conspicuously at 28 days, moncarboaluminate appears. The formation of AFm-carbonate instead of monosulfoaluminate phases is caused by the presence of calcite in the Portland cement. A comparison of the XRD scans of the hydrated cements at 90 days of hydration in Figure 8 learns that the addition of fly ash did not result in important changes in types of products formed. However the fly ash composite cements do show higher peaks for the calcium aluminate hydration products and clearly reduced portlandite peaks, both are indicative for the pozzolanic reaction of the fly ash. The reduction in portlandite peak heights was greater for the very fine fly ash, in line with the higher reactivity measured by the R3 test.

The reactivity study was complemented with compressive strength data for mortar bars containing the reference and composite cements. The data compiled in Figure 9 show that the compressive strength development in the composite cements is slower than for the reference. The very fine fly ash composite cement catches up with the Portland cement by 28 days, the medium fly ash cement stays significantly below the Portland cement at all tested ages. The increased strength gain for the very fine fly ash can be largely related to the additional pozzolanic reaction, although an improved particle packing can also be expected to contribute to the higher strength.

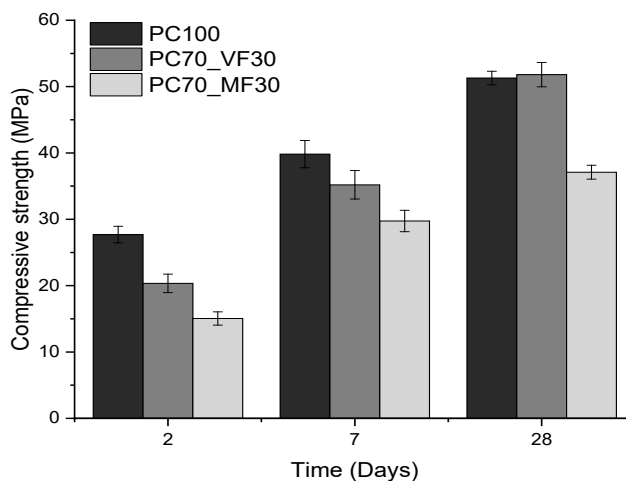


Figure 10. Mortar bar (EN 196-1) compressive strength results up to 28 days of hydration for the studied cements.

4. Conclusions

This paper described the physical properties and the chemical and mineralogical composition of fly ash fractions classified by an innovative, dry, closed-circuit classification device. The classification treatment produced four main fractions: i.e. an ultrafine fraction, a very fine fraction, a medium fraction and a coarse fraction. The ultrafine and very fine fractions had a d_{50} of 3 and 5 μm , the medium and coarse fraction 22 and 27 μm , respectively. As expected, the BET specific surface area was higher for the finer fractions; in contrast their specific gravity was higher, indicating less internal porosity or hollow cores. In terms of chemical composition the finer fractions were enriched in Al_2O_3 and depleted in SiO_2 and Fe_2O_3 , mainly reflecting concentration of quartz and iron oxide particles in the coarser fractions. In exchange the finer fractions contained higher amounts of amorphous material. The TOC increased with median particle size. Hazardous volatile elements on the other hand were considerably enriched in the finer fractions reflecting condensation on smaller particles.

The pozzolanic reactivity of the fly ash fractions measured using the R3 heat release test showed a

predominant effect of particle size. The finer the fraction, the higher the reactivity. The ultrafine fraction was about two times more reactive than the initial, non-classified fly ash. The coarse fraction was only half as reactive. Kinetic modelling indicated that secondary factors such as particle geometry need to be taken into account to fully explain the differences in reactivity. Hydration studies of cement and mortar containing the classified fly ashes confirmed the beneficial effect of fly ash fineness on reactivity by showing a.o. increased $\text{Ca}(\text{OH})_2$ consumption and strength development for finer fly ash.

4. Acknowledgments

RS, HK, ML, PN and LV gratefully acknowledge funding support by the European Institute of Innovation and Technology (EIT) RawMaterials received under PA 16390 FLAME – FLy Ash to valuable MinErals.

5. References

- [1] United Nations Framework Convention on Climate Change 2015. The Paris Agreement, Secretary-General of the United Nations, New York City, United States.
- [2] International Panel on Climate Change, 2014. Climate Change 2014: Synthesis Report. Contribution of Working Groups I, II and III to the Fifth Assessment Report of the Intergovernmental Panel on Climate Change, in: R.K. Pachauri, L.A. Meyer (Eds.), IPCC, Geneva, Switzerland.
- [3] European Commission, 2014. A policy framework for climate and energy in the period from 2020 to 2030, European Commission, Brussels, Belgium.
- [4] European Commission, 2018. A Clean Planet for all - A European strategic long-term vision for a prosperous, modern, competitive and climate neutral economy, European Commission, Brussels, Belgium.
- [5] K.L. Scrivener, V.M. John, E.M. Gartner, 2016. Eco-efficient cements: Potential economically viable solutions for a low- CO_2 cement-based materials industry, UNEP report, 64 pp.
- [6] M. De Schepper, P. Van den Heede, I. Van Driessche, N. De Belie, 2014. Life cycle assessment of completely recyclable concrete, *Materials*, 7, 6010-6027.
- [7] J.S. Damtoft, J. Lukasik, D. Herfort, D. Sorrentino, E.M. Gartner, 2008. Sustainable development and climate change initiatives, *Cement and Concrete Research*, 38, 115-127.
- [8] K.L. Scrivener, 2014. Options for the future of cement. *Indian Concrete Journal*, 88, 11-21.
- [9] A. Favier, C. De Wolf, K. Scrivener, G. Habert, 2018. A Sustainable Future for the European Cement and Concrete Industry - Technology assessment for the full decarbonisation of the industry by 2050, European Climate Foundation, Brussels, Belgium.
- [10] R. Snellings, G. Mertens, J. Elsen, 2012. Supplementary cementitious materials, *Reviews in Mineralogy and Geochemistry*, 74, 211-278.
- [11] R. Snellings, 2016. Assessing, understanding and unlocking supplementary cementitious materials, *RILEM Technical Letters*, 1, 50-55.
- [12] M. Antoni, J. Rossen, F. Martirena, K. Scrivener, 2012. Cement substitution by a combination of metakaolin and limestone, *Cement and Concrete Research*, 42, 1579-1589.
- [13] S. Adu-Amankwah, M. Zajac, C. Stabler, B. Lothenbach, L. Black, 2017. Influence of limestone on the hydration of ternary slag cements, *Cement and Concrete Research*, 100, 96-109.

- [14] K. De Weerd, M.B. Haha, G. Le Saout, K.O. Kjellsen, H. Justnes, B. Lothenbach, 2011. Hydration mechanisms of ternary Portland cements containing limestone powder and fly ash, *Cement and Concrete Research*, 41, 279-291.
- [15] K. Sideris, H. Justnes, M. Soutsos, T. Sui, 2018. Fly Ash, In: De Belie, N., Soutsos, M., Gruyaert, E. (eds.), *Properties of Fresh and Hardened Concrete Containing Supplementary Cementitious Materials*, Springer, pp. 55-98.
- [16] H.S. Pietersen, A.L. Fraay, J.M. Bijen, 1989. Reactivity of fly ash at high pH, *MRS Online Proceedings Library Archive*, 178.
- [17] Z. Yao, X. Ji, P. Sarker, J. Tang, L. Ge, M. Xia, Y. Xi, 2015. A comprehensive review on the applications of coal fly ash, *Earth-Science Reviews*, 141, 105-121.
- [18] K.H. Obla, R.L. Hill, M.D. Thomas, S.G. Shashiprakash, O. Perebatova, 2003. Properties of concrete containing ultra-fine fly ash, *ACI materials journal*, 100, 426-433.
- [19] P. Chindaprasirt, S. Homwuttiwong, V. Sirivivatnanon, 2004. Influence of fly ash fineness on strength, drying shrinkage and sulfate resistance of blended cement mortar, *Cement and Concrete Research*, 34, 1087-1092.
- [20] P. Chindaprasirt, C. Jaturapitakkul, T. Sinsiri, 2007. Effect of fly ash fineness on microstructure of blended cement paste, *Construction and Building Materials*, 21, 1534-1541.
- [21] R. Snellings, 2016. X-ray powder diffraction applied to cement, in: Scrivener, K.L., Snellings, R., Lothenbach, B.L. (eds.) *A practical guide to microstructural analysis of cementitious materials*. CRC Press, Boca Raton, pp. 107-176.
- [22] X. Li, R. Snellings, M. Antoni, N.M. Alderete, M.B. Haha, S. Bishnoi, Ö. Cizer, M. Cyr, K. De Weerd, Y. Dhandapani, 2018. Reactivity tests for supplementary cementitious materials: RILEM TC 267-TRM phase 1, *Materials and Structures*, 51, 151.
- [23] F. Avet, R. Snellings, A.A. Diaz, M.B. Haha, K. Scrivener, 2016. Development of a new rapid, relevant and reliable (R3) test method to evaluate the pozzolanic reactivity of calcined kaolinitic clays, *Cement and Concrete Research*, 85, 1-11.
- [24] S. Joseph, K. Van Balen, S. Bishnoi, Ö. Cizer, CemRS: fast and efficient modelling platform for the simulation of cementitious systems, 2016. *International RILEM Conference Materials Systems and Structures in Civil Engineering 2016 (MSSCE 2016) on Service Life of Cement-Based Materials and Structures*, pp. 573-579.
- [25] P. Termkhajornkit, R. Barbarulo, 2012. Modeling the coupled effects of temperature and fineness of Portland cement on the hydration kinetics in cement paste, *Cement and Concrete Research*, 42, 526-538.
- [26] S. Bishnoi, K.L. Scrivener, *mic*, 2009. A new platform for modelling the hydration of cements, *Cement and Concrete Research*, 39, 266-274.
- [27] K. Van Breugel, 1995. Numerical simulation of hydration and microstructural development in hardening cement-based materials (I) theory, *Cement and Concrete Research*, 25, 319-331.
- [28] M.L. Oliveira, F. Marostega, S.R. Taffarel, B.K. Saikia, F.B. Waanders, K. DaBoit, B.P. Baruah, L.F. Silva, 2014. Nano-mineralogical investigation of coal and fly ashes from coal-based captive power plant (India): an introduction of occupational health hazards, *Science of the Total Environment*, 468, 1128-1137.

- [29] M. Jones, A. McCarthy, A. Booth, 2006. Characteristics of the ultrafine component of fly ash, *Fuel*, 85, 2250-2259.
- [30] R. Snellings, X. Li, F. Avet, K. Scrivener, 2019. A rapid, robust and relevant R3 reactivity test for supplementary cementitious materials, *ACI Materials*.

Evaluation of calcined dredged sediments as supplementary cementitious materials

H. Kazemi-Kamyab¹, L. Van den Abeele¹, M. Henry², L. Haouche³, R. Snellings¹

¹ Sustainable Materials, Flemish Institute of Technological Research (VITO), Boeretang 200, B-2400 Mol, Belgium

² Centre Terre et Pierre (CTP), Chaussée d'Antoine 55, 7500 Tournai, Belgium

³ Institut Scientifique de Service Public (ISSEP), Rue de la Platinerie 12/Z, 7340 Colfontaine, Belgium

Email of the corresponding author: hadi.kamyab@vito.be

Abstract

Valorisation of the dredging sediments has gained a lot of attention over the recent years. An application route that has attracted considerable interest is the use of calcined dredged sediments as Supplementary Cementitious Material (SCM) in composite cements to replace clinker.

The present study investigates the valorisation potential of sediments dredged from three different inland waterway locations in the Belgian – French cross-border region as part of the Interreg V France-Wallonie-Vlaanderen VALSE project. The objective is to evaluate the optimum calcination temperature of the sediments at which the calcined sediments would be most reactive as SCMs. The sediment filter cake (raw) from each location was calcined at 500 °C, 600 °C, 700 °C and 800 °C. Physical and chemical characteristics were evaluated as a function of the calcination temperature.

The results show that the optimum calcination temperature was at 800°C for Brussels-Charleroi (BC) and Lens (L), and 700°C for Gent-Terneuzen (GT). The optimum calcination resulted in degradation of organic matter, which along with densification of particles and sintering, decreased the specific surface area and increased the particle size; furthermore the optimum calcination resulted in activation of clay minerals, and dissolution of CaCO₃. The R³ test method confirmed the optimum calcination temperature for each sediment to have the highest pozzolanic reactivity in the model system. Furthermore it was seen from the R³ test that all calcined sediments had comparable or even better reactivity as regular siliceous fly ashes.

Keywords: Dredged sediments, Supplementary cementitious materials, Calcination, Pozzolanic activity

1. Introduction

The buildup of sediments in ports, channels, reservoirs and dams can significantly alter their foreseen designed functionalities. In Europe the disposal of the dredged sediment by landfilling has become already an inferior option due to unwanted ecological effects, cost of landfilling, and scarcity of suitable landfilling sites. That is why valorization of the dredging sediments are of paramount importance and have gained a lot of attention.

Valorization routes for dredged sediments that have been considered include use in large-scale civil engineering works such as hydraulic or road works, use as raw material in the production of fired bricks or light-weight aggregates or use as raw material in the production of Portland clinker [1]. An application route that has received considerable recent attention is the use of calcined dredged sediments as Supplementary

Cementitious Material (SCM) in composite cements to replace clinker [2-4]. As such it could contribute to reducing the CO₂ impact of cement production. In addition careful selection and preparation of SCMs and their replacement levels can improve the rheological, mechanical and durability of concrete [5-7].

However due to the heterogeneity of the dredged sediments and different sources of contaminants such as heavy metals, and organics, most studies carried out are site specific. In order to be able to have a holistic approach toward their utilizations as an SCM, a broader investigation needs to be undertaken on a regional level. Characterizing the dredged sediments of several specific sites within a region provides the necessary information to gain better understanding of important parameters influencing their reactivity as SCMs. In this context the present study investigates the valorisation potential of sediments dredged from inland waterways in the Belgian – French cross-border region as part of the Interreg V France-Wallonie-Vlaanderen VALSE project. This region has experienced strong (historic) industrial activity resulting in increased concentrations of heavy metals and organic contamination in some areas. Dredged sediments with different composition and varying heavy metal and organic material contamination from three different locations were considered: Brussels-Charleroi (BC) channel, Gent-Terneuzen (GT) channel and Lens (SO) channel sediment.

The outcome will be to use the results obtained in the regional scale to assist in framing guidelines on influential parameters that can affect the pozzolanic activity of the calcined sediments as a SCM and also how to deal with contaminations.

2. Materials & Methods

Dredged sediments from three different locations were considered: Brussels-Charleroi (BC) channel, Gent-Terneuzen (GT) channel and Lens (SO) channel sediment. Herein for each sediment before calcination the sand fraction (>63 μm) was removed and the remaining fine fraction was dewatered using a pilot filter press. The obtained sediment filter cake (here defined as raw) was calcined for 1 hour in a box furnace under static conditions at the following temperatures 500 °C, 600 °C, 700 °C and 800 °C, in air. The following material designation is used herein:

1. For raw filter cakes: “Location-Raw”. For instance BC-Raw means the raw filter cake from Brussels-Charleroi (BC) channel.
2. Associated calcinated temperatures: “Location-Temperature.” For instance BC-500 °C means the BC raw filter cake calcined at 500 °C.

The chemical composition of the raw sediments were obtained using VARIAN Vista MPX Radial inductively coupled plasma (ICP). A sediment sample was attacked with regia water under reflux for 4 hours. After filtration, the residue undergoes alkaline fusion (in a crucible, under a Bunsen nozzle and in the presence of fluxes [NaOH and Na₂O₂]). The result of the alkaline fusion and the filtrate of the regia water attack are then analysed by inductively coupled plasma - optical emission spectrometry (ICP-OES).

Physical and chemical characteristics were evaluated as a function of the calcination temperature by means of BET N₂ sorption, laser diffraction particle size analysis, helium pycnometry, thermogravimetric analysis (TG), X-ray powder diffraction (XRD), Total Inorganic Carbon (TIC) and Total Organic Carbon (TOC) analysis, and bomb calorimetry to measure the sample calorific value.

The specific surface areas were measured using a Quantachrome Nova 3000 instrument with Brunauer–Emmett–Teller (BET) N₂ sorption method; the materials were pre-treated by degassing at 40 °C under N₂ atmosphere for 16 h.

Particle size distributions (PSD) were evaluated using a Microtrac S3500 laser diffraction setup. The powders were first pre-treated by dispersing them in distilled water and ammonium polyacrylate, followed by external ultrasonication at 270 W for 2 min.

The density of the powders was evaluated using a Micromeritics Accupyc II 1340 Helium pycnometer. Approximately 1.5 to 2 g of powders are used to carry out the analysis.

Thermogravimetric analysis (TGA) on the powders was carried out using a Netzsch STA449 F3 Jupiter. Approximately 50 mg of powders was analysed from 30 °C to 1050 °C with a heating rate of 10 °C/min under N₂ flow of 50 mL/min.

Changes in the crystalline phases were identified using X-ray powder diffraction (XRD). The XRD patterns were acquired on a X'Pert PRO diffractometer from PanAnalytical with CoK α tube operating at 40 kV and 45 mA. Diffraction scans were recorded from 3 to 120 °2 θ , with accumulated dwell time of 59.6 s, and step size of 0.013 °2 θ .

The R³ test method was used to evaluate pozzolanic reactivity of the raw and calcined sediments. In this method the SCM under investigation was mixed with excess portlandite, and water; calcite, potassium sulphate and potassium hydroxide were also added. The paste simulates the environment in which the SCM reacts in hydrating cement without the complexity of simultaneous reactions of clinker phases. The reaction of the SCM in this model environment was measured by isothermal calorimetry at 40 °C for 7 days. The heat flow of the model paste was used to obtain the cumulative heat release up to 7 days. Complementary X-ray diffraction (XRD) and TG data were used to identify reaction products and portlandite consumption. More information about this method can be found in [8, 9].

3. Results and discussion

3.1 Dredging sediment characterisation

Table 1 shows the chemical composition of the raw sediments obtained by ICP. Furthermore the total carbon and total inorganic carbon are also tabulated. It can be seen the main oxides are SiO₂, followed by Al₂O₃, Fe₂O₃, and CaO. Note that the amount of CaO in SO is two times more than BC and GT.

Table 1 - Chemical composition of the raw sediments.

Raw Sediment	Chemical composition (wt.%)											
	SiO ₂	Al ₂ O ₃	Fe ₂ O ₃	CaO	MgO	K ₂ O	Na ₂ O	SO ₃	P ₂ O ₅	LOI	TC	TOC
BC	40.8	13.9	10.0	2.6	1.1	2.1	0.5	1.0	1.1		13.18	11.97
GT	61.8	9.9	4.1	5.5	1.3	1.4	<0.7			13.3	4.50	3.62
SO	32.2	8.2	4.3	10.8	0.9	1.6	1.9	4.0	1.4		13.79	10.35

Figure 1, shows the X-ray diffraction patterns of the three raw sediments. It can be seen that all have notable presence of quartz, in descending order of signal intensity, being GT>SO>BC. All sediments also contained carbonates. The amount of calcite in BC was small while in case of SO the amount was very significant; the presence of calcite in descending order of signal intensity is as follows SO>GT>BC.

Depending on the sediment, there is more or less of the clay minerals (Clinochlore, kaolinite, and illite) and feldspar minerals (albite and microcline). However it can be seen that all have a noticeable presence of kaolinite which is well-known to transform into a reactive SCM upon calcination at the appropriate temperature [10]. The combined presence of calcite and potentially less-reactive clay minerals is also considered promising as they may react during calcination to form a reactive amorphous Ca-enriched aluminosilicate compound [4].

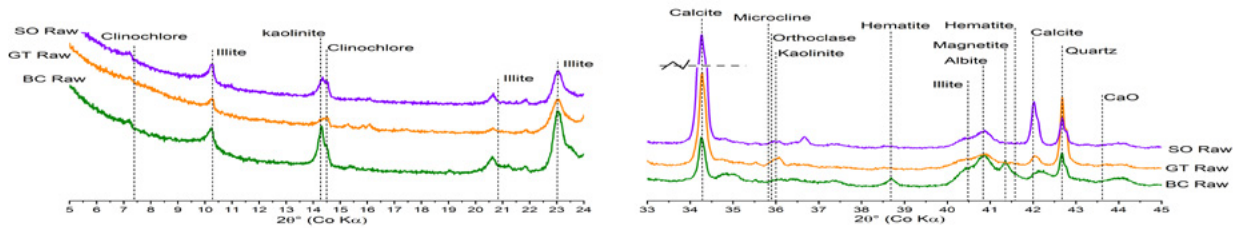


Figure 1- X-ray diffraction patterns of the raw sediments.

Table 2 shows the trace elements in the raw sediments, measured by ICP-OES. In addition the maximum allowable content values and safety limit values set by Wallonia, Flanders and France have also been tabulated. For each sediment if the value of the trace elements is below the maximum allowable content set by any of the legislations, the sediment is safe to be used in any application. However the approach of the legislations somewhat differs if one or more trace elements exceed the maximum allowable content:

1. In case of Flanders: if one or more trace elements exceed the maximum allowable content but not the safety limit, the sediment can be used in soil/bound and unbound construction applications. However if one or more trace elements exceed also the safety limit values, then leaching tests according to EN 12457-2 need to be carried out. If none of elements exceed the maximum allowable leaching limits put into effect by the legislation, then the sediment can still be used in soil/bound and unbound construction applications.
2. In case of Wallonia and France: if one or more trace elements exceed the maximum allowable content but not the safety limit, the sediment can be used in soil/bound and unbound construction applications. However if one or more trace elements exceed also the safety limit values, then leaching tests according to EN 12457-2 need to be carried out but even if none of elements exceed the maximum allowable leaching limits put into effect by legislations, extra actions need to be taken before the sediment is allowed to be used in soil/bound and unbound construction applications.
3. In case of France: For road applications, SETRA (2011) which is a guide dedicated to the valorization of alternative materials is used [11]. Note that in the absence of other standards, this guide is also used in other fields. In case of immersion of the marine sediment, a common approach for conducting a screening sediment risk assessment is to compare available chemical data on sediments with Sediment Quality Guidelines (SQGs). At the French level, SQGs are available for management of contaminated dredged sediments for several chemicals. These regulatory SQGs, named levels N1 and N2, are defined for metals and some organic compounds. Dredged sediment dispersal is permitted offshore when pollutant concentrations are lower than level 1 (N1). Dredged sediments considered as contaminated for marine environment (> N1) cannot be discharged into the sea without further ecotoxicological assessment according to GEODRISK framework [12]. Above the level N2, dredged sediments must be managed on land and are considered as wastes.

Table 2 - Trace elements concentrations in the raw sediments (units are in mg/kg of dry matter).

	Raw Sediment	As	Cd	Co	Cr total	Cu	Hg	Ni	Pb	Zn	F ⁻	CN ⁻
	BC	54.9	126.7	< 10	268.4	269.1	1.45	149.9	813.5	4790.5	437.0	109.1
	GT	12	5	11	82	76.9	3.7	26	116	591	5.41	-
	SO	21.2	< 10	14.6	125.8	855.5	1.74	61.0	480	2023.8	346.1	7.7
Wallonia	Maximum allowable content	50	6	25	200	150	1,5	75	250	1200	250	5
	Safety Limit	100	30	100	460	420	15	300	1500	2400	500	25
	Maximum allowable leaching limits	0.5	0.1	0.5	0.5	2	0.02	0.5	0.5	2.0	20.0	0.1
Flanders	Maximum allowable content	30	2	19	70	74	2.9	48	200	200	55	-
	Safety Limit	267	30	-	880	500	11	530	1250	1250	-	5
	Maximum allowable leaching limits	0.3	0.02	-	0.1	0.6	0	0.2	0.3	1.00	-	-
France	Maximum allowable content (N1)	25	1.2	-	90	45	0.4	37	100	276	-	-
	Safety Limit (N2)	50	2.4	-	180	90	0.8	74	200	552	-	-
	Maximum allowable leaching limits	0.5	0.04	-	0.5	2	0.01	0.4	0.5	4.0	10.0	-

There are significant differences on the pollutant concentrations, contained in the three raw sediments. The BC-Raw sediment surpasses the local (Wallonia) safety limit for Cd, Cr_{total}, Cu, Zn, fluoride (F⁻) and cyanide (CN⁻), while the SO-raw surpasses the local (French) safety limit for Cu, Zn, and fluoride. Table 2 shows that none of the raw sediments pass the maximum allowable content criteria set by any of the legislations. However it can be seen that while sediments BC and SO exceed the safety limit values set by the three legislations, the GT sediment passes the safety limit values set by Wallonia and Flanders, but not the French legislation. It can therefore be concluded that leaching test on final products need to be carried out to evaluate compliance to environmental legislation for cement and concrete containing (treated) BC and SO sediments.

In order to interpret the changes in physical properties such as specific gravity, specific surface area, and PSD as function of calcination temperature (Figure 2) following the alteration in the chemical characteristics of sediments as function of temperature (Figure 3) is necessary.

Figure 2.a shows the total carbon (TC) and total organic carbon (TOC) as function of calcination temperature. Note that in case of SO sediment calcinated at 500 °C and 700 °C, the measurements were

not carried out at the time of writing. Furthermore the bomb calorimetry results carried out on the three raw sediments are also shown as a 2nd y-axis in Figure 2.a. It can be seen that GT sediment has three times smaller TC and TOC compared to BC and SO which corresponds well with the calorific value of GT-raw that is approximately 3 to 4 times smaller. It can be observed that already at 500 °C, most organic matter has been decomposed and values of TC and TOC have decreased significantly; this trend continues and by 800 °C the TC and TOC values in case of BC and GT are negligible. However in case of SO, the rate of degradation of organic matter is lower with increasing calcination temperature compared to the other two sediments and it persisted up to 600 °C, and even at 800 °C but again the values of TC and TOC are very small at this heat treatment temperature. Rock-Eval pyrolysis can be carried out to better understand the source of the organic carbon in case of SO sediment [13].

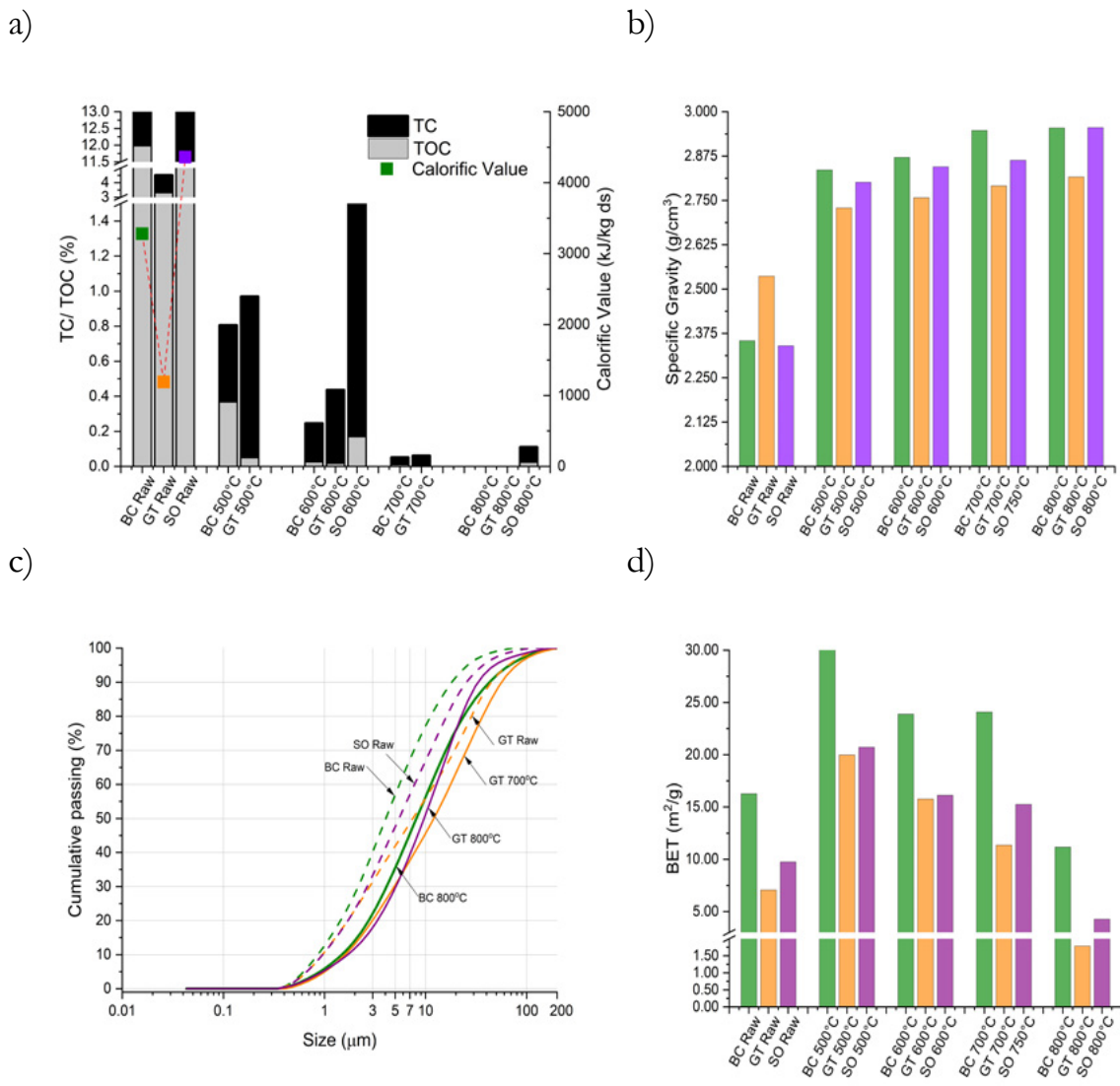


Figure 2 - Physical & chemical characterization of the sediments as function of calcinated temperature: a) Total carbon (TC), total organic carbon (TOC), and calorific value from bomb calorimetry . b) Specific gravity c) Particle size distribution (PSD) d) BET specific surface area.

Figure 2.b,c, and d show respectively the specific gravity, PSD, and specific surface area of the sediments as function of calcination temperature. It can be seen that in case of all sediments there is an increase of the specific surface at 500 °C, and thereafter they continuously decrease. In addition, the PSD shifts to coarser size with increasing calcination temperature. The specific gravity of all sediments increases with increasing calcination temperature and reaches a constant value around 700 °C to 800 °C. The abovementioned observation can be explained as following: degradation of the coarse organic matter increases the specific

surface area and specific gravity at 550 °C. Although there might be some agglomeration of particles which leads to having a small increase in the PSD, this influence is small at 500 °C. Calcination at higher temperatures leads to densification of particles due to partial sintering and formation of high temperature phases such as albite and hematite. This is also reflected in a coarser PSD, and lower specific surface area. In addition to densification and partial sintering, decomposition of organics and decarbonation of limestone are the main reasons increasing the specific gravity from 500 °C to 800 °C in all sediments.

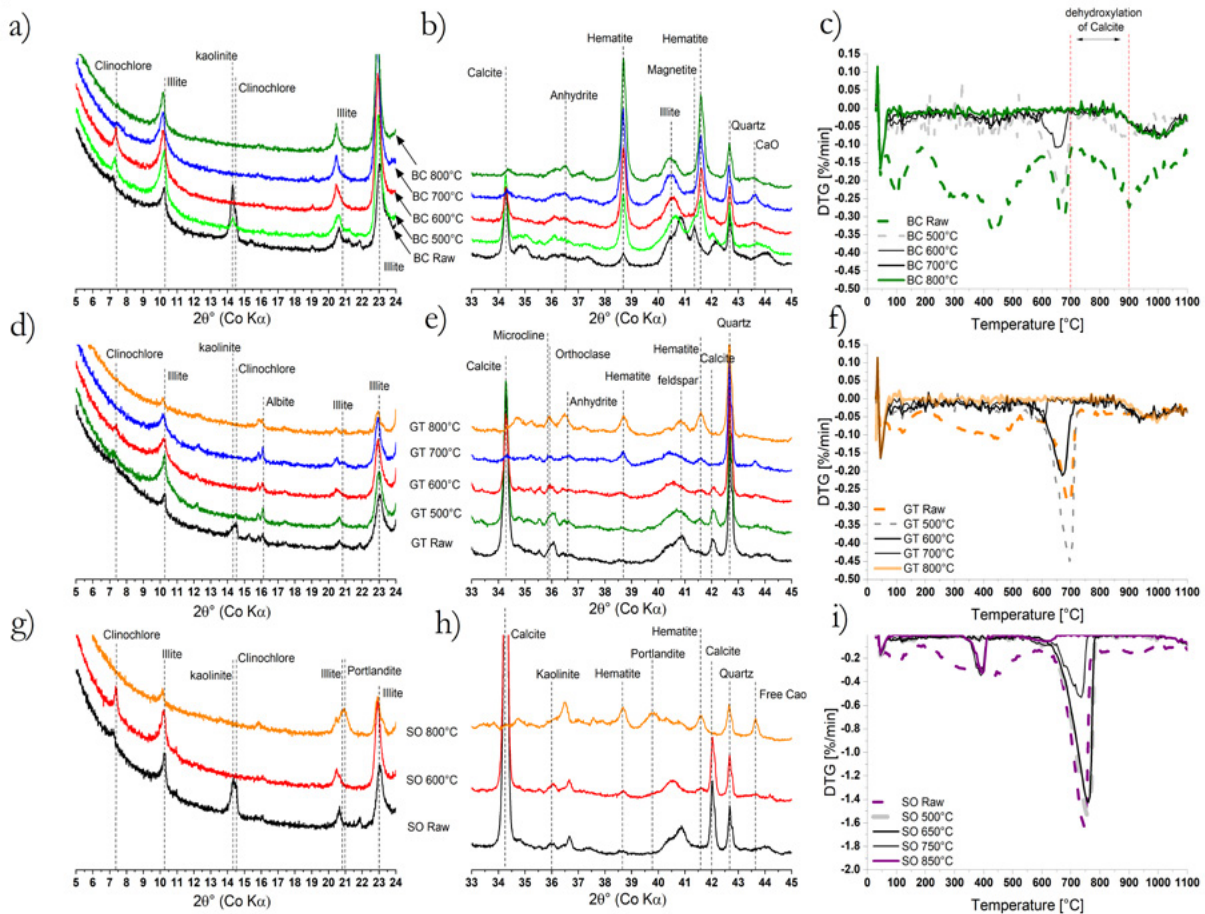


Figure 3 - Chemical characterization of sediments as function of calcination temperature.

Figure 3 shows the XRD patterns and derivative thermogravimetry (DTG) results of the sediments as function of the calcination temperature. The heat treatment has caused a mineralogical modification of clay fractions which led to reflection of some clays such as kaolinite and Illite to disappear or weaken making the sediment more amorphous. In addition both from the XRD patterns and DTG, it is clear that in all sediments calcined at 700 °C and 800 °C the calcite originally present was decomposed. In case of the SO sediment, decarbonation of the calcite was accompanied with formation of portlandite and free CaO.

3.2 R³ test

Based on the physical and chemical characterization carried out as function of temperature in the previous section, it can be inferred that the optimum calcination temperatures should be at the higher temperature range. However it is not clear what specific temperature investigated is the optimum calcination temperature in terms of pozzolanic reactivity for the calcined sediments. Therefore R³ reactivity tests were carried out on all three dredging sediments at various calcination temperatures.

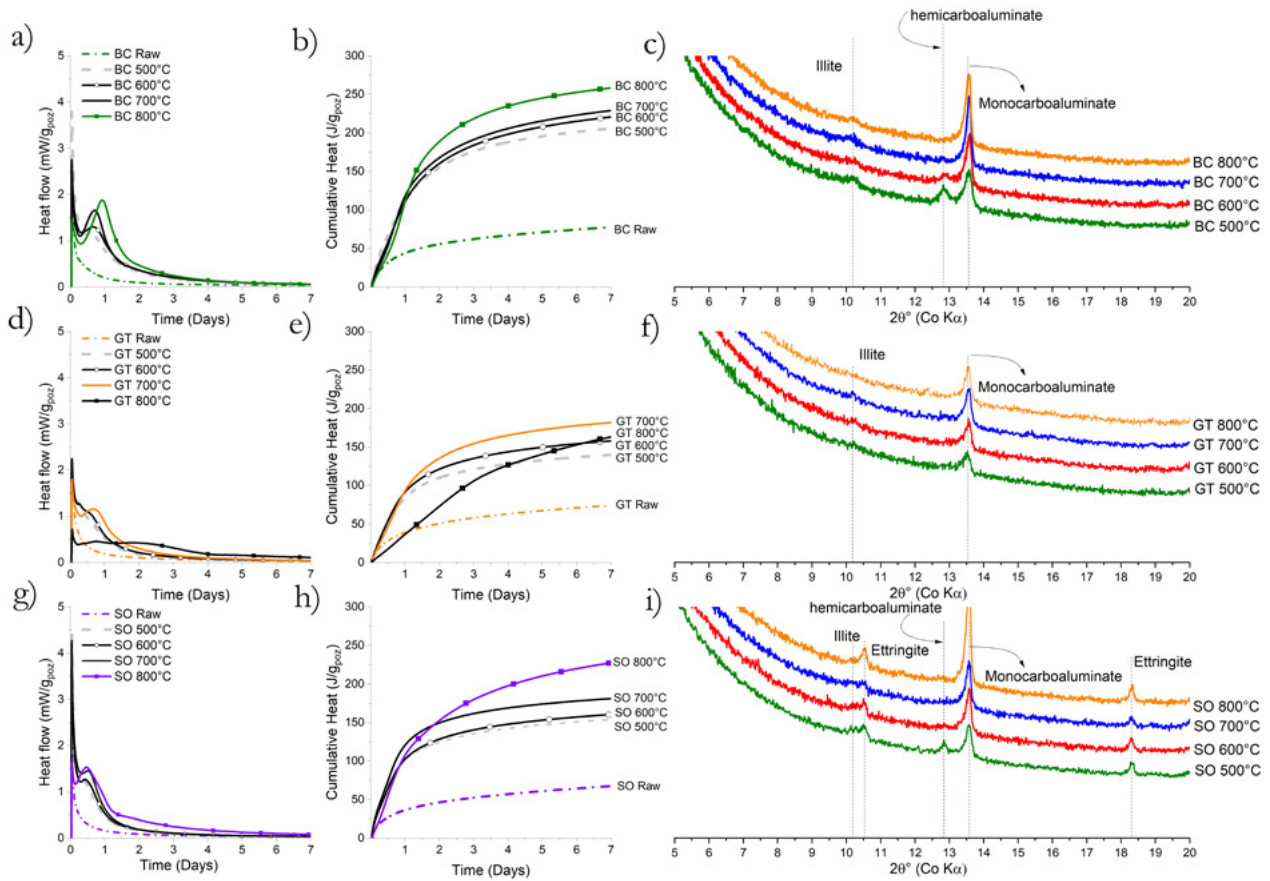


Figure 4 - R³ test results of the three calcined dredging sediment fine fractions as function of calcination temperature: a&b) heat flow and cumulative heat from the isothermal calorimetry at 40°C of the BC sediment c) XRD pattern of the BC samples after 7 days of hydration/reaction at 40°C. d&e) heat flow and cumulative heat from the isothermal calorimetry at 40°C of the GT sediment f) XRD pattern of the GT samples after 7 days of hydration/reaction at 40°C g&h) heat flow and cumulative heat from the isothermal calorimetry at 40°C of the SO sediment i) XRD pattern of the SO samples after 7 days of hydration/reaction at 40°C.

Figure 4 shows the results of the R³ test on the dredging sediments as a function of calcination temperature. It can be seen from the R³ tests, that the optimum calcination temperature for BC and SO is around 800 °C while in case of GT is around 700 °C. In case of GT calcined at 800 °C the decrease in reactivity can be linked with a recrystallization and formation of high temperature phases and thus decrease in the amorphous content coming from the clay content. The XRD measurements of the R³ pastes hydrated for 7 days at 40 °C in Figure 4 show hydration product forming; monocarboaluminate and hemicarboaluminate form in all sediments and in case of SO, ettringite is also formed. All sediments show promising pozzolanic activity at their optimum calcination temperatures. The R³ test shows that if the sediments are calcined at their optimum temperature, they are potentially more or at least as reactive as a commercial siliceous fly ash which in a R³ test shows cumulative heat in the range of 100 to 200 j/g_{poz} by the age of 7 days.

4. Conclusion

The valorisation as supplementary cementitious material of inland waterway dredged sediments from the Belgian-French cross border region was studied. To this purpose, the fine (<63 μm) fraction of sediments from the Brussels-Charleroi (BC), Lens (SO), and Gent-Terneuzen (GT) channels was recovered and calcined at 500 °C, 600 °C, 700 °C and 800 °C. The chemical and physical characterization of the raw and calcined sediments showed that thermal treatment at 500 °C to 800 °C led to distinct physical and chemical changes in the materials. These changes are summarized by calcination temperature interval as follows:

- It was seen that at 500 °C, organic matter was largely decomposed. The specific surface area increased, while the specific gravity increased and the PSD coarsened mainly due to decomposition of most of the organic matter at 500 °C. At 500 °C, the heat treatment did not cause decomposition of kaolinite and chlorite clay minerals.
- At 600 °C and higher, the decrease in organic content observed at 500 °C continued and by 800 °C it was very small. The PSD further coarsened with increasing calcination temperature, likewise the specific gravity of all sediments increased with increasing calcination temperature. Conversely, the specific surface area decreased. The main reason for the physical changes observed herein were due to decomposition of calcite, partial sintering and formation of high temperature phases such as feldspars and hematite.

The R3 SCM reactivity test was used to evaluate the optimal calcination temperature for the dredging sediments. The R3 test results clearly demonstrated that the optimum calcination temperature of Brussels-Charleroi, Lens sediments were at 800 °C and for the Gent-Terneuzen channel sediment was 700 °C.

5. Acknowledgments

The authors like to thank the financial support of the Interreg V France-Wallonie-Vlaanderen VALSE project.

6. References

- [1] S. Rakshith, D. Singh, Utilization of dredged sediments: contemporary issues, *Journal of Waterway, Port, Coastal, and Ocean Engineering*, 143 (2016) 04016025.
- [2] T.A. Dang, S. Kamali-Bernard, W.A. Prince, Design of new blended cement based on marine dredged sediment, *Construction and Building Materials*, 41 (2013) 602-611.
- [3] B. Beckstrom, D. R. Leavitt, M. C. Mesinger, B. Cutler, A. Hendricks, R. Fabricant, E. Peck, E. Stern, *Thermal Treatment for Reclamation and Beneficial Use of Contaminated Sediments*, 2014.
- [4] R. Snellings, Ö. Cizer, L. Horckmans, P.T. Durdziński, P. Dierckx, P. Nielsen, K. Van Balen, L. Vandewalle, Properties and pozzolanic reactivity of flash calcined dredging sediments, *Applied Clay Science*, 129 (2016) 35-39.
- [5] R. Snellings, L. Horckmans, C. Van Bunderen, L. Vandewalle, Ö. Cizer, Flash-calcined dredging sediment blended cements: effect on cement hydration and properties, *Materials and Structures*, 50 (2017) 241.
- [6] H. Du, S.D. Pang, Value-added utilization of marine clay as cement replacement for sustainable concrete production, *Journal of Cleaner Production*, 198 (2018) 867-873.
- [7] C. Van Bunderen, R. Snellings, L. Vandewalle, Ö. Cizer, Early-age hydration and autogenous deformation of cement paste containing flash calcined dredging sediments, *Construction and Building Materials*, 200 (2019) 104-115.
- [8] F. Avet, R. Snellings, A.A. Diaz, M.B. Haha, K. Scrivener, Development of a new rapid, relevant and reliable (R3) test method to evaluate the pozzolanic reactivity of calcined kaolinitic clays, *Cement and Concrete Research*, 85 (2016) 1-11.
- [9] X. Li, R. Snellings, M. Antoni, N.M. Alderete, M.B. Haha, S. Bishnoi, Ö. Cizer, M. Cyr, K. De Weerd, Y. Dhandapani, Reactivity tests for supplementary cementitious materials: RILEM TC 267-TRM phase 1, *Materials and Structures*, 51 (2018) 151.

- [10] R. Fernandez, F. Martirena, K.L. Scrivener, The origin of the pozzolanic activity of calcined clay minerals: A comparison between kaolinite, illite and montmorillonite, *Cement and Concrete Research*, 41 (2011) 113-122.
- [11] L. Chateau, P. Vaillant, F. Leray, A. Orsini, S. Cavellec, J. Crosnier, D. Guyonnet, G. Bellenfant, P. Piantone, B. Hazebrouck, Guide méthodologique-Acceptabilité de matériaux alternatifs en technique routière-Evaluation environnementale, in, SÉTRA. <http://www.setra.equipement.gouv.fr/Acceptabilite-de-materiaux.html>, 2011.
- [12] C. Alzieu, F. Quiniou, Géodrisk–La démarche d’analyse des risques liés à l’immersion des boues de dragage des ports maritimes, CD-ROM Geodrisk «Logiciel d’évaluation des risques liés à l’immersion des déblais de dragages des ports maritimes», Coord. C. Alzieu, Ed. Ifremer, (2001).
- [13] D. Sebag, J.R. Disnar, B. Guillet, C. Di Giovanni, E.P. Verrecchia, A. Durand, Monitoring organic matter dynamics in soil profiles by ‘Rock-Eval pyrolysis’: bulk characterization and quantification of degradation, *European Journal of Soil Science*, 57 (2006) 344-355.

The Effects of Epoxy Resin as Partial Cement Replacement on the Mechanical Properties of Concrete

G.A. Jokhio, Y. Gul, A. Abu-Tair, G. S. Wei

¹Assistant Professor, Faculty of Engineering & IT, The British University in Dubai, United Arab Emirates.

²Assistant Professor, Department of Architectural Engineering, Prince Mugrin University, AlMadina, Saudi Arabia.

³Professor, Faculty of Engineering & IT, The British University in Dubai, United Arab Emirates.

⁴Student, Faculty of Civil Engineering and Earth Resources, University Malaysia Pahang, Malaysia

Abstract

Plain concrete has low tensile strength, therefore, it is reinforced with steel for structural use. Both the production of concrete and the manufacture of steel adversely affect the environment. This can be addressed partially by increasing the efficiency of these materials in terms of their mechanical properties. The present study is exploratory in nature in that it is breaking new ground by incorporating epoxy resin as fine aggregate replacement in concrete. It was hypothesized that an increase specially in the tensile strength of concrete by the incorporation of epoxy resin will reduce the requirement of reinforcing steel. To test this hypothesis, a total of 72 concrete cubes and cylinders were made with 0%, 10%, 20%, and 30% of cement replaced by epoxy resin. These samples were tested at the curing ages of 3, 7, and 28 days. The results show that for lower values of cement replacement with epoxy, both the compressive and the tensile strength were reduced. However, when the epoxy proportion was increased, a positive change was noticed in the mechanical properties, especially the tensile strength. While the results obtained in the present study are not comprehensive, this research is a significant step towards further exploration in this area.

Keywords: Epoxy resin, cement replacement, silica, aggregate replacement, sustainable materials.

1. Introduction

Cement concrete is the most widely used material in the construction of contemporary buildings. The production of concrete is an energy intensive process that also consumes a great amount of natural resources [1]. It is stipulated that the production of cement alone is a major contributor to the emission of CO₂ gases in the atmosphere [2]. Several attempts have been made over the recent years to improve the sustainability of the construction industry with respect to the production of concrete. A significant number of these attempts have been at incorporating agricultural and industrial wastes as partial or full replacement of concrete ingredients including cement, fine aggregate, and coarse aggregate [3, 4, 5]. The most recent notable contributions in this regard have been the use of nano palm oil fuel ash and nano fly ash in concrete [6]. Some attempts have also been made at replacing concrete in less structurally intensive situations by alternative materials such as adobe [7, 8].

The manufacture of reinforcing steel is another energy intensive and environmentally expensive process.

Additionally, more often than not, it requires transportation over large distances, which adds to its adverse environmental impact. The use of reinforcing steel in concrete is necessary because concrete is generally weak at taking tensile stresses. To improve the tensile capacity of concrete and to reduce the use of reinforcing steel, several alternative reinforcement strategies have been used over recent years. Some of these strategies include the use of steel wire mesh [9], which additionally helps prevent excessive cracking; and the use of additional fibres such as kenaf [10]. These recent developments towards improving the sustainability of reinforced concrete notwithstanding, there is still great potential of the use of alternative materials and techniques in order to make this industry more environment friendly. A novel technique in this regard is the use of epoxy resin as a binding material in concrete.

Epoxy resins are petroleum derived materials. These have been used to produce, among other applications, strong coatings. Some epoxy-bonded fibre-composite materials have also been used in structural applications such as strengthening of RC beams [11]. However, no evidence was found in the literature by the authors of this paper on the use of epoxy resin as a binder replacement in the preparation of cement concrete. The present study, therefore, aims to test the hypothesis that including epoxy resin as a binder replacement will increase the tensile strength of cement concrete. It is expected that such an increase in the tensile strength without significantly compromising on the compressive strength can potentially reduce the use of cement, but more importantly, the reinforcing steel. The above hypothesis was tested experimentally. For this purpose, an experimental program was designed and carried out. The methodology adopted, the results obtained, and the conclusions drawn have been provided in the following sections.

2. Methodology

The methodology of the present study has been divided into two parts; materials, and methods.

2.1 Materials

The materials used in the present study consisted of Ordinary Portland Cement (OPC), a 50-50 mixture of common river sand and silica sand as fine aggregate, ordinary crushed stone as coarse aggregate, and epoxy resin as partial binder replacement. A total of 72 specimens were prepared. Out of the 72, 36 were cubes of 100 mm side length and the other 36 were cylinders of 150 mm diameter and 300 mm height. The cubes were used for testing the compressive strength whereas the cylinder specimens were used to test the splitting tensile strength. 4 proportions of the replacement of binder with epoxy resin were used i.e. 0%, 10%, 20%, and 30%. This yielded 18 specimens for each proportion, 9 cylinders and 9 cubes. For each proportion under investigation, 3 cylinders and 3 cubes each were tested after 3, 7, and 28 days after casting. Two sizes of coarse aggregate i.e. 10mm and 20mm were used. Table 1 presents the mix proportions used for cubes and Table 2 presents the same for cylinders.

Table 1: Details of the mix proportions used for cube samples (All quantities are in kg).

Epoxy Proportion	Cement	Epoxy Resin	Water	Fine Aggregate	Coarse Aggregate 10mm	Coarse Aggregate 20mm
0%	0.32	0	0.205	0.801	0.337	0.673
10%	0.288	0.032	0.205	0.801	0.337	0.673
20%	0.256	0.062	0.205	0.801	0.337	0.673
30%	0.224	0.096	0.205	0.801	0.337	0.673

Table 2: Details of the mix proportions used for cylinder samples (All quantities are in kg).

Epoxy Proportion	Cement	Epoxy Resin	Water	Fine Aggregate	Coarse Aggregate 10mm	Coarse Aggregate 20mm
0%	0.512	0	0.328	1.283	0.539	1.077
10%	0.461	0.0512	0.328	1.283	0.539	1.077
20%	0.41	0.102	0.328	1.283	0.539	1.077
30%	0.358	0.154	0.328	1.283	0.539	1.077

2.2 Methods

The testing methods used in the present study consisted of the compressive strength test as per ASTM C39 and the tensile splitting test as per ASTM 496. The details of the method used for specimen preparation and the testing methods used have been provided in the following subsections:

2.2.1 Specimen Preparation

For the preparation of cube as well as cylinder samples, the ingredients were mixed together in a concrete mixer. First, dry ingredients were mixed for 3 minutes and then the water was added. The concrete was mixed for another 3 minutes after the addition of water. Epoxy resin, mixed with a hardener and where applicable, was added after the addition of water and further mixed for 3 minutes.

2.2.2 Compressive Strength Test

The compressive strength of the cubic specimens was measured using the Universal Testing Machine by adopting the ASTM C39 testing standard. The compressive load was applied to the specimens at a rate of 0.25 MPa per second until failure. Figure 1 shows a specimen under compressive strength test.



Figure 1: A cubic specimen under compressive strength test.

2.2.3 Splitting Tensile Strength Test

The splitting tensile strength of the cylinder specimens was also measured using the Universal Testing Machine. For this purpose, the ASTM C496 testing standard was adopted. The standard recommends a load rate of 0.7 to 1.4 MPa per minutes. In the present study, a load rate of about 1 MPa per minute was used until the specimen failed. Figure 2 shows a specimen being subjected to the splitting tensile strength test.



Figure 2: A cylinder specimen under splitting tensile strength test.

3. Results and Discussion

The results of the compressive strength test and the splitting tensile strength along with the relevant discussion have been presented in the following subsections.

3.1 Compressive Strength Test Results

The results of the compressive strength test carried out on the cube specimens with various proportions of epoxy resin at 3, 7, and 28 days of curing age are presented in Tables 4, 5, and 6.

Table 4: Results of compressive strength test at 3 days of curing (All strength values are in MPa).

Epoxy Proportion	Sample 1	Sample 2	Sample 3	Average	Standard Deviation
0%	12.93	16.62	15.21	14.92	1.86
10%	4.02	3.62	3.04	3.56	0.49
20%	2.78	2.46	2.88	2.71	0.22
30%	15.56	15.4	15.33	15.43	0.12

Table 5: Results of compressive strength test at 7 days of curing (All strength values are in MPa).

Epoxy Proportion	Sample 1	Sample 2	Sample 3	Average	Standard Deviation
0%	20.22	17.59	19.02	18.94	1.32
10%	4.82	5.12	4.13	4.69	0.51
20%	3.81	3.76	3.82	3.8	0.03
30%	17.49	17.57	17.63	17.56	0.07

Table 6: Results of compressive strength test at 28 days of curing (All strength values are in MPa).

Epoxy Proportion	Sample 1	Sample 2	Sample 3	Average	Standard Deviation
0%	28.61	32.12	27.46	29.4	2.43
10%	4.82	4.92	5.12	4.92	0.15
20%	3.88	3.5	3.92	3.77	0.23
30%	18.78	18.56	19.41	18.9	0.44

The average compressive strength for the different epoxy resin proportions at different curing ages have been plotted in Figure 3.

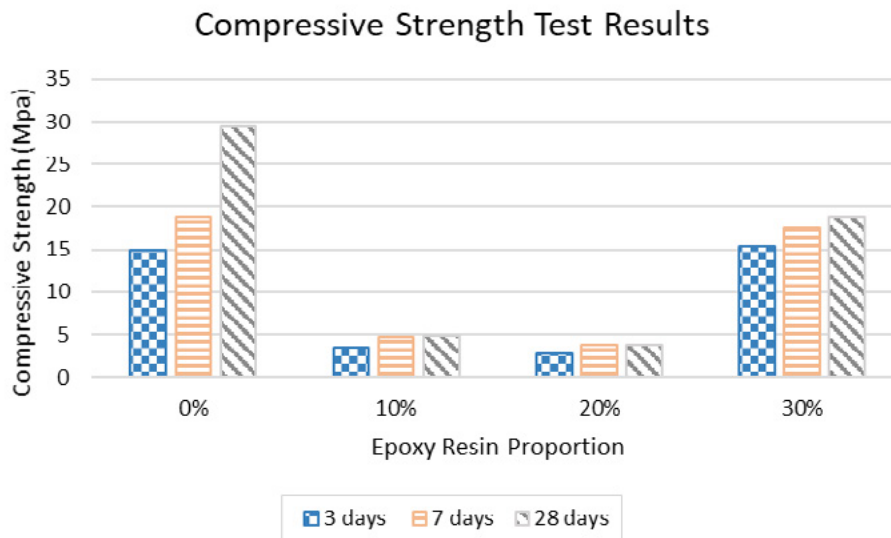


Figure 3: Average compressive strength test results.

It can be observed in Figure 3 that the compressive strength drops as epoxy resin is added in lower portions. The average compressive strength at 28 days for 10% epoxy resin is only 16.74% of that with no epoxy resin. This further drops to 12.83% when 20% epoxy resin was used. However, for epoxy resin proportion of 30%, the compressive strength seems to have bounced back to reach 64.3% of that of the control specimen. It is stipulated that the addition of epoxy resin adversely affects the effectiveness of cement as a binder and the low amount of epoxy does not produce enough of its own binding force. For larger proportion, the increase in the compressive strength may be attributed to epoxy resin. This hypothesis, however, requires further investigation to be validated.

3.2 Splitting Tensile Strength Test Results

The results of the splitting tensile strength test carried out on the cylinder specimens with various proportions of epoxy resin at 3, 7, and 28 days of curing age are presented in Tables 7, 8, and 9.

Table 7: Results of splitting tensile strength test at 3 days of curing (All strength values are in MPa).

Epoxy Proportion	Sample 1	Sample 2	Sample 3	Average	Standard Deviation
0%	0.87	0.95	1.06	0.95	0.095
10%	0.04	0.06	0.07	0.06	0.015
20%	0.11	0.19	0.23	0.18	0.061
30%	1.1	1.12	1.21	1.14	0.059

Table 5: Results of compressive strength test at 7 days of curing (All strength values are in MPa).

Epoxy Proportion	Sample 1	Sample 2	Sample 3	Average	Standard Deviation
0%	1.39	1.34	1.42	1.38	0.040
10%	0.12	0.28	0.32	0.24	0.106
20%	0.24	0.25	0.27	0.25	0.015
30%	1.65	1.48	1.73	1.62	0.128

Table 6: Results of compressive strength test at 28 days of curing (All strength values are in MPa).

Epoxy Proportion	Sample 1	Sample 2	Sample 3	Average	Standard Deviation
0%	2.25	2.21	2.28	2.25	0.035
10%	0.52	0.59	0.63	0.56	0.056
20%	0.65	0.69	0.77	0.7	0.061
30%	2.33	2.34	2.39	2.35	0.032

The average splitting tensile strength for the different epoxy resin proportions at different curing ages have been plotted in Figure 4.

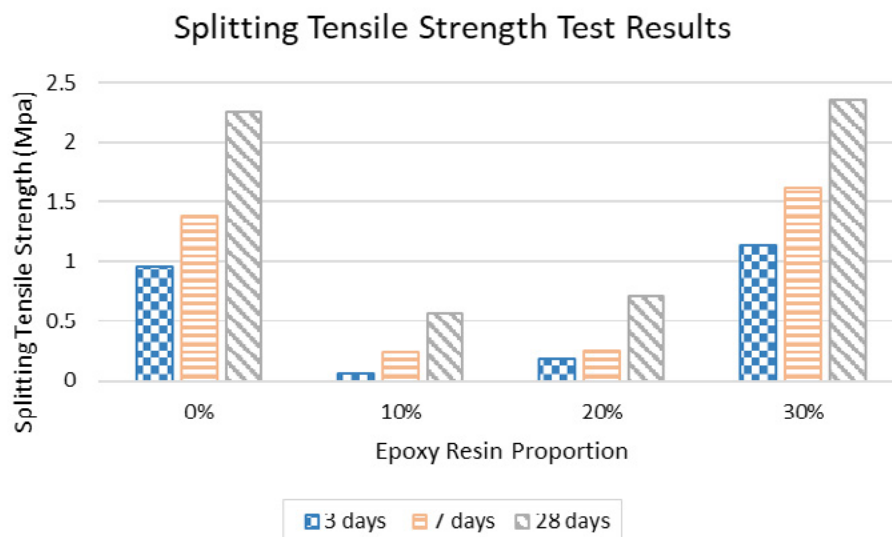


Figure 4: Average compressive strength test results.

A similar trend for the splitting tensile strength to that of the compressive strength can be observed in Figure 4. However, the drop in the tensile strength is slightly less as it drops to about 25% and 31% of the splitting tensile strength of the control specimen for the epoxy proportions of 10% and 20%, respectively. While the compressive strength for 20% epoxy proportion was less than that for 10%, the splitting tensile strength is higher for 20% epoxy proportion. More importantly, the tensile strength for the epoxy resin proportion of 30% went higher than the control specimen by about 4%. It is stipulated that a higher proportion of epoxy resin may further increase the tensile strength of concrete.

4. Conclusions

The present study was a relatively small study where only 4 proportions of epoxy resins were used. The conclusions drawn from the observed results are as follows:

The compressive strength of concrete dropped to about one-sixth of that of the control specimen when 10% cement was replaced by epoxy resin

The compressive strength of concrete dropped further to about one-eighth of that of the control specimen when 20% cement was replaced by epoxy resin

The compressive strength of concrete bounced back to about two-thirds of that of the control specimen for a higher proportion of epoxy resin replacing 30% of cement

The splitting tensile strength of concrete dropped to about one-fourth of that of the control specimen when 10% cement was replaced by epoxy resin

The splitting tensile strength of concrete slightly increased to about one-third of that of the control specimen when 20% cement was replaced by epoxy resin as compared to 10%

The splitting tensile strength of concrete went slightly higher than that of the control specimen for a higher proportion of epoxy resin replacing 30% cement

The above conclusions are based on the small size of data observed in the present study. It is recommended that further investigation in this regard be carried out to ascertain the validity of these conclusions. It would especially be of interest to find out how the higher proportions than those used in the present study may affect the compressive and the splitting tensile strength of concrete. Furthermore, the present study did not investigate the economic or environmental aspects of the use of epoxy resin in concrete. Future research in these areas is also recommended.

5. References

- [1] H. M. Hamada, G. A. Jokhio, F. M. Yahaya, A. M. Humada and Y. Gul, "The present state of the use of Palm Oil Fuel Ash (POFA) in concrete," *Construction and Building Materials*, vol. 175, pp. 26-40, 2018.
- [2] C. Meyer, "The greening of the concrete industry," *Cement and Concrete Composites*, vol. 31, no. 8, pp. 601-605, 2009.
- [3] B. H. Nagaratnam, M. E. Rahman, A. K. Mirasa, M. A. Mannan and S. O. Lame, "Workability and heat of hydration of self-compacting concrete incorporating agro-industrial waste," *Journal of Cleaner Production*, vol. 112, no. 1, pp. 882-894, 2016.
- [4] W. Tangchirapat, T. Saeting, C. Jaturapitakkul, K. Kiattikomol and A. Siripanihgor, "Use of waste ash from palm oil industry in concrete," *Waste Management*, vol. 27, no. 1, pp. 81-88, 2007.
- [5] E. Khankahje, M. W. Hussin, J. Mirza, M. Rafeizonooz, M. R. Salim, H. C. Siong and M. N. Warid, "On blended cement and geopolymer concretes containing palm oil fuel ash," *Materials & Design*, vol. 89, pp. 385-398, 2016.
- [6] H. M. Hamada, G. A. Jokhio, F. M. Yahaya and A. M. Humada, "Applications of nano palm oil fuel ash and nano fly ash in concrete," *IOP Conference series: Materials Science and Engineering*, vol. 342, no. 1, p. 012068, 2018.
- [7] G. A. Jokhio, F. M. Saad, Y. Gul, S. M. S. Mohsin and N. I. Ramli, "Uniaxial compression and tensile splitting tests on adobe with embedded steel wire reinforcement," *Construction and Building Materials*, vol. 176, pp. 383-393, July 2018.
- [8] G. A. Jokhio, Y. M. Y. Al-Tawil, S. M. S. Mohsin, Y. Gul and N. I. Ramli, "Compressive and flexural tests on adobe samples reinforced with wire mesh," *IOP Conference Series: Materials Science and Engineering*, vol. 318, no. 1, p. 012030, 2018.

- [9] S. H. Lodi, S. F. A. Rafeeqi and G. A. Jokhio, "Ferrocement constitutive model and experimental validation," *NED University Journal of Research*, vol. 7, no. 2, pp. 137-151, 2010.
- [10] S. M. S. Mohsin, A. O. Baarimah and G. A. Jokhio, "Effect of kenaf fiber in reinforced concrete slab," *IOP Conference Series: Materials Science and Engineering*, vol. 342, no. 1, p. 012104, 2018.
- [11] T. C. Triantafillou and N. Plevris, "Strengthening of RC beams with epoxy-bonded fibre-composite materials," *Materials and Structures*, vol. 25, no. 4, pp. 201-211, 1992.

Polycarboxylate Superplasticizer Modified Fly Ash: Its Effects on Fluidity and Mechanical Properties of Cement Paste

P. Liu^{a,b}, M. Qu^b, F. Wang^{a,*}, G. Hu^c, L. Yang^a, W. Zhang^a

^a State Key Laboratory of Silicate Materials for Architectures, Wuhan University of Technology, Wuhan 430070, PR China

^b School of chemistry, chemical engineering and life science, Wuhan University of Technology, Wuhan 430070, PR China

^c Laboratory of Reactions and Process Engineering (LRPG, UMR 7274), Université de Lorraine - CNRS, 1 rue Grandville, BP 20451, 54001 Nancy, France

*Corresponding author: Prof. Fazhou Wang, State Key Laboratory of Silicate Materials for Architectures, Wuhan University of Technology, Email: fzhwang@whut.edu.cn

Abstract

A polycarboxylate superplasticizer (PC) which contained PEG side chain, carboxylic groups and hydroxysilane ones, was synthesized by free radical copolymerization. It was subsequently grafted onto fly ash (FA) beads. The Si–OH groups on the surface of alkali-activated FA beads were connected to the PC molecules via covalent hydroxysilane linkage. In the PC-modified FA beads, new IR peaks appeared at 2900 and 1100 cm^{-1} and were assigned to the vibration of C–H and C–O–C groups. A peak shift in ^{29}Si NMR from -80 to -86 ppm also confirmed the successful grafting of the PC molecules onto the FA beads. Thermal analyses indicated that the PC moieties accounted for 2.1 wt.% of the modified FA beads. Compared with the crude FA and the alkali-activated one, the PC-modified FA significantly improved the workability of the cement paste, and enhanced the mechanical properties of the cement after hydration for seven days. Thus, the PC modified FA composite could serve as a promising additive for cementitious materials.

Keywords: water reducing; fly ash; alkali activation; fluidity; workability

Understanding Hydrogen Bonding in Calcium Silicate Hydrates

B. Li^{1,2}, H.J.H. Brouwers³, Q. Yu³, W. Chen^{1*}

¹State Key Laboratory of Silicate Materials for Architectures, Wuhan University of Technology, Wuhan, PR China

²School of Material Science and Engineering, Wuhan University of Technology, Wuhan, PR China

³Department of the Built Environment, Eindhoven University of Technology, Eindhoven, The Netherlands

Email of the corresponding author: chen.wei@whut.edu.cn

Abstract

The hydrogen bonding mechanisms and atomic interactions in C-S-H gels are investigated by combining ²⁹Si, ¹H solid state NMR and first principle calculation. Five distinct peaks of protons were observed in the ¹H MAS NMR spectra for C-S-H gels. The interactions between protons and silicate species are discussed in detail with well-defined first principle calculations. Amorphous portlandite and strong hydrogen bonded protons are identified. The strong hydrogen bonded protons are favored in C-S-H with high Ca/Si ratios, which is associated with Q¹ sites in the termination of silicate chains. The stronger atomic interactions between Q¹ species or silanols and water in C-S-H gel with higher Ca/Si ratio are presented than Q² species in C-S-H gel with Ca/Si ratio of 1.0. The stronger hydrogen bonds in the interlayer are expected to be an interpretation for the decrease of interlayer spacing with the Ca/Si ratio. The results are expected to pave the way to develop new components of cement with stronger hydrogen bonding features.

Keywords: calcium silicate hydrate, Ca/Si ratio, H₂O/Si ratio, hydrogen bonds, first principle calculation

1. Introduction

Hydrated Portland cement paste is a porous matrix consisting of crystals embedded in a poorly crystalline phase, the calcium-silicate-hydrate (C-S-H) gel [1]. C-S-H gel is the most abundant hydration product of Portland cement, accounting for about 50–60% by volume of hardened cement paste and making it one of the most common substances of the modern world [2]. It is also the primary binding component in cementitious materials.

C-S-H gel has a layered structure and shows similarities to 14 Å tobermorite (Ca₃Si₆O₁₆(OH)₂·4H₂O) [3, 4]. The structure of tobermorite contains layers of calcium ions linked on both sides to linear silicate chains with the ‘dreierkette’ form in such a way as to repeat a kinked pattern after every three tetrahedra [5]. Two of the three tetrahedra, named pairing tetrahedra (Q_p²), are linked together and share O-O edges with the central Ca-O part of the layer. The third tetrahedron, named bridging tetrahedron (Q_B²), shares an oxygen atom at the pyramidal apex of a calcium polyhedron and connects the dimers of pairing tetrahedra. C-S-H gel can be considered as defective tobermorite-like structure whose molar ratio of calcium to silicon varies between 0.66 and 2.0.

The local chemical environments and atomic arrangements in C-S-H gel are probed with Solid-state Nuclear

Magnetic Resonance (NMR) spectroscopy [6, 7]. The ²⁹Si NMR peaks are assigned with the assumption that chemical shifts of silicon atoms decrease with the condensation degree of (SiO₄) units, structures of which transform from isolated monomers to tetrahedrally coordinated chains [8]. The ²⁹Si NMR results show that C-S-H gel contains silicate chains with limited lengths with a 2, 5, 8... (3n-1) (n=1, 2, ...) chain length sequence [4].

Hydrogen atoms in C-S-H exist in the form of silanols, hydroxyl groups and water molecule which play an important role in atomic interactions between protons and silicate chains with hydrogen bonding. Hydrogen bonding is a special type of atomic interactions between a hydrogen atom covalently bonded to a very electronegative atom such as N, O, or F atom and another very electronegative atom, whose strengths range from 4 to 50kJ per mole of hydrogen bonds [9]. The hydrogen bonding between hydrogen-containing species and oxygen atoms has a wide range of bond length and bond strength which contributes to the internal cohesion in the C-S-H [10].

The mechanism of hydrogen bonding in C-S-H gel or hydrated cements are not sufficiently clarified, yet. Efforts have been made to study the hydrogen bonding and interactions between different silicate and hydrogen-containing species in cement hydrates or synthetic C-S-H gels [11-14]. The nanopore space in the C-S-H gel is hydrophilic because of the nonbridging oxygen atoms on the disordered silicate chains which serve as hydrogen-bond acceptor sites, based on the classical molecular simulations [13]. Glassy nature of hydrogen bonds between interlayer water and silicate chains is demonstrated because of the heterogeneity in the distribution of hydrogen bond strengths and multi-range structure [13]. ¹H-²⁹Si Heteronuclear nuclear chemical shift correlation provides information about the distance of protons to silicon atoms and interactions between protons and silicate moieties. The results from ¹H-²⁹Si Heteronuclear nuclear chemical shift correlation establishes strong interactions of the Q¹ species with water molecular [11, 12, 14].

Understanding on the mechanism of hydrogen bonds in C-S-H gels is lacking because the correlation between experimental results and underlying complex structure is lacking. A method to reveal the mechanism of hydrogen bonds in maltose anomers and C-S-H gel is proposed by a combination of first principle calculation and NMR tests [14, 15].

First principle calculations based on the Density Functional Theory (DFT) with the Gauge Including Projector Augmented Wave (GIPAW) algorithm enable the calculation of chemical shielding, which establishes a clear link between the observed spectra and underlying atomic structure [15, 16]. The mechanisms of hydrogen bonding between various silicate moieties and hydrogen groups in C-S-H can be determined by using combination of ¹H NMR and first principle calculations. Understanding the mechanisms of hydrogen bonding provides great possibilities for developing C-S-H gel with strong cohesive performance [10].

In this paper, three types of C-S-H gels with Ca/Si ratios of 1.0, 1.4 and 1.5 are synthesized. First principle calculations for ¹H chemical shifts are used to correlate the observed ¹H NMR spectra with structure of the hydrogen bonding between different silicon moieties and hydrogen groups in the C-S-H gels. The effect of Ca/Si ratios on the chemical environment of hydrogen bonds is studied.

2. Experiments

2.1 Experiments

C-S-H gels are synthesized by using pozzolanic reaction between calcium oxide and amorphous silica fume [17]. C-S-H gels with Ca/Si molar ratios of 1.0, 1.4 and 1.5 are synthesized according to the mix designs in Table 1. Calcium oxide is prepared with decomposition of calcium carbonate (AR grade, Sinopharm) at 1000°C for 10h. Amorphous silica fume (99.6% SiO₂, Shenzhen Anmisco) with a specific area of 250m²/g

is used as silicon sources. Deionized water is mixed with calcium oxide and silica fume and the water/powder mass ratio is 50. The resulting slurry is stirred under nitrogen protection for 7d at 30°C followed by filtration. The filtrates are analyzed with Inductively Coupled Plasma (ICP, Model Optima 4300DV) to determine the Ca/Si molar ratio of the filtrate. Each test is performed three times with test error smaller than 0.01mM and the mean value of the results is recorded.

The powders are washed with deionized water. No portlandite is detected in X-ray diffraction pattern (XRD, Model Rigaku MiniFlex600, Cu K α = 1.5406 Å, step size of 0.02° from 5° to 50°) after three times washing. C-S-H gels are freeze dried at 2Pa, -50°C for 24 h. The XRD patterns of the C-S-H gels are analysed (Figure 1).

The Ca/Si ratio in C-S-H is determined in two ways, including calculations from the elemental concentrations of calcium and silicon in the filtrate and measurements with X fluorescence spectrometer (XRF, Model Axios Advanced) of the C-S-H solids. The H₂O/Si molar ratios are calculated with the weight loss after calcination 1000°C for 12h. The results of Ca/Si ratios and H₂O/Si molar ratios are listed in Table 1.

Table 1 Mix design for synthesizing C-S-H and compositions of C-S-H gel

Samples	C-S-H1.0	C-S-H1.4	C-S-H1.5
Mix design			
CaO (g)	4.96	4.14	3.31
SiO ₂ (g)	5.04	6	6.69
Water (ml)	500		
Analysis of filtrate (volume 500ml)*			
Ca in filtrate (mM)	6.7	14.6	22.4
Si in filtrate (mM)	0.08	0.01	0.01
Composition of C-S-H			
Calculated Ca/Si ratio ^{&}	0.98	1.42	1.57
Measured Ca/Si ratio [#]	0.98	1.44	1.52
Measured H ₂ O/Si ratio	1.66	1.83	2.08

Note: * Determined with ICP-OES.

& Calculated from the moles of Ca and Si in the filtrates.

Determined with XRF of the powders.

¹H MAS NMR spectra are recorded on an Agilent 600 DD2 spectrometer, equipped with a 14.1T magnet, operating at a Larmor frequency of 600MHz. A 4.0mm probe is used for ¹H NMR with a spinning speed of 25.0kHz, a $\pi/2$ pulse length of 5ms, a relaxation delay of 20s and 200 scans. Tetramethylsilane is used as the reference for ¹H tests.

2.2 First principles calculation

The first principle calculations on NMR results are performed with CASTEP (Accelrys, Material Studio17.2) using DFT theory [16]. The calculation is executed in three steps, including geometry optimization, energy calculation and chemical shielding calculation. Geometry optimization and energy calculation are carried out within CASTEP using a k point grid of 4×2×1 equal to 0.04 1/Å and cut off energy of 400eV. The core-valence interactions are described with ultrasoft pseudopotentials. Little changes of unit cell and atomic positions are allowed during geometry optimization. ¹H chemical

shielding calculation is performed in the crystal frame. All-electron wave function in the presence of a magnetic field is reconstructed with the gauge including projector augmented wave (GIPAW) algorithm. The chemical shifts δ_{cal} are obtained from chemical shielding σ_{cal} with the relation

$$\delta_{\text{cal}} = \sigma_{\text{ref}} - \sigma_{\text{cal}} \quad (1)$$

Where σ_{ref} is 30.09ppm.

3. Results and discussion

3.1 XRD analysis of C-S-H gels

The XRD patterns of the three types of C-S-H gels are shown in Figure 1, which shows a typical tobermorite-like structure. Poorly resolved XRD patterns demonstrate the prominent features of heavy defects and poor long rang order in C-S-H structures. No secondary calcic phases such as portlandite are observed in all C-S-H gels, indicating that crystalline portlandite is sufficiently removed by washing with deioned water.

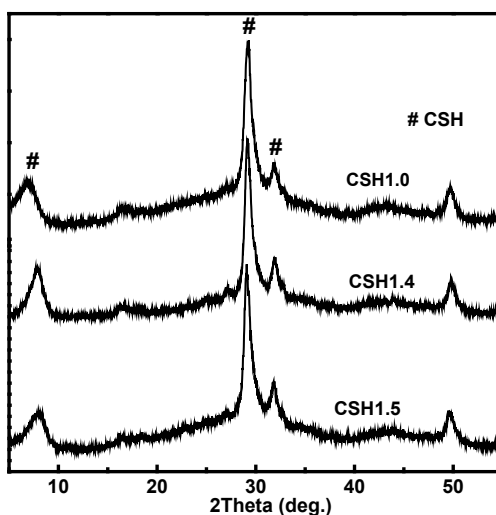


Figure 1 XRD patterns of three types of C-S-H gels after freeze drying

The position of the first diffraction peak ((020) about $2\theta=7^\circ$) shows the basal spacing of the tobermorite-like structure. The basal spacing of C-S-H1.0 is about 13\AA ($2\theta=6.78^\circ$), while the basal spacing decreases to 11.3\AA ($2\theta=7.81^\circ$) and 11\AA ($2\theta=8.02^\circ$) for C-S-H1.4 and C-S-H1.5, respectively. The change of basal spacing with Ca/Si ratio of C-S-H observed in the experiments agrees with the findings in the study of Renaudin et al [5] corresponding to about 20% contraction of the unit cell volume. The basal spacing is determined by the amount of water and the coordination requirements of the interlayer calcium ions. Removal of interlayer water and calcium ions will thus decrease the basal spacing of C-S-H. According to model proposed by Richardson, C-S-H gels with Ca/Si ratio greater than 1.4 consist of C-S-H(I) with constant basal spacing and a Ca-rich phase intermixed with C-S-H(I) [3].

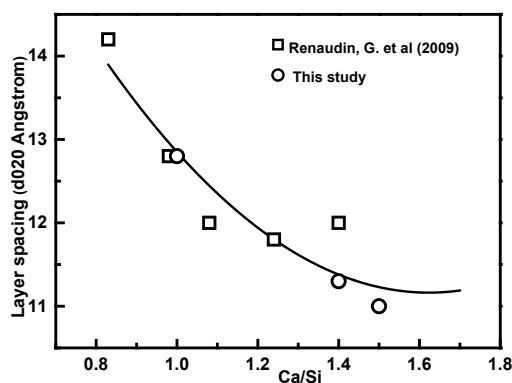


Fig. 2 Relationship between basal spacing and Ca/Si ratio of C-S-H gel plotted together with the results of [3]

3.2 ¹H NMR of C-S-H gels

Information obtained in the ¹H NMR analysis helps probing the molecular structure of C-S-H gels and the atomic interactions between hydrogen groups and silicate moieties (Figure 3). Five distinct peaks of protons are observed in the ¹H NMR spectra of C-S-H gels. The first peak at about -0.3 ppm corresponding to the hydroxyl proton in the ¹H MAS SSNMR spectra suggests the formation of portlandite in C-S-H with a Ca/Si ratio of 1.4 or 1.5. It is previously reported that portlandite is formed after excessive drying of C-S-H gels with Ca/Si ratios up to 1.5 [18]. No peaks of crystalline portlandite in the XRD patterns of C-S-H are observed (Figure 1). The hydroxyl protons identified in ¹H NMR spectra in C-S-H gels with Ca/Si ratios of 1.4 and 1.5 exist most likely in portlandite in an amorphous state. Amorphous portlandite in C-S-H gels is also traced in other studies by using nanoindentation and high energy X-ray tests [19, 20].

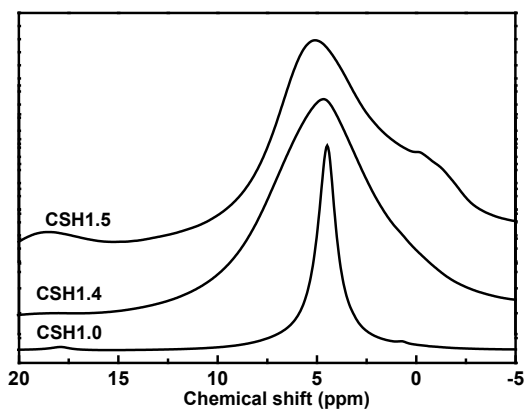


Figure 3 ¹H NMR spectra of C-S-H gels

The chemical shifts of proton species in Ca-OH, and Al-OH are between 0 and 3ppm, and those of the protons in water are between 3 and 6ppm, based on ¹H NMR studies on crystalline silicates and aluminosilicate minerals [21]. The chemical shifts of protons in Si-OH groups of silicates extend to the range between 6 and 18ppm [21].

The ¹H NMR spectrum of C-S-H gel with the Ca/Si ratio of 1.0 shows a sharp resonance peak at 4.4ppm, indicating that most protons exist as absorbed water in the interlayer, which is consistent with the observation of tobermorite. A broad and overlapped peak shifts to 5.2 and 5.6ppm in the ¹H NMR spectra of C-S-H gels with Ca/Si ratios of 1.4 and 1.5, respectively, which indicates that the protons in these C-S-H gels exist in more complex environment than those in C-S-H with a Ca/Si ratio of 1.0. Resonance peaks of the Si-

OH groups between 6-10 ppm are observed in the C-S-H gels with Ca/Si ratio of 1.4 and 1.5, whereas the peaks are absent in C-S-H gels with a Ca/Si ratio of 1.0. The deconvolution of ¹H NMR spectra of C-S-H gels with different Ca/Si ratios based on the assignment of the peaks described above is shown in Figure 4 and Table 2. The resonance peak assigned to absorbed water represents about 40-80% of the total ¹H population in all C-S-H gels with different Ca/Si ratio, which decreases with increasing Ca/Si ratio. The resonance peaks of Si-OH groups between 6-10ppm and Ca-OH in the C-S-H at about 2.5ppm is observed in C-S-H gels with Ca/Si ratios higher than 1.0. The relative fractions of Si-OH groups and Ca-OH in the C-S-H increase with the Ca/Si ratio.

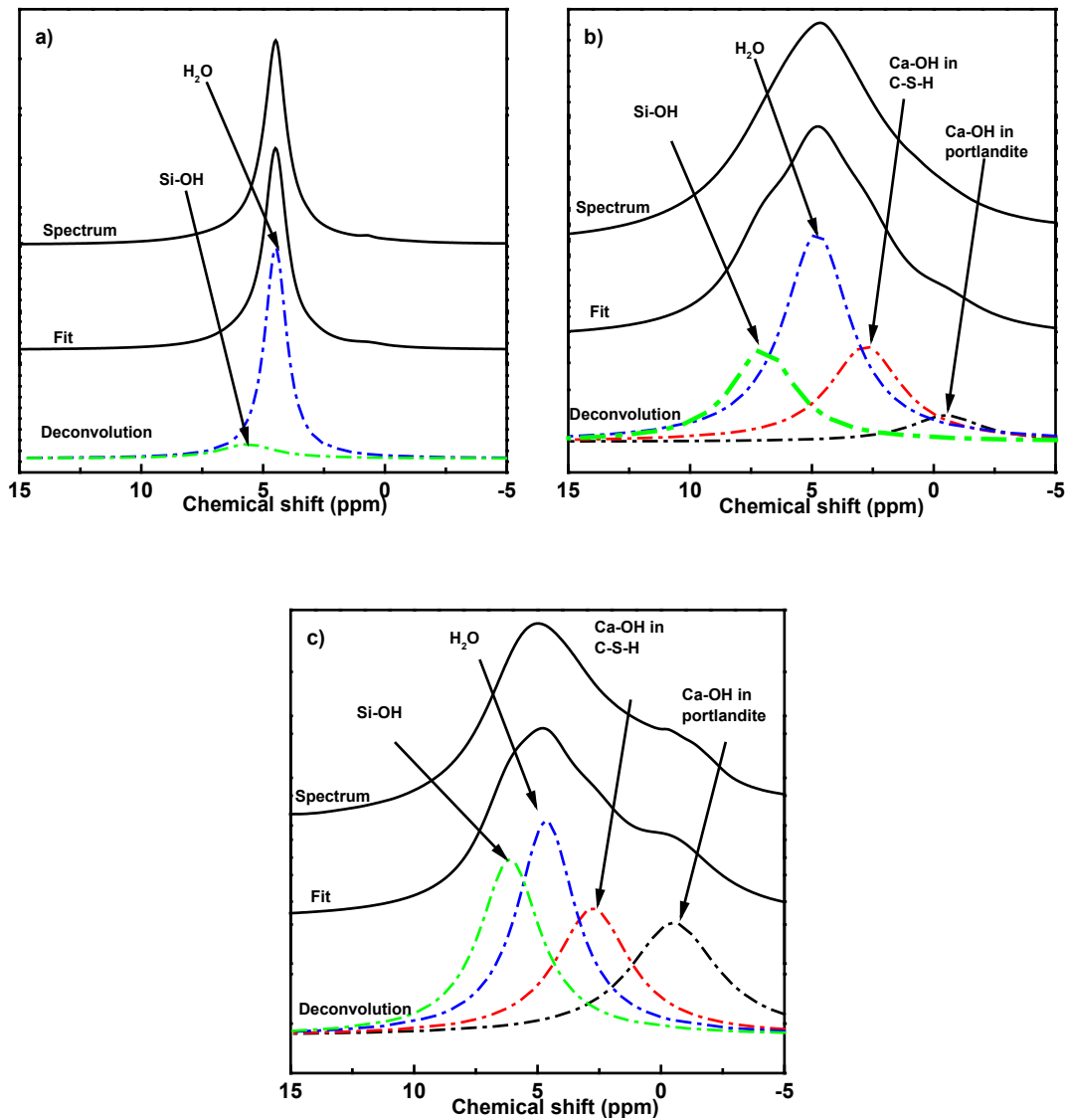


Figure 4 Deconvolution of ¹H NMR spectra of C-S-H gels. a) C-S-H1.0, b) C-S-H1.4, c) C-S-H1.5

Table 4 Quantitative results of fractions of hydrogen groups via deconvolution of ¹H NMR spectra

Samples	Si-OH	H ₂ O	Ca-OH in
	6-15 ppm	3-6 ppm	C-S-H gel 0-3 ppm
C-S-H1.0 (%)	13.8	84	3.2
C-S-H1.4 (%)	23	52	25
C-S-H1.5 (%)	33	38	29

3.3 First principle calculation of ¹H chemical shifts

The mechanism of hydrogen bonding especially the chemical environment of protons and the interactions between hydrogen containing groups and silicate chains are not known, yet. The chemical environment of protons and the distribution of hydrogen bonding between hydrogen containing groups and silicate chains are essential for establishing the structural model of C-S-H. The observed ¹H NMR results are linked to the underlying structure of hydrogen bonds with the help of first principle calculation rooting in DFT-GIPAW methods.

The structural model of C-S-H gel used in calculating the chemical shifts of protons is based on tobermorite-14 Å provided by Crystallography Open Database (as shown in Figure 5a). The protons in the tobermorite-14 Å exist in the interlayer water and silanols bonded with bridging tetrahedral silicates (Q²_B-OH).

A structural model of C-S-H gel consisting of dimers and pentamers is constructed by modifying the infinite silicate chain model following the literature [8]. The dimers and pentamers are obtained by removing some bridging tetrahedral silicates (Q²_B-OH) in the infinite chains in the structure of tobermorite. The local negative charge is compensated with H⁺, Ca²⁺ or Ca(OH)⁺ ions, forming the defective sites and increasing the Ca/Si ratios [14]. After removing a bridging silicate tetrahedron, the unbalanced charge is compensated by either adding two protons forming two silanols bonded with terminal tetrahedral silicates or adding a bridging Ca²⁺ to connect terminal tetrahedral silicates. Additional interlayer water molecular, interlayer Ca(OH)⁺ ions and Ca(OH)₂ are used to connect the defect sites through the interlayer spaces. Three types of calcium ions are distinguished in the model of C-S-H as calcium ions in main layer (Ca_M), calcium ions in interlayer (Ca_I) and calcium ions in bridging sites (Ca_B). Four proton environments are distinguished as interlayer water molecular (H₂O), silanols bonded with bridging tetrahedral silicates (Q²_B-OH), silanols bonded with terminal tetrahedron silicates (Q¹-OH) and hydroxyl associated with Ca ions (OH⁻). The constructed structure are geometry and energy optimized with CASTEP based on DFT theory. The optimized structure of the C-S-H model with the mean chemical formula of C_{1.2}SH_{1.8} and various proton environments are shown in Figure 9b).

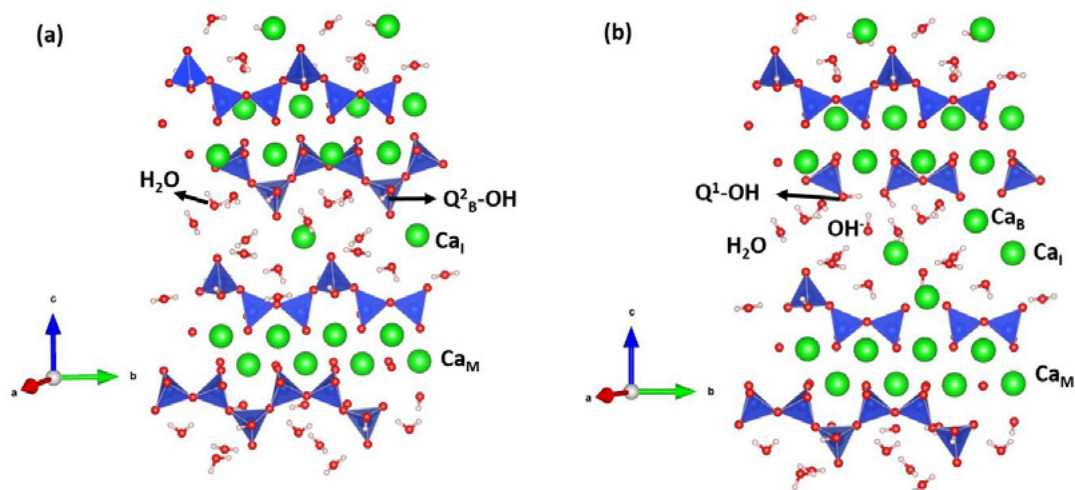


Figure 5 Geometry structures of tobermorite-14Å minerals and C_{1.2}SH_{1.8} gel. a) tobermorite-14Å and various proton environments, b) C_{1.2}SH_{1.8} gel and various proton environments

Protons in different chemical environments exist in the structure of tobermorite-14Å and constructed model of C-S-H gel. The hydrogen bonds are classified into three types according to the donors in the

bond. Three different structure units containing protons and oxygen atoms are labeled as TH (silanols bonded with tetrahedral silicates (T)), W (water molecular) and OH (hydroxyl groups bonded with calcium ions). Nine different hydrogen bonds involving the different donators and acceptors are named as W---W, W---T(Q²) and W---T(TH)(Q¹) etc.

The observed NMR chemical shifts are compared with the calculated values, aiming to correlate the underlying structure of hydrogen containing groups which are shown in the C-S-H model to the observed spectra. Hydrogen bonds affect greatly the isotropic ¹H chemical shifts. A well-established linear relationship between ¹H isotropic chemical shifts and distance of hydrogen bonds ($d_{O-H...O}$) has been reported by experiment if the proton is bonded to oxygen atoms [6, 21]. The accurate values of $d_{O-H...O}$ are calculated from the C-S-H model used in the calculation, with which the correlation between ¹H isotropic chemical shifts and hydrogen bonds are established. The linear relationship between the calculated ¹H chemical shift and values of $d_{O-H...O}$ is shown in Figure 6.

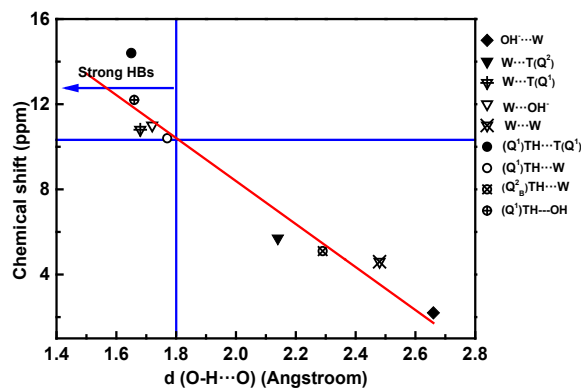


Figure 6 Relationship between calculated ¹H chemical shift and value of $d_{O-H...O}$ (HBs: Hydrogen Bonds)

The comparison between the observed ¹H chemical shifts and the calculated values shows much higher overlapped ranges of protons in water and silanols groups than that indicated from the literatures [12]. Protons in water molecule resonate from 3 to 11ppm, while peaks of protons in silanols bonded with tetrahedral silicates ranges between 10 and 14ppm, leading to broaden and overlapped peaks observed in the ¹H NMR spectra of C-S-H gels with the Ca/Si ratio of 1.4 and 1.5. The highly overlapped ranges of protons are due to the different distance and strength of hydrogen bonds which influence shielded effect to protons. Thus, the hydrogen bonds should be taken into consideration to reasonably analyze the ¹H NMR of C-S-H or cement based materials.

There is a linear correlation between the calculated ¹H chemical shift and the values of $d_{O-H...O}$: $\delta_{iso} = 28.587 - 10.10 d_{O-H...O}$ with δ_{iso} in ppm and $d_{O-H...O}$ in Å (Figure 6). The protons in Ca-OH involved in the hydrogen bond labeled as OH---W resonate at about 2.5ppm, suggesting an average $d_{O-H...O}$ value of about 2.7Å and rather weak hydrogen bonds. Protons in hydroxyl groups serves as a weak donator in hydrogen bonds. Most protons in C-S-H gels exit in water whose ¹H chemical shifts spread in a wide range and has various values of $d_{O-H...O}$. The protons resonating at 4.6ppm is involved in hydrogen bond named as W---W and have an average $d_{O-H...O}$ value of 2.37Å, which is the dominant chemical environment of protons in C-S-H with Ca/Si ratio of 1.0. The protons in water forming the hydrogen bonds with Q¹ sites (W---T(TH) (Q¹)) show higher chemical shifts at 10ppm than those with Q² sites (W---T (Q²)) and have an average value of $d_{O-H...O}$ about 1.84Å. The observation suggests stronger hydrogen bonding between water and Q¹ sites than those with Q² site in the silicate chains, which agrees with the ranking of strength of hydrogen bonds proposed in the literature [13]. Nonbridging oxygen atoms in Q¹ sites serve as stronger hydrogen-bond acceptor

sites than bridging oxygen atoms in Q² sites. The protons in forming hydrogen bonds with water show similar observation that hydrogen bonding between Si-OH groups in Q¹ sites and water ((Q¹)TH---W) are stronger than those between Si-OH groups in Q_B² sites ((Q_B²)TH---W) with water. In conclusion, the Q¹ sites enhance the internal cohesions with water and hydrophilicity of the silicate main chain.

Hydrogen bonds whose the average value of $d_{\text{O-H}\cdots\text{O}}$ is lower 1.8Å are defined as strong hydrogen bonds (shown in Figure 10). The strong hydrogen bonding are dominated by (Q¹)T-H---T(Q¹), (Q¹)T-H---W, W---OH, W---T(Q¹) and (Q¹)TH---OH. Strong hydrogen bonding between terminal silanol and terminal silicate sites shows the internal cohesions between the parallel chains, which are present in the minerals suolunite and acts as the major interactions between dimes in the structure [10]. The hydroxyl groups bonded with calcium ions serve as strong acceptors for hydrogen bonds, which forms the strong bonding with water (W---OH) and terminal silanol ((Q¹)TH---OH). The strong hydrogen bonding between terminal silanol and hydroxyl acts as the interlayer affinity in the structure of C-S-H gel.

4. Conclusions

The observed ¹H NMR results are correlated with the underlying structure of hydrogen bonds, aiming to reveal the mechanism of hydrogen bonding. The main conclusions can be drawn as followings.

1. Amorphous portlandite exists in C-S-H gels with high Ca/Si ratios.
2. Chemical shifts of protons in C-S-H gel are affected greatly by the hydrogen bonds. Protons in water and silanol resonate in a highly overlapped range. Hydrogen bonds should be taken into consideration to reasonably analyze the ¹H NMR of C-S-H or cement based materials.
3. Strong hydrogen bonding between water and terminal silicate sites or silanol are revealed, which enhance the hydrophilicity of silicate chains in the C-S-H gel.
4. The strong hydrogen bonding between terminal silanol and hydroxyl bonded with calcium ions in C-S-H gel with high Ca/Si ratio is observed, which acts as the affinity in the interlayer space of C-S-H gel, and consequently decreased basal spacing with increasing Ca/Si ratio.

5. Acknowledgment

This research has been financially supported by the National Natural Science Foundation of China (grant numbers 51672199); the Fundamental Research Funds for the Central Universities (grant number WUT: 2017-YB-008□2019III018GX); and the 111 Project (No. B18038).

6. References

- [1] B. Lothenbach, A. Nonat, Calcium silicate hydrates: Solid and liquid phase composition, *Cem Concr Res*, 78 (2015) 57-70. <https://doi.org/10.1016/j.cemconres.2015.03.019>.
- [2] H.F.W. Taylor, *Cement Chemistry*, 2nd ed., Thomas Telford, London, 1997.
- [3] I.G. Richardson, Model structures for C-(A)-S-H(I), *Acta crystallographica Section B, Structural science, crystal engineering and materials*, 70 (2014) 903-923. <https://doi.org/10.1107/S2052520614021982>.
- [4] I.G. Richardson, Tobermorite/jennite- and tobermorite/calcium hydroxide-based models for the structure of C-S-H: applicability to hardened pastes of tricalcium silicate, β-dicalcium silicate, Portland cement, and blends of Portland cement with blast-furnace slag, metakaolin, or silica fume, *Cem Concr Res*, 34 (2004) 1733-1777. <https://doi.org/10.1016/j.cemconres.2004.05.034>.
- [5] G. Renaudin, J. Russias, F. Leroux, F. Frizon, C. Cau-dit-Coumes, Structural characterization of C-S-H

and C–A–S–H samples—Part I: Long-range order investigated by Rietveld analyses, *J Solid State Chem*, 182 (2009) 3312-3319. <https://doi.org/10.1016/j.jssc.2009.09.026>.

[6] G. Renaudin, J. Russias, F. Leroux, C. Cau-dit-Coumes, F. Frizon, Structural characterization of C–S–H and C–A–S–H samples—Part II: Local environment investigated by spectroscopic analyses, *J Solid State Chem*, 182 (2009) 3320-3329. <https://doi.org/10.1016/j.jssc.2009.09.024>.

[7] X. Pardal, F. Brunet, T. Charpentier, I. Pochard, A. Nonat, ²⁷Al and ²⁹Si solid-state NMR characterization of calcium-aluminosilicate-hydrate, *Inorganic chemistry*, 51 (2012) 1827-1836. <https://doi.org/10.1021/ic202124x>.

[8] P. Rejmak, J.S. Dolado, M.J. Stott, A. Ayuela, ²⁹Si NMR in Cement: A Theoretical Study on Calcium Silicate Hydrates, *J Chem Phys C*, 116 (2012) 9755-9761. <https://doi.org/10.1021/jp302218j>.

[9] G.A. Jeffrey, *An introduction to hydrogen bonding*, Oxford university press, New York, 1997.

[10] C. Dharmawardhana, M. Bakare, A. Misra, W.-Y. Ching, J. Bullard, Nature of Interatomic Bonding in Controlling the Mechanical Properties of Calcium Silicate Hydrates, *J Am Ceram Soc*, 99 (2016) 2120-2130. <https://doi.org/10.1111/jace.14214>.

[11] F. Brunet, P. Bertani, T. Charpentier, A. Nonat, J. Virlet, Application of ²⁹Si Homonuclear and ¹H-²⁹Si Heteronuclear NMR Correlation to Structural Studies of Calcium Silicate Hydrates, *J Phys Chem B*, 108 (2004) 15494-15502. <https://doi.org/10.1021/jp031174g>.

[12] A. Rawal, B.J. Smith, G.L. Athens, C.L. Edwards, L. Roberts, V. Gupta, B.F. Chmelka, Molecular Silicate and Aluminate Species in Anhydrous and Hydrated Cements, *J Am Chem Soc*, 132 (2010) 7321-7337. <https://doi.org/10.1021/ja908146m>.

[13] M. Youssef, R.J.M. Pellenq, B. Yildiz, Glassy Nature of Water in an Ultraconfining Disordered Material: The Case of Calcium–Silicate–Hydrate, *J Am Chem Soc*, 133 (2011) 2499-2510. <https://doi.org/10.1021/ja107003a>.

[14] A. Kumar, B.J. Walder, A. Kunhi Mohamed, A. Hofstetter, B. Srinivasan, A.J. Rossini, K. Scrivener, L. Emsley, P. Bowen, The Atomic-Level Structure of Cementitious Calcium Silicate Hydrate, *J Phys Chem C*, 121 (2017) 17188-17196. <https://doi.org/10.1021/acs.jpcc.7b02439>.

[15] J.R. Yates, T.N. Pham, C.J. Pickard, F. Mauri, A.M. Amado, A.M. Gil, S.P. Brown, An Investigation of Weak CH...O Hydrogen Bonds in Maltose Anomers by a Combination of Calculation and Experimental Solid-State NMR Spectroscopy, *J Am Chem Soc* 127 (2005) 10216-10220.

[16] M. Profeta, F. Mauri, C.J. Pickard, Accurate First Principles Prediction of ¹⁷O NMR Parameters in SiO₂ Assignment of the Zeolite Ferrierite Spectrum, *J Am Chem Soc*, 125 (2003) 541-548.

[17] X. Pardal, I. Pochard, A. Nonat, Experimental study of Si–Al substitution in calcium-silicate-hydrate (C-S-H) prepared under equilibrium conditions, *Cem Concr Res*, 39 (2009) 637-643. <https://doi.org/10.1016/j.cemconres.2009.05.001>.

[18] E. Pustovgar, R.P. Sangodkar, A.S. Andreev, M. Palacios, B.F. Chmelka, R.J. Flatt, J.B. d'Espinoise de Lacaille, Understanding silicate hydration from quantitative analyses of hydrating tricalcium silicates, *Nature communications*, 7 (2016) 10952. <https://doi.org/10.1038/ncomms10952>.

[19] F. Puertas, M. Palacios, H. Manzano, J.S. Dolado, A. Rico, J. Rodríguez, A model for the C-A-S-H gel formed in alkali-activated slag cements, *J Eur Chem Soc*, 31 (2011) 2043-2056. <https://doi.org/10.1016/j>.

jeurceramsoc.2011.04.036.

[20] S. Grangeon, A. Fernandez-Martinez, A. Baronnet, N. Marty, A. Poulain, E. Elkaim, C. Roos, S. Gaboreau, P. Henocq, F. Claret, Quantitative X-ray pair distribution function analysis of nanocrystalline calcium silicate hydrates: a contribution to the understanding of cement chemistry, *Journal of applied crystallography*, 50 (2017) 14-21. <https://doi.org/10.1107/S1600576716017404>.

[21] J.P. Yesinowski, H. Eckert, G.R. Rossman, Characterization of Hydrous Species in Minerals by High-Speed MAS-NMR, *J Am Chem Soc*, 110 (1988) 11367-11375. <https://doi.org/10.1021/ja00213a007>.

Concrete with High-purity Volcanic Glass Powder Manufactured from Pyroclastic Deposit through Dry Gravity Classification and Pulverization

T. Noguchi¹, A. Tomoyose¹, K. Sodeyama² and K. Higashi³

¹Department of Architecture, The University of Tokyo, 7-3-1 Hongo, Bunkyo-ku, Tokyo, Japan

²Kagoshima Prefectural Institute of Industrial Technology, 1445-1 Oda, Hayato-cho, Kirishima-shi, Kagoshima, Japan

³Principle Co., Ltd., 1-17-8 Kamoike, Kagoshima-shi, Kagoshima, Japan

Abstract

Utilization of natural pozzolan such as volcano-related materials in concrete as a supplementary cementitious material can contribute to establishment of low-carbon society and resource circulation society. Volcanic-related materials generally comprise not only glass but also crystal mineral and clay mineral, which may cause undesirable properties in concrete. The authors developed the technology for dividing volcanic-related materials into crystalline mineral, pumice, high-purity volcanic glass, and clay fraction toward total utilization of volcanic-related materials as construction materials. In this study, concrete containing high-purity volcanic glass powders with different fineness are investigated regarding fresh properties, strength development, chloride ion penetration and CO₂ reduction. Experimental works were conducted using 7 types of volcanic glass powders with replacement ratios of 5%, 10% and 20% in concrete with water-to-binder ratios of 20% and 50% for the investigation of fresh properties and strength development. Another experiment on chloride ion penetration in concrete was also conducted using concrete with water-binder ratio of 60% containing volcanic glass powders with replacement ratios of 20%. As a result, it was found that volcanic glass powders gave excellent contribution to the improvement of flowability like fly ash, the enhancement of strength like silica fume, and the restraint of chloride ion penetration like ground granulated blast-furnace-slag. Volcanic glass powders can also contribute to the reduction of CO₂ emission because the content of portland cement can be largely reduced to obtain the same strength in concrete with 100% portland cement.

Keywords: Volcanic glass powder, Supplementary cementitious material, Strength development, Chloride ion diffusion, CO₂ reduction

1. Introduction

Ancient concrete used in the Pantheon in Rome contains volcanic ejecta, which is known as pozzolana. One popular technique to reduce CO₂ emissions stemming from concrete production and construction involves the use of these natural pozzolans as supplementary cementitious materials (SCMs) [1]. Volcanic activity is common in Japan, and one of the earliest researches to use volcanic ejecta as SCM began more than 110 years ago in Hokkaido, the northern part of Japan [2, 3]. Subsequently, many studies were done on the applications of domestic natural pozzolan as SCM, and have been recently reviewed by Cai et

al. [4]. Although concrete made with volcano-related materials had been manufactured practically until 1960's, artificial materials have been chosen as a replacement. The reaction of natural pozzolans is due to volcanic siliceous glass [5], but volcanic ejecta generally comprises not only glass but also crystal mineral and clay mineral in their natural conditions [6], which may lead to typical undesirable properties of natural pozzolans; large variety, variability, and high water demand [7].

In the previous researches [8-11] on the total utilization of pyroclastic flow deposits as construction materials, the authors clarified that dry gravity classification is effective in dividing Ito-shirasu into crystalline mineral, pumice, high-purity volcanic glass, and clay fraction. Through a separating machine made by combining a gravity separator with a winnowing sorter, the amorphous content of volcanic glass increased to 88% when that of raw material is about 60%. As the mechanism of the machine is shown in Figure 1, winnowing with the action of the vibration fluid bed can sort particles by density, particle size, and terminal velocity with low energy consumption.

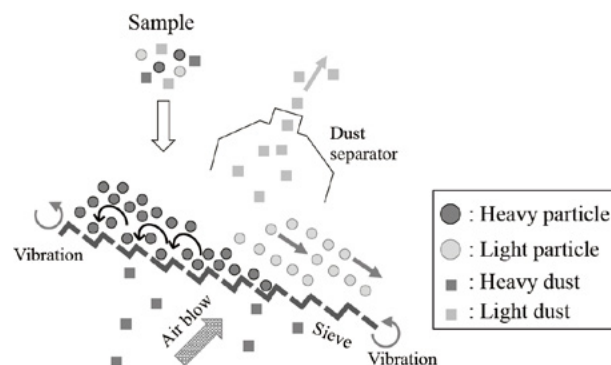


Figure 1: The mechanism of the separating machine for dividing Ito-shirasu.

We have also reported earlier that, when using this material pulverized to a BET specific surface of 15m²/g by a jet mill as a SCM, a replacement ratio of 10% in high strength concrete with a water-to-binder ratio (W/B) of 0.2 leads to fresh properties (microfiller effect) and strength development comparable to those of silica fume. In normal concrete with a W/B of 0.6, a replacement ratio of 5% to 20% leads to strengths higher than that of concrete with no SCM beginning from an age of 7 days, and the strength increases as the replacement ratio increases. Immersion tests in saltwater revealed that the apparent diffusion coefficient decreases to as low as 15% and 10% with replacement ratios of 10% and 20%, respectively, when compared with those of concrete with no replacement. Volcanic glass powder (VGP) was thus found to provide excellent resistance to chloride ion penetration. Furthermore, a replacement ratio of up to 20% does not impair the carbonation resistance. The long-term strength development and durability have also been investigated with a replacement ratio of 20%.

In this study, concrete containing volcanic glass powders with different fineness are investigated from a more practical aspect.

2. Experimental program

2.1 Manufacturing process of VGP

Ito-shirasu used in this investigation was delivered from Kanoya-city, Kagoshima Prefecture in Japan by a mine operator without any pretreatment as shown in Figure 2. The mineral composition of particle size fractions and the chemical composition of the raw material reported in the previous research [12] are presented in Figure 3. As to mineral components, the fraction over 2.4g/cm³ is defined as crystalline, under 2.4g/cm³ defined as amorphous, and in particular under 1.5g/cm³ as pumice in this figure. After sieving Ito-shirasu to under 5mm, Ito-shirasu is divided into five substances by a dry gravity separator. Volcanic

glass powder was manufactured through dry gravity classification and pulverization as shown in Figure 4. First, classified volcanic glass is crushed by a roller mill to a mean particle size of 5.1 μ m. This was then pulverized and classified using three devices, namely, a jet mill, an air classifier, and a cyclone, with the resulting coarse and fine powders being recovered by cyclones and dust collectors, respectively.

2.2 Properties of VGP

The basic properties of seven VGPs are shown in Table 1; the BET specific surface area measured by N₂-adsorption, amorphous content based on heavy liquid separation using zinc bromide ($\rho=2.4\text{g/cm}^3$), and chemical composition by fluorescent X-ray analysis.

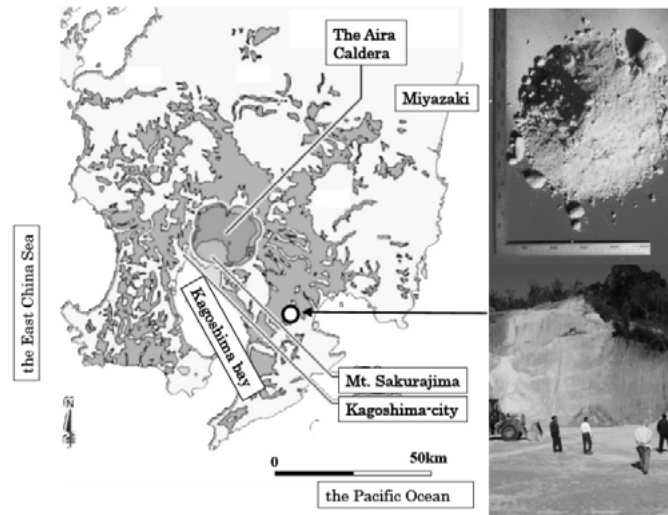


Figure 1: Distribution of shirasu and location of sampling site.

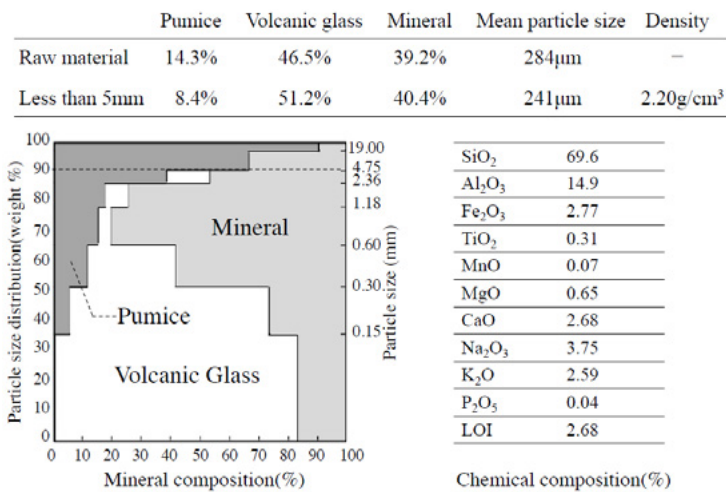


Figure 3: Mineral composition of particle size fractions and chemical composition of Ito-shirasu.

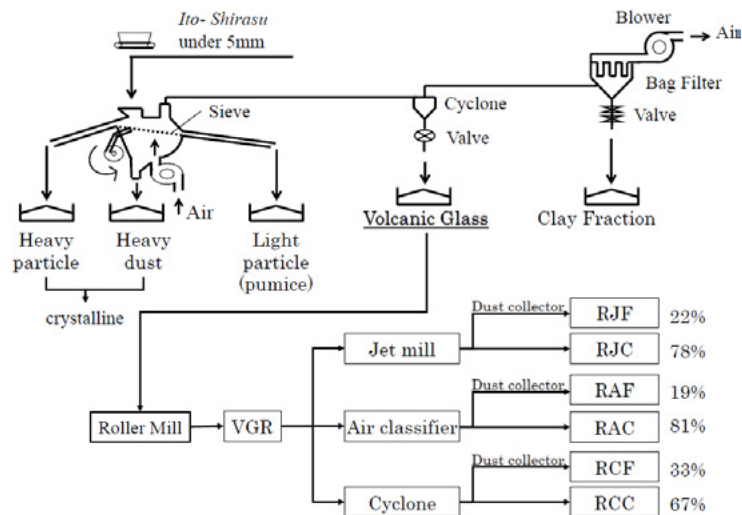


Figure 4: Dry gravity classification and pulverization for manufacturing volcanic glass powder.

Table 1: Basic properties of VGPs.

Marks	VGR	RJF	RJC	RAF	RAC	RCF	RCC
SiO ₂	73.9	72.4	74.3	72.6	74.2	73.0	74.3
TiO ₂	0.20	0.21	0.20	0.21	0.20	0.21	0.19
Al ₂ O ₃	12.8	13.3	12.6	13.2	12.7	13.1	12.6
Fe ₂ O ₃	1.89	2.33	1.76	2.26	1.83	2.38	1.78
MnO	0.05	0.06	0.05	0.06	0.05	0.06	0.05
MgO	0.30	0.37	0.26	0.34	0.29	0.32	0.28
CaO	1.44	1.56	1.40	1.55	1.42	1.51	1.39
Na ₂ O	3.78	3.57	3.91	3.60	3.71	3.59	3.75
K ₂ O	3.34	3.36	3.38	3.30	3.37	3.32	3.35
P ₂ O ₅	0.03	0.04	0.03	0.04	0.03	0.04	0.03
LOI	2.25	2.81	2.02	2.84	2.14	2.47	2.25
BET surface area (m ² /g)	6.4	16.1	4.2	15.2	5.1	12.0	3.6
Glass content (%)	85.7	88.6	87.4				

Table 2: Materials used.

Material	Properties	Marks	
Binder	Cement	Normal portland cement, density: 3.24 g/cm ³	N, NPC
		Low-heat portland cement, density: 3.24 g/cm ³	L, LPC
	SCM	VGP, SF, FA	SCM
Fine aggregate		Crushed lime, density: 2.67g/cm ³	S1
		Crushed tight sand, density: 2.62 g/cm ³	S2
Coarse aggregate		Crushed tight sand, density: 2.64 g/cm ³	G1
		Crushed lime, density: 2.70 g/cm ³	G2
Chemical admixture		High-range water-reducing admixture	SP1
		Air-entraining and high-range water-reducing admixture	SP2
		Air-entraining and water reducing admixture	SP3
		Air-entraining admixture	AE

Table 3: Factors and level, mixing proportions.

Series	W/B	Cement	W (kg/m ³)	SCM/B (%)	S1:S2	s/a (%)	SCM used	Chemical admixture used	Target air content (%)	Target slump (cm)
I	0.20	L	160	10	4:6	45.2	SF + 6 VGP	SP1	2.0±1.0	Slump flow 65±10
II	0.50	N	167	25	2.5:7.5	42.8	FA + 6 VGP	SP2+AE	5.0±1.0	Slump 18±2.5
III	0.60	N	183	5 10 20	2.5:7.5	50.8	RF RC VGR	SP3 + AE	5.0 ± 1.5	Slump 18±2.5

2.3 Mix proportion and test method

The experimental program for three types of VGP was divided into four series, and tests were conducted on concrete mixtures. A forced-action double-axis mixer was used for mixing. Referring to the JIS test method for the activity indices for silica fume (SF) and fly ash (FA), the W/B and replacement ratio were set at 20% and 10%, respectively, in Series 1, whereas they were set at 50% and 25% in Series 2, respectively. The materials and mixture proportions are listed in Tables 2 and 3, respectively. The reference SCM for Series 1 (W/B=20%) was SF. Its target air content and slump flow were 2.0±1.0% and 65±10cm, respectively. The reference SCM for Series 2 (W/B=50%) was FA. Its target air content and slump were 5.0±1.5% and 18±2.5cm, respectively. The chemical admixture dosage was adjusted to achieve the target air content and slump. Compression specimens (φ100×200mm cylinders) were fabricated after testing the fresh properties, namely, the slump (only for Series 2), slump flow, air content, concrete temperature, time to 50cm flow, and time to end-of-flow (only for Series 1). Compression tests were conducted at standard curing ages of 1, 4, and 13 weeks.

In Series III, the influence of VGP on the chloride diffusion of concrete was experimentally examined. Tests were performed on concrete specimens (W/B=60%) of three different sizes of VGP (RF, RC and VGR) with a replacement ratio of 20% and OPC for reference, according to the JSCE standard “Test method for apparent diffusion coefficient of chloride ion in concrete by submergence in salt water”. After cutting off 25mm slices from the top and bottom ends of each cylinder, concrete specimens were cured in a water bath at 20°C. The curing period was 28 days. Specimens were coated with epoxy excepting the circular placing surface and immersed in a 10% NaCl solution at 20°C for 42 weeks. The total chloride ion profile was determined by cutting four 10 mm slices from each cylinder so that the centers of the slices would be the points at depths of 5, 20, 35, 50 and 65 mm from the uncoated surface. These were crushed to less than 150 μm and subjected to ion chromatography to quantify chloride ions in accordance with JIS A 1154 (Method of test for chloride ion content in hardened concrete).

In Series IV, the relational expressions between the binder-water ratio (B/W) and the 28-day compressive strength were experimentally determined to evaluate the environmental performance of concrete containing VGP on a practical basis. Tests were conducted at a ready-mixed concrete plant with actual shipping experience. All materials excepting VGP were the same as those normally shipped from the plant. Trial mixtures of RF, RC, and VGR were prepared with a fixed replacement ratio and three levels of W/Bs. Table 4 tabulates the test levels, proportioning factors, and fresh test results. The replacement ratio was 20% for RF, RC and VGR. RF was also tested with replacement ratios of 5% and 10%. The target slump and air content were 18±3cm and 4.5±1.5%, respectively, for all mixtures. Compression tests were conducted at 28 days after standard curing.

Table 4: Test levels, proportioning factors and fresh test results.

SCM-replacement	W/B (%)	W (kg/m ³)	SP dosage (B*wt%)	AE dosage (B*wt%)	Slump (cm)	Air (%)
RF-20%	60	172	0.80	0.3	19.0	5.9
	50	170	0.90	0.0	19.0	5.7
	35	174	0.90	0.0	19.0	5.9
VGR-20%	60	172	0.65	0.2	19.0	5.9
	50	170	0.65	0.1	19.0	4.6
	35	174	0.80	0.0	20.0	3.4
RC-20%	60	172	0.65	0.0	20.0	5.4
	50	170	0.60	0.1	20.0	4.9
	35	174	0.95	0.1	20.0	3.7
RF-5%	60	172	0.70	0.0	18.5	5.8
	50	170	0.90	0.0	20.5	4.8
	40	172	0.70	0.0	19.0	3.5
RF-10%	60	172	0.70	0.0	18.0	5.2
	50	170	0.90	0.0	20.0	5.4
	40	172	0.85	0.0	21.0	4.0

3. Experimental results

3.1 Fresh properties

Table 5 gives the fresh properties immediately after mixing and chemical admixture dosage of Series I. All VGPs are found to provide slump flows equal to or greater than SF with smaller chemical admixture dosages. In comparison with SF with a mean diameter of 0.1µm, the size of VGP is large. It is therefore presumed that agglomerations are prone to be dispersed due to the small van der Waals forces, requiring a small chemical admixture dosage. The time to 50-cm flow of the coarse powders is longer than that of fine powders, with substantial viscosity and dilatancy to cause resistance to shoveling with a cement shovel. Though the time to 50-cm flow with the three fine powders is longer than that with SF, the consistency was sufficiently practicable. Powders with a BET specific surface of 12m²/g or greater contain sufficient amounts of fine particles to fill the spaces between cement particles, increasing the packing factor of the binder. This presumably achieves a microfiller effect comparable to SF. Based on these results, it is judged that, in fresh concrete with a W/B of around 20%, fine powders with a BET specific surface of 12m²/g or more provide a flowability-improving effect, while the effect is less evident with coarse powders with a BET specific surface of 5m²/g or less.

However, it can be said that VGP is a supplementary cementitious material that is expected to produce a sufficient effect of improving the workability of low W/B mixtures as demonstrated in the present results, provided that its physical properties including grading are rectified during the process of crushing and classification and that impurities including clay minerals are removed.

Table 6 gives the fresh properties and chemical admixture dosage of Series II. The mixing time was the same for all VGPs. The dosage of the high-performance air-entraining and water-reducing admixture for fine powders to achieve the target slump is higher than FA, whereas the admixture dosage to achieve the target slump and air content with coarse powders was the same as SF. The use of VGP reduces the slump flow by 15%, leading to fresh concrete with a high yield value. This is presumably due to the effect of the angular shape of crushed VGP particles in contrast to spherical FA particles. However, coarse powders with a BET specific surface of 5m²/g or less show sufficiently practicable viscosity comparable to FA. It can therefore be said, from these results, that the target slump and air content were achievable in fresh concrete with a W/B of around 50% by using the same dosage of a chemical admixture as FA, which is effective in improving the concrete flowability.

Table 5: Fresh properties and chemical admixture dosage of Series 1.

Type pf SCM /BET surface area (m ² /g)	Slump flow (cm)	Air (%)	Time to 500mm flow (sec)	Time to end-of-flow (sec)	SP1 dosage (B*wt%)
RJF/16.1	74.0×74.8	2.1	5.3	97	1.40
RAF/15.2	73.2×75.0	2.1	5.8	118	1.40
RGF/12.0	73.8×72.2	1.8	5.5	92	1.40
RJC/4.2	74.0×73.8	1.8	6.3	95	1.30
RAC/5.1	72.4×71.1	1.9	6.8	102	1.20
RGC/3.6	69.8×68.2	1.9	8.3	103	1.20
SF/17.7	69.0×68.0	2.9	4.3	79	1.60

Table 6: fresh properties and chemical admixture dosage of Series II.

Type pf SCM /BET surface area (m ² /g)	Slump (cm)	Air □%□	SP2 Dosage (B*wt%)	AE dosage (B*wt%)
RJF/16.1	18.5	5.8	1.10	0.40
RAF/15.2	19.5	5.8	1.10	0.40
RGF/12.0	19.0	5.6	1.10	0.40
RJC/4.2	19.5	5.8	0.83	0.40
RAC/5.1	19.0	5.7	0.83	0.40
RGC/3.6	18.0	5.5	0.83	0.40
FA/1.4	20.0	5.9	0.83	0.40

3.2 Strength development

Figure 5 shows the compressive strength with a W/B of 20%. At an age of 4 weeks, the strength with VGPs is equal to or higher than with SF. At 13 weeks, the strength is equal to or lower than SF. It has been reported that, if the W/B is constant, then a 1% increase in the air content reduces the strength by 4% to 6%. The air content with SF is higher than that with VGP by around 1% in a fresh state. It follows that, even if the strength with VGP is reduced by 5%, it can be regarded as roughly comparable to SF up to 4 weeks. Figure 6 shows the compressive strength with W/B=50%. The strength with fine powders is approximately 20% higher than with FA, while that with coarse powders is equivalent to that with FA, at all ages.

Figure 7 shows the strength development. With W/B=20%, the strength gains with SF from 4 to 13 weeks are greater than with any of the VGPs, but the slopes from 7 to 28 days are similar for all specimens. With W/B=50%, similar tendencies are found in the strength development over time in both cases of FA and VGP.

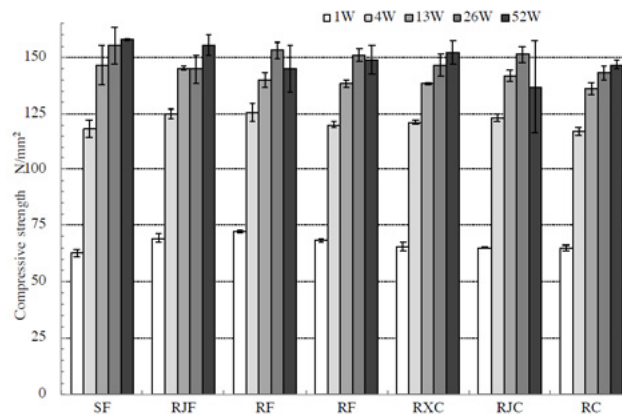


Figure 5: Compressive strength with a W/B of 20% in Series I.

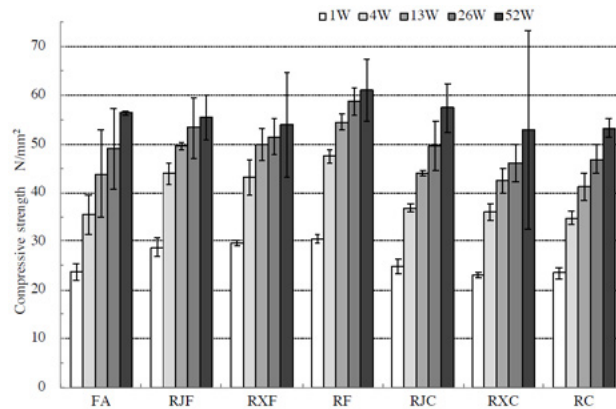


Figure 6: Compressive strength with a W/B of 50% in Series II.

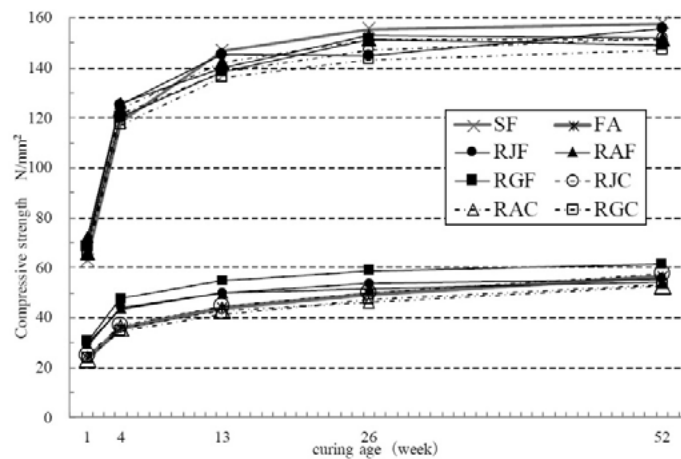


Figure 7: Strength development.

Figure 8 shows VGP's BET specific surface and the relative strength ratio to SF at W/B=20%. The strongest correlation between the relative strength ratio and the BET specific surface is observed at 1 week, with the strength being equivalent with SF even at a BET specific surface of 3m²/g. With a BET specific surface of 12m²/g or greater, the strength is equal to or higher than with SF. However, both the slope of the approximate lines and the correlation coefficients decrease over time, ending up with a strength equivalent to that with SF with all specific surfaces at 4 weeks and a strength equal to or lower than that with SF even with 15m²/g or more at 13 weeks. The reaction rate of SF in place of 10% of cement in a paste with W/B=22% is reported to rapidly increase up to 7 days and slows down thereafter. Though the strength development mechanism of VGP can slightly differ from that of SF due to the different glass percentage and chemical composition, it is presumed that the strength test results of VGP correlate well with the BET specific surface at 1 week and delayed reaction of particles with smaller BET specific surfaces proceeds thereafter. However, the results that strength ratio to SF is 100% or higher up to 4 weeks but is less than SF at 13 weeks imply the effects of factors other than reactions, such as void percentage. Elucidation of strength development related to age remains a subject for future research.

Figure 9 shows the relative strength ratio to FA with W/B=50%. A closer correlation than 20% W/B is observed between VGP's BET specific surface and strength ratio to FA, though with a slight scatter at 13 weeks. According to a former research on pastes with a replacement ratio of 20% and a W/B of 40%, the

reaction ratio of Type II fly ash specified in JIS A 6201 is around 10% at 7 days and 42% to 53% at 555 days, being affected by the amount, chemical composition, and fineness of the glass phase. Since the only difference among the six types of VGPs in the present study is fineness, the obtained strength development presumably corresponds with the BET specific surface, which is closely related to fineness. However, the slightly low strength ratio to FA at 13 weeks requires further observation of long-term strength to elucidate the strength development mechanism.

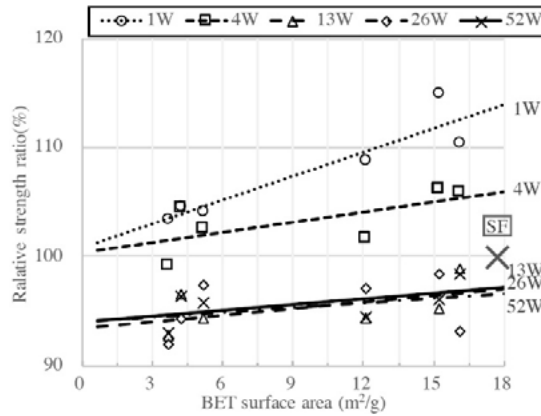


Figure 8: VGP's BET specific surface and the relative strength ratio to SF at W/B=20%.

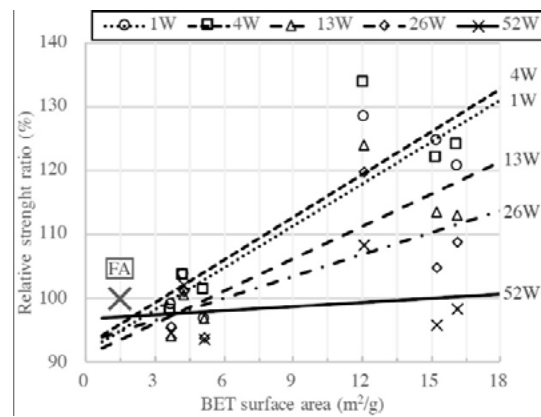


Figure 9: VGP's BET specific surface and the relative strength ratio to FA at W/B=50%.

Resistance to chloride ion penetration

Figure 10 shows the results of immersion tests on concrete specimens in 10% saltwater for 42 weeks after 4-week water curing. The concretes with W/B=60% were OPC and concretes containing RF, VGR, and RC in place of 20% of cement. The chloride contents in the surfaces and deeper inward of concrete containing VGPs are significantly lower than those of OPC. Concrete containing RF or VGR not only shields the penetration of chlorides at a depth of 20mm but also inhibits its penetration at 10mm. Even concrete containing RC with the smallest BET specific surface is found to shield chloride ion penetration at 35mm. Though the shielding effect of RC is weaker than those of RF and VGR, it significantly improves the chloride ion resistance of concrete when compared with OPC. The apparent diffusion coefficients of OPC, RF, VGR, and RC regarding all chloride ions are 4.00, 0.16, 0.20, and 0.60cm²/year, respectively. VGPs with a larger BET specific surface show a smaller apparent diffusion coefficient of chloride ions. In the case of a replacement ratio of 20%, even the apparent diffusion coefficient of RC with a BET specific surface of approximately 3m²/g is less than 20% of that of OPC. The diffusion coefficients of VGR and RF with BET specific surfaces of approximately 7m²/g and 11m²/g, respectively, are less than 20% and less than 10%, respectively, of that of OPC.

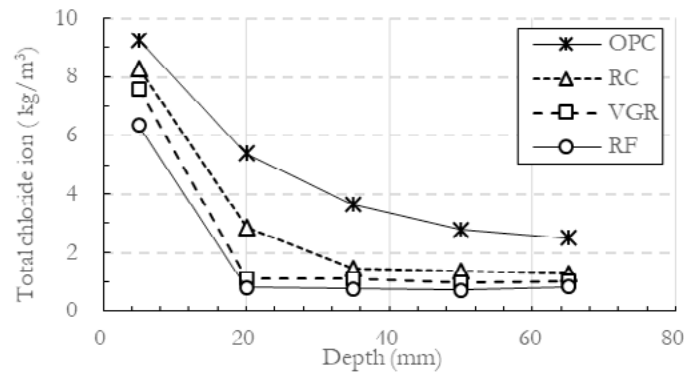


Figure 10: Chloride ion penetration in 10% saltwater for 42 weeks.

3.3 W/B-strength relation and contribution to CO2 reduction

Figure 11 shows the approximate lines calculated from the compression test results and the B/W-strength relational expressions. The relational expression for OPC in the figure is the expression adopted for the actual ready-mixed concrete made of the same materials and shipped by the plant. Due to approximation of trial mixtures with three levels by $n=1$, the scatter of the results of 20%-replaced RF is wider than that of OPC approximated by $n=4$. RF with a BET specific surface of 11m²/g shows a higher strength than OPC with the same B/W even with a replacement ratio of 5%, and the effect remains up to a replacement ratio of 20%. The strength of VGR with a BET specific surface of 7m²/g is slightly higher than OPC. That of RC with a BET specific surface of 3m²/g is slightly lower than OPC. In Series 2, the strength development is comparable to fly ash with a W/B of 50% and replacement ratio of 25%. It can therefore be regarded as equivalent to general fly ash of JIS Type II, which is available on the market in Japan. A higher strength at 91 days is therefore expected.

Figure 12 shows the unit cement reduction determined from calculation by the relational expression for proportioning to achieve compressive strengths of 30, 40, and 50MPa. The unit water content of OPC proportioning for general slump control is assumed to be 180kg/m³, whereas the unit water content in the flow control using VGP is assumed to be 170kg/m³. By assuming the proportioning control strength as 50MPa, the cement content can be reduced by more than 100kg even with a replacement ratio of 10% at which the carbonation rate coefficient decreases. With a 20% replacement, the cement content can be reduced by 150kg. Also, with RC, the B/W-strength relational expression of which is lower than cement, the cement demand to obtain the same strength becomes smaller, as the replacement ratio is 20%. Reductions of more than 50kg are therefore achieved at all strength levels.

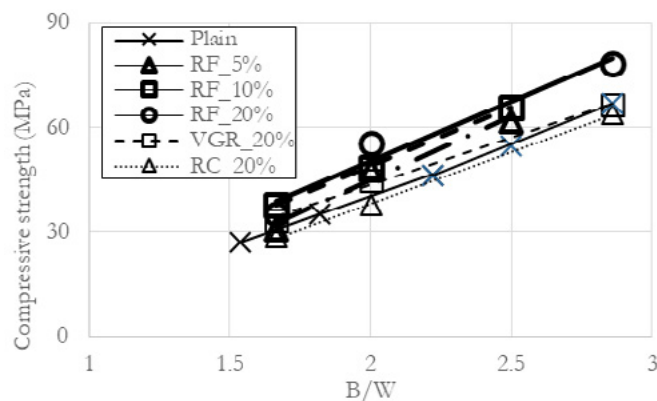


Figure 11: B/W-compressive strength relation

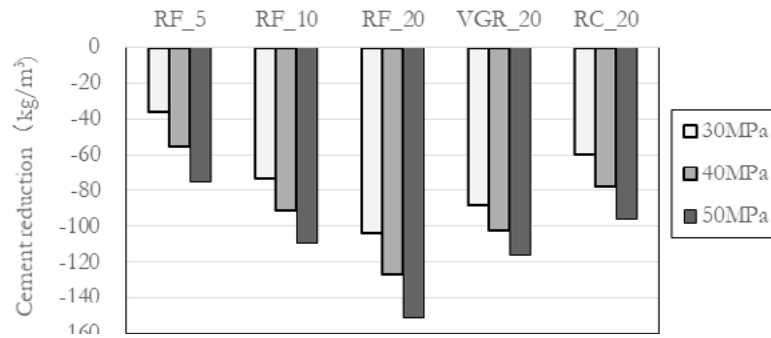


Figure 12: Unit cement reduction to achieve compressive strengths of 30, 40 and 50MPa.

4. Conclusions

The findings regarding concrete made using volcanic glass powder obtained in this study include the following:

(1) Fresh properties

With a W/B of around 20%, VGP powder with a BET specific surface of 12m²/g or more has a flowability-improving effect, while such an effect is judged as being weak with a BET specific surface of 5m²/g or less. With a W/B of around 50% or more, a replacement ratio exceeding 10% of VGP with a BET specific surface of 12m²/g or more increases the chemical admixture demand for achieving the target slump increases. With a BET specific surface of 5m²/g or less, however, the target slump and air content can be achieved with a chemical admixture dosage equivalent to JIS Type II fly ash with a replacement ratio of 25%.

(2) Strength properties

With a W/B of around 20%, the BET specific surface of VGP correlates with the strength, demonstrating the strength-developing performance equivalent to SF with a BET specific surface of around 5m²/g, and that equal to or higher than SF with a BET specific surface of 12m²/g. At four weeks, the correlation between the BET specific surface and strength becomes weak, demonstrating a strength-developing performance equivalent to SF. At an age of 13 weeks, the correlation becomes even weaker, with the strength being equivalent or lower than SF. With a W/B of around 50% or more, a strength equivalent to JIS Type II fly ash is obtained with a BET specific surface of around 3m²/g. The strength becomes 20% higher than fly ash with a BET specific surface of 12m²/g or more, with correlation between the BET specific surface and the strength being observed up to 91 days.

(3) Durability and CO₂ reduction

The use of VGP with a BET specific surface of around 3m²/g at a replacement ratio of 20% provides sufficient resistance to chloride ion penetration, being sufficiently effective in reducing the amount of portland cement consumption.

5. Acknowledgment

This research is supported by JSPS Grant-in-Aid for Scientific Research (A) with No. 18H03803 entitled “Carbon-minus Recyclable High-performance Concrete”.

6. Reference

[1] K. Kupwade-Patil, C. de Wolf, S. Chin, J. Ochsendorf, AE. Hajiah, A. Al-Mumin, O. Büyükoztürk,

Impact of Embodied Energy on materials/buildings with partial replacement of ordinary Portland Cement (OPC) by natural Pozzolan volcanic Ash, *J Clean Prod* (2018) 177: 547-554. <https://doi.org/10.1016/j.jclepro.2017.12.234>

[2] I. Hiroi, The Preparation and Use of concrete Blocks for Harbour Works, *Transactions, ASCE* (1904) LIV. Part A (10): 211-220

[3] I. Hiroi, On Long-time Tests of Portland Cement, Hydraulic Lime, and Volcanic Ashes, *J College Engrg, Tokyo Imperial Univ* (1920) X (7): 155-172

[4] G. Cai, T. Noguchi, H. Degée, J. Zhao, R. Kitagaki, Volcano-related materials in concretes: a comprehensive review, *Environ Sci Pollut Res* (2016) 23 (8): 7720-7243, <https://doi.org/10.1007/s11356-016-6161-z>

[5] R. Snellings, G. Mertens, J. Elsen, Supplementary Cementitious Materials. *Rev Mineral Geochem* (2012) 74 (1): 211-278, <https://doi.org/10.2138/rmg.2012.74.6>

[6] S. Shipley, A. M. Sama-Wojcicki, Maps Showing Distribution, Thickness, and Mass of Late Pleistocene and Holocene Tephra from Major Volcanoes in the Pacific Northwest of the United States; a Preliminary Assessment of Hazards from Volcanic Ejecta to Nuclear Reactors in the Pacific Northwest (1983), USGS, MF-1435, <https://doi.org/10.3133/mf1435>

[7] R. Snellings, Assessing, Understanding and Unlocking Supplementary Cementitious Materials, *RILEM Tech Lett* (2016) 1 (1): 50-55, <https://doi.org/10.21809/rilemtechlett.2016.12>

[8] A. Tomoyose, T. Noguchi, K. Sodeyama, K. Higashi, Experimental study on using differentiated shirasu by gravity concentration and classification as concrete material, *CAJ Proc Cem Concr* (2016) 70 (1): 580-587, <https://doi.org/10.14250/cement.70.580>

[9] A. Tomoyose, T. Noguchi, K. Sodeyama, K. Higashi, Stability of volcanic silicate powder for concrete manufactured from shirasu through gravity classification and pulverization, *CAJ Proc Cem and Concr* (2017) 71 (1): 674-681, <https://doi.org/10.14250/cement.71.674>

[10] K. Sodeyama, A. Tomoyose, T. Noguchi and K. Higashi, Total Utilization of Shirasu as Construction Materials through Dry Gravity Classification and Pulverization, *J Soc Mat Sci, Japan* (2017) 66 (8): 574-581, <https://doi.org/10.2472/jsms.66.574>

[11] A. Tomoyose, T. Noguchi, K. Sodeyama and K. Higashi, Fundamental study about volcanic glass classified from Ito-shirasu by gravity classification, *Proc Jpn Concr Ins* (2017) 38 (1): 151-156

[12] Tomoyose, A. et al.: Utilization of volcanic ejecta as a high-performance supplementary cementitious material by gravity classification and pulverization, *RILEM technical letters*, Vol.3, pp.66-74, 2018.12, <https://doi.org/10.21809/rilemtechlett.2018.66>

Manufacturing high-performance supplementary cementitious materials from pyroclastic deposit through dry gravity classification and pulverization

A. Tomoyose¹, T. Noguchi¹, K. Sodeyama², K. Higashi³

¹Department of Architecture, The University of Tokyo, 7-3-1 Hongo, Bunkyo-ku, Tokyo, Japan

²Kagoshima Prefectural Institute of Industrial Technology, 1445-1 Oda, Hayato-cho, Kirishima-shi, Kagoshima, Japan

³Principle Co., Ltd., 1-17-8 Kamoike, Kagoshima-shi, Kagoshima, Japan

Abstract

Volcanic ejecta and deposits, which are pozzolanically reactive, have long been known to improve the durability of concrete. Nevertheless, it has also been pointed out that the use of a natural pozzolan as a supplementary cementitious material (SCM) can pose problems of low workability and slow strength development. Also, in addition to the low performance as a natural SCM, its composition and physical properties are widely variable and significantly scattered when compared with industrial by-products. The authors have been conducting studies on the total utilization of volcanic deposits for applications suitable for respective properties by classifying them by floating speed difference and particle diameter. Pyroclastic flow deposits called “Ito-Shirasu” which erupted out in 29,000 years ago covers an area of about 3,427 km², and it forms extensive pyroclastic plateaus with a layer about 10 meters to 200 meters thick in the southern regions of Kyushu, Japan. The amount of sediments of Ito-Shirasu is estimated to have a volume of 75 billion m³. It includes a crystal mineral and an amorphous silicate and so on, therefore it has the properties of both a fine aggregate and a SCM owing to its pozzolanic reaction. They reported that sorting out particles less than 2.4 g/cm³ by dry gravity classification and removal of smaller clay fraction by bag filter is technically effective to recover high purity volcanic glass from Ito-shirasu.

This study provides a possibility to produce high performance SCMs in volcanic regions worldwide from volcanic ejecta, which have been regarded as a low performance SCM, by sorting out a high purity volcanic glass by the same method using an air table.

Keywords: Volcanic glass, natural pozzolan, supplementary cementitious material, dry gravity classification

1. Introduction

A quest for supplementary cementitious materials (SCMs) with a reactivity allowing them to be used as a replacement for Portland cement has been under way worldwide, with industrial byproducts including ground-granulated blast-furnace slag and fly ash being globally applied to actual construction. However, an expected reduction in the output of such materials, particularly fly ash, was pointed out already in 2007 [1], amid the trend to cope with the environmental problems. Then in December 2015, the Paris Agreement

was adopted to urge the world to take measures against greenhouse gas emissions, edging out coal-fired power generation.

Though the term “pozzolan” is widely used today to describe a reactive material for concrete regardless of whether it is natural or artificial, it is derived from “pozzolana,” natural volcanic ejecta, which was used as a material for concrete in the Roman era. Volcanic ejecta and deposits, which are pozzolanically reactive, have long been known to improve the durability of concrete. No standard has been available for these materials due to their being no industrial products, with their physical properties widely varying. Volcanic ejecta and deposits have therefore not been actively employed for construction under the circumstances where laws and regulations require engineers to refer to standards. However, with a shift from specification codes to performance-based codes in sight, active use of natural resources in the future of north America has been highlighted [2].

Nevertheless, it has also been pointed out that the use of a natural pozzolan as a supplementary cementitious material can pose problems of low workability and slow strength development [3]. Also, in addition to the low performance as a natural SCM, its composition and physical properties are widely variable [4] and significantly scattered [5] when compared with industrial byproducts.

The wide variety of natural pozzolans are classified by their origins as shown in Figure 1. They are broadly divided into two categories: primary volcanic and sedimentary. Diatomaceous earth and white earth fall in the sedimentary category due to their undergoing hydrothermal action during the depositional process. The volcanic category includes zeolitised tuff, or volcanic tuff, which is also altered by diagenetic processes. Though zeolite is a sedimentary rock diagenetically crystallized after being ejected and deposited, it shows reactivity with lime when finely pulverized by a base-change reaction. Excepting the group of diatomaceous earth, all natural pozzolans are derived from volcanic rock and volcanic minerals [6]. All these natural pozzolans contain such impurities as quartz and feldspar, along with amorphous silica (volcanic glass, VG), which causes reactivity. However, in many cases these are studied and used as they are, through the processes of pulverization and classification (mostly into a particle smaller than 45 μm)[6].

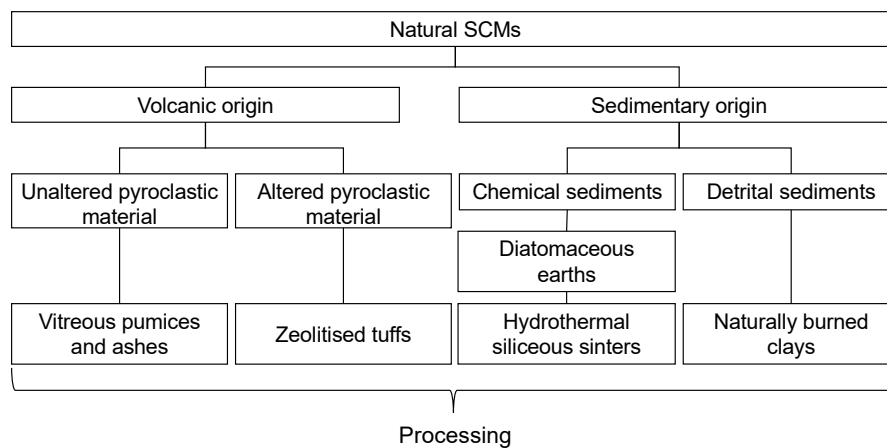


Figure 1: General classification scheme of natural supplementary materials. Processing usually involves crushing grinding, and size separation, mostly under 45 μm

The authors have been conducting studies on the total utilization of volcanic deposits for applications suitable for respective properties by classifying them by floating speed difference and particle diameter. This is done by using equipment referred to as an air table, which is based on a principle shown in figure 2. We have already blended the heavy particle and heavy dust fractions dry-classified by the air table from pyroclastic flow deposits (Ito-Shirasu), which is categorized as unaltered matter of volcanic origin, and

found that the blend can be used as fine aggregate in the same manner as crushed sand [7]. Furthermore, based on the analysis of the mineral composition and amorphous content of classified light dust, sorting out particles less than 2.4 g/cm³ by dry gravity concentration and removal of smaller clay fraction by bag filter is technically effective to recover high purity VG from raw material. The authors demonstrated that, by pulverizing this VG to around 1 μm, a slump flow and 7-day and later strength equal to or greater than silica fume can be obtained when used for concrete at W/B = 0.2 even with smaller dosages of chemical admixtures. When used at W/B = 0.6, the concrete demonstrated excellent strength development from an age of 7 days even when up to 20% of normal Portland cement was replaced with VG. That concrete also showed no reduction in the carbonation rate coefficient, indicating extremely high resistance to chloride ion penetration [8].

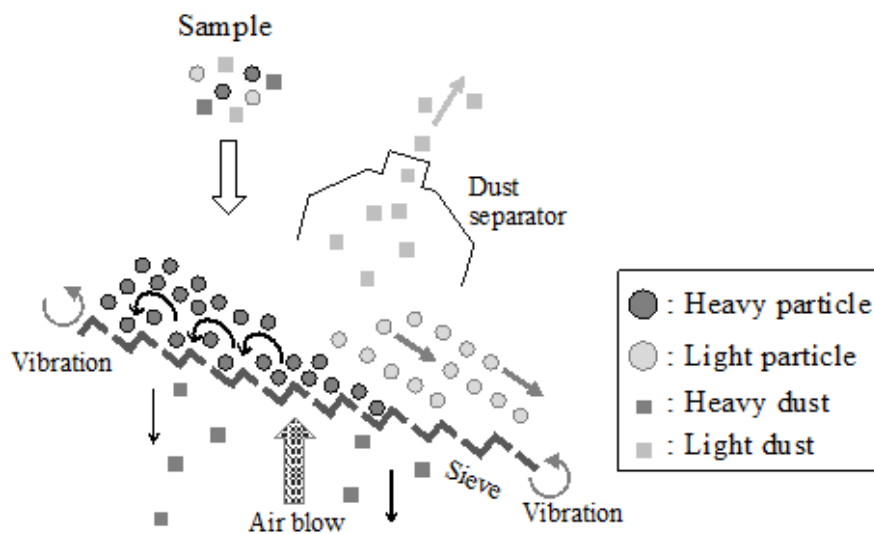


Figure 2: Mechanism of air table; dry gravity classification. The particles are almost classified according to the density and diameter.

This study aims to verify whether the effect of dry classification of volcanic deposits by an air table is limited only to Ito-Shirasu, which spreads over Southern Kyushu of Japan, or whether it is more universal, by analyzing its deposition principle and powder properties.

2. Test materials and procedures

2.1 Method of producing volcanic glass powder

Similarly to a former report [9], unprocessed Ito-Shirasu was obtained from a mining firm in Kagoshima Prefecture. The test material was prepared by drying the part passing a 5 mm sieve to a water content of 1% or less. Figure 3 shows details of the classifier used. This equipment consisting of an air table along with a cyclone and dust collector classifies the material into five components. The classifying conditions include the material feed, pore size of the sieve, concavo-convex shape, inclination angle, rotation frequency, vibration amplitude, and air flow. The density and size of each component can be adjusted by setting these conditions [9]. The particles are classified according to the density and mean size as listed in Table 1 along with the recovery rate. Most crystal minerals are recovered as heavy particles 1 mm or more in diameter and heavy dust less than 1 mm in diameter, while pumice is recovered as light particles. Among the light dust, fine particles recovered by the cyclone include high purity VG. The super fine part not recovered at the cyclone is recovered by the dust collector as the clay fraction (CF).

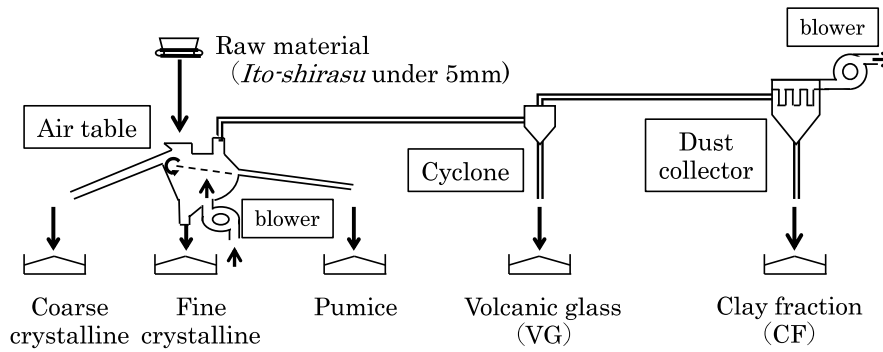


Figure 3: the dry classifier used. An air table along with cyclone and dust collector classifies Ito-shirasu into five elements.

Table 1: Recovery rate, density and mean size of components

	Coarse crystalline	Fine crystalline	Pumice	VG	CF
Recovery rate (%)	12	21	19	46	2
Density (g/cm ³)	2.63	2.66	1.81	2.36	2.37
Particle mean size (μm)	1137	330	742	83.5	4.1

Figure 4 shows the size distributions of VG recovered by the cyclone and CF recovered by the dust collector measured by a laser diffractometer. The mean size of the fraction recovered by the dust collector is 4 μm, representing the fine particle fraction slightly contained in the ore, though the two curves partly overlap due to dry classification.

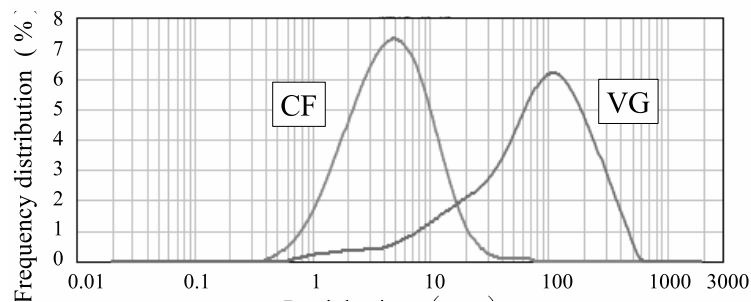


Figure 4: Particle size distribution of VG and CF

The sorted VG and CF were crushed and classified as shown in figure 5. Volcanic glass primary-crushed by a roller mill into a powder (VGR) is pulverized and classified using three devices: a jet mill, air classifier, and cyclone. The fractions recovered by the dust collector (RJF, RAF, and RCF) are referred to as fine powder. The fractions recovered by the cyclone (RJC, RAC, and RCC) are referred to as coarse powder. These fractions, including the primary-crushed VGR, are referred to as volcanic glass powder (VGP). Also, the CF, including its crushing, are collectively referred to as clay powder.

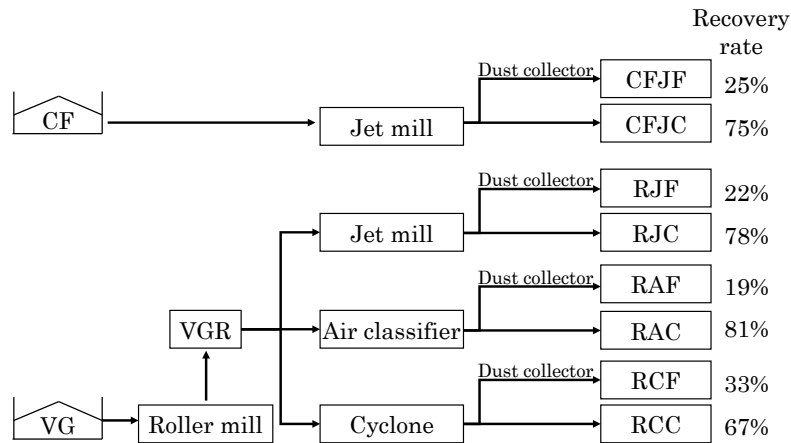


Figure 5: Manufacturing process of volcanic glass powder and clay powder

2.2 Chemical composition and ignition loss

Calibration curves of the standard minerals were prepared by the glass bead method for VGP and clay powder using lithium tetraborate as the flux, and their chemical compositions were measured by XRF. The ignition loss was calculated from the loss values obtained from samples dried for more than 12 h at 105°C and then ignited at 1,000°C for 1 h.

2.3 Thermogravimetric analysis, water vapor adsorption, BET specific surface

Prior to heating, measurement samples for thermogravimetric analysis 20 to 30 mg in mass were vacuum-dried for more than 12 h to eliminate the effect of adsorption water in the atmosphere. These were then heated from the room temperature (approximately 20°C) to 1,100°C at a rate of 10°C/min with measurement intervals of 30 sec.

The water vapor adsorption isotherm was measured at 25°C using an automatic vapor adsorption meter. The specific surface was then determined by the BET method. The measurement cell containing the sample was vacuumed and dried for 3 h at 105°C to eliminate the effect of adsorption water.

2.4 MB adsorption

Adsorption of methylene blue (MB) was determined in accordance with JCAS I-61: 2008 (Test method for methylene blue adsorption of fly ash). Based on the preliminary test results, a MB solution was added to samples weighed to between 0.05 and 0.10 g, and the absorbance was measured by suction filtration. The MB adsorption of samples was calculated by preparing calibration curves from the absorbance by blank tests. Six types of VGP and three types of clay powder were used as the materials.

3. Results and discussion

3.1 Chemical composition and ignition loss

Table 2 tabulates the results of chemical composition and ignition loss measurements. As shown in figure 6, the SiO₂ content of both VGP and clay powder negatively correlate with the ignition loss. The SiO₂ content and ignition loss of VGP are more than 72% and less than 3%, respectively, but after pulverization and classification, the SiO₂ content tends to slightly decrease in the fine powder fraction and slightly increase in the coarse powder fraction, with the difference being around 2 percentage points. As for clay powder, the SiO₂ content and ignition loss of CF are 65% and 4.5%, respectively, but the difference between those of the fine powder fraction (CFJF) and coarse powder fraction (CFJC) after pulverization and recovery are greater than those of VGP, being around 10 percentage points for SiO₂ content and around 3 percentage

points for ignition loss.

Table 2: Chemical composition and LOI of the materials

Sample	VGR	RJF	RJC	RAF	RAC	RCF	RCC	CF	CFJF	CFJC
SiO ₂	73.9	72.4	74.3	72.6	74.2	73.0	74.3	64.4	60.5	69.2
TiO ₂	0.20	0.21	0.20	0.21	0.20	0.21	0.19	0.30	0.33	0.24
Al ₂ O ₃	12.8	13.3	12.6	13.2	12.7	13.1	12.6	16.0	16.9	13.7
Fe ₂ O ₃	1.89	2.33	1.76	2.26	1.83	2.38	1.78	7.03	8.26	5.07
MnO	0.05	0.06	0.05	0.06	0.05	0.06	0.05	0.07	0.08	0.06
MgO	0.30	0.37	0.26	0.34	0.29	0.32	0.28	0.75	1.09	0.52
CaO	1.44	1.56	1.40	1.55	1.42	1.51	1.39	1.47	1.62	1.45
Na ₂ O	3.78	3.57	3.91	3.60	3.71	3.59	3.75	2.22	1.75	2.59
K ₂ O	3.34	3.36	3.38	3.30	3.37	3.32	3.35	3.21	3.05	3.76
P ₂ O ₅	0.03	0.04	0.03	0.04	0.03	0.04	0.03	0.03	0.04	0.03
LOI	2.25	2.81	2.02	2.84	2.14	2.47	2.25	4.47	6.37	3.44

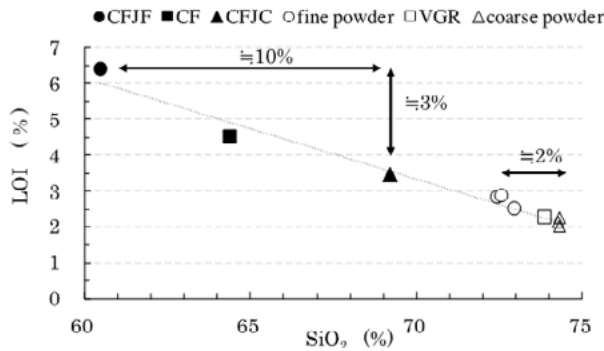


Figure 6: Relation between SiO₂ and LOI

Volcanic glass is subjected to weathering action of water, undergoing hydration and elution, and follows a weathering sequence shown in Fig. 7, ultimately being modified to a clay mineral (halloysite)[10]. SiO₂ is prone to elution through chemical changes, leaving compositions rich in H₂O and Al₂O₃. Clay powder can therefore be regarded as being in a later stage of weathering in terms of chemical composition than VGP. In either case, fine powder shows a composition at a later stage of weathering than coarse powder, with the difference between fine and coarse powders of clay powder being greater.

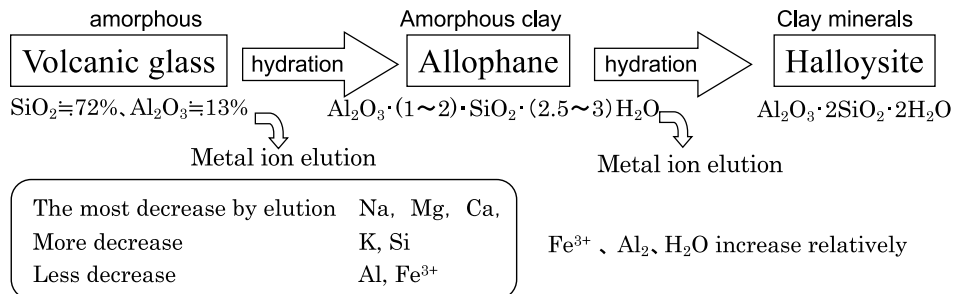


Figure 7: Weathering sequence of volcanic glass

3.2 Properties of adsorbed water

Figure 8 shows the thermogravimetric curves of three types of clay powder and three types of VGP from

among the results of thermogravimetric analysis tests. The mass losses of CFJF and CF are significant, being 8% and 6%, respectively. Those of CFJC and RJF are similar at around 4%, but their ignition losses differed at 3.4% and 2.8%, respectively. This is presumably because the mass loss of RJF during drying at 105°C for pretreatment before ignition loss measurement is greater as shown in the different low temperature ranges of their TG curves. The mass losses of RJC and VGR are both below 3%, demonstrating similar trends to the ignition loss results. Since volcanic glass derived from magma is reported to contain moisture equivalent to ignition loss [11], the losses in the TG curves are considered to be attributable to reduction in the moisture content, but the differential thermogravimetric curves shown in figure 9 demonstrate different trends of the peak temperatures of dehydration. One peak is found at around 250°C for VGP including those not shown in the figure. This is a typical peak of volcanic glass [12]. The shift of this temperature toward a lower temperature as the sample is crushed to smaller particles was also confirmed in the tests [12]. For clay powder, peaks are found at less than 100°C, around 250°C, and 450°C. The large peak at less than 100°C is a tendency observed in allophane, an amorphous clay of weathered volcanic glass, indicating the presence of physical adsorbed water or interlayer water, which result from weathering-induced hydration and are not dehydrated by vacuum drying. Similar water is also found to be present in CF and CFJF.

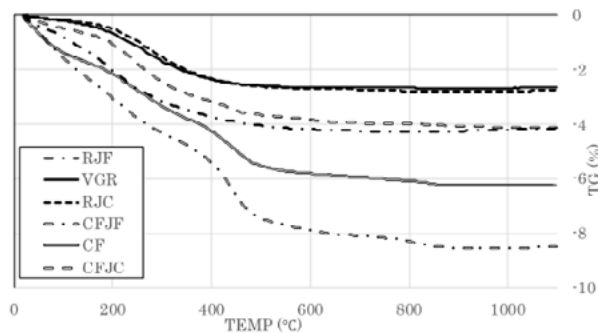


Figure 8: Thermogravimetric curves of VGP and clay powder

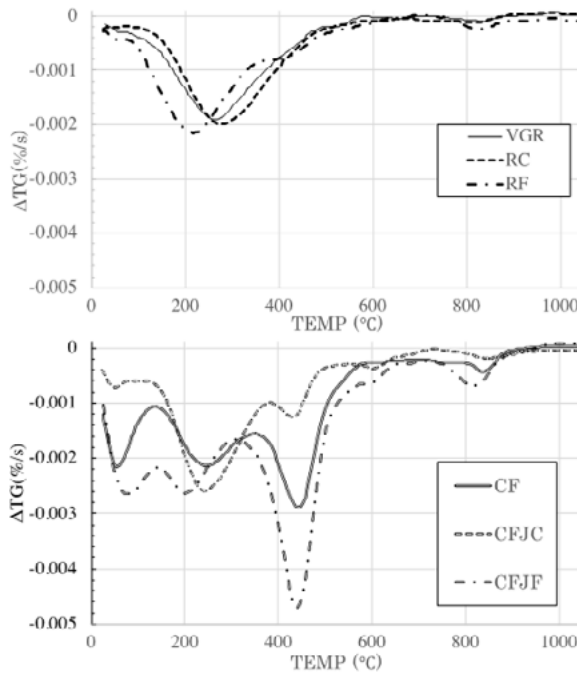


Figure 9: Differential thermogravimetric curves of VGP and clay powder

At the peaks of 450°C, slight endothermic shoulders are observed in all clay powders and in DTA as well. These are considered to be the dehydration of water bound by further hydration or of structural water

(hydroxyl), suggesting an indication of clay mineralization [10].

Figure 10 shows part of the obtained water vapor adsorption isotherms. The adsorption and desorption curves of RJF are separated, being hysteretic similar to Type II or Type H4 that suggest the presence of slit-shaped pores and micropores according to the classification by IUPAC [13]. CF shows hysteretic curves close to Type III or Type V, with adsorption being small in low pressure ranges less than 0.1, which demonstrates that adsorption does not occur while the interaction between vapors is greater. The total adsorption of CF is high, though its hydrophilicity can be low, with the difference between adsorption and desorption being large. Therefore, once water is adsorbed, it tends to be hard to be desorbed. Regarding TG curves for which the pretreatment is vacuum drying, CF shows a dehydration peak of ΔTG at less than 100°C. Therefore, the adsorbed water is mostly not desorbed at normal temperatures and low pressure, demonstrating properties close to allophane, which is used as a desiccant-adsorbent. Table 3 shows the BET specific surface determined from the water vapor adsorption at a pretreatment temperature of 105°C and the nitrogen gas adsorption at a pretreatment temperature of 300°C. CF was incalculable, as no linearity in the plots was found in the relative pressure range of 0.05 to 0.35. In contrast to SF, VGP and FA show BET specific surfaces by water vapor adsorption greater than that by nitrogen adsorption. In vapor adsorption, water is adsorbed selectively by hydrophilic sites, whereas nitrogen is an adsorbate that covers the entire powder surfaces uniformly. The surface physical properties can therefore be discussed by using different adsorbates. Since the BET specific surface is calculated in the relative pressure range of 0.05 to 0.35, the amount of water vapor adsorption of VGP in the low pressure range turned out to be great due to its high hydrophilicity.

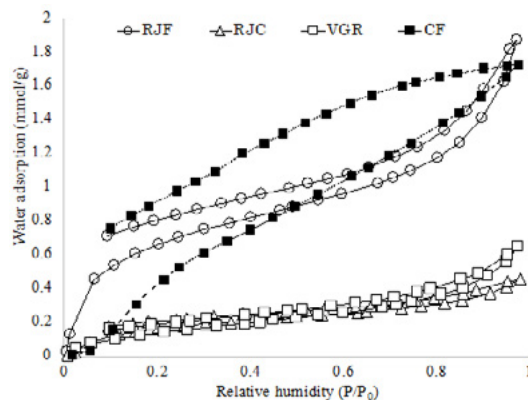


Figure 10: Thermogravimetric curves of VGP and clay powder

Table 3: BET surface area determined from water and nitrogen

Sample	VGR	RJF	RJC	RAF	RAC	RCF	RCC	CF	SF	FA
Water adsorption BET (m ² /g)	10.0	41.9	11.2	23.6	8.4	18.6	6.4	-	14.4	7.1
Nitrogen adsorption BET (m ² /g)	7.1	16.1	4.2	12.4	5.1	10.7	3.7	31.4	20.2	1.5

3.3 BET specific surface area and adsorption

Figure 11 shows the relationship between the mean particle size and the BET specific surface. The BET specific surface of VGP increases as the mean size decreases. On the other hand, clay powder shows no particular trend between the mean particle size and the BET specific surface. The BET specific surfaces of CF and CFJF are particularly large, being twice as large as that of VGP with similar mean size. The state of

particle surfaces can differ from that of VGP.

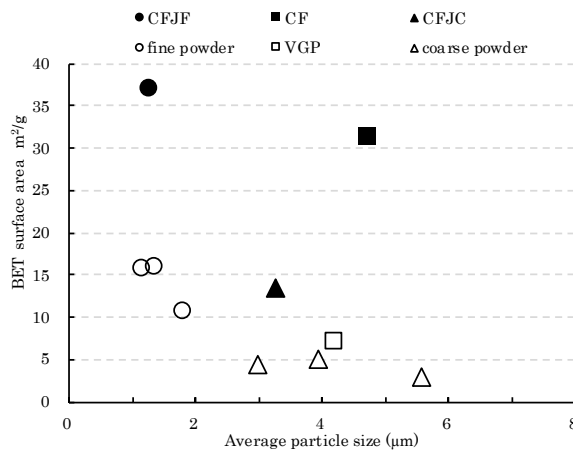


Figure 11: Relationship between mean particle size and BET surface area of VGP and Clay powder

Figure 12 shows the relationship between the BET specific surface and the MB adsorption. The BET specific surface and MB adsorption of VGP are closely correlated, with all sizes meeting the requirement to be not more than 1.20 g/100 g (12.0 mg/g) by EN 197-1: 2000 for the MB adsorption of limestone as a cement component. On the other hand, clay powders exceed this limit, with the adsorption tending to be above the approximate line for VGP.

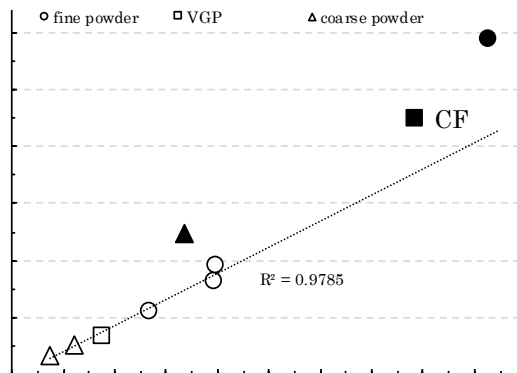


Figure 12: Relationship between BET surface area and MB adsorption of VGP and Clay powder

Focusing on the fact that silica is lost during the process of weathering, leaving alumina, the ratio of SiO₂ to Al₂O₃ (silica-alumina ratio) has been proposed as a most simple index to the degree of weathering [14]. Figure 13 shows the relationship between the silica-alumina ratio and the MB adsorption per unit BET specific surface. The chemical compositions of CFJF and CF represent particularly high degrees of weathering among the clay powders. Their MB adsorption is also 30% greater than that of VGP. When compared with CFJF and CF, the degree of weathering of CFJC is closer to that of VGP, but the value of adsorption is nearly twice as large as that of VGP. As for VGP, the degree of weathering of fine powder is slightly higher than coarse powder in terms of chemical composition, but their MB adsorptions can be regarded as being on the same level from their respective mean values and standard deviations. The adsorption of a polycarboxylate-based dispersant per unit area of powders of the same types (i.e., powders with the same compositions) is reported to be constant [18]. If this applies to MB, then fine and coarse powders of VGP can be regarded as the same powder from the aspect of dispersant adsorption, but clay powder cannot be regarded as the same type as VGPs. Also, the unit adsorption of CFJC is the largest,

though its degree of weathering is not as high as CF and CFJF.

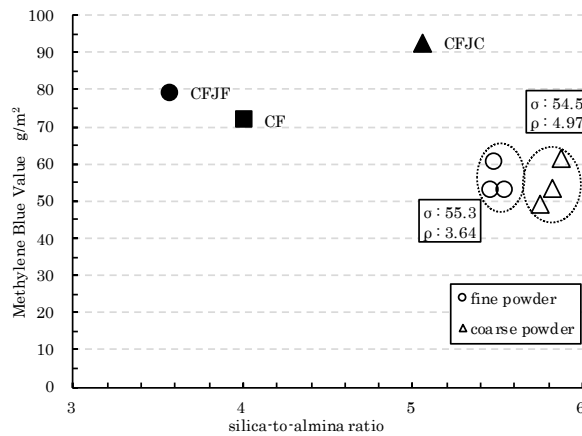


Figure 12: Relationship between BET surface area and MB adsorption of VGP and Clay powder

4. Discussion

In the field of natural disaster science, the refractive index of volcanic glass is used as an index to the progress of weathering of a cliff, as it increases under the effect of hydration. Also, the particle structure of a glass shard is explained as a structure consisting of a non-hydrated core surrounded by a hydrated rim, since the refractive index of crushed glass shards is widened toward the lower side [15]. Volcanic glass is a most weatherable material, and the smaller the particle, the faster the weathering proceeds, changing to a different soft material under chemical weathering action [16]. In view of these findings and the results of the present study, figure 14 shows the particle properties and process of crushing/classification.

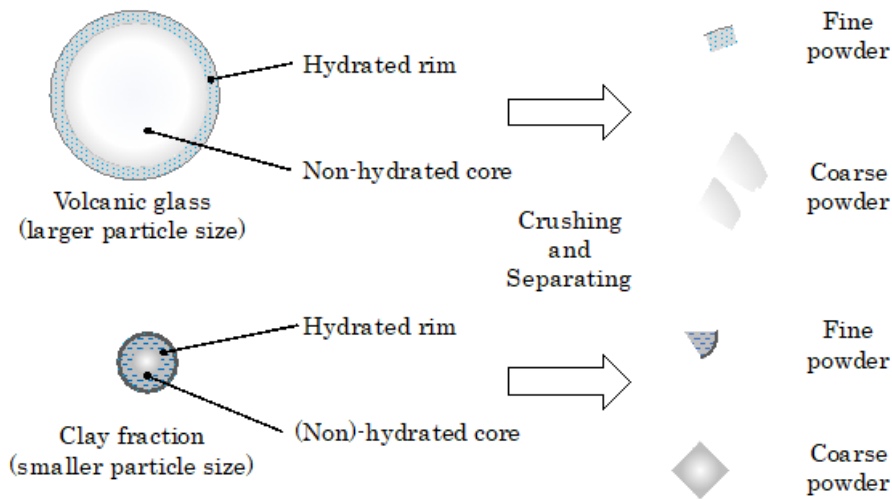


Figure 14: Particle contained in volcanic ejecta and deposits and their crushing process

Both VG and CF have a structure with a hydrated rim on the surfaces, and layers closer to the surface are softer and more prone to be pulverized during the crushing process, tending to be recovered by a dust collector. This agrees with the fact that fine and coarse powders have different chemical compositions and ignition losses. Based on the adsorption per unit area and the results of thermoanalysis of CFJC, it is considered that CF with a smaller particle size with hydration proceeding more to the core layer leads to a thicker hydrated surface rim. CFJF in particular has a concentrate of highly weathered surface layer. In other words, crushing after removing heavily weathered fine particles is effective in manufacturing unweathered high purity VGP, which is a high performance SCM, from volcanic deposits.

Whereas basaltic magma with low viscosity causes moderate volcanic activity, rhyolitic magma is generally said to cause violent and explosive eruption. In other words, magma with a large SiO₂ content is said to cause explosive eruption. The deposits of volcanic materials excepting gasses are classified into three types: pyroclastic fall deposit, pyroclastic flow deposit, and lava. Pyroclastic fall deposit results from a Plinian eruption shown in figure 15, whereas pyroclastic flow deposit results from a pyroclastic flow.

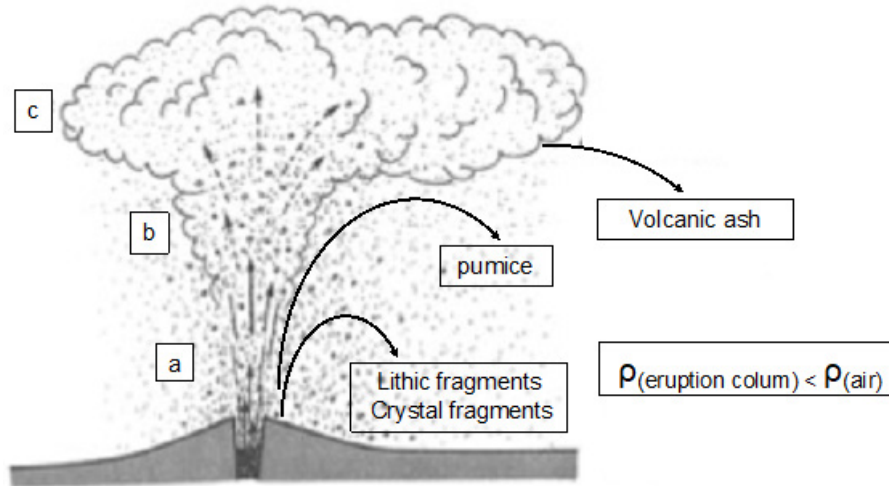


Figure 15: Diagram of Plinian eruption

A Plinian eruption, an explosive one represented by the eruption of Mount Vesuvius in 79 AD, forms an eruptive column made of gases, magma and rocks crushed to pieces, and fragments of minerals directly above the crater for half an hour to several days. The temperatures of this column higher than the surrounding atmosphere cause convection (b in the figure). The top of the eruptive column is formed where the density of the column equals the surroundings (c) and spreads horizontally. Low-density particles including volcanic ash and pumice are horizontally blown by the wind out of the regions of b and c and begin to fall when their speed decreases to the point of equilibrium between air resistance and gravity; ‘terminal speed’. Since smaller particles are carried farther away due to their lower terminal speed, they are subjected to classification while flying. The material deposited near the crater is referred to as fall pumice. The material 2 mm or less in size is referred to as volcanic fall ash. Both are uniform in size and contain little crystal minerals or lithic fragments. There can be a case where weathered materials subjected to hydration are included, but high purity volcanic glass can be sorted out by the cyclone and dust collector of the present device for air classification. Collapse of an eruptive column leads to a so-called pyroclastic flow. A large-scale flow is formed by gravitational collapse of an eruptive column, which is regarded as a phenomenon of a rapid outflow of unclassified pumice, volcanic ash, and rock fragments with volcanic gases as shown in figure 16. A theoretical calculation has shown that, when an eruptive column of 2 to 3 km in height collapses, the resulting pyroclastic flow runs over a distance of 20 to 30 km, traversing ridges with a relative elevation of 200 to 300 m. Coarse particles tend to be entrapped among fine particles due to the weak classifying action.

Though such ejecta, which is also referred to as tephra, is derived from magma, it also includes ‘accessory’ materials derived from the old volcanic body near the magma reservoir and conduit and ‘accidental’ materials, which are fragments of the basement rock. Their quantitative ratios vary depending on the scale and pattern of eruption and distance from the eruption source. After deposition, extraneous materials from the surrounding ground can be normally included during various stages of turning into soil. In view of the use as a SCM in the field of concrete, pyroclastic deposits resulting from explosive eruption of magma with a high SiO₂ content are advantageous from the aspect of the amount of resources, but they simultaneously

entail abundant impurities other than pozzolantically reactive volcanic glass.

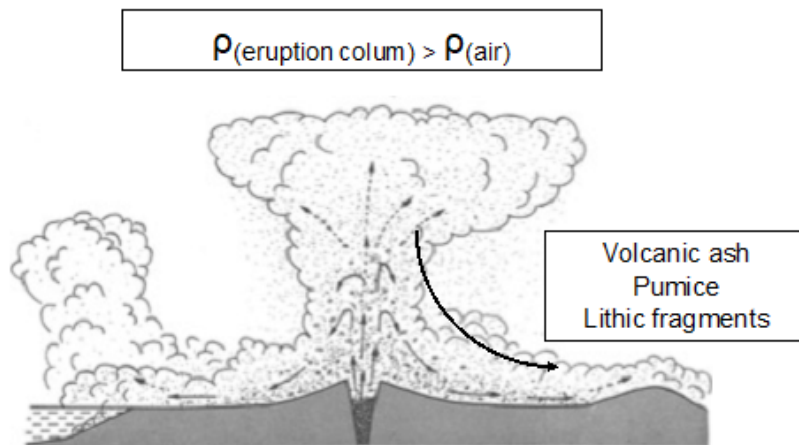


Figure 16: Diagram of Pyroclastic eruption

Ito-Shirasu presently under study is a large-scale pyroclastic flow sedimentation with an estimated reserve of 75 billion m³, but amorphous materials including pumice were reported to account for around 60%, while crystal minerals were approximately 40%. Also, the fine fraction of CF with a recovery ratio of 2% showed indications of weathering. According to the results of research into volcanic glass and other minerals contained in volcanic ejecta from Cascade Range in North America [17], the densities of pumice, glass shards, and lithic fragments were 0.7 to 1.2 g/cm³, 2.35 to 2.45 g/cm³, and 2.7 to 3.2 g/cm³, respectively. That of crystalline materials and crystal fragments was 2.6 to 5.2 g/cm³. Therefore, our findings from volcanic deposits in Japan that volcanic glass can be perfectly sorted out both with a density limit of 2.4 g/cm³ and with a diameter limit of around 5 μm can be applicable to volcanic ejecta from Cascade Range. Physical densities of particles should, even beyond national borders, fall in constant ranges when considering the mechanisms acting on volcanic ejecta -- eruption of volcanic glass onto the ground and rapid cooling thereafter, crystallization within the underground magma, rocks present on the ground, weathering after deposition, and so on. In that sense, this study provides a possibility to produce high performance SCMs in volcanic regions worldwide from volcanic ejecta, which have been regarded as a low performance material, by sorting out a high purity volcanic glass by the same method using an air table.

5. Acknowledgment

This research is supported by JSPS Grant-in-Aid for Scientific Research (A) with No. 18H03803 entitled “Carbon-minus Recyclable High-performance Concrete”.

6. Reference

- [1] K. L. Scrivener, R. J. Kirkpatrick, 2008, Innovation in use and research on cementitious material, Cement and Concrete Research, Vol.38, pp.128-136, <https://doi.org/10.1016/j.cemconres.2007.09.025>
- [2] R. D. Hooton, 2008, Bridging the gap between research and standard, Cement and Concrete Research, Vol.38, pp.247-258, <https://doi.org/10.1016/j.cemconres.2007.09.012>
- [3] J. S. Damtoft, J. Lukasik, D. Herfort, D. Sorrentino, E. M. Gartner, 2008, Sustainable development and climate change initiatives, Cement and Concrete Research, Vol.38, pp.115-127, <https://doi.org/10.1016/j.cemconres.2007.09.008>
- [4] R. Snellings, G. Mertens, J. Elsen, 2012, Supplementary Cementitious Materials, Reviews in Mineralogy and Geochemistry, Vol.74 (1), pp.211-278, <https://doi.org/10.2138/rmg.2012.74.6>

- [5] R. Snellings, 2016, Assessing, Understanding and Unlocking Supplementary Cementitious Materials, RILEM Technical Letters 1, pp.50-55, <https://doi.org/10.21809/rilemtechlett.2016.12>
- [6] P. K. Mehta, P. J. M. Monteiro, 2006, CONCRETE Microstructure, properties, and Materials third edition, McGraw-Hill Companies, pp.295-315
- [7] A. Tomoyose, T. Noguchi, K. Sodeyama, K. Higashi, 2018, Total utilization of pyroclastic flow deposits as construction materials through dry gravity classification and pulverization, Proceedings of the 8th International Concrete of Asian Concrete Federation, Vol.1, pp.475-481
- [8] A. Tomoyose, T. Noguchi, K. Sodeyama, K. Higashi, 2018, Utilization of volcanic ejecta as a high-performance supplementary cementitious material by dry gravity classification and pulverization, RILEM Technical Letters, Vol.3, pp.66-74, <https://doi.org/10.21809/rilemtechlett.2018.66>
- [9] K. Sodeyama, A. Tomoyose, T. Noguchi and K. Higashi, 2017, Total Utilization of Shirasu as Construction Materials through Dry Gravity Classification and Pulverization, Journal of the Society of Materials Science, Japan, Vol. 66, Issue 8, pp. 574-581, <https://doi.org/10.2472/jsms.66.574>
- [10] S. Iwao, 1985, Nendo no Jiten, Asakura Publishing Co. Ltd, ISBN 4254162286 (in Japanese)
- [11] H. Taniguchi, 1972, Studies on Si⁴⁺ ion, Al³⁺ ion and H₂O(+) in volcanic glasses by means of infrared absorption and other methods, the journal of the Japanese association of Mineralogists, Petrologists and economic geologists, Vol. 67, Issue 9, pp.291-300, <https://doi.org/10.2465/ganko1941.67.291> (in Japanese)
- [12] H. Tateyama, K. Kimura, K. Jinnai, K. Tsunematsu, 1982, Changes on bloating properties of volcanic glass by weathering, Journal of the clay society of Japan, Vol.22, Issue 1, pp.1-10, <https://doi.org/10.11362/jcssjendokagaku1961.22.1>(in Japanese)
- [13] K. S. W. Sing, D. H. Everett, R. A. W. Haul, L. Moscou, R. A. Pierotti, J. Rouquerol, T. Siemieniowska, 1985, Reporting physisorption data for gas/solid systems with special reference to the determination of surface area and porosity, Pure and applied chemistry, Vol.57, No.4, pp.603-619, <https://doi.org/10.1351/pac198557040603>
- [14] B. P. Ruxton, 1968, Measures of the degree of chemical weathering of rocks, the journal of geology, vol. 76, No. 5, pp.518-527, DOI: [10.1086/627357](https://doi.org/10.1086/627357)
- [15] T. Yamashita, T. Danhara, 1995, Problem in measuring refractive indices of younger tephra glass shards: effect of thin hydration layer, the geological society of Japan the 102nd annual meeting, p.112, https://doi.org/10.14863/geosocabst.1995.0_112_2 (in Japanese)
- [16] H. Tsukamoto, S. Mizutani, 1988, Clay Minerals in Weathering Process and Their Transformation, Journal of the Japan Society of Engineering Geology, Vol.29, Issue 3, pp.231-241, <https://doi.org/10.5110/jjseg.29.231> (in Japanese)
- [17] S. Shipley, A. M. Sama-Wojcicki, 1983, Maps Showing Distribution, Thickness, and Mass of Late Pleistocene and Holocene Tephra from Major Volcanoes in the Pacific Northwest of the United States; a Preliminary Assessment of Hazards from Volcanic Ejecta to Nuclear Reactors in the Pacific Northwest, USGS, MF-1435, <https://doi.org/10.3133/mf1435>
- [18] A. Ohta, T. Uomoto, 1999, A Study of the Dispersing Effects of Polycarboxylate-Based Dispersant on Fine Particles, Concrete research and technology, Vol.10, Issue 2, pp.131-140, https://doi.org/10.3151/crt1990.10.2_131

Early hydration of C₂S doped with combination of S and Li

M. Boháč¹, T. Staněk¹, A. Rybová¹, A. Zezulová¹, F. Bellmann², H.-M. Ludwig²

¹Physical Chemistry Dep., Research Institute for Building Materials, 62400 Brno, Czech Republic

²F.A. Finger-Institute of Building Materials Science, Bauhaus University Weimar, 99423 Weimar, Germany

Abstract

Production of low-energy cements would result in energy saving and lower CO₂ emissions related to reduced consumption of fuel and high-grade limestone as a raw material. Belite rich clinker, made more reactive by doping with combination of S and Li, could possibly be one of the low-energy alternatives for Portland cement clinker. Paper describes the preparation of doped belite and deals with its early hydration and reactivity. Belite rich clinkers were prepared in laboratory in high-temperature solid state synthesis. Pure substances were used for the preparation of raw meal and clinker. Early hydration heat flow development of cement pastes was monitored by isothermal calorimetry, changes in phase composition by “in-situ” X-ray diffraction and TGA/DTA and microstructure by SEM-SE. Heat flow exotherms were correlated with quantified phase composition at given time. Heat related to C₃S hydration measured by isothermal calorimetry is proportional to its content and the position of its peak and maximum changes with increased Li content. Doping of the C₂S by the S or the combination of S and Li significantly increases the reactivity of the C₂S-rich cement. The formation of C-S-H products is a continuous process that depends mainly on C₃S during first 6 hours and then is supported by slow reaction of β-C₂S. The reactivity of C₂S is affected by the timing of the hydration of other clinker phases. Two generations of portlandite formation detectable as a double endotherm on TGA/DTA can be attributed to hydration of C₃S and β-C₂S.

Keywords: belite clinker, S, Li, doping, early hydration

1. Introduction

The manufacture and use of concrete produce a wide range of environmental and social consequences. The cement industry is together with the energy production and transportation industries one of the three primary producers of carbon dioxide, a major greenhouse gas. The share of cement production in total anthropogenic CO₂ emissions has been rising steadily and is now estimated by some sources to be around 10% [1], or about 6% of the total anthropogenic greenhouse gases [2].

Although energy use and release of CO₂ are closely related in the usual cement manufacturing industry, it is the release of CO₂ to the atmosphere rather than the consumption of energy which is of chief concern. Decarbonation of limestone (CaCO₃) results in the release of CO₂ and, since natural limestone and chalk are the only large-scale sources of calcium available to the cement industry, this CO₂ release is only reducible by changing the chemical composition of the cement [3].

Clinker is the main constituent of the cement. The clinker is mixed with a few per cent of gypsum and finely ground to make the cement. The clinker typically has a composition in the region of 67% CaO, 22% SiO₂, 5% Al₂O₃, 3% Fe₂O₃ and 3% of other components, and normally contains four major phases,

called alite (C3S, Ca₃SiO₅), belite (C2S, Ca₂SiO₄), aluminate phase (C3A, Ca₃Al₂O₆) and ferrite phase (C4AF, Ca₂AlFeO₅). Several other phases, such as alkali sulfates and calcium oxide, are normally present in minor amounts [4].

Recently, there are four classes of alternative clinker system that deserve serious attention with respect to global reductions in concrete-related CO₂ emissions [5]; reactive belite-rich Portland cement clinkers (RBPC), belite-ye'elimite-ferrite clinkers, carbonatable calcium silicate clinkers, magnesium oxides derived from magnesium silicates.

RBPC belong to the same family as ordinary Portland cement (OPC) in terms of clinker mineralogy, i.e. they are in the C2S-C3S-C3A-C4AF system. The difference in clinker composition between RBPC and OPC lies mainly in the belite/alite ratio. For RBPC the belite content is more than 40 % and alite normally less than 35 %, making belite the most abundant phase in RBPC, as opposed to alite in OPC. The manufacture of RBPC therefore leads to lower specific energy consumption and CO₂ emissions, and also has the additional practical advantage of requiring less high-grade (low-silica) limestone as a raw material [5]. The ideal clinkering temperature for RBPC is usually close to 1350 °C, which is about 100 °C lower than the average for OPC, which can lead to somewhat lower kiln heat consumption and permit more use of low-grade kiln fuels.

Physical or chemical activation, e.g. rapid clinker cooling or minor element doping may be needed in some cases to make the belite sufficiently reactive. As an example, the use of 0.5–1.0% SO₃ in the raw meal combined with rapid clinker cooling can lead to the formation of reactive belite in the clinker. Staněk and Sulovský [6] reported the principle of activation during preparation of belite-rich clinkers with an increased Ca:Si ratio in the structure of dicalcium silicate and partial substitution of SiO₄⁴⁻ by SO₄²⁻. Activation was realized by the addition of sulfate ions, which in the structure of belite substitute SiO₄, caused an increased entry of Al₂O₃ into the belite and increased the CaO:SiO₂ in belite. The sulfur addition to the clinker also stabilized the hydraulically more active monoclinic alite M1 modification. The clinker for its preparation, contained only around 20 wt.% of alite, was burned at a temperature of 1350 °C and was activated by the addition of about 5% SO₃ (related to the bulk clinker weight). It contained a small proportion of anhydrite.

Specific kiln fuel requirements and CO₂ emissions of RBPC are typically about 10 % below those for OPC. Lower emissions of NO_x and SO_x are commonly observed when making RBPC, due mainly to the lower burning temperature. On the other hand, it requires about 5 % more electric power to grind RBPC to the same fineness as OPC, due to the greater hardness of belite relative to alite [5].

Pure C2S exhibits five polymorphic forms, depending on temperature and pressure during formation [7], all are metastable except the γ (orthorhombic) form. In Portland cement the equilibrium temperature between α (hexagonal) and α' is 1280 °C and the conversion reaches a maximum rate at 1100 °C. With decreasing cooling rate, the α' H (orthorhombic) phase tends to dominate, and finally the belite is composed entirely of this form, which transforms into β -C2S (monoclinic) after passing through the α' L (orthorhombic) form [8].

Belite is a major phase in active belite cements and is chiefly present in the α and α' modifications, stabilized either by rapid cooling in the temperature range 1300-900 °C [8], or by the use of higher alkali levels [9]. It has been suggested that the hydraulic activity of β -C2S is related to the calculated strength of the Ca-O ionic bond [10]. A study of the relationship between crystal structure and hydraulic activity, including synthetic β -C2S and samples separated from Portland cement, indicates that the electric field strength at the site of the Ca²⁺ ions in the crystal lattice determines the hydraulic activity [11].

Paper deals with reactive C₂S-rich clinkers doped with a combination of S and Li. Early hydration properties of cements prepared from the clinkers were monitored by isothermal calorimetry, XRD-in situ and inner standard method, DTA-DTG and SEM-SE. Paper brings comparison of reactivity and phase development during early hydration of S and Li doped belite clinkers and undoped belite clinker.

2. Methodology

2.1 Materials

Belite clinkers, prepared by high-temperature solid state synthesis, were doped with S and combination of S and 2 % or 4 % of Li in form of CaSO₄.2H₂O and LiCO₃. Pure compounds were used to prepare the clinkers. The composition of the raw meal constituents was calculated on the composition of belite. The raw meal composition and phase composition of burned clinkers are given in Table 1 and 2. Clinker tablets were prepared from raw meal which was homogenized for 2.5 hours. Clinkers were burned in Kanthal furnace at 1400 °C with 12 hours of soaking time. Thereafter, the clinkers were quickly cooled in the air when they were placed on a metal substrate after being removed from the furnace. For isothermal calorimetry, X-ray and DTA testing, clinkers were ground in a vibratory mill for 1 minute.

Table 1: Raw meal composition for clinker preparation

	C ₂ S	C ₂ S S	C ₂ S S 2Li	C ₂ S S 4Li
	wt. %			
CaCO ₃	75.41	74.98	72.34	69.70
SiO ₂	24.59	21.16	21.16	21.16
LiCO ₃	-	-	3.66	7.32
CaSO ₄ .2H ₂ O	-	3.86	3.86	3.86

2.2 Methods

The development of heat flow and total hydration heat was monitored by isothermal calorimetry (TAM Air – TA Instruments) on samples of cements prepared from synthesized clinkers. Calorimetric measurements were performed at 25 °C for 7 days on cement pastes with w/c = 0.4 when 5 grams of cement was used for individual test. Samples were stored under laboratory conditions at 25 °C for 24 hours prior to the experiment. Before inserting the ampoules pastes into the calorimeter, each cement sample was mixed with water and stirred at 2 rpm for 1 minute outside the calorimeter. The measurement itself started 1 minute after the addition of the mixing water.

The in-situ X-ray diffraction analysis was performed on Bruker D8 Advance apparatus with Cu anode ($\lambda K\alpha = 1.54184 \text{ \AA}$) and variable divergence slits at Θ - Θ reflection Bragg-Brentano para focusing geometry, scan range 7-50 2 Θ , scan step size 0.039°. Data were processed using EVA software. The duration of individual scans was approximately 20 minutes; duration of the whole experiment was 24 hours. The paste (w/c=0.4) was placed in a sample holder and covered with kapton foil to prevent carbonation. In case of C₂S S 2Li sample, the phase composition over time (0, 45, 90, 360, 720, and 2880 minutes) was monitored using the inner standard method. As a standard, 20 wt.% fluorite was used. After each time interval the hydration was stopped by isopropyl alcohol and acetone. The phase composition of burned clinkers was determined using Rietveld refinement. Since the inner standard method was used the amorphous content was not quantified.

The sample C₂S S 2Li was investigated by thermal analysis. The samples were prepared following the same procedure as for XRD. The hydration process of the paste was stopped by isopropyl alcohol and acetone after 45, 90, 360, 720 and 2880 min of hydration. Combined TGA/DTA data were obtained using STA 449 F3 Jupiter (by Netzsch). The samples were tested in Pt crucibles at a heating rate 10 °C/min, from 35 °C to 1000 °C. The sample atmosphere was synthetic air (50 ml/min, ratio N₂/O₂ was 80/20).

Development of microstructure at 45, 90, 360, 720, and 2880 minutes of hydration of the sample C₂S S 2Li was observed by scanning electron microscope ZEISS EVO LS10 in secondary electrons (SE). SE micrographs were taken at 100x, 500x, 1000x, 2000x and 5000x magnification, EHT 15 kV, WD 12 mm and I probe 80pA. Samples were sputtered with gold before SEM SE analyses.

Table 2: Phase composition of burned clinkers

	C ₂ S	C ₂ S S	C ₂ S S 2Li	C ₂ S S 4Li
	wt. %			
β-C ₂ S	27.1	42.5	80.7	82.5
γ-C ₂ S	72.7	27.3	1.0	1.1
C ₃ S	-	27.7	9.9	2.9
CaO free	0.2	2.5	7.7	10.0
anhydrite	-	-	0.7	3.5

3. Results and discussion

3.1 Isothermal calorimetry

Early hydration exothermic reactions were monitored by isothermal calorimetry during 7 days of hydration (Figure 1). Exothermic reactions are related to dissolution of amorphous and crystalline phases (Table 2), growth, nucleation and precipitation, complexation and adsorption processes. Main contributors of the evolved heat during hydration are portlandite - Ca(OH)₂ (CH) and C-S-H. These phases are hydration products of clinker phases C₃S and C₂S and CaO. Understanding the mechanism of cement hydration involve the study of the kinetics of individual mechanistic steps [12].

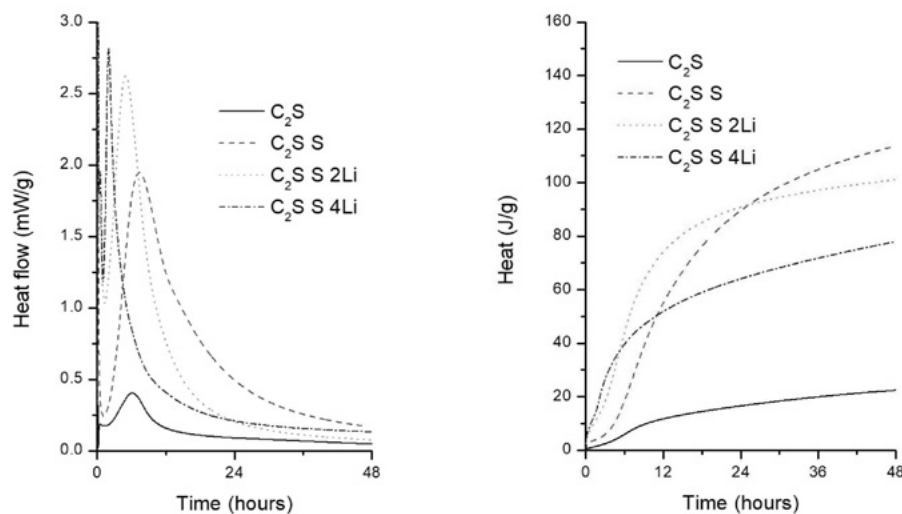


Figure 1: Heat flow and total heat development during 48 hours of hydration

When in contact with water, the initial reactions' exotherms include wetting and dissolution/dissociation of molecular units from the surface of a solid. Despite the fact that the measurement started after 1 min after water addition, the first exotherm is still controlled by CaO content in the sample. Total heat evolved in the time interval between 1st and 60th min of hydration is proportional to CaO content in the samples (Table 2): C₂S – 1.1 J/g, C₂S S – 3.4 J/g, C₂S S 2Li – 9.2 J/g, C₂S S 4Li – 11.4 J/g. The CaO reaction during initial period of hydration exhibits large signal overshadowing other reactions. Samples with Li contains also anhydrite which is also expected to react during the initial period of hydration. Despite considerably lower solubility of anhydrite comparing to gypsum, anhydrite still serves in the presence of alkali solvent as a retarder of the setting forming ettringite (AFt) during the initial reactions contributing to total heat.

Anhydrite in this belite rich system deserves further research since it plays an important role in terms of hydration mechanism and performance of hardened material in systems with OPC and CSA [13].

Period of slow reactions is followed by acceleration period which is characterized by the main peak related to hydration of C3S. Despite the fact that the heat related to C3S hydration is proportional to its content, the position of the peak and its maximum changes with increased Li content. With higher Li contents the temperature of the maximum increases and the position moves to earlier times. Total heat development during 7 days of hydration show that doping of the belite with the S and the combination of S and Li dramatically increases the reactivity of the resulting cement (Figure 1). The combination of S and Li accelerates the heat evolution during first days compared to doping with the S only.

C2S hydration is very slow and heat contribution is considerably lower. C2S reactions are represented by minute peaks in deceleration period where diffusion is the controlling process of hydration. In principle, it is claimed that both hydraulically highly active and nearly inactive forms may be possible for all belite modifications and the measured strength generation depends on the experimental conditions like burning temperature, cooling rate, foreign oxide content, etc. [14]. The reactivity of C2S is affected by the timing of the clinker phases hydration. Since the hydration of C2S take part mainly in deceleration period, the lack of water, space and smaller number of fine and more reactive particles are parameters affecting C2S hydration kinetics.

3.2 Phase analysis

From results of phase composition of burned clunkers, it can be stated that the enhancement of β -polymorph of dicalcium silicate is the criteria of doping with S and combination of S and Li. Vice versa the content of γ -polymorph of dicalcium silicate decreases with the doping (Table 2). C3S formation is significantly suppressed with increasing Li content. Recent study [15] clarifies this effect of Li by significant reduction in the temperature of the clinker melt formation and a decrease in its viscosity. Lithium causes a partial to complete decomposition of the alite into microcrystalline mixture of belite and free CaO depending on Li₂O content and cooling rate.

The phase composition was monitored by XRD hydration in situ during 24 hours of hydration. Sample C2S contains mainly γ -C2S with a small amount of β -C2S and a minimum of CH (CH peak is overlapped with peaks of C2S and a slight amorphous hump). In the course of 24 hours the phase composition does not change considerably. Sample C2S S contains β -C2S and γ -C2S, C3S and CH. Although the raw material composition was designed so that the resulting CaO : SiO₂ + SO₃ ratio would match belite, relatively high amount of C3S is probably caused due to release of a part of SO₃ during synthesis. At the beginning, amorphous hump and intensity of CH peaks are increasing. From 160 min on, there is no longer a hump and CH peaks are clearly visible and their intensities increase. After 800 min., there is no change. Sample C2S S 2Li contains β -C2S, C3S and CH. CH peaks appear right at the beginning and gradually increase their intensity reaching their maximum at around 360 min (Figure 2).

β -C2S intensities have a very slight decrease at the beginning, otherwise unchanging. C3S intensities also decrease from the start. Sample C2S S 4Li contains β -C2S, C3S, CH and anhydrite. At the beginning, a pronounced amorphous hump disappears around 200 min. From 200 min, anhydrite is visible and then its signal stays invariant. CH grows from 80 to 1200, then its intensities stay unchanged. Detailed XRD and DTA analyses were done on sample C2S S 2Li. Hydration of the sample was stopped after 0, 45, 90, 360, 720 and 2880 minutes. Phase composition including amorphous phase was determined. CaO reacts completely within first minutes of hydration, which is demonstrated as a large exothermic signal in isothermal experiments (Figure 1). C3S content decrease and increase of amorphous content and

CH content are in good correlation with the main calorimetric peak. β -C2S reacts very slowly showing continuous content decrease (Figure 3).

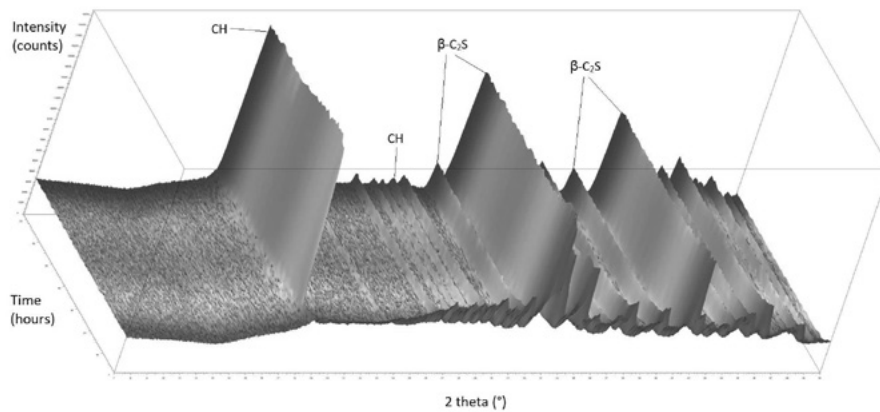


Figure 2: XRD, hydration in situ, sample C2S S 2Li, 24 hours

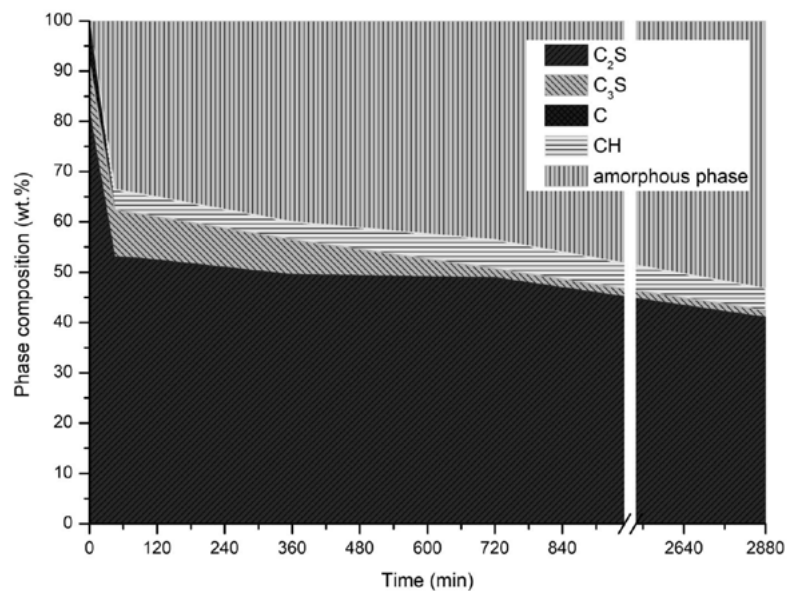


Figure 3: XRD, inner standard method, phase composition during 2 days of hydration, sample C2S S 2Li

Quantitative analysis of effluent fluids with calculation of phases for single processes was done by DTA-TGA on sample C2S S 2Li. The phase composition of the sample was determined after 45, 90, 360, 720 and 2880 minutes of hydration. Position and intensity of main endotherms were monitored at selected time intervals during hydration (Figure 3, Tables 3 and 4). Processes of H₂O release from C-S-H and AFt overlap each other. Taking in account recrystallization of AFt, continuous increase of C-S-H content can be seen on endotherm which changes its position from 76-127 °C during 48 hours of hydration. CH endotherm moves its minimum as the crystal size increases. From 720th minute on, double endotherm of CH is visible. This double endotherm can be explained as a second generation of CH, which might indicate the presence of another source. From the results of calorimetry and XRD, it is obvious that this source is β -C₂S which starts to react later than C₃S. Furthermore, the C₃S content stays the same after 720 minutes of hydration (Figure 3). Based on the intensities and positions of endotherms, it is likely that two generations of CH differing in crystal size are formed. Second generation, that is detectable from about 6 hours of hydration onwards, grows simultaneously with first generation.

Table 3: Quantification of effluent gases or phases* from thermographs (wt. %), sample C2S S 2Li

	45	90	360	720	2880
	min				
H ₂ O; C-S-H, AFt	0.21	0.18	0.47	1.22	1.72
H ₂ O; CH	1.5	1.56	1.36	1.84	2.07
CH*	6.17	6.42	5.59	7.57	8.51
CO ₂ ; calcite* (minor peak)	0.15	0.16	0.4	-	0.14
CO ₂ ; calcite* (larger peak)	0.71	0.41	1.07	1.19	1.47
CO ₂ ; calcite* (sum)	0.86	0.57	1.47	1.19	1.61
calcite*	1.96	1.30	3.34	2.71	3.66

Table 4: Position of endotherms (°C), sample C2S S 2Li

	45	90	360	720	2880
	min				
C-S-H, AFt	76	96	99	116	127
CH	443	441	451	441, 468	474, 489
calcite (main peak)	762	739	777	774	788

3.3 Microstructure

Development of the structure during hydration of C2S S 2Li cement paste was observed by SEM in secondary electrons. The microstructure after 45 min, 90 min, 360 min, 720 min and 2880 min is given in Figure 4. A study [16] that has discussed the microstructure of a similar system after 90 and 180 days of hydration revealed similar C-S-H fibrous structures, that was transformed into dense aggregates of globular morphology at later ages (180 days). The studied structure shows platy larger CH crystals with undergrowth of fine fibrous C-S-H after 45 min and 90 min of hydration and continuous recrystallization of CH and densification of C-S-H on the surface of the particles after 2880 min of hydration. Based on SEM-SE, it is not possible to distinguish C-S-H formed from C3S and C2S hydration, yet it is the goal of further microstructural studies. Nevertheless, the densification of C-S-H from 720 min on, taking into account the phase analyses, can be supported by C2S hydration.

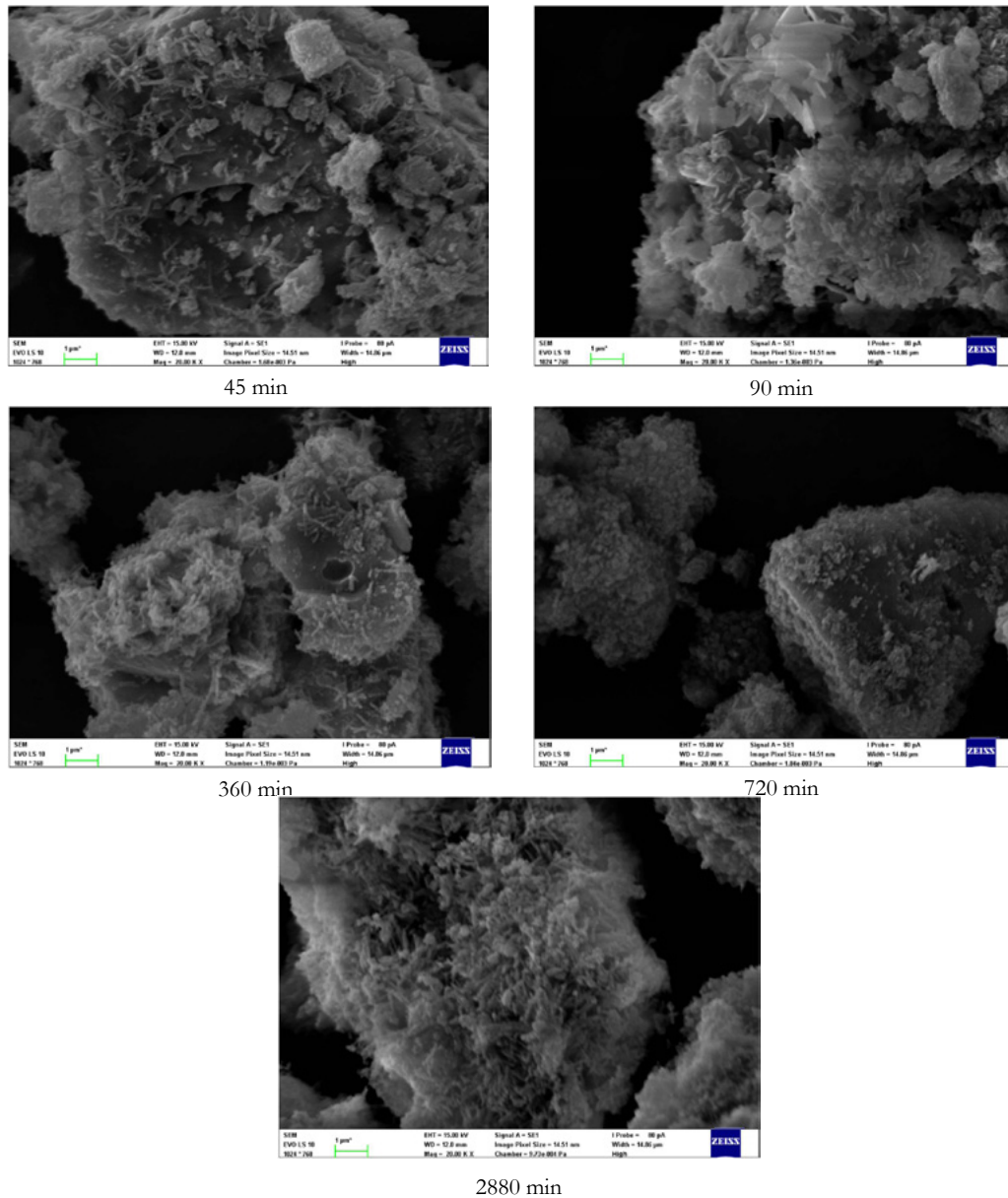


Figure 4: SEM micrographs of sample C2S S 2Li during 48 hours of hydration, 20000x.

4. Conclusions

Heat related to C3S hydration measured by isothermal calorimetry is proportional to its content and the position and maximum of heat flow peak changes with increased Li content. The reactivity of β -C2S is affected by the timing of the hydration of other clinker phases. Based on heat development, the formation of C-S-H products is a continuous process that relates mainly to C3S hydration during first 6 hours which is then supported also by slow reaction of β -C2S. Results of thermal analyses show the presence of double portlandite endotherm in DTA curves revealing two generations of portlandite attributed to C3S and C2S hydration. This finding is in agreement with changes in phase composition and position of exotherms determined by XRD-in situ and inner standard method, isothermal calorimetry and densification of C-S-H on the surface of the anhydrous particles studied by SEM.

5. Acknowledgment

Thanks are due to project No. 19-05762S financed by the Czech Science Foundation.

6. References

- [1] Boden, T, Andres, B, Marland, G 2016 Global CO₂ Emissions from Fossil-Fuel Burning, Cement Manufacture, and Gas Flaring: 1751–2013, Oak Ridge National Laboratory, Oak Ridge
- [2] IEA, WBCSD, Cement Technology Road-map 2009 Carbon Emissions Reductions up to 2050, OECD/IEA.; WBCSD, Paris.; Conches-Geneva, Switzerland, 2009
- [3] Lea, F M, & Hewlett, PC (2004). *Lea's chemistry of cement and concrete*. New York: Elsevier Butterworth-Heinmann.
- [4] Taylor, HFW. *Cement Chemistry*, 2nd Edition. Thomas Telford, London, 1997.
- [5] Gartner, E, Sui, T (2017). Alternative cement clinkers. *Cement and Concrete Research*, <http://dx.doi.org/10.1016/j.cemconres.2017.02.002>
- [6] Staněk, T, Sulovský, P (2015). Active low-energy belite cement. *Cement and Concrete Research* 68 203–210.
- [7] Hanic, F, Kamarad, J, Stracelsky, J, Kapralik, J (1987). The p-T diagram of Ca₂SiO₄. *British Ceramic Society Transactions and Journal* 86: 194-198.
- [8] Sahu, S (1994). Developments in low energy clinkers. *Ceramics-Silikáty* 38: 191-200.
- [9] Stark, J, Müller, A (1988). International development trends in low-energy cements. *Zement-Kalk-Gips* 41: 162-164.
- [10] Xiuji F, Xinmin M, Congxi T (1994). Study on the structure and characteristic of dicalcium silicate with quantum chemistry calculations. *Cement and Concrete Research* 24: 1311-1316.
- [11] Tsurumi, T, Hirano, Y, Kato, H, Kamiya, T, Daimon, M (1994). Crystal structure and hydration of belite. *Cement Technology (The American Ceramic Society)* 19-25.
- [12] Bullard, JW, Jennings, HM, Livingston, RA, Nonat, A, Scherer, GW, Schweitzer, JS, Scrivener, KL, Thomas, JJ (2011). Mechanism of cement hydration. *Cement and Concrete Research* 41: 1208–1223.
- [13] Pelletier, L, Winnefeld, F, Lothenbach, B (2010). The ternary system Portland cement–calcium sulphoaluminate clinker–anhydrite: Hydration mechanism and mortar properties. *Cement and Concrete Composites* 32: 497–507
- [14] von Lampe, F, Seydel, R (1989). On a new form of β-belite. *Cement and Concrete Research* 19: 509-18
- [15] Staněk, T, Rybová, S, Zezulová, A, Boháč, M (2019). Formation of clinker containing lithium. *Materials Science Forum* 955: 50-55
- [16] Goni, S, Guerrero, A (2007). SEM/EDX Characterization of the Hydration Products of Belite Cements from Class C Coal Fly Ash. *Journal of the American Society* 90, 12, 3915-3922

Safe Use of Sustainable Building Materials: A reappraisal of Adobe

T. Li Piani^{1,2,3}, J. Weerheijm^{1,2}, L. Koene³ and L. J. Sluys¹

¹ Technical University of Delft (TU Delft), Computational Mechanics, Civil Engineering Faculty, Delft, The Netherlands

²TNO, Defence, Safety and Security, The Hague, The Netherlands

³ Netherlands Defence Academy (NLDA), Den Helder, The Netherlands

Abstract

Adobe is a sustainable masonry made of sundried earthen bricks and mortar. A critical analysis of the normative bodies currently available for the material characterization of adobe is addressed in this paper. Guidelines, prescriptions and requirements related to test methods, materials selection and properties contained in the available building codes for adobe around the world are discussed in this study. The physical and mechanical properties of adobe presented in literature are addressed, with particular attention to the most recent scientific findings produced by the authors over the last five years of research. These have been assessed in several experimental campaigns as well as corresponding numerical simulations aimed at physically-mechanically characterizing the behaviour of various soil mixtures, adobe bricks and mortar under different environmental (humidity content and temperature) and loading conditions (in tension and compression) in the static and dynamic regimes. On the basis of these findings, some issues have been identified in relation to the knowledge currently condensed in the prescriptions, requirements and procedures of the available norms for the material characterization of adobe. A final series of guidelines is aimed at orienting future research on adobe as well as fostering the process of updating its current normative body. The importance of a normative update for adobe is cogent in relation to the need for a sustainable conversion of the current product and production processes inherent to building industry in order to satisfy requirements for safety and sustainability to structural design.

Keywords: adobe; material; properties; standardization; characterization.

1. Introduction

Goal number 11 of the UN urban agenda is concerned with making cities inclusive, safe, resilient and sustainable. The introduction of the concept of sustainability in the building construction industry is urgent because of its current impact on the increasing threats inherent to natural material scarcity and global pollution. Construction industry nowadays influences up to half of the total anthropogenic emissions of dioxin in the atmosphere and is responsible for more than one third of the total energy and water use. A relevant portion of these contributions regards only the material production phase [1]. Thus, sustainable alternatives to current building practices are cogent priorities and researches aimed at reducing the environmental impact of building materials while respecting performance requirements have been recently started around the world. For example, biological fibers have been recently tested as sustainable alternatives

to steel in reinforced concrete and natural binders or aggregates have been partially replacing Portland cement in concrete [2]. Alternatives to baking processes such as air drying procedures are studied for baked clay bricks [3]. Most of the aforementioned practices, despite being applied to new materials, are far from being new. In particular, they belong to the tradition of adobe. In adobe masonry, bricks are made of soil mixed with natural fibers locally available in the field. Mixtures are then cast in moulds and sundried without baking [4]. Fiber inclusion as well as air drying contribute to the eco-sustainability of adobe as a material. Adobe is fully disposable and recyclable. It causes almost null carbon footprint and ensures also higher acoustical and thermal performance than classical modern materials. Therefore, this material has recently gained renovated attention also in Europe within trends of sustainable architecture [5]. Unfortunately, the effects inherent to air drying and fiber inclusion as well as other sustainable practices tied to adobe tradition on its mechanical performance have not been addressed yet. In fact, use of adobe decayed in industrialized societies in favour of artificial building materials with higher performance and standardized production methods [6]. As a result, most of the adobe buildings in the world are currently not designed according to any standard. However, more than two billion people still live in earthen dwellings spread mainly in regions of developing countries involved into military operations or prone to severe earthquakes and building heritage of adobe can be encountered in Europe as well [7]. Thus, in the specific case of adobe, sustainability is intertwined with other global urgencies inherent to safety and housing affordability tasks [8]. As a result, a comprehensive characterization of earthen material is of paramount importance nowadays. Normative efforts for the material characterization of adobe have started about fifty years ago in different areas of the world. The first attempts to characterize earthen materials for constructions relate to standards in Germany [9], [10] and in New Zealand [11] and the most widely used reference nowadays according to literature studies is the Australian earth building handbook [12]. Other guidelines can be found in different areas of the world, including Mexico, Peru, California and Spain [13]–[15]. In codes for adobe, indications about material selection and characterization test requirements are often lacking, scarce or not consistent among the different guidelines. This occurs also because adobe is a site dependent material whose properties vary based on the local resources availability and building traditions, that prevented an uniform treatment of the subject. Nevertheless, it has been the lack of definite knowledge on the mechanical properties of earthen mixtures that mostly prevented a shared standardization process of adobe similarly to modern building materials. Comprehensive studies on the mineralogical, physical and mechanical properties of adobe are still rare in literature: if this is true in statics, literature production on the dynamic performance of adobe is almost null [16]. However, research efforts toward the mechanical characterization of adobe have been focusing in the last decades [17]–[19]. Over the last five years, research by the authors has been devoted to comprehensively studying the properties of adobe. Earthen bricks and mortar with different soil and fiber proportions have been physically as well as mechanically studied at different humidity contents [20]. In particular, the role of fibers and water content have been experimentally studied also in the dynamic regime, in ranges of strain rates which cover earthquakes and ballistic impacts [21]. These studies resulted in theories, analytical models and numerical frameworks developed to assess the material performance of adobe from statics to dynamics, including to address the effects of its mineralogical composition at a meso-scale on the material response [21]–[23]. In this paper, the resulting updated knowledge gained on its physical-mechanical performance serves as a critical normative review on the material characterization of adobe. Normative guidelines, prescriptions and requirements condensed in the heterogeneous normative production currently available around the world have been confronted against the recent physical evidences collected for adobe. In the following paragraphs, a review of characterization norms is presented into three subjects: soil selection, sample testing and material requirements. From the normative-experimental, analytical and numerical comparison, issues and knowledge gaps have been identified in some existing prescriptions, requirements and procedures currently available for the material characterization of adobe.

Therefore, final recommendations are meant to support the development of a normative framework/body for adobe as well as give a perspective on future research.-

2. Material Characterization of Adobe in three steps

Material standardization derives from a shared definition of soil selection, test methods and product performance. In the following paragraphs, a normative review is based on the analysis of these three main subjects.

2.1 Material Selection

Traditional adobe bricks result from mixtures of clay, silt, sand, water and air. In most cases, bricks' soil is mixed with natural fibers while mortar contains limited or no fiber amounts. Despite already back in the 90's scientific papers in literature recommended a proper characterization of the soil granulometry, plasticity and compaction properties of adobe with building purposes, importance on the selection and identification practices of soil mixtures for earthen building applications is still not reflected in current design codes [24]. All codes for adobe currently available agree in selecting soils with no organic content and avoiding soluble salts above 0.5-2% [11], [12], [14]. Thus, top soil shall not be used. Potable water is recommended for mixing soil. Granulometry ranges are the most common recommendation contained in current building codes for adobe as indications of the cohesion properties of the final product [12], [14]. Guidelines mainly focus on the quantitative evaluation of clay amount in the mixture. In fact clay is the binder for the cohesionless granular fraction of the soil and is responsible for providing strength to the dried material [20], [25]. All codes agree that a minimum of 10% by weight of clay should be present in the mixture [12]. However, recommended ranges vary also significantly around the different normative bodies, including in experimental characterization campaigns found in literature [20]. As a result, maximum recommended clay percentage and foremost relative proportions with the larger size aggregates are still not defined neither agreed [4], [12]. For instance, maximum aggregate size recommended can range between 5 mm to 25mm [12]–[14]. This uncertainty happens because the adopted mixture is dependent on local availability of raw resources and an optimal clay amount is also determined by its mineralogical family and mutual proportions with the larger particles of the soil mixture. Expansive clay such as smectite or montmorillonite are highly cohesive but also cause shrinkage cracks in the resulting adobe bricks [25]. In this regards the use of expansive soil (i.e. “black earth”) is sometimes discouraged in codes [11], but studies in literature reveal that an optimum balance between expandable and non expandable soil is possible and desired to ensure adequate strength to the brick [26]. Permitted ranges of soil components in the different codes are resumed in Figure 1. As a result of the possible combinations available in literature, consistency in the normative assessment of the optimal ranges of soil particles for earthen building purposes is lacking. The (loose) ranges contained in the Australian standard include the best quantitative soil mixture compositions for building purposes identified by the authors for adobe in [20] from a literature survey. Besides availability of raw materials, quantity of clay as well as other soil elements and including mixing water depend on a vernacular building practice typical for adobe. It consists of mixing soil with natural fibers. This practice is tied to earthen architecture and dates back to ancient Egypt [6]. It takes roots in the need for limiting shrinkage cracks naturally forming in the brick during curing process under sun [19]. In fact, fibers ensure better drainage systems [27]. Recommended materials are e.g. rice, barley, maize, wheat and including animal hair. Obviously, inclusion of fibers necessarily influences the initial mineralogical composition and the mixing water content and has an impact also on the physical-mechanical behaviour of the final product. However, despite a consolidated practice, the assessment of the mixture properties after fiber inclusion is currently not regulated by characterization standards for adobe. Instead, judgment of its opportunity in soil mixtures in codes is deputized again to the user and regulated only by not defined limits of not “*excessive use*” [12].

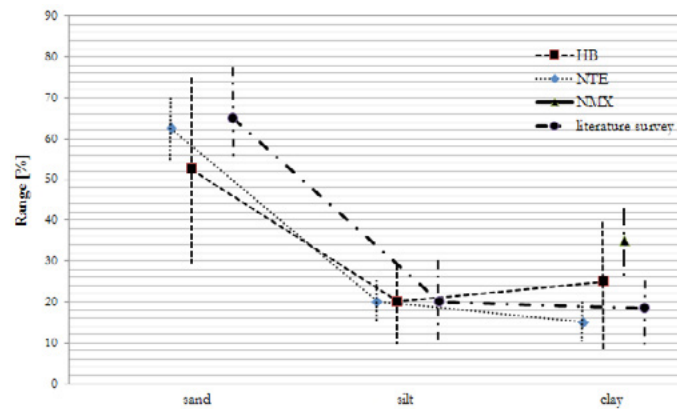


Figure 1: Granulometry ranges for soil mixtures of adobe for building purposes according to Australian (HB), Peru (NTE) and New Mexico (NMX) codes compared with the results of a survey by the authors from literature.

Actually, fiber inclusion in adobe guidelines is often considered as a stabilization technique of otherwise unsuitable soil compositions and suggested as an alternative to the introduction of cementitious bituminous binders recommended for highly clayey soils [11]–[13]. In this regard, fibers are suggested to improve the mechanical properties in hardness and strength, especially in tension [11]. The current interpretation on the role of fibers in many building codes for adobe is instead in contradiction with the main experimental trends recently observed for fibrous adobe in the field [20], [21].

The most common effect described in literature when adding natural fibers to soil mixtures is a decay of the initial mechanical properties of the resulting brick, namely strength and elastic modulus [19], [20]. This is valid both for flexure and compression and at different loading rates in the static and dynamic regimes [21]. According to [20], higher amounts of clay were needed to partially recover the initial brick strength of a given soil mixture, if mixed with fibers, at the expenses of cracking problems after curing due to large clay amounts (Figure 2). These effects on the mechanical performance of adobe have been interpreted by the authors as the consequence of a loss of cohesion in the meso-structure of the soil mixture after fibers insertion. Particles can be separated by fibers and interaction between clay floccules to bind the cohesion less fraction of the mixture is less effective [21]. This particularly happens for fiber amounts above 10% b.w. However, also cases in which fibers strengthen the soil mixture can be encountered in literature [28], [29]. This happens because cohesion of the brick’s macro-structure results from the mineralogical properties and relative proportions of the soil and by the material, quality and quantity of the added fibers, including their mutual interactions with clay binders at the meso-scale. This interpretation suggests that an optimum mixture of fiber and soil elements capable of reducing shrinkage and enhancing the mechanical performance exists. However, only a few codes currently prescribe cohesion tests for characterization purposes and they all require them to be performed only on the soil before fiber mixing [12]. Laboratory tests are recommended only in very few standard [9], [12]. In most of the cases, they imply the evaluation of Atterberg limits but only few quantitative indications are found, despite in broad ranges (16-30 for the plastic index and 30-50 for the liquid index) [12]. Quantitative evaluations inherent to soil plasticity as indication of soil consistency (without fibers) in standard are instead more commonly related to simple in field tests such as the Ribbon test, with an acceptance rate of 60-120mm for the broken pieces [12].

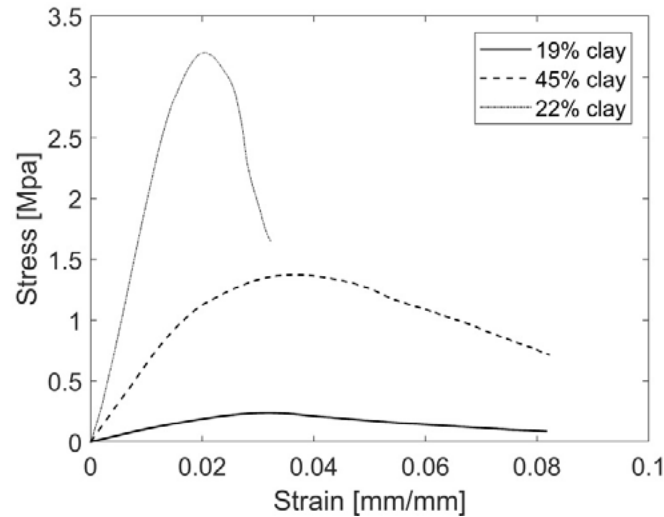


Figure 2: Experimental stress-strain curves of two adobe bricks containing about the same fiber content ($\cong 30\%$ b.w.) and different percentages in clay ($\cong 20\%$ and $\cong 45\%$) and one brick containing only clay (22%) tested statically (rate of 1mm/min) in compression at laboratory conditions [20].

2.2 Material Testing

As emerged in the material selection phase, test methods and requirements inherent to the characterization of adobe components are not comprehensively neither consistently registered among the available codes [9]-[15]. A representative list of characterization tests required according to three different normative bodies on adobe is provided in Table 1. In adobe building codes, in-field tests are still considered as acceptable alternatives to more rigorous laboratory test methods. In-field tests are recommended provided the presence of the persons responsible for final construction, despite most of earthen dwellings in the world are still designed and fabricated by owners themselves, often without the necessary specialist technical competences [30]. Also the level of sophistication of the testing procedures and requirements rely on the user judgement on the importance of the building project [11]. Some characterization tests in codes are even fully sensorial, such as the smell test to verify the presence of organic matter in soil mixtures [12]. The most widely used test to determine the grading of a soil mixture is the sedimentation bottle test, in which the shaking of a jar containing loose soil is aimed at ascertaining approximate fine and sand particles [12]. Instead, sieving and hydrometer tests are strictly recommended only in few norms [9]. In 2017, granulometry tests were performed by the authors using the BS 1377-2 norm for classification methods on soils for civil engineering purposes (Figure 3a-b) [31]. In fact, this code also includes the preliminary treatment of soil mixtures with natural fibers. Tests were performed starting from cured bricks of several mineralogical compositions.

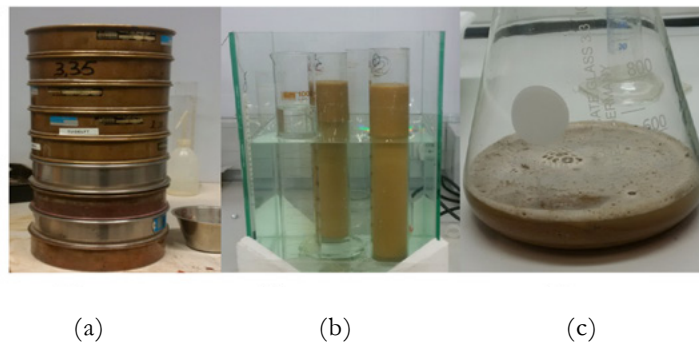


Figure 3: Sieving (a) and hydrometer (b) test, with preliminary chemical treatment of fibers (c) in [20]

This implied the preliminary desegregation of the product into its original soil mixture. Later, organic

content was excluded using mechanical and chemical treatments (Figure 3c). Dissolution was accomplished using hydrogen peroxide. In case of soil mixed with significant amounts and large sized fibers, this process required more cycles of chemical treatment.

Also the mechanical characterization of adobe is not solely prescribed according to laboratory standards but in-field compressive and flexural tests are often possible and still preferred [11]–[14]. However, mechanical properties can be rigorously derived from the standard commonly used for modern materials such as concrete. Compression tests on adobe samples were performed in [20] using UNI EN 772-1 for modern masonry materials [32]. Required levels of plane parallelisms for testing purposes were achieved using mechanical rectification procedures which did not cause visible damage and achieved precisions included in standard tolerance (Figure 4 a-b). The interposition of layers of materials of significantly different properties like cement mortar is not recommended for plane parallelism purposes for adobe.



Figure 4: Sanding paper (a) and machine (b) used for rectification purposes and wooden strip interposition between steel rolls in a three point bending test (c) [20], [21]

Static three point bending tests were performed by the authors according to UNI EN 12390-5 [33]. In this case, no indentation occurred when wooden stripes between adobe surfaces and steel rolls were interposed (Figure 4c). Literature studies and norms for adobe indicate that applied deformation rates above 5 mm/min may be not adequate for testing soft earthen materials. This limit is generally respected in literature studies and suggested by the authors. Displacement controlled tests at velocities of 1-2 mm/min are suggested especially for soft adobe tested in compression and tension [20]. Higher values are discouraged also because the mechanical properties of adobe have been recently found to be sensitive to the applied loading rate [21].

Table 1: List of main tests required for the characterization of adobe components according to the Australian (HB), New Zealand (NZS) and Mexico (NMX) codes, distinguishing in-field test (*in italic*) from laboratory tests and denoting with * tests without quantitative requirement limits

Property	HB	NZS	NMX
Grading	Bottle test		
	Sieving/sedimentation	*	*
Organic content	Smell test*	*	*
Plasticity	Casagrande test		
	Ribbon test	*	*
	Touch test		
Durability&Erosion	Water retention test*	Wet/dry test*	
	Water absorption test*	Spray test*	Water retention test*
	Spray test*		
Shrinkage	Box test	Box test*	*
Density	Oven drying*		*
Compression	Uniaxial test	Uniaxial test	Uniaxial test
	Drop test	Drop test	
Tension	Bending test		
	Flexure test	Flexure test*	Flexure test*

If methods of investigation are uncertain, material performance requirements in codes are controversial

as well. As shown in Table 1, prescribed values for important physical and mechanical properties are often lacking or incomplete. Not strictly quantitative recommendations that rely on the arbitrary judgment of the user according to the specific need and destination of the product are often encountered in codes for the assessment of many parameters [11], [12]. This is the case for instance for the smell or the wet/dry in-field tests. When not lacking, test limits are often not uniform among different sources. Most of the quantitative requirements normed in codes for adobe nowadays focus on the assessment of minimum strength values in compression and tension. However, there is often no agreement about the minimum required performance and the assessment of other important mechanical parameters for masonry design is missing.

2.3 Material Performance

2.3.1 Physical Properties

Mixtures of adobe are casted in moulds and dried under the sun for a minimum of 28 days in an exterior environment before testing [11], [12]. Both literature references and current standard for adobe recommend to protect bricks from wind and rain during drying [11]. It is known that natural fibers explicate their role during this phase. They fasten this process facilitating draining through cavities and prevent the formation of severe shrinkage cracks [34]. Shrinkage is abundant during drying of earthen materials and is allowed also according to codes, provided that shrinkage cracks do not jeopardize the material properties of the product [11], [13]. Caution is recommended in [11] if short fine cracks spread randomly at the surface of the brick are observed. In [12], it is preferred to exclude products with crack lengths above 7 cm. Only [10] recommends quantitative limits of 2% for the property of linear shrinkage. Shrinkage cracks represent a significant issue especially in case of high amounts of expandable clays in soil mixtures or in absence of fibers. Therefore, it can represent a threat especially for mud mortar. Characterization of mud mortar receives very little attention in codes and it is treated only in [9], [11]. Despite its importance on the overall performance of adobe walls is recognized in literature, physical tests on mortar are usually prescribed only if different soil materials than for the bricks is used. This implies neglecting the influence of fibers during production of material and life cycle of the structure. Different shrinkage rates between bricks and mortar can be responsible for initial loss of adherence and de-cohesion issues which may soon affect structural integrity. Unfortunately, also scientific studies on the material characterization of adobe mortar are lacking and only two references concerning the physical mechanical assessment of mud mortar have been found in literature [20], [35]. In [20] physical tests for the determination of density and moisture content were performed on various types of bricks and mortar for the same curing conditions. They confirmed that mortar is denser and characterized by higher shrinkage rates than fibrous bricks (Figure 5).



Figure 5: Picture of mortar just casted(a) and after five days since pouring(b): volumetric shrinkage of about 18%[22]

Even if the same soil is used for bricks and mortar, also the corresponding values for the property of density are different after 28 days of curing. Density in adobe is significantly influenced by fiber addition and its inclusion in the mixture significantly reduces the density of the resulting brick. This is a common trend observed in literature and quantified in [21]. Density was determined on two types of bricks with the same mineralogical composition but with only one mixed with 18%b.w. of fibers. Tests showed that average

density of the fibrous samples was more than 30% lower than the fiber free homologous bricks. As a result of different compositions, density values among different bricks also greatly vary in literature. They usually range between 800 kg/m³ for fibrous mixtures to 1800 kg/m³ for clayey bricks [20], [21]. This range is close to the one recommended in standards for adobe (1200 kg/m³ – 2000 kg/m³) [12]. Tested mortar in [20] showed a density of 1400 kg/m³ whereas the one in [35] was almost 2000 kg/m³.

In codes, durability performance of cured adobe is addressed mainly using in-field tests. The most common property evaluated (without specific restrictions) is erosion against water simulating raining conditions or dry/wet cycles to which adobe walls may be exposed to during its life cycle [11]-[12]. Instead, the assessment of the moisture content at 28 days of drying before wall fabrication is not required by codes. It is generally assumed that water content after curing is lower than 4% [11]. This is not always the case and actually depends on the internal composition of the product. This was inferred in [20] during an experimental campaign aimed at testing the mechanical performance of bricks and mortar made with different clay and fiber percentages. Bricks mixed with 30%b.w. of fiber and containing 45%b.w. of clay contained more than 6% of water after 28 days of curing, whereas the same fiber amount in a mixture with half of the clay almost halved its initial moisture level for the same environmental conditions (Figure 6). This suggests that 28 days are not always sufficient to ensure a fully dried product. Furthermore, presence of fibers in the mixture has been found to have a relatively minor influence on the final level of water content at cured conditions of bricks [21], [23], [36]. In particular, for certain amount of fibers, it is found that water content increases significantly with the increment of the clay proportion in the mixture. This is interpreted as a consequence of the fact that the areas of the mixtures surrounding fibers are fully dried after 28 days. Thus, the final water content depend on the spatial distribution of the fibers in the mixture, with particular concern to concentrations of clay. In fact, water can still be retained by floccules of clay due to its affinity toward water: it swells in its presence and it shrinks in its absence [25].

Finally, the eco-efficiency of the material in terms of physical properties such as thermal resistance are not contemplated by codes, with the exception of [12] where a typical range of the expected performance is included between 0.25-0.6 m²K/W.

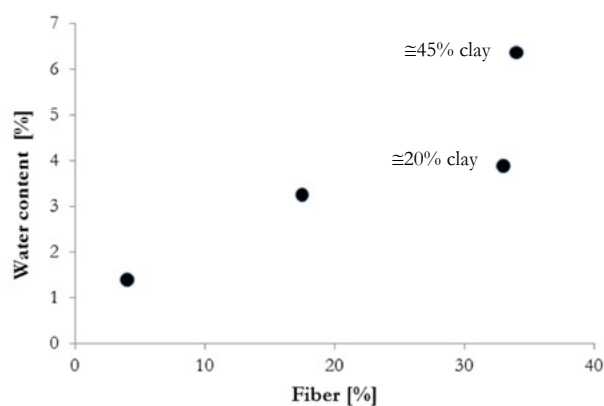


Figure 6: Water content at 28 days of curing for four different adobe bricks as a function of the mixing fibers: focus on the moisture content for two bricks with similar amount of fiber but different clay percentages [20].

2.3.2 Mechanical Properties in Compression

For adobe, assessing the interstitial water content of earthen components prior to construction is of paramount importance. Not only it is already known that water affects the durability performance of the structure due to erosion phenomena during the life cycle of the structure [4] but it also directly influences the nominal strength of the bricks and mortar and thus of the overall walls. Guidelines consider adobe

bricks as fully dried after 28 days of curing, when the water content is expected to be lower than 4% [11]. However, also water levels below 2% are sufficient to determine a significant decrement in the parameters in strength, whereas a minor influence is exerted in deformation. This has been experimentally found testing different types of adobe bricks at different induced moisture levels (including oven drying the samples) [20], [21]. Tests revealed an increment in strength for progressively lower water contents in the bricks. This trend has been observed for all the tests performed, both in static and dynamic regimes and also when mixtures contain fibers (Figure 7).

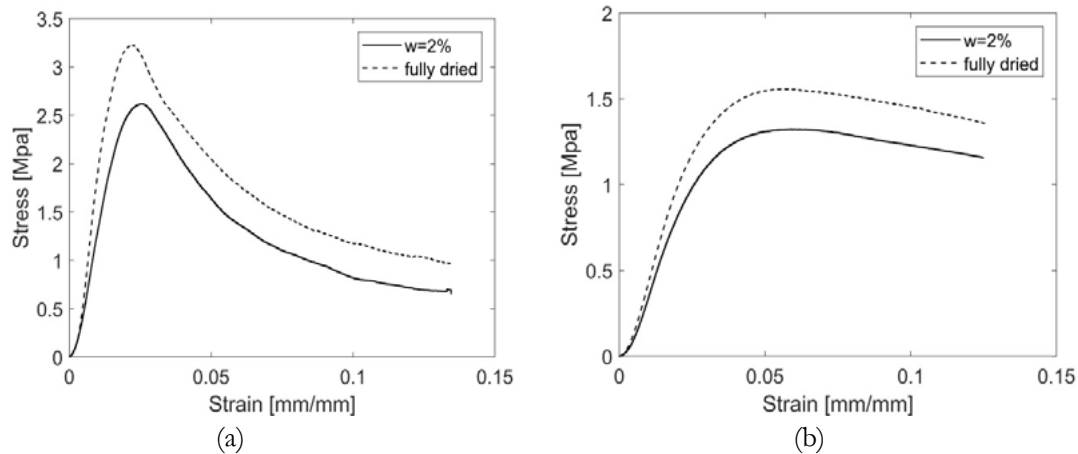


Figure 7: Stress-Strain curves in compression for fiber free adobe bricks (a) and fibrous bricks (b) air dried at laboratory conditions ($w \cong 2\%$) and dried in the oven (reduction of about 20% in strength)[21]

However, the rate of decay of the strength of adobe due to interstitial water has been quantified in [20] as a function of the mineralogical composition of the mixture. By testing samples with different clay and fibers at certain drying conditions, it was revealed that the mineralogical composition of adobe can accelerate or decrease the loss of the mechanical property. In particular, statistical regression of experimental data on adobe resulted in the law of eq.1 for the prediction of strength at a given humidity as a function of its internal composition, namely fiber, clay and water contents [16]:

$$f_b \sim \frac{\text{clay}}{\text{fiber}} w^{-\frac{\text{clay}}{\text{fiber}}} \tag{1}$$

Where w stands for water and all variables are expressed in volumetric percentages. Examples of these laws are shown in Figure 8 for one type of brick and mortar experimentally tested. The shape of the law in eq. 1 recalls the trend previously derived for baked clay bricks in [3], where the rate of decay increased for higher clay contents. As expected from the formulation in eq.1, the rate of strength decay experimentally derived for adobe mortar (with low or no fiber content) is in general higher than for adobe bricks and it is found to be similar to one of the slopes determined in [3] for only clay bricks.

The mechanical testing procedures and prescribed values in compression of the brick after curing are covered the best by current standards. Table 2 summarises the quantitative requirements in strength prescribed by four different codes for adobe. Recommendations in the different sources are not fully consistent in the prescribed test setup as well as in the required performance levels. However, the minimum values for strength prescribed by codes after aspect ratio correction are in average consistent with the values usually found for adobe bricks and mortar in literature, although lower values than prescribed requirements can also be encountered in the field [6]. Figure 9a shows the nominal strength distribution for adobe after elaboration of a database collecting more than 150 static characterization tests in literature supplemented with authors data [20]. Most common values for adobe range between 0.8MPa and 2MPa. The average

value of strength is found to be about 1.28 MPa, with 0.95 percentile of about 0.29 MPa.

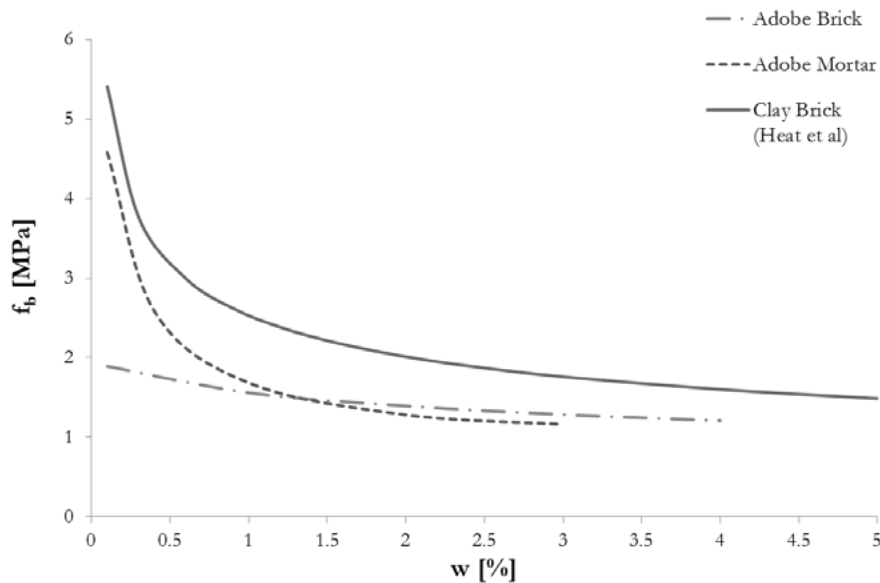
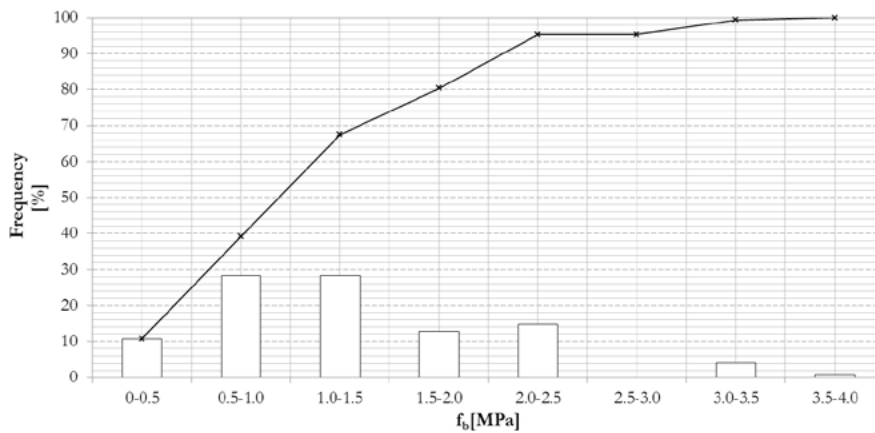


Figure 8: Compressive strength law for adobe dependent on water content. Examples of predicted trends for one type of adobe brick and one type of adobe mortar using eq.1, compared with law derived in [3] for clay bricks

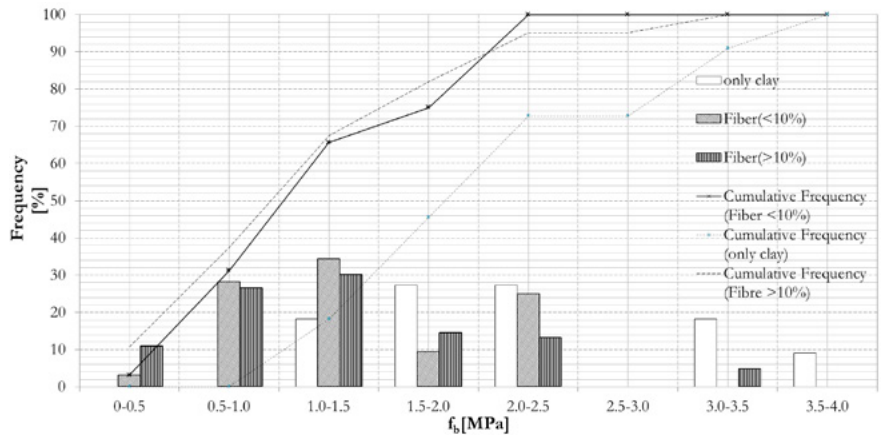
On the other hand, in almost 40% of the test cases, strength of adobe bricks was lower than 1 MPa. The unconfined values of strength are usually determined in literature using the aspect correlation factors commonly prescribed for concrete [37]. Instead, codes in [12] and [11] prescribe a more conservative law for adobe and recommend slenderness's of 3-5 as representative of the unconfined strength (Figure 10). Applying this law to the available tests in the database, the average strength is equal to 1.19 MPa, with 0.95 fractile of about 0.2 MPa.

Table 2: Prescribed strengths (and additional indications) for four building codes on adobe

Standard	Requirement	Indication
NZS	Minimum > 0.9 MPa	after aspect ratio correction (Figure 10)
NTE	80% fractile > 0.85 Mpa	after aspect ratio correction
NMX	Average > 2 MPa	on flat direction/no geometry info
HB	Average > 1 MPa	after aspect ratio correction (Figure 10)



(a)



(b)

Figure 9: Relative frequency (histogram) and cumulative frequency (line) for the unconfined strength of adobe in literature (including data from authors) considering all data (a) or disaggregating data according to fiber ratios in the mixtures (b)

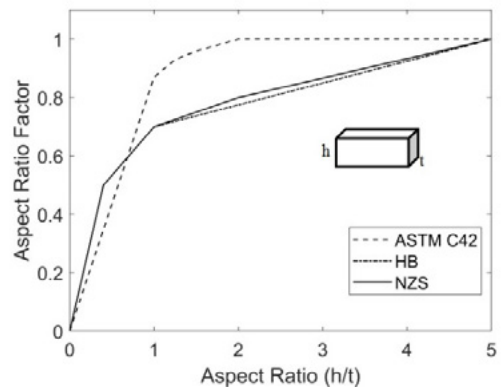
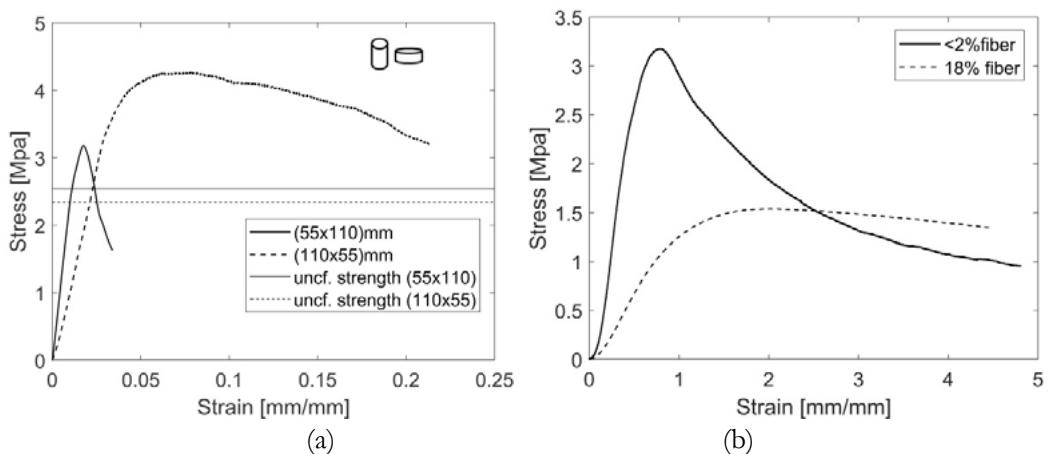


Figure 10: Aspect ratio correction law in strength for concrete compared with the laws proposed in the Australian and New Zealand code for adobe

Despite the specific shape of the curves in Figure 9, there are almost no systematic studies publicly available in literature on the size and shape dependencies of adobe [38]. Preliminary size dependence studies by the authors reveal a significant sensitivity to sample dimensions in the response in strength and deformation (Figure 11a). However, derived values for nominal strength are consistent with the aspect ratio laws depicted for adobe in Figure 10.



(a)

(b)

Figure 11: Stress - strain curves and unconfined strength values after aspect ratio correction in HB (Figure 10) for two adobe cylinders with same soil and fiber compositions but different slenderness

(a) or with the same geometry but different fiber percentages (b) tested in uniaxial compression at laboratory conditions in [21]

As for shape dependence, in [38] a correlation between tests on cylinders and cubes was found with a slope of 0.94. Furthermore, aside the role of water content, the mechanical characterization of adobe in standards does not address the influence of fiber content on strength, despite that most common trends in literature relate fiber in soil mixtures to a decay of the mechanical parameters of the material (Par. 2.1). However, recognizing this role is not always easy in literature. In Figure 9b, the same data plotted in Figure 9a are disaggregated according to the relative presence of fibers in the mixture, organized in three categories: fiber free (<2 b.w.%), low fiber ratio (<10%b.w) and high fiber ratios (>10 % b.w). From Figure 9b, fiber free samples do not possess strength values lower than 1 MPa, whereas fibrous bricks have a significant statistical incidence in the 0.5-1MPa and 1.0-1.5 MPa ranges. However, fibers can confer to the brick also values of strength above 3MPa. As explained in Par. 2.1. the outcome of fiber inclusion depends also on the specific characteristics of the applied soil. However, there are only few systematic studies aimed at quantitatively addressing the role of fibers in adobe bricks [39]. Tests by the authors [21] showed that parameters in strength and stiffness are significantly affected by fibers whereas their inclusion is always accompanied by an enhanced ductility and retarded failure (Figure 11b). The major contribution associated to the presence of fibres in the mixture on the mechanical performance of adobe is indeed related to the material ductility. Fibers allow the bridging of the stress through cracks, limiting their entity and holding together the vital cores of the matrix until large deformation stages.

Indications on the elastic stiffness of adobe bricks are not provided in standards. Data in literature reveal a significant scatter in values, with ranges between 10 MPa and 2500 MPa. However, most common values lie between 50 MPa and 200 MPa (Figure 12). The only reference to this parameter in standards relates to the stiffness of the adobe wall, which should be designed as 300 times the corresponding strength in [11]. Calculating E as a ratio of the strength reduces the scatter in value associated to stiffness, since strength and stiffness are found to react in a similar manner to clay, fiber and water contents in the mixture [21]. However the recommended value in standards is lower than the ratios commonly encountered for adobe bricks. Considering only data set in [20], $E=60-80f_b$, whereas considering data in literature $E=120-180f_b$ [40].

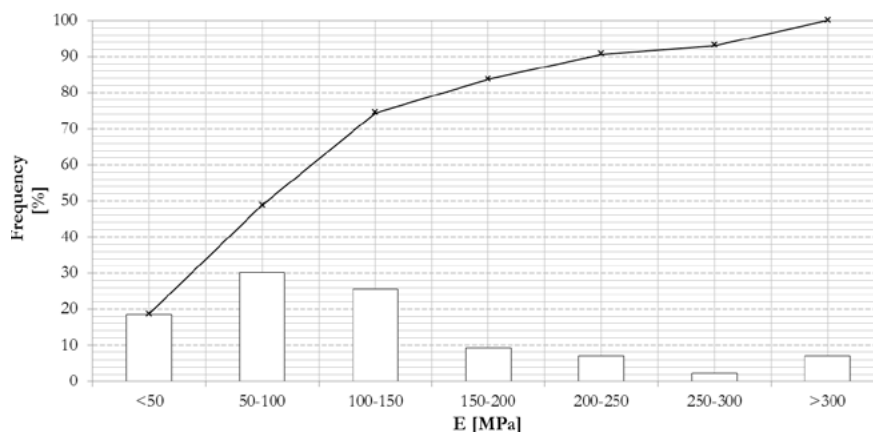


Figure 12: Relative frequency (histogram) and cumulative frequency (line) of the elastic stiffness of adobe

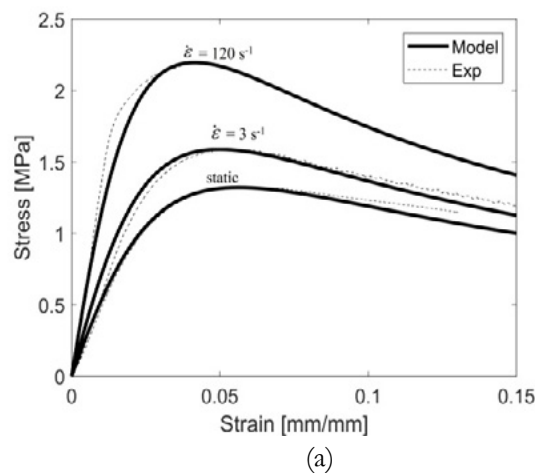
Besides the assessment of the mechanical parameters in compression, the definition of the entire curve in compression is of paramount importance for masonry materials. In fact, deformation curves can be used to develop constitutive models for non linear analyses [41]. Research has revealed that constitutive models originally developed for concrete can be used to address the curve of response of bricks and mortar of

adobe. In [21] a constitutive model has been developed to assess the stress-strain plots of adobe bricks made of different mineralogical composition and water content and subjected to various loading rates, from statics to dynamic impact (Figure 13a). The law recalled in eq. 2 takes roots from the Popovics' model developed for cement geo-pastes in statics [42]. It properly addresses the typical non linearity observed in the curves of response of adobe in compression, characterized by micro-cracking processes starting in the pre-peak phase of the curve and in the final quasi-brittle softening behaviour [18], [43]. Parameter n in eq. 2 controls the amount of non linearity in the uniaxial response and calibration with experimental data in [17] makes the parameter a function of fiber content (n ranges between about 1.5 and 3.5 in adobe and decreases with increasing fiber amounts). Furthermore, the model in eq. 2 modifies the original formulation in [42] implementing rate dependent functions of logarithmic shape $f(\text{DIF})$ for the uniaxial assessment of adobe in dynamics [21] (Figure 13b).

$$\sigma = f(\text{DIF}) E \left(\frac{n}{n-1 + \left(\frac{\dot{\epsilon} f(\text{DIF}) E}{\text{DIF} \dot{\epsilon}_0} \right)^n} \right) \epsilon \tag{2}$$

In fact, the response of adobe at high strain rate loadings has been recently experimentally assessed [21]. Strain rates in the order of 120 s^{-1} were achieved using Hopkinson bar tests. Tests revealed that adobe is a material sensitive to the deformation rate. The dynamic increase factor of the mechanical property of strength for adobe lies in the lower boundary of the cloud of data usually associated to concrete (Figure 13b) [44]. From the same Figure it is shown that if soil mixtures are provided with fibers, rate sensitivity of adobe decays. This is consistent with interpreting a reduction of cohesion after fiber inclusion. Instead water content in the mixture enhances sensitivity to the deformation rate for a physical principle of viscosity called Stefan effect (Figure 13b) [21].

The scarcity of constitutive models describing the non linear response in compression up to failure for adobe is reflected in the lack of numerical models for the material simulation of bricks and mortar [45]. Constitutive models as in eq. 2 can be implemented in numerical frameworks, together with the definition of damage or plasticity surfaces. In [22], a smoothed Mohr Coloumb damage surface implemented in a finite element isotropic damage model with exponential softening damage evolution laws was suitable for interpreting the damage process of soil based masonry materials loaded in compression. This constitutive law has been validated against a wide range of loading conditions, including impact penetration tests on adobe walls [23].



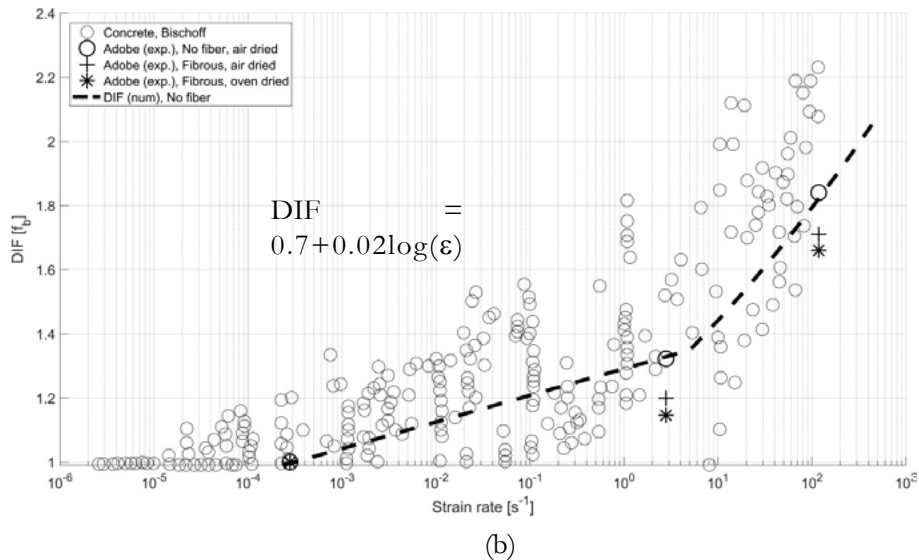


Figure 13: Experimental-numerical stress strain curves in compression for a fibrous adobe ($n=1.7$) compressed at three different loading rates from statics to high velocity impacts using eq. 2 (a) equipped with dynamic increase factor functions (DIF) experimentally derived in [21] (b)

2.3.3 Mechanical Properties in Tension

As for many quasi brittle materials used in masonry, correctly addressing the response of adobe in tension is very important. The mechanical characterization of adobe in tension in current codes mainly concerns the evaluation of its strength parameter. Quantitative values are evaluated mainly from flexural tests, despite literature studies suggest that splitting tests better reproduce the uniaxial tensile state [38]. Experimental data available for adobe in tension in literature and including tests in [20] is shown in Figure 14 similarly to Par. 2.3.1. Averages and 0.95 percentile values respectively are about 0.4 MPa and 0.15 MPa. According to codes, average values for strength of 0.34 MPa is prescribed in [13], while a minimum of 0.25 MPa is requested in [9]-[11]. This requirement is met by 65% of the experimental data for adobe in tension available in literature (Figure 14).

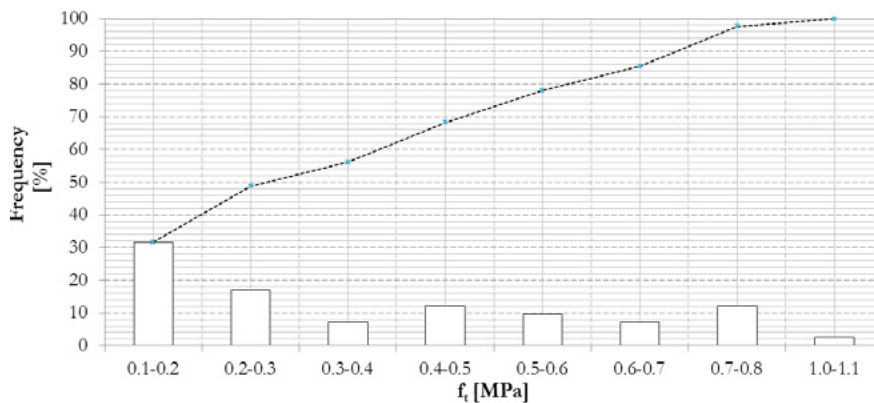


Figure 14: Relative frequency (histogram) and cumulative frequency (line) for the tensile strength for adobe using data in literature (including authors')

Disaggregating data in tension according to the possible presence of fibers in the mixture as in Par. 2.3.1., also in tension mixing soil with fibers statistically results to a lower strength performance in average (Figure 15a). In [45], bending tests at the same laboratory conditions have revealed an enhancement of ductility in the response of adobe when fibers are added to the mixture (Figure 15b). With a value of 0.7 MPa, adobe mortar (fiber free) tested in [20] possesses one of the highest values of tensile strength encountered in literature for adobe.

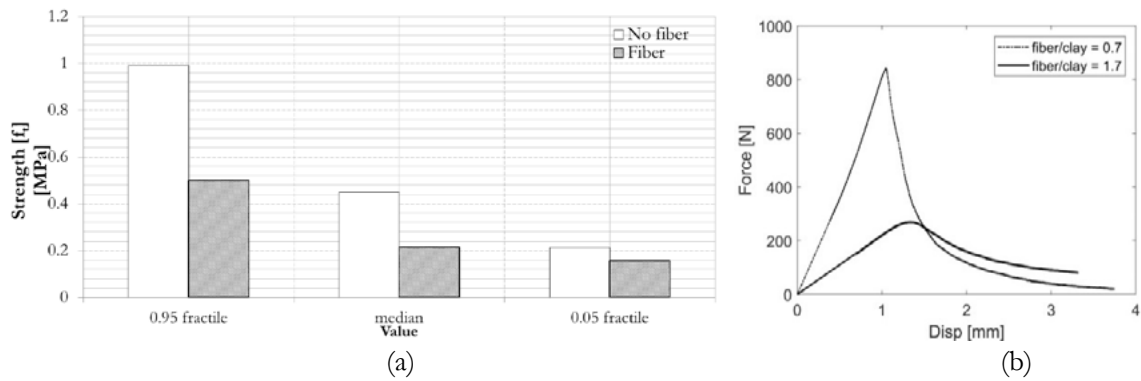


Figure 15: Relative frequency for the tensile strength of adobe bricks disaggregated for fiber free and fibrous adobe samples (a) and Force – displacement plots in bending tests in [16] on two adobe bricks with different fiber proportion ratios (b).

Tensile strength relates to the parameter in compression in ranges between $0.18f_b$ [6] and $0.4f_b$ [28]. In [16], this ratio ranges between $0.3f_b$ and $0.7f_b$, with a median equal to $0.57f_b$. These values are in general higher than the minimum levels suggested in [11], included between 10% and 20% of the compressive strength [11]. The failure process of adobe in tension is typically more brittle than in compression. A localized failure has characterized bricks and mortar subjected to bending tests in [20], independently from water content and fiber inclusion in the mixture. Typical curves of response are characterized by an elastic phase followed by softening with exponential shape (Figure 15b). In [22], numerical simulations of bending tests on adobe using a local damage finite element model recently developed for the simulation of bricks and mortar at various loading conditions showed that a constitutive law in RILEM TC 162 [46] originally prescribed for steel fiber reinforced concrete is suitable to numerically assess the localized damage failure experimentally observed in adobe in flexure (Figure 16). The adopted constitutive model in tension is linear elastic with an elastic modulus being the same as in compression until the attainment of the stress level associated to the first crack in bending, which anticipates softening.

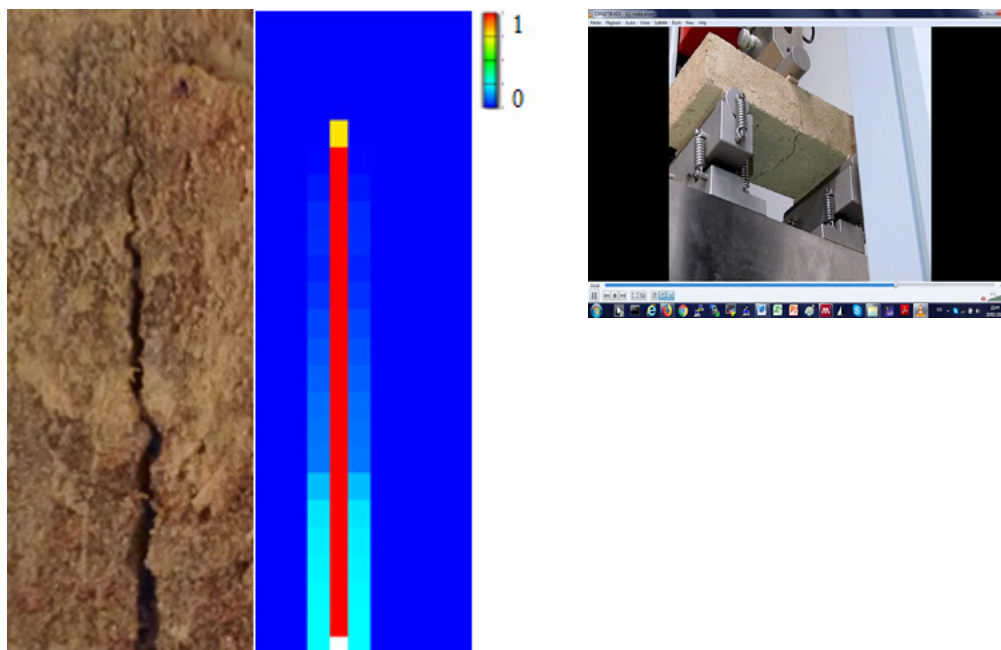


Figure 16: Experimental crack and numerical damage (using RILEM TC) localized in the middle of a brick subjected to bending test using the *adobe delta damage model* in [22], a finite element model for the simulation of adobe bricks

3. Final Recommendations and Conclusions

A review of the codes currently available for the material characterization of adobe bricks and mortar is reported in this study. The prescriptions provided by the normative bodies for adobe around the world related to test methods, soil selection and material properties have been critically addressed. They have been compared with the most recent scientific findings produced for adobe regarding the assessment and interpretation of its physical-mechanical properties. To this end, the experimental data, theoretical interpretations and numerical elaborations produced by the authors over the last years on adobe have been used as main reference. From the analysis, lack of knowledge, consistency and completeness in the current normative body stand out and a normative and knowledge update is needed. Among others, two areas of improvement are deemed as priority:

- Definition of a shared set of identifying properties for the physical-mechanical performance of adobe components, both bricks and mortar. The assessment of the drying conditions preliminary to tests on samples is a priority and the set of maximum moisture levels before mechanical characterization is necessary. The influence of moisture on the mechanical performance must be integrated both at an experimental characterization and at a material design level. Moisture content dependent strength laws should be considered when designing for the life cycle of the structure. Required properties should not solely relate to the characterization of the mechanical parameters of the resulting brick but rather to the evaluation of its original soil. If the minimum requirements in strengths by codes are generally consistent with mean experimental values found in literature, soil particle distributions tests are not sufficient to certify suitability of adobe as a building material. Assessment of fiber properties and amounts in the brick before mechanical characterization in codes is necessary. A comprehensive physical study on the mixture is needed, with particular reference to the plasticity and cohesive property assessment. These must not only be determined on the raw soil, but also directly on the final mixture used to produce the brick, namely including the assessment of fiber-soil mixtures properties. At a research level, the identification of the materials, quantity and orientation of mixing fibers which ensures durability, ductility and strength to bricks and mortar of given mineralogical compositions is a priority task.
- Homogenization of test procedures, methods and requirements for each targeted property. Simplistic identification tests in the field must be preferably substituted by laboratory tests because they are often not sufficient to determine exhaustive information of fundamental properties for adobe. Standard methods can be adapted from codes for modern building materials for masonry applications. Furthermore, for each property, acceptable ranges of values or minimum requirements should be carefully defined to ensure prescribed levels of safety. These values should concern the properties in strength and deformation of the brick as well as the physical properties of the mixture. Given the site dependency inherent to soil selection, prescriptions are expected in terms of ranges for the soil distribution properties and in terms of strict minimum requirements for cohesion, durability and plasticity properties. At a research level, new building production and construction processes capable of removing randomness in the manual production of adobe bricks can help to ensure safety in contexts of scarcity.

4. References

- [1] Transitieteam Bouw, "Circulaire Bouweconomie," p. 38, 2018.
- [2] J. Reis, "Fracture and flexural characterization of natural fiber-reinforced polymer concrete," *Constr. Build. Mater.*, vol. 20, no. 9, 2006.

- [3] A. Heath, P. Walker, C. Fourie, and M. Lawrence, “Compressive strength of extruded unfired clay masonry units,” *Proc. Inst. Civ. Eng. Constr. Mater.* 162 3, vol. 162, no. 3, pp. 105–112, 2009.
- [4] R. Coffman, N. Agnew, G. Austin, and E. Doehne, “Adobe mineralogy: characterization of adobes from around the world,” *6th Int. Conf. Conserv. Earthen Archit. Las Cruces, New Mex. U.S.A., Oct. 14-19, 1990*, vol. 1, no. May, pp. 424–429, 1990.
- [5] G. Minke, “Building with earth: Design and Technology of a sustainable architecture,” *Birkhauser*, 2009.
- [6] D. Silveira and et al., “Mechanical properties of adobe bricks in ancient constructions,” *Constr. Build. Mater.*, vol. 28, no. 1, pp. 36–44, 2012.
- [7] “Centre de recherche et d’application en terre <http://craterre.org/>.” .
- [8] G. R. Wekerle and P. S. B. Jackson, “Urbanizing the security agenda,” *City*, vol. 9, no. 1, pp. 33–49, 2005.
- [9] “DIN 18952: Methods of test for earth (1956), 2008.”
- [10] “Lehmbau Regeln. Begriffe; Baustoffe; Bauteile. Braunschweig/Wiesbaden, Germany: Friedr. Vieweg & Sohn Verlagsgesellschaft mbH, 1999.”
- [11] NZS 4298, “NZS 4298 (1998): Materials and workmanship for earth buildings,” *New Zeal. Tech. Committe*, vol. 4298, p. 91, 1998.
- [12] *HB 195 - 2002 The Australian earth building handbook-Standards Australia International, NSW 2001*. 2001.
- [13] *New Mexico Earthen Building Materials Code - Title 14, Chapter 7 (Part 4), 2004*. New Mexico.
- [14] *Sencico Norma Tecnica Edificacion, NTE E 0.8 Adobe, 2000*. .
- [15] “California Code of Regulations for Adobe in New Constructions, Title 24, Part 10.” 2011.
- [16] M. Larcher *et al.*, “Dynamic Increase Factor of Masonry Materials: Experimental Investigations,” in *ISIEMS, International Symposium for the Interaction of Munitions with Structures*, 2013, p. 10.
- [17] H. Varum, A. Costa, D. Silveira, H. Pereira, J. Almeida, and T. Martins, “Structural Behaviour Assessment and Material Characterization of Traditional Adobe Constructions,” *AdobeUSA 2007, El Rito, NM, USA* , no. January, 2007.
- [18] R. Illampas, I. Ioannou, and D. C. Charmpis, “Adobe bricks under compression : Experimental investigation and derivation of stress – strain equation,” *Constr. Build. Mater.*, vol. 53, pp. 83–90, 2014.
- [19] S. Yetgin, O. Cavdar, and A. Cavdar, “The effects of the fiber contents on the mechanic properties of the adobes,” *Constr. Build. Mater.*, vol. 22, no. 222–227, 2006.
- [20] T. Li Piani, D. Krabbenborg, J. Weerheijm, L. Koene, and L. J. Sluys, “The Mechanical Performance of Traditional Adobe Masonry Components: An experimental-analytical characterization of soil bricks and mud mortar,” *J. green Build.*, vol. 13, no. 3, pp. 17–44, 2018.
- [21] T. Li Piani, J. Weerheijm, M. Peroni, L. Koene, G. Solomos, and L. J. Sluys, “Dynamic Characterization of Adobe in compression: The effect of fibres with soil binders,” in *FraMCoS-X : Fracture Mechanics of Concrete and Concrete Structures*, 2019.

- [22] T. Li Piani, J. Weerheijm, L. Koene, and L. J. Sluys, “The Adobe delta damage model: A locally regularized rate-dependent model for the static assessment of soil masonry bricks and mortar,” *Eng. Fract. Mech.*, vol. 206, pp. 114–130, 2019.
- [23] T. Li Piani, J. Weerheijm, and L. J. Sluys, “Ballistic model for the prediction of penetration depth and residual velocity in Adobe: A new interpretation of the ballistic resistance of earthen masonry,” *Def. Technol.*, vol. 14, no. 5, pp. 4–8, 2018.
- [24] H. Houben and H. Guillaud, *Earth construction: a comprehensive guide*. ITDG Publishing, 1994.
- [25] E. W. Smith, “Adobe bricks in New Mexico, Circular 188, New Mexico Bureau of Mines and Mineral Resources.” p. 89, 1982.
- [26] G. S. Austin, “Adobe as a building material,” *New Mex. Bur. Mines Miner. Resour. Socorro*, pp. 69–71, 1984.
- [27] E. Quagliarini, S. Lenci, and M. Iorio, “Mechanical properties of adobe walls in a Roman Republican domus at Suasa,” *J. Cult. Herit.*, vol. 11, no. 2, pp. 130–137, 2010.
- [28] A. Caporale, F. Parisi, D. Asprone, R. Luciano, and A. Prota, “Comparative micromechanical assessment of adobe and clay brick masonry assemblages based on experimental data sets,” *Compos. Struct.*, vol. 120, pp. 208–220, 2015.
- [29] E. Quagliarini and S. Lenci, “The influence of natural stabilizers and natural fibres on the mechanical properties of ancient Roman adobe bricks,” *J. Cult. Herit.*, vol. 11, no. 3, pp. 309–314, 2010.
- [30] A. A. Hammond, “Prolonging the life of earth buildings in the tropics,” *Build. Res. Pract.*, vol. 1, no. 3, pp. 154–163, 1973.
- [31] *BS 1377-2: 1990, Methods of test for soils for civil engineering purposes, Classification tests.* .
- [32] *UNI EN 772-1:2015 “Test Methods for masonry elements”. Title 1: Determination of compressive strength”. .*
- [33] “UNI EN 12390-5: “Tests on hardened concrete. Title 5: Bending tests on concrete specimens’, 2009.”
- [34] A. Agarwal, “Mud as a Traditional Building Material,” *Chang. Rural Habitat; Ed. by Brian Brace Taylor. Singapore Concept Media/ Aga Khan Award Archit.*, vol. 1, pp. 137–146, 1975.
- [35] R. Aguilar, M. Montesinos, and S. Uceda, “Mechanical characterization of the structural components of Pre-Columbian earthen monuments: Analysis of bricks and mortar from Huaca de la Luna in Peru,” *Case Stud. Constr. Mater.*, vol. 6, pp. 16–28, 2017.
- [36] T. Li Piani, L. Koene, J. Weerheijm, and L. J. Sluys, “The Ballistic Performance of Adobe Masonry: An analytical model for penetration in soil bricks and mortar,” in *International Symposium on Ballistics Impacts on Structures (17th ISIEMS)*, 2017.
- [37] “ASTM C42: Standard Test Method for Obtaining and Testing Drilled Cores and Sawed Beams of Concrete.”
- [38] D. Silveira, H. Varum, and A. Costa, “Influence of the testing procedures in the mechanical characterization of adobe bricks,” *Constr. Build. Mater.*, vol. 40, no. March, pp. 719–728, 2013.
- [39] Ş. Yetgin, Ö. Çavdar, and A. Çavdar, “The effects of the fiber contents on the mechanic properties

of the adobes,” *Constr. Build. Mater.*, vol. 22, no. 3, pp. 222–227, 2008.

[40] A. Caporale, F. Parisi, D. Asprone, R. Luciano, and A. Prota, “Critical surfaces for adobe masonry: Micromechanical approach,” *Compos. Part B Eng.*, vol. 56, no. January, pp. 790–796, 2014.

[41] J. Ingham, D. Biggs, and L. R., “Uniaxial Compressive Strength and Stiffness of Field-Extracted and Laboratory-Constructed Masonry Prisms,” *J. Mater. Civ. Eng.*, vol. 26, no. 4, pp. 567–575, 2014.

[42] Popovics, “A numerical approach to the complete stress strain curve of concrete,” *Cem. Concr. Res.*, vol. 3, pp. 583–599, 1973.

[43] T. Li Piani, J. Weerheijm, L. Koene, and L. J. Sluys, “Modelling the mechanical response of Adobe components under uniaxial loadings,” in *European Conference on Computational Mechanics (ECCM 6)*, 2018.

[44] P. H. Bischoff and S. H. Perry, “Compressive behaviour of concrete at high strain rates,” *Mater. Struct.*, vol. 24, no. 6, pp. 425–450, 1991.

[45] T. Li Piani, J. Weerheijm, L. Koene, and L. J. Sluys, “Modelling the Mechanical Response of Adobe Components under Uniaxial Loading,” *Key Eng. Mater.*, vol. 774, pp. 650–657, 2018.

[46] “RILEM TC 162-TDF: Test and design methods for steel fibre reinforced concrete. Sigma-epsilon design method. Final Recommendation,” 2003.

Microstructural changes in porosity due to carbonation of fly ash blended pastes assessed by dynamic vapour sorption

Y. Villagrán-Zaccardi^{1,2}, N. Alderete¹, N. De Belie¹

¹Magnel Laboratory for Concrete Research, Department of Structural Engineering, Faculty of Engineering and Architecture, Ghent University, Tech Lane Ghent Science Park, Campus A, Technologiepark Zwijnaarde 60, B-9052 Ghent, Belgium

²LEMIT, CONICET, 52 entre 121 y 122 s/n, 1900 La Plata, Argentina

Abstract

Blended cement pastes are usually reported to carbonate faster than ordinary Portland cement (OPC) pastes due to the reduced portlandite content caused by the pozzolanic action. Moreover, the effect of carbonation on the pore structure of hydrated cement paste may be variable depending on the binder. On the one hand, calcium carbonate precipitates and clogs the pore network. On the other hand, decalcification of C-S-H may cause shrinkage, and potentially microcracking that increases pore connectivity. When fly ash is included in the system, the situation becomes quite different from ordinary Portland cement paste. As the pozzolanic reaction consumes portlandite, carbonation is more likely to progress by decalcifying C-S-H. Blended cement pastes are therefore more susceptible to microstructural changes due to carbonation. In this paper, we assessed the overall effect of carbonation on the porosity of well-cured fly ash blended cement paste by dynamic vapour sorption (DVS). This technique allows determining the pore structure from the quantification of water uptake by condensation of water vapour at different relative humidities. The Barrett, Joyner and Halenda (BJH) method, based on the Kelvin model, was applied for computing the volume of mesopores (0.002-0.05 μm). The Dubinin–Radushkevich (DR) equation was used to calculate the volume of micropores ($<0.002 \mu\text{m}$). Samples with 20, 30, and 40% replacement ratios of OPC by fly ash were prepared and cured for one year before carbonating them in an accelerated chamber with 1% CO_2 . Despite the advanced age of the pastes, considerable reductions due to carbonation in the volume of mesopores and micropores were registered.

Keywords: fly ash, carbonation, porosity, DVS

1. Introduction

The dynamic vapour sorption (DVS) test helps in the description of the pore structure of cementitious materials by measuring the equilibrium between the mass water content of the sample and the relative humidity (RH), at a constant temperature. Water molecules are relatively smaller than those of gases CO_2 or N_2 [1], and this advantage allows water molecules to penetrate smaller pores and ink-bottle pores as well. Also, it is very convenient that no degassing process of the sample prior to the measurements is necessary, hence possible microstructural damage is avoided. Furthermore, the test can be performed at room temperature, which is a practical and realistic approach for most applications. The sorption isotherms obtained from the test are used afterwards to calculate specific surface area and pore size distributions (PSDs) of samples.

The most applied theories of adsorption that mathematically describe the results are the Barrett, Joyner and Halenda (BJH) method [2] for the calculation of the pore size distribution in the mesopore range, and the Dubinin–Radushkevich (DR) equation [3] for the calculation of the pore size distribution in the micropore range. These models include a number of simplifications that should be considered. For instance, for the computation of the specific surface, a monolayer of adsorbate is assumed to be uniformly distributed on pore walls, but this surface is never completely covered until the saturated vapour pressure is reached [4]. Another important aspect is that calculations of the pore size distribution consider cylindrical pore shapes for the distribution [2].

Changes in pore structure of carbonating blended cementitious mixes occur over time and in relation to the reaction degree of the supplementary cementitious material and the affectation of hydration products by their reaction with carbon dioxide. Even developing at a relatively slow pace, when fly ash is added to concrete there is normally an improvement in durability-related properties of the cementitious material [5-8]. Nevertheless, the carbonation of fly ash blended mixes has particular implications. The consumption of calcium hydroxide by the pozzolanic reaction of the fly ash and the dilution effect of the portland cement reduce the alkaline reserve of the material that offers resistance to carbonation. As a result, the carbonation front progresses more rapidly than in unblended mixes with the same porosity. Moreover, the relative amounts of calcium hydroxide and C-S-H suffering carbonation are modified with the inclusion of fly ash [9-10], and the effect of carbonation on porosity differs from the case of plain Portland cement pastes. Whereas carbonation of calcium hydroxide partially contributes in clogging the pore structure, carbonation of C-S-H causes the opposite effect when increasing porosity.

Previous studies have dealt with the effect of carbonation on the pore structure of fly ash blended cement pastes. Techniques such as mercury intrusion porosimetry, scanning electron microscopy and the X-ray attenuation method have been applied for describing the changes in the microstructure. These techniques are effective in describing the total porosity, but they are imperfect for connecting these changes to different pore size ranges due to the potential affectation of the microstructure caused by the procedure or the preconditioning required. Results from DVS tests can complement previous descriptions of carbonated fly ash blended paste, in relation to the particular capabilities of the method, which requires no preconditioning.

2. Methodology

2.1 Materials

The mineralogical and chemical compositions, and particle size distribution of the Class F fly ash and ordinary Portland cement (OPC, CEM I, 42.5 N) used in this study are presented in Tables 1, 2 and 3, respectively. The mineralogical compositions were determined by Rietveld analysis of the X-ray diffraction patterns. These analyses were performed by adding 10% w/w of internal standard (zincite) to apply the PONKCS method and determine the content of amorphous phases as well. The particle size distributions were measured by laser diffractometry. The values of the refractive/absorption indexes considered in this analysis were 1.73/0.1 and 1.56/1 for the OPC and fly ash, respectively.

Pastes were prepared with 20, 30, and 40 % w/w replacement ratios of OPC by fly ash. The water to binder was 0.40 in all cases. These samples were cured in a conditioned room at $(20 \pm 2) ^\circ\text{C}$ and $(95 \pm 5) \% \text{RH}$ for 360 days for assuring nearly the maximum possible reaction degree of the fly ash.

Table 1. Mineralogical composition of the fly ash and OPC, determined by XRD/Rietveld analysis (and PONKCS method for the amorphous content) (%).

Material	C ₃ S	C ₂ S	C ₃ A	C ₄ AF	Gypsum	Quartz	Magnetite	Calcite	Amorphous
OPC	60.2	22.0	10.8	2.7	4.2	nd	nd	0.04	nd
Fly ash	nd	nd	nd	nd	nd	5.9	1.2	nd	91.9

nd = not determined

Table 2. XRF chemical compositions of raw materials (%).

Material	Na ₂ O	MgO	Al ₂ O ₃	SiO ₂	SO ₃	K ₂ O	CaO	Fe ₂ O ₃	Free CaO
OPC	0.27	0.95	4.91	20.74	2.96	0.77	64.67	1.52	0.2
Fly ash	1.08	1.92	23.50	54.19	0.94	3.38	3.02	7.92	0.1

Table 3. Particle size distribution of OPC and fly ash (µm).

Material	d10	d50	d90
OPC	3.1	16.3	57.9
Fly ash	2.1	15.0	89.3

2.2 Methods

After the curing period, samples were ground and sieved between 500–1000 µm. This range of particle size for the samples was considered as a good compromise between DVS test duration and practicality [11]. Portions of the samples were immediately conditioned by removing free water by solvent exchange with isopropanol for 15 min and dried under vacuum afterwards. Then, approximately 5 mg was tested for DVS. The device was set at 20 °C, with a dm/dt < 0.002 wt.%/min as a detection limit to continue to the following RH level. The RH levels at which samples were subsequently equilibrated included 5-10-20-30-40-50-60-70-80-90-98 % RH. Since these samples were predried under vacuum, they were first increasingly tested for adsorption up to 98 % RH and then a complete desorption process was performed. Other portions of the samples were put in a carbonation chamber (60 % RH, 1 % CO₂) for six weeks to allow them to carbonate. Afterwards, small fractions of the samples were crushed and sprayed with phenolphthalein solution to confirm full carbonation by no colour change. Then, portions of the samples were conditioned and tested for DVS with the previously described set-up. Each DVS test demanded approximately 7 days to be completed.

The BJH method [2] was used for the calculation of the pore size distribution in the mesopore range (0.002-0.05 µm [12]). This method, based on the Kelvin model, considers that capillary and adsorbed water phases exist in cylindrical pores and calculations of the pore size distribution are made by step-by-step iterative calculations [1]. The DR equation [3] was used to calculate the pore size distribution in the micropore range (<0.002µm). The method is based on the assumptions of a change in potential energy between the gas and adsorbed phases.

3. Results and discussion

Figure 1 presents the DVS isotherms. Carbonated pastes are drawn with dashed lines, and uncarbonated pastes are drawn with continuous lines. Small increases in the mass water contents for each RH are noted as the content of fly ash increases. This effect of fly ash is showing an increased overall porosity due to a dilution effect of the OPC [5]. An exception should be made for 20 and 30 % uncarbonated samples, as between these two the paste with the 30 % fly ash content showed the lowest water content. However, the difference between these two series is very small, and it can be therefore considered within the variability of the test. In general, a significant variation in the desorption branches between 40 and 30 % RH is observed.

This change is produced near the RH generally considered key for separating free water from interlayer water [1]. The device required a much more extended stabilization period during the step from 40 to 30 % RH, and a steeper desorption curve is presented in this particular range. Further analyses for this situation are possible, but they have no implications for the comparative study aimed in this work. More significant hysteresis is also noted for uncarbonated samples. Hysteresis commonly points at the presence of ink-bottle effects, and the observed attenuation suggests a reduction in the tortuosity caused by an increased accessibility of all pores when samples are carbonated.

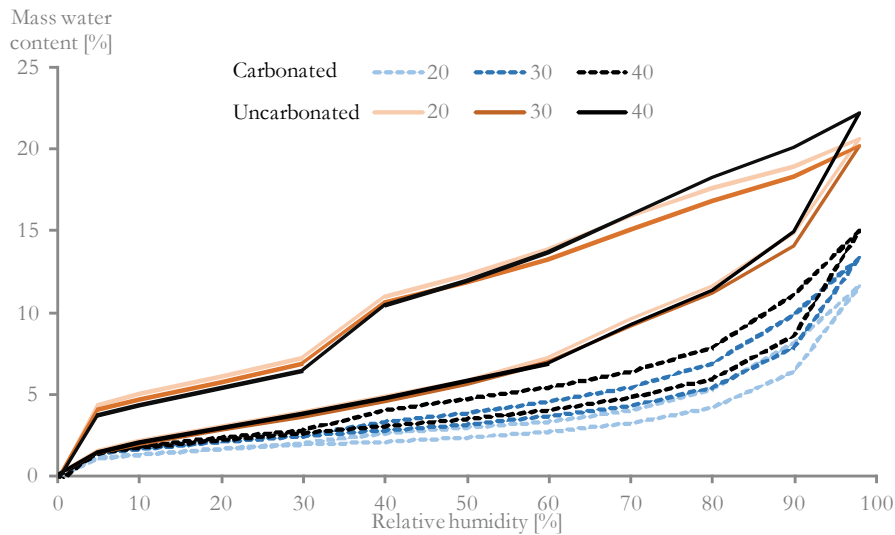


Figure 1: Sorption isotherms of the samples.

Figure 2 presents the pore volume and pore specific surface area of samples calculated from the DVS isotherms data. The replacement ratio of OPC by fly ash did not cause significant differences in the micro and meso pore volumes or the specific surface area of the pore structure. The long curing period promoted a reaction degree very close to the maximum possible in the mixes, and compared to the 20% paste, the higher dilution effect in the 40% paste seems to be compensated by the reaction of the fly ash. In this case, uncarbonated 40% paste must have had a significantly lower content of calcium hydroxide than the the 30 and 20% pastes, and this is certainly defining the effect of carbonation on the pore structure depending on the replacement ratio. Accelerated carbonation produced a notorious decrease in the volume of micro and meso pores in the mixtures. The decrease is smaller with a higher replacement ratio, showing the connection between the pore volume reduction due to carbonation and the initial content of calcium hydroxyde in the samples. Several authors [13-16] have indicated that carbonation of calcium hydroxyde contributes to the clogging of the pore structure, whereas carbonation of C-S-H produces a detrimental effect instead. In relative terms, similar reductions due to carbonation were found for the mesopore and micropore size ranges. Accelerated carbonation also caused the specific surface to decrease. The relative reduction due to carbonation in the specific surface area is greater than the reduction in pore volume. However the number of tests is insufficient and this outcome requires to be confirmed by additional testing, this indication is also in agreement with the reduced hysteresis. When the comparative analysis is made on the basis of the same porosity, a slight coarsening of the pore structure caused by carbonation is suggested by the decreased pore specific surface area. Overall, the relative pore size distribution seems to remain the same, so the effect of carbonation would be homogeneous over the whole pore size range. The suggested coarsening might be explained by microcracking, which typically has a totally different structure than innate porosity. As during carbonation the previous consumption of portlandite by the fly ash promotes decalcification of C-S-H, the microcracking may be associated to ‘carbonation shrinkage’. Additional results from other experimental techniques would be valuable for assessing the complete pore size range in the pastes (i.e. covering also

larger pores) and confirming this hypothesis.

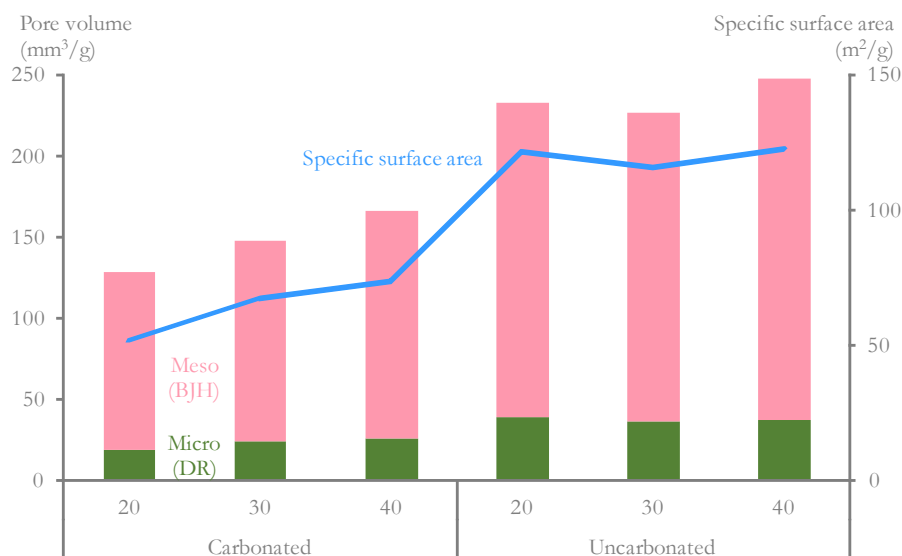


Figure 2: Computed pore volume and specific surface area.

The results in the present study differ from the findings from Wu and Ye [9], where increased porosity in fly ash blended pastes was registered by mercury intrusion porosimetry, and Cui et al [17], where similar results were found by the extended X-ray attenuation method (XRAM), for fly ash contents of 30, 50 % or higher. These studies attributed the increase in porosity to carbonation of C-S-H, which is probably enhanced when they apply accelerated carbonation at 3 % CO₂. In agreement, a previous study considering accelerated carbonation at 10 % CO₂ [18] also found a decrease in capillary porosity due to carbonation with 35 and 50 % fly ash, whereas an increase in capillary porosity was detected for 67 % fly ash. In the present study the CO₂ concentration was only one-third and one-tenth of the values in previous works (i.e., a closer value to natural exposure), and clogging of the pore structure seems to be the main effect. Moreover, no high fly ash contents were included in the present study, so our analysis is limited to 40 % fly ash at the most, and it is possible that the situation is different for higher fly ash contents. For example, Shah et al [19] suggest that reductions in porosity are to be expected whenever high replacement ratios, with a consequent full consumption of portlandite, are applied. Conversely, with replacement ratios of up to 40 %, Chindaprasirt and Rukzon [20] found similar results to those presented in the present work. It is therefore clear that significant attention should be put on the replacement ratio and the CO₂ concentration when assessing the impact of carbonation on fly ash blended paste.

4. Conclusions

- A small increase in porosity was measured in fly ash blended pastes, in connection with a dilution effect due to a limited reactivity of the fly ash, even after 1 year of curing.
- Significant reductions in the volumes of micro and mesopores due to accelerated carbonation (1 % CO₂) of fly ash blended cement pastes were detected by dynamic vapour sorption tests. This reduction was registered for replacement ratios between 20 and 40 % w/w of OPC by fly ash.
- The reduction in the pore specific surface area of fly ash blended pastes due to the carbonation seems more significant in relative terms than the reduction in pore volume. The contrast between both parameters can be interpreted as a suggestion of a slight coarsening of the meso/micro pore structure due to carbonation, probably due to the development of carbonation shrinkage caused by the reduced portlandite content as a result of the pozzolanic reaction. This hypothesis is supported by a concurrent reduction in the tortuosity of pastes due to carbonation. Confirmation studies including tests with other

techniques that assess larger pores are necessary.

5. Acknowledgement

The participation of Yury Villagrán-Zaccardi in this publication is possible thanks to partial funding received from ANPCyT through PICT 2017-0091 Prest BID.

6. References

- [1] Baroghel-Bouny V., (2007), Water vapor sorption experiments on hardened cementitious materials. Part I: Essential tool for analysis of hygral behavior and its relation to pore structure, *Cement and Concrete Research* 37, 414-437.
- [2] Barret E., Joyner L., Halenda P., (1951), The determination of pore volume and area distributions in porous substances - computations from nitrogen isotherms, *Journal of the American Chemical Society* 73, 373-380.
- [3] Dubinin M., (1975), Physical adsorption of gases and vapors in micropores, *Progress in Surface and Membrane Science* 9, 1–70.
- [4] Dollimore D., Spooner P., Turner A., (1976), The BET method of analysis of gas adsorption data and its relevance to the calculation of surface areas, *Surface Technology* 4, 121-160.
- [5] Van den Heede P., Gruyaert E., De Belie N. (2010), Transport properties of high-volume fly ash concrete: Capillary water sorption, water sorption under vacuum and gas permeability. *Cement and Concrete Composites* 32, 749–756.
- [6] Saha A. K. (2018), Effect of class F fly ash on the durability properties of concrete. *Sustainable Environment Research* 28, 25–31.
- [7] Bijen J. (1996), Benefits of slag and fly ash. *Construction and Building Materials*, 10(5), 309–314.
- [8] Chindaprasirt P., Jaturapitakkul C., Sinsiri T. (2005), Effect of fly ash fineness on compressive strength and pore size of blended cement paste. *Cement and Concrete Composites*, 27(4), 425–428.
- [9] Wu B., Ye G. (2017), Development of porosity of cement paste blended with supplementary cementitious materials after carbonation, *Construction and Building Materials* 145, 52–61.
- [10] Van den Heede P., De Schepper M., De Belie N. (2019), Accelerated and natural carbonation of concrete with high volumes of fly ash: chemical, mineralogical and microstructural effects, *Royal Society Open Science* 6, 181665.
- [11] Snoeck D., Velasco L.F., Mignon A., Van Vlierberghe S., Dubruel P., Lodewyckx P., De Belie N., (2014), The influence of different drying techniques on the water sorption properties of cement-based materials, *Cement and Concrete Research* 64, 54–62.
- [12] IUPAC (1972), *Manual of symbols and terminology. Appendix 2. Pt. 1. Colloid and surface chemistry, Pure Applied Chemistry.*
- [13] Borges P., Costa J., Milestone N., Lynsdale C., Streatfield R. (2010), Carbonation of CH and C-S-H in composite cement pastes containing high amounts of BFS, *Cement and Concrete Research* 40, 284–292.
- [14] De Belie N., Kratky J., Van Vlierberghe S. (2010), Influence of pozzolans and slag on the microstructure of partially carbonated cement paste by means of water vapour and nitrogen sorption experiments and

BET calculations, *Cement and Concrete Research* 40, 1723–1733.

[15] Gruyaert E., Van den Heede P., De Belie N. (2013), Carbonation of slag concrete: Effect of the cement replacement level and curing on the carbonation coefficient – Effect of carbonation on the pore structure, *Cement & Concrete Composites* 35, 39–48.

[16] Groves G., Rodway D., Richardson I. (1990), The carbonation of hardened cement pastes, *Advances in Cement Research* 3, 117–125.

[17] Cui D., Banthia N., Wang Q., Sun W. (2019), Investigation on porosity of partly carbonated paste specimens blended with fly ash through dual CT scans, *Construction and Building Materials* 196, 692–702.

[18] Lammertijn S. and De Belie N. (2008) Porosity, gas permeability, carbonation and their interaction in high-volume fly ash concrete, *Magazine of Concrete Research* 60 (7), 535–545.

[19] Shah V., Scrivener K., Bhattacharjee B., Bishnoi S. (2018) Changes in microstructure characteristics of cement paste on carbonation, *Cement and Concrete Research* 109, 184–197.

[20] Chindapasirt P. and Rukzon S. (2009) Pore Structure Changes of Blended Cement Pastes Containing Fly Ash, Rice Husk Ash, and Palm Oil Fuel Ash Caused by Carbonation, *Journal of Materials in Civil Engineering* 21 (11), 666-671.

Isothermal Calorimetric Study on Heat Evolution and of Apparent Activation Energy of Alkali-activated Slag/Fly ash Pastes

S. Zhang¹, Y. Zuo¹, Z. Li¹, G. Ye^{1,*}

¹Microlab, Section Materials and Environment, Faculty of Civil Engineering and Geosciences, Delft University of Technology, Stevinweg 1, 2628 CN, Delft, The Netherlands

*G.Ye@tudelft.nl

Abstract - Alkali-activated slag/fly ash (AASF), as an environmental-friendly binder system for construction materials, has recently attracted great attention from both academic and industrial communities. Towards its wider engineering application, it is crucial to have a better understanding of the temperature induced effects by different curing regimes and the temperature sensitivity on the thermal properties of this system, for instance the apparent activation energy. However, the available information on the apparent activation energy of AASF system is still quite limited.

The present study is aimed at investigating the role of alkali activator (AA) chemistry on the reaction kinetics of AASF at early age. The binder is made of 50 wt.% blast furnace slag and 50 wt.% fly ash. Four AA moduli ($\text{SiO}_2/\text{Na}_2\text{O}$ ratio = 0.8, 1.0, 1.2 and 1.5) were used for the mixture preparation. The effect of AA modulus on the heat evolution was studied by performing isothermal calorimetry test up to 160 h at ambient temperature. The total heat release was studied through curve fitting using exponential model. Furthermore, the apparent activation energy of AASF pastes was determined using incremental methods and its variation over wide range of early age reaction was studied. It was found that the AA modulus evidently influences the heat evolution of AASF. The cumulative heat release reached the maximum value at AA modulus of 1.0, followed by at 0.8, 1.2 and 1.5. This trend is well in line with the changes of the apparent activation energy of AASF mixtures. In addition, it was confirmed that the apparent activation energy of AASF was not only related to the chemistry of reactants but also reaction-stage dependent. Particularly it varied significantly at the very early age of reaction.

Keywords: Activation energy; alkali-activation; isothermal calorimetry; Slag; Fly ash

1. General introductions

Alkali activated materials (AAMs), derived by the reaction of an alkali metal source (solid or dissolved) with a solid (alumino)silicate powder [1, 2], are considered as an environmental friendly binder and one of the best alternatives for ordinary Portland cement (OPC). These materials show comparable or even better performances and less energy consumption at the same time when compared to the traditional cementitious binders. Furthermore, concrete made of alkali activated materials also provide added advantage regarding the greenhouse gas emission, i.e. an reduction of up to 80% compared with concrete made of OPC [3]. Up till now, the most intensively studied system of AAMs is based on blast furnace slag and class F fly ash. This is mainly due to their large quantity of annual production as well as their relatively stable chemical composition. Previous studies on AASF have focused on microstructure development,

nature of reaction products and mechanical properties [4-6]. However, few studies have paid attention to the heat evolution related properties especially the apparent activation energy of AASF. As an important parameter for engineering predictions and applications of AASF with regards to different temperature curing regime, the knowledge of the apparent activation energy of AASF binder system is crucial .

Compared to that within traditional cementitious systems, the data concerning the apparent activation energy of AASF is currently still scarce. Most previous results were related to alkali-activated slag (AAS). For instance, Fernandez et al [7] determined apparent activation energy to be 57.6 kJ/mol in AAS system activated by sodium hydroxide and sodium silicate. Zhou [8] studied the kinetics of hydration of AAS and the apparent activation energy was determined to be 53.63 kJ/mol. Only one work related to apparent activation energy in AASF was found [9] and the value calculated was 53.1 kJ/mol.

Therefore, this work aims to further investigate the influence of mixture parameters, especially the AA modulus, on the heat evolution and to determine the apparent activation energy of AASF systems by isothermal calorimetry testing.

2. Experimental program

2.1 Materials and mix design

The solid precursors used in this study were ground granulated blast furnace slag (GGBS) and Class F fly ash (FA) according to ASTM 618. Material density is 2890 kg/m³ for slag and 2440 kg/m³ for fly ash. The d50 particle size is 17.88 μm for slag and 33.19 μm for fly ash. The chemical compositions deduced from X-ray Fluorescence along with other properties of the precursors (including LOI at 950 °C and fineness passing 45 μm) are shown in Table 1.

Table 1. Chemical compositions and properties of raw materials

Oxide (wt %)	SiO ₂	Al ₂ O ₃	Fe ₂ O ₃	CaO	MgO	SO ₃	Na ₂ O	K ₂ O	LOI	Fineness, % passing 45μm
Slag	32.91	11.84	0.46	40.96	9.23	1.60	-	0.33	1.15	95
Fly ash	52.90	26.96	6.60	4.36	1.50	0.73	0.17	-	3.37	81

As reported previously by the authors [10], the major crystalline phases in fly ash are quartz, mullite and hematite, while the blast furnace slag contains mainly amorphous phases. The reactivity of slag could be indicated by its abundant amorphous content (over 98%). On the other hand, the reactivity of fly ash is reflected by its reactive silica content of 43.04% and reactive alumina content of 15.51%. Sound mechanical properties have been achieved using both solid precursors.

To study the heat evolution of AASF, three levels of alkali activator (AA) moduli (ratio of SiO₂ wt.%/ Na₂O wt.% within AA) were considered for preparation of AASF pastes with fixed binder combination of 50 wt.% blast furnace slag and 50 wt.% Class F fly ash. The detailed mixture designs are shown in Table 2. Na₂O wt.% content (in alkali activator with respect to total binder mass) was kept constant to be 4 wt. %. In addition, the water to binder (w/b) ratio was chosen to be 0.32 to maintain adequate workability for all the paste mixtures. The mixtures were named M0.8, M1.0, M1.2 and M1.5 accordingly, with the number representing the AA modulus.

Table 2 Mixture design of AASF

Mixture	Slag (wt.%)	Fly ash (wt.%)	w/b ratio	Na ₂ O (wt.%)	Modulus
M0.8					0.8
M1.0					1.0
M1.2	50	50	0.32	4.0	1.2
M1.5					1.5

The alkaline activator was prepared by dissolving NaOH pellets (analytical grade, purity ≥ 98%) and sodium silicate (Na₂O: 8.25 wt.%, SiO₂: 27.50 wt.%) in distilled water. The activator was cooled down to room temperature prior to mixture preparation.

2.2 Isothermal calorimetry

Isothermal calorimetry was conducted using a TAM-Air-314 isothermal conduction calorimeter. Calibration of the heat flow channels was carried out prior to measurements. The solid precursors were firstly hand mixed for 5 min. Afterwards, the alkaline activator solution was added and the batches were mixed for additional 2 min using a head-mixer with speed of 1600 rpm. Approximately 5g of freshly mixed paste was introduced into a small glass ampoule and was immediately loaded into the heat flow channels along with the reference ampoule. Two replicates for each mixture were measured. Heat release was recorded for a period of 160 h. For the tests carried out at 40 °C, the solid precursors, alkali activator and reference ampoules were stored in 40 °C oven before the tests. Extra caution has been paid to minimize the decrease of temperature during mixing and sample transfer.

2.3 Ultimate total heat and global reaction degree through curve fitting

The global reaction degree of AASF is also calculated using cumulative heat release data by the aid of curve fitting using exponential model shown in Equation 5.

$$Q(t) = Q_{max} \exp\left(\frac{-t}{\tau}\right)^\beta \quad (5)$$

where Q_{max} corresponds to the ultimate total heat at completion of reaction; τ and β are parameters associated with time and shape in the exponential model. This model along with Knudsen linear dispersion model, have been proven somewhat adequate for Q_{max} prediction and has been previously used in alkali-activated systems [11, 12], especially when the data before the induction period is neglected. Finally, the reaction degree $\alpha(t)$ could be then calculated by Equation 6

$$\alpha(t) = \frac{Q(t)}{Q_{max}} \quad (6)$$

where $\alpha(t)$ was determined for all AASF mixtures reacted under 20 °C and 40 °C for later calculation of apparent activation energy using incremental method.

2.4 Apparent activation energy determination

Arrhenius's theory as shown in Equation 1 has been proven to be an effective tool to study the temperature related effects and combined rate sensitivity of hydration reactions in cementitious systems. The Arrhenius equation is written as:

$$k(T) = A \exp\left(\frac{-E_a}{RT}\right) \quad (1)$$

where k is the temperature sensitivity rate constant, T is the absolute temperature (K). A is a constant (pre-exponential factor that varies for different chemical reaction), E_a is the activation energy (kJ/mol), R is the

universal gas constant (J/(mol.K)).

Arrhenius equation could be rewritten using two sets of rates constants at different temperature:

$$k(T_1) = k(T_2) \exp \left[\frac{-E_a}{RT} \left(\frac{1}{T_1} - \frac{1}{T_2} \right) \right] \quad (2)$$

This study used the incremental method or ‘rates’ method to determine the apparent activation energy E_a of AASF as has been previously used for OPC pastes [13, 14]. Assuming the calorimeter is calibrated properly, the rate constant k equals to the power of heat flow measured for a given reaction degree α and reaction temperature T :

$$k(T) = P(\alpha, T) \quad (3)$$

Therefore, in order to calculate E_a , two sets of heat flow data were used which enables calculation of E_a as a function of reaction degree α continuously.

$$E_a = R \left[\frac{T_1 T_2}{T_1 - T_2} \ln \left(\frac{P_{\alpha_0}^{T_1}}{P_{\alpha_0}^{T_2}} \right) \right] \quad (4)$$

It is worth noting that a huge simplification is made here to use E_a for the entire alkali activation and geopolymerization processes. Evidently, E_a is also sensitive to different reaction stages as the microstructure changes with elapse of time. However, considering the great difficulties to distinguish the different individual reactions within geopolymerization, E_a acquired in this way can still give further insights on temperature dependent reaction kinetics of the global reaction.

3. Results and discussions

3.1 Heat evolution and reaction degree

The heat flow curves of mixture M0.8-M1.5 under the temperature of 20 °C and 40 °C are shown in Figure 1. In general, the heat flow curve is characterized by two calorimetric peaks, The first peak is due to the wetting and dissolution of precursors particles and the second broader peak corresponds to the formation of reaction products. Compared to the heat flow at 20 °C, an evident increase of heat flow intensity could be found at 40 °C. In addition, the intensity and the time of appearance of the second peak are positively correlated and both of them change with increasing AA modulus. More specifically, with increasing AA modulus, both the intensity and time of appearance of the second peak first increase and then decline after reaching the maximum when AA modulus is 1.2. This trend indicates AA modulus has a significant influence over the early age of heat evolution, and therefore the early age reaction kinetics of AASF. It is commonly acknowledged that the early age reaction kinetics of AASF is dominated by two processes, i.e. the dissolution of Ca, Si, Al species from the solid precursor and Si oligomer dissociation presented in AA, and the geopolymerization of useful?? species to form various reaction products. Previous studies by ²⁹Si NMR and FTIR proved that higher amount of silica species with low polymerization degree (monomers) is favoured at lower AA modulus [15, 16], A lower polymerization degree of silica species can promote the gel formation. However, by lowering the AA modulus, the total amount of available species within AA is also reduced, which might have negative impact over the very early geopolymerization process. The experimental data and corresponding curve fitting using exponential model were presented in Figure 2 (a) and (b). For the calculation of total reaction heat, it is worth noting that the initial data related to the heat flow of first peak was not taken into consideration. The reason is to avoid the testing error induced during the mixing and transferring of the AASF mixtures. This is in accord with previous studies [7, 17, 18].

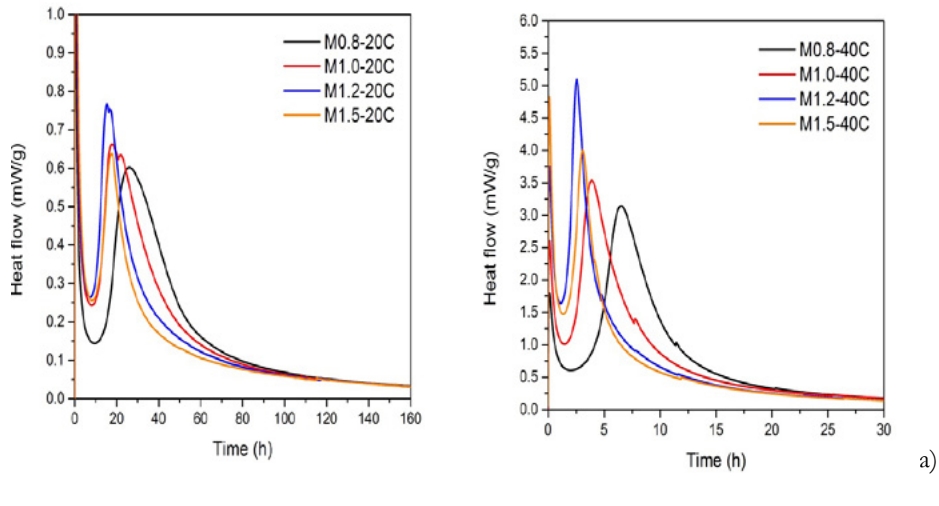


Figure 1 Heat flow of AASF mixtures at different temperature: (a) 20°C; (b) 40°C.

As expected, the cumulative heat for AASF at 40 °C were evidently higher than that at 20 °C due to the facilitating effect on reaction kinetics induced by a higher temperature. At 7d, M1.0 has the highest cumulative heat release followed by M0.8, M1.2 and M1.5. This trend is not consistent with the trend of the heat flow of the main reaction peak, which reached maximum when AA is 1.0. Therefore, it seems that a faster early age reaction is neither necessary nor sufficient for a higher reaction cumulative heat of AASF. In this study, the higher cumulative heat release of certain AA modulus could be related to the early age dissolution of species and the following-up geopolymerization process. With increasing AA modulus, the pH of AA drops [16]. Although in this way the early age dissolution is slowed down, higher AA modulus also increase the total amount of available species for geopolymerization in the liquids. Hence, an optimum activating conditions for overall reaction would exist which is favoured by its higher total heat release and higher amount of main reaction products.

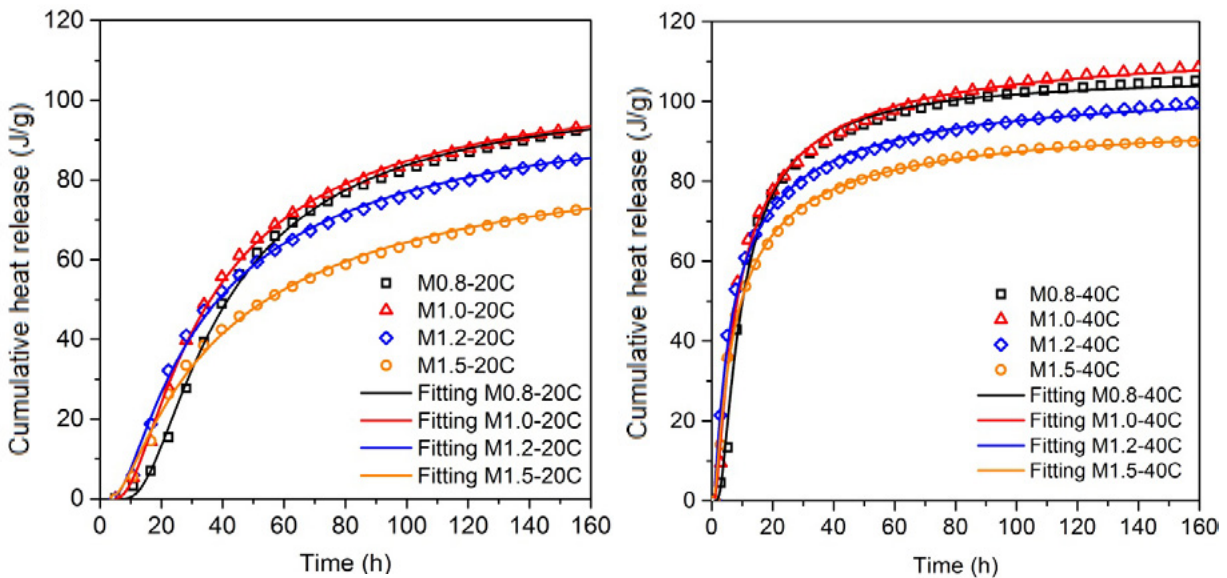


Figure 2 Cumulative heat release of AASF mixtures and curve fitting using the exponential model: (a) 20°C; (b) 40°C

The fitted parameters of exponential model for Q_{max} are presented in Table 3. As could be seen in Table 3, the accuracy of fitting (Adjusted R-Square) is rather satisfactory, implying the effectiveness of using exponential model for total heat fitting in AASF. In addition, the Q_{max} obtained exhibit identical trend with

increasing AA modulus when comparing with corresponding total heat release Q_{160h} of AASF up to 160h.

Table 3 Fitted parameters of exponential model for maximum total heat

Mixture		M0.8		M1.0		M1.2		M1.5	
		20 °C	40 °C	20 °C	40 °C	20 °C	40 °C	20 °C	40 °C
Total heat at 160h	Q_{160h}	92.8	105.1	93.6	108.5	85.7	99.8	73.1	89.9
	Q_{max}	103.55	106.65	107.46	114.95	103.30	106.80	94.47	97.24
Fitting parameters	τ	33.33	8.03	28.49	6.73	27.53	5.27	31.70	5.79
	β	1.41	1.22	1.14	0.86	0.95	0.73	0.84	0.78
Adjusted R-Square	r^2	0.998	0.996	0.999	0.996	0.998	0.996	0.997	0.997

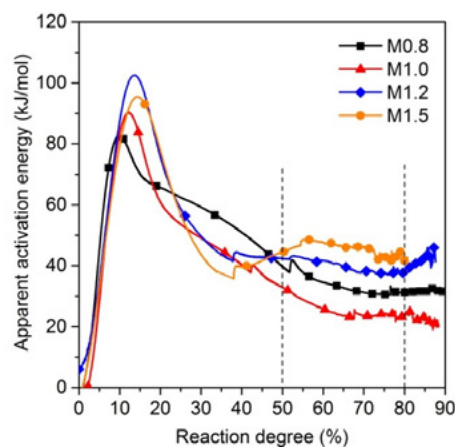


Figure 3 Apparent activation energy E_a as a function of reaction degree

According to previous studies of E_a of alkali-activated systems, comparison of related results is made and is shown in Table 4. It could be found that E_a determined in AASF is in general lower than those determined in AAS systems and close to the value determined in AASF systems. However, it is crucial to notice that by changing AA modulus, the global chemical reaction is already changed. E_a as one of its reflections, therefore, cannot be directly used to compare the chemical nature and ultimate total heat release of different AASF systems.

Table 4 Apparent activation energy E_a for different alkali-activated systems

E_a	Solid precursor	Activator (Liquids)	Reference
57.6	GGBS	NaOH+Na ₂ SiO ₃ (Na20% = 4%)	Fernandez et al [7].
53.6	GGBS	NaOH+Na ₂ SiO ₃	Zhou et al [8].
48.2 ± 2.9	GGBS	9M NaOH	Sun & Vollpracht [20]
48.2 ± 5.9	80%GGBS+20%FA	8M NaOH+Na ₂ SiO ₃	Joseph et al [9].
24.6 ~ 46.4	50%GGBS+50%FA	NaOH+Na ₂ SiO ₃ (Na20% = 4%)	Present study

4. Conclusions

The present study is aimed at investigating the role of alkali activator (AA) chemistry on the early age reaction kinetics of AASF made of 50 wt.% blast furnace slag and 50 wt.% fly ash. The effect of AA modulus on the heat evolution and cumulative reaction heat release was studied. Additionally, the apparent activation energy was determined using the incremental method and its variation over wide range of early age reaction was studied.

It was found that the AA modulus evidently influences the heat evolution of AASF. The cumulative heat release at 160h reached the maximum value at AA modulus of 1.0, followed by at 0.8, 1.2 and 1.5. This trend

is inversely related to the changes of the apparent activation energy E_a of AASF mixtures. Disagreement of the trend of early age heat flow and that of total reaction heat implies that a faster early age reaction does not necessarily result in a higher reaction total heat of AASF. The calculated E_a varies from 24.6 to 46.4 kJ/mol, which is in generally close to the values reported for GGBS based alkali activated systems. Furthermore, this study confirmed that the apparent activation energy of AASF was not only related to the chemistry of reactants but also reaction-stage dependent. Particularly it varied significantly at the very early age of reaction.

5. Acknowledgements

This research is carried out in Microlab, Delft University of Technology and supported by the Netherlands Organisation for Scientific Research (NWO), Grant No.729.001.013 and National Natural Science Foundation of China (NSFC), Grant No. 5151101050. Additionally, the second and third author would like to thank the financial support from China Scholarship Council (CSC).

7. References

1. Shi, C., D. Roy, and P. Krivenko, Alkali-activated cements and concretes. 2006: CRC press.
2. Davidovits, J., Geopolymers. *Journal of Thermal Analysis and Calorimetry*, 1991. 37(8): p. 1633-1656.
3. Duxson, P., et al., The role of inorganic polymer technology in the development of 'green concrete'. *Cement and Concrete Research*, 2007. 37(12): p. 1590-1597.
4. Ismail, I., et al., Modification of phase evolution in alkali-activated blast furnace slag by the incorporation of fly ash. *Cement and Concrete Composites*, 2014. 45: p. 125-135.
5. Puertas, F. and A. Fernández-Jiménez, Mineralogical and microstructural characterisation of alkali-activated fly ash/slag pastes. *Cement and Concrete composites*, 2003. 25(3): p. 287-292.
6. Lee, N.K. and H.K. Lee, Reactivity and reaction products of alkali-activated, fly ash/slag paste. *Construction and Building Materials*, 2015. 81: p. 303-312.
7. Fernández-Jiménez, A. and F. Puertas, Alkali-activated slag cements: kinetic studies. *Cement and concrete research*, 1997. 27(3): p. 359-368.
8. Huanhai, Z., et al., Kinetic study on hydration of alkali-activated slag. *Cement and Concrete Research*, 1993. 23(6): p. 1253-1258.
9. Joseph, S., S. Uppalapati, and O. Cizer, Instantaneous activation energy of alkali activated materials. *RILEM Technical Letters*, 2018. 3: p. 121-123.
10. Zhang, S., et al., Waste glass as partial mineral precursor in alkali-activated slag/fly ash system. *Cement and Concrete Research*, 2017. 102: p. 29-40.
11. Chithiraputhiran, S. and N. Neithalath, Isothermal reaction kinetics and temperature dependence of alkali activation of slag, fly ash and their blends. *Construction and Building Materials*, 2013. 45(0): p. 233-242.
12. Ravikumar, D. and N. Neithalath, Reaction kinetics in sodium silicate powder and liquid activated slag binders evaluated using isothermal calorimetry. *Thermochimica Acta*, 2012. 546(0): p. 32-43.
13. Poole, J.L., et al., Methods for calculating activation energy for Portland cement. *ACI Materials*

Journal, 2007. 104(1): p. 303-311.

14. Broda, M., E. Wirquin, and B. Duthoit, Conception of an isothermal calorimeter for concrete—Determination of the apparent activation energy. *Materials and Structures*, 2002. 35(7): p. 389-394.
15. Criado, M., et al., Effect of the $\text{SiO}_2/\text{Na}_2\text{O}$ ratio on the alkali activation of fly ash. Part II: ^{29}Si MAS-NMR Survey. *Microporous and Mesoporous Materials*, 2008. 109(1): p. 525-534.
16. Jansson, H., D. Bernin, and K. Ramser, Silicate species of water glass and insights for alkali-activated green cement. *Aip Advances*, 2015. 5(6): p. 067167.
17. Fernández-Jiménez, A., F. Puertas, and A. Arteaga, *Determination of kinetic equations of alkaline activation of blast furnace slag by means of calorimetric data*. *Journal of thermal analysis and calorimetry*, 1998. 52(3): p. 945-955.
18. Carette, J. and S. Staquet, Monitoring and modelling the early age and hardening behaviour of eco-concrete through continuous non-destructive measurements: Part I. Hydration and apparent activation energy. *Cement and Concrete Composites*, 2016. 73: p. 10-18.
19. Kada-Benameur, H., E. Wirquin, and B. Duthoit, Determination of apparent activation energy of concrete by isothermal calorimetry. *Cement and concrete research*, 2000. 30(2): p. 301-305.
20. Sun, Z. and A. Vollpracht, Isothermal calorimetry and in-situ XRD study of the NaOH activated fly ash, metakaolin and slag. *Cement and Concrete Research*, 2018. 103: p. 110-122.

Uncovering strength developing regularities of ultra-high performance concrete cured under high temperature

Z. Liu^{1,3}, Z. Shui¹, R. Yu^{1*}, Q. Song^{1,2}

¹State Key Laboratory of Silicate Materials for Architectures, Wuhan University of Technology, Wuhan 430070, China;

²School of Materials Science and Engineering, Wuhan University of Technology, Wuhan 430070, China.

³International School of Materials Science and Engineering, Wuhan University of Technology, Wuhan 430070, China

Abstract

Early studies suggested that fly ash has low volcanic ash activity and is an inert material in the early stage of hydration. It only acts as a filling agent and does not react with other substances. In fact, the activity of volcanic ash depends on factors such as the volcanic ash activity of the fly ash and the maintenance system. In addition to its pozzolanic activity, fly ash can also act as a micro-aggregate in the slurry to improve the microstructure and macroscopic properties of UHPC. To study the influence of different curing conditions on the mechanical properties of UHPC replacing parts of cement with fly ash, the current work replaced 20% of the cement content for fly ash to obtain a UHPC sample. The compressive strength, flexural strength and pore structure of Ultra High Performance Concrete under steam curing and hot water curing conditions were studied. The results of strength test reveal that the compressive strength can be improved by heated curing, especially hot water curing, which allowed the highest strength to reach 139 MPa after 48 hours. The results of the pore structure indicate that the cumulative pore volume of UHPC decreases with increasing curing time. And the cumulative pore size of hot water curing is lower than that of steam curing.

Keywords: Ultra-High Performance Concrete(UHPC), Fly ash, Curing system, pore structure

1. Introduction

In 1994, Larrard applied the concept of high packing density to concrete technology and first proposed the concept of Ultra-high Performance Concrete (UHPC) [1]. UHPC is defined as a cementitious composite with a compressive strength of more than 150 MPa and good ductility and durability[2, 3]. Typical UHPC includes very high levels of cement, silica fume, quartz powder, quartz sand, steel fibers and superplasticizers [4].UHPC is characterized by extremely low porosity and extremely high bulk density. It is because UHPC contains a great quantity of particles with low diameter and extremely low W/B[5]. Due to the addition of fibers, UHPC has a flexural strength of 15 MPa and an elastic modulus of 45 GPa [6]. At the International Conference on Ultra-High Performance Fiber Reinforced Concrete (UHPRFC) held in Marseille, France in 2009, the experts hold that UHPRFC is low-carbon, environmentally friendly and has excellent performance. It can be used to build low-carbon concretes structures and will be developed in the future.

As various mineral admixtures are increasingly used in cement-based materials, fly ash has also begun to be used in the preparation of UHPC. Ultra-high performance concrete with different content of fly ash has

different degrees of mechanical strength improvement, and reduces the porosity of UHPC samples and the content of calcium hydroxide in uhpc samples[7]. Therefore, the use of cement-fly ash-silica ash as a cementitious material for the preparation of UHPC has become more common.

The macro performance and microstructure of UHPC are closely related to the maintenance system. The best curing technique for UHPC was found to be heat curing[8]. Thermal curing can significantly promote cement hydration and pozzolanic reactions, thereby improving the mechanical properties of UHPC. Different curing conditions and curing time will also affect the performance of UHPC[9].

Based on this, the mechanical properties of UHPC for 95C steam curing and 95C hot water curing were studied. First, the modified Andersen & Andreasen model [10, 11]was used to obtain a densely packed concrete skeleton. Then, the properties of the UHPC cured at different systems are evaluated.

2. Methodology

2.1 Materials

In this study, the cementitious materials are Portland cement type 2 (52.5), fly ash and silica fume, and their chemical compositions are evaluated by X-ray fluorescence (XRF)as shown in Table 1. Fine aggregates are natural river sand with particle size of 0-0.6mm and apparent density of 2.6g/cm³. A polycarboxylic ether-based superplasticizer is used to adjust the workability of the UHPC.

Table 1:The chemical composition of cementitious materials(%)

Compound	Na ₂ O	MgO	Al ₂ O ₃	SiO ₂	P ₂ O ₅	SO ₃	K ₂ O	CaO	Fe ₂ O ₃	LOI
Cement	0.09	1.61	4.18	19.2	0.09	3.35	0.78	64.93	3.32	2.49
SF	0.13	0.47	0.25	94.65	0.17	0.69	0.84	0.36	0.15	2.29
FA	0.33	0.23	38.01	46.44	0.06	0.69	0.88	7.5	3.12	2.79

2.2 Methods

2.2.1 Mix design of UHPC

In this study, the modified Andreasen and Andersen model[10, 11] is used to design a dense particle packing skeleton, to improving the overall performance of the UHPC. The modified A & A model acts as a target function, as show in Eq.(1)

$$P(D) = \frac{D^q - D_{min}^q}{D_{max}^q - D_{min}^q}$$

Where $P(D)$ represents the percentage of particles smaller than size D to the total, D is the particle size (μm), D_{max} means the maximum particle size(μm); D_{min} means the minimum particle size(μm) and q is dispersion coefficient. In this study, the q value is fixed at 0.23.

By adjusting the composition of the raw materials, the optimized grading curve is approximated to the target curve calculated by the modified A & A model. In addition, the recipe of designed UHPC is shown in Table 2 and the particle size distributions of the ingredients, target and optimized grading curves of UHPC mixtures are shown in Figure 1.

Table 2:Recipe of the designed UHPC (kg/m³).

	C	FA	SF	Sand	Water	Sp
UHPC	660	200	188	990	195	34

(C: Cement, FA: Fly Ash, SF: Silica Fume, Sand: ϕ :0-0.6 mm; Sp: superplasticizer, solid content=18.2%).

2.2.2 Casting and Curing

First, add powder materials such as cement, silica fume, fly ash and sand to the mixer for 1 min. Second,

mix 90% of the water and superplasticizer and add to the mixer to stir at low speed until it is slurried. Third, add the remaining water and stir at high speed for 2 minutes to mix well. Last, Stir at low speed for 1 min to make the bubbles slowly dispatched. The fresh UHPC was cast in the moulds with the size of 40mm*40mm*160mm and were vibrated on the shaking table for 4 min[12].

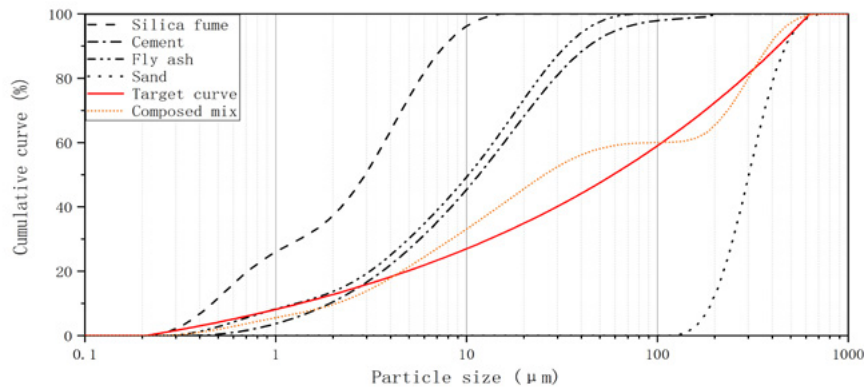


Figure 1: Particle size distributions of the ingredients, target and optimized grading curves of UHPC mixtures.

After 20 hours of standard curing in the curing room, the moulds were removed for hot water curing and steam curing respectively. The curing box heats up at a rate of 10 °C per hour. When temperature reaches 95 °C, the timing starts.

2.2.3 Mechanical properties

After high temperature for 6, 12, 18, 24, 48, 72, 96 and 120 hours, the compressive strength of the specimens are tested according to Chinese standards GB17671-1999. At least three specimens are tested for each batch.

2.2.4 Pore structure analysis

The pore structure (total porosity and pore size distribution) of the UHPC is measured by a micromeritics mercury porosimeter (named AutoPore IV-9500, pore size range: 3 nm-360 µm). Specimen is soaked in acetone firstly, and then dried in a vacuum atmosphere at 65 ± 2 °C for 4 h[13].

2.2.5 Hydration heat test

The hydration heat test was carried out using a TAM Air eight-channel isothermal microcalorimeter. The hydration heat test was carried out using a mortar having the same water-cement ratio (water-cement ratio = 0.21) as the concrete, and the quality of the test sample was determined according to the same total specific heat capacity as the inert reference sample. In this test, water was used as a reference sample, and the specific heat capacity of water was 4.2×10³ J/(kg·°C).

3. Results and discussion

3.1 Mechanical properties

Figure 2 and figure 3 shows the test results of UHPC compressive and flexible strength under different curing systems and different time. As can be seen from the figure, after steam curing at 95 °C or hot water curing at 95 °C for 48h, the compressive strength reaches 136MPa and 139MPa respectively. The flexible strength reached the highest after 18h of curing. We can also find that whether cured at steam or cured at hot water 24 h can be considered to be a stage boundary. In the earlier stage(0-24h), the compressive strength and flexible strength of UHPC is growing quickly. In the later stage(24-120h), there was no significant increase of the strength of UHPC. The strength of hot water curing is slightly higher

than that of steam curing.

The above phenomenon may be caused by changes in the microstructure of the concrete. In the earlier stage, as the hydration reaction proceeds rapidly, the hydration products continue to increase, the capillary pores continue to decrease, and the compressive strength and flexural strength increase rapidly. In the later stage, as the hydration proceeds further, the newly formed hydration product exceeds the volume of the capillary pores, and the micro-cracks in the concrete continuously generate and disappear. The strength is generally unchanged, but exhibits fluctuations[14-16]. The strength of the test piece for hot water curing is slightly higher than that of the same age test piece for steam curing[8, 17, 18]. This may be due to the difference between steaming and hot water curing heat transfer media, which are condensed water and hot water, respectively.

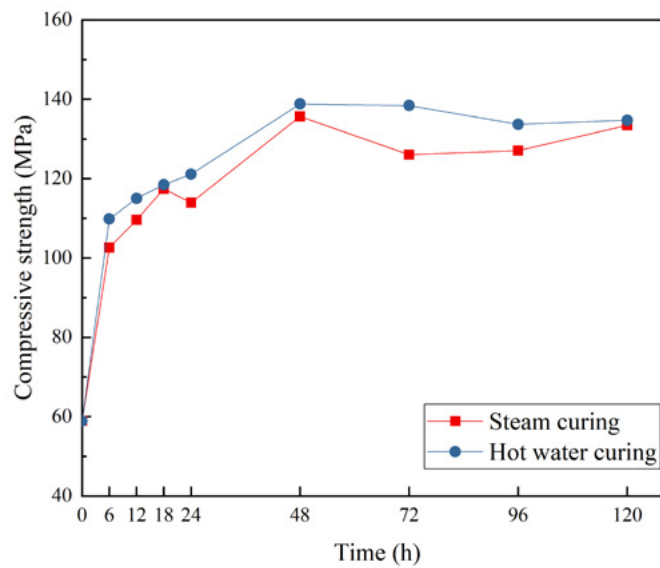


Figure 2: Compressive strength of UHPC cured at different systems (Steam curing, Hot water curing)

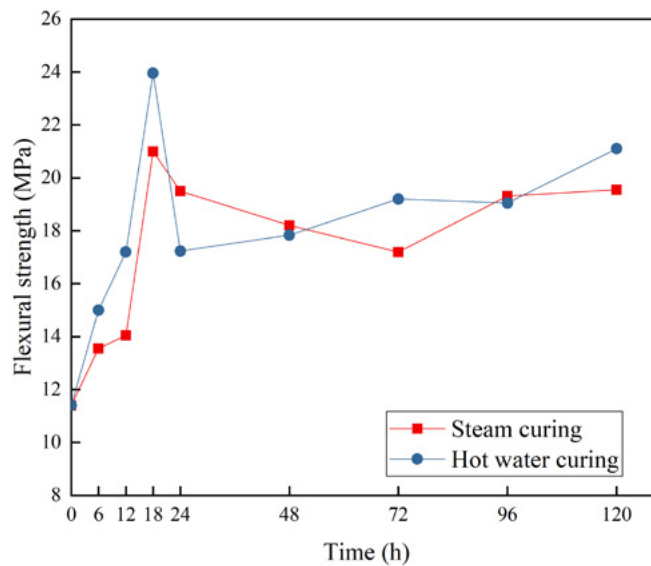


Figure 3: Flexible strength of UHPC cured at different systems (Steam curing, Hot water curing)

At the beginning of the heating, the steaming mainly passes steam and radiates heat. When steam first

meets the surface of a cold concrete, it immediately condenses into water, releasing a large amount of heat. Because the temperature gradient is too large, the thermal conductivity of concrete is small, resulting in large temperature stress, which has a great destructive effect on the concrete structure. In contrast, the heat transfer rate of hot water curing is relatively constant, because the concrete is immersed in water, and the water temperature rises slowly, and the damage to the concrete structure is small. During the constant temperature, due to the hydration reaction, the internal temperature of the concrete is higher than the external temperature, and the external heat is radiated, and the internal moisture is evaporated outward. While curing at steam, the moisture in the UHPC is easily vaporized, transferred, and forms a directional channel that affects UHPC strength[19].

3.2 Effect of curing condition on UHPC pore structure

The pore size distribution and cumulative pore volume of UHPC with different curing systems curing for 18h, 48, 120h are illustrated in Figs.4.

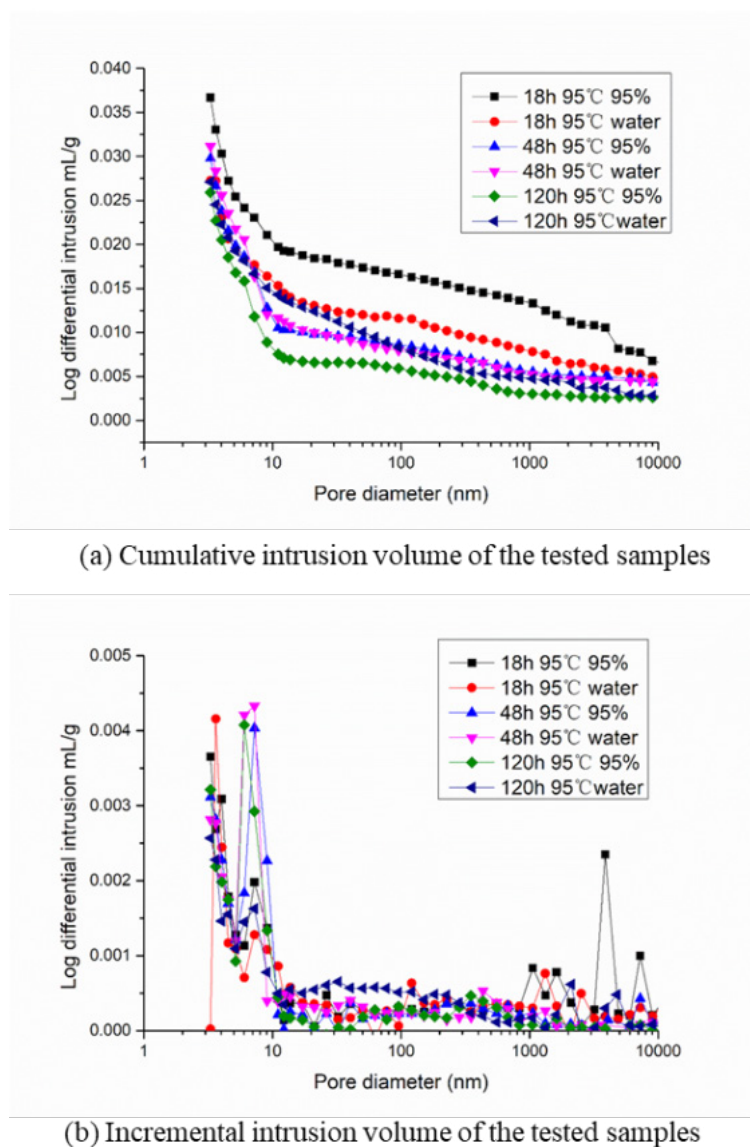


Figure 4: Pore size distributions of UHPC with different curing systems curing for 18h, 48h, 120h. It can be seen that as the curing time is extended, the cumulative pore volume of the UHPC is continuously reduced. And the cumulative pore size of hot water curing is lower than that of steam curing. This also

confirms the assumption that steam curing will form a directional channel inside the UHPC.

It can be seen from Figure 4 that most of the pore diameter is less than 30 nm, and it is known that pores within 30 nm are harmless or less harmful[20]. This means that this part of the pores has little negative impact on UHPC properties, while those close to 100 nm can significantly reduce concrete performance. It can also be found that as the curing time increases, the large pores are constantly changing into small holes. This is consistent with the findings of other researchers[21-23].

3.3 Hydration heat test

Fig.5 is the hydration exotherm of the slurry of the UHPC at room temperature. The hydration heat release curve can be divided into three stages. The first stage: slow hydration stage, the cumulative heat release of cement is less, the chemical reaction is slow, and the time of this stage is prolonged due to the addition of fly ash. In the second stage, the hydration heat is rapidly accumulating, and a severe hydration reaction occurs at this stage, releasing a large amount of heat, and the hydration heat curve is suddenly increased. In the third stage, the slow hydration stage, in which the hydration heat release rate is slowed down and the hydration heat release is less.

In the slow hydration stage (0-6h), the hydration heat release is only 6.4% of the final hydration heat release, the degree of reaction of the cement is still very low, and the concrete strength is at a lower level. In the second stage (6-48h), the hydration heat release is 80.3% of the final hydration heat release. With the rapid progress of hydration, the mechanical properties of concrete also increase rapidly. In the slow hydration stage, the hydration heat release is about 13.3% of the final hydration heat release, and the concrete strength does not increase significantly at this stage, but the internal structure is improved.

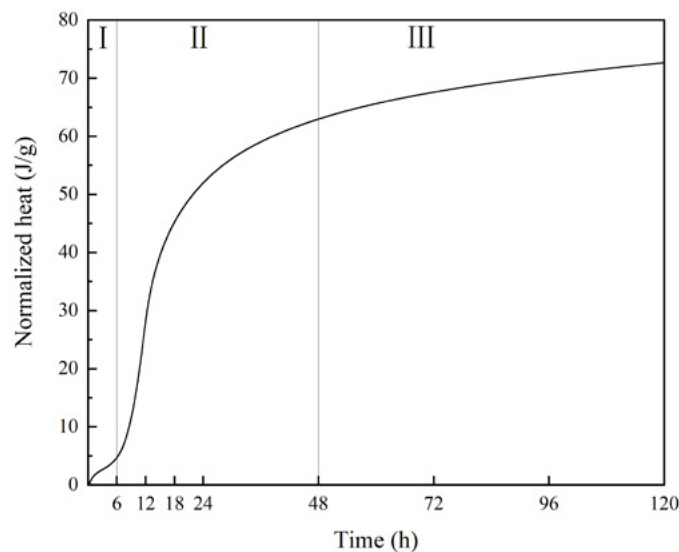


Figure 5: Hydration heat emission of cement pastes

4. Conclusions

This study explored the effects of curing systems on the development of mechanical strength and microstructure of concrete. According to the experimental results, the following conclusions can be drawn:

1. At the same temperature, the hot water curing strength is slightly higher than the steam curing. This is due to the difference in heat transfer medium. Due to the small thermal conductivity of concrete, the instability of steam heat transfer leads to large temperature stress inside the concrete, which has a great destructive effect on the concrete microstructure.

2. Under high temperature curing conditions, concrete strength rises rapidly in the early stage, and high temperature curing after peaking causes fluctuations in strength. This is because high temperature promotes hydration to generate more hydration products and microcracks are continuously generated and repaired.

5. Acknowledgment

The authors acknowledge the financial supports of National Nature Science Foundation Project of China (No. 51608409), National Nature Science Foundation Project of China (51679179), Major science and technology project in Zhongshan city, Guangdong province (2017A1021), Yang Fan plan of Guangdong Province (201312C12), Open research project of Advanced Engineering Technology Research Institute of Wuhan University of technology in Zhongshan city (WUT201802).

6. References

1. Larrard, F.o.d., *Concrete mixture proportioning : a scientific approach*. Modern concrete technology. 1999, London ; New York: E & FN Spon. xvii, 421 p.
2. Li, Y., K.H. Tan, and E.-H. Yang, *Influence of aggregate size and inclusion of polypropylene and steel fibers on the hot permeability of ultra-high performance concrete (UHPC) at elevated temperature*. Construction and Building Materials, 2018. **169**: p. 629-637.
3. Schmidt, M. and E. Fehling, *Ultra-high-performance concrete: research, development and application in Europe*. ACI Special publication, 2005. **228**: p. 51-78.
4. Lee, M.J., et al., *The Study of UHPC Precast Concrete Containing Incinerator Fly Ash*. Journal of Testing and Evaluation, 2018. **46**(1): p. 160-167.
5. Xu, Y., et al., *Experimental studies and modeling of creep of UHPC*. Construction and Building Materials, 2018. **175**: p. 643-652.
6. Fehling, E. and S. Sturwald, *Flexural Behaviour of UHPC with Fibres and Rebars*. Fib Symposium Prague 2011: Concrete Engineering for Excellence and Efficiency, Vols 1 and 2, 2011: p. 535-538.
7. Chen, T., X. Gao, and M. Ren, *Effects of autoclave curing and fly ash on mechanical properties of ultra-high performance concrete*. Construction and Building Materials, 2018. **158**: p. 864-872.
8. Prem, P.R., A.R. Murthy, and B.H. Bharatkumar, *Influence of curing regime and steel fibres on the mechanical properties of UHPC*. Magazine Of Concrete Research, 2015. **67**(18).
9. Ng, S., et al., *Effect of storage and curing conditions at elevated temperatures on aerogel-incorporated mortar samples based on UHPC recipe*. Construction And Building Materials, 2016. **106**: p. 640-649.
10. Song, Q., et al., *Steel fibre content and interconnection induced electrochemical corrosion of Ultra-High Performance Fibre Reinforced Concrete (UHPRFC)*. Cement and Concrete Composites, 2018. **94**: p. 191-200.
11. Yu, R., P. Spiesz, and H.J.H. Brouwers, *Mix design and properties assessment of Ultra-High Performance Fibre Reinforced Concrete (UHPRFC)*. Cement and Concrete Research, 2014. **56**: p. 29-39.
12. Huang, H., et al., *Influence of formwork wall effect on fiber orientation of UHPC with two casting methods*. Construction and Building Materials, 2019. **215**: p. 310-320.
13. Wang, X., et al., *Development of a novel cleaner construction product: Ultra-high performance concrete incorporating lead-zinc tailings*. Journal of Cleaner Production, 2018. **196**: p. 172-182.

14. Yu, R., P. Spiesz, and H.J.H. Brouwers, *Effect of nano-silica on the hydration and microstructure development of Ultra-High Performance Concrete (UHPC) with a low binder amount*. Construction and Building Materials, 2014. **65**: p. 140-150.
15. Buck, J.J., D.L. McDowell, and M. Zhou, *Effect of microstructure on load-carrying and energy-dissipation capacities of UHPC*. Cement and Concrete Research, 2013. **43**: p. 34-50.
16. Sadrmomtazi, A., S. Tajasosi, and B. Tahmouresi, *Effect of materials proportion on rheology and mechanical strength and microstructure of ultra-high performance concrete (UHPC)*. Construction and Building Materials, 2018. **187**: p. 1103-1112.
17. Shen, P., et al., *Experimental investigation on the autogenous shrinkage of steam cured ultra-high performance concrete*. Construction and Building Materials, 2018. **162**: p. 512-522.
18. Mosaberpanah, M.A. and O. Eren, *Effect of quartz powder, quartz sand and water curing regimes on mechanical properties of UHPC using response surface modelling*. Advances in Concrete Construction, 2017. **5**(5): p. 481-492.
19. Du, H., S. Du, and X. Liu, *Durability performances of concrete with nano-silica*. Construction and Building Materials, 2014. **73**: p. 705-712.
20. Fan, Y.-f. and H.-y. Luan, *Pore structure in concrete exposed to acid deposit*. Construction and Building Materials, 2013. **49**: p. 407-416.
21. Wang, Z., et al., *Experimental and numerical investigation of the interfacial properties of non-steam-cured UHPC-steel composite beams*. Construction and Building Materials, 2019. **195**: p. 323-339.
22. Kang, S.-H., S.-G. Hong, and J. Moon, *The effect of superabsorbent polymer on various scale of pore structure in ultra-high performance concrete*. Construction and Building Materials, 2018. **172**: p. 29-40.
23. Lee, N.K., et al., *Microstructural investigation of calcium aluminate cement-based ultra-high performance concrete (UHPC) exposed to high temperatures*. Cement and Concrete Research, 2017. **102**: p. 109-118.

Depth of penetration for steel-tube-confined concrete targets penetrated by rigid sharp-nosed projectiles

Q. Tan¹, D. Song², Z. Jiang²

¹ College of Aerospace Science and Engineering, National University of Defense Technology, Changsha, 410073, P.R. China.

² Undergraduate School, National University of Defense Technology, Changsha, 410072, P.R. China.

Abstract

Steel-tube-confined concrete (STCC) targets have excellent anti-penetration performance as a result of the confinement effect of steel tube to in-filled concrete. Therefore, establishing engineering models to predict depth of penetration (DOP) of STCC targets has application value for the potential application of STCC in protective structures. When the STCC targets are impacted by rigid sharp-nosed projectiles, dynamic cylindrical cavity-expansion model is used to get the approximate solutions of pressure at cavity wall with the inclusion of confinement effect and establish the formulas of DOP for STCC targets in this paper. Firstly, several assumptions including Heok-Brown criterion describing concrete in comminuted region, confinement effect of steel tube to in-filled concrete and incompressibility of concrete etc., are made to establish the basic equations of dynamic cylindrical cavity-expansion model. And then, approximate solutions of pressure at cavity wall are gained under the possible response modes including “elastic-cracked-comminuted”, “cracked-comminuted” and “full-comminuted”. Moreover, the scope of application and procedure of numerical solution are also derived. Lastly, on the basis of approximate solutions of pressure at cavity wall, an engineering model is proposed to predict the DOP of STCC targets normally penetrated by rigid sharp-nosed projectiles, and the existing tests of STCC targets normally penetrated by armor piecing projectile (APP) are used to validate the DOP formulas. The comparison results show that the engineering model in this paper is in good agreement with the results of penetration experiments, which further reveals that the engineering model is applicable to the calculation of DOP of the STCC targets normally penetrated by the rigid sharp-nosed projectiles with an impact velocity less than 830 m/s.

Keywords: Penetration mechanics, depth of penetration (DOP), dynamic cylindrical cavity-expansion; steel-tube-confined concrete (STCC), finite targets.

1. Introduction

With the rapid development of weapons and ammunition, a variety of concrete structures and protective facilities are facing more and more serious threat of projectile impact, such as the concrete protective walls of nuclear power plant and concrete shelters of protective engineering [1, 2]. As concrete is easy to crack or fracture under projectile impact, it has been a critical issue to improve the strength, ductility and toughness of concrete under impact loading [3], in which steel-tube-confined concrete (STCC) is one of the effective ways [4, 5]. STCC targets have excellent penetration resistance in comparisons with unconfined concrete targets. The penetration tests performed by Wan et al. [4] revealed that steel tube could restrict the radial

displacement of the in-filled concrete and development of radial cracks, and the damage was restrained within the element of STCC targets when impacted by projectiles; the depth of penetration (DOP) of STCC targets can be reduced by 10%–20% than that of semi-infinite targets. Therefore, proposing an appropriate DOP model for STCC targets is of significant importance to conveniently and efficiently expand the application of STCC to protective structures.

DOP models based on spherical or cylindrical cavity-expansion approximation have been extensively used [6, 7]. The spherical cavity-expansion (SCE) approximation model is shown to be suitable to deep penetration problems of semi-infinite targets impacted by ogival nose rigid projectiles [8, 9], while the cylindrical cavity-expansion (CCE) approximation model is more applicable to perforation problems with ductile hole-growth and deep penetration problems of semi-infinite targets impacted by rigid conical or other sharp-nosed projectiles or [10–12]. The CCE approximation model has been employed to solve the penetration problems of dry porous rock [13, 14], soil [15] and concrete [16, 17] targets. Mastilovic and Krajcinovic [18] proposed CCE approximation model for semi-infinite targets on the assumption that the target is divided into elastic, process (damaged), crushed (comminuted) and cavity zones, and material in crushed (comminuted) zone yields according to the Mohr–Coulomb (M–C) criterion. Forrestal and Tzou [19] also used M–C criterion to capture the mechanical performance of concrete in the comminuted zone.

Macek and Duffey [20] regarded the targets as incompressible materials, and proposed a finite SCE approximation model for the analysis of rigid ogival-nose projectiles obliquely penetrating into geological medium to consider the effect of free surface at the initial stage. On the basis of incompressible M–C material and the SCE approximation model for semi-infinite targets proposed by Forrestal and Tzou [19], Warren et al. [21, 22] proposed a dynamic finite spherical cavity-expansion (FSCE) approximation model for the targets obliquely impacted by projectiles. With targets treated as incompressible M–C material, Fang et al. [23] constructed a decay function to include the free-surface effect for geological targets by assuming that plastic-cracked-elastic response region exists during the cavity-expansion process. Chen et al. [24] proposed a fast algorithm to predict penetration trajectory in simulation of a rigid steel projectile obliquely penetrating into a limestone target and the effect of cratering and free surface, and separation-reattachment phenomenon were involved. However, the models mentioned above do not include the influence of lateral free boundary and also do not account for the confinement effect of restraints imposed on the target material. Zhen et al. [25] established a finite cylindrical cavity-expansion (FCCE) approximation model for perfect elastic-plastic compressible and incompressible materials with the inclusion of the influence of the lateral free boundary. On the basis of assumptions of incompressible material and the Modified-Griffith (M–G) criterion [26, 27], which shows the same form with Hoek–Brown (H–B) criterion [28, 29], Meng et al. [30] proposed a dynamic FSCE approximation model and DOP model for confined concrete targets normally impacted by rigid projectile. The results showed that under high confinement, the empirical constant m in the M–G criterion was recommended to be above 15 on the basis of triaxial experiments. However, in the practical application to calculation of DOP for armor piercing projectile (APP) with conical core normally penetrating into STCC targets in Ref. [4], the calculated results with m ranged between 6 and 8 agree well with the test results, i.e., the value of m in Ref. [30] is lower than the recommended values. The reason is that under conditions that there is no coarse aggregate within concrete of the targets in Ref. [4] and the penetration resistance is overestimated by the FSCE approximation model. Moreover, the geometric shape of an STCC target with finite lateral dimensions and tunneling cavity response is approximately cylindrical when the STCC target is normally penetrated by rigid conical or other sharp-nosed projectiles, which is close to the FCCE models.

On the basis of the above backgrounds and problems, a dynamic FCCE approximation model is proposed to analyze the stress distribution during the penetration process and predict the DOP of STCC targets

normally impacted by rigid conical or other sharp-nosed projectiles. Firstly, a dynamic FCCE approximation model is established for STCC targets with the H–B criterion and incompressible material, and the equations of stresses and displacements in STCC targets are proposed. Moreover, formula of the DOP for STCC targets based on the dynamic FCCE approximation model is developed and then the relevant penetration tests of STCC targets are employed to validate the DOP model.

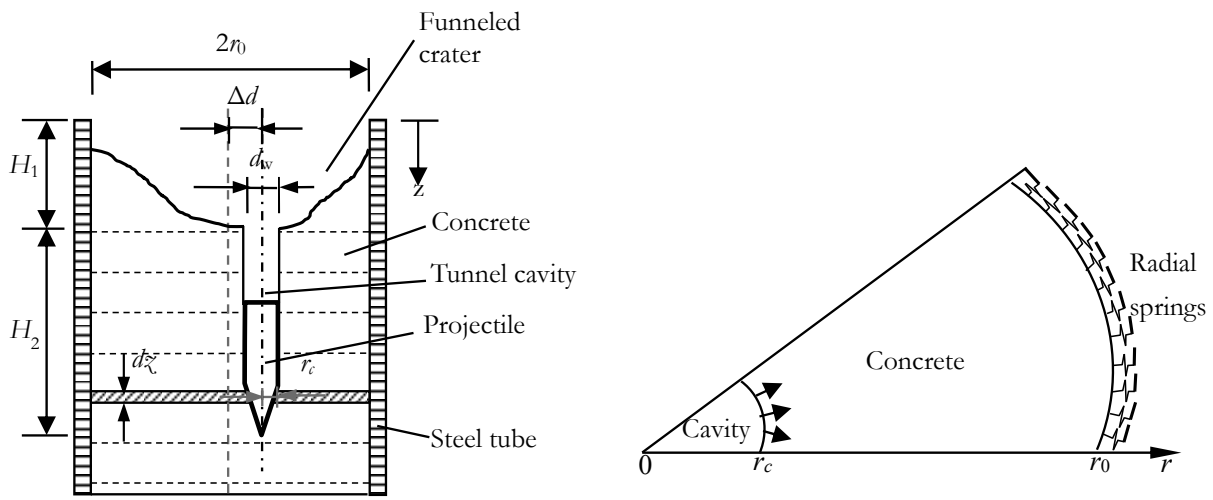
2. Dynamic FCCE model for STCC targets

2.1 Simplification of penetration problems

On the basis of the above backgrounds and problems, a dynamic FCCE approximation model is proposed to analyze the stress distribution during the penetration process and predict the DOP of STCC targets normally impacted by rigid conical or other sharp-nosed projectiles. Firstly, a dynamic FCCE approximation model is established for STCC targets with the H–B criterion and incompressible material, and the equations of stresses and displacements in STCC targets are proposed. Moreover, the key parameters on cavity-expansion process, radial stress at cavity wall and critical cavity radii are also analyzed. Lastly, formula of the DOP for STCC targets based on the dynamic FCCE approximation model is developed and then the relevant penetration tests of STCC targets are employed to validate the DOP model.

The penetration process of projectiles into STCC targets includes the cratering and tunneling stages [4], as shown in Fig. 1 (a). Generally, the DOP in the cratering stage (H_1) is based on empirical formula according to experimental results, while the DOP in the tunneling stage (H_2) is usually calculated by analytical models based on cavity-expansion approximation models. Like the results of cavity-expansion approximation model for semi-infinite targets [8–12], FCCE approximation model is expected to be more applicable to analyze the penetration problem of STCC targets normally penetrated by rigid conical or other sharp-nosed projectiles.

For FCCE approximation model, the STCC targets can be idealized as infinitely thin layers normal to the impacting direction and particles of the target material move in a radial direction during the penetration process shown in Fig. 1 (a). And then the penetration analysis can be simplified to one dimensional problem, as shown in Fig. 1 (b).



1a) Penetration process of STCC target 1b) Diagram for process of cavity expansion

Figure 1: Schematic diagram for FCCE models.

Like the dynamic FSCE approximation model for confined concrete targets proposed by Meng et al. [30], some assumptions are further employed to establish the dynamic FCCE approximation model for STCC targets.

(1) Target concrete is a fully incompressible material with Poisson’s ratio $\nu=0.5$. By ignoring the compressibility and strain-softening of concrete, the cavity-expansion pressure would be overestimated; and if shear dilatancy, strain-rate, strain-hardening of concrete are not included, the cavity-expansion pressure would be underestimated. Therefore, under low and medium penetration velocity, the above effects of concrete material generally offset each other, which indicates the incompressible material assumption of target concrete is reasonable [30–32]. Additionally, incompressible material assumption excludes the effect of stress wave and thus greatly simplifies the problem with possible analytical solutions.

(2) Confinement effect of steel tube to concrete is equivalent to a series of linear radial springs with stiffness (K) shown in Fig. 1 (b). As for the circular STCC targets, the equivalent confining stiffness (K) is shown in Eq. (1) [4].

$$K = \frac{E_s \delta}{r_0^2} \tag{1}$$

Where E_s , δ and r_0 are the elastic modulus, thickness and internal radius of steel tube, respectively.

(3) Finite cavity-expansion is assumed as a concentric cylindrical cavity expanding at a constant velocity \dot{r}_c from initial radius zero to the radius of r_0 . Under low and medium penetration velocity, elastic, cracked and comminuted regions generally appear in the STCC targets [30]. A typical finite cavity-expansion process includes three phases, i.e., “elastic-cracked-comminuted” “cracked- comminuted” and “completely comminuted” phases, as shown in Fig. 2. In Fig. 2, r_c , r_{cr} and r_p are the cavity radius, radius of the interface between the elastic and cracked zones and radius of the interface between the cracked and comminuted zones, respectively.

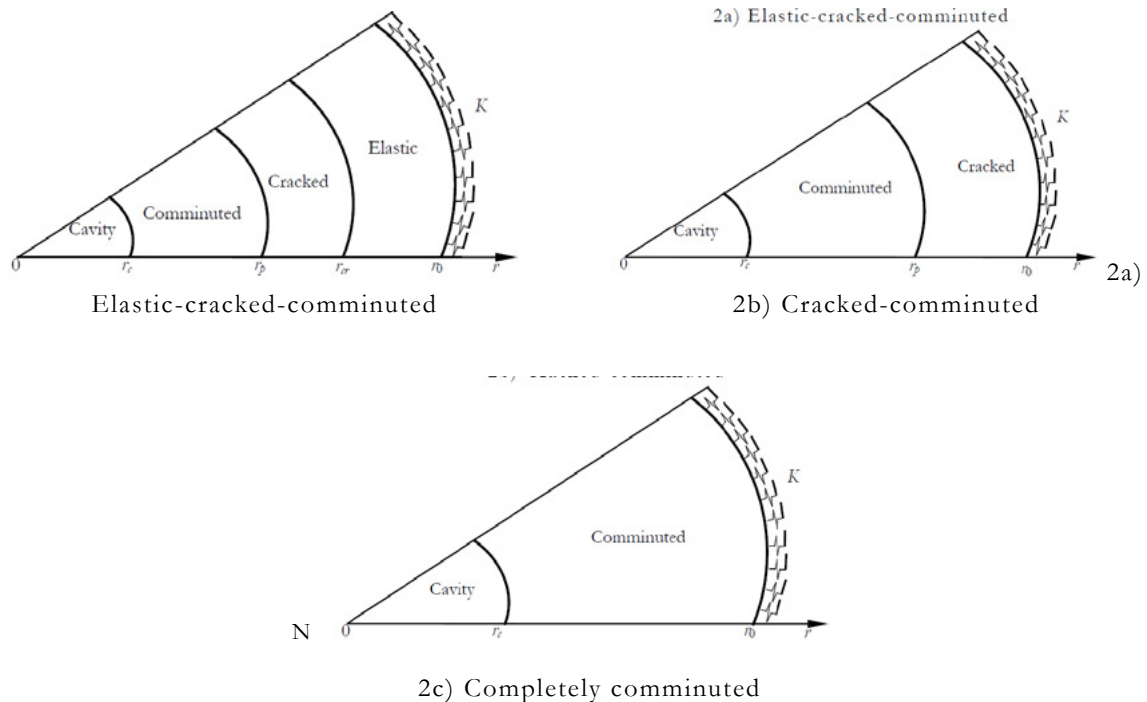


Figure 2: Schematic diagram of a typical cavity-expansion process.

For “elastic-cracked-comminuted” phase shown in Fig. 2 (a), the elastic zone is surrounded by the radius r_0 of core concrete as the outer boundary. When the cracked zone expands to the outer boundary of core concrete ($r_{cr}=r_0$), the elastic zone disappears; and the first phase comes to end ($r_c=r_{c1}$, r_{c1} is a critical cavity radius).

For “cracked-comminuted” phase shown in Fig. 2 (b), the cracked zone takes the radius r_0 of core concrete as the outer boundary, i.e., $r_{cr}=r_0$; when the comminuted zone reaches the outer boundary of the core

concrete, the cracked zone disappears, then the second phase ends ($r_p=r_0$, $r_c=r_{c2}$, r_{c2} is another critical cavity radius and larger than r_{c1}).

For “completely comminuted” phase shown in Fig. 2 (c), the external radius of the comminuted zone is r_0 , i.e., $r_p \equiv r_0$; and the third phase ends when the elastic constraint fails.

Moreover, in cracked zone, the radial stress of the incompressible target concrete is continuous with the circumferential stress $\sigma_\theta=0$, and the radial stress gets to equal the uniaxial compressive strength (σ_u) at the interface between the comminuted and cracked zones. In elastic zone, the circumferential stress is equal to the uniaxial tensile strength (σ_t) at the elastic-cracked interface.

(4) As strength performance of confined concrete is similar to that of the surrounding rock, the nonlinear H–B criterion is used to describe the confined concrete in comminuted region under triaxial compression [30]. The equation of H–B criterion is Eq. (2) for intact rock [28, 29].

$$\frac{\sigma_1}{\sigma_u} = \frac{\sigma_3}{\sigma_u} + \sqrt{m \frac{\sigma_3}{\sigma_u} + 1} \tag{2}$$

Where, σ_u , σ_1 and σ_3 are the uniaxial compressive strength, first and third principal stresses respectively, measured positive in compression; and m is an empirical constant.

For cylindrical coordinate system, equilibrium equation of axial stress (σ_z) is shown in Eq. (3) and further simplified according to assumption (1) ($\nu=0.5$).

$$\sigma_z = \delta(\sigma_r + \sigma_\theta) = \frac{1}{2}(\sigma_r + \sigma_\theta), \quad \sigma_r > \sigma_\theta \tag{3}$$

Where σ_z , σ_r and σ_θ are the axial, radial and circumferential stresses, respectively, and taken positive in compression.

Generally, the three principal stresses in cylindrical coordinate system meet relationship of Eq. (4).

$$\sigma_1 = \sigma_r, \sigma_2 = \sigma_z, \sigma_3 = \sigma_\theta \tag{4}$$

Transforming Eq. (2) into the function of σ_r can give Eq. (5).

$$\frac{\sigma_\theta}{\sigma_u} = \frac{\sigma_r}{\sigma_u} + \frac{m}{2} \sqrt{m \frac{\sigma_r}{\sigma_u} + n} \tag{5}$$

Where $n = m^2/4 + 1$.

2.2 Basic equations

For solutions of FCCE approximation model, as the density of concrete keeps constant according to assumption (1), the equations of momentum and mass conservation and the relations between particle velocity and displacement in the cylindrical coordinates are as follows [12].

$$\frac{\partial \sigma_r}{\partial r} + \frac{\sigma_r - \sigma_\theta}{r} = -\rho \left(\frac{\partial v}{\partial t} + v \frac{\partial v}{\partial r} \right) \tag{6}$$

$$\frac{\partial(r-u)^2}{\partial r} = 2r \tag{7}$$

Where u and v are displacement and velocity of particle, respectively, with outward motion considered positive; ρ is the density of material.

The particle velocity can be obtained by time derivative of the particle displacement.

$$v = \frac{\partial u}{\partial t} + v \frac{\partial u}{\partial r} \quad (8)$$

At cavity wall ($r=r$), the particle displacement (u) is equal to the cavity radius ($r=r$), and integral of Eq. (7) would get

$$(r-u)^2 = r^2 - r_c^2 \quad (9)$$

Derivation of time from Eq. (9) gets

$$v = \frac{r_c}{r} \dot{r}_c \quad (10)$$

At the interface between concrete and steel tube ($r=r_0$), the boundary conditions can be expressed as

$$\sigma_r(r=r_0) = Ku_0, \quad u_0 = u(r=r_0) = r_0 - \sqrt{r_0^2 - r_c^2} \quad (11)$$

According to assumption (3) about the elastic-cracked and cracked-comminuted interfaces, the stresses at the interfaces are

$$\sigma_\theta(r=r_c^+) = -|\sigma_t| \quad (12)$$

$$\sigma_r(r=r_p^-) = \sigma_u \quad (13)$$

On the basis of assumption (3) with a constant cavity-expansion velocity (\dot{r}_c), integrating Eq. (10) with Eq. (6) obtains

$$\frac{d\sigma_r}{dr} + \frac{\sigma_r - \sigma_\theta}{r} = -\rho \dot{r}_c^2 \left(\frac{1}{r} - \frac{2r_c^2}{r^3} \right) \quad (14)$$

Furthermore, when compressibility of concrete is ignored according to assumption (1), the continuous conditions at interface are obtained as follows [19].

$$u_2 = u_1, v_2 = v_1, \sigma_{r2} = \sigma_{r1} \quad (15)$$

Where figure subscripts (1 and 2) represent the front and rear of the interfaces, respectively.

2.3 Solutions of concrete responses

2.3.1 Elastic-cracked-comminuted phase ($r_c < r < r_0$)

In the elastic region ($r_c \leq r \leq r_0$, $r_c < r$), relationships between strain and displacement can be described with Eq. (16) under the conditions of small deformation.

$$\varepsilon_r = -\frac{\partial u}{\partial r}, \quad \varepsilon_\theta = -\frac{u}{r} \quad (16)$$

Derivative of r for Eq. (9) and in combination with Eq. (16) could gain the relationship between strain and displacement.

$$\varepsilon_r - \varepsilon_\theta = -\left(\frac{\partial u}{\partial r} - \frac{u}{r} \right) = \left(\frac{r_c}{r} \right)^2 \left(1 - \frac{r_c^2}{r^2} \right)^{-\frac{1}{2}}$$

Using the Hooke law with assumption (1) ($\nu=0.5$) and ignoring the high-order terms of Eq. (17) get

$$\sigma_r - \sigma_\theta = \frac{2E}{3} \left(\frac{r_c}{r} \right)^2 \quad (18)$$

At the elastic-cracked interface ($r=r_{cr}$), substituting Eq. (12) into Eq. (18) gets

$$\sigma_r = \frac{2E}{3} \frac{r_c^2}{r_e^2} - |\sigma_t| \quad (19)$$

Combining Eq.(14) with Eq. (18) can obtain

$$\frac{d\sigma_r}{dr} = -\frac{2E}{3} \frac{r_c^2}{r^3} - \rho \dot{r}_c^2 \left(\frac{1}{r} - \frac{2r_c^2}{r^3} \right) \quad (20)$$

Integral of Eq. (20) with the boundary conditions of Eq. (11) gains the radial stress (σ_r).

$$\sigma_r = \frac{E}{3} \left(\frac{r_c^2}{r^2} - \frac{r_c^2}{r_0^2} \right) - \rho \dot{r}_c^2 \left(h \frac{r}{r_0} + \frac{r_c^2}{r^2} - \frac{r_c^2}{r_0^2} \right) + K_0 \left[1 - \left(1 - \frac{r_c^2}{r_0^2} \right)^{\frac{1}{2}} \right] \quad (21)$$

The circumferential stress (σ_θ) in elastic region is gotten by combining Eq. (21) and Eq. (18).

$$\sigma_\theta = -\frac{E}{3} \left(\frac{r_c^2}{r^2} + \frac{r_c^2}{r_0^2} \right) - \rho \dot{r}_c^2 \left(h \frac{r}{r_0} + \frac{r_c^2}{r^2} - \frac{r_c^2}{r_0^2} \right) + K_0 \left[1 - \left(1 - \frac{r_c^2}{r_0^2} \right)^{\frac{1}{2}} \right] \quad (22)$$

Combining Eq. (21) with Eq. (19) can gain the equation of interface radius (r_{cr}).

$$\frac{E}{3\sigma_u} \left(\frac{r_c^2}{r_e^2} + \frac{r_c^2}{r_0^2} \right) - \frac{|\sigma_t|}{\sigma_u} = \frac{K_0}{\sigma_u} \left[1 - \left(1 - \frac{r_c^2}{r_0^2} \right)^{\frac{1}{2}} \right] - \frac{\rho \dot{r}_c^2}{\sigma_u} \left(h \frac{r_e}{r_0} + \frac{r_c^2}{r_e^2} - \frac{r_c^2}{r_0^2} \right) \quad (23)$$

The critical cavity radius r_{c1} is gained by definition of $r_{cr}=r_0$ in Eq. (23). The “elastic-cracked-comminuted” phase would come to end if $r_{cr}=r_0$, and then Eq. (23) can be further simplified as

$$\frac{K_0}{\sigma_u} \left[1 - \left(1 - \frac{r_{c1}^2}{r_0^2} \right)^{\frac{1}{2}} \right] + \frac{|\sigma_t|}{\sigma_u} = \frac{2E}{3\sigma_u} \frac{r_{c1}^2}{r_0^2} \quad (24)$$

It can be seen from Eq. (24) that r_{c1}/r_0 is only related to the parameters of the targets (Kr_0/σ_u , $|\sigma_t|/\sigma_u$ and E/σ_u) but independent of the cavity-expansion velocity.

In the cracked region ($r_p \leq r \leq r_{cr}$), according to assumption (3), there is no circumferential stress, i.e., $\sigma_\theta=0$, and then integral of Eq. (14) gains

$$\sigma_r = \frac{C}{r} - \rho \dot{r}_c^2 \left(1 + 2 \frac{r_c^2}{r^2} \right) \tag{25}$$

Where, C is the integral constant.

Moreover, on the basis of the continuous conditions of the radial stress (σ_r) related to Eq. (15), substituting Eq. (19) into Eq. (25) can provide C as

$$C = r_e \left[\frac{2E}{3} \left(\frac{r_c}{r_e} \right)^2 - |\sigma_t| + \rho \dot{r}_c^2 \left(1 + 2 \frac{r_c^2}{r_e^2} \right) \right] \tag{26}$$

The integral constant (C) can be further simplified by substituting Eq. (13) in to Eq. (25).

$$C = r_p \left[\sigma_u + \rho \dot{r}_c^2 \left(1 + 2 \frac{r_c^2}{r_p^2} \right) \right] \tag{27}$$

Integration of Eqs. (26) and (27) gains the relationship between r_p and r_{cr} , as shown in Eq. (28).

$$r_{cr} \left[\frac{2E}{3} \left(\frac{r_c}{r_{cr}} \right)^2 - |\sigma_t| + \rho \dot{r}_c^2 \left(1 + 2 \frac{r_c^2}{r_{cr}^2} \right) \right] = r_p \left[\sigma_u + \rho \dot{r}_c^2 \left(1 + 2 \frac{r_c^2}{r_p^2} \right) \right] \tag{28}$$

Interface radii r_{cr} and r_p can be solved by combining Eq. (23) and Eq. (28).

If the cracked zone is absent during the FCCE process, by definition of $r_{cr} = r_p$ in Eq. (28), it gets

$$\frac{r_c}{r_e} = \frac{r_c}{r_p} = \sqrt{\frac{3(\sigma_u + |\sigma_t|)}{2E}} \tag{29}$$

Integration of Eqs. (23) and (29) can gain the cavity-expansion velocity ($\dot{r}_{c,max}$) for response mode exchange, i.e., $\dot{r}_{c,max}$ is the maximum cavity-expansion velocity for the “elastic-cracked- comminuted” phase during the FCCE process; and there is no cracked zone in targets at initial expansion if cavity-expansion velocity exceeds $\dot{r}_{c,max}$, which belongs to hypervelocity penetration problems.

$$\dot{r}_{c,max} = \left\{ \frac{\left[\frac{E}{3\sigma_u} \left(\frac{r_c}{r_0} \right)^2 + \frac{\sigma_u - |\sigma_t|}{2\sigma_u} - \frac{K_0}{\sigma_u} \left[1 - \left(1 - \frac{r_c^2}{r_0^2} \right)^{\frac{1}{2}} \right] \right] \sigma_u}{\frac{r_c^2}{r_0^2} - h \frac{r_c}{r_0} + \frac{1}{2} h \frac{3(\sigma_u + |\sigma_t|)}{2E} - \frac{3(\sigma_u + |\sigma_t|)}{2E}} \rho \right\}^{\frac{1}{2}} \tag{30}$$

It can be seen from Eq. (30) that $\dot{r}_{c,max}$ is related to the geometric and mechanical parameters of the targets.

Then, combining Eq. (25) with Eq. (26) gets

$$\sigma_r = \frac{r_{cr}}{r} \left[\frac{2E}{3} \left(\frac{r_c}{r_{cr}} \right)^2 - |\sigma_t| + \rho \dot{\epsilon}^2 \left(1 + 2 \frac{r_c^2}{r_{cr}^2} \right) \right] - \rho \dot{\epsilon}^2 \left(1 + 2 \frac{r_c^2}{r^2} \right) \quad (31)$$

In the comminuted region ($r_c \leq r \leq r_p$), transformation of Eq. (5) gives

$$\sigma_r - \sigma_\theta = \sigma_u \left(\sqrt{m \frac{\sigma_r}{\sigma_u} + n} - \frac{m}{2} \right) \quad (32)$$

Combining Eq. (32) with Eq. (14) provides

$$\frac{d\sigma_r}{dr} = \frac{\sigma_u \left(\frac{m}{2} - \sqrt{m \frac{\sigma_r}{\sigma_u} + n} \right)}{r} - \rho \dot{\epsilon}^2 \left(\frac{1}{r} - \frac{2r_c^2}{r^3} \right) \quad (33)$$

Eq. (33) is a nonlinear ordinary differential equation, and could be solved by Runge-Kutta method with the boundary conditions of Eq. (13).

2.3.2 Cracked-comminuted phase ($r_{c1} \leq r_c < r_{c2}$)

In the cracked region ($r_p \leq r \leq r_0$), radial stress (σ_r) can still be obtained by Eqs. (25) and (27). The equation of boundary conditions is still Eq. (11) at $r=r_0$, and then the integral constant C in Eq. (25) can be gained by combination of Eqs. (25) and (11).

$$C = r_0 \left[K_0 \left[1 - \left(1 - \frac{r_c^2}{r_0^2} \right)^{\frac{1}{2}} \right] + \rho \dot{\epsilon}^2 \left(1 + 2 \frac{r_c^2}{r_0^2} \right) \right] \quad (34)$$

The radial stress (σ_r) can be gained by substituting Eq. (34) into Eq. (25).

$$\sigma_r = \frac{r_0}{r} \left[K_0 \left[1 - \left(1 - \frac{r_c^2}{r_0^2} \right)^{\frac{1}{2}} \right] + \rho \dot{\epsilon}^2 \left(1 + 2 \frac{r_c^2}{r_0^2} \right) \right] - \rho \dot{\epsilon}^2 \left(1 + 2 \frac{r_c^2}{r^2} \right) \quad (35)$$

In the comminuted region ($r_c \leq r \leq r_p$), the solution procedure of the control equation Eq. (33) with the boundary conditions of Eq. (13) is similar to that in the “elastic-cracked-comminuted” phase.

At the cracked-comminuted interface, the Eq. (36) is gotten by integrating Eqs. (27) with (34).

$$\frac{Kr_0}{\sigma_u} \left[1 - \left(1 - \frac{r_c^2}{r_0^2} \right)^{\frac{1}{2}} \right] + \frac{\rho \dot{\epsilon}^2}{\sigma_u} \left(1 + 2 \frac{r_c^2}{r_0^2} \right) = \frac{r_p}{r_0} \left[1 + \frac{\rho \dot{\epsilon}^2}{\sigma_u} \left(1 + 2 \frac{r_c^2}{r_p^2} \right) \right] \quad (36)$$

When the “cracked-comminuted” phase ends, the comminuted region has just reached the outer boundary of the targets. Therefore, the critical cavity radius (r_{c2}) is obtained by definition of $r_p=r_0$, and then Eq. (36) can be transformed into

$$\left(\frac{r_{c2}}{r_0}\right)^2 = 1 - \left(1 - \frac{\sigma_u}{K_0}\right)^2 \tag{37}$$

It is shown in Eq. (37) that r_{c2}/r_0 is correlated closely with dimensionless confinement stiffness Kr_0/σ_u , which can reflect the confinement effect of the outer tube to concrete to a certain degree. The applicable maximum confinement $(Kr_0)_{\max}$ can be obtained by the substitution of the critical condition $r_{c1} = r_{c2}$ into Eqs. (24) and (37).

$$\frac{\sigma_u}{(K_0)_{\max}} = 1 - \sqrt{1 - \frac{3(\sigma_u + |\sigma_r|)}{2E}} \tag{38}$$

There will be no “cracked-comminuted” phase if $Kr_0 > (Kr_0)_{\max}$, and the cavity-expansion process just includes “elastic-cracked-comminuted” and “completely comminuted” phases.

2.3.3 Completely comminuted phase ($r_c \geq r_{c2}$)

In the completely comminuted phase, the comminuted zone has reached the outer boundary of the targets, i.e., $r_p \equiv r_0$. The boundary conditions and control equation would be Eqs. (11) and (33), respectively, and the solution procedure of radial stress σ_r is also similar to the “elastic-cracked-comminuted” phase.

As equations of stresses for the three possible phases of FCCE models are complex, numerical solutions of the radial stress and circumferential stress at the cavity wall can be solved by Runge-Kutta method according to a standardized and classified procedure shown in Fig. 3, which is similar to the procedure for FSCE models reported by Meng et al. [30]. The procedure generally includes five steps: (1) Collecting and defining the initial conditions; (2) Discussing the applicability of the dynamic FCCE model; (3) Calculating the two critical cavity radii; (4) Determination of the response phases; (5) Solving the stresses at cavity wall at different phases, as shown in Fig. 3.

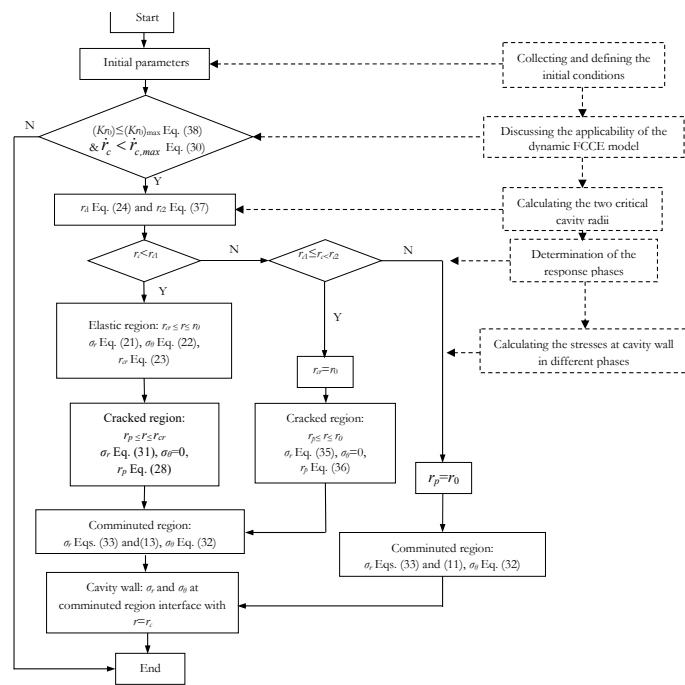


Figure 3: Flowchart and steps for calculation of pressure at cavity wall.

3. DOP model for STCC targets based on the FCCE model

3.1 DOP formula of STCC targets

The penetration process of the STCC targets normally penetrated by rigid projectiles includes the cratering and tunneling stages [4] and the formula of total DOP (H) is

$$H = H_1 + H_2 \quad (39)$$

Where H_1 is the DOP of the cratering stage with $H_1 = kd$, k is an empirical constant and d is the diameter of projectile; H_2 is the DOP of the tunneling stage obtained by the FCCE model.

For the confined concrete targets, the tunneling stage DOP (H_2) can be calculated by Eq. (40) according to Ref. [30]

$$H_2 = \frac{2M}{\pi d^2 \rho NB} \ln \left(1 + \frac{NB \rho V_1^2}{A \sigma_u} \right), \quad V_1^2 = \frac{4M V_0^2 - Ak \pi d^3 \sigma_u}{4M + k \pi d^3 \rho NB} \quad (40)$$

Where, N is the shape factor of the projectile nose [34, 35]; V_1 is the velocity of projectile at beginning of the tunneling stage, which can be equal to the impact velocity of projectile (V_0) for APP [30]; A and B are constants, obtained by curve-fitting of the numerical solutions of the dynamic FCCE governing equations with Eq. (41) between a series of σ_{rc} and the given $\dot{\epsilon}_c$.

$$\frac{\sigma_{rc}}{\sigma_u} = A + B \frac{\rho \dot{\epsilon}_c^2}{\sigma_u} \quad (41)$$

Where σ_{rc} is calculated with the FCCE model described above. Therefore, the total DOP (H) is the sum of H_1 and H_2 .

$$H = H_1 + H_2 = kd + \frac{2M}{\pi d^2 \rho NB} \ln \left(1 + \frac{B \rho V_1^2}{A \sigma_u} \right) \quad (42)$$

3.2 Validation of the DOP model

Penetration tests of STCC targets in Ref. [36] were selected to validate the DOP model in the Section 3.1. In Ref. [36], 9 specimens were designed, as shown in Table 1. All the tubes of the targets had the same dimension and the diameter, wall thickness and length of the tubes were 140 mm, 3.5 mm and 350 mm, respectively. Self-compacting concrete was filled in the steel tube and the unconfined compressive strength and splitting tensile strength of the standard specimens at the time of test (age 35 d) were 56.3 MPa and 5.66 MPa, respectively.

The test set-ups, procedures and methods were also the same as those in Ref. [4]. The damage parameters of the STCC targets were summarized in Table 1. Where, Δd is the distance from the center of ballistic crater to the center of target, r_0 is the radius of confined concrete, as shown in Fig. 1; V_L is the volume of the crater volume, which is measured by sand-filling method; H is the total DOP; H_1 is the depth of the funneled crater and correlated with the diameter of projectile. Based on the tested H_1 , the empirical constant k is deduced by rounding the numbers of the averaged values according to the designed penetration velocity range. The results show that for the 12.7 mm APP, k is related closely to the impact velocity V_0 , approximately, $k=4$ for $V_0 = 820$ m/s–830 m/s, $k=3$ for $V_0 = 700$ m/s–710 m/s and $k=2$ for $V_0 = 600$ m/s–610 m/s.

Table 1: Damage parameters of targets in Ref. [36].

Specimens number	Diameter/ thickness of steel tube (mm)	V_0 (m/s)	Δd (mm)	$\Delta d/r_0$ (%)	V_L (mL)	$H_1=kd$ (mm)	H (mm)	Average value of k	Notes
C140-1	140/3.5	-	-	-	-	-	142*		Perforation of steel tube
C140-2	140/3.5	820.7	6.4	9.1	270	42.0	173.0	4	
C140-3	140/3.5	829.9	13.0	18.6	252	45.5	181.0		
C140-8	140/3.5	-	3.0	4.3	290	45.0	172.1*		Unmeasured velocity
C140-6	140/3.5	703.0	4.0	5.7	235	40.0	126.8	3	
C140-7	140/3.5	710.5	3.0	4.3	190	34.0	129.2		
C140-4	140/3.5	603.0	0	0	195	36.0	92.0		
C140-5	140/3.5	599.3	4.0	5.7	84	29.0	80.6*	2	Unseparated steel sleeve
C140-9	140/3.5	611.8	2.0	2.9	172	26	93.5		

Notes: “-” denotes the unmeasured data; “*” signifies the perforation or the abnormal cases of the concrete or projectiles, which would be considered as invalid during the penetration-depth analysis.

The hard core of 12.7 mm APP can be considered to be rigid during the penetration process and the velocity loss of hard core during the cratering stage can be neglected [4, 36]. Therefore, the parameters of projectile of the DOP model can be replaced by those of the hard core during the tunneling stage, i.e., $d=d_w$ and $V_1=V_0$ in Eq. (40), where d_w is the diameter of hard core. The relevant parameters of the 12.7 mm APP and STCC targets in Ref. [36] are as follows: $d=12.7$ mm, $d_w=7.5$ mm, $M=9.8$ g, $N=0.8$; $E_s=198$ GPa; $K_0/\sigma_u=192$, $\delta=3.5$ mm, $r_0=66.5$ mm, $r_c=d_w/2=3.75$ mm, $\sigma_u=4.3$ MPa, $|\sigma_t|=5.6$ MPa, $E=3375 \times \sqrt{\sigma_u}=24869.9$ MPa, $\rho=2420$ kg/m³; the constant of k is valued according to the deduced results in Table 1.

As m between 8 and 26 is recommended in Ref. [30], $m=10, 15, 20$ and 25 are tentatively selected and the corresponding constant coefficients A and B were fitted with Eq. (41) as described in Section 3.1. One of the fitted results for $m=25$ is shown in Fig. 4, and the fitted parameters A and B are 4.96 and 9.44, respectively, with the correlation coefficient (R^2) 0.998. And then, the tested DOP (the DOP and impact velocity are averaged for the specimens with valid measured results) and calculated DOP are compared as shown in Table 2.

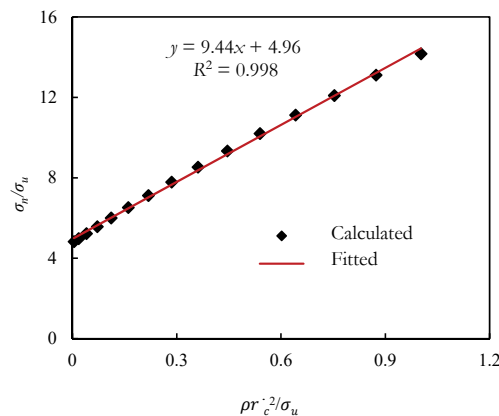


Figure 4: Curve-fitting of coefficients A and B ($m=25$).

The results in Table 2 show that the relative error decreases with the increasing values of m , and the optimal values are gained with $m=25$ where the relative error is about 8% except that of the targets with the impact velocity about 600 m/s (The possible reason is that the projectiles do not completely normally impact the STCC targets under the lower impact velocity [36]).

Table 2: Resistance coefficient and DOP of FCCE model for STCC targets.

r_0/δ (mm)	σ_u (MPa)	r_c/r_0	Kr_0/σ_u	m	A	B	k	V_0 (m/s)	Tested	Calculated	Relative
									DOP (mm)	DOP (mm)	error (%)
66.5/3.5	54.3	0.056	192	10	4.53	7.21	4	825.4	177.0	188.6	6.6
							3	706.7	128.0	160.5	25.4
							2	607.4	92.8	133.2	43.6
							4	825.4	177.0	175.9	-0.6
				15	4.75	8.18	3	706.7	128.0	149.4	16.7
							2	607.4	92.8	123.7	33.4
							4	825.4	177.0	168.2	-4.9
							3	706.7	128.0	142.8	11.5
				20	4.88	8.89	2	607.4	92.8	118.1	27.3
							4	825.4	177.0	163.1	-7.9
							3	706.7	128.0	138.3	8.1
							25	4.96	9.44	2	607.4

The comparisons of several DOP models for STCC targets including Li–Chen model [34, 35], FSCE model [30] and FCCE model in this paper, are shown in Fig. 5. As for Li–Chen model, in cratering stage, $H_1=2d$, and d is replaced with d_w in tunneling stage; H_2 is calculated by Eq. (40) with $V_1=V_0$, $B=1$, $\sigma_u=f_c$, $A=S$ and $S=72f_c^{0.5}$. For FSCE model and FCCE model, $m=25$ is selected.

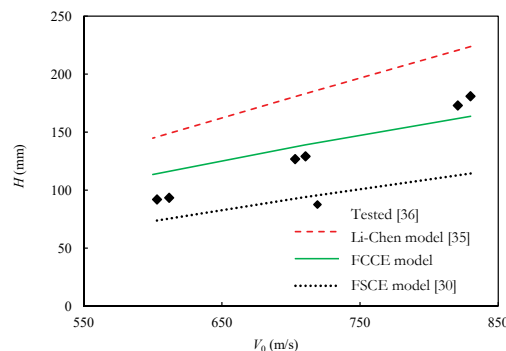


Figure 5: Comparison between the predicted models and tested results in Ref. [36].

As shown in Fig. 5, the results of DOP calculated by Li–Chen model are much larger than those of tests with the relative error as high as 23.7%–57.5%, while the results of DOP calculated by FSCE model are smaller than those of tests with the relative error of 5.9%–25.1%. However, the relative error between the results calculated by Eq. (42) in this paper and the tested data is less than 8% except that the targets with the impact velocity about 600 m/s. Generally, it is shown that the DOP of STCC targets calculated by engineering model based on H–B criterion and FCCE model is obviously superior to that of the Li–Chen model. It is because that the constraint effect of the steel tube on concrete is not considered in Li–Chen model. It should point out that all the DOP of the engineering models are discrete with the impact velocity about 600 m/s, which may be due to the oblique penetration of the projectiles [36].

In order to further testify the applicability of the DOP model in this paper, Table 3 presents the comparison between the DOP model based on FCCE model and the tests in Ref. [4]. The parameters of penetrators, i.e., 12.7 mm APP, are identical to Ref. [36]. The parameters of STCC targets in Ref. [4] are as follows: $\sigma_u = 35.8$ MPa, $|\sigma_t| = 5.9$ MPa, $E_s = 198$ GPa, $\delta = 3.5$ mm (4.5 mm) and $r_0 = 53.5$ mm (52.5 mm). Since the in-filled concrete of targets was designed without coarse aggregate, the value of m should be smaller than that of concrete with coarse aggregate in Ref. [36]. Therefore, m (10, 15 and 20) is tentatively selected for that concrete without coarse aggregate in Ref. [4]. The tested (the DOP and impact velocity are averaged for the specimens with valid measured results) and calculated DOP data are compared as shown in Table 3.

Table 3: Resistance coefficients and DOP for STCC targets in Ref. [4].

r_0/δ (mm)	σ_u (MPa)	r_c/r_0	Kr_0/σ_u	A	B	m	k	V_0 (m/s)	Tested DOP (mm)	Calculated DOP (mm)	Relative error (%)
				8.07	4.78	10				216.4	9.6
53.5/3.5		0.070	362	8.81	5.44	15		825.9	197.4	199.0	0.8
				9.33	5.94	20				188.3	-4.6
				9.69	4.43	10				208.9	10.0
52.5/4.5	35.8	0.071	474	10.74	5.02	15	4	820.7	189.8	191.7	1.0
				11.48	5.49	20				181.1	-4.6
				6.15	6.32	10				206.0	-2.4
66.5/3.5		0.056	291	6.56	7.23	15		819.0	211.1	190.0	-10.0
				6.87	7.92	20				179.9	-14.8

It can be seen from Table 3 that when $m=15$, the calculated results of the FCCE model are generally consistent with the experimental data in Ref. [4], with the maximum disparity of 10.0%. And the comparison results further shows that the DOP model based on the dynamic FCCE models can predict the DOP of the STCC targets normally impacted by rigid conical nosed projectile.

Furthermore, the comparisons of DOP models based on the dynamic FSCE model [30] and FCCE model ($m=15$) for STCC targets with $r_0=53.5$ mm and $\delta=3.5$ mm in Ref. [4] normally impacted by 12.7 mm APP ranging from 600 m/s to 830 m/s are shown in Fig. 6.

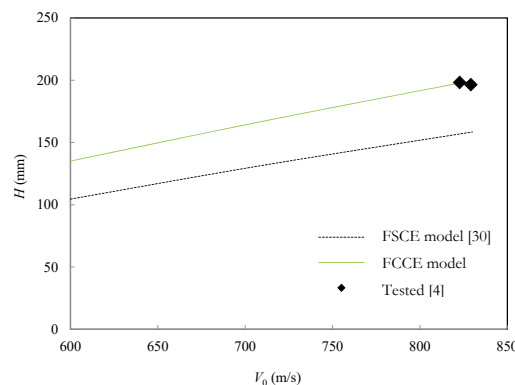


Figure 6: Comparison of the predicted models with tested results in Ref. [4].

It is shown that the DOP obtained by FCCE model are 26%–29% higher than that obtained by FSCE model with impact velocity ranging from 600 m/s to 830 m/s. Especially, for the tested STCC targets (D6#, D7#) in Ref. [4] normally impacted by 12.7 mm APP ranging from 822.7 m/s to 829.1 m/s, the DOP obtained by FCCE model agrees well with tested results with the maximum relative error about 1%, while

the relative error between tested results and the DOP obtained by FSCE model is about -25%. Therefore, the DOP model based the dynamic FCCE model is more applicable to predict the DOP of STCC targets penetrated by rigid conical projectiles with a proper value of m .

4. Conclusions

Based on the assumptions of incompressibility and H-B criterion, a dynamic FCCE model has been developed to analyze the penetrating process and stresses at cavity wall of the STCC targets, followed by a DOP model of STCC targets normally penetrated by rigid sharp-nosed projectiles. And the relevant penetration tests of STCC targets by 12.7 mm APP were used to testify the DOP model based on the FCCE model. The results of DOP for the STCC targets based on the dynamic FCCE model have the optimal consistence with those of the relevant penetration experiments in comparisons with the results based on the dynamic FSCE and Li-Chen models, which shows that under the conditions of a proper m , the DOP model based on the dynamic FCCE model is more applicable to predict the DOP of STCC targets penetrated by rigid conical or other sharp-nosed projectiles with an impact velocity below 830 m/s.

5. Acknowledgment

The research reported in the paper is part of the Natural Science Foundation of Hunan Province, China (No. 2018JJ2470) and the Project supported by National Natural Science Foundation of China (No. 51308539). The financial support is highly appreciated.

6. References

1. Kamal IM, Eltehwewy EM, 2012, Projectile penetration of reinforced concrete blocks: Test and analysis, *Theoretical and Applied Fracture Mechanics*, 60: 31–37.
2. Bruhl JC, Varma AH, Johnson WH, 2015, Design of composite SC wall to prevent perforation from missile impact, *International Journal of Impact Engineering*, 75: 75–87.
3. Tai YS, 2009, Flat ended projectile penetrating ultra-high strength concrete plate target, *Theoretical and Applied Fracture Mechanics*, 51: 117–128.
4. Wan F, Jiang ZG, Tan QH, Cao YYY, 2016, Response of steel-tube-confined concrete targets to projectile impact, *International Journal of Impact Engineering*, 94: 50–59.
5. Jiang ZG, Wan F, Tan QH, Liu F, 2016, Multi-hit experiments of steel-tube-confined concrete targets, *Journal of National University of Defense Technology*, 38(3): 117–123. (In Chinese)
6. Ben-Dor G, Dubinsky A, Elperin T, 2015, Analytical engineering models for predicting high speed penetration of hard projectiles into concrete shields: A review, *International Journal of Damage Mechanics*, 24(1): 76–94.
7. Anderson CE, 2017, Analytical models for penetration mechanics: A Review, *International Journal of Impact Engineering*, 108: 3–26.
8. Forrestal MJ, Warren TL, 2008, Penetration equations for ogive-nose rods into aluminum targets, *International Journal of Impact Engineering*, 35: 727–730.
9. Kong XZ, Wu H, Fang Q, Ren GM, 2016, Analyses of rigid projectile penetration into UHPCC target based on an improved dynamic cavity expansion model, *Construction and Building Materials*, 126: 759–767.
10. Forrestal MJ, Warren TL, 2009, Perforation equations for conical and ogival nose rigid projectiles into

aluminum plate targets, *International Journal of Impact Engineering*, 36: 220-225.

11. Forrestal MJ, Luk VK, Brar NS, 1990, Perforation of aluminum armor plates with conical-nose projectiles, *Mechanics of Materials*, 10: 97-105.
12. Johnsen J, Holmen JK, Warren TL, Børvik T, 2017, Cylindrical cavity expansion approximations using different constitutive models for the target material, *International Journal of Protective Structures*, 1-27.
13. Forrestal MJ, Longcope DB, Norwood FR, 1981, A model to estimate forces on conical penetrators into dry porous rock, *Journal of Applied Mechanics-Transactions of the ASME*, 48(1): 25–29.
14. Forrestal MJ, 1986, Penetration into dry porous rock, *International Journal of Solids and Structures*, 22(12): 1485–1500.
15. Forrestal MJ, Luk VK, 1992, Penetration into soil targets, *International Journal of Impact Engineering*, 21: 427–444.
16. Guo X J, He T, Wen HM, 2013, Cylindrical cavity expansion penetration model for concrete targets with shear dilatancy, *Journal of Engineering Mechanics ASCE*, 139(9): 1260–1267.
17. Yankelevsky DZ, Feldgun VR, Karinski YS, 2017, Rigid projectile penetration into a concrete medium: A new model, *International Journal of Protective Structures*, 8(3): 204141961772154.
18. Mastilovic S, Krajcinovic D, 1999, High-velocity expansion of the cavity within a brittle material, *Journal of the Mechanics and Physics of Solids*, 47: 577–610.
19. Forrestal MJ, Tzou DY, 1997, A spherical cavity-expansion penetration model for concrete targets, *International Journal of Solids and Structures*, 34: 4127–4146.
20. Macek RW. and Duffey AD, 2000, Finite cavity expansion method for near-surface effects and layering during earth penetration, *International Journal of Impact Engineering*, 24: 239–258.
21. Warren TL, Poormon KL, 2001, Penetration of 6061-T6511 aluminum targets by ogive-nosed VAR 4340 steel projectiles at oblique angles: experiments and simulations, *International Journal of Impact Engineering*, 25: 993–1022.
22. Warren TL, Hanchak SJ, Poormon KL, 2004, Penetration of limestone targets by ogive-nosed VAR 4340 steel projectiles at oblique angles: experiments and simulations, *International Journal of Impact Engineering*, 30: 1307–1331.
23. Fang Q, Kong XZ, Hong J, Wu H, 2014, Prediction of projectile penetration and perforation by finite cavity expansion method with the free-surface effect, *Acta Mechanica Solida Sinica*, 27: 597–611.
24. Chen XG, Zhang D, Yao SJ, Lu FY, 2017, Fast algorithm for simulation of normal and oblique penetration into limestone targets, *Applied Mathematics and Mechanics-English Edition*, 38(5): 671–688.
25. Zhen M, Jiang ZG, Song DY, Liu F, 2014, Analytical solutions for finite cylindrical dynamic cavity expansion in compressible elastic-plastic materials, *Applied Mathematics and Mechanics-English Edition*, 35: 1039–1050.
26. Zuo JP, Li HT, Xie HP, Peng SP, 2008, A nonlinear strength criterion for rock-like materials based on fracture mechanics, *International Journal of Rock Mechanics and Mining Sciences*, 45(4): 594–599.

27. Zuo JP, Liu HH, Li HT, 2015, A theoretical derivation of the Hoek-Brown failure criterion for rock materials, *Journal of Rock Mechanics and Geotechnical Engineering*, 7: 361–366.
28. Eberhardt E, 2012, The Hoek-Brown failure criterion, *Rock Mechanics and Rock Engineering*, 45(6): 981–988.
29. Hoek E, Martin CD, 2014, Fracture initiation and propagation in intact rock-A review, *Journal of Rock Mechanics and Geotechnical Engineering*, 6: 287–300.
30. Meng CM, Tan QH, Jiang ZG, Song DY, Liu F, 2018, Approximate solutions of finite dynamic spherical cavity-expansion models for penetration into elastically confined concrete targets, *International Journal of Impact Engineering*, 114: 182–193.
31. Warren TL, Forrestal MJ, 1998, Effect of strain hardening and strain-rate sensitivity on the penetration of aluminum targets with spherical-nosed rods, *International Journal of Solids and Structures*, 35: 3737–3753.
32. He T, Wen HM, Guo XJ, 2011, A spherical cavity expansion model for penetration of ogival-nosed projectiles into concrete targets with shear-dilatancy, *Acta Mechanica Solida Sinica*, 27(6): 1001–1012.
33. Iravani S, 1996, Mechanical properties of high-performance concrete, *ACI Materials Journal*, 93(5): 416–426.
34. Chen XW, Li QM, 2002, Deep penetration of a non-deformable projectile with different geometrical characteristics, *International Journal of Impact Engineering*, 27: 619–637.
35. Li QM, Chen XW, 2003, Dimensionless formula for penetration depth of concrete target impacted by a non-deformable projectile, *International Journal of Impact Engineering*, 28: 93–116.
36. Meng CM, Song DY, Jiang ZG, Liu F, Tan QH, 2018, Experimental research on anti-penetration performance of polygonal steel-tube-confined concrete targets, *Journal of Vibration and Shock*, 37(13): 3–9. (In Chinese)

Ballistic performances of multi-layered Ultra-high Performance Fibre Reinforced Concrete

Y.Y.Y. Cao ¹, M. Sluijsmans ¹, Q.L. Yu ¹, H.J.H. Brouwers ¹

¹ Department of the Built Environment, Eindhoven University of Technology, the Netherlands

Abstract

The security problem of protective infrastructures is a critical consideration. Ultra-High Performance Fibre Reinforced Concrete (UHPFRC) is a newly-developed material with superior mechanical properties, and excellent damage tolerance. These characteristics make UHPFRC a potential solution for increasing the resistant capacities of the infrastructures subjected to impacts. In this study, a series of high-velocity bullet impact tests are conducted to investigate the ballistic performances of UHPFRC targets consisting of one to three layers, and the influences of the fibre re-arrangement in the layered structure on the ballistic properties are analysed. The in-service 7.62 mm bullets are used in the experiments and the impact velocity is around 830 m/s. The diameter and thickness of the UHPFRC targets are 275 mm and 90 mm, respectively. The tested UHPFRC targets have an identical total fibre content, but different fibre amounts in the individual layers. The experimental results present that steel fibres play a significant role in prohibiting the development of cracks under bullet impact, thus reducing the damage area in the front and back faces of the target. Moreover, the UHPFRC targets with two and three layers show smaller penetration depths than their single-layered counterpart, which indicates the positive effects of the layered structure on enhancing the impact resistance.

Keywords: Ultra-high performance concrete, Layered structure, High-velocity bullet impact

1. Introduction

Ensuring the security of protective infrastructures against weapons is a critical consideration in both civil and military fields. These infrastructures have a high risk of being exposed to bullet impacts generated in terrorist attacks or military activities. To improve the impact resistance of these infrastructures, utilizing Ultra-High Performance Fibre Reinforced Concrete (UHPFRC) is one of the solutions considering its ultra-high strength and outstanding damage tolerance [1–3]. Increasing attentions have been paid to study the response of UHPFRC under penetration. For example, Yu et al. [4] investigated the ballistic performances of UHPFRC targets against 7.62 mm bullets and confirmed the advantageous resistance of UHPFRC material. Sovják et al. [5,6] transportation hubs, protective or defence structures are at exposure risk to extreme load event such as blast loading or direct armed attack. This kind of loading is typical by its rapid increase in release of energy in a very short time. It is believed that emerging cementitious materials such as Engineered Cementitious Composite (ECC and M_aca et al. [7] experimentally evaluated the behaviour of UHPFRC under bullet penetration and obtained that the optimal resistance can be achieved by the UHPFRC reinforced with 2% fibres.

When a concrete target is under impact, there are generally three regions in the target, as shown in Figure 1.

(1) The impact region is crushed by the bullet and a crater is generated; the stress waves after many times

of reflections inside the target result in cracks around the crater.

(2) The middle tunnel region is mainly under compression with confining pressure, and a tunnel is formed as the bullet passes by.

(3) At the rear region of the target, the compressive waves reflect to be tensile ones, causing the cracking and scabbing in the rear surface.

Previous studies suggest that adding steel fibres to Ultra-High Performance Concrete (UHPC) matrix can result in a prominent improvement of its tensile strength [8]; however, fibres contribution to the compressive strength of UHPFRC is relatively limited [9,10] limited data is available on the influence of the steel fiber length and dosage on UHPC mechanical and durability performance. Therefore, in this study, a number of UHPC mixtures with varying steel fiber lengths (8 mm (0.31 in. Considering the above two points, i.e. the stress distribution in the concrete target and the effects of fibre on the UHPFRC properties, one can suppose that fibres are not fully utilized when they are distributed in the whole volume of a UHPFRC target. Designing layered target with different fibre amounts at different regions can be one of the approaches to increase the fibre efficiency. Due to the complexity of the casting process, few studies can be found concerning layered concrete target. Among the limited studies, Quek et al. [11] developed a cementitious target containing four layers: the impact and the rear layers are reinforced with hybrid fibres, the second layer is composed of tough aggregates, and the third layer is plain mortar. Their penetration tests presented that the developed layered target has superior ballistic resistance than the plain mortar. With regards to UHPFRC, very few investigation on the penetration resistance of layered UHPFRC targets can be found in the literature. The previous study [12] conducted by the authors confirms the advantages of applying layered structure to UHPFRC under the static bending, however, the dynamic penetration response of layered UHPFRC is not addressed. Lai et al. [13] designed a double-layered UHPFRC composite with an anti-penetration layer (without fibres) and a crack resistance layer (with fibres), the investigation showed that the designed layered composite has an improved impact resistance. But the composite in their study is filled with a large amount of aggregates or fibres in the two layers respectively, i.e. it is not a UHPFRC composite in the strict meaning.

This paper presents the ballistic performances of the layered UHPFRC targets against the in-service 7.62 mm bullet. The penetration depth in UHPFRC targets with one to three layers incorporating different amounts of steel fibres are compared. The results from this paper can promote a better understanding about the effects of fibres and the layered structure on the penetration resistant capacity of UHPFRC.

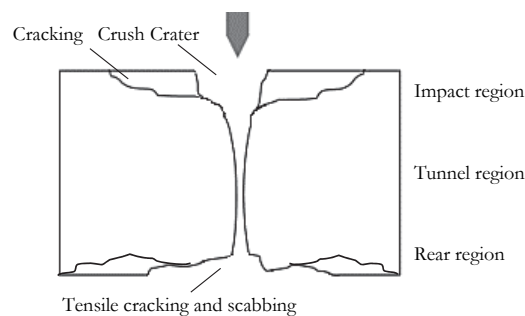


Figure 1: Illustration of a concrete target under penetration.

2. Methodology

2.1 Target design

Cylinder targets with the diameter of 275 mm and thickness of 90 mm were casted. Parameters of the designed targets are listed in Table 1, in which U0 is the plain UHPC target without fibres, UF1-3 are the

layered UHPFRC targets with one to three layers, respectively. Note that UF1-3 have the same total fibre amount, i.e. the equivalent fibre volume fraction for the three targets is 1%.

Table 1: Designed targets in the study.

Target	Layer thickness			Fibre dosage		
	Impact layer	Middle layer	Rear layer	Impact layer	Middle layer	Rear layer
	mm	%				
U0	90	-	-	0	-	-
UF1	90	-	-	1	-	-
UF2	45	-	45	2	-	0
UF3	30	30	30	1.5	0	1.5

The raw materials and the recipe used for the UHPFRC target are given in Table 2. The fractions of the materials were calculated applying the Brouwers mix design method [14,15] the features of \”Japanese and Chinese Methods\” are discussed, in which the packing of sand and gravel plays a major role. Here, the grading and packing of all solids in the concrete mix serves as a basis for the development of new concrete mixes. Mixes, consisting of slag blended cement, gravel (4-16 mm. Two groups of coarse basalt aggregates were used in the target with size fractions of 2-5 mm and 5-8 mm. The straight steel fibre in the UHPFRC has a length of 13 mm and a diameter of 0.2 mm. The amounts of water and superplasticizer adding into the UHPFRC mixtures are adjusted with the fibre amount to achieve a satisfying flowability.

Table 2 Recipes of the UHP(FR)C: CEM = Portland cement I 52.5 R, LP = limestone powder, mS = micro-silica, S = sand, BA = basalt aggregate, W = water, SF = steel fiber, SP = superplasticizer.

Materials	CEM	LP	mS	S	BA 2-5	BA 5-8	W	SP	SF
	kg/m ³	kg/m ³	kg/m ³	kg/m ³	kg/m ³	kg/m ³	kg/m ³	kg/m ³	%
V _f = 0%							149	9.4	0
V _f = 1.0%	588	156.8	39.2	839.9	413.2	232.3	157	8.5	1.0
V _f = 1.5%							157	12.5	1.5
V _f = 2.0%							157	16.5	2.0

2.2 Mixing and casting

The mixing and casting of the UHP(FR)C were conducted at room temperature (20 ± 1 °C). The mixing procedure of the UHPC and the UHPFRC is given below: dry mixing of all powders and sand for 2 minutes; adding 75% of the water while mixing; after 2 minutes, adding the superplasticizer and the remaining water; mixing for 4 minutes and adding the steel fibres (for UHPFRC); mixing until the mixture is slurred; then adding the basalt aggregates and mixing for 3 minutes.

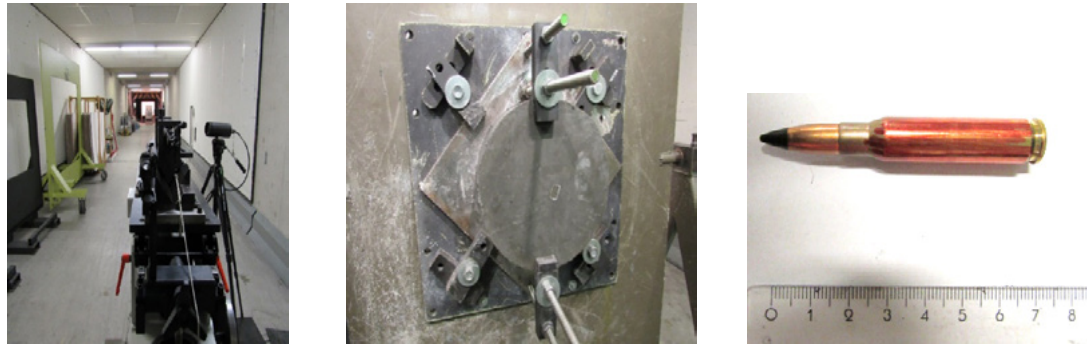
Cylindrical moulds with a diameter of approximately 275 mm were used for casting the targets. For the layered UHPFRC targets, the time interval between casting each layer is about 45 min, which is determined by considering both the experimental operability and the interfacial bond strength. More information about the casting method can be found in [12]. The cast targets were covered with plastic sheet and demoulded after 24 hours. Then the samples are curing in water at room temperature until the day of testing.

2.3 Testing methods

The experimental set-up and the 7.62 mm armour-piercing incendiary bullet utilized for the penetration tests are shown in Figure 2. The bullet was launched by the system given in Figure 2a and the impact

velocity around is 830 m/s. The target was held by a specially designed fixing frame that constrains the movement of the target, as presented in Figure 2b.

The damage level of the target is assessed by the penetration depth, which is measured as the distance from the impact surface to the deepest point in the target. In order to obtain the accurate penetration depth, the targets were cut along the axial direction by a saw cutting machine after the penetration tests.



(a) Launch system

(b) Fixing frame

(c) 7.62 mm Bullet

Figure 2: Penetration test set-up and the bullet.

3. Results and discussion

3.1 Penetration depth

The compressive strengths of the UHPC and the UHPFRC with 1 to 2% of fibres at the day of the penetration tests are within the range of 149 to 159 MPa, and the difference on the strength is too small to cause significant influences on the impact resistance. The penetration depths of the UHPFRC targets are plotted in Table 3. Note that no penetration depth is collected for U0 as the bullet went through the target, i.e. perforation occurred in the case of U0.

Table 3 Penetration depth.

Target	Velocity	Penetration depth	Note
	m/s	mm	
U0	838.9	-	perforation
UF1	838.5	62	penetration
UF2	838.0	59	penetration
UF3	836.0	54	penetration

As summarized in Table 3, the multi-layered UHPFRC target can provide a superior impact resistance and therefore results in a reduced penetration depth. To be precise, the penetration depths in UF2 and UF3 are 15% and 5% smaller than that in UF1, respectively. These reductions of the penetration depth can be attributed to the re-arrangement of the fibres in the target by the layered structure. Among the tested samples, UF3 with fibres purposefully reinforced in the impact and the rear layers archives the smallest penetration depth. In the impact region of UF3 the concentrated steel fibres, on the one hand, provide a better control of the tensile cracks in the surface and increase the tensile strength of the target; on the other hand, they work as a mesh wire to trap the travelling bullet and slow down its velocity. Moreover, fibres in the rear region of UF3 can contribute to the reduction of the cracking area caused by the tensile waves, as well as help to keep the rear surface remaining intact, which creates an additional restraint to the bullet.

3.2 Failure pattern

The failure pattern of the targets are given in Figures 3 - 6. As can be observed in Figure 3, U0 disintegrated into pieces due to the lack of fibres and the bullet perforated the target with a residual speed. The rear region of U0 is more seriously damaged than the impact region, indicating the stronger reflected tensile waves at the rear surface and a dampened tensile wave at the impact surface. The targets reinforced with steel fibres, viz. UF1-3, remained intact after the penetrations and the bullets were stopped inside the targets. Few cracks are observed in the impact and rear surfaces of UF1 and UF3 thanks to the application of fibres which inhibit the propagation of cracks. The rear surface of UF2 (Figure 5b) has some large cracks as no fibre is added in its rear layer. However, the rear layer of UF2 did not break into several pieces as U0 did, which is attributed to the reduced velocity of the bullet when it arrived at the rear layer and the constraint effects provided by the impact layer on the rear layer.

An important feature shown in Figures 5 and 6 is that cracking exhibited in the side surface of the layered targets along the interface and the crack is more obvious in the double-layered target (UF2) than in its triple-layered counterpart (UF3). As suggested by the previous study [12], the layer interface is the weakest part in the layered composite that the bond strength usually tends to be smaller than the tensile strength of the layer material. When the reflected tensile waves reach to the layer interface, cracking can occur if the amplitude of the tensile wave is higher than the bond strength. Although cracks are observed in the interface, no layer delamination occurs during the penetration tests, reflecting the rationality of the casting method. Moreover, the interface cracking process of the layered target can also promote the energy absorption of the target through the networks of micro-cracks [11], and thus contributes to the reduction of the penetration depth.

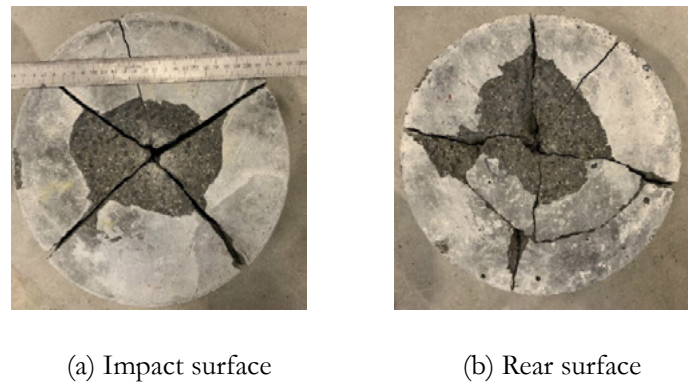


Figure 3: Failure pattern of U0.

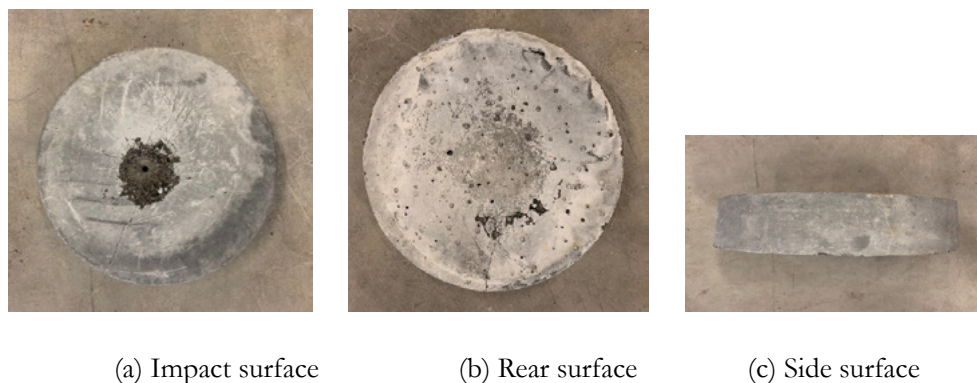


Figure 4: Failure pattern of UF1.

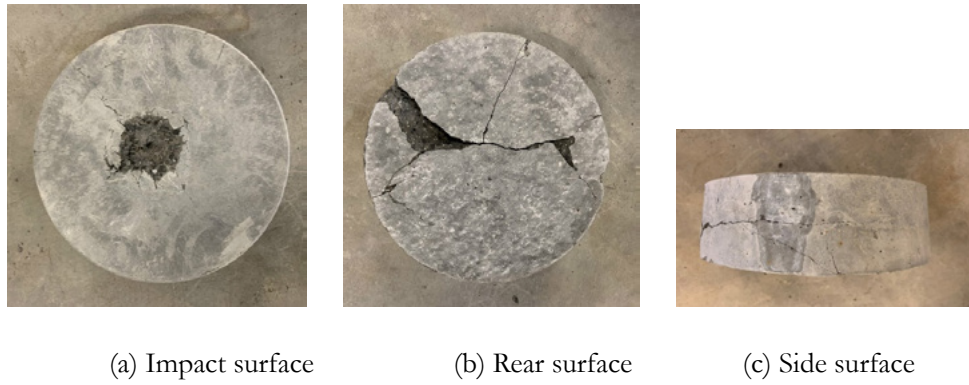


Figure 5: Failure pattern of UF2.

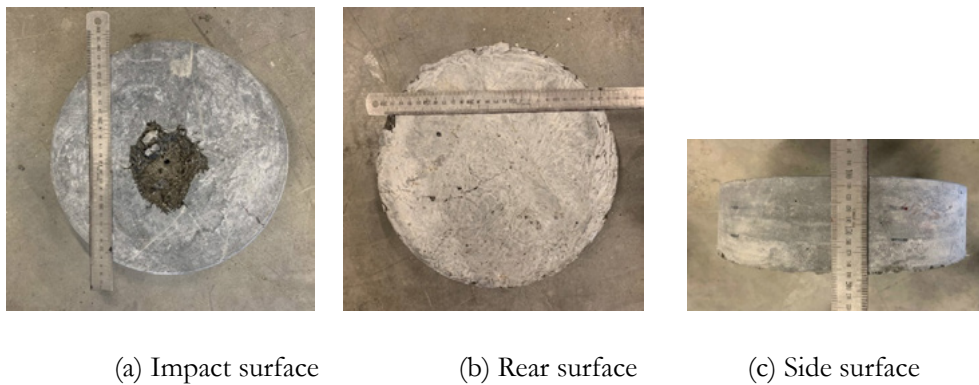


Figure 6: Failure pattern of UF3.

4. Conclusions

This study investigates the ballistic performances of layered UHPFRC targets against 7.62 mm bullet impacting at around 830 m/s. The tested UHPFRC targets have an identical total fibre content, but different fibre amounts in the individual layers. The penetration depth and the failure pattern of the tested targets are analysed in the study. The experimental results show that the UHPC target without fibres disintegrated into several pieces under the impact while the UHPFRC targets remained intact, which indicates the significance of adding fibres in the target. Moreover, the layered structure benefits the impact resistance of the UHPFRC targets, and the penetration depth in the double and triple-layered UHPFRC targets are approximately 13.8% and 8.3% smaller than its single-layered counterpart. This study promotes a better understanding about the fibres effects on the ballistic performance of UHPFRC, benefits the more efficient utilization of steel fibres in UHPFRC target, and contributes to the design of UHPFRC protective structures for both civil and military fields.

5. Acknowledgment

This research was carried out under the funding of China Scholarship Council and Eindhoven University of Technology. Furthermore, the authors wish to express their gratitude to Ing. D. Krabbenborg from the Dutch Defense Academy and the following organizations for conducting the penetration experiments: Ministerie van Defensie, Defensie Materieel Organisatie, Kenniscentrum Wapensystemen en Munitie, and Bureau Kleinkaliber.

6. References

[1] Yu R. Development of sustainable protective Ultra-High Performance Fibre Reinforced Concrete (UHPFRC). Eindhoven University of Technology, 2015.

- [2] Li PP, Yu QL. Responses and post-impact properties of ultra-high performance fibre reinforced concrete under pendulum impact. *Compos Struct* 2019;208:806–15. doi:10.1016/j.compstruct.2018.10.071.
- [3] Cao YYY, Yu QL, Brouwers HJH, Chen W. Predicting the rate effects on hooked-end fiber pullout performance from Ultra- High Performance Concrete. *Cem Concr Res* 2019;120:164–75. doi:10.1182/blood-2016-03-705590.
- [4] Yu R, Spiesz P, Brouwers HJH. Energy absorption capacity of a sustainable Ultra-High Performance Fibre Reinforced Concrete (UHPFRC) in quasi-static mode and under high velocity projectile impact. *Cem Concr Compos* 2016;68:109–22. doi:10.1016/j.cemconcomp.2016.02.012.
- [5] Sovják R, Vavříník T, Zatloukal J, Máca P, Mičunek T, Frydrýn M. Resistance of slim UHPFRC targets to projectile impact using in-service bullets. *Int J Impact Eng* 2015;76:166–77. doi:10.1016/j.ijimpeng.2014.10.002.
- [6] Sovják R, Vavříník T, Máca P, Zatloukal J, Konvalinka P, Song Y. Experimental investigation of ultra-high performance fiber reinforced concrete slabs subjected to deformable projectile impact. *Procedia Eng* 2013;65:120–5. doi:10.1016/j.proeng.2013.09.021.
- [7] Máca P, Sovják R, Konvalinka P. Mix design of UHPFRC and its response to projectile impact. *Int J Impact Eng* 2014;63:158–63. doi:10.1016/j.ijimpeng.2013.08.003.
- [8] Nguyen DL, Ryu GS, Koh KT, Kim DJ. Size and geometry dependent tensile behavior of ultra-high-performance fiber-reinforced concrete. *Compos Part B Eng* 2014;58:279–92. doi:10.1016/j.compositesb.2013.10.072.
- [9] Abbas S, Soliman AM, Nehdi ML. Exploring mechanical and durability properties of ultra-high performance concrete incorporating various steel fiber lengths and dosages. *Constr Build Mater* 2015;75:429–41. doi:10.1016/j.conbuildmat.2014.11.017.
- [10] Savino V, Lanzoni L, Tarantino AM, Viviani M. Simple and effective models to predict the compressive and tensile strength of HPFRC as the steel fiber content and type changes. *Compos Part B Eng* 2018;137:153–62. doi:10.1016/j.compositesb.2017.11.003.
- [11] Quek ST, Lin VWJ, Maalej M. Development of functionally-graded cementitious panel against high-velocity small projectile impact. *Int J Impact Eng* 2010;37:928–41. doi:10.1016/j.ijimpeng.2010.02.002.
- [12] Cao YYY, Li PP, Brouwers HJH, Sluijsmans M, Yu QL. Enhancing flexural performance of ultra-high performance concrete by an optimized layered-structure concept. *Compos Part B Eng* 2019;171:154–65. doi:10.1016/j.compositesb.2019.04.021.
- [13] Lai J, Wang H, Yang H, Zheng X, Wang Q. Dynamic properties and SPH simulation of functionally graded cementitious composite subjected to repeated penetration. *Constr Build Mater* 2017;146:54–65. doi:10.1016/j.conbuildmat.2017.04.023.
- [14] Brouwers HJH, Radix HJ. Self-compacting concrete: Theoretical and experimental study. *Cem Concr Res* 2005;35:2116–36. doi:10.1016/j.cemconres.2005.06.002.
- [15] Wang X, Wang K, Taylor P, Morcoux G. Assessing particle packing based self-consolidating concrete mix design method. *Constr Build Mater* 2014;70:439–52. doi:10.1016/j.conbuildmat.2014.08.002.

Effect of MgO, nitrate intercalated LDH and Calcined-LDH on chloride resistance of alkali-activated fly ash /slag mortar

T. Liu¹, Y. Chen¹, Q.L.Yu¹, H.J.H. Brouwers¹

¹Department of the Built Environment, Eindhoven University of Technology, 5600 MB, Eindhoven, the Netherlands

Abstract

Layered double hydroxides (LDHs) are the major secondary reaction products of alkali activated slag. The formation and absorptive performance of LDHs can be affected by factors such as the amount of magnesium oxide (MgO) and the structure of LDHs, making it possible to absorb the chloride ions Cl^- in alkali activated materials (AAMs). Meanwhile, Calcined layered double hydroxides (CLDHs) have the potential to act as a more effective chloride adsorbent than the original LDHs because of the reconstruction of LDH-like structure in AAMs matrix. The effects of MgO, LDHs- NO_3 and CLDHs on mitigating the chloride penetration in alkali activated fly ash and slag blends (AAFS) were investigated in terms of the chloride ingress in AAMs matrix. The objective is to explore the mechanism of LDHs formation with MgO, LDHs and CLDHs addition in alkali-activated materials. In this research, nitrate intercalated Mg-Al layered double hydroxide (Mg-Al-LDH- NO_3) was successfully synthesized with the co-precipitation method followed by subsequent washing and aging treatment. Calcined Mg-Al layered double hydroxide was obtained by thermal treatment of MgAl-LDH- NO_3 at 500 °C for 3 hours. The results of the rapid chloride migration test (RCM) revealed the ability of the CLDH, LDH and MgO to absorb the chloride ion in mortars. Furthermore, the microstructure of nitrate intercalated LDH and CLDH materials were analyzed by scanning electron microscopy (SEM).

Keywords: Alkali activated materials, LDH, MgO, Chloride penetration, RCM.

1. Introduction

Corrosion of steels by chloride attack plagues the durability of steel reinforced concrete, which often occurs in reinforced concrete structures built in the marine environment and saline regions. Large amounts of military and civil structures are exposed to the marine environment, and the main cause of corrosion in these concrete structures is the chloride ingress [1]. Severe corrosion, which often occurs in reinforced concrete structures, can be due to penetration of chloride ions, causing local destruction of the passive layer and leading to localized corrosion. Consequently, the usability and load bearing capacity are decreased, even leading to the failure of the structure. As a result, approximately 3.4% of the global GDP (\$2.5 Trillion USD) is spent each year to prevent and repair the infrastructure damage caused by chloride-induced corrosion [2].

To address this issue, many protecting methods to prevent chloride ingress have been discussed [3,4], for instance, adding new chemical inhibitors and applied on the surface of reinforcing bars. Layered double hydroxides (LDHs) are the typical reaction product of alkali activated slags [5], and the structure of LDHs makes it possible to adsorb the Cl^- in AAMs. MgO can promote the formation of LDHs in AAMs matrix,

which results in a higher chloride binding capacity of AAMs [6]. A higher MgO dosage (8%) leads to more hydroxalite-like phase to form [7]. Consequently, the binding ability of chloride ion in AAMs is increased. However, one issue when using MgO in AAMs causes concerns because the hydration product of LDHs is controlled by many factors, e.g. M^{2+}/M^{3+} ratio [8], thus it is not easy to control the LDHs content in AAMs by simply adding MgO. The most common type of LDHs in nature is the mineral hydroxalite that is a Mg–Al type LDHs intercalated with carbonate ions. The interlayer anions can be exchanged with other anions and the affinity order of anion is demonstrated by Costa et al. [9] as:



Thus, Mg-Al- NO_3 show better chloride binding ability in Ordinary Portland Cement (OPC) due to the higher affinity of chloride than nitrate [10,11]. The Mg-Al- NO_3 LDH was synthesized by Xu et al. [10], which could later exchange NO_3^- with Cl^- , therefore immobilizing chloride ion as an adsorbent. Furthermore, several methods, using LDH-like chemical products, have been developed in cement concrete structure [12]. For instance, the thermal treatment of Mg-Al- CO_3 LDH at 500 °C had been operated by Sato et al. [13]. The calcined layered double hydroxide (CLDH) shows the increased binding capacity of anions because of the reconstruction of LDH-like structure in cementitious matrix, which is shown in Fig. 1 [12].

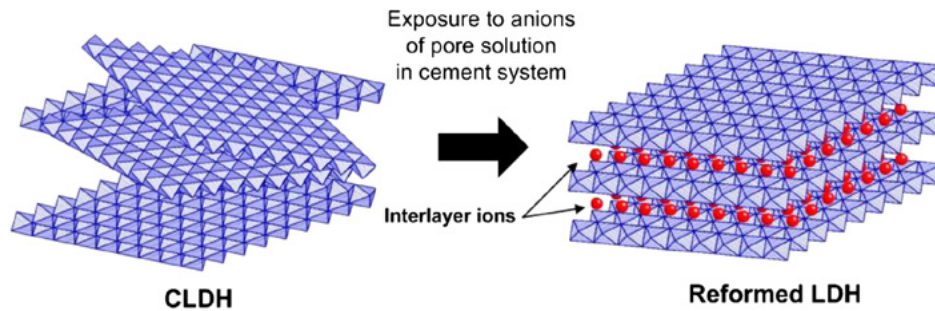


Figure 1 Schematic illustration of reforming layered structure of CLDH by adsorbing anions[12].

Yoon et al. [12] simulated the behavior of CLDHs in hardened Portland cement paste by utilizing the Langmuir’s equation and Freundlich’s equation. The analytic results showed the CLDHs rebuild the layered structure in a cementitious environment, thereby demonstrating the feasibility of applying CLDHs in concrete. Ke et al. [14,15] reported that the binding ability of CLDHs in sodium carbonate-activated slag pastes and mortars also showed the decreased porosity with the incorporation of 5 wt. % CLDHs, and the lower chloride migration coefficient than the samples without CLDH. In this article, the MgO, synthetic nitrate intercalated LDH and calcined LDH were utilized to replace the mass content of the AAFS binder (defined as FA + GGBS) to investigate their effects on the chloride penetration resistance of the AAFS mortars. The X-ray diffraction was applied to detect the crystalline phases of the AAFS samples. The chloride resistance was revealed by the RCM test, besides, the effects of the dosages of these materials in AAFS samples were discussed.

2. Experimental program

2.1 Materials

Class F fly ash, and ground granulated blast-furnace slag (GGBS) were utilized in this research. The chemical composition of the fly ash and GGBS were measured by X-ray fluorescence (XRF) and are shown in Table 1.

Table 1: Chemical composition of the fly ash and GGBS

Compound	MgO	Al ₂ O ₃	SiO ₂	SO ₃	K ₂ O	CaO	TiO ₂	Fe ₂ O ₃	Cl	LOI*□ %□
Fly Ash	1.137	25.576	53.892	2.905	1.601	5.441	1.503	7.883	0.062	3.79
GGBS	9.023	13.093	31.246	5.15	0.299	39.067	1.4	0.679	0.043	1

*LOI = loss on ignition at 1000□

Table 2: Composition of the water glass

	SiO ₂	Na ₂ O	H ₂ O
Wt. %	27.69%	8.39%	63.92%

The activator used in this research was prepared by mixing NaOH solution and sodium silicate solution, and the SiO₂/ Na₂O molar ratio is 1.5. The composition of the water glass is shown in Table 2. MgO (96% purity) was added to replace the AAMs binder at different mass percentage (2 wt. % and 4 wt. %)

Mg-Al-NO₃ LDH was prepared by a co-precipitation method [10]. Solution A containing Mg (NO₃)₂·6H₂O and Al(NO₃)₃·9H₂O with Mg/Al molar ratio of 3.0 (M[Mg²⁺] + M [Al³⁺] = 1.0 mol/L) and solution B containing 1.75 mol/L NaOH and 0.75 mol/L NaNO₃ were simultaneously dripped into 50 ml deionized water in a 500 mL container with magnetic stirring under N₂ atmosphere. The pH value of the mixture was maintained at 10.0±0.5. After this, the resulting suspension was aged at 65 °C for 24 h in a thermostatic bath. The final precipitate was filtered, washed thoroughly, and dried in vacuum at 90 °C for 24 h.

Calcined layered double hydroxide (CLDH) was prepared from the synthesized nitrite intercalated LDH using a heating rate of 5°C /min till 500°C and then kept constant for 3h. Afterwards the material was cooled down naturally in the furnace to 105°C before it was moved to a sealed centrifuge tube and kept in a desiccator under vacuum [14].

2.2 Sample preparation

The alkali activated samples were consisting of GGBS and fly ash, and the MgO, LDH and CLDH replaced 2 wt. % and 4 wt. % by mass of the alkali activated binder. GGBS / FA mass ratio was 7:3 (See the sample ID in Table 3). All the mortar samples were casted in the Ø 100 mm × 200 mm cylindrical moulds.

Table 3: Mix design of the mortars using different additions

Sample ID	Binder (g)					Sand (g)	Na ₂ O/Precursor	W/B*
	Slag	Fly Ash	MgO	LDHs(NO ₃)	CLDHs			
A0	70	30	-	-	-	300	7%	0.4
M2	68.6	29.4	2	-	-	300	7%	0.4
M4	67.2	28.8	4	-	-	300	7%	0.4
L2	68.6	29.4	-	2	-	300	7%	0.4
L4	67.2	28.8	-	4	-	300	7%	0.4
C2	68.6	29.4	-	-	2	300	7%	0.4
C4	67.2	28.8	-	-	4	300	7%	0.4

* W/B = Water/Binder mass ratio (where binder is defined as FA + GGBS)

2.3 Test methods

2.3.1 Scanning electron microscopy

The samples were selected from the synthetic LDH and CLDH powder. The microscopic analysis was performed using a JSM-IT100 InTouchScope™ Scanning Electron Microscope (SEM).

2.3.2 X-ray diffractometry

X-ray diffractometry (XRD) analysis was performed by using a Co tube (40kV, 30mA) with a scanning range from 5° to 90° 2θ, applying a step 0.01° and 1 s/step measuring process. The qualitative analysis was carried out by the Highscore Plus and the PDF database of ICDD.

2.3.3 Non-steady-state migration experiments

The Ø 100×100 mm cast cylinder mortars were used and cut into 50 ± 2 mm thick slice from the central portion. After sawing, brushing and washing away any burrs from the surfaces of the samples, and wiping off the excess water from the surfaces, the cylinder samples were put in the vacuum container for vacuum treatment for 3 hours with the pressure in the range of 10-50 mbar (1-5 kPa), and then immersed in the saturated Ca(OH)₂ solution for 18±2 hours. Subsequently, the non-steady-state migration experiments were tested according to the NT Build 492 [16].

The samples subjected to the accelerated NT Build 492 procedure, AgNO₃ solution was used to reveal the chloride penetration depths.

The non-steady-state migration coefficient is calculated from Equation (2):

$$D_{nssm} = \frac{0.0239(273+T)L}{\pi \times 0.0738 \sqrt{(273+T)L \cdot x_d}} \quad (2)$$

Where:

D_{nssm} : non-steady-state migration coefficient, ×10⁻¹² m²/s;

U : absolute value of the applied voltage, V;

T : average value of the initial and final temperatures in the anolyte solution, °C;

L : thickness of the specimen, mm;

x_d : average value of the penetration depths, mm;

t : test duration, hour.

The RCM test set-up was shown in Fig. 2.



Figure 1: RCM test set-up

3. Results and discussion

3.1 Characterization of the synthetic LDH and CLDH

The X-ray diffraction patterns of the synthetic LDH and CLDH are presented in Fig. 3. Most peaks were consistent with the typical XRD patterns of $Mg_6Al_2(OH)_{16}(NO_3)_2 \cdot 4H_2O$, corresponding to hydrotalcite-like phase (PDF 00-089-0460). The characteristic peak of Mg-Al-LDHs was observed at 13.6° , corresponding to crystal plane [003]. Cavani et al. [17] investigated the crystal phase of different anion intercalated hydrotalcite, which exhibited the same XRD pattern. Meanwhile, the characteristic peaks of Mg-Al-CLDH were detected at 41.2° , 51.3° and 75.6° , which were similar with the experimental results reported by Kanazaki et al. [18].

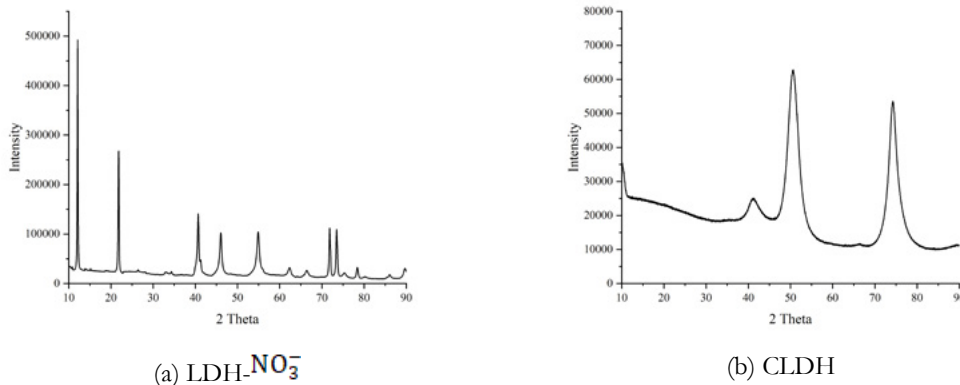


Figure 2: X-ray diffractogram and structure of LDH and CLDH

The layered structure of the LDHs and CLDHs were shown in Fig. 4. The size of the layered products LDH (Fig. 4(a)) is about $1 \mu m$ in length, which is in agreement with the previously reported SEM micrographs [19]. The micrographs of CLDH (Fig. 4(b)) showed the layered structure without rules. And the raw CLDH in Fig. 4 (b) has plate-like particles with sharp edges [12]. Due to the non-homogeneity of the CLDHs, the formed LDH particles from reconstruction of CLDHs may not be homogeneous for all particles [12].

3.2 Hydration products of AAFS

The XRD patterns of the samples showed that the primary hydration products of C-S-H, hydrotalcite and Mullite were identified in all AAFS samples.

The main characteristic peak of hydrotalcite was identified at 13.6° . However, Ke et al. [20] reported the main peak of XRD pattern for similar hydrotalcite-like phase after filtration was centered at 11.6° . The shift in the hydrotalcite-like peak is attributed to the partly carbonation of the LDH. As we can see in Fig. 5, the

crystalline phases in the AAFS samples exhibited the same reaction products.

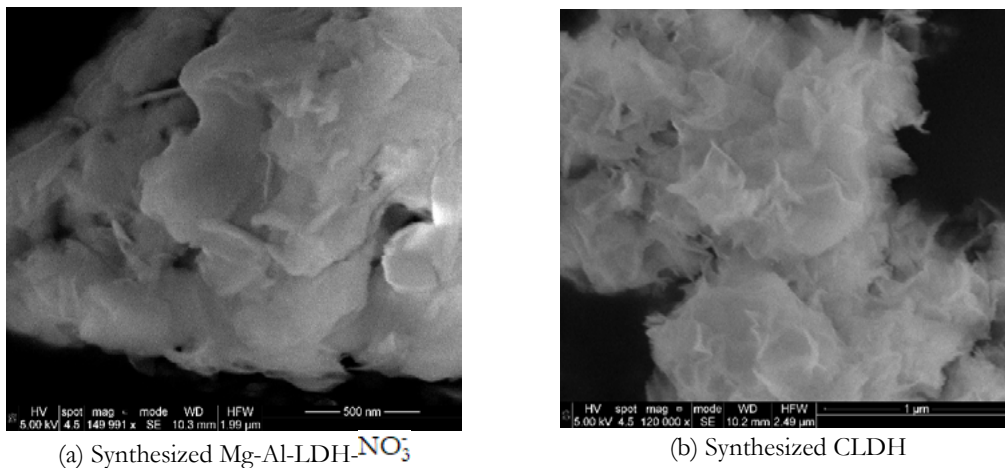


Figure 3: SEM micrographs of LDH and CLDH

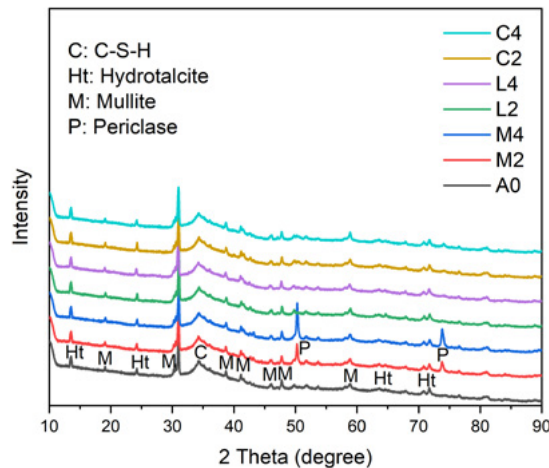


Figure 4: X-ray diffractogram of samples at 28-day curing age

Periclase was identified in specimens prepared with MgO addition (M2 and M4), which indicated that the MgO was not fully reacted with slag to form LDH [6]. However, according to previous study [7], the content of LDH formed from MgO in AAFS environment had the potential to grow over time, due to the solid phase reaction of MgO in alkali-activated cement.

The XRD patterns of L2, L4, C2 and C4 demonstrated almost the same intensity of hydrotalcite. The CLDH phase was not found in the XRD patterns while the emerged peak of hydrotalcite-like phase appeared, which proved that the CLDH completed the reconstruction process in AAFS to form the LDH [21].

3.3 Chloride resistance of AAFS

The penetration depths of the chloride in the AAFS samples confirmed a low degree of the chloride attack (shown in Fig. 6). All the ternary AAFS (M2, M4, L2, L4, C2 and C4) exhibited better chloride penetration resistances than the reference sample A0, reflected by the lower chloride diffusion coefficients of ternary AAFS samples than that of reference sample A0.

The chloride diffusion coefficients of all samples were listed in Table 4 and the chloride penetration depths were marked with the black lines in Fig. 6, where chloride penetration started in each sample from bottom to top. Moreover, the chloride diffusion coefficients (shown in Table 4) of C2 and C4 were $4.11 \times 10^{-12} \text{ m}^2/\text{s}$ and $2.88 \times 10^{-12} \text{ m}^2/\text{s}$, respectively, much lower compared to other samples. The experimental results were in line with the previous study [12], which demonstrated the CLDH in hardened AAFS paste can reduce the chloride content.

The coefficients of M2 and M4 were $4.68 \times 10^{-12} \text{ m}^2/\text{s}$ and $4.55 \times 10^{-12} \text{ m}^2/\text{s}$, respectively. And the coefficients of L2 and L4 were $6.91 \times 10^{-12} \text{ m}^2/\text{s}$ and $4.49 \times 10^{-12} \text{ m}^2/\text{s}$, respectively. It showed that the chloride banding capacity was increased with the increase of the MgO and LDH dosage. Meanwhile, the coefficient of M2 was lower than the L2 at 47.6% while M4 was higher than L4 at 1.3%, which showed that the content of LDH had an obvious influence on chloride resistance in AAFS system.

Combined with XRD results and chloride diffusion coefficients, the M2 and M4 samples had the same level of the chloride resistance with L2 and L4 at 28 days, but the MgO in M2 and M4 would continue forming the LDHs-like phase to absorb the chloride ion. The addition of CLDH in hardened AAFS could mitigate more chloride penetration than the addition of LDH and MgO.

Table 4: Chloride diffusion coefficients calculated from the RCM test in mortar cured for 28 days.

Sample ID	A0	M2	M4	L2	L4	C2	C4
Chloride diffusion coefficient ($\times 10^{-12} \text{ m}^2/\text{s}$)	5.42	4.68	4.55	6.91	4.49	4.11	2.88

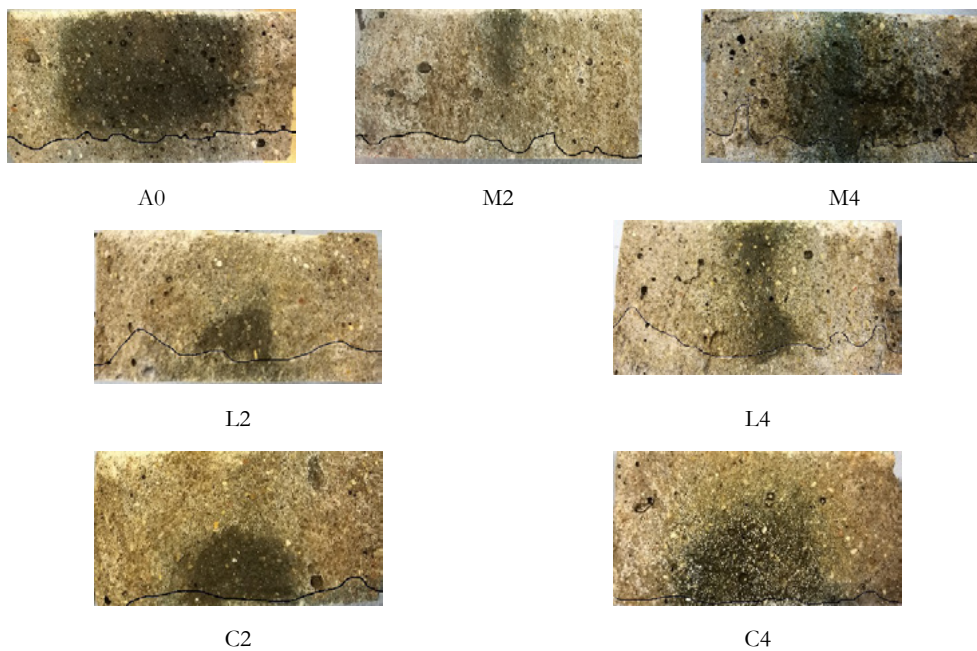


Figure 5: Boundary of chloride penetration in 28-day curing age

4. Conclusions

The effects of MgO, LDH and CLDH additions on the chloride resistance in AAFS were examined by the XRD, SEM and RCM tests. The experimental data indicated that the ternary AAFS could resist the chloride ingress better than the slag/fly ash blends mortars.

The CLDH could reconstruct the LDH in AAFS system, however the MgO was not fully reacted in AAFS at the age of 28 days and still had potential to form more LDH in AAFS. Based on the results of this study, the MgO and CLDH have potential in preventing the chloride ingress in the AAFS.

5. Acknowledgment

This research was supported by the Department of the Built Environment at Eindhoven University of Technology. Ing. A.C.A. Delsing is acknowledged for the experimental support on analytical analysis.

6. References

- [1] C. Tennakoon, A. Shayan, J.G. Sanjayan, A. Xu, Chloride ingress and steel corrosion in geopolymer concrete based on long term tests, *Mater. Des.* 116 (2017) 287–299. doi:10.1016/j.matdes.2016.12.030.
- [2] J. Osio-Norgaard, J.P. Gevaudan, W. V. Srubar, A review of chloride transport in alkali-activated cement paste, mortar, and concrete, *Constr. Build. Mater.* 186 (2018) 191–206. doi:10.1016/j.conbuildmat.2018.07.119.
- [3] H. Tatematsu, T. Sasaki, Repair materials system for chloride-induced corrosion of reinforcing bars, *Cem. Concr. Compos.* 25 (2003) 123–129. doi:10.1016/S0958-9465(01)00059-2.
- [4] Y. Tian, C. Dong, G. Wang, X. Cheng, X. Li, Zn–Al–NO₂ layered double hydroxide as a controlled-release corrosion inhibitor for steel reinforcements, *Mater. Lett.* 236 (2019) 517–520. doi:10.1016/j.matlet.2018.10.177.
- [5] R.J. Myers, J.S.J. van Deventer, F. Puertas, R. San Nicolas, S.A. Bernal, R. Mejía de Gutiérrez, J.L. Provis, MgO content of slag controls phase evolution and structural changes induced by accelerated carbonation in alkali-activated binders, *Cem. Concr. Res.* 57 (2014) 33–43. doi:10.1016/j.cemconres.2013.12.003.
- [6] H.N. Yoon, S.M. Park, H.K. Lee, Effect of MgO on chloride penetration resistance of alkali-activated binder, *Constr. Build. Mater.* 178 (2018) 584–592. doi:10.1016/j.conbuildmat.2018.05.156.
- [7] M. Ben Haha, B. Lothenbach, G. Le Saout, W. F., Influence of slag chemistry on the hydration of alkali-activated blast-furnace slag — Part I: Effect of MgO, *Cem. Concr. Res.* 41 (2011) 955–963. doi:http://dx.doi.org/10.1016/j.cemconres.2011.05.002.
- [8] Y. Chen, Z. Shui, W. Chen, G. Chen, Chloride binding of synthetic Ca–Al–NO₃ LDHs in hardened cement paste, *Constr. Build. Mater.* 93 (2015) 1051–1058. doi:10.1016/j.conbuildmat.2015.05.047.
- [9] D.G. Costa, A.B. Rocha, W.F. Souza, S. Shirley, X. Chiaro, A.A. Leitão, Comparative Structural , thermodynamic and electronic analyses of ZnAlAn – hydrotalcite-like compounds (An – Cl – , F – , Br – , OH – , CO₃ – or NO₃ –): An ab initio study *Applied Clay Science Comparative Structural , thermodynamic and electronic analy*, *Appl. Clay Sci.* 56 (2018) 16–22. doi:10.1016/j.clay.2011.11.014.
- [10] J. Xu, Y. Song, Y. Zhao, L. Jiang, Y. Mei, P. Chen, Chloride removal and corrosion inhibitions of nitrate, nitrite-intercalated Mg–Al layered double hydroxides on steel in saturated calcium hydroxide solution, *Appl. Clay Sci.* 163 (2018) 129–136. doi:10.1016/j.clay.2018.07.023.

- [11] H. Ye, Nanoscale attraction between calcium-aluminosilicate-hydrate and Mg-Al layered double hydroxides in alkali-activated slag, *Mater. Charact.* 140 (2018) 95–102. doi:10.1016/j.matchar.2018.03.049.
- [12] S. Yoon, J. Moon, S. Bae, X. Duan, E.P. Giannelis, P.M. Monteiro, Chloride adsorption by calcined layered double hydroxides in hardened Portland cement paste, *Mater. Chem. Phys.* 145 (2014) 376–386. doi:10.1016/j.matchemphys.2014.02.026.
- [13] T. Sato, T. Wakabayashi, M. Shimada, Adsorption of Various Anions by Magnesium Aluminum Oxide, *Am. Chem. Soc.* 25 (1986) 89–92.
- [14] X. Ke, S.A. Bernal, J.L. Provis, Controlling the reaction kinetics of sodium carbonate-activated slag cements using calcined layered double hydroxides, *Cem. Concr. Res.* 81 (2016) 24–37. doi:10.1016/j.cemconres.2015.11.012.
- [15] X. Ke, S.A. Bernal, O.H. Hussein, J.L. Provis, Chloride binding and mobility in sodium carbonate-activated slag pastes and mortars, *Mater. Struct. Constr.* 50 (2017). doi:10.1617/s11527-017-1121-8.
- [16] Nordtest Method, NT Build 492, (1999) 1–8.
- [17] F. Cavani, F. Trifirò, A. Vaccari, Hydrotalcite-type anionic clays: Preparation, properties and applications., *Catal. Today.* 11 (1991) 173–301. doi:10.1016/0920-5861(91)80068-k.
- [18] E. Kanazaki, A thermally induced metastable solid phase of Mg/Al-layered double hydroxides by means of in situ high temperature powder X-ray diffraction, *J. Mater. Sci. Lett.* 17 (1998) 371–374. doi:10.1023/A:1006570730849.
- [19] Y. Chen, Z. Shui, W. Chen, Q. Li, G. Chen, Effect of MgO content of synthetic slag on the formation of Mg-Al LDHs and sulfate resistance of slag-fly ash-clinker binder, *Constr. Build. Mater.* 125 (2016) 766–774. doi:10.1016/j.conbuildmat.2016.08.086.
- [20] X. Ke, S.A. Bernal, J.L. Provis, Uptake of chloride and carbonate by Mg-Al and Ca-Al layered double hydroxides in simulated pore solutions of alkali-activated slag cement, *Cem. Concr. Res.* 100 (2017) 1–13. doi:10.1016/j.cemconres.2017.05.015.
- [21] Y. Lin, Q. Fang, B. Chen, Metal composition of layered double hydroxides (LDHs) regulating ClO₄ adsorption to calcined LDHs via the memory effect and hydrogen bonding, *J. Environ. Sci. (China).* 26 (2014) 493–501. doi:10.1016/S1001-0742(13)60462-3.

Recent development on sustainable ultra-high performance concrete design with low cement consumption: a review

P.P. Li, Q.L. Yu, H.J.H. Brouwers

Department of the Built Environment, Eindhoven University of Technology, 5600 MB, the Netherlands.

Abstract - Ultra-high performance concrete (UHPC) is a relatively new building material with a relatively high consumption of cement compared to the conventional concrete, which causes the economic and environmental burdens. This paper aims to review the recently reported methods on developing sustainable UHPC with low cement consumption. The hybrid replacement by supplementary cementitious materials (SCMs), high-volume substitution by filler powders, inclusion of coarse aggregate, and two-stage casting method have been summarized. Furthermore, the thermal and chemical activation on SCMs, and the mineral plasticization effect of substitute material are discussed. Lastly, further research trends are identified.

Keywords: ultra-high performance concrete, sustainable, low cement, SCMs.

1. Introduction

Ultra-high performance concrete (UHPC) is a relatively novel cementitious construction material with excellent mechanical properties, durability and impact resistance [1]. During the past few decades, it has drawn great attention from both researchers and engineers. Richard et al. developed the reactive powder concrete (RPC) in 1993, which was characterized by a large amount of reactive powder, fine quartz powder without any coarse aggregate, very low water content and high superplasticizer dosage, utilization of steel fibre, special treatment (pre-setting pressurization and heat-treating) [2]. RPC showed a dense microstructure, excellent toughness and ultra-high strength over 150 MPa. A few years later, De Larrard proposed the term of 'ultra-high performance concrete' with high packing density [3]. Although, the special mix design methods of UHPC are beneficial for the excellent performance that allows to design thin and light concrete structures with long service life. They also cause problem of high binder or cement consumption, usually more than 900 kg/m² that is about 3 times more than that in conventional concrete. The large amount of cement utilization results in a high energy consumption and increased costs of UHPC material and structure, consequently limiting the engineering applications. Therefore, designing sustainable UHPC with relatively low cement consumption has been attempted by more and more researchers nowadays.

Currently, substitution of partial cement by cheaper and sustainable supplementary cementitious materials (SCMs) has been investigated to develop sustainable UHPC [4], including such as ground granulated blast slag (GGBS), fly ash, bottom ash, silica fume, glass powder etc. Yu et al. developed eco-friendly UHPC with different mineral admixtures uses, which showed better properties than the reference mixture [5]. Kang et al. used 16.5% of rice husk ash as pozzolanic admixture and internal curing agent in UHPC [6]. However, cement reduction by the traditional replacement methods is usually very limited, mostly less than 30%, to avoid sacrifice of too much properties of UHPC due to dilution effect. More efficient measures are needed to achieve much low-cost and eco-friendly UHPC with low cement content, but meanwhile without decreasing too much or even improving the performance of UHPC.

The aim of this review is to summarize the current novel methods to develop the sustainable UHPC with low cement consumption, including using ternary or quaternary SCMs, adding minerals with plasticization effect, activating weak-active binder by thermal and chemical methods, introducing coarse aggregate, casting UHPC by two-stage method. Furthermore, research needs are identified and suggestions are given.

2. Hybrid utilization of SCMs

To develop more sustainable UHPC, higher contents of cheap and eco-friendly substitution materials are desired to be utilized in UHPC system. To overcome or partly compensate the negative effect (e.g. dilution effect of cement) of SCM on the properties of UHPC, hybrid utilization of SCMs is probably a good method rather than blending a single SCM. Kang et al. found that UHPC with ternary binder (63% cement + 17% rice husk ash + 20% GGBS) even showed slightly better properties compared to the binary blends (83% cement + 17% rice husk ash), especially under the thermal curing conditions [6]. As shown in Figure 1, the workability, 28d strength and volume stability were much better, except for the slightly lower early age strength. The positive combination of GGBS and RHA was probably due to the mesoporous amorphous structure of RHA, which absorbed aqueous water at early age and thereafter provided water for further hydration for the GGBS at the later stage. Shi et al. designed UHPC with cement-silica fume-slag binder considering the hydration and microstructure [7]. It revealed that there existed optimum hybrid blending proportions between those three raw materials for the best flowability or compressive strength, as illustrated in Figure 2. They indicated that hybrid utilization of SCMs had some certain positive synergistic effects on hydration and thus improved the performance of UHPC system.

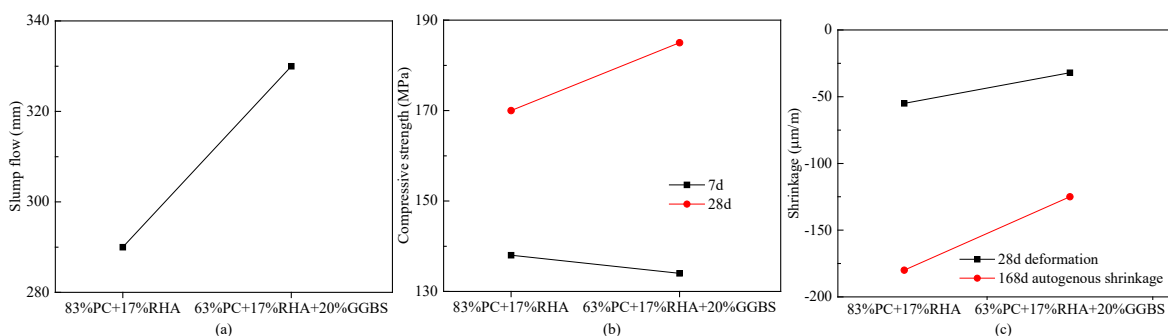


Figure 1: Properties between ternary (PC+RHA+GGBS) and binary (PC+RHA) blends [6].

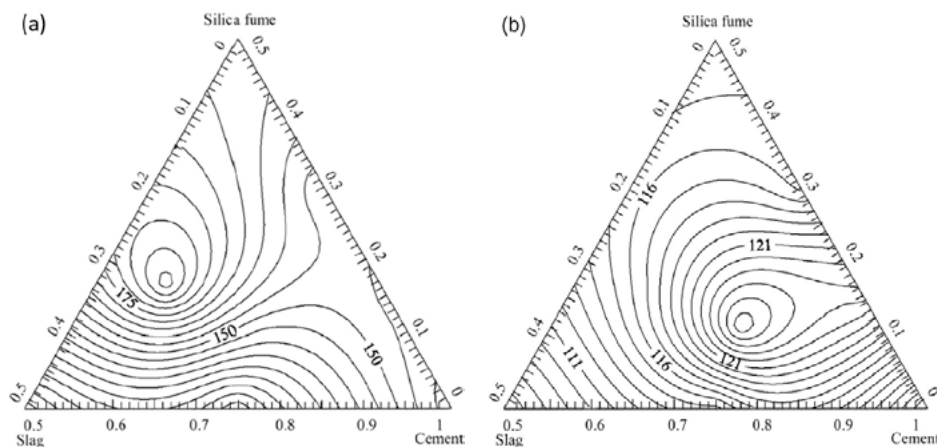


Figure 2: (a) flowability and (b) 56d compressive strength of UHPC with cement-silica fume-slag binder [7].

Arora et al. reported binder phase selection for UHPC from commonly available cement replacement and

fine filler, namely fly ash (F), slag (S), microsilica (M), metakaolin (K) and limestone (L) [8]. The strategies to select optimum binders were mainly based on packing and rheology. As shown in Figures 3, the ternary and quaternary blends, with a total cement replacement of 30%, were selected and suggested for sustainable application, which had better packing densities and rheological properties than pure cement or binary blends. After the optimization, UHPC mixtures with ternary or quaternary binders showed lower cement consumption, but only slightly lower or even higher compressive strength, as shown in Figure 4.

K ₁₀	M ₁₀	M ₂₀	F ₂₀	F ₃₀	S ₂₀	S ₃₀	
F ₁₀ K ₁₀	F ₂₀ K ₁₀	S ₁₀ K ₁₀	S ₂₀ K ₁₀	F ₁₀ M ₁₀	F ₂₀ M ₁₀	S ₁₀ M ₁₀	S ₂₀ M ₁₀
F ₂₀ L _{10a}	F ₂₀ L _{10b}	F ₂₅ L _{5a}	F ₂₅ L _{5c}	S ₂₀ L _{10a}	S ₂₀ L _{10b}	S ₂₅ L _{5a}	S ₂₅ L _{5b}
F _{17.5} K _{7.5} L _{5b}	F _{17.5} K _{7.5} L _{5c}	F _{17.5} M _{7.5} L _{5b}	F _{17.5} M _{7.5} L _{5c}	S _{17.5} K _{7.5} L _{5b}	S _{17.5} K _{7.5} L _{5c}	S _{17.5} M _{7.5} L _{5b}	S _{17.5} M _{7.5} L _{5c}

Figure 3: UHPC matrix selection based on packing and rheology. The subscript numbers represent the % by mass of SCMs replacing cement [8].

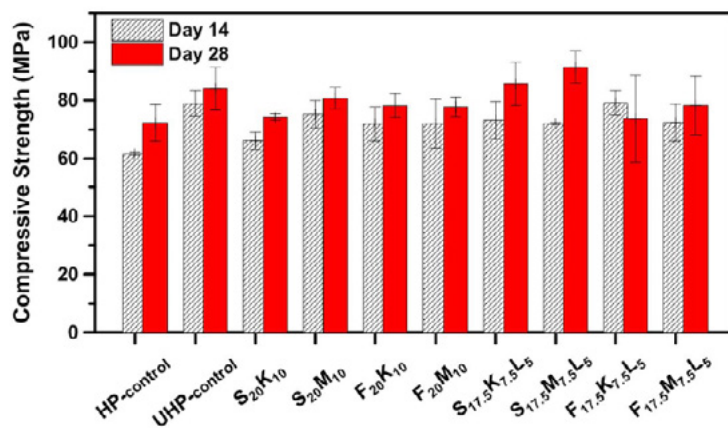


Figure 4: Compressive strength of UHPC with ternary and quaternary blends [8].

To further prove the hybrid benefit of SCMs, our study proposed to evaluate the synergy of quaternary blends (cement-slag-silica-limestone) compared to binary (cement-slag) and ternary binders (cement-silica-limestone),

$$synergy = \frac{(X_{ref} - X_B) + (X_{ref} - X_T)}{X_{ref} - X_Q} - 1 \tag{1}$$

where X represents the properties of UHPC pastes, and subscripts represent the mixtures with reference cement (ref), binary (B), ternary (T) and quaternary (Q) binders. A positive synergy (>0) indicates that quaternary blends have less adverse influence than binary and ternary blends. Normally, positive values of synergy in terms of 28d compressive strength, fibre-to-matrix bond and total free shrinkage were observed in the sustainable UHPC pastes with quaternary binders, as shown in Figure 5. The positive synergy was probably attributed to optimized total particle size distribution and reasonable mineral composition, e.g. Ca/Si ratio.

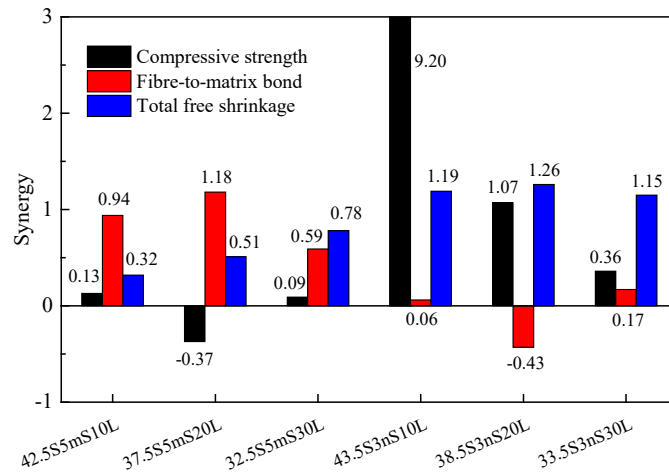


Figure 5: Synergy of quaternary binders compared to binary and ternary ones (S = slag, mS = micro-silica, nS = nano-silica, L = limestone, the number in mixture name means % by mass of SCMs replacing cement).

To sum up, hybrid utilization of SCMs such as ternary and quaternary binders is more appropriate to design sustainable UHPC instead of simple binary blends, due to the positive synergetic effect on hydration kinetics, optimization of mineral composition, whole packing density, rheology behaviour and even internal curing.

3. Mineral additions with plasticization effect

UHPC is characterized as relatively high superplasticizer dosages, in order to decrease the low water amount and the porosity, thus increase the packing density, microstructure and mechanical properties. Therefore, it is potentially desirable to use some mineral additions that possess plasticization effect to replace cement in sustainable UHPC, in order to decrease the water demand and compensate the probable negative dilution effect. Some carbonate fillers, e.g. limestone powder, show good plasticization effect, which can greatly enhance the workability of concrete [9,10]. Even though, limestone powder has negative dilution effect on cement because of its limited solubility and reactivity, the function as a mineral plasticizer can reduce the water demand to obtain a desirable flow ability. A less water utilization tends to a better compactness, which can overcome or partly compensate the negative dilution effect.

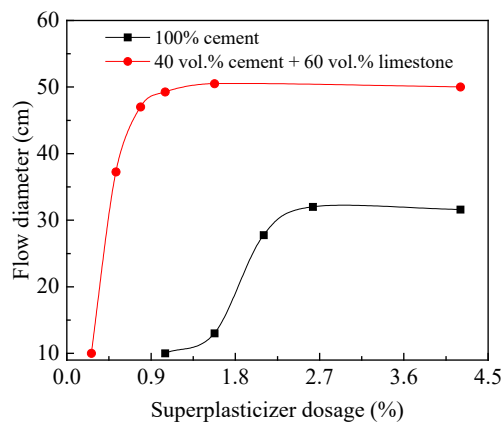


Figure 6: Spread flow of cement-limestone pastes (water = 200 kg/m³).

Figure 6 shows the spread flow of cement-limestone paste with a fixed water content (200 kg/m³). Replacing cement by high-volume limestone fillers, e.g. 60 vol.%, the mini-slump flow was significantly enhanced. In addition, the saturation dosage of superplasticizer was greatly decreased from about 2.3% to 0.7% by the

mass of powder. In other words, high-volume limestone powder substitution could not only decrease the cement consumption, but also improve the compactness by largely reducing both water content and superplasticizer dosage. Furthermore, a lot of cement grains were not completely hydrated due to the very low water-to-cement ratio. Limestone powder addition could increase the hydration degree of cement because of the increased water-to-cement ratio, as proven in Figure 7(a) [11]. The improved compactness and hydration degree contributed to higher compressive strength with 34% and 54% limestone powder, while a slightly lower strength with a further higher amount of limestone powder, e.g. 74%, as shown in Figure 7(b) [11]. It can be concluded that some minimal additions with good plasticization effect can be used to replace high volume of cement in sustainable UHPC.

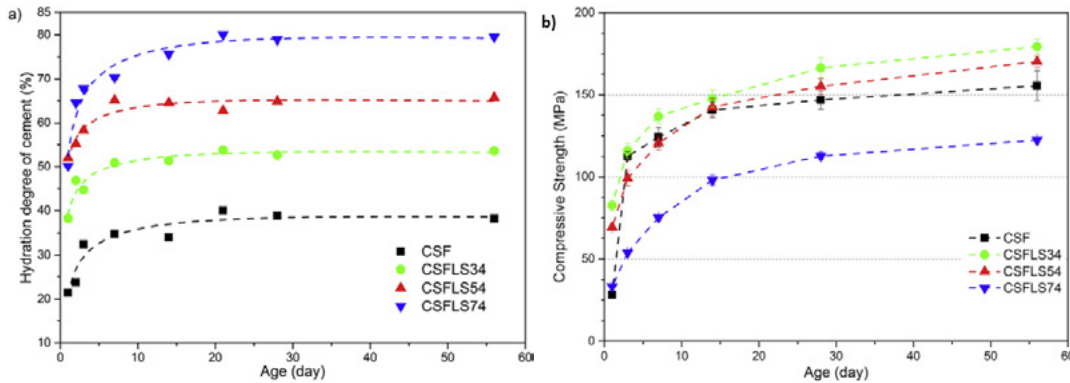


Figure 7: (a) hydration degree and (b) compressive strength of UHPC with limestone powder [11].

4. Thermal and chemical activation

If too much SCM is used, the performance usually tends to decrease. Abdulkareem et al. used GGBS to replace cement with 30%, 50% and 80% by the volume [12,13]. As shown in Figure 8, 50% and 80% volume-substitution rates caused a considerable reduction on compressive strength development. The negative influence was mainly attributed to the dilution of the more reactive cement and alkali environment. Hence, activations on the hydration of SCM and cement by increased thermal and alkaline environments are probably efficient solutions.

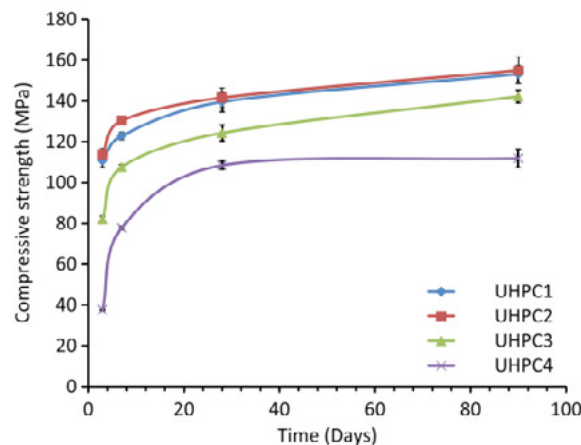


Figure 8: Compressive strength of UHPC with different contents of GGBS, the volume-substitution rates of cement by GGBS are 0, 30%, 50%, 80% for UHPC1, UHPC2, UHPC3 and UHPC4, respectively [13].

When different contents of alkalis (e.g. KOH) were added in UHPC with large amounts of slag, the compressive strength could be improved, especially at early ages, as shown in Figure 9. Slag particles reacted rapidly and promoted the formation of hydrates. More hydration products were generated to fill the

porosity and improve the strength in alkali-activated UHPC. In addition, relatively low content of KOH, namely 3.39 kg/m³, seemed to be enough to activate the combined binders. And further higher contents only showed effect on 3 days strength instead of later strength development.

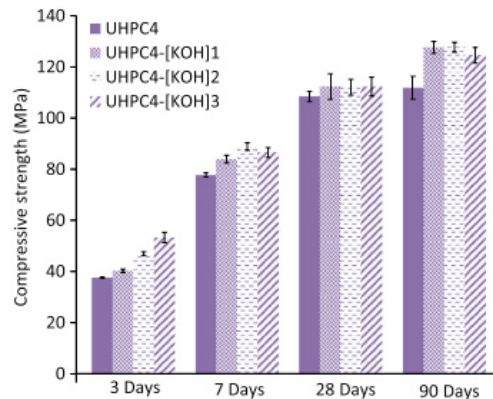


Figure 9: Compressive strength of UHPC with chemical activation, the used concentrations are 3.39 kg/m³, 6.78 kg/m³ and 10.17 kg/m³ for [KOH]₁, [KOH]₂ and [KOH]₃, respectively [13].

The sustainable UHPC incorporating high content of GGBS can also be activated by high temperatures curing. Figure 10 shows the 90 days compressive strength of sustainable UHPC with GGBS, by using a thermal curing with 90 °C from 48 h to 72 h after mixing. Compared to the results in Figure 8, the thermal activation significantly enhanced the compressive strength, attributed to the faster hydration reaction rate of both cement and slag under higher temperatures. Furthermore, the thermal-activated UHPC with a high content of GGBS could even acquire a higher mechanical strength than the reference without any GGBS.

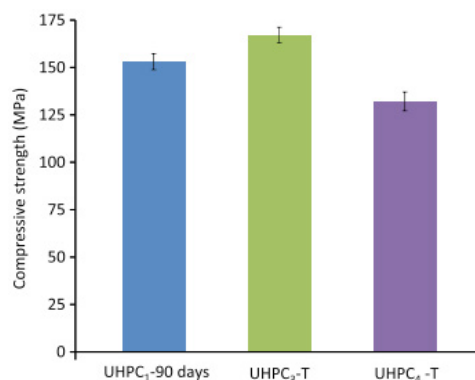


Figure 10: 90 days compressive strength of UHPC with thermal activation, a temperature of 90 °C is applied from 48 h to 72 h after mixing [13].

5. Introducing coarse aggregates

The aggregate-to-powder ratio is another key factor to determine the cement consumption. Traditional UHPC is usually developed without utilizing any coarse aggregate. Recently, coarse aggregates are attempted to be introduced into UHPC system, in order to reduce the powder content, as well as strengthen the impact resistance [14,15] and volume stability [16]. Liu et al. investigated the content effect of coarse aggregate with the particle size between 8 mm to 20 mm on tensile behaviour of UHPC, as shown in Figure 11 [17]. With the increase of coarse aggregate content up to 40%, both first-crack and maximum tensile strength tended to have a decrease. But considering the benefits of coarse aggregate on powder reduction, the strength decrease was tolerable.

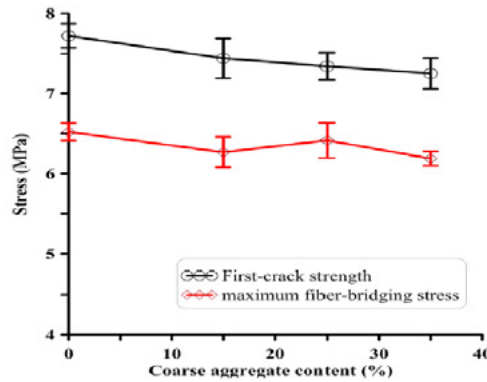


Figure 11: Tensile properties of UHPC on coarse aggregate content [17].

Our previous study investigated the size effect of coarse aggregate on properties of UHPC [18]. The basalt aggregates were selected to match the high-strength of UHPC matrix. As illustrated in Figure 12, the optimum powder content was diminished from 800 kg/m³ to 700 kg/m³, when the maximum basalt aggregates size increased from 8 mm to 16 mm. It revealed that less powder/cement content was demanded for UHPC incorporating coarser aggregates. Although the powder consumption was reduced (Figure 12(b)), the compressive strength was still comparable to the mixture with more powder content and finer aggregates in Figure 12(a). With the inclusion of coarse aggregates, the optimal particle size distribution and compactness could be changed, resulting in less powder demand but comparable strength [18].

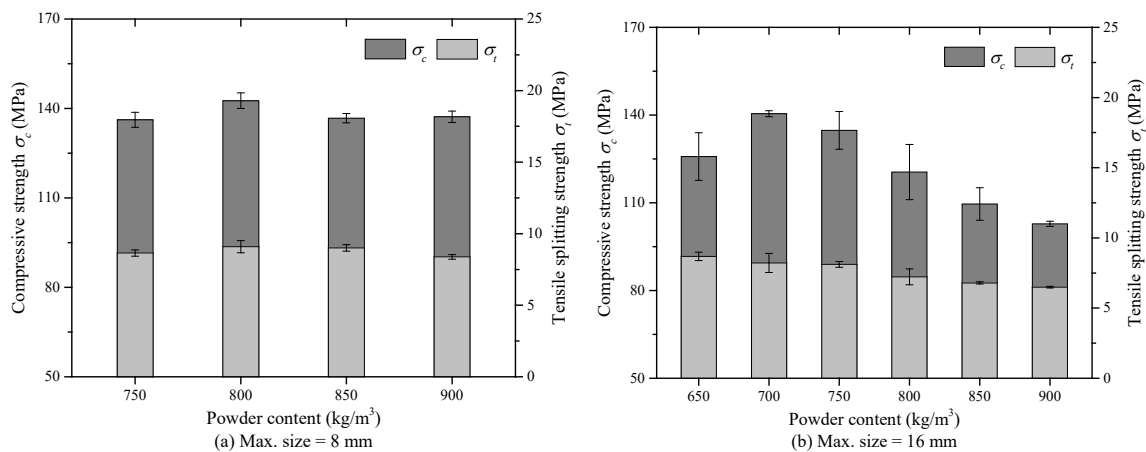


Figure 12: strength of UHPC with different powder contents [18].

6. Two-stage casting method

As analysed above, utilization of coarse aggregates is an efficient way to design sustainable UHPC with low cement consumption. However, the aggregates normally occupy rather limited volume, around 36% of total UHPC mixture [19]. How to increase the granular skeleton volume and decrease the powder content is still an issue in UHPC system. Two-stage concrete (TSC) is a type of concrete that makes full potential to enlarge the volume of aggregate [20]. The coarse aggregates are firstly pre-placed in the concrete mould, then grout is injected into the voids between the aggregates by gravity pressure, as illustrated in Figure 13 [21]. The volume of coarse aggregate skeleton could easily achieve 55% based on the drying packing density of coarse aggregates themselves, which is much higher than that in the conventional UHPC.

Thus, it is of great interest to develop low-cement UHPC by the two-stage casting method. To meet the requirement of high strength in two-stage UHPC, high strength coarse and ultra-high performance grout are needed. Our research showed that the concept of two-stage UHPC was successfully designed with very low cement consumption between 340 kg/m³ and 450 kg/m³, and compressive strength between

120 MPa-150 MPa. Figure 14 shows the binder (mainly cement) efficiency of TS-UHPC that was defined as compressive strength normalized by binder amount. The designed TS-UHPC achieved the advantages of both UHPC (high strength) and TSC (low binder consumption), resulting in a relatively high binder efficiency between 0.19 MPa/(kg/m³) and 0.42 MPa/(kg/m³).

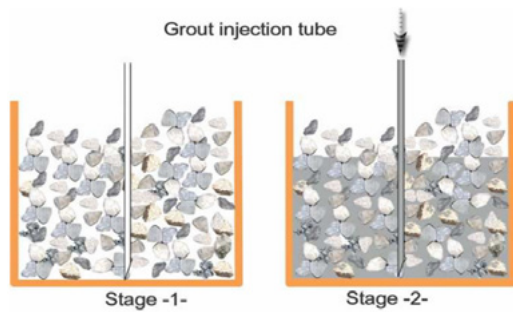


Figure 13: Casting procedure of two-stage concrete [21].

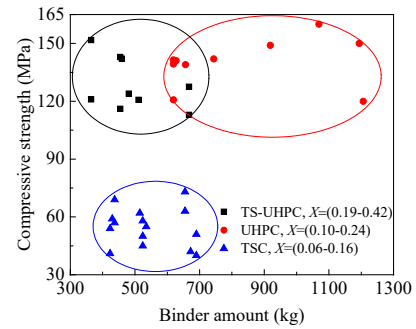


Figure 14: Binder efficiency of TS-UHPC.

7. Conclusions and recommendations

Based on the reviews and discussions above, the following conclusions can be drawn:

1. Appropriate ternary and quaternary blends with SCMs have positive synergistic effect on both fresh and hardened properties of UHPC with low cement, due to improved particle packing, mineral proportion, hydration production and microstructure.
2. Certain minerals possessing plasticization effect, e.g. limestone powder, can be used to replace cement in sustainable UHPC without sacrificing properties, attributed to the less water and superplasticizer demands.
3. Thermal curing and alkalis addition are efficient to activate the hydration and then compensate the negative dilution effect, when a high volume of SCMs is used to partly substitute cement in UHPC.
4. Introducing coarse aggregates in UHPC is an efficient attempt to reduce the powder demand. Although coarser aggregates tend to decrease the mechanical strength of UHPC, appropriate contents and particles sizes would limit the negative influences.
5. The concept of two-stage UHPC is successfully designed with very low cement consumption between 340 kg/m³ and 450 kg/m³, and compressive strength between 120 MPa-150 MPa.

Based on the previous studies, the following researches need to be further investigated to develop sustainable UHPC with low cement consumption:

1. More ternary and quaternary binders for UHPC are needed to be developed for sustainable UHPC, considering not only mechanical strength but also durability.
2. More raw materials possessing mineral plasticization effect should be investigated, under the condition of lower water amount and superplasticizer.
3. The thermal and chemical activations adversely increase the cost and energy consumption. Hence, efficient thermal curing regimes and optimum alkalis contents should be proposed by considering both cost and performance of UHPC, in the cases of different SCMs conditions. And the compatibility between superplasticizer and chemical activation also should be carefully researched.

4. More possible materials for granular skeleton in TS-UHPC need to be researched, such as ceramic or metal to improve some special properties, e.g. impact resistance.

8. Acknowledgment

The research was carried out with funding by the China Scholarship Council and Eindhoven University of Technology.

9. References

- [1] Wang D, Shi C, Wu Z, Xiao J, Huang Z, Fang Z. A review on ultra high performance concrete: Part II. Hydration, microstructure and properties. *Constr Build Mater* 2015;96:368–77.
- [2] Richard P, Cheyrezy M. Composition of reactive powder concretes. *Cem Concr Res* 1995;25:1501–11.
- [3] de Larrard F, Sedran T. Optimization of ultra-high-performance concrete by the use of a packing model. *Cem Concr Res* 1994;24:997–1009.
- [4] Shi C, Wu Z, Xiao J, Wang D, Huang Z, Fang Z. A review on ultra high performance concrete: Part I. Raw materials and mixture design. *Constr Build Mater* 2015;96:368–77.
- [5] Yu R, Spiesz P, Brouwers HJH. Development of an eco-friendly Ultra-High Performance Concrete (UHPC) with efficient cement and mineral admixtures uses. *Cem Concr Compos* 2015;55:383–94.
- [6] Kang SH, Hong SG, Moon J. The use of rice husk ash as reactive filler in ultra-high performance concrete. *Cem Concr Res* 2019;115:389–400.
- [7] Shi C, Wang D, Wu L, Wu Z. The hydration and microstructure of ultra high-strength concrete with cement–silica fume–slag binder. *Cem Concr Compos* 2015;61:44–52.
- [8] Arora A, Aguayo M, Hansen H, Castro C, Federspiel E, Mobasher B, et al. Microstructural packing- and rheology-based binder selection and characterization for Ultra-high Performance Concrete (UHPC). *Cem Concr Res* 2018;103:179–90.
- [9] Bentz DP, Ferraris CF, Jones SZ, Lootens D, Zunino F. Limestone and silica powder replacements for cement: Early-age performance. *Cem Concr Compos* 2017;78:43–56.
- [10] Kang SH, Jeong Y, Tan KH, Moon J. The use of limestone to replace physical filler of quartz powder in UHPFRC. *Cem Concr Compos* 2018;94:238–47.
- [11] Huang W, Kazemi-Kamyab H, Sun W, Scrivener K. Effect of cement substitution by limestone on the hydration and microstructural development of ultra-high performance concrete (UHPC). *Cem Concr Compos* 2017;77:86–101.
- [12] Abdulkareem OM, Ben Fraj A, Bouasker M, Khelidj A. Mixture design and early age investigations of more sustainable UHPC. *Constr Build Mater* 2018;163:235–46.
- [13] Abdulkareem OM, Ben Fraj A, Bouasker M, Khelidj A. Effect of chemical and thermal activation on the microstructural and mechanical properties of more sustainable UHPC. *Constr Build Mater* 2018;169:567–77.
- [14] Peng Y, Wu H, Fang Q, Liu JZ, Gong ZM. Impact resistance of basalt aggregated UHP-SFRC/fabric composite panel against small caliber arm. *Int J Impact Eng* 2016;88:201–13.

- [15] Li PP, Yu QL. Responses and post-impact properties of ultra-high performance fibre reinforced concrete under pendulum impact. *Compos Struct* 2019;208:806–15.
- [16] Dittmer T, Beushausen H. The effect of coarse aggregate content and size on the age at cracking of bonded concrete overlays subjected to restrained deformation. *Constr Build Mater* 2014;69:73–82.
- [17] Liu J, Han F, Cui G, Zhang Q, Lv J, Zhang L, et al. Combined effect of coarse aggregate and fiber on tensile behavior of ultra-high performance concrete. *Constr Build Mater* 2016;121:310–8.
- [18] Li PP, Yu QL, Brouwers HJH. Effect of coarse basalt aggregates on the properties of Ultra-high Performance Concrete (UHPC). *Constr Build Mater* 2018;170:649–59.
- [19] Stengel T, Schießl P. Life cycle assessment (LCA) of ultra high performance concrete (UHPC) structures. Woodhead Publishing Limited; 2014.
- [20] Abdelgader HS. How to design concrete produced by a two-stage concreting method. *Cem Concr Res* 1999;29:331–7.
- [21] Abdelgader HS, S E-BA. Investigations on some properties of two-stage (pre-placed aggregate) concrete. NTCC2014 Int. Conf. Non-Traditional Cem. Concr., 2015.

Suitability of phenolphthalein indicator method for alkali activated concrete

O. O. Ojedokun¹, P.S. Mangat¹

¹Centre for Infrastructure Management, Materials and Engineering Research Institute, Sheffield Hallam University, Sheffield S1 1WB, UK.

Abstract

Alkali activated cementitious materials (AACM) concrete is a sustainable alternative to Portland cement PC concrete by reducing CO₂ emitted during the production of PC by 60%. Fundamental investigations on alkali activated concrete (AACM) has been on their engineering properties with less emphasis on the service life and durability properties. The carbonation effect on concrete is crucial for its service life prediction. This paper investigates the suitability of phenolphthalein indicator method to determine the carbonation front in AACM. The geopolymerisation products of AACM are different from the hydration products of PC concrete and consequently, the carbonation process of these two types of concrete is expected to be different. Three mixes of AACM 1, 2, 3 and control PC concrete were produced and cured in water (20 ± 2°C) for 27 days and then in laboratory air (20 ± 2°C, 65% R.H) for 42 days. A total of twenty-four cylindrical specimens with 50mm diameter X 60mm depth were produced. All the specimens were exposed to 5% CO₂ inside a carbonation chamber at 20 ± 2°C and 65% R.H for 327 days. Carbonation depths were determined by phenolphthalein indicator method on twelve specimens. Powder samples were obtained from the carbonated and non-carbonated zones of the other twelve specimens to measure the pH of the carbonated concrete and powder. Results show that the pH of the carbonation in AACM concrete and mortar are above threshold 9 while it was below 9 in PC concrete. This suggests that phenolphthalein indicator method is inappropriate to determine the carbonation of alkali activated cementitious materials (AACM) concrete

Keywords: Alkali activated cementitious materials (AACM) concrete, carbonation depths, phenolphthalein indicator method, carbonated and non-carbonated zones.

1. Introduction

Research findings show attractive attributes of alkali activated cementitious materials (AACM) concrete as a construction material over Portland cement (PC) concrete. These attributes include low CO₂ emission and energy demand during its production [1, 2], superior strength and pore properties [3], lower bound chloride ingress [4]. However, limited knowledge on the durability properties and in-service performance of AACM exists in literature. Field applications of AACM are restricted due to the limited knowledge of its structural behaviour when subjected to exposure to corrosion initiators such as carbonation.

Carbonation in PC concrete reduces the pH of its pore solution to below 9 [5, 6]. This occurs when atmospheric carbon dioxide, CO₂, dissolves in the concrete pore solution to form carbonic acid HCO₃ which then reacts with the main hydration products of concrete, Ca(OH)₂ and C-S-H, to form calcium carbonate CaCO₃ [7, 8]. The hydroxyl ion (OH)₂ within the pore solution is displaced by this reaction thereby depleting the protective passive film around the reinforcing steel in concrete. The progression of these reactions results in carbonation induced corrosion of reinforcement in the presence of oxygen and water.

AACM concrete does not contain calcium hydroxide, $\text{Ca}(\text{OH})_2$, which can react with carbonic acid, HCO_3^- , to produce calcium carbonate CaCO_3 , unlike PC concrete which has calcium hydroxide $\text{Ca}(\text{OH})_2$ as its hydration product. The reaction of atmospheric CO_2 with the geopolymerisation and hydration compounds of AACM and PC concrete respectively is dependent on the amount and type of these compounds.

The carbonated zone of PC concrete is determined by the phenolphthalein indicator test [9]. Spraying phenolphthalein solution on carbonated concrete surfaces indicates the depletion of $\text{Ca}(\text{OH})_2$ within the concrete matrix, which is not present in AACM concrete. Therefore, the use of phenolphthalein indicator method to determine the carbonation front may not give a true extent of carbonation in AACM concrete. The suitability of the phenolphthalein indicator method for AACM concrete will be addressed in this study.

The chemistry of carbonation in PC concrete is fairly well documented while limited knowledge is available for AACM concrete [10]. Like other durability properties, the carbonation of AACM is significantly influenced by its pore chemistry which is significantly different from that of PC concrete. The mechanism of carbonation in PC concrete is represented in equation 1 -3:



Bicarbonate ions are formed when CO_2 reacts with water at the carbonated zone (equation 1). These bicarbonate ions dissociate near the non-carbonated zone within the PC concrete to form carbonate ions due to the high pH of the pore solution (equation 2). The carbonate ions precipitate as calcium carbonate (CaCO_3) crystals when they react with the hydration product of PC concrete ($\text{Ca}(\text{OH})_2$) (equation 3). These crystals are present in PC concrete in two forms: vaterite and calcite, the metastable vaterite turns to calcite over time [11]. This process will continue until all the hydration product, $\text{Ca}(\text{OH})_2$, of PC concrete is consumed by the carbonate ions. The pH of PC concrete drops because of the low calcium ions present in the pore solution due to this process. The phenolphthalein test for PC concrete is suitable for detecting these chemical layers in PC concrete.

The carbonation effect on AACM concrete by using the accelerated testing method may have overestimated its actual degradation in service life [12]. A change in AACM pore solution equilibria may induce accelerated carbonation compared to under natural carbonation giving a higher apparent carbonation rate [12]. Published results on the carbonation of AACM concrete are inconsistent in comparison with PC concrete. For example, high depths of carbonation were recorded for silicate-activated blast furnace slag concrete compared with PC concrete under accelerated carbonation conditions 10-20% CO_2 and 70% R.H. [13, 14]. Other studies show that the depth of carbonation of alkali activated blast furnace slag concrete and mortar is comparable to those of PC concrete or mortar [15]. The author [15] concluded that the refinement of the pore structure of alkali activated blast furnace slag concrete is responsible for its carbonation resistance, however, a high relative humidity of 90% was used for the accelerated carbonation test which would slow the diffusion of CO_2 within the concrete matrix and invalidate the author's results.

The rate of carbonation in concrete is a slow process which sometimes takes years to manifest. Concrete structures in large cities are susceptible to carbonation due to human activities involving high emissions of CO_2 , up to 1% by volume of air [16]. The carbonation chamber used in the laboratory for accelerated testing was maintained at 5% CO_2 concentration, 65% relative humidity and a temperature of $20 \pm 2^\circ\text{C}$ to achieve the optimum rate of carbonation in both AACM and the control PC concrete. The diffusion parameters of the concrete pores have considerable influence on the rate of carbonation. The diffusion

rate of CO₂ within a concrete matrix is four orders of magnitude slower than O₂ when its pores are fully saturated while its diffusion remains inactive when the concrete pores are insufficiently saturated [16–18].

2. Experimental Programme

2.1 Materials and mixes

Details of AACM mixes 1, 2 and 3 and the control PC concrete are given in Table 1. AACM and PC concrete were produced from ground granulated blast furnace slag (GGBS) and ordinary Portland cement CEM 1 of grade 42.5R [19] respectively. 10 mm uncrushed gravel, 6 mm limestone and a medium grade sand of 80% particle size passing 1mm sieve were used as coarse and fine aggregates. The activator dilutions of 0%, 3.88% and 7.76% were used to prepare AACM 1, 2 and 3 mixes respectively. Liquid/binder ratio 0.47 was used for both AACM and PC concrete mixes. AACM mixes contained 2% by binder weight of shrinkage reducing admixtures (SRA) made from Alkyl-ether and 0.75% by binder weight of retarder R42 made from a blend of high grade polyhydroxycarboxylic acid derivatives. The shrinkage reducing admixture also enhances workability while the retarder reduces the setting time of AACM concrete.

Table 1: Composition of AACM 1, 2, 3 and the control PC concrete

Mix	Binder Content (%)	Fine Agg. (%)	Coarse Agg. (%)		Liquid/Binder Ratio	Activator Dilution (%)	R42 (% by weight of binder)	SRA
			10mm Gravel	6mm Limestone				
AACM 1	25	18	29.3	15.7	0.47	0	0.2	0.5
AACM 2	25	18	29.3	15.7	0.47	3.88	0.2	0.5
AACM 3	25	18	29.3	15.7	0.47	7.76	0.2	0.5
Control PC	20	26	28.9	15.5	0.47(w/c)	-	-	-

*R42 is the retarder; SRA is the shrinkage reducing admixture

2.2 Specimen preparation

The concrete specimens were cast in a 0.0625m³ (150kg) capacity Cretangle mixer. AACM and PC concrete specimens were cast in plastic cylinders of 50mm diameter X 60mm depth as shown in Fig. 1 in two layers and compacted on a vibrating table. Self-adhesive bitumen tape was fixed at the bottom of the plastic cylinder moulds before casting to prevent the concrete from pouring out (Fig. 2). The specimens were cured in the laboratory air (20 ± 2°C, 65% R.H.) for 24hrs while covered with polythene sheets. They were left in the moulds to prevent the ingress of CO₂ through the bottom face and circumference of the specimens. The specimens were wet cured for 27days at a temperature of 20 ± 2°C followed by dry curing for 42days at 65% R.H. and a temperature of 20 ± 2°C until the change in their unit weight was less than 0.2% in a 24-hour period to reduce its moisture content. The specimens were then placed inside the carbonation chamber exposed to 5% CO₂ concentration at 65% relative humidity and temperature of 50°C for 327days. After exposure to 5% CO₂ concentration for 327days, the specimens were grouped into two batches. The first batch of AACM and PC concrete specimens were used to determine the depth of carbonation with the phenolphthalein test [9]. Powder samples were collected at the carbonated and non-carbonated zones in the second batch for pH analysis. A total of 24 specimens were produced for both AACM and the control PC concrete, 6 specimens per each mix in Table 1.



Fig. 1: Casting concrete specimens in cylindrical plastic moulds



Fig. 2: Self-adhesive tape fixed at the bottom of cylindrical moulds

2.3 Test Procedure

The cylindrical specimens were removed from the carbonation chamber after 327 days exposure. These specimens were removed from their plastic moulds (sleeves) and split into halves vertically along their depths as shown by section A-A in Fig. 3. The splitting tensile strength procedure was adopted to break the cylinders into two longitudinal halves. The depth of carbonation was determined by spraying phenolphthalein on the exposed (split) surface of one broken half of each cylinder according to standard procedure [9]. However, phenolphthalein was not applied to the surface of the second half of each cylinder.

The depth of carbonation profile obtained from the first half cylinder was marked on the second half of the cylinder that was not sprayed with phenolphthalein. This was carefully chiselled out to obtain concrete chunks of the carbonated and non-carbonated zones. This procedure was performed on six specimens for each AACM and PC concrete to obtain enough concrete chunks for the test. The chunks were ground to powder and passed through a 150 μm sieve to obtain concrete powder for the carbonated and non-carbonated zones (Fig. 4).

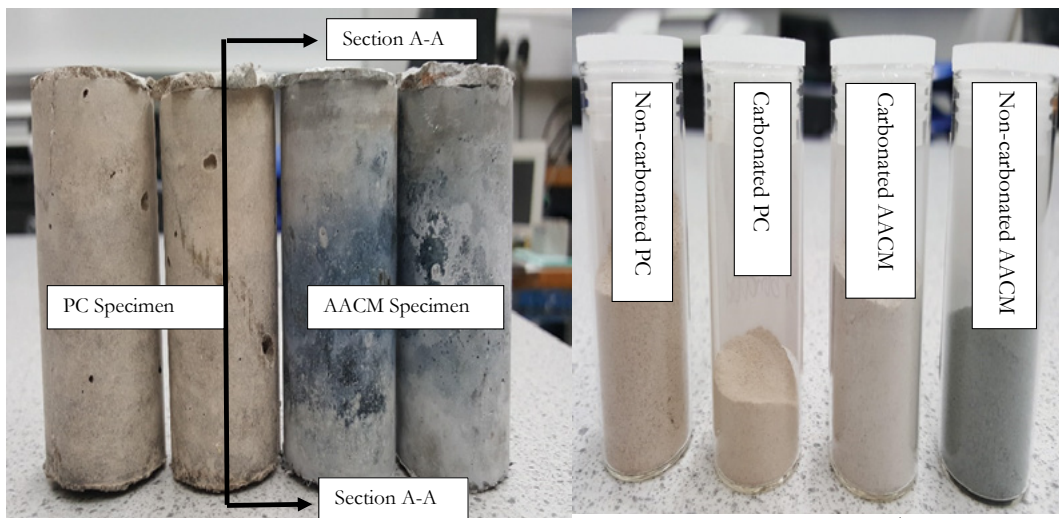


Fig. 3: Demoulded cylinders showing the section A-A of splitting concrete/mortar powder stored in air-proof plastic vials

Fig. 4: AACM and OPC

A second set of powder test samples was similarly obtained by removing the coarse aggregate particles from the concrete chunks. The concrete pieces were crushed to separate the coarse aggregate particles from the matrix and they were removed by sieving. The remaining mortar material was ground to obtain mortar powder for the carbonated and non-carbonated zones. pH analysis was performed on these carbonated and non-carbonated powder samples.

2.3.1 pH Analysis

The ex-situ leaching method of concrete [20] was adopted to obtain the solution used for the pH analysis of the concrete and mortar samples. This was carried out by dissolving 5grams of the powder sample in distilled water at a liquid/solid ratio of 1:1 in an air-tight plastic vial. The solution was shaken thoroughly for 2mins to ensure a homogenous mix of the powder. The powder solution in an air-tight plastic vial was left undisturbed for 5hrs to allow for leaching. The concrete powder solution was then filtered to obtain a solution that does not contain powder particles. A double junction electrode connected to a benchtop meter 3-in-1 was dipped inside the filtered solution to measure its pH. This device measures pH ranging from 0.00 to 14.00 and can measure sample volumes as small as 0.2mL with an accuracy of ± 0.01 .

3. Results and discussion

3.1 Depth of carbonation

The carbonation depths of AACM and PC concrete is shown in Fig. 5. The carbonated and non-carbonated zones are marked on the broken faces of both AACM and PC concrete (Fig. 5).

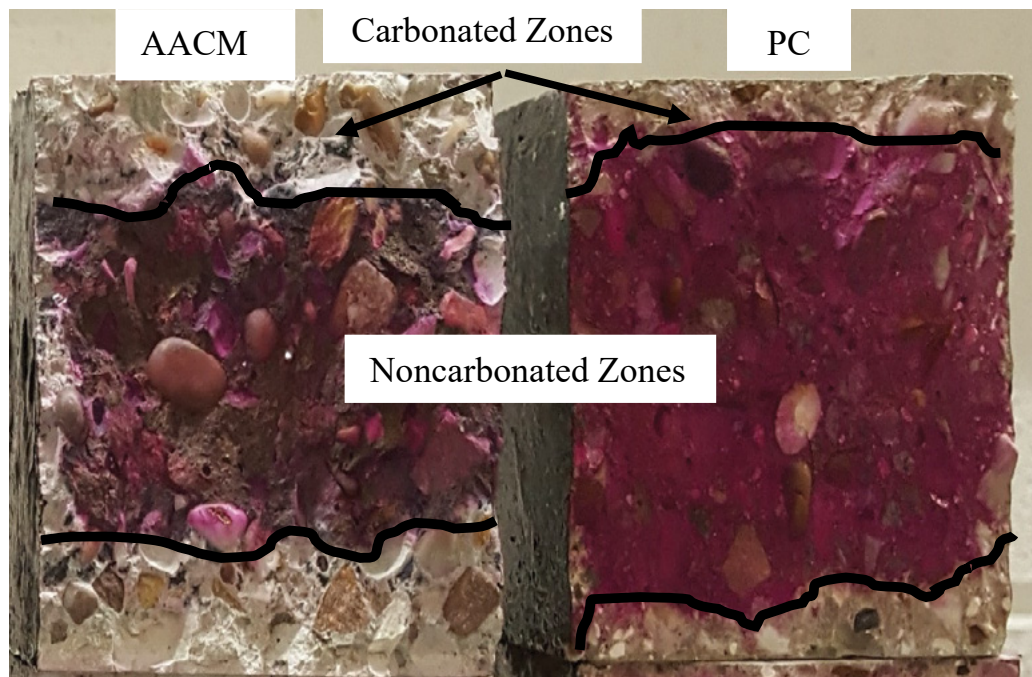


Fig. 5: showing the carbonation and non-carbonated zones in AACM and PC concrete

Fig. 5 shows that the depths of carbonation front which occurred at the two opposite faces exposed to CO₂ while the other opposite two faces coated with bitumen paint have insignificant carbonation front. This shows that the bitumen paint is an effective barrier to CO₂ diffusion in concrete. The presence of optimum moisture content and CO₂ within the concrete matrix resulted in the decalcification of the Ca-rich gel binder within the concrete matrix.

Increase in the depth of carbonation is observed in AACM concrete than the control PC concrete as shown

in Fig. 5. The average carbonation depth in AACM 1, 2 and 3 are 25.19, 26.75 and 29.25mm respectively while it is 14.13mm for PC concrete after 327days exposure.

Increase in the depth of carbonation was observed for water-glass activated slag mortar [21]. The author [21] observed a much deeper and intense carbonation between 28 and 120 days while moderate increase in the carbonation depth was observed between 120 and 240 days. The specimens were cured in a closed chamber containing K_2CO_3 solution, kept at a relative humidity of 43.2%. The chamber was saturated with CO_2 twice daily with unknown concentration of the CO_2 .

3.2 pH of carbonated zone

The pH of the powder solutions extracted from AACM and PC concrete and mortar at the carbonated zones is shown in Fig. 6.

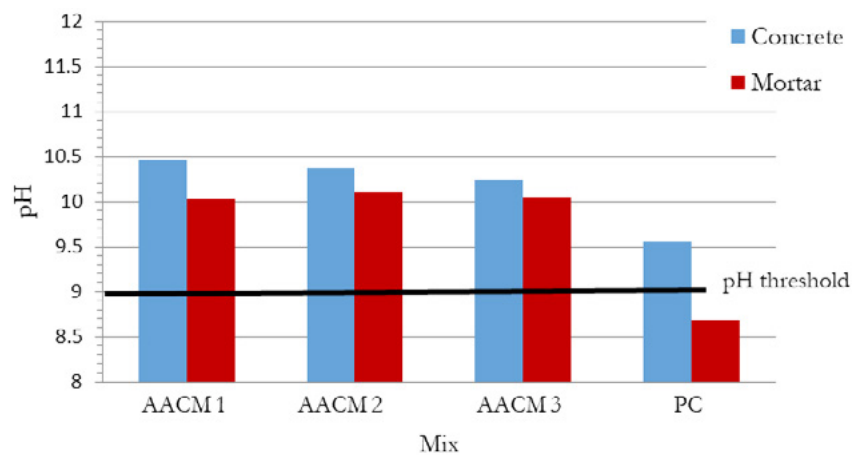


Fig. 6: pH of AACM and PC powder solutions after 327days exposure to 5% CO_2 .

The pH of the concrete powder solutions at the carbonated zones of AACM 1, 2, 3 and PC concrete are above the carbonated threshold of 9 as shown in Fig. 6. The pH values are 10.62, 10.46, 10.37, 10.25 and 9.56 for AACM 1, 2, 3 and PC concrete respectively. The pH of the mortar solution is also greater than the threshold value of 9 for all AACM mixes whereas the PC mortar has a pH value significantly lower than the threshold of 9. The high pH exceeding the carbonation threshold in AACM mortar solution is an indication that the phenolphthalein indicator method fails to detect carbonation in AACM concrete compared with PC concrete having pH of 8.69. The phenolphthalein indicator method produces no colour change when the pH of the pore solution is about 9 for PC concrete at the carbonated zone. However, in the case of AACM the phenolphthalein indicator method show no colour change when the pH of pore solution is above 10 at the carbonated zone (Fig. 6). The colourless change at the carbonated zone indicates the absence of $Ca(OH)_2$ [16]. Since $Ca(OH)_2$ is absent from the AACM pore solution, an alternative method besides using the phenolphthalein indicator method for assessing the carbonation in AACM is required.

The pH of mortar solutions at the carbonated zones for both AACM and PC are lower than that of the concrete. The pH of the mortar solutions of AACM 1, 2, 3 and PC at the carbonated zones are 10.33, 10.02, 10.1, 10.05 and 8.69 respectively. The difference in their solution pH is due to the release of alkaline content by the aggregate present in the concrete. PC concrete which had the highest aggregate content of 70.4% compared with 63% for AACM (Table 1) shows the highest pH difference between the solution extracted from concrete powder and mortar powder. The differences in pH between concrete and mortar for AACM 1, 2, 3 and PC concrete are 4.2%, 2.6%, 1.95% and 9.1% respectively.

3.3 Activator Dilution

The influence of activator dilution on the pH of powder solution from AACM concrete and mortar at the carbonated zones is shown in Fig 7.

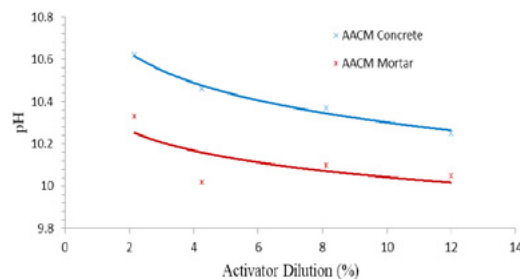


Fig. 7: Influence of activator on the pH of AACM concrete and mortar solutions at carbonated zones

The difference in the pH of solutions extracted from AACM concrete and mortar powder at the carbonated zones is fairly constant at different activator dilution (Fig. 7). This is because the aggregate content of 63% is constant in AACM 1, 2 and 3 mixes are the same (Table 1). The release of alkaline content by the aggregate present in the AACM 1, 2 and 3 accounts for the increase in the pH of solutions extracted from the AACM mortar. On the other hand, carbonation reacts chemically with AACM mortar while the aggregate in the concrete will influence the diffusion rate of CO₂ and moisture due to the interfacial transition zones around the aggregate.

The pH of solutions extracted from AACM concrete and mortar powders is highest at the lowest activator dilution (Fig. 7). The differences in the pH of AACM concrete and mortar solutions for different activator dilution are attributed to their porosity [3] which affected the rate of carbonation. AACM with 0% activator dilution has the lowest porosity of 4.64%, followed by 3.88% activator dilution which has 6.67% porosity while 7.76% activator dilution has the highest porosity of 7.71% under 3days wet curing (20 ± 2°C) following 24days dry curing (20 ± 2°C, 65% R.H) [3]. The corresponding pH values of AACM concrete are 10.46, 10.3 and 10.25. The other factor influencing the difference in pH in both AACM concrete and mortar solutions is the aggregate content. Yinghong [22] studied the leaching of alkali content of an open graded recycled coarse aggregate and the adverse effect of carbonation on the pore solution. The author [22] observed an increased pH of the pore solution due to leaching of alkali content from the recycled coarse aggregate. The alkali content of the recycled coarse aggregate is consumed during carbonation. However the release of pH-dependent constituents that cause the drop in pH is delayed by the dense structure of concrete [22]. AACM represented in Fig 7 is denser at 0% activator dilution than at 7.76% activator dilution, which is the reason for the differences between the pH of concrete solution and mortar solution at higher and lower activator dilution.

3.4 Relationship between carbonation depth and porosity

The relationship between carbonation depth at 327days exposure to 5% CO₂ and effective porosity of AACM 1, 2 and 3 mixes at 28 days is shown in Fig 8. Details of the pore properties and the effective porosity of AACM mortar mixes are reported in the authors' previous publication [3]. The following linear relationship is established between the effective porosity and the depth of carbonation with a correlation of 0.98:

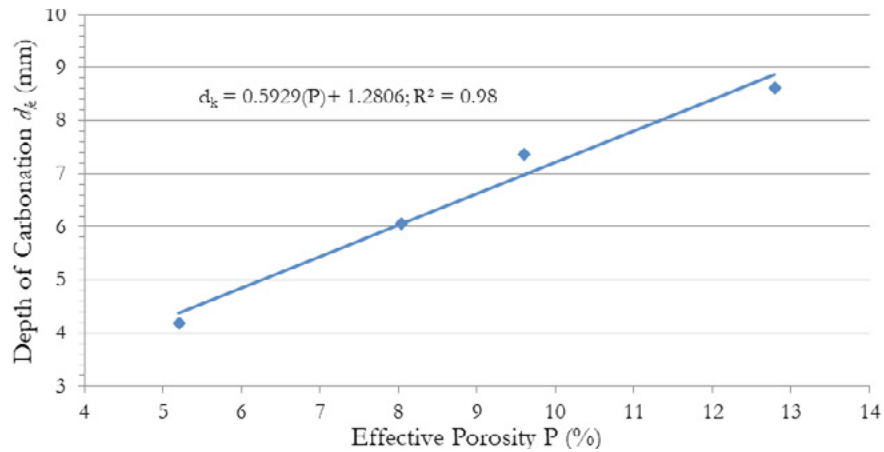


Fig. 8: The relationship between depth of carbonation d_k and effective porosity of AACM concrete

$$d_k = 0.5929(P) + 1.2806 \text{ with } R^2 = 0.98.$$

where; d_k is the depth of carbonation (mm) and P is the effective porosity (%).

The depth of carbonation increases with greater porosity. Concrete diffusivity which is a function of porosity is a major controlling factor for carbonation [16]. The ingress of CO_2 and moisture from the environment into the concrete is inhibited by decreasing porosity. The carbonation process is complicated because it involves the transport of liquid and gas which cannot be represented simply with Fick's law [23]. Lagerblad [11] stated that it is difficult to apply the Fick's law equation because of the simultaneous inward and outward diffusions involving carbonate and calcium ions. The pore structure is altered during the inward and outward diffusions involving carbonate ions and calcium ions by reacting with the concrete matrix. For PC concrete, a dense pore structure evolves as the outward diffusion of CaCO_3 forms precipitates that block the concrete pores. In the case of AACM, the calcium ions from the geopolymerization products disintegrate by a process termed decalcification and diffuse outward into the environment. Whilst the chemical compound (CaCO_3) formed during carbonation in PC concrete blocks the pores, the disintegration of calcium ion due to decalcification in AACM concrete enlarges the pores.

4. Conclusions

This paper investigates the suitability of using phenolphthalein indicator method to determine carbonation front in alkali activated concrete AACM. Twenty-four AACM and PC concrete were produced and cured in water ($20 \pm 2^\circ\text{C}$) for 27 days and then in laboratory air ($20 \pm 2^\circ\text{C}$, 65% R.H) for 42 days. These specimens were exposed to 5% CO_2 inside a carbonation chamber at $20 \pm 2^\circ\text{C}$ and 65% R.H for 327 days. Phenolphthalein indicator method was used to determine carbonation front of the AACM and PC concrete specimens. Powder samples were collected from the carbonated zones and their pH was determined. The following conclusions can be drawn from the study.

- The pH of mortar solutions at the carbonated zones for alkali activated cementitious materials (AACM) concrete is greater than the threshold of 9 while the corresponding PC mortar is below 9. For example, the pH of mortar solutions of AACM 1, 2, 3 and PC at the carbonated zones are 10.33, 10.02, 10.1, 10.05 and 8.69 respectively. This suggests that the application of phenolphthalein solution on faces of AACM produces pH higher than 9. The phenolphthalein method of determining the carbonation in AACM does not give a true representation and may not be an appropriate method for investigating the carbonation depth.
- The release of alkaline content by the coarse aggregate present in the AACM and PC concrete results in higher pH in concrete than the mortar excluding the coarse aggregate particles. The difference is

greater with increasing coarse aggregate content.

- Activator dilution with water increases the pH of carbonated AACMs (mortar and concrete). The porosity of AACMs also increases with activator dilution as they both provides a linear relationship between the two parameters. For example, AACM with 0% dilution has the lowest porosity of 4.64%, followed by 3.88% activator dilution which has 6.67% porosity while 7.76% activator dilution has the highest porosity of 7.71% under 3days wet curing ($20 \pm 2^{\circ}\text{C}$) and 24days dry curing ($20 \pm 2^{\circ}\text{C}$, 65% R.H). The corresponding pHs of AACM are 10.46, 10.3 and 10.25.
- The relationships between porosity and depth of carbonation in AACM concrete is as follows:

$$d_k = 0.5929(P) + 1.2806 \text{ with } R^2 = 0.98.$$

where; d_k is the depth of carbonation (mm) and P is the effective porosity (%).

5. Acknowledgment

The authors gratefully acknowledge the support of the Materials and Engineering Research Institute, Sheffield Hallam University and the funding provided to the second author for postgraduate study by the Tertiary Education Trust Fund, Ministry of Education, Federal Republic of Nigeria. The authors also acknowledge the award by the UK - India Newton - Bhabha programme through funding provided by Innovate UK, EPSRC (EP/P026206/1) and the Government of India for research on alkali activated cementitious materials AACMs.

6. References

1. Scrivener KL, Kirkpatrick RJ (2008) Innovation in use and research on cementitious material. *Cem Concr Res* 38:128–136. <https://doi.org/10.1016/j.cemconres.2007.09.025>
2. Madlool NA, Saidur R, Hossain MS, Rahim NA (2011) A critical review on energy use and savings in the cement industries. *Renew. Sustain. Energy Rev.* 15:2042–2060
3. Mangat PS, Ojedokun OO (2018) Influence of curing on pore properties and strength of alkali activated mortars. *Constr Build Mater* 188:337–348. <https://doi.org/10.1016/j.conbuildmat.2018.07.180>
4. Mangat, P.S. and Ojedokun OO (2019) Bound chloride ingress in alkali activated concrete. *Constr Build Mater* 212:375–387. <https://doi.org/https://doi.org/10.1016/j.conbuildmat.2019.03.302>
5. Ho DWS, Lewis RK (1987) Carbonation of concrete and its prediction. *Cem Concr Res.* [https://doi.org/10.1016/0008-8846\(87\)90012-3](https://doi.org/10.1016/0008-8846(87)90012-3)
6. Papadakis VG, Fardis MN, Vayenas CG (1992) Effect of composition, environmental factors and cement-lime mortar coating on concrete carbonation. *Mater Struct* 25:293–304. <https://doi.org/10.1007/BF02472670>
7. Hobbs DW (2001) Concrete deterioration: causes, diagnosis, and minimising risk. *Int Mater Rev* 46:117–144. <https://doi.org/10.1179/095066001101528420>
8. Johannesson B, Utgenannt P (2001) Microstructural changes caused by carbonation of cement mortar. *Cem Concr Res* 31:925–931. [https://doi.org/10.1016/S0008-8846\(01\)00498-7](https://doi.org/10.1016/S0008-8846(01)00498-7)
9. BS EN 14630 (2006) Products and systems for the protection and repair of concrete structures — Test methods — Determination of carbonation depth in hardened concrete by the phenolphthalein method

10. John L. Provis, Deventer JSJ van (2014) Alkali-Activated Materials State-of-the-Art Report, RILEM TC 224-AAM
11. Lagerblad B (2005) Carbon dioxide uptake during concrete life cycle – State of the art
12. Bernal SA, Provis JL, Brice DG, et al (2012) Accelerated carbonation testing of alkali-activated binders significantly underestimates service life: The role of pore solution chemistry. *Cem Concr Res* 42:1317–1326. <https://doi.org/10.1016/j.cemconres.2012.07.002>
13. Byfors K, Klingstedt G, Lehtonen V, et al (1989) Durability of Concrete Made With Alkali-Activated Slag. In: *Third International Conference Proceedings. Fly Ash, Silica Fume, Slag, and Natural Pozzolans in Concrete*. pp 1429–1466
14. Bakharev T, Sanjayan JG, Cheng Y-B (2001) Resistance of alkali-activated slag concrete to carbonation. *Cem Concr Res* 31:1277–1283
15. Deja J (2002) Carbonation aspects of alkali activated slag mortars and concretes. *Silic Ind* 37–42
16. Neville AM (2011) *Properties of Concrete*. Pearson Education Limited
17. Papadakis VG, Vayenas CG, Fardis MN (1991) Experimental Investigation and Mathematical-Modeling of the Concrete Carbonation Problem. *Chem Eng Sci* 46:1333–1338. [https://doi.org/10.1016/0009-2509\(91\)85060-b](https://doi.org/10.1016/0009-2509(91)85060-b)
18. Houst YF (1996) The role of moisture in the carbonation of cementitious materials *TT - Bauinstandsetzen und Baudenkmalpflege: eine internationale Zeitschrift. Restor Build Monum an Int J = Bauinstandsetz und Baudenkmalpfl eine Int Zeitschrift* 2:67–82
19. BS EN 206 (2014) *Concrete — Specification, performance, production and conformity*. British Standards Institution
20. Plusquellec G, Geiker MR, Lindgard J, et al (2017) Determination of the pH and the free alkali metal content in the pore solution of concrete: Review and experimental comparison. *Cem Concr Res* 96:13–26. <https://doi.org/10.1016/j.cemconres.2017.03.002>
21. Puertas F, Palacios M, Vázquez T (2006) Carbonation process of alkali-activated slag mortars. *J Mater Sci*. <https://doi.org/10.1007/s10853-005-1821-2>
22. Qin Y, Yang H (2015) Carbonation dominates the acid intake of recycled concrete aggregate subjected to intermittent leaching. *Constr Build Mater* 89:110–114. <https://doi.org/10.1016/j.conbuildmat.2015.04.038>
23. Collepardi, M., Marcialis, A, and Turriziani R (1970) The Kinetics of Chloride ions Penetration in Concrete. *II Cem* 67:157–164

Activation of binary binder containing fly ash and cement with red mud as alkali source and application in controlled low strength materials

B. Yuan¹, S. Yuan^{1,2}, C. Straub³, W. Chen^{1,2}

¹ Wuhan University of Technology, 1 School of Material Science and Engineering

² State Key Lab of Silicate Materials for Architectures

³ Eindhoven University of Technology, Department of the Built Environment

Email of the corresponding author: chen.wei@whut.edu.cn

Abstract

The feasibility of using red mud as alkali source in alkali-activated fly ash and cement based binary binder for controlled low strength material (CLSM) is investigated. The red mud contains NaOH and Na₂CO₃ that can be used as the alkali source. The incorporation of red mud increases the pH of pore solutions in the mixtures by the direct dissolution of NaOH and the reaction of Na₂CO₃ with portlandite released from the cement hydration. The increased pH accelerates the hydration of the fly ash cement binary binder, contributing to the strength development. The red mud also act as micro-filler that refines the pore structure, reducing the amount of harmful pores. The mechanical performance is promoted after incorporating red mud, which is mainly attributed to the accelerated hydration of the fly ash cement binary binder and the refinement of red mud on the pore structure.

Keywords: Red mud; alkali source; fly ash-cement blends; controlled low strength materials.